CENTRAL LASER FACILITY

RUTHERFORD APPLETON LABORATORY

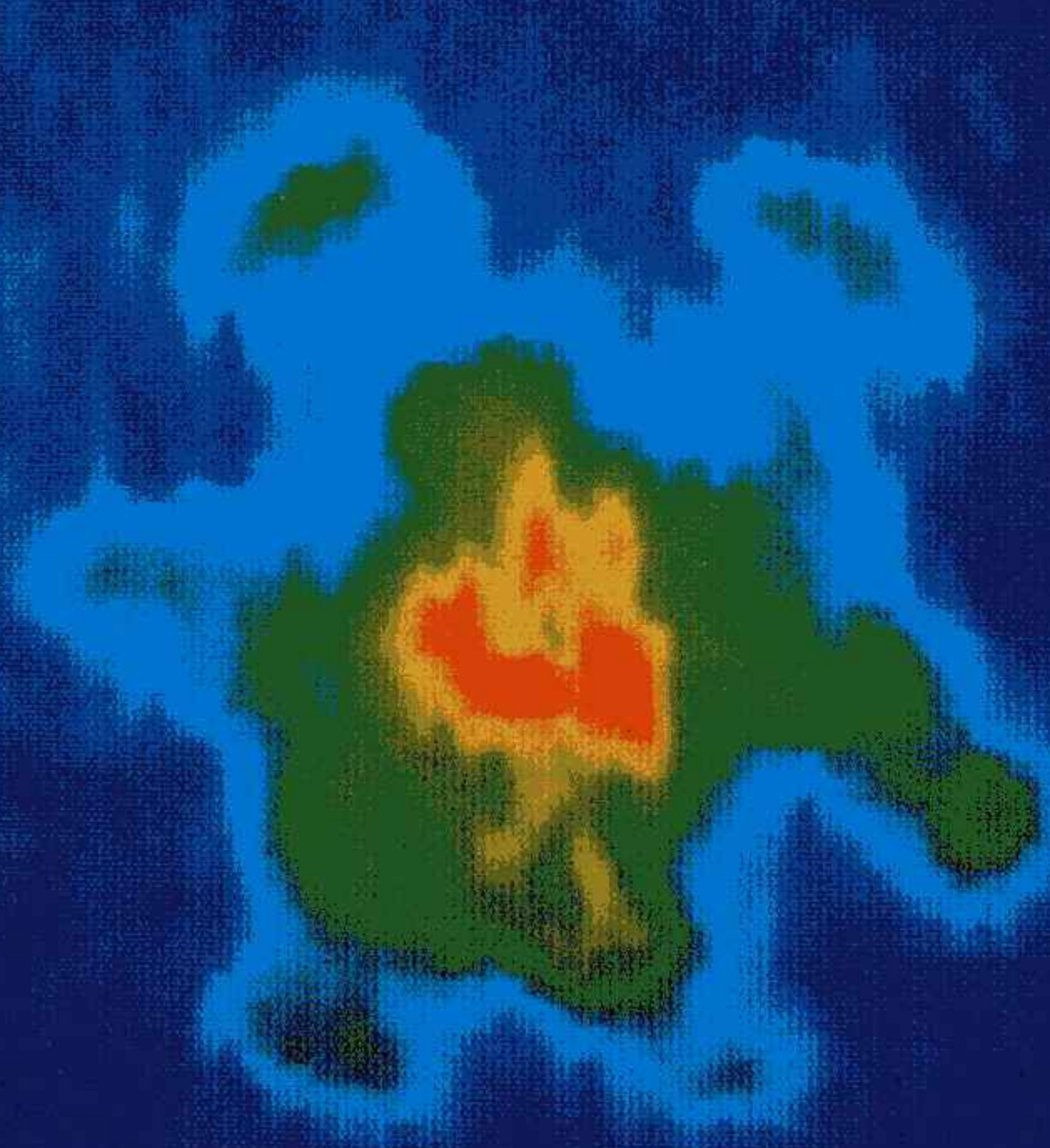

# ANNUAL REPORT 1990
# RAL-90-026

# ANNUAL REPORT TO THE LASER FACILITY COMMITTEE 1990

Cover: False colour pinhole picture of a NUHART implosion

Science and Engineering Research Council

"The Science and Engineering Research Council does not accept any responsibility for loss or damage arising from the use of information contained in any of its reports or in any communication about its tests or investigations"

## ACKNOWLEDGEMENTS

As always, the production of this report has depended on the teamwork of the section editors and document preparation specialists. Thanks are due to Chris Ayling and Katharine Higgs for their wordprocessing, to Jan Smith for diagram tracing, to Roger Chittock, Colin Danson, Abdeslem Djaoui, Chris Edwards, Malcolm Gower, Andrew Langley, Tony Parker, Stuart Ramsden, Allan Ridgeley, Steven Rose, Ian Ross, Mick Shaw, Phil Taday, Greg Tallents, Bill Toner, Mike Towrie and Edmond Turcu who acted as section and chapter editors, and to Nic Allen and Peter Rodgers for overall subediting work and organisation.

The camera-ready format adopted this year for the first time, has also meant that much of the preparation has been carried out by facility users in their own Institutes and thanks are due to them and their support staff also. The RAL reprographic service has produced the report with the assistance of Borough Press (Wiltshire) Ltd for the printing of the cover.

M H Key (general editor)

# PREFACE

The year to 31 March 1990 covered by this report, has been characterised by intensive operation and development of our laser facilities for a wide range of experimental research by UK University and Polytechnic research teams, their overseas collaborators and facility staff. Significant scientific results were obtained and, whilst highlighting some may not do justice to the full breadth of the work described in this report, certain achievements stand out.

The Neodymium Glass Laser Facility Vulcan came into operation at a 2-fold enhanced power level following the final stage of its upgrading completed in July. There followed a period of operation for users with 6-beam energy in the infrared routinely at 1.6 kJ in subnanosecond pulses. Over a thousand high energy target shots were delivered to a series of experiments. Outstanding among these were optimisation of thermonuclear yield from laser-driven implosions, giving a record neutron yield for Vulcan and resulting in an excellent source for particle probing experiments; the first powder diffraction patterns from polycrystalline media using laser-generated X-rays were obtained; and in X-ray laser research the germanium collisionally excited laser was developed to a high gain system and initial steps were made towards its application in X-ray microscopy.

With the high power KrF laser Sprite, a major achievement was the demonstration of 50% efficient combining of 7 laser beams into a single Raman Stokes beam of exceptionally low beam divergence, 40 psec pulse duration and high contrast ratio. The beam was focused to more than $10^{17}$ W cm$^{-2}$ on target. These results give considerable confidence in the KrF pumped Raman laser for future large laser facilities. Design studies for the Working Group on the European Laser Facility (ELF) resulted in novel concepts being developed for this important initiative.

Multidisciplinary research carried out with the numerous smaller lasers of the Laser Support Facility (LSF) was exceptionally active this year with more lasers in regular use. Chemists reported new results in reaction dynamics, using jet cooled spectroscopy, on radical-radical and insertion reactions , and from time resolved resonance Raman scattering, on reaction intermediates in solution. Biologists made major progress in study of the repair of DNA damaged by both UV photons and X-rays, including an observation of potential significance for research on carcinogenesis: that exposure to UV light increases the resistance of cells to an antibiotic by a factor of more than 100. Measurements of the transient change in absorbance in photosynthesis established that transfer of excitation occurs in less than a picosecond. Physicists reported novel work on quantum well structures and multiphoton ionisation.

In writing a preface to last year's Annual Report, I highlighted the new policy for the operation and development of the CLF which had been agreed following the report of the CLF Review Panel, chaired by Professor Challis, and following also from SERC's participation in technical studies and negotiations for a European Laser Facility (ELF). This year has been the first in which the new policy has been implemented and it has brought significant changes.

The work of the CLF has been more formally structured into three programmes comprising the two major operational facilities, Vulcan, and the LSF, and one main research and development programme in high power KrF lasers. The management of the CLF has been restructured accordingly as presented in the first section which follows.

The impact of these changes on the LSF has been straightforward and beneficial. Its resources have been increased by about 45% both through provision for purchasing of new lasers (30%) and increased manpower and operating funds (10%). The result has been improved quality and variety of available facilities and better supporting R&D activity, leading to enhanced multidisciplinary scientific output by a growing and diversifying user community.

The effect on Vulcan has been mixed. The completion of the previous five year programme of upgrades gave the machine its highest ever performance capability. A reduction in operating funds made it necessary, however, to cut back on provision of spares and therefore to restrict the operational power for the users to a cautious level and also to cut back on development of diagnostic instrumentation for the support of experiments. Difficulty was experienced in achieving the planned abrupt change in expenditure and plans were modified during the year with some resources diverted from the other programmes to increase operating funds to a level about 25% less than the historical average.

The KrF laser development work was given a major (50%) boost of resources. The initial objective was to demonstrate, using the Sprite facility, the principles of the novel optical and Raman multiplexed laser architecture.

A parallel activity initiated during the year provides evaluation of prototype pulsed power technology and electron beam diodes for larger KrF laser amplifiers.

Separately funded work was also undertaken , notably for the Scientific and Technical Working Group on ELF in the form of detailed technical studies of KrF and Neodymium glass laser options. Members of the user community also participated in the evaluation of the scientific case for ELF. Nonlinear optics research and development of an excimer laser-driven, high repetition rate XUV source in the European Eureka initiative completed this category.

Detailed descriptions of the three programmes and of the separately funded activities are given in the four major sections of this report.

The year has been successful and exciting if at times stressful, and many new avenues have been opened up for the future.

My thanks are due to the staff of the CLF who have worked with dedication in support of Facility users throughout the year. My thanks go also to the users of the Facility without whose enthusiasm and ideas it could not operate.

**Professor M H Key**
**Head of the Central Laser Facility**

# ORGANISATION AND MANAGEMENT OF THE CENTRAL LASER FACILITY

W T Toner

The Central Laser Facility (CLF) is funded by the Science Board of the Science and Engineering Research Council and the programme is managed by the Laser Facility Committee (LFC) chaired by Professor R J Donovan FRSE (members of the LFC are listed in Appendix A). The LFC delegates responsibility to the Director of the Rutherford Appleton Laboratory for the operations of the facility.

The allocation by the Board to the CLF for the period covered by this report, April 1989 to March 1990, was £3.3M. An additional allocation of £63K was made to support the work of the European Laser Facility Scientific and Technical Working Group. Fifty six man years of effort were used and the staff costs and overheads amounted to 50% of the allocation. The resources were divided between the three programmes of the facility as follows:-

| | |
|---|---|
| VULCAN Operations | 36% |
| Laser Support Facility Operation and Development | 25% |
| KrF Laser Development | 27% |

Support of users' travel and subsistence and provision for CLF administration comprised a fourth programme which used 12% of resources. The figure for VULCAN includes capital expenditure of £150,000 committed in earlier years for the Phase I development. This programme is now completed. The figure for the Laser Support Facility includes £250,000 for a major upgrade of equipment.

The major facilities provided by the CLF and their principal scientific applications are listed in Table 1. The Nd Glass laser VULCAN is the main facility for experiments using high power lasers by UK user groups and their overseas collaborators. The results of this work are contained in Section A of this report.

The KrF laser Sprite was used for a thorough investigation of the optical multiplexing and Raman beam combining architecture which it is proposed to use in future systems, which could replace VULCAN in the mid 1990's or be constructed as part of a European Laser Facility. A developmental Marx generator and pulse forming line are being built to test the pulse power concepts for very large lasers of this type. A detailed account of this work is given in Section B.

The Laser Support Facility and small scale R&D work some of which is supported by other funding sources, accounts for 25% of the Science Board allocation. The programme covers all areas of research supported by the Science Board and the experiments are frequently multidisciplinary in in character. Results from the scheduled programme of the LSF make up Section C of this report. Section D contains reports of other research and development work by Facility staff.

A target preparation service, an engineering support group and a small group giving theoretical support by maintaining computer codes service all CLF activities. Figure 1 shows the present divisional and group structure of the CLF.

Use of the CLF by UK research workers in Higher Education Institutes (HEI's) is free of charge to those successful in a peer review process. The cost of travel to the facility and some incidental costs of the research are borne by the CLF out of its allocation from the Board. The costs of research assistants and expenditure in HEI laboratories may be sought by application to the SERC for a research grant. The Laser Facility Committee funds users wholly or mainly using the CLF with an annual committment allocation of £420 K. The subject committees of the Science Board also award grants to users of the Facility.

TABLE 1: Major Facilities and Programmes at the CLF

| Nd glass laser facility | Laser Support Facility | High Power KrF Laser Facility |
|---|---|---|
| VULCAN | LSF | SPRITE |
| Laser plasma interactions and energy transport | Photochemistry<br>Photobiology<br>Nonlinear optics | Ultra high intensity pico-second laser source |
| Laser compression of matter and dense plasmas | High field atomic physics<br>Laser Loan Pool<br>Raman facility | Research and development in Raman beam combining and novel architectures for high power lasers. Research and development in large scale KrF amplifiers |
| XUV lasers and applications of laser produced plasma sources | Picosecond laser<br>High repetition rate<br>X-ray source | Short pulse laser plasma energy transport processes |
| Target Preparation Service<br><br>Theoretical support service | | |

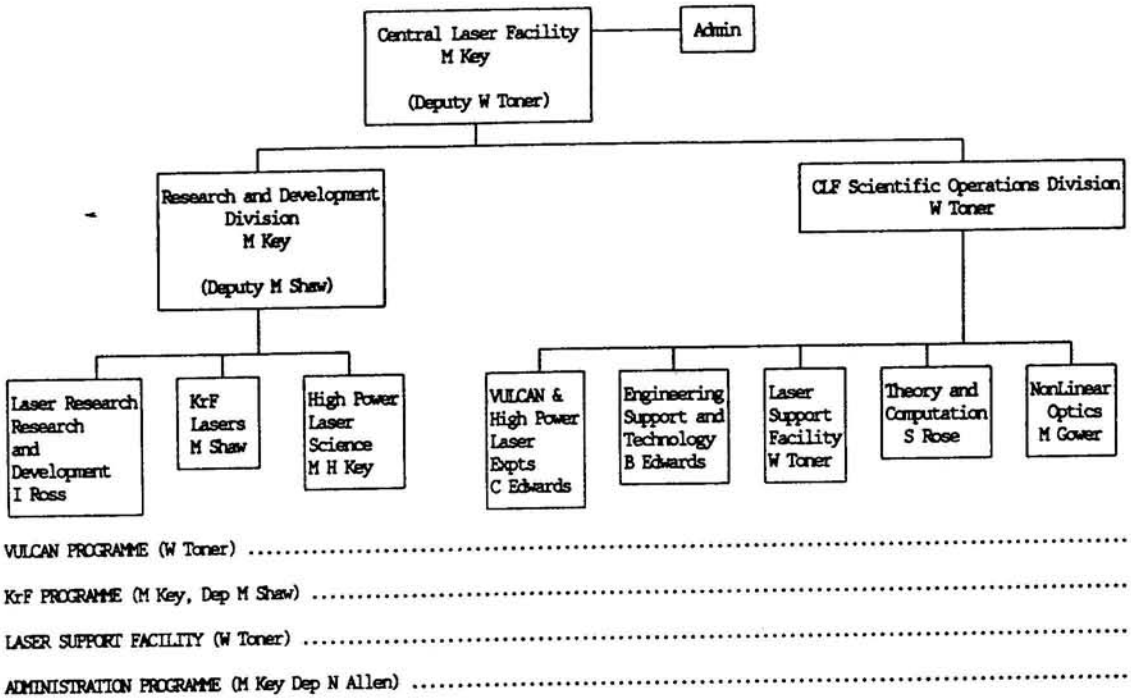


Figure 1: Divisional and Group Structure of the Central Laser Facility and Programme Management

Grant holders may bid for time on the facilities of the CLF by application to one of the two selection panels: the High Power Laser Panel chaired by Dr D C Robinson and the Laser Support Facility Panel charied by Professor R N Dixon FRS (Panel members are listed in Appendix B). The panels meet three time a year to determine the relative priority of the bids for time in a specific four month schedule period. A small proportion of the time may be allocated by the Panels to applicants without grant support. Following the recommendation of the Panels as to priority, and taking account of logistical factors, schedules are prepared by CLF staff which are then discussed, modified as necessary and approved by open committees of facility users.

The SERC encourages use of the CLF by industry or other organisations on the basis of payment for the full cost of laser time. Such use is limited to 10% of available laser time.

International collaboration in the research programme is extensive through collaborative participation in approved experiments of UK University groups and through agreements negotiated with the CLF and SERC.

The annual policy meeting of the LFC is attended by 2 foreign members, Dr S Witkowski of the Max Planck Institut fur Quantenoptik, Garching and Prof E Fabre of Ecole Polytechnique.

# A DETAILED CHARACTERISATION OF THE Ne-LIKE GERMANIUM SOFT X-RAY LASER

D Neely,[1] C L S Lewis,[1] J Uhomoibhi,[1] D O'Neill,[2] S A Ramsden,[2]
M H Key,[3] B Shiwai,[3] N Tragin[3] and G J Tallents[4]

[1]Queens University Belfast
[2]University of Hull
[3]Rutherford Appleton Laboratory
[4] University of Essex

## INTRODUCTION

An extensive study and characterisation of the Ne like Ge 3p—3s XUV lasing scheme using massive stripe targets operating in an ablative mode was carried out at RAL during 1989 on two separate experiments following previously reported work on electron collisional excitation systems at LLNL[1,2] and NRL.[3] In the first experiment[4,5] three 1.05μm beams from the Vulcan glass laser delivering on target ≈600J in total were used, and the gain coefficients at maximum irradiance of five 3p—3s transitions and one previously unobserved 3d—3p transition were measured. Pointing direction and divergence of the output beam at each wavelength was studied as a function of target length; double passing the beam using a multi layer concave mirror was tried; the temporal history of the lasing lines was recorded for different driving laser pulse durations and, an attempt to study the effect of incident irradiance (by changing the target width) was made, but this led to inconclusive results.

The objectives set for the second experiment were :-

1. Investigate the possibility of increasing the duration of the quasi cw gain phase of the plasma.
2. Measure the dependence of the gain and emmisivity of the strong J = 2—1 lines at 23.2 and 23.6 nm as a function of incident laser intensity.
3. Compare the XUV output beam powers obtained using 1.06 and 0.53μm driving beams of similar intensity.
4. Locate and measure the size and position of the gain region in the plasma w.r.t the target surface for both the 23.2 and 23.6nm lines.
5. Measure the vertical beam divergence obtained when using 100 and 200μm wide massive targets. This was to check on the vertical divergence assumed previously to estimate the total output power in each line.

With the above objectives set, it was decided to use only 100μm wide massive stripe targets.

## EXPERIMENTAL

The target chamber was set up to use six beams in total from the Vulcan glass laser in an off axis line focus geometry[6] , with either three beams incident onto the target from the West side in 1.06μm light, or alternatively three beams from the East side in 0.53μm light. Each beam was set to give an 11—14mm length line focus, and hence it was possible by placing the beams end to end to illuminate uniformly over the full length up to 32mm of target or, by stacking the beams on top of each other to achieve higher intensities at up to 14mm of target length. Targets were positioned on axis using two split field microscopes, with which it was possible to achieve a pointing accuracy of better than ±2 mrad. The targets consisted of a 1.0μm deep layer of Ge, 100μm wide, which was deposited on a 1cm wide 25μm thick mylar support. After testing various methods of attaching the mylar support to a brass holder, it was found that using thin stripes of a flexible sticky tape to fix the mylar to the brass gave the best results as tested on a target surface quality monitor. The target surface quality monitor consists simply of an expanded spatially filtered parallel HeNe beam, which is incident onto the target through a 32mm x 1mm mask with spacing bars of 300μm width every 4mm. The reflection of this beam from the target surface over a range of incident angles is examined both visually via a CCD TV camera and photographically recorded using polaroid. If the target is flat then the reflected beam remains 1mm wide and the spacing between the bars remains constant. If however the surface is not flat then it acts as a curved mirror and depending on which way the target is bent either the reflected beam width will change or the spacing between the bars will not be constant. It is therefore easy to quickly select the best targets from a batch, and afterwards calculate the exact surface deviations from perfect using the photographic record.

An axial, flat-field, grazing incidence spectrometer was used as the primary diagnostic of lasing in the plasma. This diagnostic used as recording media either Kodak 10101 film (calibrated at M.P.Q.[7]) to give an absolute time integrated intensity measurement or, a streak camera / intensifier combination with a CsI coated 1.0μm thick Al photocathode, to record, on individually calibrated pieces of HP5 film, time resolved relative intensity measurements. In the case of time integrated measurements an axial fiducial wire was placed just in front of the film to give a reference for the target surface plane on each shot. For time resolved measurements the start of the laser pulse was inferred from the commencement of continuum emission. The axial spectrometer was operated in either an angle resolving mode (Fig 1a) or in a space resolving mode (Fig 1b). In the angle resolving mode each position at the focal plane corresponds to photons emitted from the plasma having a different angular deviation $\varphi$ from the axis, with the spectrometer having a maximum field of view of ±2.2°. Hence, it was possible to record both the XUV lasing beams pointing and divergence in one dimension on a single shot at each wavelength. To record both the horizontal and vertical beam divergences for a given type of target it was necessary to first record the horizontal information on one shot and then rotate the whole spectrometer through 90° and record the vertical information on the next shot. In the space resolving mode a 51.3±0.5μm wide slit was placed 14.5mm away from the target with the slit orientated normally to the grating surface. This set up gave a magnification of ≈33 at the spectrometer focal plane and a field of view of ≈650μm. Because the XUV lasing beams are emitted from a small region of the plasma and have a specific

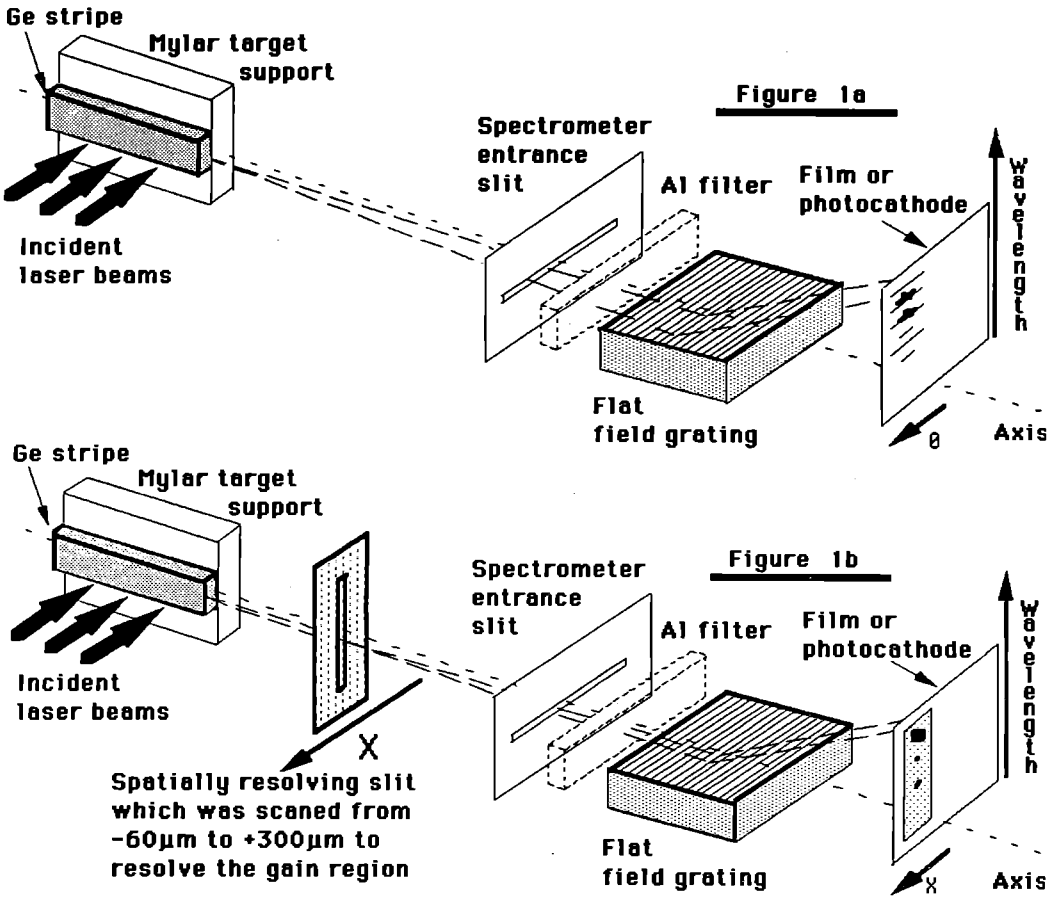


Figure 1(a+b): Schematic diagrams showing the target geometry with the axial flat field grazing incidence spectrometer in angle resolving (Fig 1a), and space resolving (Fig 1b) modes.

pointing, it was necessary to scan the slit across the axis on a series of shots to locate the position where it intercepted the maxima of the XUV lasing beams. This enabled a determination to be made of the spatial location of the gain region since adequate reproducibility of the target positioning and beam pointing had previously been demonstrated. Wide spectral entrance slits of widths 25μm, 80μm and 500μm were used to deliberately degrade the resolution of the instrument thus broadening the recorded line widths on film to 20—250μm, and making the final automatic digitisation of results much simpler. The lasing lines were normally so bright that signal to background continuum emission ratios presented no problems when operating the spectrometer at low resolution.

A spatially resolving TLAP crystal spectrometer was used to record the Ne and F like resonance lines in the 0.75→1.05nm region from the plasma on Industrex C type film. This spectrometer was operated to give a spatial resolution of 60μm along the length of the plasma at a magnification of 0.9 with line widths ≈20mÅ being limited by source broadening. The absolute intensities and ratios of the Ne and F resonance lines from the plasma correlated well with the incident intensity, hence this diagnostic proved to be useful in monitoring the illumination uniformity along the plasma length. A 2D spatial imaging camera consisting of two orthogonally crossed, spatially displaced slits, to give differential magnification was used to monitor the line focus width (25μm resolution) along the full plasma length (200μm resolution) . The 1.2KeV filtered image from this device was recorded using a phosphor screen/intensifies combination and individually calibrated pieces of HP5 film.

## FILM ANALYSIS

A 2D microdensitometer scan of each piece of film was carried out to obtain the density profile across the lasing lines as a function of position on film. The density profile was then converted to intensity (using the appropiate calibration curve for 10101 or HP5) and an integration under the line width was carried out at each point on the film. The spatial intensity profile of the lasing lines so obtained was then converted into the appropiate format for the type of measurement being made, (Angular, Spatial or Temporal) and an output file containing the data created.

## RESULTS

The peak output intensity $\varnothing_{max}$ for a non-saturated Doppler broadened spontaneous emission amplifier of length L, gain $\alpha$ per cm and emissivity $\varepsilon$ is given by :-

$$\varnothing_{max} = \frac{\varepsilon}{\alpha} \frac{(\exp \alpha L - 1)^{3/2}}{(\alpha L \exp \alpha L)^{1/2}} \qquad --(1)$$

Where $\alpha$ and $\varepsilon$ are functions of the target irradiance and depend on the specific transition. Using targets of lengths .89cm,1.4cm and 2.2cm the irradiance from a 1ns pulse was varied between a maximum of 3 x $10^{13}$ W/cm$^2$ (operating the driving laser at maximum energy) and a minimum of 0.4 x $10^{13}$ W/cm$^2$ (threshold of observation of lasing activity). Graphs were constructed of the peak intensity output for the two brightest lasing lines 23.2 and 23.6nm, as a function of irradiance, for each target length (due to lack of space only 23.6nm data is presented here) . In order to fit a function describing the intensity output for a given target length against irradiance two assumptions were necessary. These were :-

1. Both $\alpha$ and $\varepsilon$ are smooth slowly changing continuous functions thus implying that $\emptyset_{max}$ would also be a smooth slowly changing continuous function.
2. The experimentally observed output would always be less than or equal to that produced by a perfect target shot under ideal conditions due to imperfections in target fabrication, alignment or uniformity of the driving laser beams.

Using these assumptions a simple power law equation (using only two constants $A_{(L)}$ and $B_{(L)}$) could describe the growth of observed peak line intensity $\emptyset_{fit}$ as a function of irradiance, I, for each target length L, and was of the form :-

$$\emptyset_{fit} = A_{(L)}\ I^{B_{(L)}} \qquad \text{---(2)}$$

Fits obtained using this equation are shown on Fig 2. The sources of experimental error shown on this graph arose from uncertainty of the thickness of the Al filter ≈±5%, which corresponded to an uncertainty in transmission of up to ±25%, the observed modulation of the spatial profiles on film giving rise to an additional uncertainty of ≈±7.5%, and errors in the laser energy calorimetry estimated at ≈±5% from energy calibration only shots. The uncertainty error of a fit $E_{(I,L)}$ at a given irradiance I, and for a particular target length L, was taken to be the average uncertainty of the closest data points for that target length to the required irradiance.

To extract $\alpha$ and $\varepsilon$ from the data an error weighted form of equ(1) as shown below in equ(3) was used :-

$$\frac{\partial}{\partial(\alpha,\varepsilon)} \sum_{L} \frac{(\emptyset_{fit}-\emptyset_{max})^2}{E_{(I,L)}} = 0 \qquad \text{---(3)}$$

This fit was carried out between 0.7→ 2.0 x $10^{13}$ W/cm$^2$ and the resultant values of $\alpha$ and $\varepsilon$ are shown as the heavy lines on Figs (3) and (4). To determine the bounds within which $\alpha$ and $\varepsilon$ lie, then $\emptyset_{fit}$ in equ(3) was replaced by $\emptyset_{fit}+E_{(I,L)}$ or $\emptyset_{fit}-E_{(I,L)}$ to give the maximum deviations for $\alpha$ and $\varepsilon$, and the upper and lower bounds so obtained are represented by the thin lines on Figs (3) and (4). Fig (3) shows the gain rising steeply at low irradiances from 1.4 ±0.5 cm$^{-1}$at an irradiance of 0.7x $10^{13}$ W/cm$^2$ to 4.4±0.5cm$^{-1}$ at an irradiance of 2.0 x $10^{13}$ W/cm$^2$. To a first order approximation the rate of change of gain with irradiance above 0.9 x $10^{13}$ W/cm$^2$ is given by :-

$$\frac{\partial \alpha}{\partial I} = 3.78 - 1.19 \times (I / 10^{13} \mathrm{Wcm^{-2}}) \qquad \text{---(4)}$$

and using this equation to extrapolate the gain curve further up, then a maximum gain of 5.2±0.7cm$^{-1}$

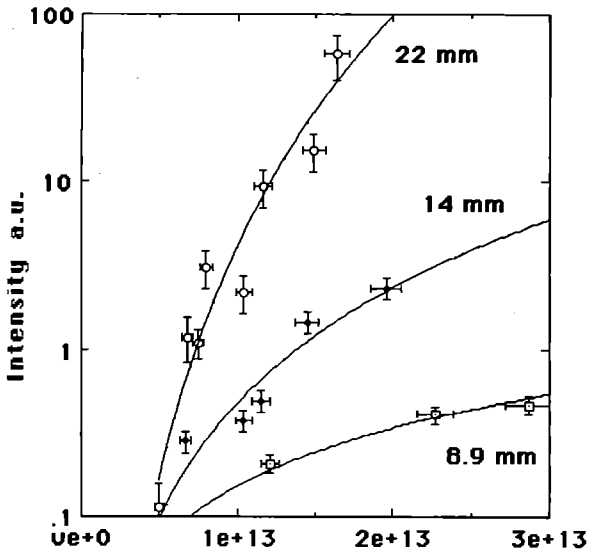


Figure 2: The peak intensity data, and fit, for the 23.6nm lasing line plotted against incident irradiance for targets of lengths 0.89, 1.4 and 2.2cm.

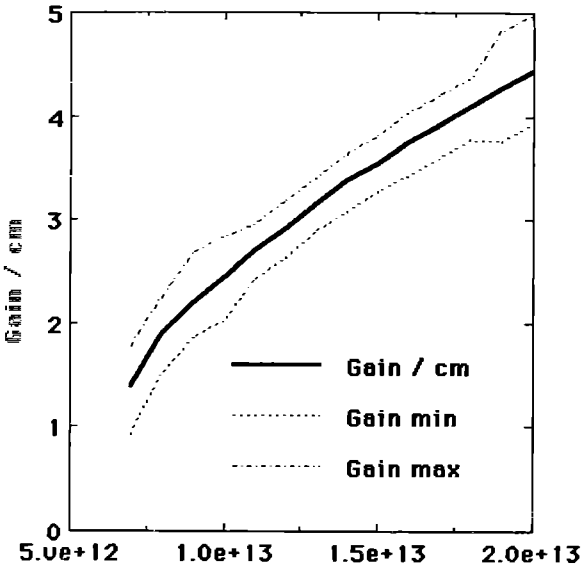


Figure 3: The experimentally observed gain per cm of the 23.6nm lasing line plotted against target irradiance.

would be achieved at a target irradiance of 3.2±.4 x $10^{13}$ W/cm$^2$. The large uncertanities inherent in extracting $\varepsilon$ from the data shown in Fig (1) using equations (2) and (3) is due to the fact that $\emptyset_{max}$ scales linearly with $\varepsilon$, but exponentially with $\alpha$ and L. Hence small uncertanities in $\alpha$ lead to much larger uncertanities in $\varepsilon$ with the average uncertanity as shown on Fig (4) being≈+50%→−40%. The data shown in Fig (4) however shows a slight tendency for $\varepsilon$ to unexpectedly fall with increased irradiance (increasing gain) over the range 0.7→2.0 x $10^{13}$ W/cm$^2$.

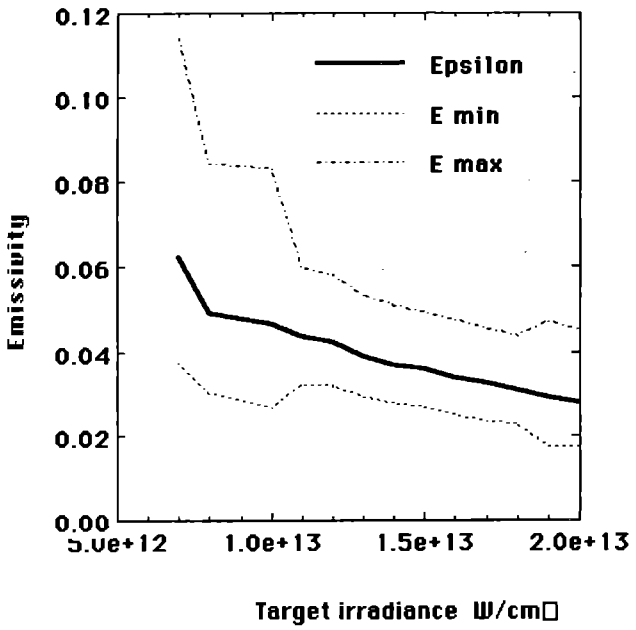


Figure 4: The experimentally measured emmisivity of the 23.6nm lasing line plotted against target irradiance.

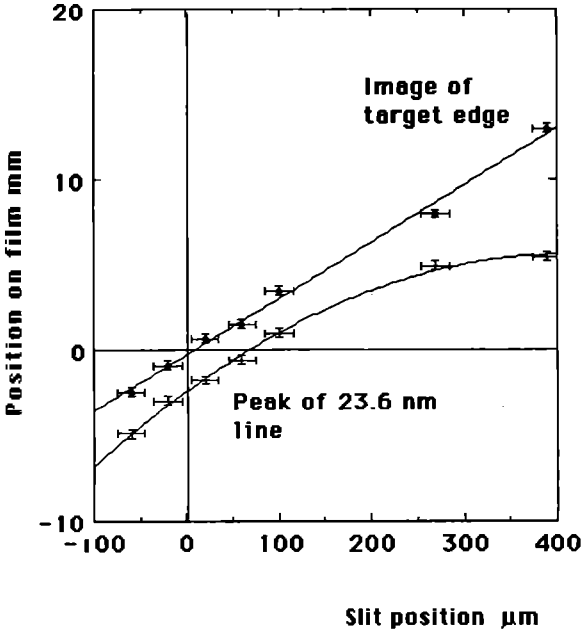


Figure 5: A graph showing the position on film of the soft x-ray continuum image of the target edge and, the peak of the 23.6nm emission as a spatially resolving slit parallel to the target surface is scanned across the axis.

A summary of the results from the gain region scan for the 23.6nm line is presented on Fig (5) which shows both the positions of the target edge (straight line) and peak of the 23.6nm line emission (curved line) on film for the seven data shots taken in this sequence. The recorded soft X-ray continuum images of the target edges provides both, an accurate calibration of magnification 33.2±0.2, obtained from the slope of the straight line fit to the data and also, the absolute positioning error of 8µm of the slit w.r.t the target surface is obtained from the horizontal intercept with the axis. The curvature of the fit to the 23.6nm lasing beam emission is attributed to the lasing beam's divergence and pointing as it leaves the plasma being spatially dependent (due to travelling through a plasma where both gain and refractive index are spatially varying). Hence, when scanning a slit across which transmits different portions of the beam at each spatial position, this effect is observed. From the position where the fit to the peak of the 23.6nm emmision crosses the horizontal axis, it is possible to deduce that the gain region is located 60±5.0µm from the target surface and, from the FWHM recorded on film, the width of the gain region was estimated from deconvolution to be 28±7µm. Similar results were also obtained for the 23.2nm line.

Two data shots were taken using 1.4cm targets in 0.53µm laser light at an irradiance of $1.2 \times 10^{13}$ W/cm$^2$. The observed lasing line intensities were only ≈10—20% of that obtained using identical targets under similar irradiance conditions but in 1.06µm light and, this is attributed to a reduction of the gain coefficient. It is estimated that $\alpha(2\omega) \approx 0.6\alpha(\omega)$ under these conditions. It can be concluded therefore that it is much more efficient for this lasing scheme to use the energy from the driving laser in 1.06µm light rather than 0.53µm since, not only is higher gain achieved for similar energies on target but, also the conversion efficiency losses of ≈40—50% in converting the driving laser beams from 1.06µm to 0.53µm are not present.

The temporal FWHM of the XUV lasing beams were measured for driving laser pulse widths of 0.6, 1.0 and 1.8ns. Increasing the driving laser pulse width from 0.6 to 1.0ns increased the FWHM of the 23.2 and 23.6nm lines from 320±20ps to 370±20ps and on further increasing of the driving laser pulse to 1.8ns no increase in the XUV lasing beams FWHM was apparent. However since the driving laser becomes energy limited for pulses of greater than 1.0ns it is not clear whether the lower incident power level affected this result and further analysis of the data obtained will be necessary before coming to a final conclusion.

On a few long length (2.2cm), high irradiance shots in which the filtering on the axial spectrometer was deliberately reduced to bring up the exposure of the weaker 19.6, 24.7 and 28.6nm lines, it was noticed that a very faint line at 19.9nm Fig (6) had a weak polar distribution and an apparent non linear growth with length. Following the observation of this line which is believed to be a previously unobserved although theoretically predicted[8] 3p—3d transition with a 2s hole in the core configuration ($1s^2\,2s^1\,2p^5$), a reanalysis was undertaken of data from the first experiment from targets of lengths 0.9—3.2cm which were also exposed to record the weaker lasing lines. This data again showed the 19.9nm (19.895 ±0.003nm) lasing line to be weaker than any of the 3s—3p lines. However, it was possible to measure a gain coefficient of slightly under 1.0cm$^{-1}$ which is believed to be the first time soft X-ray lasing action involving an inner shell transition has been observed.

The measurements made of beam pointing and divergence in the horizontal direction, as a function of target length, from 100µm wide targets produced, as expected, similar results to those obtained in the first experiment[4,5] from 200µm wide targets. However, the beam divergence measured in the vertical direction from 200µm and 100µm wide targets of 2.2cm length were 25.0±1.0mrad and 20.0±1.0mrad respectively. The divergence measured for the 200µm target matches

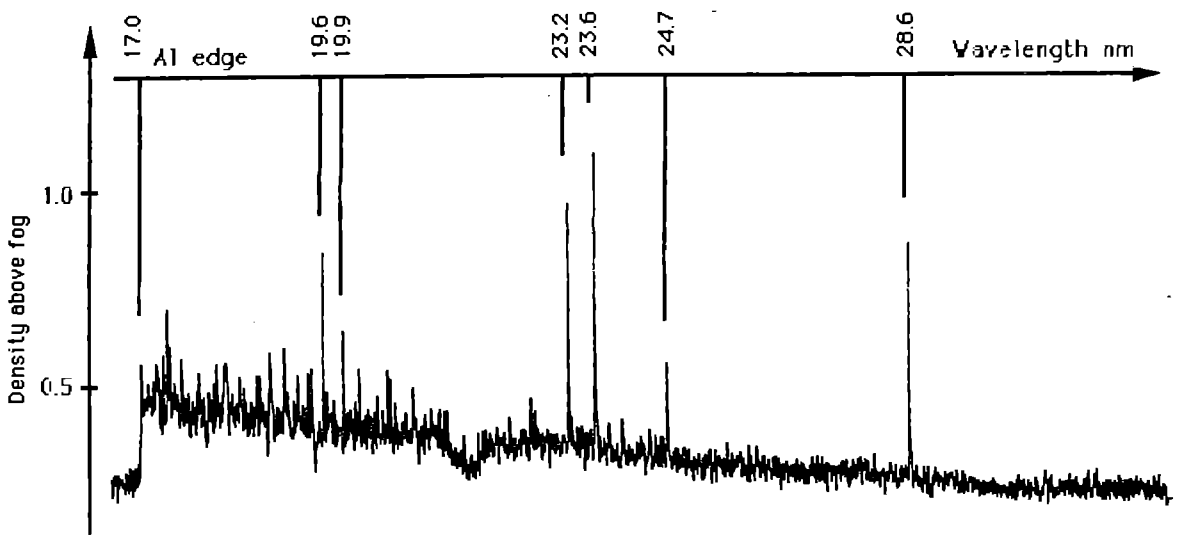


Figure 6: A densitometer trace showing five 3p—3s and one 3d—3p lasing transition from a 3.2cm length massive target.

closely that initially assumed in calculating the output powers in the first experiment. However the divergence observed from the 100μm target is much larger than was expected and will be investigated further in the next experiment.

## CONCLUSION / FUTURE AIMS

The sucessful measurement of, the maximum gain duration possible (≈370ps), the gain and emmisivity scaling of the 23.2 and 23.6nm lines and the exact location of the gain region, wrt the target surface, has enabled a further experiment to be planned in detail. In the next experiment it is hoped to achieve output powers of ≈1MW, on the 23.2 and 23.6nm lines using a drive/amplifier target design as shown in Fig (7). This target design will use two spatially off-set targets to feed the maximum output from one target into the second target when it is at maximum gain. This arrangement will allow us to utilise the full power of Vulcan (1.8KJ/1ns) in collisionally pumped lasing schemes for the first time.

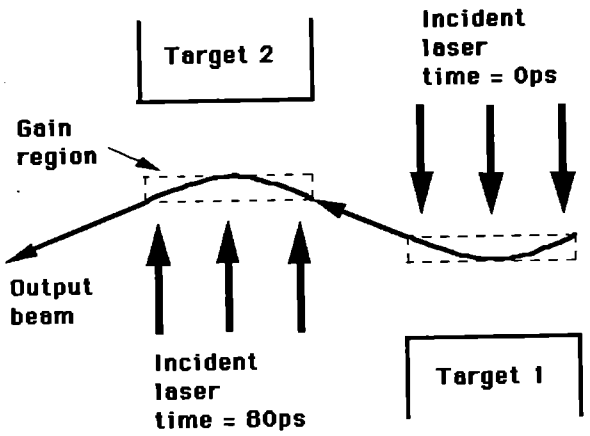


Figure 7: A schematic diagram showing the intended off-set target design for the next X-ray laser experiment.


1 D L Mathews et al,
Phys Rev Lett 54, 110-3 (1985)
2 D L Mathews et al,
J Opt Soc Am 4, 588 (1987)
3 T N Lee, E A McLean and R C Elton
Phys Rev Lett 59, 115 (1987)
4 C L S Lewis et al
RAL Annual Report 13-18 (1989)
5 D M O'Neill et al
J Opt Com 75, 406-412 (1990)
6 C Chenais - Popovics et al
RAL 87-041 Annual Report P6-12 1987
7 K Eidmann, personal communication 1989
8 R C Elton, T N Lee and E A McLean
Jour de Physique Colloque C9, Vol 48 P395 1987

# A PRELIMINARY INVESTIGATION OF THE Ni-LIKE SAMARIUM SOFT X-RAY LASER

D Neely,[1] C L S Lewis,[1] J Uhomoibhi,[1] D O'Neill,[2] S A Ramsden,[2]
M H Key,[3] B Shiwai,[3] N Tragin[3] and G J Tallents[4]

[1]Queens University Belfast
[2]University of Hull
[3]Rutherford Appleton Laboratory
[4] University of Essex

Soft X-ray lasing in a Ni-like collisional excitation 4d–4p scheme (analagus to the Ne like 3p–3s scheme but showing more favourable Z scaling to shorter wavelength) was first demonstrated using Ni-like Europium (Z=63) at LLNL[1]. An exploding foil type target geometry, illuminated using a 0.53μm 1ns laser pulse, at an irradiance of $7 \times 10^{13}$ Wcm$^{-2}$ led to the observation of gains of $\approx 0.6$ cm$^{-1}$ and $\approx 1.1$cm$^{-1}$ on the J=0–1 transitions at wavelengths of 6.58 and 7.1nm respectively.

Following our inference, in the Ne-like lasing scheme, that higher gains were achieved from massive targets[2,3], when illuminated in 1.06μm rather than 0.53μm light a preliminary attempt at observing the lasing lines from a Ni-like system illuminated at 1.06μm was made. Two shots on 2.2cm long samarium massive stripe targets (a 0.5μm deep 100μm wide layer of Sm deposited on a 50μm thick mylar support) were taken at an irradiance of $2.8 \times 10^{13}$Wcm$^{-2}$ using three 0.6ns duration laser beams. The same chamber set-up and diagnostics as described previously[3] were used, with only the axial flat field spectrometer (operated in a low spectral resolution angle resolving mode) requiring alterations. Because the wavelength range of interest was now 6—8nm, it was necessary to use a double reflection filter[4] on the axial flat field spectrometer. The reflection filter ensured that no sub 4nm radiation in higher order overlaid the spectral region of interest. A 0.4nm thick protective plastic Formvar filter was also required to stop any target debris from damaging the reflection filter's gold coated surfaces.

## RESULTS / CONCLUSION

The X-ray crystal spectrometer observing 4-3 lines in the 0.7-1.1nm range showed that good illumination uniformity along the target length on shot #04291089 had been obtained. On shot #05291089 however illumination uniformity was much poorer (due to problems of beam obscuration on the almost transparent layer of Sm). From the densitometer trace of the axial spectra on shot #04, two lines showing a marked polar distribution (as expected from lasing lines emitted from a small gain region) were noted. The polar distributions of these lines at wavelengths of 6.9±0.2nm and 7.5±0.2nm, as shown on Fig 1, contrasts significantly with that of all the other observed lines. The 7.5 and 6.9nm lines are at the correct wavelength positions expected for the Ni like Sm J=0–1 transitions and were observed to have an intensity ratio of ≈2:1. On shot #05 which was non uniformly illuminated the intensities of the 7.5 and 6.9nm lines were only ≈20% of those on shot #04, whilst those of other lines were very similar to before. All of the above data is consistent with the observed 7.5 and 6.9nm lines being the two J=0-1 Ni-like Sm lasing transitions which are exhibiting gain from a small region of the plasma.

A future Ni-like soft X-ray laser experiment using massive stripe targets is planned, in which it is hoped to characterise the gain and pulse properties as a function of target irradiance and atomic number.

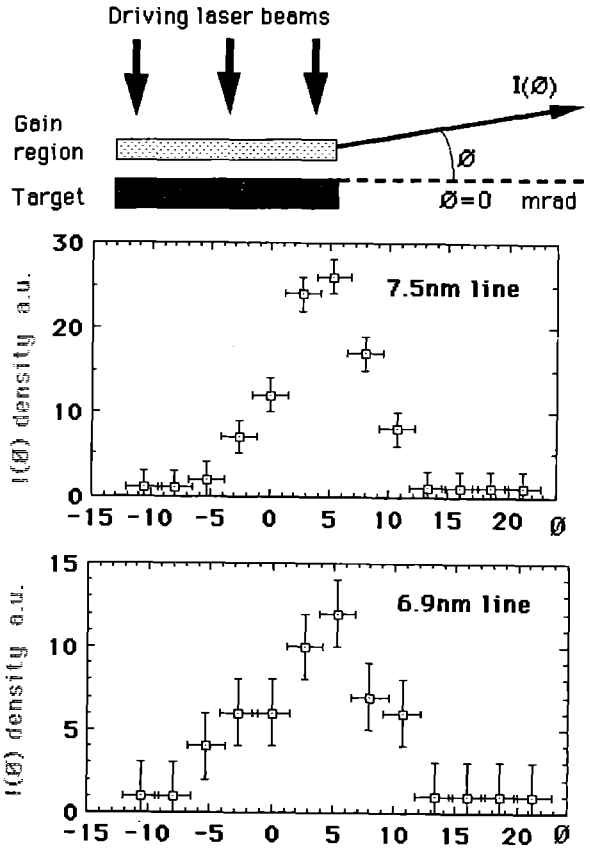


Figure 1: Densitometer traces showing the polar distributions of the 6.9 and 7.5nm J=0-1 Ni-like Sm lasing lines.

1 B J MacGowan, S Maxon, P L Hagelstein, C J Keane, R A London, D L matthews, M D Rosen, J H Scofield and D A Whelan
Phys. Rev. Lett. 59, 2157 (1987)

2 T N Lee, E A McLean, and R C Elton
Phys. Rev. Lett. 54, 1185 (1987)

3 D Neely, C L S Lewis, J Uhomoibhi, D O'Neill, S A Ramsden, M H Key, B Shiwai, N Tragin and G J Tallents
RAL annual report A1.2 (1990)

4 C L S Lewis, D Neely and A R Damerell
RAL annual report A6.4 (1990)

# Characterisation of a Schwartzchild Condenser for use in an X-ray Laser Imaging Microscope

R.E. Burge, A.G. Michette and A.M. Rogoyski

Physics Dept., King's College, London

## INTRODUCTION

The structure of an X-ray imaging microscope using an X-ray laser as the source of monochromatic illumination is illustrated in fig. b). A multi-layer Schwartzchild (SC) matched to the X-ray source is required to act as the condenser lens. The SC should be designed to match the beam divergence of the X-ray source and have a narrow bandwidth centred on the X-ray wavelength 23.6 nm.

## THE SCHWARTZCHILD CONDENSER

An Ealing Electo-optic X15 reflecting (SC) objective (25-0506) was purchased and this was coated with 50 layers of Si/Mo by the Ovonics Corp. Inc. USA. Ovonics made the layers of Si/Mo equally thick. A theoretical calculation using Henke data showed that the bandwidth and combined reflectivity of both surfaces were 2.6 nm and 7.3% respectively. An experimental measurement has recently been made and a preliminary analysis gives a bandwidth of 2.4 nm centered on a wavelength of 23.3 nm. The reflectivity was measured to be 3+1%. A narrower bandwidth is required in order to reduce the magnitude of the plasma background in relation to the line. This can be achieved by reducing the thickness ratio of the more absorbing to less absorbing layer.

A preliminary investigation of the suitability of a SC condenser lens has been made in a short run using the X-ray laser. The general arrangement of the system is shown in fig. a). A 400 nm Al filter was placed between the X-Ray source and the SC to remove the visible components of the radiation. A film holder loaded with S101 film had a 400 nm Al window to prevent scattered visible light from reaching the film. The predicted beam deflection was 10 mrad with a devergence of 6 mrad. The SC was placed at 1000 mm from the source to match the divergence of the source and was displaced horizontally and was tilted to align its axis with the estimated deflection angle of the emission.

## PRELIMINARY RESULTS

The first four shots were taken with the film at varying distances from the anticipated image of the source. The images obtained were annuli intersected by three spokes which arose because of the SC construction. From the diameter of these images and their relative positions it was possible to locate the focus of the SC. A secondary image was observed (possibly due to a pin hole in the Al filter). The secondary image was eliminated by the use of a 750 um diameter source aperture. An attempt was made to record the focused image in a PMMA film. However, very accurate focusing would be necessary to obtain the flux density required to record an image in PMMA. Facilities for accurate focusing were not available on this run. To test if visible or uv light is present in the beam a mylar film placed in the path gave zero intensity on the S101 film. Transmission by the Al window and nearly total absorption of a Mg filter indicates that the X-Ray wavelength transmitted by the SC lie in the band 170 - 250 nm.

The X-Ray flux reaching the film was determined from the optical density, area and the film calibration. At the beginning of the run 32 mm Ge targets were used but, owing to the low output from Vulcan, a switch to 24 mm targets was made. The flux from the 32 mm targets were generally higher than the flux from the 24 mm targets. The variation shot to shot was of the order of a factor five. The max. flux recorded was 9.2x10-9 joules corresponding to $10^9$ photons but typical energies were much lower than this.

It was not possible from these results to ascertain whether this energy was in the laser line or the plasma background. In order to try to establish this an angular distribution of the source was obtained by observing the intensity measured on the right and left of the annuli image and then repeating at other angles. This showed a peak at about 5 mrad with a cut off at 15 mrad. This is now believed to be due to badly positioning the 750 um source aperture rather than the laser peak.

## CONCLUSIONS

Future experiments should be conducted with high lasing outputs and with an accurately positioned source aperture which matches the laser emission area of the source. The focused image of the source should be investigated with a photoresist recording medium. A zone plate could then be introduced to project this image on to a S101 film or a CCD array detector. Finally an object could be placed at the SC focus which could be imaged into the recording medium.

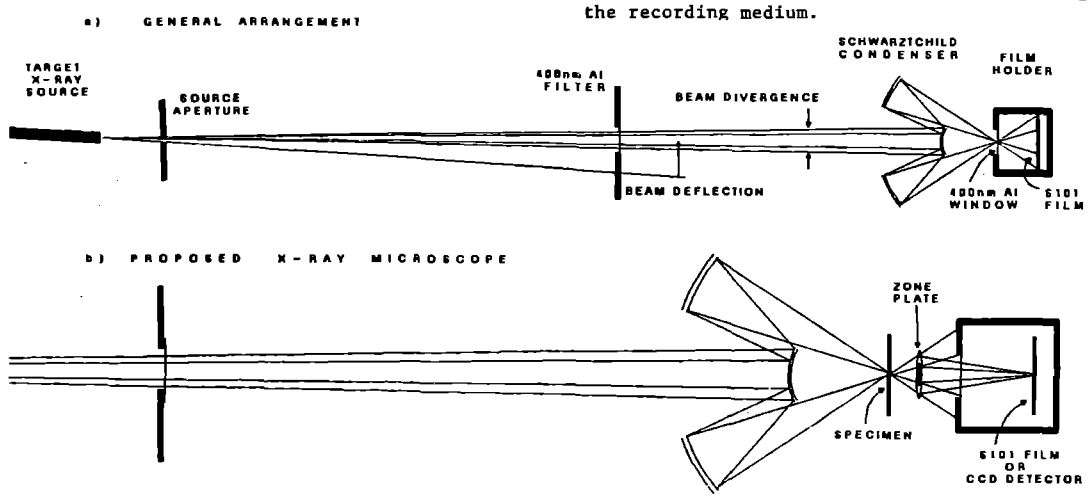

# SHORT PULSE PUMPING OF BALMER-α SODIUM LASER

H. Azuma[1], K. Yamakawa[1], S.A. Ramsden[2], Y. Kato[1], T.Tachi[1], M.Nishio[1], H. Shiraga[1], G.J. Pert[3], S.J. Rose[4] and S. Nakai[1]

[1] Institute of Laser Engineering, Osaka University, Suita, Osaka, 565 Japan
[2] University of Hull, Hull, HU6 7RX England, UK
[3] University of York, York, YO1 5DD England, UK
[4] Rutherford Appleton Laboratory, Chilton, Didcot, Oxfordshire OX11 0QX England, UK

## INTRODUCTION

In a typical mode of operation of the recombination-pumped Balmer-α (Hα) laser the heating laser pulse is terminated before significant expansion of the plasma so that the plasma can cool rapidly to produce population inversion during collisional-radiative cascade decay to lower electronic states.[1] The characteristic time of plasma expansion to the density at which gain occurs is given approximately by

$$\tau \sim 5 \times 10^{-7} Z^{-4} \qquad (1)$$

where Z is the nuclear charge and τ is in sec.[2] In an experiment on C VI Hα at 18.2 nm where a carbon fibre was irradiated by a 90 ps laser pulse[3], the pulse duration was shorter than the characteristic time of $\tau \sim 380$ ps given by eq. (1). Target irradiation with a shorter pulse is required in order to scale the recombination Hα laser to shorter wavelengths since τ depends strongly on Z. For example, $\tau \sim 34$ ps for Na XI (Z = 11). Laser intensity should be increased as $I_L \sim Z^4$ in order to increase the electron temperature as $T_e \sim Z^2$ for producing fully-stripped ions.

In a previous experiment[4,5] a planer stripe (and foil) target was irradiated with a laser pulse of 130 ps duration at 351 nm wavelength at an irradiation intensity of $I_L \sim 3 \times 10^{14}$ W/cm². Positive gains on Hα transitions of Na XI at 5.42 nm and Mg XII at 4.55 nm were obtained in this experiment. However, the laser pulse duration of 130 ps was too long compared with the characteristic time given by eq. (1). Here we present results of an experiment on Na XI Hα when a target is irradiated with a laser pulse of 28 ps duration. Compared with the previous experiment, approximately a factor of three improvement in gain has been obtained by target irradiation with a laser pulse of shorter duration and smaller energy.

## EXPERIMENTAL

A short pulse was generated by using a fibre-grating pulse compressor and then amplified with a high power glass laser. A stable, transform-limited laser pulse of 100 ps duration, 1.052 μm wavelength and 0.5 μJ energy from a mode-locked and Q-switched Nd: YAG oscillator[6] was transmitted through a polarization-preserving single mode fibre of 9 μm core diameter and 1 m length. The frequency-chirped pulse from the fibre was compressed with a pair of gratings of 1800 lines/mm placed at an incidence angle of 75° and separated by 3.8 m. A spectral window placed between the gratings eliminated the lowest and highest frequency components from the chirped pulse in order to reduce the pedestal which accompanied the compressed pulse[7]. The shape of the compressed pulse observed with a streak camera of 10 ps resolution (Hamamatsu C979) is shown in Fig 1. It has a width of 28 ps at half-maximum. It is accompanied with a pedestal whose rise time is ∿ 100 ps and whose front portion has an energy ∿ 5%

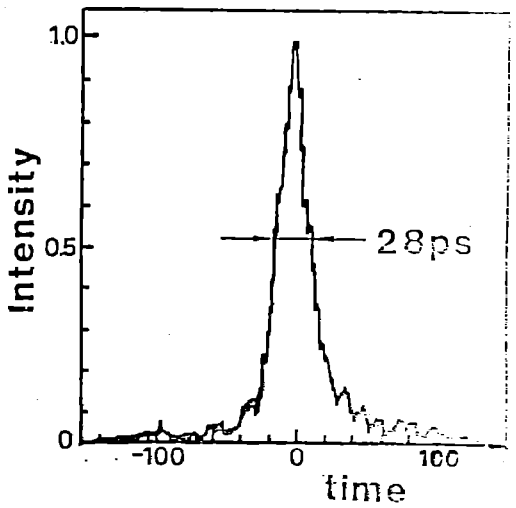


Fig 1 A streak-camera trace of a compressed pulse.

of that of the main pulse. The position of the spectral window was adjusted to reduce the front portion of the pedestal since it contributes to formation of a preformed plasma. This energy fraction is reduced to less than 2.5% after frequency conversion to second harmonic. It should be noted that except for this pedestal there was no prepulse which often exists in passively mode-locked oscillators.

The compressed pulse was amplified with the Gekko MII phosphate glass laser[8] whose final output aperture is 20cm. The amplified beam of 18cm diameter was frequency-doubled to 526 nm with a 4-segmented KDP crystal with a conversion efficiency of approximately 60%. The laser beam was line-focused onto a target with a combination of a negative cylindrical lens and an f/3 aspheric lens. The size of the line-focus determined from the x-ray emission pattern was 4.5 mm in length and 30 μm in width. The laser energy on target was determined from the laser energy measured outside the vacuum chamber and the calibrated transmittance of the focusing optics. The maximum energy on target was 25J at 526 nm corresponding to an intensity of $6.6 \times 10^{14}$ W/cm².

The line-focused laser beam irradiated a thin foil target in which NaF of varying thicknesses (0.12 μm to 0.45μm) was coated on the laser-irradiation side of a 0.2 μm-thick parylene film. The width of the foil was 4.5mm. The position of the line focus was carefully adjusted so that the edge of the foil facing the axial spectrometer was always covered by the laser beam. Spectra of the x-ray emission on-axis and 21.5° off-axis were measured with two grazing-incidence spectrometers equipped with x-ray film (Kodak 101-07) for time-integrated recording.[5] The ratio of the line intensities emitted along ($I_a$) and transverse ($I_t$) to the x-ray laser axis is

given by $I_a/I_t = [\exp(gL)-1]/(gL)$ where g is the gain coefficient and L is the gain length. The gain length L (~4.5 mm) was determined from an x-ray emission pattern taken for each shot. Therefore we can determine g from $I_a/I_t$ for various spectral lines in each shot. The relative sensitivity of the two spectrometers and the characteristic response of the Kodak 101-07 film were carefully calibrated in order to determine $I_a/I_t$ accurately.

# RESULTS

Typical axial and transverse spectra near the Na XI Hα line obtained in this experiment are shown in Figs 2(a) and 2(b), respectively. A 0.45 μm-thick NaF target was irradiated at 6.0 X $10^{14}$ W/cm² with a 23J, 28 ps laser pulse for this shot. The Na XI Hα is composed of a doublet structure: $3d^2D_{5/2}-2p^2P_{3/2}$ at 5.419 nm and $3d^2D_{3/2}-2p^2P_{1/2}$ at 5.406 nm, and is closely overlapped with NaIX $4p^2P^o-2s^2S$ at 5.386 nm and F IX $5d^2D_{5/2}-2p^2P^o_{3/2}$ at 5.353 nm. These four lines were deconvolved as shown. Relative to the nearby NaIX and FIX lines, the Na XI Hα doublets are stronger in the axial spectrum and weaker in the transverse spectrum. The absolute values of $I_a/I_t$, determined from the relative sensitivity of the two instruments, are shown in Fig 2(c). The $I_a/I_t$ of Na XI $3d^2D_{5/2}-2p^2P_{3/2}$ is 2.8 ± 0.7. The uncertainties on the values of $I_a/I_t$ arise from errors in calibration and in the deconvolution of each line. From this ratio, the time-integrated gain coefficient of the Na XI Hα was determined to be g = 4.0 ± 1.0 $cm^{-1}$.

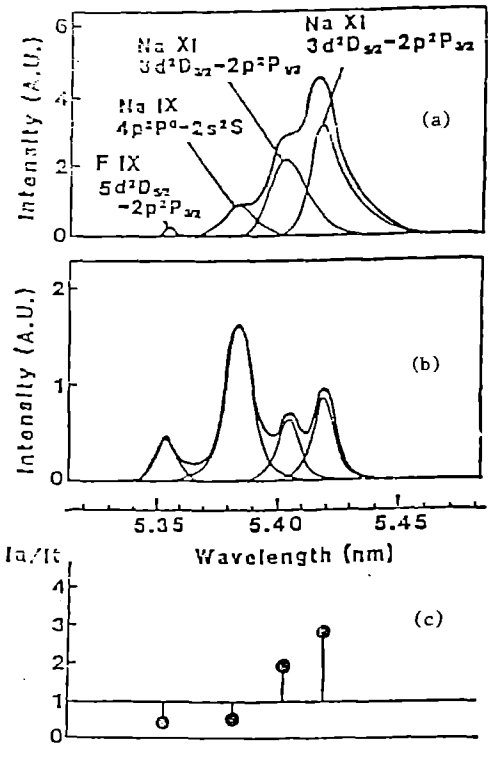


Fig 2 Axial (a) and transverse (b) spectra of Na XI Hα doublet and nearby lines and the Ia/It ratio for each line (c) for target irradiation with a 28 ps, 23J laser pulse.

Dependence of gain on the laser energy was studied using a target of 0.45 μm thick NaF coating. The results presented by open circles in Fig 3 show that gain is observed reproducibly when the laser energy exceeds approximately 20J, and becomes strongly negative when the irradiation energy is reduced to half. Other points in Fig 3 correspond to the gain when the NaF thickness was varied from 0.45μm to 0.12μm. There appears to be no strong dependence of gain on the coating thickness.

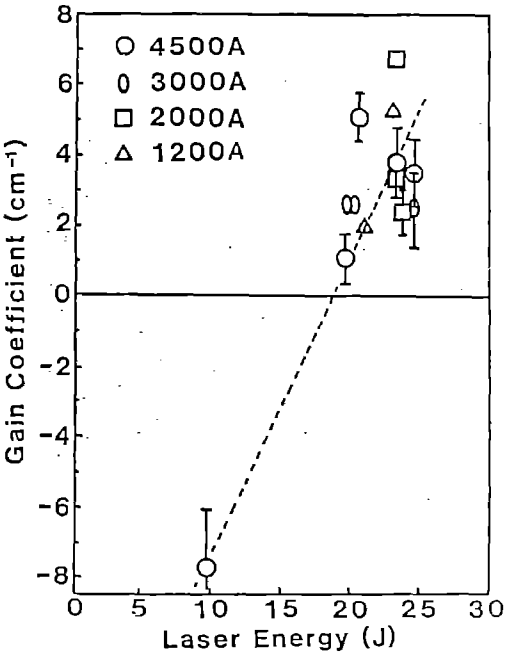


Fig 3 Dependence of the time-integrated gain coefficient of Na XI Hα J = 5/2-3/2 on laser energy.

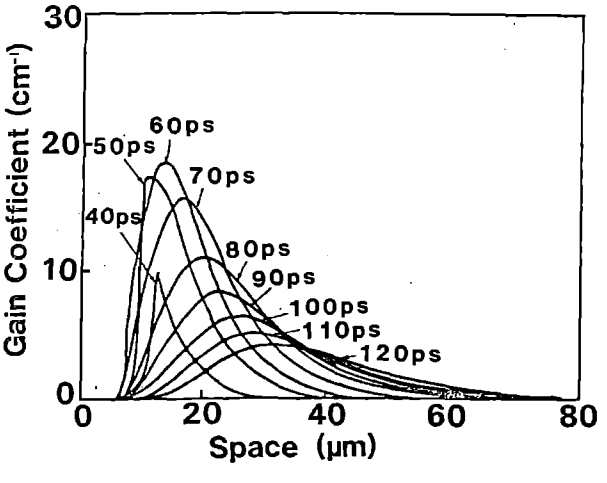


Fig 4 Result of computer simulation on spatial distribution of gain at different times after laser irradiation.

Figure 4 shows the calculated spatial distribution of the gain coefficient of NaXI Hα at different times, where t = 0 corresponds to the peak of the laser pulse. The gain increases sharply from 40 ps and becomes maximum at 60 ps taking a value of g = 18 $cm^{-1}$. The intial depth from the surface of the plasma element which yields this maximum gain is 0.1 μm. The maximum gain is created at ∿15 μm from the initial target surface and the gain region has a width of ∿15μm. Time dependence of the spatially-averaged gain calculated form Fig 4 has a peak value of g ∿ 11$cm^{-1}$. The space- and time-average gain is g ∿ 5 $cm^{-1}$ which is in close agreement with the experimental result that we have obtained. Note that Ly-α trapping has been neglected in the calculation shown in Fig 4, reflecting the result of the recent study on F IX Hα[9]. This suggests that a time- and space-resolved measurement may give a very high gain as predicted in Fig 4.

# SUMMARY

In summary, a NaF foil target was irradiated with a laser pulse of 28 ps duration and 532 nm wavelength at an irradiation intensity of up to 6.6 X $10^{14}$ $W/cm^2$. A space- and time- integrated gain coefficient of g ∿ 4 ± 1 $cm^{-1}$ was obtained for Na XI Hα at 5.42 nm. This value is approximately three times higher than the value obtained previously in target irradiation with a 130 ps laser pulse. Computer simulation of the present experiment suggests a peak gain, local in space and time, of g ∿ 18 $cm^{-1}$.

We would like to thank the laser group for operation of the Gekko MII laser and M Takagi and the target group for fabricating the targets. S A Ramsden thanks Monbusho for inviting him as a Guest Professor to Osaka University to carry out this work.

1. G.J. Pert, J. Phys. B9, 3301 (1976) and B12, 2067 (1979).

2. G.J. Pert, Topical Meeting on High Density Physics with Subpicosecond Laser Pulses, Sept 11-13, 1989, Snowbird, Utah.

3. C. Chenais-Popovics, et al., Phys. Rev. Lett., 59, 2161 (1987).

4. Y. Kato, et al., OSA Proceedings on Short Wavelength Coherent Radiation: Generation and Applications, edited by R.W. Falcone and J. Kirz (Optical Society of America, Washington, DC, 1988), Vol. 2, pp. 47-51; H. Nishimura, et al., ibid. pp. 137-140.

5. Y. Kato, et al., Appl. Phys., to be published in Jan., 1990.

6. D. Kuizenga, IEEE J. Quant. Electr. QE-17, 1694 (1981).

7. J.P. Heritage, et al., Appl. Phys. Lett., 47, 87 (1985).

8. Y. Kato, et al., Appl. Phys Lett., 38, 72 (1981).

9. M. Grande et al., Opt. Comms., 74, 309, 1990.

# RECENT ADVANCES IN THE TECHNIQUE OF POINT PROJECTION SPECTROSCOPY

S.J.Davidson, D.Neely, C.L.S.Lewis and D.O'Neill

Queens University Belfast

## INTRODUCTION

Point projection spectroscopy[1] using Bragg crystals has been finding increasing application in the measurement of absolute absorption in the X-ray region. The technique has found use in measurements of X-ray laser hydrodynamics[2], aluminium coronal measurements[2], and recently in high density, K-shell aluminium absorption experiments. [3]

Since the last annual report there has been progress on the theoretical modelling of the latter experiment. The improved calculation shows the degree of detailed agreement with experiment achievable when Bragg spectroscopy is coupled with point projection techniques.

The use of Bragg crystals however fundamentally limits the technique to measurements in the hard X-ray region above ~500eV. For plasmas up to a hundred eV this precludes the measurements of transitions contributing to the Rosseland mean and excludes many transitions of astrophysical interest.

Recent measurements will be described in which the the technique of point projection spectroscopy has been extended into the soft X-ray region. This has been achieved by using a flatfield grating as the dispersive element in place of the Bragg crystal.

## IMPROVED MODELLING OF K-SHELL EXPERIMENTS

Data from the aluminium K-shell experiment [4,5] (Fig.1a) was previously compared with a calculation which explicitly included a limited number of detailed configurations and represented further configurations, with spectator electrons in the 3 and 4 shells, as configuration averages. This calculation showed broad agreement with experiment but did not agree in detail with the experimental data.

An improved calculation [6] has now been carried out using the LINES code which generates spectra based on LTE populations and atomic data from the CATS code (a modified version of R.D.Cowans programs [7]). For each ion stage of ground state $1s^2 2s^2 2p^m$ all possible configurations of the form

$$1s^w 2s^x 2p^y (nl)^z$$

were considered, where the occupation numbers were restricted to

$$w = 1,2$$

$$| x+y-m-2 | \leq 1$$

$$Z \leq 1$$

The $1s^2$ and $1s\,(nl)^1$ configurations were considered for the helium like ion and $(nl)^1$ configurations were considered for the hydrogen like ion. All possible excited electron orbitals with $n \leq 10$ and $l \leq 4$ were considered.

This calculation used the previously estimated conditions for the experimental data (40eV and 0.013g/cc with a viewed thickness of $5 \times 10^{-5}$ g/cm$^2$ and an instrumental resolution of 0.7eV) to predict the transmission expected from the experiment (Fig.1b).

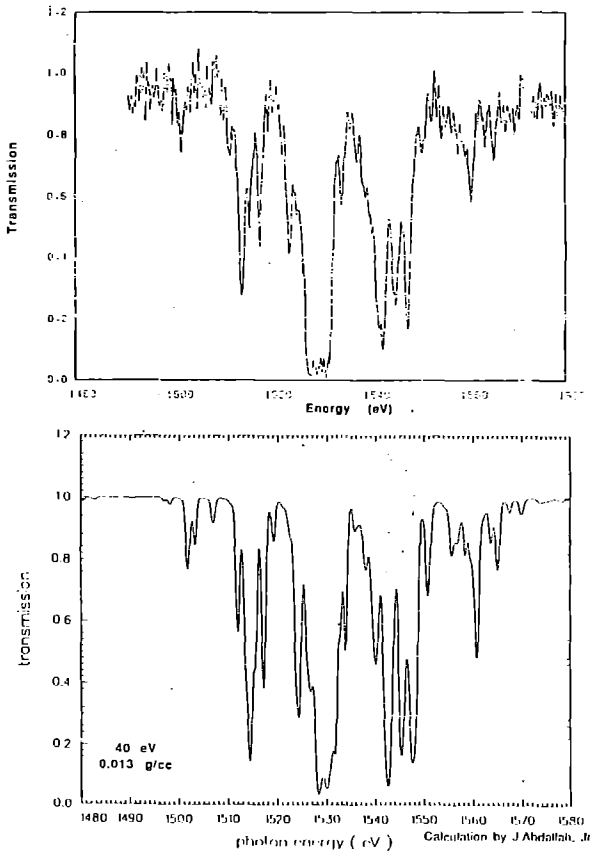


Figure 1. Aluminium K-shell absorption -comparison of experimental measurement (upper graph) with new calculation (lower graph)

The sensitivity of K-shell absorption as a diagnostic of target conditions is demonstrated in figure 2 which shows the calculated effect of changing the conditions by 5eV. Noticable changes in the absorption spectra occur for changes as small as 1eV.

## SOFT XRAY POINT PROJECTION SPECTROSCOPY

The geometry used for the aluminium K-shell measurements has been modified to allow absolute absorption measurements in the soft X-ray region below 500 eV by replacing the Bragg crystal with a soft X-ray spectrometer [8] (Fig.3). The spectrometer, a flatfield grazing incidence device using non-uniformly ruled gratings[9] was positioned with the entrance slit 6 cm from the backlighting source.

The sample placed about 3cm from the backlighting source, was heated by the soft X-rays from the rear of laser heated gold foil which was irradiated with 200J of 0.53μm laser light in 400pS. The size of the heating foil was limited to 1000μm or 500μm diameter in order to achieve reasonable conversion efficiencies.

The backlighting source of X-rays was provided by a second beam irradiating a 200μm disc of material with ~60J of 0.53μm laser light in 100pS. The size of this back-lighting source was a compromise between the

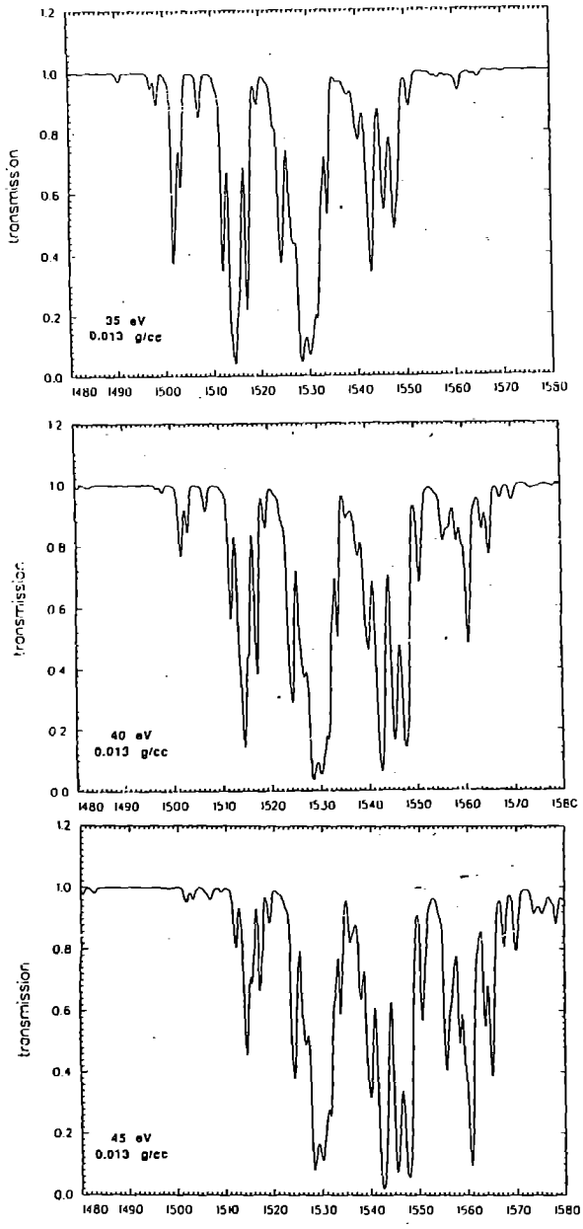


Figure 2. Calculations show that K-shell spectroscopy is potentially a good diagnostic of sample conditions

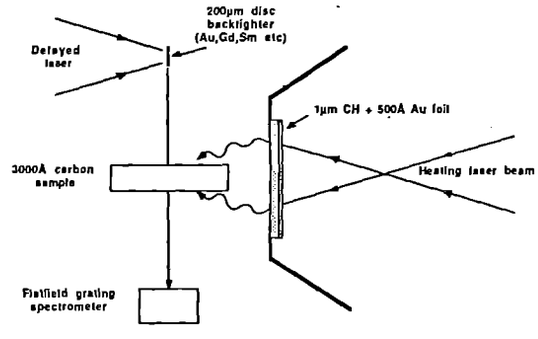


Figure 3. Experimental geometry for soft X-ray point projection spectroscopy

need to have a small source so that, the probed region of the heated sample did not have large gradients due to the limited extent of the heating source and the need to fill the grating when the spectrometer entrance slit is placed at a distance from the backlighting source.

The backlighter material was chosen to provide a bright short lived emission of limited spatial extent. An experimental survey of the emission spectra of elements of differing atomic number using a 20μm slit to spatially resolve the extent of the emission perpendicular to the backlighter foil ( Fig.5) showed that regardless of the atomic number of the backlighting material, the spatial extent of the continuum emission was always in the range 50-100μm. However line emission particularly, for low-Z elements, extended over hundreds of microns .

Time resolved measurements (Fig.4) indicated that the continuum emission for medium and high-z materials essentially followed the laser pulse typically having a FWHM of 100pS. A low intensity tail containing a few percent of the energy did however persist for a few hundred pS. Line emission in general lasted longer and in particular the low-Z line emission lasted for many hundreds of picoseconds.

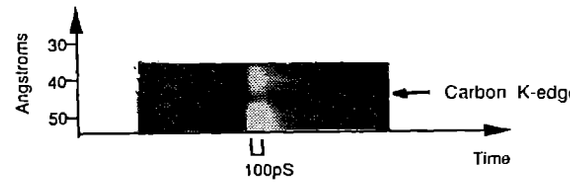


Figure 4. Streak of thulium spectrum in the region of the carbon K-edge
(Note. small scale structure due to photo cathode imperfections)

The low-Z line spectra provide estimates of the amount of higher order contributions to the spectrum. A correction for higher order contributions must be made if quantitative measurements of absorption are to be achieved.

Two versions of the flatfield gratings[10] are commercially available with 1200 and 2400 l/mm respectively. Both are designed to work with a 235 source to grating distance and 237 mm grating to detector distance. Using such a geometry the 2400 grating covers the spectral range 150-700eV and the 1200 covers the range 30-400eV

The 2400 l/mm grating is relatively insensitive to higher order contributions (Fig.6) but the 1200 l/mm spectra can show multiple orders up to 12th order (Fig.7).The use of a double reflection filter described elsewhere in the annual report can help remove the effects of multiple orders, but for measurements in the softer regions of the spectrum using the 1200 l/mm grating a trade off between sensitivity and higher order contributions is inevitable.

Kodak 101 film was used to make the measurements The film calibration was carried out by Dr Klauss Eidmann of the Max-Plank-Institute Fur Quantenoptic. The film saturates at density 1.2 and has a fog level density of 0.05 This obviously limits the dynamic range of any absorption measurement. The brightness of the unattenuated backlighting spectrum is therefore a critical issue if quantitative measurements of absorption are required. The experimentally measured characteristic curve was used to plot of the difference between the density due to unattenuated X-rays and the density due to X-rays passing through the sample as a function of sample transmission. (Fig 8.) This clearly demonstrates the importance of ensuring that the unattenuated density is in the range 0.7 - 1.0.

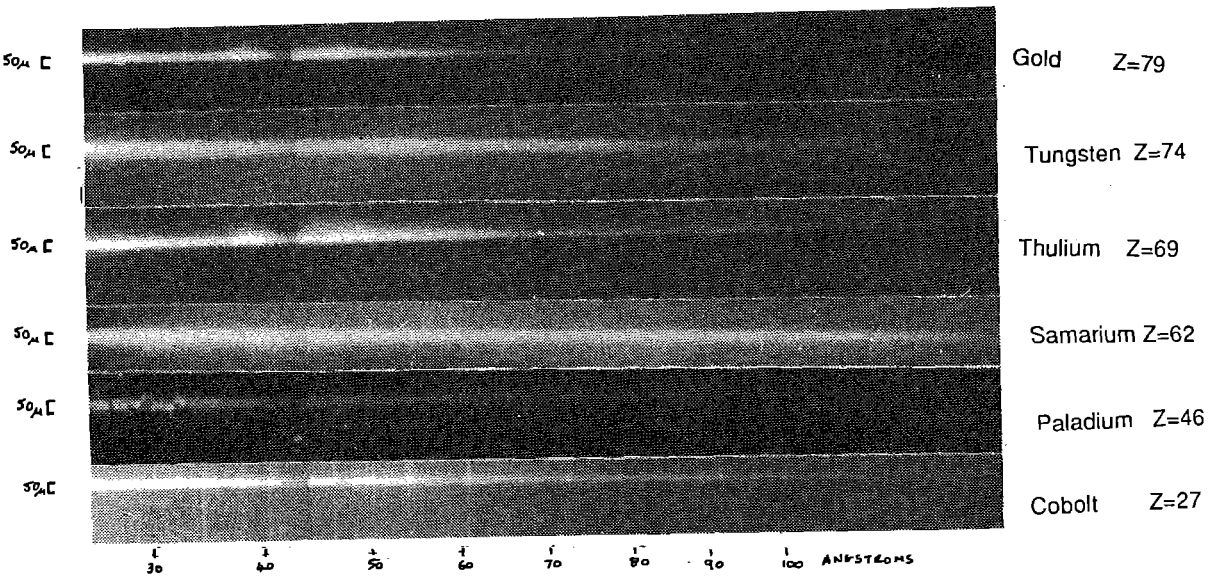


Figure 5. Typical spatially resolved measurements using 2400 l/mm grating

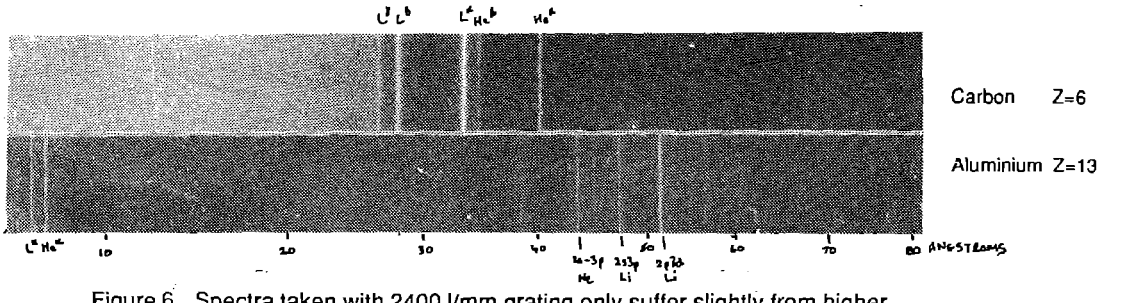


Figure 6. Spectra taken with 2400 l/mm grating only suffer slightly from higher order contributions. (Note aluminium emission lines at 7.176 and 7.872Å)

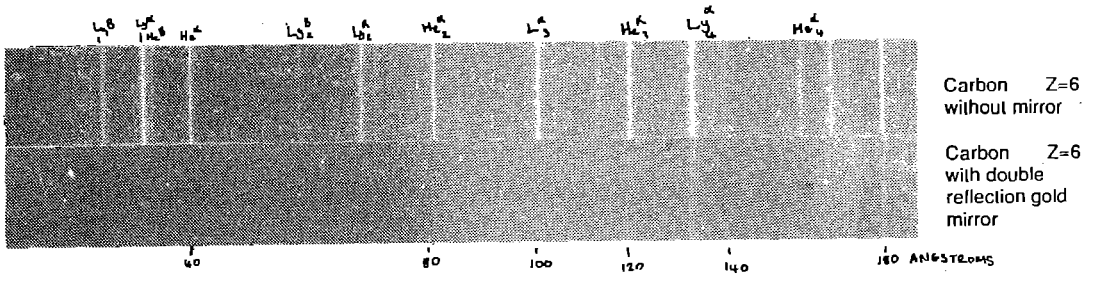


Figure 7. Carbon spectra using 1200 l/mm grating shows many high order contributions. Double gold mirror removes shorter wavelength multiple order contributions

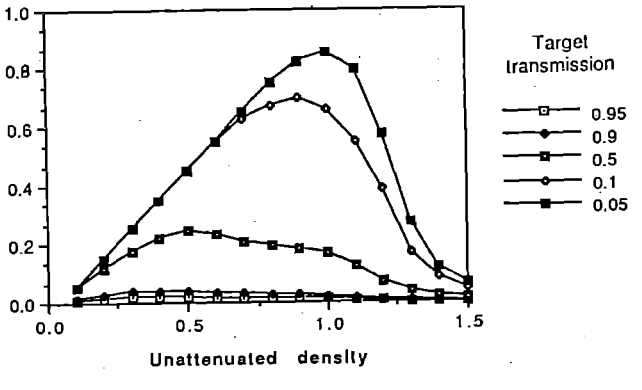


Figure 8. Difference in density on film due to target absorption, for a given target transmission as a function of density on film due to unattenuated backlighter.

Recently measurements have been carried out on the Vulcan Laser at the Rutherford Appleton Laboratory using the geometry described above to measure the absorption of a 3000Å (Parylene-E) plastic sample placed perpendicular to the heating source. The backlighter in this particular measurement was gadolinium.

The result of the measurement shown in figure 9. The carbon K-shell absorption spectra is qualitatively similar to the aluminium K-shell spectra in that the spectrum consists of 1s-2p and 1s-3p absorption lines corresponding to the various ionstages present in the plasma.

Detailed analysis of this and other carbon K-shell spectra as well as aluminium L-shell measurements will be reported at a later date.

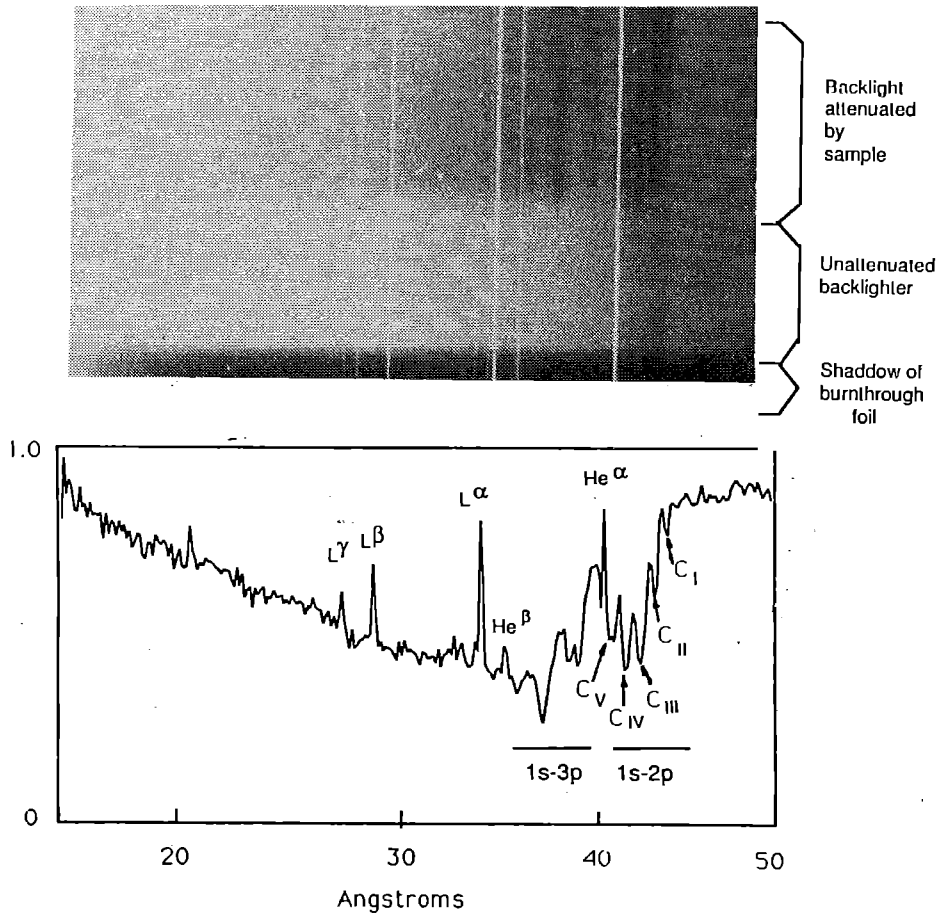


Figure 9. Soft Xray absorption spectrum of K-shell carbon

## CONCLUSIONS

The improved calculations of the K-Shell aluminium absorption has demonstrated the power of the point projection technique using Bragg spectroscopy. The extension of the technique to the soft X-ray region using grating spectroscopy has been demonstrated, allowing the technique to be applied to a much larger range of transitions.

## REFERENCES


1 C.L.S.Lewis and J.McGlinchey,Opt. Comm. , 53, 179 (1985)

2 D.O'Neill, C.L.S.Lewis, D.Neely, S.Davidson "Investigation of short pulse expanding plasmas"1989 Annual report to the LFC Section A1.6

3 S.Davidson, C.L.S.Lewis, D.O.Neill, "1s-2p Term structure in Aluminium "1989 Annual report to the LFC, section A1.4

4 S.J.Davidson, C.L.S.Lewis, D.O'Neill " K.Shell absorption spectra of an aluminium plasma", Proceedings 19th ECLIM ,Madrid 1988

5 S.Davidson, C.C.Smith, J.M.Foster, K.A.Warburton and S.Rose, Appl.Phys. Letts. 52, 10 (1988)

6 J.Abdallah Jr. and R.E.Clark "Transmission calculations for aluminium" To be published in Phys. Rev. 'A'

7 R.D.Cowan "Theory of Atomic Spectra"(University of California Press,Berkeley 1981)

8 G.P.Keihn, T.Garvey, R.Smith, O.Willi, A.Damerell and J.Westcane, SPIE Vol 831,150, (1987)

9 N.Nakamo,H.Kuroda,T,Kita,T.Harada,Appl.Opt. 23,14 p2386 (1984)

# SUB-NANOSECOND X-RAY POWDER DIFFRACTION

J.S. Wark, N.C. Woolsey, D. Riley

Clarendon Laboratory, University of Oxford, Parks Road, Oxford, OX1 3PU.

## INTRODUCTION

Over the past few years we have been using the x-rays emitted from laser-plasmas to study the lattice parameters of single crystals under shock-compression.[1,2] This novel technique has led to a number of notable firsts including the direct measurement of tensile strain under shock-breakout,[3] and a measurement of unit-cell shape as a single crystal of lithium flouride undergoes hydrostatic compression. So far all our work has concentrated on single crystals for the simple reason that it is well known that the diffracted intensity is sufficient to enable single-shot diffraction measurements to be made. However, an extension of the technique to incorporate powdered samples would be beneficial for two main reasons. Firstly, the majority of materials which have been studied by conventional shock-wave techniques, and which are used in 'real-world' engineering applications are powdered - e.g. the small crystallites constituting a metal bar. Secondly, one of the major long-term aims of our work is to gain an understanding on the lattice level of the mechanisms involved in shock-induced phase transitions. The transitions which are of most interest are the non-displacive transitions, i.e. the crystal cannot simply slip from one lattice type to another, but a total rearrangement of the atoms via a disordered phase is necessary. Such a transition is found in KCl which is believed to transform from the NaCl (face centred cubic lattice) to CsCl structure (simple cubic lattice) within two nanoseconds above a shock pressure of just 20 kilobars.[4] In such a rearrangement of atoms we do not expect the new phase to be formed as a single crystal, and thus the observation of such phenomena will require a means of studying powders. Indeed, in an experiment in 1988 we observed the diffraction from a single crystal of KCl disappear when it was compressed above the phase change point.

## THE SEEMAN-BOHLIN CAMERA

The diffracted signal from a powder is inherently several orders of magnitude less than that from a single crystal due to the random orientation of the small crystallites with respect to the x-ray source. Thus to gain a diffracted signal from a powder in a single laser shot it is necessary to use a focussing geometry such as that shown in Fig.1, which is known as a Seeman-Bohlin camera. This camera relies on the principle that the angle subtended by a chord to any point on the circle on a given side of the chord is the same. Thus if a powdered sample is placed on the circumference of a circle, and the x-ray source is also on the circumference, then all of the crystallites that are oriented such that they meet the Bragg condition for a particular (hkl) reflection will diffract to the same point on that circle. We made some simple calculations that indicated that the integrated diffracted intensity from such an arrangement should be comparable to the diffraction from a single crystal, and thus be recordable in a single laser shot.

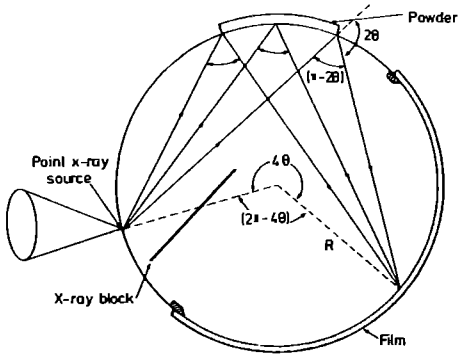


Fig.1: A schematic diagram of the Seeman-Bohlin camera.

## EXPERIMENT

On the basis of these calculations a camera was manufactured in the Clarendon laboratory workshops. The diameter of the circle on which the target, powder, and film are placed is 15cm. This camera was tested in an experiment in TA2. LiF powder with a grain size of order 25$\mu$m was placed on the powder holder, and a sub-nanosecond x-ray source was created by focussing a 600psec beam of 0.53$\mu$m light containing about 50J to a tight spot on a titanium target. The curved film pack was placed in a position to record

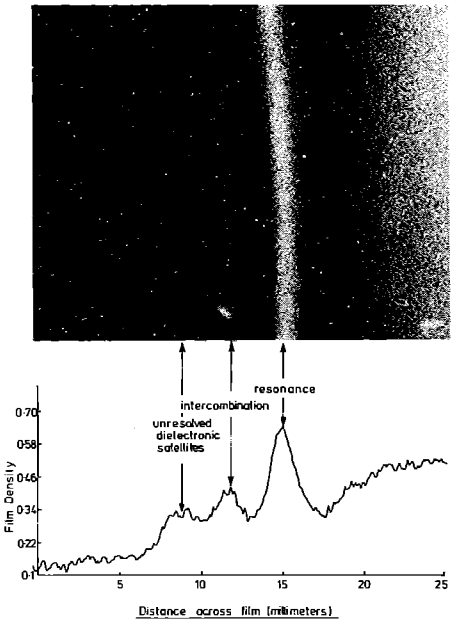


Fig.2: Diffracted spectrum of titanium helium-$\alpha$ from LiF (220) powder.

diffraction of titanium helium-$\alpha$ from the (220) planes of the LiF powder. A typical result is shown in Fig.2. The titanium lines are clearly visible, and the integrated reflectivity is indeed comparable to that from a single crystal. It should be noted that the reflection shown here - (220), only has a reflectivity of 48% compared to that of the strongest (200) line. The slight fogging to the higher energy side of the resonance line is believed to come from fluorescence from the edge of an x-ray beam block. Experiments using a c.w. x-ray source are planned to optimise the focussing conditions and to minimise the background fluorescence. Having clearly demonstrated the feasibility of the camera, we are now in a position to laser-shock the powders simultaneously with the x-ray flash.

## REFERENCES

1. J.S. Wark, R.R. Whitlock, A. Hauer, J. Swain, and P.J. Solone, Phys. Rev. B Rap. Comm. 35, 9391 (1987).
2. J.S. Wark, R.R. Whitlock, A. Hauer, J. Swain, and P.J. Solone, Phys. Rev. B 40, 5705 (1989).
3. J.S. Wark, G. Kiehn, R.R. Whitlock, D. Riley, and N.C. Woolsey, submitted to J. Appl. Phys. (1990).
4. D. Hayes, J. Appl. Phys. 45, 1208 (1974).

# DIRECT MEASUREMENTS OF COMPRESSIVE AND TENSILE STRAIN DURING SHOCK BREAKOUT BY USE OF SUB-NANOSECOND X-RAY DIFFRACTION

J.S. Wark, G. Keihn+, R.R. Whitlock*, D. Riley, and N.C. Woolsey

Clarendon Laboratory, University of Oxford, Parks Road, Oxford OX1 3PU.

+Blackett Laboratory, Imperial College, Prince Consort Road, London SW7 2BZ.

*Naval Research Laboratory, Washington, D.C. 20375, U.S.A.

## INTRODUCTION

It has long been known that tensile stress can develop in the interior of a body when two decompression waves collide.[1] If this stress is of sufficient amplitude it will cause separation of the material and 'spalling' will occur.[2] This phenomenon can occur when a compressive shock wave is reflected from the back surface of a body. This rarefaction wave can interact with the rarefaction wave caused by release of the shock driving pressure at the front surface to give rise to the tensile stress.

One of the major problems in this area is that the dynamic stresses and strains occur within the body of the material, making direct measurements of such parameters difficult; most diagnostic techniques rely on measurements at the surface. In the experiment described here we have directly measured tensile strains during shock breakout by using sub-nanosecond x-ray diffraction. This technique has recently been used to study shock-launching in single crystals.[3,4]

## EXPERIMENT

The experiment was performed using the VULCAN laser system at the Central Laser Facility. A schematic diagram of the experiment is shown in Fig. 1. One arm of the laser containing 100J of 1.05$\mu$m light in a pulse of 1 nsec (FWHM) was focused to a 1.5cm spot onto a 50$\mu$m thick silicon (111) single crystal (2d = 6.28 A). The front (irradiated) surface of the crystal was coated with 100nm of aluminium and 18$\mu$m of $(CH)_x$ plastic to ensure abrupt absorption of the laser light and increased strength and duration of the applied pressure pulse.[4,5] A second laser beam, synchronous but delayed with respect to the shock driving beam, was focused to a tight (<100$\mu$m) spot on a separate titanium target. This frequency-doubled beam contained 25J of 0.53$\mu$m light in a pulse length of 1 nsec (FWHM). The resultant laser-plasma was a prolific source of x-ray line radiation. The resonance line(2.612A), intercombination line (2.625A), and associated dielectronic satellites (around 2.635A) of helium-like titanium were Bragg diffracted from the rear surface of the shocked crystal and recorded on a Kentech x-ray streak camera. The temporal resolution, as determined by the slit width, was 50psec.

## RESULTS

Typical data recorded on the streak camera are shown in Fig 2. Fig.2(a) shows the unresolved titanium spectrum recorded by diffraction from the rear surface of an unshocked crystal. Fig. 2(b) shows the time-resolved spectrum during shock breakout. Also shown on the diagram are the values of compression or tension corresponding to the observed shift in Bragg angle, where the shift is measured from the resonance line for tension, and from the dielectronic satellites for compression. In interpreting this data it should be recalled that the x-rays are diffracting from all the various interatomic spacings in a region of the crystal from the rear surface down to a probe depth several microns below the surface. In diffraction from such highly strained crystals this probe depth will be determined by photoelectric absorption rather than extinction. The 1/e depth for 2.6A radiation in silicon is 15.4$\mu$m, which at a Bragg angle of 24.5 degrees corresponds to a depth of 6.4$\mu$m below the surface of the crystal. Of course the x-rays must both enter and exit from the crystal, so diffraction exiting the surface from a region 6.4$\mu$m below

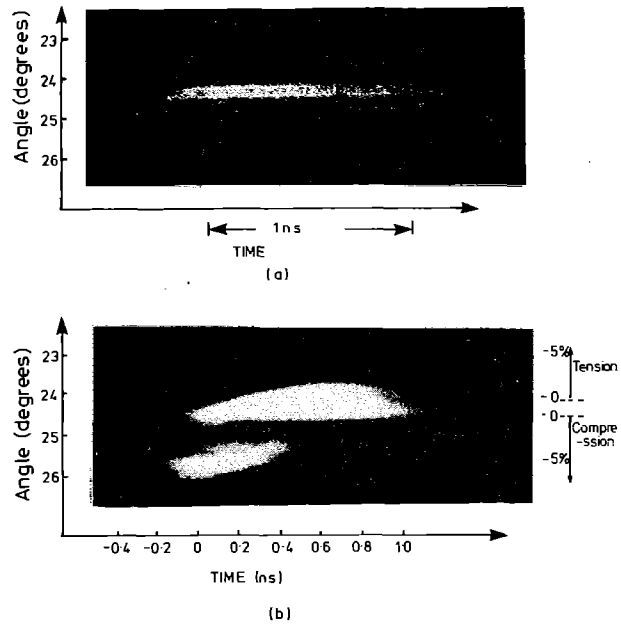


Fig.2: (a) Streak camera record of the diffraction of the helium-like titanium lines from the rear surface of an unperturbed crystal and (b) the diffracted spectrum from the rear surface during shock breakout.

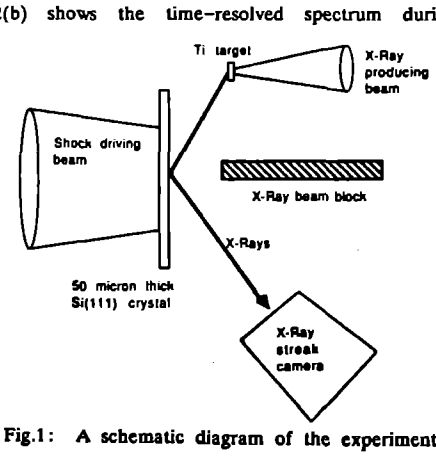


Fig.1: A schematic diagram of the experiment.

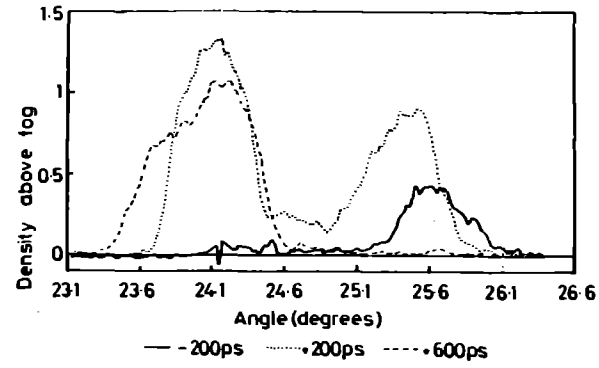


Fig.3: Densitometer tracings of Fig.2(b) corresponding to the times shown.

will be reduced by $(1/e)^2$ from that entering the surface. The intensity of the diffracted signal will also be a function of the strain gradient, and more detailed calculations of the diffracted signal are given below.

Fig.3 shows lineouts through the spectrum from the shocked crystal at the three times indicated. Zero time has been taken to be the time when the crystal is first observed to go into tension. It can be seen that at -200 ps the x-rays are probing the crystal in a state of compression, the maximum compression being 5.9% ± 0.5%; later at 200 ps the x-rays are being diffracted from both regions of compression and regions of tension; and finally at 600 ps the x-rays are being diffracted from a region of pure tension, with a maximum observed tension of 3.9% ± 0.5%. These three regimes correspond to the times when the reflected wave has not yet collided with the rarefaction wave due to release of pressure at the front surface; the time during collision of the rarefaction waves; and the time when the reflected wave has gone so far through the front surface rarefaction wave that the x-rays can no longer probe the compressed region.

The response of the crystal has been modelled using the one-dimensional lagrangian hydrocode 'Medusa'.[5] The code has been modified to include a Birch-Murnaghan equation of state for the silicon. We have also assumed that the response of the silicon is totally elastic even though the Hugoniot elastic limit of silicon, which occurs at a compression of 2.6% in the (111) direction,[6] has been exceeded. This assumption has been made as the elastic-plastic transition is expected to take far longer than the timescales involved in this experiment . The results for the strain-depth profiles are shown in Fig.4. It can be seen that after the wave is reflected the maximum compressive strain is reduced. When the rarefaction waves meet the material goes into tension. At a certain time the rear few microns of the material are in tension whilst the rest of the crystal is in a state of compression.

The x-ray diffraction from the shocked crystal has been modelled by a code based on dynamical diffraction theory as applied to strained crystals.[7-10] The code has been described elsewhere[4] and for the sake of brevity we will not reproduce it here. The code calculates the reflectivity as a function of angle around the Bragg angle for a crystal with a given strain-depth profile. The reflectivity calculations are shown in Fig. 5. For direct comparison with experimental data these rocking curves have been convolved with the line shapes of typical helium-like titanium radiation. The line shape for this particular shot is not known, and line shape is also a function of time, but as the shifts in diffraction angle are several times larger than the angular width of the helium-like complex this should not give rise to large errors. The calculated reflected x-ray intensities have been converted to density using a film calibration curve obtained from density step-wedges recorded on the experimental data. It can be seen that there is good qualitative agreement between the experimental and calculated results.

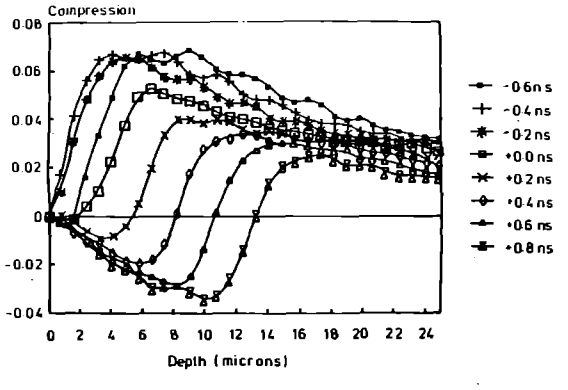


Fig.4: 'Medusa' calculations for the strain profiles for an absorbed irradiance of $2x10^{10}Wcm^{-2}$. Zero time is taken to be the point when the material first goes into tension to facilitate comparison with the experimental data.

DISCUSSION

Although there is good qualitative agreement between the experimental and predicted diffracted profiles care should be taken in interpreting fine details in the experimental data. This is because diffraction for different lattice spacings comes from different irradiated regions of the crystal. Thus non-uniformities in the shock-driving laser beam can manifest

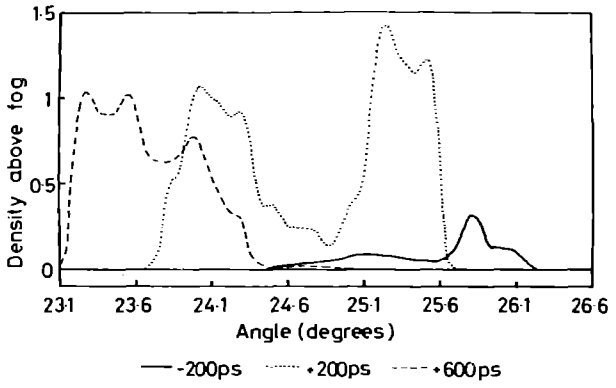


Fig.5: Computed x-ray diffraction data for the strain profiles shown in Fig.4. In calculating these curves the rocking curve has been convolved with a typical line profile, and converted to film density. At each time the integrated reflectivity has been set equal to the corresponding experimental integrated reflectivity.

themselves as detail in the diffraction data. Time-integrated pictures with 100 psec x-ray pulses have shown non-uniformities in peak compressions of only 10%, so we do not expect the gross structure to be altered. Future experiments are planned to address the problem of beam uniformity. A further factor that should be taken into account is the parallelism of the crystal. If the shock front is not parallel to the rear surface of the crystal the temporal resolution will be degraded. We have measured the crystal to be parallel to 1.5$\mu$m over 1cm, and have calculated that this will contribute less to the temporal resolution than the quoted 50psec due to the slit width.

CONCLUSION

In conclusion we have used sub-nanosecond x-ray diffraction to measure the interatomic spacings over a range of several microns at the rear surface of a laser-shocked single crystal during shock breakout. We have observed the crystal go into a state of dynamic tension as the rarefaction waves collide. The experimental results are in good agreement with predictions from a combination of hydrocode and diffraction theory. This technique allows us to measure dynamic strain within a crystal, and thus appears to be a promising diagnostic tool for the study of spallation

REFERENCES

1. B. Hopkinson, Trans. R. Soc. (Lond.) 213A, 437 (1914).
2. B. Hopkinson, "Brittleness and Ductility", Scientific Papers, p64, Cambridge U. Press, London (1910).
3. J.S. Wark, R.R. Whitlock, A. Hauer, J.E. Swain, and P.J. Solone, Phys. Rev. B Rap. Comm. 35, 9391 (1987).
4. J.S. Wark, R.R. Whitlock, A. Hauer, J.E. Swain, and P.J. Solone, Phys. Rev. B 40, 5705 (1989).
5. J.P. Christiansen, D.E.T.F. Ashby, and K.V. Roberts, Comp. Phys. Comm. 7, 271 (1974).
6. W.H. Gust and E.B. Royce, J. Appl. Phys. 42, 1897 (1971).
7. S. Takagi, Acta Crystallogr. 15, 1311 (1962).
8. J. Burgeat and D. Taupin, Acta Crystallogr. A24, 99 (1968).
9. B. Klar and F. Rusticelli, Nuovo Cimento 13B, 249 (1973).
10. C.R. Wie, T.A. Tombrello, and T. Vreeland Jr., J. Appl. Phys. 59, 3743 (1986).

# THOMSON SCATTERING RESULTS OF MULTI-PHOTON IONISATION OF HYDROGEN BY A 1μm LASER BEAM

[1]A.K.L. Dymoke-Bradshaw, [1]A.E. Dangor and [2]A.E. Dyson.

[1]Imperial College of Science, Technology and Medicine.
[2]Ecole Polytechnique, France.

ABSTRACT

We describe an experiment in which a fully ionised plasma was generated in hydrogen gas using multiphoton ionisation by an intense 1.053μm laser beam.

Light scattered by the plasma was observed to be anomalous and had a spectrum that cannot be fitted to classical Thomson scattered profiles.

In a certain range of fill pressures the forward scattered spectrum was highly asymmetric showing a large single sideband upshifted by $\omega_p$, indicating full ionisation. The corresponding down shifted sideband was not observed. The intensity in the upshifted sideband varied with density, peaking at about 1.4 $10^{17}$ $cm^{-3}$, and is estimated to be more than $10^3$ times that expected from a thermal plasma.

The scattered profiles at 90° and in the forward direction were symmetric but the data are poor fits to classical Thomson profiles.

INTRODUCTION

This experiment was intended to complement our work on the Beat Wave Accelerator[1] for which we need to generate a very uniform plasma with a density of approximately 1.0 $10^{17}cm^{-3}$. Earlier work indicated that such a plasma could be generated with an intense 0.5μm laser beam focussed into hydrogen gas. The gas pressure being set for the required final plasma density. Thermal expansion and ponderomotive forces on the plasma are not very significant on the timescale of the experiment (~200ps). Thomson scattering from the plasma, of laser light used for the plasma creation, indicated that a very uniform density region extended over at least 8mm along the focal direction of an f/20 focussing system. It was thought that the beatwave experiments could be considerably simplified if one of the 1μm beating beams could be used for plasma creation removing the need to provide a dedicated 0.5μm beam. Consequently the experiment described here was performed in order to test the efficacy with which the 1μm laser light can ionise hydrogen gas.

Thomson scattering with 1μm laser light is not normally considered practical in plasmas as the cross section is very small ($\sigma$=6.6 $10^{-29}$ $m^2$) and the quantum efficiency of detectors is very low (<0.1%). Fortunately the parameter range in which we are interested is of low temperatures and high densities. Consequently the experiment is just feasible.

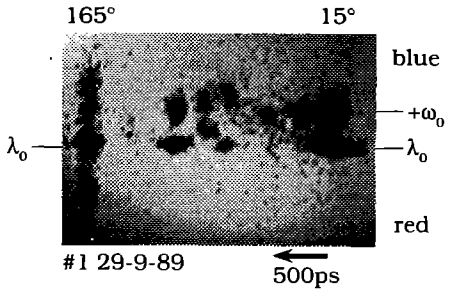


Figure 2 Typical Scattered spectra

The experimental layout is shown in figure 1. Light was collected at both 15° and 165°. Light from the latter angle was relayed back into the 15° collecting optics 2ns after the 15° scattered light. The detector, a Hadland 675 S1 streak camera, was used to resolve temporally the two scattered signals. As only one scattering channel was available, the 90° scattering experiments were done on different shots.

SUMMARY OF EXPERIMENTAL PARAMETERS

**Laser** YLF 1.053μm, 50 to 100 joules, pulse length 100 and 200 ps, beam diameter 100mm, polarisation vertical.

**Focussing** f/20 focussing optics, spot radius 200μm, Raleigh length ±8mm, intensity 4 to 8 $10^{14}Wcm^{-2}$.

**Scattering Channels** Angles 15, 165 and 90° in the horizontal plane, collecting aperture f/5, spatial resolution 300μm vertically and 400 or 2000 μm horizontal (90° or 15° and 165°), temporal resolution 100ps.

**Plasma parameters** $n_e$ ~ 0.6 to 3.6 $10^{17}cm^{-3}$ (equivalent to hydrogen fill pressures of 1 to 6 torr), $T_e$ ~ 25eV, $\omega_p$ ~ 1.4 to 4.3 $10^{13}s^{-1}$, $\lambda_D$ ~ 15 to 4.8 $10^{-6}$cm, $v_{osc}/v_{the}$ ~ 1.8 to 3.6. ($v_{osc}$ is the quiver velocity of electrons in the field of the laser, $v_{the}$ is the thermal velocity of electrons).

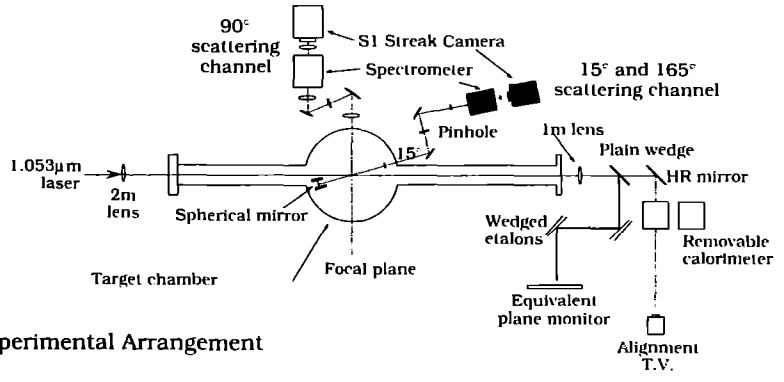


Figure 1 Experimental Arrangement

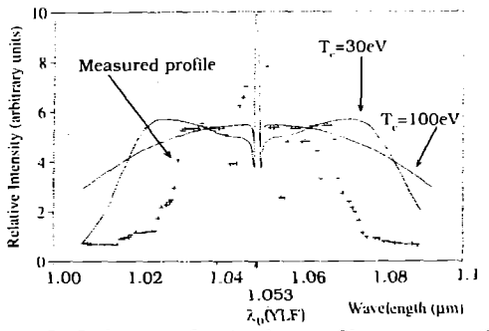


Figure 3 Only poor fits to the profiles are possible

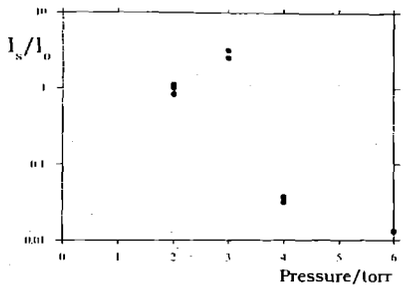


Figure 6 Plot of normalised side band intensity v. fill pressure.

EXPERIMENTAL RESULTS

Typical data from the 15° and 165° scattering channel for a 3 torr shot is shown is shown in figure 2. The first light to arrive is from the 15° scattered light and has a single blue sideband. 2ns later the 165° signal arrives. This is much more symmetric and shows a classical shape although attempts to fit it to theoretical spectra produce a poor fit, see figure 3. For the 15° data the sideband position corresponds to a fully ionised plasma with the density expected from the initial fill pressure of hydrogen. The data indicate that full ionisation is obtained over pressures in the range 1 to 6 torr, see figure 4.

The anomalous signal levels can clearly be seen from figure 5. Here several spectral profiles from the 15° channel are shown for various fill pressures. The red side bands are visible only for the higher pressures whilst the blue sideband intensity is very dependent upon the initial fill pressure as shown in figure 6. The degree of enhancement at 15° has been estimated by comparing the signal levels with those obtained at 165° and correcting for the known angle dependent factors. The enhancement is about $10^3$ times thermal.

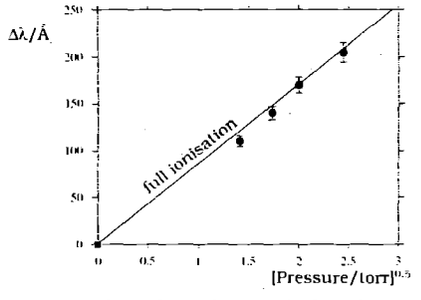


Figure 4 Plot of sideband shift v. [Pressure]$^{0.5}$

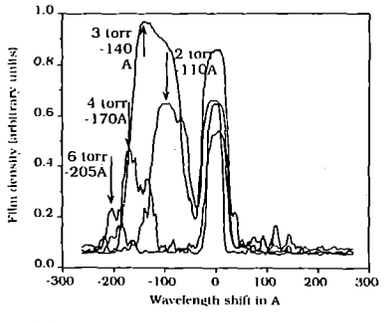


Figure 5 Spectra scatterd at 15° for various pressures

CONCLUSIONS

The production of sidebands of unequal intensity with the blue being very strong is quite unexpected an awaits further measurement and also a theoretical investigation. It is not at all clear what mechanism could generate such a scattered spectrum. The cylindrical nature of the symmetry of the experiment would indicate that both sidebands would be driven by any non-linear process. In figure 7 the layout of the scattering vectors for the 15° scattering is shown. There is a small but finite difference in the wave vectors of the plasma waves that give rise to the red and blue sidebands. It should be noted that due to the finite incident and collecting angles of the optical system the blue sideband does cover a plasma wave travelling perpendicular to the laser beam. However, the contribution from such a wave to the scattered signal does not peak at 3 torr, but continues rising until pressures well beyond the 6 torr limit covered in the experiment.

FUTURE EXPERIMENTS

It is hoped to extend the experimental work described here in a further experiment. In an attempt to learn more about the plasma turbulence the experiment will be designed so that a far greater range of plasma waves can be probed. This will use a fibre optically coupled scattering system, which will permit the collection lens to be moved around with ease to cover different angles.

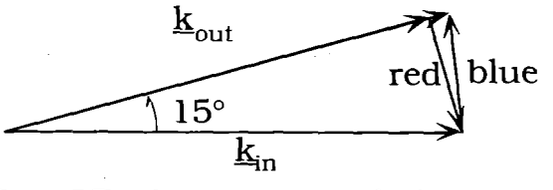


Figure 7 The plasma wave vectors for the 15° scattering

REFERENCES

1 *Annual Report to the Central Laser Commitee* Rutherford Appleton Laboratory Report RAL-89-045 (1989)

# SHOCK VELOCITY MEASUREMENTS USING A FIBRE-OPTIC REFLECTOMETER SYSTEM

[1]G. McCall, [2]T.A. Hall, [3]A.K.L. Dymoke-Bradshaw, [3]A.E. Dangor and [2]Z. Ahmed.

[1]Los Alamos National Laboratory, NM, U.S.A.
[2]University of Essex
[3]Imperial College of Science, Technology and Medicine.

ABSTRACT

We describe experiments using a novel technique to measure the shock pressure inside a laser-driven target. The technique relies upon reflectometry from a shock front using optical fibres embedded in a target.

INTRODUCTION

An important quantity which determines the performance of a laser driven implosion is the pressure produced by the surface ablation of the target. Also, many target designs use a shaped laser pulse to produce a pressure profile which increases with time. Estimates of the ablation pressure by others have inferred the driving pressure from detailed measurements of the plasma expanding from the surface of a target or by the time-integrated measurement of foil acceleration. Measurements of shock breakout at the rear surface of a target have used targets which had steps at the rear. These experiments, however, produce large perturbations in the target pressure profile, and the time and spatial resolution are rather poor. With the technique we describe here the pressure in the interior of a thick target is found by measuring the shock velocity as a function of position using detectors which are well-matched to a target material for which the equation of state is known to high accuracy. The method used here is intended to solve several of the other problems associated with the shock breakout technique as well. The method is based on the results obtained in a preliminary experiment carried out with the laser at the University of Essex.

The results can provide an accurate measurement of the hydrodynamic coupling of a laser beam to a target. They may also provide information on the weakening of shock waves as a result of two-dimensional effects such as lateral propagation of a wave and beam asymmetries. Calculations using computer codes aid the analysis of the experiments.

A secondary aim of the experiment is to investigate the feasibility of using the visible light emitted by a shocked fibre to make a spectroscopic measurement of the fibre temperature and, thus, the pressure. Recent measurements by L. Veeser of LANL indicate that the light intensity can give an accurate measurement of the pressure in the megabar pressure range, and the spectral measurement should be even more accurate. The shock velocity measurement will provide a calibration for this technique.

BACKGROUND

Shock waves in a solid satisfy simple physical relations, the Hugoniot relations, which allow all of the material parameters in the set of density, pressure, shock velocity, and particle velocity to be determined if any two of the parameters are known. If the strength of the shock wave is large, the relations simplify further and the calculation of unknown parameters becomes almost trivial. The importance of these well known observations is that shock and particle velocities are relatively easy to measure while the pressure in a material is usually difficult to measure. If the velocities are known, the pressure is simply the product of the shock velocity, the particle velocity, and the initial density. Further, there is a unique relation between shock velocity and particle velocity which has been determined for many materials by either measurement or calculation. Therefore, a measurement of shock velocity alone can, in many cases, determine the pressure in a material. Of course, the conditions are only determined at the shock front, and the time delay between a change of pressure behind the front and a change of velocity at the front must be estimated, but this is a fairly straightforward process.

Work supported by the CLF at the University of Essex in 1987 has led to the development of a technique which may solve many of the problems associated with older methods of shock propagation measurement. It was found that the reflectance of a shock wave was very low (less than 2 percent) and that the reflectance of a fibre optic tip when shocked, fell dramatically and rapidly. Measurements indicated extinction of reflected light in less than 0.1ns.

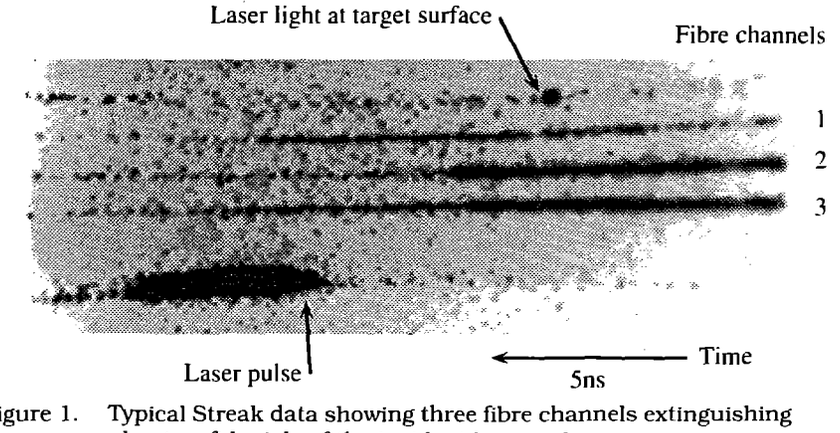


Figure 1. Typical Streak data showing three fibre channels extinguishing plus two fiducials of the incident laser pulse.

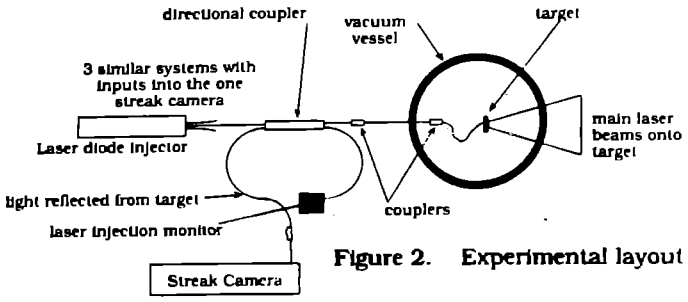


Figure 2. Experimental layout

## METHOD

The targets consisted of a group of optical fibres entering from the rear of a copper disc. The fibres extended to various depths into the target and occupied various radial positions. The overall diameter of the bundle was approximately 1 mm and the number of fibres varied from 2 to 3. The variation of the axial positions of the fibres was approximately 100μm. The ends of the fibres were coated with a thin coating of chromium. A 100ns pulse from an 832nm, 20mW laser diode was injected into each fibre using a fibre optic directional coupler, and the light reflected from the metallic coating was sent back through the fibre to the slit of an S1 streak camera. The camera recorded the reflected light as a function of time, and a sharp reduction in reflectivity was seen when the shock wave generated by main laser irradiation struck the end of the fibre. The measurements were done using a single 6ns pulse of 0.53μm light formed by overlapping four beams from the Vulcan laser system. Figure 2 shows the layout of the experiment.

In the technique described here all of the signals were of the same amplitude and therefore the dynamic range of the camera does not have to be large. The fibres were matched to the substrate, and the radial separation of the fibres was small, so that the diagnostic perturbed the shock very slightly. The transit time of the light in the fibres was used to place the expected arrival times of the indication of the shock front at convenient positions in the streak so that they did not interfere with one another. The streak record length could be a very small fraction of the shock transit time as all the signals are delayed by an estimated amount so that they arrive at the camera at the same time. The use of single mode fibre optics allows long delays with very high bandwidth. The visible light from a shocked fibre was not filtered out and in some shots did cause some confusion. This will be amended on future experiments. By careful measurement of the fibre length from the target to the streak camera the relative arrival times of the shock at the fibre tips can be deduced. The fibre lengths were measured with an optical time domain reflectometer made by Opto-Electronics, Inc. With this device a short (150ps) laser pulse is injected into the fibre via a directional coupler. Light reflected from the tip of the fibre is detected and its arrival time compared with the injection time. Using sampling and averaging techniques the device is able to measure the fibre length with an accuracy of a several picoseconds. It is not practical to measure the lengths of a fibre with a ruler as this requires removing the fibre from the experiment. The fibre lengths were also changed frequently to allow for the expected arrival times of the signal. The target fabrication technique resulted in an inability to predict accurately the fibre position in the target. These were measured after the target was drilled, just prior to inserting the fibres.

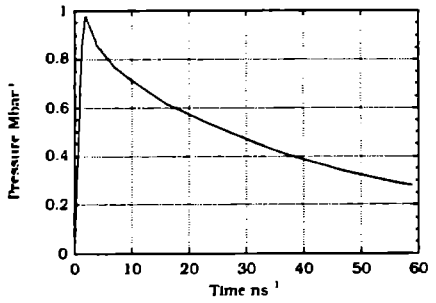


Figure 3. Simulation results of the pressure at the target surface.

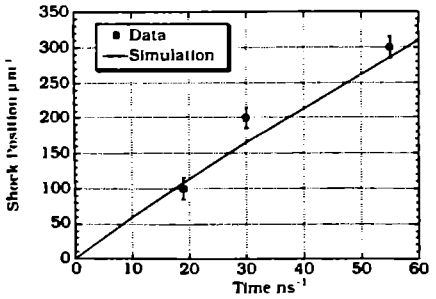


Figure 4. Simulation and experimental results of the motion of the shock front.

## RESULTS

Figure 1 shows typical raw data from the streak camera. The fall in the recorded intensity of the light reflected from the fibre tip when the shock arrives can be seen clearly. The background light level is due to reflections from various connectors in the system. This could be improved by using fibre splicing techniques instead of couplers. On some shots, however, after the signal initially falls there is a rise in signal level. This was not observed in earlier experiments where a narrow band (832nm) filter was placed in front of the detector. It is likely that this is light emission from the shock. Such emission has been observed in other shock experiments performed at LANL.

The results obtained for the shock velocity position as a function of time were compared with simulations with LASNEX performed at LANL. Whilst this work is still under way some initial results are shown in figures 3 and 4. Figure 3 shows the simulated pressure at the surface of the target as a function of time. Figure 4 using the same simulation shows the shock position as a function of time with the experimental data superimposed. Good agreement can be seen implying that the pressure time history at the target surface is reasonable. An absorption coefficient of 80% was used in the simulation along with the measured laser temporal history and measured focal spot size.

## CONCLUSIONS

We have shown that the technique although still in need of some refinement is capable of providing accurate information regarding the velocity of shocks inside materials. With more channels it will be possible to measure shock acceleration and coalescence.

# STUDY OF INSTABILITIES IN LONG SCALELENGTH PLASMAS WITH AND WITHOUT LASER BEAM SMOOTHING TECHNIQUES

T. Afshar-rad, M. Desselberger, L. Gizzi, F. Khattak and O. Willi[1]
and A. Giulietti[2]

[1]The Blackett Laboratory, Imperial College of Science, Technology and Medicine, London SW7 2BZ, U.K.

[2]Istituto di Fisica Atomica e Molecolare del C.N.R., 56100 Pisa, Italy

## INTRODUCTION AND BACKGROUND

The interaction of intense laser light with large underdense plasmas is of great interest for inertial confinement fusion since fusion pellets will be surrounded by large plasma coronas. Under these conditions various parametric instabilities such as Stimulated Brillouin Scattering (SBS), Stimulated Raman Scattering (SRS) and laser beam filamentation may be very effective in reducing the laser-plasma coupling efficiency, in the production of high energy electrons and in the nonuniform heating of the plasma corona. To simulate fusion conditions, plasmas with scalelengths of up to 1mm were produced by focussing four green laser beams of the CLF high power VULCAN laser system onto thin foil targets in a line focus configuration. A delayed green laser beam was focussed axially into the preformed underdense plasma with an electron temperature and density of about 0.5 keV and 0.1 $n_c$ respectively. The levels of SRS and SBS generated were recorded [1]. Laser beam filamentation and whole beam self-focusing was clearly observed [2,3]. Further, direct experimental observations showed that a significant level of the SRS and SBS were being generated in the filamentory structures [4,5]. When the incident laser beam was smoothed either by Random Phase Plate Arrays (RPPA) or Induced Spatial Incoherence (ISI) a significant reduction in the absolute levels and the virtual suppression of filamentation was observed [5-7].

## PRESENT EXPERIMENTAL INVESTIGATION

In this contibution experimental results of a recent investigation (February,1990) are reported. The preformed plasma was again formed by a line focus configuration using four heating beams irradiating a thin aluminium foil target (700nm thick, 0.7mm long, 0.3mm wide). However, in this experiment the heating beams were also smoothed by ISI in contrast to previous measurements in order to produce a more uniform preformed plasma. The two pairs of opposing green laser beams were smoothed using an ISI and RPPA combination and superimposed in a line focus configuration. Typical irradiances of $10^{14}$W/cm$^2$ were used. Either an ISI smoothed infrared (1.05 $\mu$m) laser beam or a broadband beam (the ISI beam with the echelons removed ) delayed by 2.2 ns was focussed axially into the plasma. An extensive set of diagnostics was used to investigate the plasma conditions of the preformed plasma and the nonlinear interaction of the laser beam with the plasma.

Measurements were made of the absolute levels of SBS backscattering with the broadband beam ($\Delta\omega/\omega$ = 0.1%) or with an ISI laser beam to study the effect that spatial incoherence played in the reduction of the backscattered instabilities. At the time of interaction the nominal electron density was about 0.3 $n_c$ ($n_c$=1.1x10$^{21}$ cm$^{-3}$ is the critical density for the infrared laser light) and the electron temperature was about 500 eV of the preformed plasma. The uniformity of the preformed plasma was investigated transversely to the exploding foil target by using optical Moire deflectometry techniques with a probe wavelength of 350 nm. The density profile was also measured interferometrically with 350 nm probe beam propagating along the axis of the preformed plasma. The electron temperature of the plasma was obtained from time resolved x-ray streak spectroscopy. The backscattered Brillouin signal generated by the interaction beam was imaged out via the incident focussing lens onto a calibrated photodiode. In addition, time resolved SBS spectra were recorded with a S1 optical streak camera. A four frame x-ray pinhole camera with a gating time of about 150 ps was used to observe the x-ray emission of the preformed plasma and of the interaction beam.

Figure 1 shows the absolute levels of SBS backscattering for the ISI and broadband interaction beams as a function of the incident irradiance.

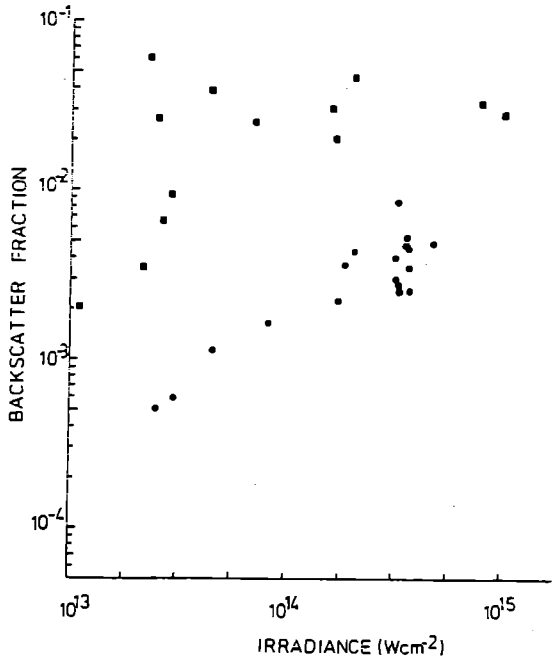


Fig. 1. Variation of SBS backscatter fraction with average irradiance for an ISI (illustrated by the solid circles) and broadband (squares) interaction beam.

The focal spot of the interaction beam was 140 $\mu$m in diameter and was kept constant for all the data shots. For the broadband laser beam a threshold at an irradiance of about 3x10$^{13}$ Wcm$^{-2}$ is observed with a saturation level between 2 to 6% of the incident laser energy. For the ISI interaction beam an exponential behaviour is seen with an average SBS value of 0.5% at an irradiance of 7x10$^{14}$ Wcm$^{-2}$. The SBS backscattering levels are significantly higher than observed in a previous experiment [4,5] in which a green interaction beam was used, the plasma was less uniform and the electron density was lower (by about a factor of 3) during interaction. However, SBS levels were also recorded in the present experiment for thinner targets (500nm thick). For these targets a similar electron density ( 0.1$n_c$) as used previously is expected. However, the level of SBS did not vary significantly when compared with thicker targets. The estimated electron density is consistent with backscattered Simulated Raman Scattering (SRS) which

was detected by diodes filtered with narrowband interference filters. For the 700nm targets virtually no SRS backscatter is observed. On the other hand, clear SRS signals (at a wavelength of about 1.5 $\mu$m) are seen with the 500 nm. These results indicate that the electron density was below 0.25 $n_c$ during interaction.

For some of the data shots anomolously high levels of SBS (larger by about a factor of 8 compared to the data shown in fig.1) were observed when an ISI interaction beam was used. On these shots the x− ray framing camera images as well as the optical probing diagnostic indicated that whole beam self−focusing may have occurred. A channel like structure was observed in the x−ray emission with a diameter of about 40 $\mu$m. In addition, a substantially higher transmitted laser energy was measured at the output plane of the the preformed plasma.

In conclusion the absolute levels of SBS in long scalelength underdense homogenous preformed plasmas were measured for a broadband laser beam and a beam smoothed by ISI which interacted axially with the preformed plasma. Whole beam self−focusing of the ISI interaction beam may have been observed for some of the shots.

REFERENCES

1. O. Willi, D. Bassett, A. Giulietti and S. Karttunen, Opt. Commun. 70, 487 (1989).

2. S. Coe, T. Afshar−rad and O. Willi, Opt. Commun. 73, 299 (1989).

3. S. Coe, T. Afshar−rad and O. Willi, submitted to Europhys. Lett.

4. T. Afshar−rad, O. Willi, S. Coe, To be published.

5. O. Willi, T. Afshar−rad, S. Coe and A. Giulietti, Phys. Fluids, accepted.

6. S. Coe, T. Afshar−rad, M. Desselberger, F. Khattak, O. Willi, A. Giulietti, Z. Q. Lin, W. Yu and C. Danson, Europhys. Lett. 10, 31 (1989).

7. C. Danson, R. Bann, D. Pepler, N. Rizvi, I. Ross, P. Rumsby, R. Jackson, S. Coe, T. Afshar−rad, M. Desselberber and O. Willi, LFC Annual Report RAL−89−045, 141 (1989).

# MEASUREMENT AND ANALYSIS OF RADIATION TRANSPORT IN LASER IRRADIATED TARGETS.

J. Edwards, V. Barrow, O. Willi and S.J. Rose[+]
Imperial College, London, UK.
[+]Rutherford Appleton Laboratory, UK.

The transport of radiation, in particular of soft X-rays, is a major energy transport mechanism in laser produced plasmas when short wavelength lasers are used. The use of short wavelength light is advantageous for major programmes such as Inertial Confinement Fusion (ICF) since the production of suprathermal electrons is reduced and the laser radiation is absorbed more efficiently. However, a significant fraction of the absorbed laser energy is converted into soft X-ray radiation because the absorption takes place at high electron densities. Recent measurements showed that up to 80% of the incident laser energy can be converted into soft X-ray radiation for 0.26 $\mu$m laser light incident on gold targets [1,2]. Consequently, an understanding of radiation transport in plasmas under these conditions is very important for the interpretation and analysis of the plasma dynamics. Here the first temporally and spectrally resolved observations of soft X-ray radiation transported through plastic foil targets are described.

Thin foil plastic (parylene, $C_8H_8$) targets 0.1 $\mu$m and 5 $\mu$m thick, overcoated with 0.1 $\mu$m of gold on the front side were irradiated with a single VULCAN laser beam. The frequency doubled green ($\lambda$ = 0.53 $\mu$m) laser light 700 ps in duration was focussed onto target with an F/2.5 aspheric doublet lens producing an irradiance between $1x10^{14}$ and $5x10^{14}$ $Wcm^{-2}$ at the target surface. The focal spot size was measured with an X-ray pinhole camera filtered for the 1.5 keV energy range and was typically 400 $\mu$m (FWHM) in diameter. The soft X-ray radiation transported through the rear side of the thin foil targets was time resolved using a grazing incidence flat field spectrometer coupled to an XUV streak camera. The instrument used a 2400 lines per millimetre grating. The temporal and spectral resolution was 50 ps and 0.2 Å respectively. The soft X-ray radiation was reflected into the spectrograph by a highly polished silica mirror set at a grazing incidence angle of 2.5° acting as a high frequency cut off filter for radiation above approximately 1 keV.

Numerical simulations were carried out for a 5 $\mu$m target using a multi-group radiation transport model[3] coupled to the 1-D Lagrangian hydrodynamics code MEDUSA. The radiation transport calculation uses 116 energy groups in the 0 to 100 keV energy range with a resolution of 10 eV below 800 eV. Because the radiation field is not isotropic, the model distinguishes between inwardly and outwardly moving photons and each group is transported separately. Group averaged Planck mean opacities are calculated at the material temperature, in-line with the hydrodynamics using an average-atom screened-hydrogenic approximation in LTE, based on the model XSN[4]. Only bound-free and free-free transitions are considered in the model. The behaviour of the laser irradiated thin gold layer was not calculated in the code because of the marked non-LTE behaviour of the X-ray emitting region of the gold plasma which could not be accurately calculated by our LTE model. Therefore, several assumptions are made about the emission from the gold at time t and frequency $\nu$. Firstly, because the spectrograph is not absolutely calibrated, it is assumed that the spectrum at the peak of the radiation pulse is Planckian characterised by a radiation temperature $T_{RMAX}$ with additional components due to M, N and O shell emission bands consistent with measurements[5]. Secondly, it is assumed that the radiation is isotropic in the half plane because the focal spot diameter is very much larger than the target thickness. The radiative flux $F(\nu,t)$ incident on the plastic foil from the heated gold layer is then taken to be

$$F(\nu,t) = \pi\, B(T_{RMAX},\nu)\, f(\nu,t)$$

where f is the measured temporal behaviour of the radiation at frequency $\nu$ and time t and B is the Planck function.

Small inaccuracies in the gold spectral emission do not cause any serious errors in the material heating. Simulations were carried out with and without the inclusion of M, N and O emission bands. No signifiant differences in the overall predicted results were seen. $T_{RMAX}$ was estimated to be 115 eV from absolute measurements which were taken under similar experimental conditions. This corresponds to an overall laser to X-ray conversion efficiency of approximately

Figure 1. Experimental (right) and predicted spectra from the rear of a 5 $\mu$m CH target coated with 0.1 $\mu$m of gold.

12% towards the rear which is consistent with spectra taken on ultra thin 0.1 $\mu$m plastic substrates and other measurements[6]. Simulations were also carried out with values of $T_{RMAX}$ of 100 and 130 eV corresponding to X-ray conversion efficiencies of 7 and 20%, respectively.

Figure 1 shows a time resolved X-ray spectrum (right) in the 15 to 70 Å spectral wavelength range of the radiation transported through the rear of a 5 $\mu$m thick plastic foil target which was overcoated with 0.1 $\mu$m of gold on the surface facing the laser beam. The gold layer was irradiated at an intensity of $1.5 \times 10^{14}$ $Wcm^{-2}$. Note the clear presence of a sharp edge-like feature (A) at around 45 Å in the XUV spectrum and the apparent early turn on of radiation on the longer wavelength side of (A). In addition, away from the edge, the emission of radiation towards longer wavelength appears to be progressively retarded with respect to that at shorter wavelength. Finally, the position of (A) appears to move gradually towards higher energies later in time as the foil becomes heated. The maximum shift of this feature is measured to be 0.9 $\pm$ 0.2 Å or 5.5 $\pm$ 1.2 eV. For comparison a 3-D plot (left) of the predicted intensity of radiation in units of $Wm^{-2}Å^{-1}$ into $2\pi$ str transported through a 5 $\mu$m plastic foil target as a function of time and wavelength for $T_{RMAX}$ = 115 eV. At each time spectral emission profiles as a function of wavelength were obtained from a 1-D integration of the radiative transfer equation through the heated thin foil target at the mid point of each energy group in the 10 to 70 Å wavelength region. In common with the experiment, the simulations show a clear edge which is due to the carbon K-edge, the early turn on of radiation just below (in energy) and well above the edge, progressively retarded emission of radiation towards longer wavelength away from the edge and a gradual shift in the edge position as the foil is heated.

Figure 2 (left) shows the variation of the intensity as a function of wavelength of the experimental data of figure 1 close to the peak emission. The shaded band shown results from the envelope formed by several densitometer traces taken within $\pm$ 150 ps of the peak of the emission. The time interval of $\pm$150 ps is the estimated uncertainty in the peak of the emission from the gold as the time resolved spectrograph was not absolutely timed. The relative response of the instrument was estimated by taking the various components such as filters, mirror, grating and streak camera photocathode into consideration. In comparison with the experimental data, the predicted rear side spectra for a 5 $\mu$m plastic foil target at the peak of the radiation pulse for three different values of $T_{RMAX}$ (100, 115 and 130 eV) are shown in figure 2. Note the significant shift in the carbon K-edge for the different temperatures. In addition, the assumed soft X-ray spectrum for 115 eV incident on the plastic target is shown in figure 2.

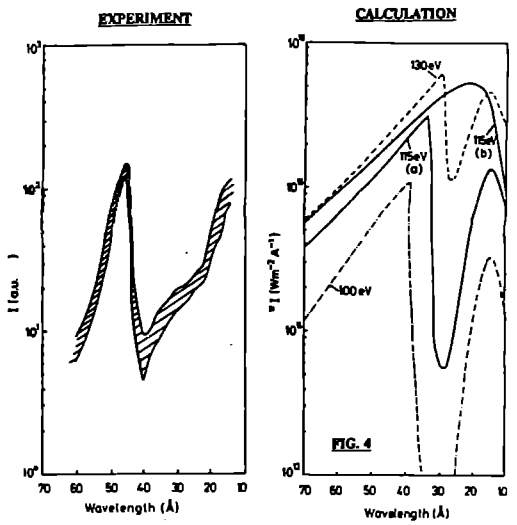


PREDICT EDGE POSITION AT LOWER WAVELENGTH

Figure 2. Experimental spectrum from the rear of a 5$\mu$m CH target near peak emission and the predicted spectra for different X-ray conversion efficiencies at the same time. Curve marked (b) is the assumed incident spectrum from the gold layer for a radiation temperature of 115 eV.

The position of the edge feature in the experimental data is at approximately 45 Å which corresponds to the cold carbon K-edge position. Maximum shifts of about 1 Å were seen during the heating phase. In contrast, much larger shifts of the carbon K-edge positions are predicted in the simulations depending on the temperature of the heated material. For example, a shift of more than 10 Å towards shorter wavelength is seen for a peak radiation temperature of 115 eV.

Although the code calculations are in overall agreement with the experiment, the small apparent shift in the experimental edge position is not predicted by any of the values of $T_{RMAX}$ in figure 2. Indeed, it is only predicted if a value of $T_{RMAX}$ = 75 eV is used. In this case the radiation does not burn through a 5 $\mu$m thick target, leaving a layer of cold material towards the rear of the foil. This cold layer attenuates strongly in the wavelength region between 24 and 44 Å which is contradictory to the experimental observations. In addition, a radiation temperature of 75 eV corresponds to a conversion efficiency of only 2% which is well below the conversion efficiencies published for green laser light at an irradiance of around $10^{14}$ $Wcm^{-2}$. It is unlikely that a photoionization K-edge will be predicted in the position observed experimentally, for the predicted plasma conditions, even when a more detailed bound-free opacity spectrum is used. The ionization energies of K-shell electrons from Be-, Li-, He- and H-like isolated carbon ions have been calculated to be 339, 360, 391 and 490 eV respectively using a multi-configuration Dirac-Fock atomic physics code [7]. (For comparison, the model used here in the radiation transport calculation gives 328, 360, 394 and 490 eV. These values were obtained by calculating the eigenvalue of a K-shell electron using the screening coefficients, employed in our model, for the respective ions in their ground states. The abundance of lower ionization stages in the target for the predicted conditions is negligible). The continuum lowering can be estimated from the ion sphere model as $3Ze^2/2R_0$, where $R_0$ is the ion sphere radius. For carbon, this can be written approximately as $13Z[\rho(gcm^{-3})]^{1/3}$ eV. Taking the typical plasma conditions near the peak of the pulse, $\rho \approx 0.1$ $gcm^{-3}$ and $Z \approx 5$, the continuum lowering is approximately 30 eV. Therefore, for all ionization stages $C^{2+}$ to $C^{5+}$, the K-edge positions are predicted to be above 310 eV (i.e. below 40 A), in contrast to the observed edge feature at a wavelength closer to 45 A. We suggest that the small shift in the edge position may be due to the filling in of the photoabsorption below the shifted K-edge by line absorption. The edge in figure 1 would then correspond to the side of a strong carbon absorption line. This explanation

is supported by the plasma conditions predicted to exist in the foil. At the peak of the pulse, the density in the target is approximately constant at 0.1 $gcm^{-3}$ and the temperature varies from approximately 100 eV near the front of the foil to just below 30 eV at the rear. The average degree of ionization calculated by the model decreases from just over 5 at the front of the target to approximately 3.5 at the rear. Therefore, a large number of bound-bound transitions (including satellites) will exist in the soft X-ray energy region due to an abundance of several different ionic species in the plasma. The closest carbon resonance transition to the experimentally observed edge feature is the He-like $1s^2$-1s2p line at 40.268 Å. Improvements to the opacity calculations to include both the distribution of ionic states around the average in both the bound-free and bound-bound transitions is underway to assess whether this is the correct explanation for the discrepancy. A further possible explanation is that the bright feature below 45 A in figure 1 originates from the gold plasma. This would correspond to emission from the gold O shell . However, time resolved spectra of gold emission through ultra thin plastic foil targets 0.1 $\mu$m thick, which are too thin to significantly affect the transmitted radiation, suggest that this is not the case.

In summary, radiation transport through thin foil plastic targets has been studied both experimentally and computationally. The simulations include multi-group radiation transport and an average atom opacity calculation which are performed in-line with the hydrodynamics. Overall agreement is obtained between the experimental observations and the simulations. In detail, however, the small shift in the carbon K-edge observed in transmission during the heating is not predicted theoretically. This may be due to one,(or some combination) of the following: an overestimate of the material heating; continuum lowering; bound-bound transitions; structure in the gold emission.

REFERENCES


1. R L Kauffman, Lawrence Livermore National Laboratory Annual Report 85, ed. by M L Rufer and P W Murphy, UCRL-50021-85, 1986.
2. R Kodama, K Okada, N Ikeda, M Mineo, K A Tanaka, T Mochizuki an C Yamanaka, J Appl Phys 59, 3050 (1986).
3. A description of an older version of the model can be found in RAL report, RL-83-040 (1983) by S Rose and R G Evans. The description of the new model will be presented for publication shortly.
4. W A Lokke and W H Grasberger, Lawrence Livermore National Laboratory Report, UCRL-52276, 1977.
5. K Eidmann and T Kishimoto, Appl Phys Lett 49, 377 (1986).
6. W C Mead et al, Phys Fluids, 26, 2316 (1983).
7. I P Grant, B J McKenzie, P H Norrington, D F Mayers and N C Pyper, Comp Phys Comm, 21, 207, (1980).

# VUV PROBING OF PLASMA JET STRUCTURES IN THE SUPERCRITICAL PLASMA REGION

T. Afshar-rad, M. Desselberger, L. Gizzi and O. Willi

The Blackett Laboratory, Imperial College, London.

## INTRODUCTION AND BACKGROUND

In order to achieve the symmetric compressions vital for laser fusion, it is of paramuont importance to study the significance of thermal instabilities. These instabilities may form jet structures which, in turn, may affect target symmetry. This asymmetry may seed other instabilities such as Rayleigh-Taylor.

After the first experimental evidence of jet formation was provided by us (1) from experiments performed at the CLF in the early 1980's, considerable theoretical interest was stimulated. A number of mechanisms for the formation of the plasma jet structures have been proposed in theoretical studies (2-7). These are mainly unstable processes caused by interactions between the electrons and magnetic fields of a plasma and include: the collisional Weibel, thermomagnetic, Ohmic and Nernst effects (for a review of these see reference (2) and the references therein). Additionally, a non-thermomagnetic effect - Radiation Cooling - has been proposed by R. Evans (RAL).

Until now, no experiment has clearly identified the instability mechanism(s), nor has any evidence been obtained of the effect of the instabilties on the ablation rate or on thermal smoothing. Of particular importance to the ICF programme is the question of whether the jets exist only in the subcritical region (all experimental work until now has provided information only about the subcritical region) or whether they extend into the supercritical regions, where their effects are potentially far more detrimental.

The experiment described below was performed recently at the CLF and sought to address the issues described above.

## EXPERIMENTAL INVESTIGATIONS

The novel experimental technique used is based on only recently available multilayered mirror technology for use in the VUV spectral region. The experimental arrangement used is shown in Fig. 1. As is well known, optical probing is limited to the sampling of relatively low density regions $n_e < n_{crit}$, since the optical probe rays are refracted out of the imaging optics by the steep plasma density gradients. Shorter wavelengths are refracted less and simulations show that VUV probe wavelengths ($\lambda$ approx. 100A) will, in combination with the imaging technique used in this experiment, effectively probe the conduction region $n_e > n_{crit}$ up to several times the critical density. Further, this imaging system was combined with the novel technique of Soft X-ray/VUV Moire Deflectometry to quantitatively measure plasma density gradients. Image shadowgraphy was used to determine the presence of plasma jet structures.

The backlighter source was generated by irradiating a Ni target at typical intensities of $5x10^{14}$ $Wcm^{-2}$. The main or object targets used for the density gradient investigations were planar CH disc targets at typical irradiances of $5x10^{13}$ $Wcm^{-2}$. Simulations were carried out prior to the experiment using the 1-D Lagrangian hydrocode MEDUSA and a radiation transport code to determine expected density scalelenghts, refraction angles and attenuation of the backlighter signal. For the plasma jet structure investigations, 50$\mu$m Al wires were used at irradiances of $5x10^{13}$ $Wcm^{-2}$. Again, calculations made prior to the experiment indicated that the refraction due to the plasma jet structures was detectable by the proposed system. The imaging system consisted of spherical multilayered mirrors operating at a wavelength of 180A with a bandwidth of 20A.

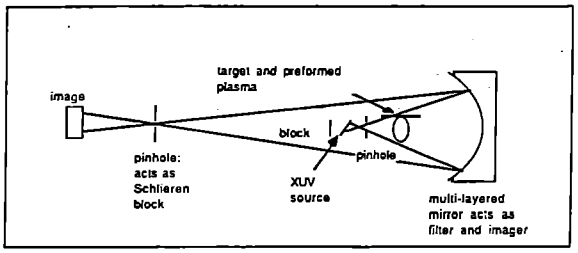


Fig. 1: Experimental Arrangement

The principal result of this experiment is that plasma jetting was clearly observed under several different conditions. These images provide the first evidence of their existence in the conduction region. One such image is shown in Fig. 2.

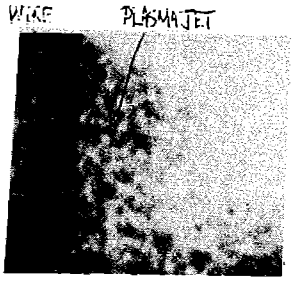


Fig.2: XUV image of Al wire showing jet structure

It must be stated that in this experiment, no attempt was made to optimise the technique in terms of spatial and temporal resolution or VUV source brightness. The feasibility of the technique, however, has been clearly demonstrated by the results.

## SUMMARY AND CONCLUSION

The novel and quantitative VUV probing technique described has been demonstrated to be experimentally feasible. Further refinements in terms of spatial and temporal resolution have been developed and much further work in applying this technique remains.

## REFERENCES

1. "Self-generated magnetic fields in laser produced plasmas," presented at the 7th Annual Conference in Plasma Physics, Cambridge, UK (1980); O. Willi, P. Rumsby, C. Hooker, A. Raven and Z. Lin, Optics Communications 41, 110 (1982).
2. M.G. Haines, Phys. Rev. Lett. 47, 917 (1981) and references therein.
3. R.G. Evans, J. Phys. D Appl. Phys. 14, L173 (1981)
4. I. Limpoukh and V.B. Rozanov, Sov. J. Quantum Electro 14, 955 (1984)
5. M.G. Haines, Can. J. Phys. 64, 914 (1986)
6. E.M. Epperlein, Plasma Physics and Contr. Fusion 27, 1027 (1985)
7. E.M. Epperlein and A.R. Bell, Plasma Physics and Contr. Fusion 29, 85 (1987)

# STUDIES OF RAYLEIGH TAYLOR INSTABILITY BY ALPHA PARTICLE BACKLIGHTING

A P Fews, M J Lamb*, M Savage*

University of Bristol,
* Queens University Belfast,

## INTRODUCTION

We have performed an experiment to investigate Rayleigh Taylor instability in accelerated planar foils by an α-particle backlighting technique. This has several unique advantages over more conventional methods.

In this technique, an α-particle source from a DT implosion produces a bright pulse of particles which are used to shadow a separately driven foil. Each α-particle loses range, determined by the local thickness of the foil at the time of passage of the particle.

Since both the position and range of each particle are individually determined, any variation of thickness, even of sub micron scale, will be recorded. In addition, a shadow image of the driven foil will be produced, of spatial resolution limited by source size and multiple coulomb scattering in the driven plasma.

Previously, the thickness distribution thus recorded was blurred due to Doppler broadening of the spectrum, but this effect has now been eliminated due to maximum entropy unfolding of the transmitted foil spectrum from the source spectrum. In the future we hope to measure the source shape separately, which will allow the possibility of unfolding the foil image from the source size and scattering effects described above. This would then offer the possibility of obtaining spatially and spectrally sharp images of the foil at the instant the α-particles passed through. In addition, other charged particles (eg protons and tritons) would be used. Since these have different times of flight, it would be possible to obtain several images of the same foil at different times into the drive.

## EXPERIMENTAL

Fig. 1 shows the basic layout. The foil is driven towards the α-source, and particles travel through the foil to the CR-39 detector. The system is entirely co-linear - the drive beam passes through the CR-39 which is placed over the backlight lens. The α-particle data is assembled into 3D images - (2 spatial directions by 1 thickness dimension), and moments of these images may then be plotted (eg image of mean thickness, or standard deviation of thickness). In general these images show a feature at the edge of the foil where the particles passing through the foil overlap with those going round the edge of the foil. In addition, several of the driven foils show large scale features, which must correspond to large scale non-uniformities in the drive beam.

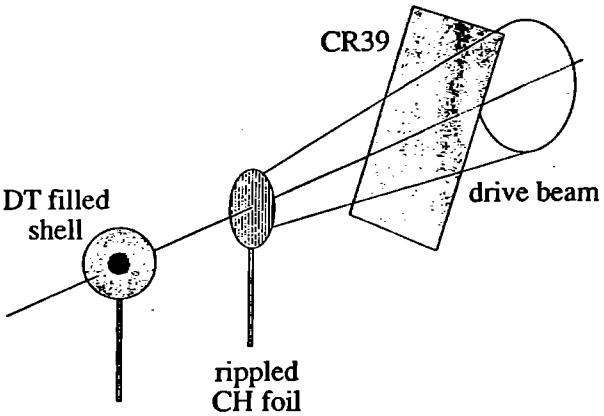


Figure 1. The basic experimental configuration. Particles from the implosion shadow the foil and are detected in the CR-39, placed over the backlighting lens, ensuring the detection axis is co-linear with the drive axis.

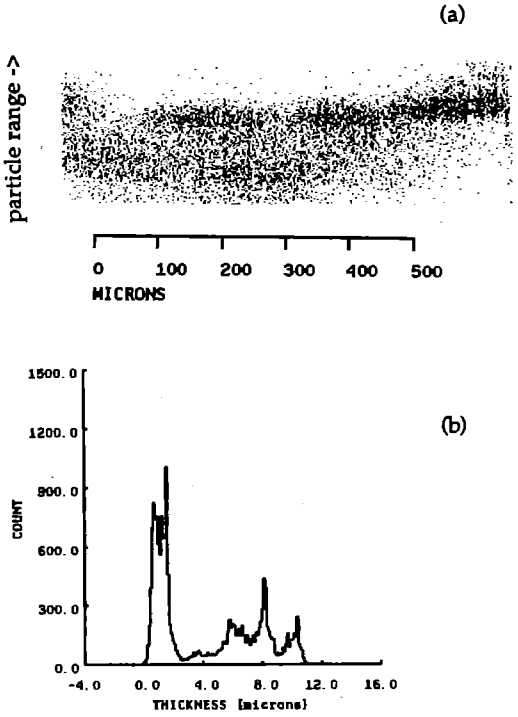


Figure 2. 2(a) shows a line section through the shadow image. The horizontal direction is position across the foil, and the vertical direction is particle range. Lower points correspond to low range (high foil thickness). 2(b) is the thickness spectrum from the centre of this foil, unfolded from the source spectrum.

## RESULTS

Some typical results are shown in Figure 2. Fig 2(a) shows a line section through the shadow image. The horizontal direction is position across the foil, and the vertical direction is particle range. Lower points correspond to low range (high foil thickness). At the right hand side of the plot, the distribution is tightest, corresponding to particles direct from the source. Throughout the rest of the plot a wide distribution can be seen, indicating a very broad distribution of

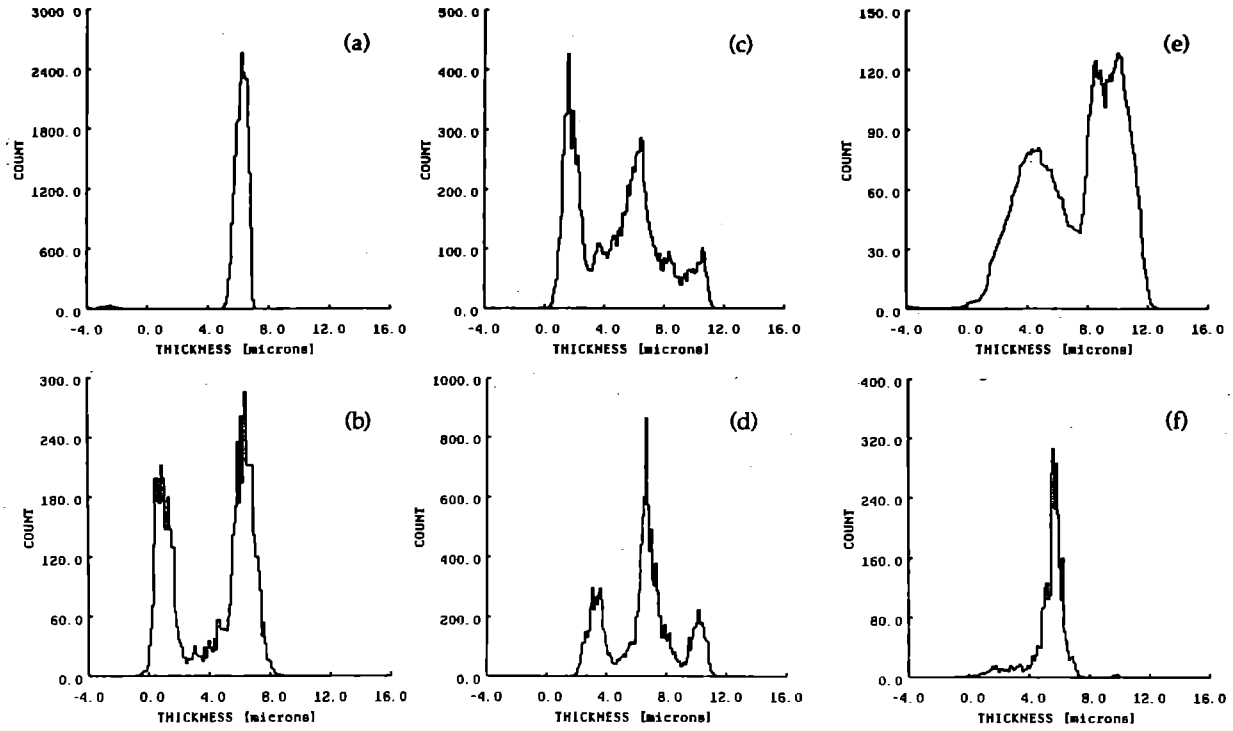


Figure 3. Some thickness spectra. 3(a) is an undriven planar foil. 3(b) is an undriven foil with deep cuts, producing two separated peaks, as expected. 3(c) is a foil with 1μm seed probed at 1.0ns. 3(d) is as for (c) but probed at 0.5ns. 3(e) is a driven planar foil driven similarly to (c), probed at 2.0ns. 3(f) is a driven planar foil, probed at 2.0ns , as (e), but driven with random phase plate illumination.

thicknesses, some parts of the foil having been thinned away to zero. The foil was of initial thickness 8μm with 1μm depth seed modulations of period 20μm. The particles probed the foil 1.5 ns into a drive pulse of intensity $1.1 \times 10^{13}$ W.cm$^{-2}$. Two regions may then be sampled : the thickness spectrum in the centre of the foil, and the particle source spectrum outside the foil. These can then be unfolded with a maximum entropy technique to produce a spectrally sharp thickness spectrum. The result of this is shown in Fig 2(b). Several features can be clearly seen. A large peak close to zero thickness indicates that parts of the foil have thinned away to zero. A small peak at the original foil thickness (8μm) indicates some regions of the foil which have probably not been ablated/driven. Some features to either side of this show that regions of the foil have been thickened above the initial thickness and others thinned.

The principle results from this experiment are these unfolded thickness spectra, which are able to give a unique measurement of the foil conditions. Fig. 3 shows some typical spectra. Fig 3(a) is an undriven planar foil. Fig 3(b) is an undriven foil with 6μm deep cuts, producing two separated peaks, exactly as expected. The width of these peaks is determined by effects of target thickness over the region sampled, and by limitation of the unfolding technique caused by the source width (exceptionally large in this case) This latter effect should be eliminated in the next experiment by using random phase plate illumination on the implosion drive. Fig.3(c) is a foil with 1μm seed probed at 1.0ns. Fig 3(d) is as for (c) but probed at 0.5ns. Note that Fig 2(b), Fig 3(c) and Fig 3(d) form a sequence of shots probed with the same intensity on the same foil type, but probed at 1.5, 1.0 and 0.5 ns,respectively, into the probe. It can be seen clearly that as the probe time gets later, the peak at the original thickness of 8 μm decreases in height, and the peak close to zero thickness increases. Fig 3(e) is a driven planar foil driven similarly to Fig 3(c), probed at 2.0ns. The driven planar foils do not show a peak at zero thickness, and reach the same induced modulation at a later time than the seeded foils. However, if the planar foils were driven with a smooth drive, then no mass modulation should have been observed due to Rayleigh-Taylor instability.

Fig 3(f) is a driven planar foil, probed at 2.0ns , as Fig 3(e), with the same probe intensity, but driven with random phase plate illumination. This was the only RPP shot, all the other driven non phase plate shots showing a large modulation. In contrast, this plot shows no increased modulation, as expected from a driven foil with no seed modulations. There is, however, a small tail to the left of this peak, which is a feature not seen on the undriven foils. This could indicate some small residual spikes in the RPP focal spots.

These results may be interpreted as showing that unsmoothed beams and the foil seeding both have a significant effect in inducing mass modulations in the foils.To observe the Rayleigh-Taylor instability, it will be necessary to use smooth beams on seeded foils. Non uniformities in the drive of unsmoothed beams always burn through regions in the foil whilst other regions seem unmoved from their initial thicknesses.

We plan to repeat this experiment, using RPP beams to drive both the foil and the implosion, and hope to achieve sharp spectra, and reasonable spatial resolution.

# LASER COMPRESSION OF HIGH ASPECT RATIO DEUTERIUM TRITIUM FILLED SHELLS.

A P Fews[1], M J Lamb[2], M Savage[2], T A Hall[3],
Z Ahmad[3],E Koresheva[4],Y A Zakharenkov[4], A.Ridgeley[5]
[1]University of Bristol
[2]Queen's University Belfast
[3]University of Essex
[4]Lebedev Institute,Moscow
[5]Rutherford Appleton Laboratory.

## INTRODUCTION

We have carried out a systematic investigation of implosions of high aspect ratio DT filled shells, using both conventional and random phase plate (RPP) drive. Maximum alpha particle yields of $3 \times 10^9$ have been achieved. A primary aim of this work is to develop such implosions as a source of thermonuclear particles in order to probe other laser produced plasmas with application to studies of Rayleigh–Taylor instability and to measurements of plasma stopping power.

## EXPERIMENTAL DETAILS

The targets were typically 600 $\mu$m diameter glass shells of 1$\mu$m wall thickness, and filled with 2–3 atmospheres of DT. Drive energies of up to 800J at $2\omega$ were used in pulse lengths

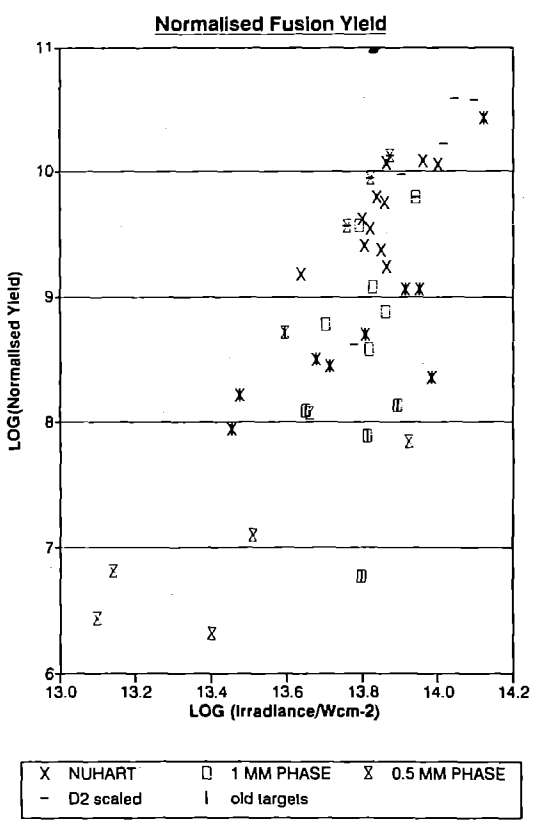


Figure 1. Scaled thermonuclear yield.vs Irradiance.

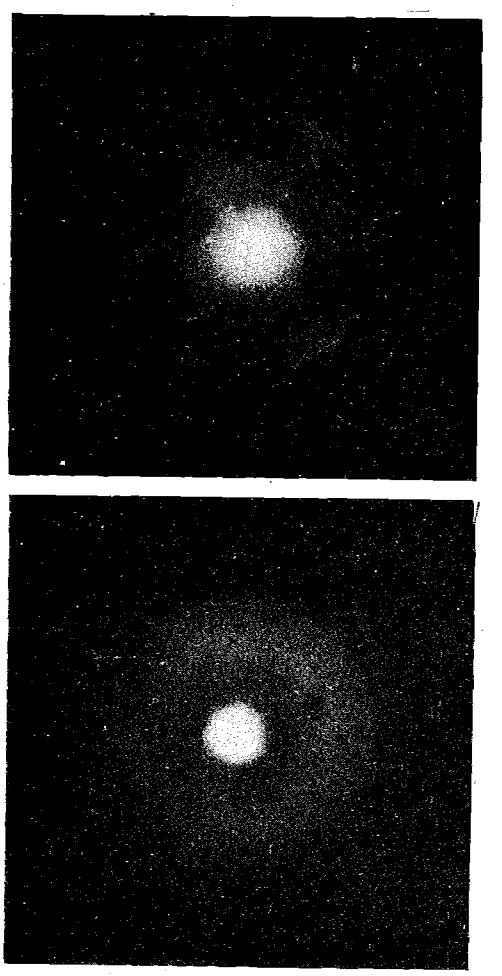

(a)

(b)

Figure 2. X–ray pinhole images. (a) NUHART,shell diameter 741 $\mu$m, (b) RPP 0.5mm zones, shell diameter 440$\mu$m.

600 – 900 ps. The implosions were diagnosed by a wide variety of diagnostics:

(a) Three near–orthogonal X–ray pinhole cameras.
(b) Three near–orthogonal alpha particle cameras viewing in the opposite directions to the X–ray cameras.
(c) A space resolving X–ray streak camera.
(d) Two space resolving X–ray spectrometers.
(e) Neutron scintillation counter.
(f) Alpha particle and proton energy spectrum measurement and yield measurement based on CR–39 plastic detector.
(g) Neutral particle detectors, discussed in section A3.6.

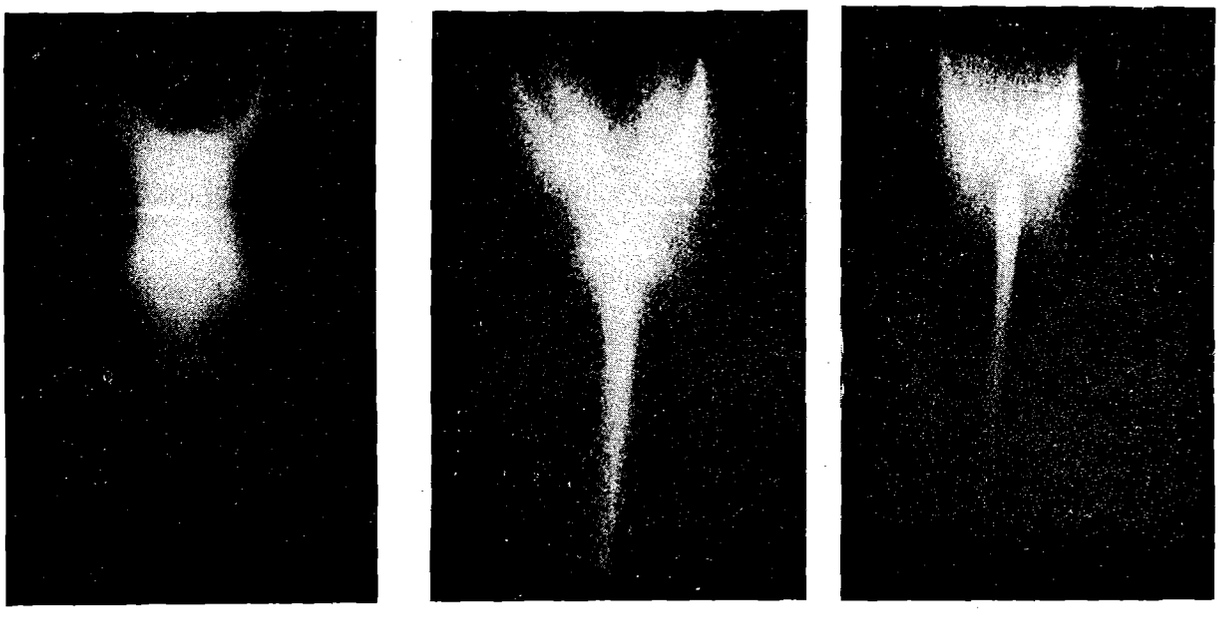

(a) (b) (c)

Figure 3. X–ray streak pictures. (a) NUHART, (b) RPP with 1mm zones, (b) RPP with 0.5mm zones. Space is horizontal, time is vertical.

## THERMONUCLEAR YIELDS

Thermonuclear alpha particle yields of $3x10^9$ have been obtained from NUHART mode implosions, and $6x10^8$ from RPP driven implosions. Proton yields of up to $1.2x10^8$ have also been observed in NUHART implosions of deuterium filled shells. These indicate that alpha particle yields of $10^{10}$ should be obtained from targets optimally matched to the available laser energy.

Fig. 1 shows the variation of thermonuclear yield, normalised to a standard target, plotted against average irradiance. Old targets refer to DT targets which had been stored in liquid nitrogen for 9 months. It can be seen that the higher yields were all obtained from the NUHART mode, and that random phase plate drive results in lower yields, both in absolute terms and in relation to that predicted by our model [1]. In fact the RPP data points lie below the NUHART line by approximately the factor of 20 which represents the enhancement of NUHART yields over conventional uniform drive.

## IMAGING

Fig 2 shows two examples of X–ray pinhole images. Fig 2(a) shows a typical image from a NUHART implosion. The wall emission from the focused beam spots can be clearly seen. Fig 2(b) shows the corresponding image from a random plate plate implosion. The drive in this case is nearly uniform producing weak wall emission, and a more uniform core.

The alpha particle images are described elsewhere (see section A3.3). Alpha particle and proton core images were obtained with spatial resolution 5–10$\mu$m, comparable to the X–ray pinhole images. These thermonuclear particle images were obtained by maximum entropy unfolding of penumbral aperture images. They show core sizes which are comparable to the hard X–ray cores seen, but the individual core shapes (X–ray and alpha particle) are not directly relatable. For most of the shots, three near orthogonal images were taken, and we hope to develop three dimensional reconstruction of these images in the near future.

## X–RAY STREAK IMAGES

Fig.3 shows examples of space resolved X–ray streak images showing the implosion dynamics. Fig 3(a) shows a streak image from a NUHART implosion. Emission from the collapsing walls and from the rather broad implosion core can be clearly seen. Fig 3(b) shows a X–ray streak from a RPP shot driven with 1mm zones, and Fig 3(c) an RPP shot driven with 0.5mm zones in the phase plate, giving the largest focal spot size. This latter image shows uniform wall emission with a compact central core – similar features may also be seen on both the X–ray pinhole and spectrometer images. The implosion times were well matched to the laser pulse duration.

SPECTRAL IMAGES

Fig.4 shows space resolved X–ray spectra from a series of shots showing H–like and He–like silicon line and continuum emission. The spatial magnification has been chosen to be unity so that each line feature in the spectrum is a complete monochromatic image of the source. Fig 4(a) shows a NUHART implosion, Fig 4(b) show a RPP implosion with 1mm zones, and Fig 4(c) shows a RPP implosion with 0.5mm zones giving a larger focal.spot size. The spatial structures observed in the H–like and He–like lines are distinctly different showing that they originate from different regions of the target. Note also the sharp core feature observed in the continuum emission in the RPP shots. A densitometer trace of Fig 4(a) is shown in Fig 4(d).

Fig.5 shows an example of alpha particle spectra from a NUHART implosion. Fig 5(a) shows a typical range spectrum. The distribution is comparatively broad, caused

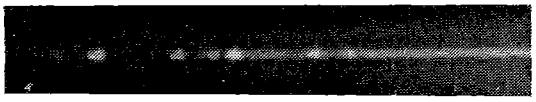

(a)

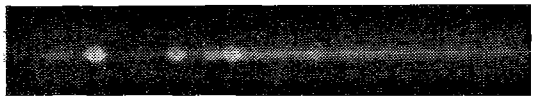

(b)

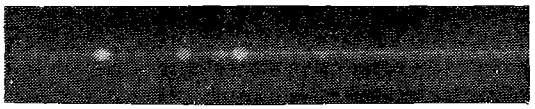

(c)

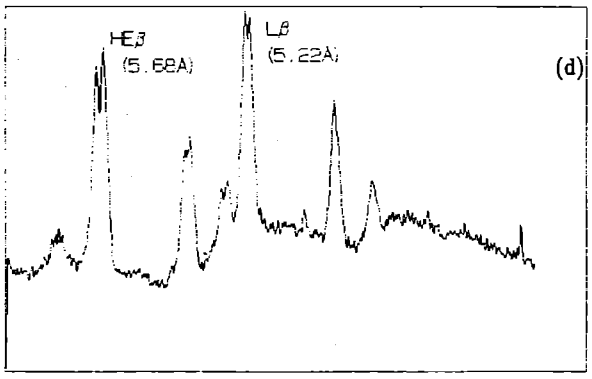


(d)

Figure 4. X–ray spectra from (a) a NUHART implosion, (b) a RPP implosion with 1mm zones and (c) a RPP implosion with 0.5mm zones in the phase plate. (d) shows a microdensitometer trace of (a).

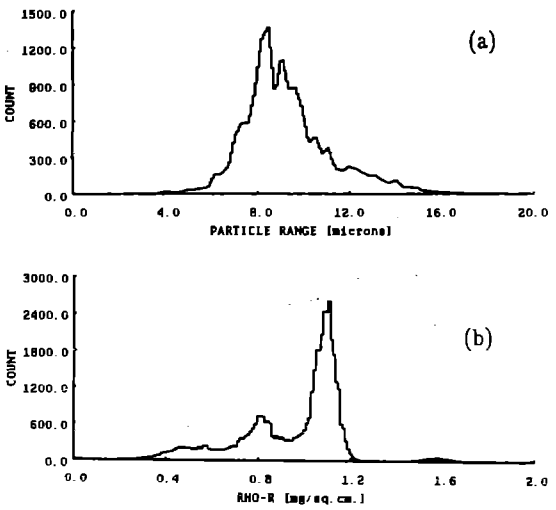


Figure 5. Alpha particle spectra from a NUHART implosion. (a) shows the range spectrum and (b) shows the corresponding $\rho$.R spectrum from (a) with the Doppler contribution unfolded.

by a high core temperature giving rise to a large Doppler width, and also to large scale non–uniformities in the imploded shell at the time it was probed by the escaping alpha particles. These two effects can be separated, by a maximum entropy unfolding of the measure alpha particle range loss spectrum from the (gaussian) Doppler contribution, which can be directly determined from the proton range loss spectrum because the proton width is six times the alpha particle width at a given temperature.Fig 5(b) show the result of unfolding Fig 5(a). The structure in the $\rho$.R distribution caused by the shell structure is much more clearly visible. In general, unfolded spectra from different directions on the same shot show the same central feature, but all have different shapes to the tail of the distributions, indicating large scale anisotropies in the imploded shell. These features are always present on the low range–high $\rho$.R side of the main peak. Spectra recorded on RPP shots give a lower core temperature and show less additional core broadening. Unfolded spectra from RPP shots show a small peak due to shell structure to the high range–low $\rho$.R .

REFERENCES

1. M H Key, M J Lamb, A P Fews et al, Optics Communications,71,184,(1989).

# THERMONUCLEAR PARTICLE IMAGING

A P Fews, M J Lamb*,M Savage*

University of Bristol,
* Queens University Belfast,

## INTRODUCTION

Images of thermonuclear particle emission from implosions of DT filled microballoons have been generated with spatial resolution 5-10 microns. Both α particle and proton images have been produced. Two separate techniques have been investigated: maximum entropy unfolding of penumbral images; and the use coded apertures of the "PNP" type. Superior results were obtained from the penumbral apertures and these will form the basis of future experiments.

## PENUMBRAL IMAGING

Circular penumbral apertures of 200±0.5 μm were used, placed at a distance ~8mm from the target. The best images contain ~$10^5$ particles, from implosions of yield >$10^9$. The noise level is usually negligible. The particles were detected in CR-39 plastic approximately 200mm from the target. Since the field of view in the geometry used was only 1mm diameter, these assemblies were mounted on active pinhole camera bodies in order to achieve the required alignment accuracy. The maximum entropy technique[1,2] was used to unfold the images, because of its many advantages, in particular, the suppression of noise and non significant features in the image, and the consequent production of source images where any features observed must be statistically significant. A major advantage of computationally unfolded images is that the spatial resolution may be determined at the analysis stage when the quality of the data is known, unlike coded apertures where the mask pixel size must selected beforehand.

The α particle and proton images obtained are of high quality: each particle is individually located in the image to ±1μm spatially and its energy is simultaneously measured to an accuracy comparable to the straggling limit. Since the energy of each particle is determined, energy slices through the image may be taken, and separately unfolded. The set of source images thus obtained, each at a different particle energy, may then be recombined and images of the resultant structure produced. Thus in the case of α particles, images of the shell structure at the time of thermonuclear reaction have been made. In the case of protons, because of their low energy loss rate, accurate images of core temperature may be produced from the known relationship of the Doppler broadening of the spectral width. These images may then be related to the microballoon geometry and to known inhomogeneities in the laser drive, both large scale (beam balance effects) and small scale (beam non-uniformity effects).

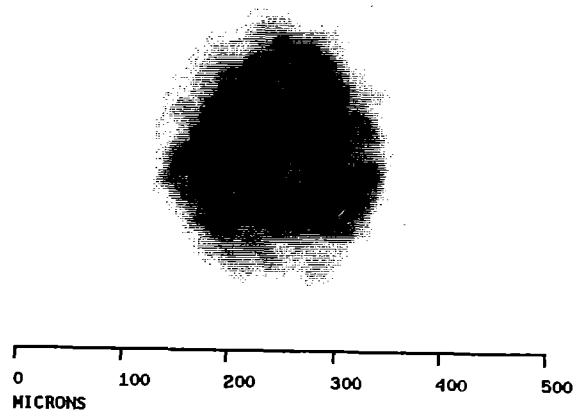


Figure 1. An α particle image of a typical high yield shot.

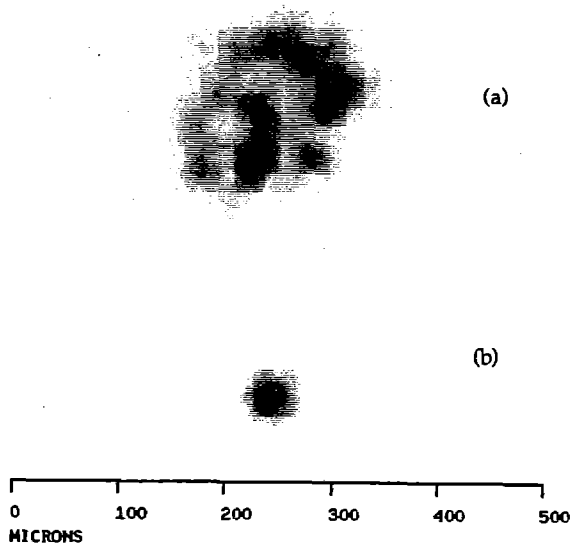


Figure 2. Proton core images. Fig 2(a) shows a good NUHART implosion, Fig 2(b) a good random phase plate implosion image.

The images were unfolded using the established maximum entropy technique[1] but the computational time required was significantly reduced by compressing the point spread function prior to the unfolding and the development of a new method of updating the coefficients, in order to obtain fast convergence of the iterations.

## RESULTS

Fig 1 shows an α particle image from a typical high yield shot (6/19/10/89, yield=3x$10^9$). The core can be seen to be large, ~$^1/_3$ of the initial microballoon diameter of ~660μm. The spectral width is also large, from both α particles and protons indicating both a high core temperature and many shell inhomogeneities (See Section A3.2). Note that the original images are printed in colour and much information has been lost in producing the black and white copies given here. In the recent implosion experiment, described in detail in section A3.2, X ray pinhole cameras gave hard X-ray images in the

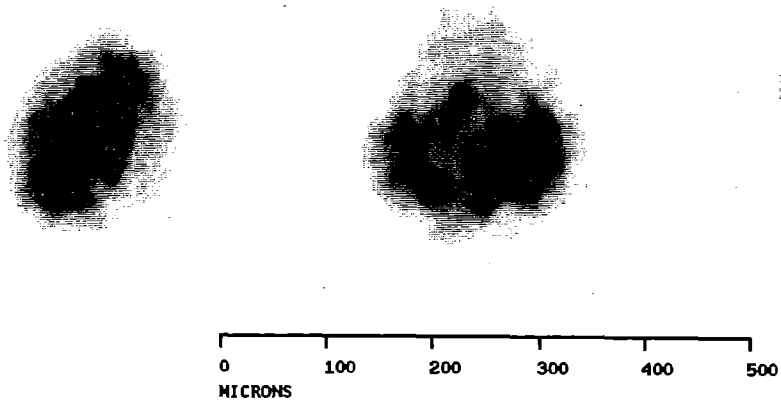


Figure 3. Three near orthogonal α particle views of shot 4/18/10/89.

diametrically opposite direction to the α cameras. Since both α particles and hard X rays will easily penetrate the target both cameras should give the same view of the plasma. Preliminary analysis suggest that the core sizes seen in α particles and X rays correlate well, although core shapes are different in many cases. A further example is given in Fig.2(a) which shows a proton image of shot 2/25/10/89 (proton yield=$8x10^7$), which shows more structure and a greater variation of emissivity than Fig. 1 - some central regions of this cores shows little or no particle emission. This could give further insight into any fuel/shell mixing that may occur. In general, higher yield implosions, expressed both as high absolute yield and high relative to model predictions, have large core sizes of thermonuclear emission, with visible structure and occasionally with three fold symmetry. Poorer implosions are generally more variable in size. Core images generated from implosions driven by random phase plates can also show variability in size. However, most of these shots are similar to Fig 2(b), shot 11/25/10/89 which is a proton image showing a very much smaller core, with a central feature of ~20μm diameter. The corresponding spectral distribution is also much narrower. Despite their lower yield, random phase plate drive therefore offers excellent prospects for generating thermonuclear particle sources.

In general 3 orthogonal α particle or proton cameras are used, in order to allow development of a 3D source calculation. Fig 3 shows 3 near orthogonal views in α particles of shot 4/18/10/89, which gave a yield $3x10^9$. The procedures to generate a 3D source reconstruction from the raw images are currently being developed, and it is then hoped to better relate the image generated to the drive parameters.

## PNP IMAGING

Thermonuclear Core Images have also been produced using PNP (Pseudo Noise Product) coded aperture masks. This method[3,4] consists of using a mask constructed from the product of two PN sequences. The technique used here is a refinement of our previous design[5]. The method has the advantage that, due to their close relationship to Hadamard matrices, an unfolding matrix may be easily computed and no iteration is required. Masks were fabricated based on 2 x 2 cycles of a 63 x 63 period sequence. Alignment of the image with the mask was achieved using a set of fiducial holes at the edge of the mask. Despite the stated merits of PNP masks for dealing with noise, the source images produced contain a low noise background over the entire source area - a feature not present on the maximum entropy penumbral images. However, comparison with reconstruction of simulated images suggests that this is principally caused by particles scattering off the edges of the mask and disturbing the reconstruction. Also the spatial resolution is determined by the pixel size, in the present case to ~18μm from a pixel size of 15.5μm. The images also contain two types of artifact - (i) spatial features caused by small inaccuracies in the construction of the mask, which although too small to see by eye disrupt the unfolding procedure; and (ii) spectral features caused by particles losing energy by traversing edges and corners of the mask substrate.

Although the results obtained for α particle images are inferior to penumbral images, improved fabrication of the PNP masks could still make a contribution for imaging of very weak emissions, for example secondary reaction products.

## REFERENCES

1. S. F. Gull and G. J. Daniell, Nature 27, 686, (1978).
2. M. W. Johnson, "Metric: An algorithm of maximum entropy reconstruction using iterative multiple constraints"; RAL report 1988.
3. S. R. Gottesman and E. J. Schneid, IEEE Transactions in Nuclear Science, 33, 745, (1986).
4. E. D. Nelson and M. L. Fredman. Journal of the Optical Society of America, 60, 1964, (1970).
5. Annual Report to the Laser Facility Committee, Rutherford Appleton Laboratory Report RAL-89-045 Section A6.6 (1989).

# NEUTRAL PARTICLE DETECTION OF LASER IMPLOSION.

T.A.Hall[1],Z.Ahmad[1],Y.A.Zakharenkov[2],M.J.Lamb[3],M.Savage[3], P.Fews[4].
[1] University of Essex, Colchester
[2] Lebedev Institute of Physical Science USSR, Moscow
[3] Queen's University, Belfast
[4] Bristol University.

A diagnostic technique to study the laser implosion of microshell targets based on time of flight mass-spectrometry of neutral particles was conducted using the 12-beam 'VULCAN' laser on implosion of high aspect ratio glass shell targets.

## INTRODUCTION.

The sources of neutral atoms in laser produced plasma have been previously recognised[1] to be from ion recombination in the plasma corona due to unheated parts of the imploded shell itself.

The earlier works showed that for ablatively driven implosion, a considerable part of the shell mass had average ionisation degree of less than unity[2].Thus high density and low temperature provided conditions for a significant number of low charged ions in the very beginning of the expansion motion. The velocities of such recombination atoms did not exceed the implosion velocity of the shell [3]. Therefore time of flight measurement was suitable because of temporal separation of plasma and imploded shell atoms.

Only neutral atoms and x-rays were allowed to reach the detector by applying an electrostatic ion deflector in the path of the flight .The signal of neutral particles could then be processed to obtain a velocity distribution of the neutral particles[5].

The optical imaging diagnostic, on the other hand , could give more information as to where the origin of the neutral particles [1].

## EXPERIMENT.

The laser energy used was in the range of 500-800 J, wavelength of 0.53 um and pulse duration of 600 ps.The targets used were DT and DD filled shells of high aspect ratio, having diameter, 500-700 um and wall thickness of 0.75-1.3 um. Some shots were taken using empty thick glass (2.3 um) and plastic shells up to 11 um thick. These conditions were described more fully in the later section.

Two different techniques of focussing the laser beam onto the target were employed. One was NUHART to provide non-uniform irradiation and the other was to provide a uniform irradiation, by placing random phase plates of specified thicknesses infront of the incoming laser beams. These would enable an investigation on the influence of different focussing conditions in detecting neutral particles.

The viewing axis of the neutral particle detector was chosen so as to enable detection of particles from the cold areas of the target surrounded by three hot spots. The detector, either secondary electron multiplier or microchannel plate camera, was placed at a distance L = 110 cm from the target. An ion collector to detect plasma ion signals was placed at L = 90 cm. Pinhole of diameter 50-100 um was also used inside the vacuum chamber at a distance of 5-25 cm from the target.

The detector signal were observed from an oscilloscope connected to the electron multiplier or on photographic film in tight contact with fiber optics screen of the microchannel plate.The x-ray exposure to the highly sensitive microchannel plate was eliminated using the method of time gated feeding voltage [4] . Fig.1 summarised the experimental setup.

## RESULT AND DISCUSSION.

Figure 2(a) and 2(b) showed the typical data of DT filled glass shells, obtained from secondary emission electron multiplier. Fig.2(a) was from uniform irradiation of target with diameter 615 um and wall thickness 1.01um. The ion structure revealed two maximums.The first corresponded to $v_i$=8.2x10$^7$ cm/s, which originated from the hot areas of the target. The second maximum had $v_i$=3.5x10$^7$ cm/s with a characteristic long tail down to $v_i$=1.53x10$^7$ cm/s.

The velocity of the observed atoms ranged at (0.75-4.05)x10$^7$ cm/s.In comparison with the ion trace, the neutral atoms could be divided into two parts; the fast atoms due to recombination of ions from the cold areas, and the slow atoms from residual target mass.

Fig. 2(b) was that of uniform irradiation with diameter 592 um and wall thickness 1.1 um. The ion velocity ranged 7.5x10$^7$ (1st max) down to 1.12x10$^7$ cm/s with a slight emphasis at 3.46x10$^7$ cm/s. The neutral atom signals showed velocity range of (0.76-3.76)x10$^7$ cm/s.

The observed spectra could be explained using images from microchannel pinhole camera. Fig.3 showed a pinhole image of plastic shell with diameter 266.4 um and wall thickness of 9.2 um. The time gating corresponded to (0.8-1.8)x10$^7$ cm/s. It was observed that the slow atoms not only come from the target,but from the glass support stalk as well. This might be the consequence of radiation heating or conduction from the target and the effects of focussed laser radiation propagating other than the target. An x-ray static image was used to locate the position of the target center.

The signals from the electron multiplier traces could be processed to obtain a velocity spectra of neutrals by the following relation [1] ;

$$\frac{dN}{dv} = \frac{L_T I_n}{Ke \Gamma R_n v_n^2 \Omega_n} \qquad (1)$$

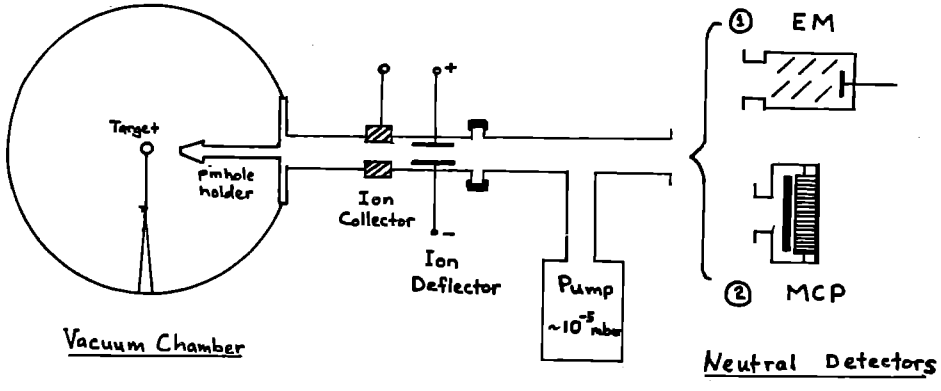


Fig.1 Schematic diagram of the experimental set up.

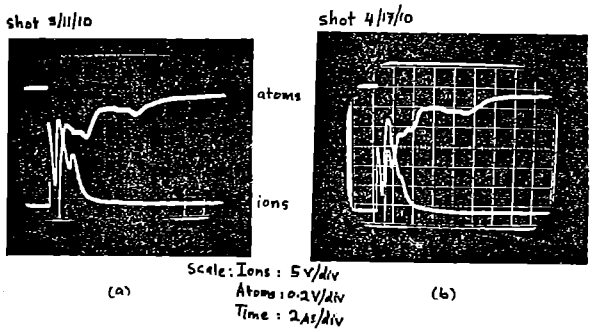


Fig.2 Oscilloscope trace of ion and neutral signals.

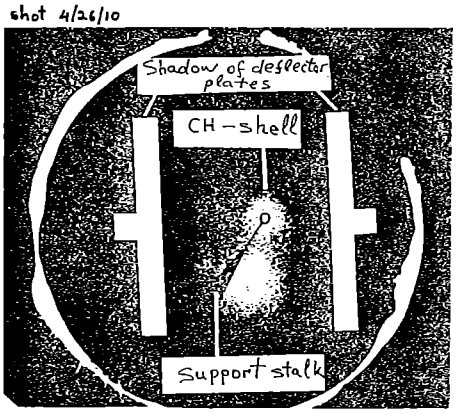


Fig.3 Image from MCP pinhole camera.

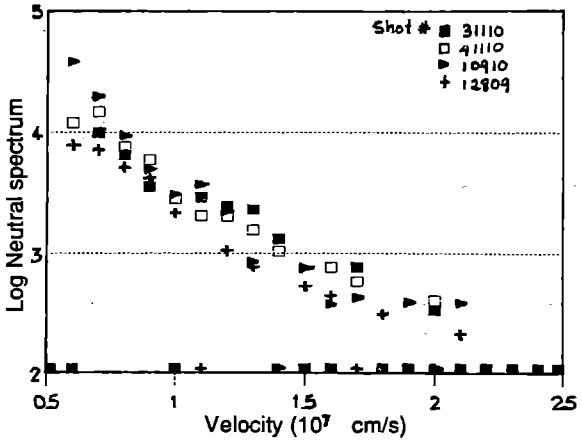


Fig.4 Neutral velocity spectrum (non-uniform irradiation).

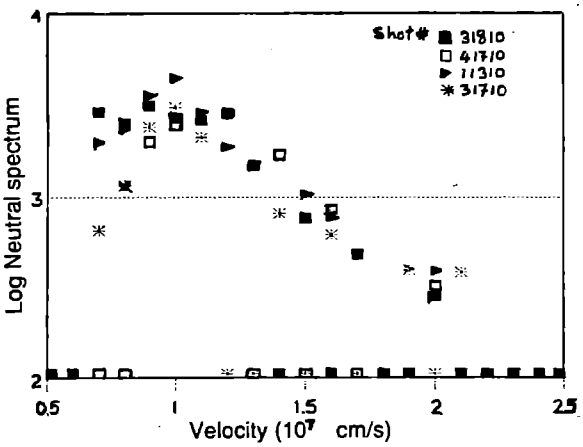


Fig.5 Neutral velocity spectrum (uniform irradiation).

where $L_r$ is the distance of deflector from the target, $I_n$ , the detector current, K, the multiplier amplification factor , $\Gamma^+$ ,the secondary electron emission coefficient , $v_n$, the velocity of the atoms and, $\Omega_n$, the solid angle.

An analysis based on the initial data produced various velocity spectra. Fig.4 showed various spectra from different types of targets, which were irradiated non-uniformly ,from 4 different shots. All the spectra showed a rather high level of atoms with velocities less than $1.0 \times 10^7$ cm/s.

Fig. 5 showed a group of spectra obtained from uniform target irradiation of 4 different shots. All showed a maximum around $1.0 \times 10^7$ cm/s.The precise reason for the difference between the uniform and non-uniform illumination is not clear at the present time. The low velocity neutrals from the non uniformly irradiated targetscould be from indirectly heated parts of the target or perhaps from the target support stalk. Such emissions were observed on some shots as shown in fig. 3 but further experiments will be necessary to resolve this issue.

It is important to note that the coefficient of amplification of secondary electron emission used in these analysis was still an estimate. Since this coefficient is energy dependent, it would be wrong to consider the results presented here as anything other than preliminary. A further analysis is in progress to make use of a better correction factor as well as to study other correlations.

CONCLUSIONS.

It was possible to detect neutral atoms emission from laser implosion of microshells using the method described in this experiment. The analysis of atoms spectra enabled one to distinguish the origin of separate emission of neutral atoms from various regions of the target.The influence of different target irradiation could be studied further. The prospect of using this method in experiments with ablatively driven targets seemed promising.

REFERENCES.

1.A.A.Erokhin,Yu.A.Zakhrenkov,A.A.Karnaukhov. A.S.Shikanov,Z.Ahmad,T.A.Hall (to be published in JETP letters)

2.Yu.A.Zakharenkov,A.A.Karnaukov,V.Ya.Karpov et al.Sov.Phys.Plasma Phys 1988, v.14(5),p367.

3.N.G.Basov,E.Woloski,S.Denus,Yu.A.Zakharenkov et al. Sov. J.Plasma Phys 1988,v.14(1),p47-50.

4.A.A.Erokhin,Yu.A.Zakharenkov,A.A.Karnaukhov et al .Sov. Phys. Plasma Phys.1989, v.15(9)p1076.

5.S.Denus,J.Farny,M.Grudzien et al. Laser and Particle Beams 1986. v.4 pt 3,4, p 507-514.

6.RAL annual report 1989.

# K-absorption edge spectroscopy of laser shocked solids

D. Riley*, S.J. Rose+, O. Willi* and T. Afshar-Rad+

* Blackett laboratory, Imperial College

+ Rutherford-Appleton Laboratory

A recent experiment in target area east has demonstrated a blue-shift of the K-absorption edge of chlorine in a laser compressed solid[1]. The cluster beam facility was used to create a shaped laser pulse by delaying four of the 0.53μm, 800ps FWHM laser beams by 700ps with respect to the remaining beam. The pulse ratio created could be arbitarily set and a ratio of 8:1 was used during the experiment. The effect was to drive two shocks into the target where they coalesced[2], producing a high compression at a relatively low temperature.

The targets were planar, 1mm square and consisted of a sandwich of three plastic layers. The central layer was C-parylene ($C_8H_7Cl$) with a density of 1.29g/cc and was 15μm thick. The outer layers where E-parylene (CH) , of density 1.1g/cc and 20μm thick. The shock driving beams where focussed onto a 250-400μm focal spot with a peak irradiance of about $5x10^{14}$ $W cm^{-2}$. The rear surface of the target was coated with 250nm of bismuth and was irradiated by a separate 70ps pulse at approximately $10^{15}$ $Wcm^{-2}$ on a focal spot 160μm in diameter. The M-band bismuth emission which passed through the compressed region was recorded with a toroidally curved Bragg crystal coupled to a X-ray streak camera. An active pinhole camera was used to monitor the superposition of the backlighting beam with the shock driving beams. The K-edge of the chlorine atoms in the central layer is at approximately 4.4 Å. This wavelength is within the range of the quasi-continuum M-band emission from the bismuth. Figure 1 shows densitometer scans of spectra taken both with and without compression of the target. For the compressed case the peak irradiance was $4.4x10^{14}$ $Wcm^{-2}$. the backlighter was timed to 100ps after the peak of the main pulse. The average shift of the k-edge is approximately 13eV to the blue. The temperature and density of the central layer at this time is predicted from the MEDUSA hydrocode[3] which was successfully used to model the shock velocities in an earlier shock coalescence experiment[2]. The predicted average density was 5.4g/cc with a maximum variation of 15%. The predicted temperature was 13eV with all cells in the simulation within 3ev of this value.

The shift in the edge was modelled using the same techniques as in earlier work[4]. The contributions to the edge shift are considered to come from three sources. Firstly, the change in ionisation state of the chlorine increases the binding energy of the k electrons. The average ionisation state is determined from the Thomas-fermi model for the conditions predicted by MEDUSA. This is then used in an MCDF atomic physics code[5] to calculate the k-shell ionisation energy for the free ions. The second contribution is the continuum lowering caused by the presence of the surrounding plasma. this is determined by a simple ion-sphere model. In which each ion is surrounded by a uniform cloud of electron charge, such that each ion sphere is electrically neutral. The third contribution is due to the change in the free electron degeneracy. degenerate electrons will occupy the lower energy free states, thus forcing ionised k electrons to higher states, which produces a blue shift of the edge.

For the compressed case in figure 1 the contributions are to the edge shift are calculated to be +48.1eV from the change in ionisation, -54.4eV from continuum lowering, and +16.1 eV from the change in electron degeneracy. This predicts a net shift of 9.8eV, in reasonable agreement with the experimental results.

The observation of a blue shift is in contrast to the red-shifts observed in a previous experiment. The reason for this is believed to be that in the earlier experiment the bismuth was heated by the main shock driving beam and thus the target was radiatively pre-heated before the compression. Thus resulting in lack of electron degeneracy. The degeneracy parameter is defined as $\eta = \mu/kT$ where $\mu$ is the

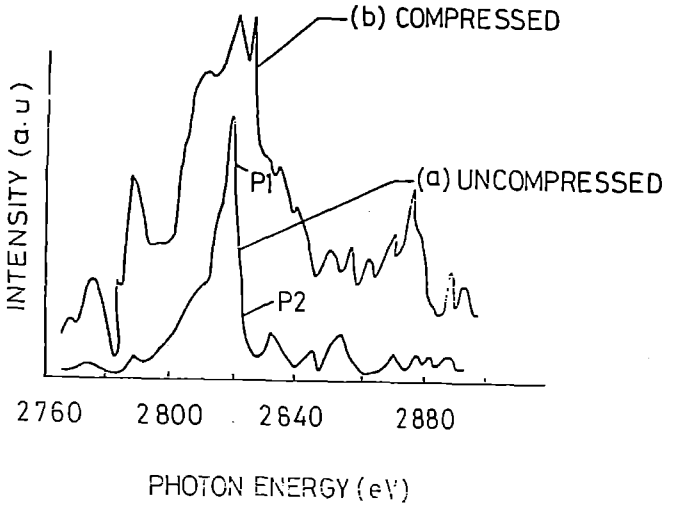


**Figure 5**
**Absorption edge spectra for (a) unshocked and (b) shocked case.**

chemical potential from the Thomas-Fermi theory. For the compressed case in figure 1 $\eta$ is calculated to be 1.9, compared to 0.2 for the previous experiment. A more detailed description of the experiment can be found in reference 1. The shift is relatively small compared to the individual contributions and so we have to be cautious in assessing the success of the modelling compared to experiment. However, the major conclusion from the experiment and those in reference 3 is that the simple theoretical treatment used, is capable of reproducing the direction and magnitude of the k-edge shifts in laser compressed solids.

1. D. Riley, O. Willi, S.J. Rose and T. Afshar-Rad, Europhys. Lett. **10** (2) pp135-140 (1989)

2. Coe et al, Appl.Phys.Lett. **53** 2383 (1988)

3. Christiansen et al, Comput. Phys. Commun. **7** p271 (1974)

4. Bradley et al, Phys.Rev.Lett., **59** 2995 (1987)

5. Grant et al, Comput. Phys. Commun. **21** 207 (1980): McKenzie et al, Comput. Phys. Commun. **21** 233 (1980)

# RAMAN SCATTERING FROM DENSITY CAVITIES

H C Barr, T J M Boyd and A P Mackwood

University of Wales, Bangor

## INTRODUCTION

The continuing interest in stimulated Raman scattering (SRS) from laser-produced plasmas is sustained both for its intrinsic interest and on account of its role in laser fusion studies. Various aspects of SRS are still not fully understood. Two in particular are of special concern in that each is present ostensibly in experiments over a wide range of parameters. The first concerns the spectrum. Almost all experiments show spectral features, at odds with the predictions of conventional theory, exhibiting peak emission at wavelengths between $\lambda_0$ and $2\lambda_0$ ($\lambda_0$ being the laser wavelength). The short wavelength cutoff is easily explainable in terms of Landau damping but the gap on the long wavelength side is more mysterious and has attracted a flurry of speculative interpretations. The second anomaly concerns the observation of emission at intensities typically an order of magnitude below the conventional convective threshold. Explanations have invoked filamentation, density ripples, localised density maxima, plateaus or minima, enhanced Thomson scattering arising from fluxes of hot electrons, and collisions. There is also debate concerning the nature - absolute or convective - of the instability at densities away from the quarter critical density.

First, it should be recognized that SRS can almost always be absolute. It is absolute in a homogeneous plasma. In an inhomogeneous plasma some feedback into a resonance will cause temporal growth (above a certain threshold) and this feedback will always be present by virtue of reflections due to the inhomogeneity (and/or interaction between resonances). Such reflections occur everywhere that the plasma is inhomogeneous and not just at geometrical reflection points. It acts as a distributed feedback mechanism, excluded when using WKB theory. Stringent conditions on the phases of the interacting waves determines the eigenfrequencies. Thresholds will be high if the feedback is weak and vice-versa. The second question is whether there is also a significant regime of only convective amplification to a level which is observable at intensities below the absolute instability thresholds or at frequencies distinct from the eigenfrequencies. The answer, in general, is no if damping is weak and feedback high. Convective regimes which give sufficiently large gain will be indistinguishable from absolute growth. A third issue concerns the sensitivity of the absolute growth to changes in parameters and hence to detuning. Weak damping and strong feedback give rise to sharp resonances, with spatial amplification of off-resonant frequencies negligible. If damping is strong, thresholds are raised but large amplifications become possible at off-resonant frequencies.

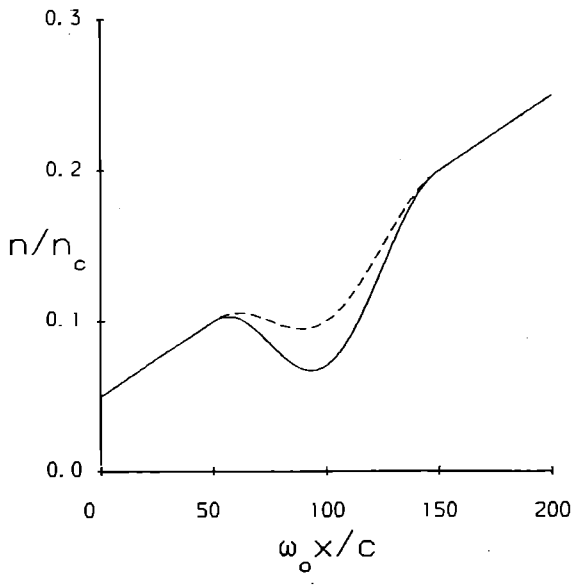


Figure 1: The density profile

We have recently employed a code in which SRS may be studied in an arbitrary but specified density profile where the frequency of the waves is controllable and hence that fields across boundaries can be made rigorously continuous. This ensures that there are no spurious reflections to mask the physics. The model has been described elsewhere. In short, the full coupled wave equations for SRS, Laplace-transformed in time, are solved over a domain that includes both back (SRBS) and forward (SRFS) scattering resonances as well as allowing for wave reflections. The density profile of interest is attached to infinite portions of homogeneous plasma in a continuous manner. The laser intensity is also assumed continuous across the boundaries. The coupled wave equations are easily solved analytically in the homogeneous regions giving four independent solutions. In the absence of the laser driver these represent left and right travelling plasma and scattered light waves. The laser couples these. If these homogeneous portions are at nonresonant densities for the frequencies being considered the coupling gives rise to small nonresonant changes to the dispersion of the freely propagating waves. Even so it is important to include these to eliminate all spurious reflections at the boundaries. This procedure ensures that the boundaries are transparent to all waves. Boundary conditions for absolute instability allow only outward propagating waves. For convective regimes we measure gain by choosing boundary conditions which allow waves to propagate into the inhomogeneous plasma or by having noise sources within the plasma (we use the former mostly).

In what follows we present results for SRS from a plasma in which density cavities occur. Plasma waves trapped in a cavity have quantised frequencies. If this is approximated by a parabolic well of scale length L then the frequencies are

$$\omega_n^2 = \omega_p^2 + \sqrt{3} V_t \omega_p (2n+1)/L \qquad (1)$$

where n=0,1,2.... At densities away from quarter critical backscattering involves high mode numbers (shorter wavelengths) while forward scatter involves the low mode numbers. Scattering from a density minimum (cavity) is qualitatively and quantitatively similar to that from a density maximum for intensities above the threshold intensity for scattering from the density maximum (see last year's report[1]). In this regime the strong growth washes out the interference effects impicit in (1). At lower intensities the two cases are qualitatively different. First, the thresholds are reduced to zero (in the absence of damping) as one might expect since the plasma wave suffers no losses by convection (alternatively one can regard it as having its group velocity reduced to zero). Second, the growth rates for SRS in which the plasma is trapped are comparatively slow. Third, forward scattering grows absolutely (without invoking any coupling to backscatter) but are even more slowly growing. However the plasma waves involved in forward scattering, having smaller wavenumbers than those for backscatter, are trapped by shallower cavities ($\delta n/n \geq 3V_t^2/c^2$). They are also much less susceptible to Landau damping and hence can have lower thresholds than the backscattering resonances. Therefore, there may be more SRS activity at thresholds below even that for the localised density maximum than is supposed.

RESULTS

We show here the properties of SRS in a density profile as shown in Fig.1 having a cavity/bump superposed on a monotonic density ramp. Such a profile has been proposed by Drake et.al.[2,3] as a possible candidate to explain observations of SRS which appear to imply that SRS must grow absolutely over a range of densities on what is apparently a monotonic density ramp. As we have said above, while it is not difficult to obtain absolute instability, it is somewhat more difficult at the same time to obtain the required low thresholds. Drake suggested that scattering from such "local" density maxima can explain the observed thresholds. The accompanying minimum is also a site of interesting SRS behaviour. The maximum density was chosen to be 0.25 $n_c$ allowing propagation of most forward scattered light out of the system and hence providing only low feedback between back and forward scattering resonances. Two depths of cavity were investigated: a shallow cavity which is sufficient to trap only the SRFS plasma waves and a deep cavity, akin to the profile suggested by Drake et al., which traps both SRBS and SRFS plasma waves.

The shallow cavity case shows that thresholds and growth rates for SRBS at both the density maximum and minimum are virtually identical but that SRFS, having trapped plasma waves, grows absolutely from zero threshold.

Fig.2 shows the thresholds for the deep cavity. The lower frequencies correspond to resonance on the steepened part of the profile where there is insufficient feedback to sustain absolute growth. The first plotted threshold corresponds to scattering from the density maximum and agrees with the Rosenbluth expression for scattering from a density maximum. Subsequent points correspond to scattering away from the density maximum until we reach the first zero threshold corresponding to the highest order trapped plasma wave for SRBS (n=23 in this case, c.f. eq.(1)). The complete set of trapped plasma waves is seen here. In most of these both back and forward scatter are involved although dominated by the backscattering. However the low order modes participate in forward scattering only. These show that the cavity can make SRFS absolute. The scaling of growth rate with laser intensity is complex at low intensities. Growth is not monotonic with laser intensity.

The addition of Landau damping illustrates the differential effect on back and forward scattering. Fig.3 shows this for a temperature of 1.7KeV. The absolute growth of SRBS within the cavity is easily suppressed while the forward scattering survives. This figure also shows the gain contour above which a gain in excess of exp(2π) for SRBS is achieved. It indicates that significant amplification is achieved at all frequencies and at intensities not much different from those giving absolute instability. The rapid rise of this with scattered frequency is the Landau cut-off ($\omega_s = 0.7\omega_0$ implies a $k\lambda_d$=0.3). In the case of SRFS, the regions of the $(v_0,\omega_s)$ parameter space giving in gains excess of exp(2π) appear as loops centred on the absolute instability thresholds but these are too small to be resolved on this figure. It should then be asked to what extent such sharp resonances are easily detuned by noise, turbulence, ion waves (due to stimulated Brillouin scattering for example) or other agency. This will be discussed elsewhere.

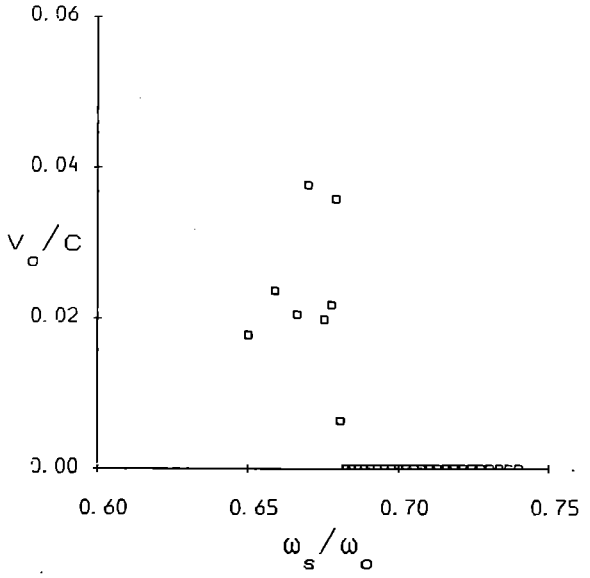


Figure 2: Threshold intensities versus scattered frequency in the absence of damping ($I_0 \lambda_0^2 = 5.48\ 10^{18}\ (v_0/c)^2$ W cm$^{-2}\mu$m)

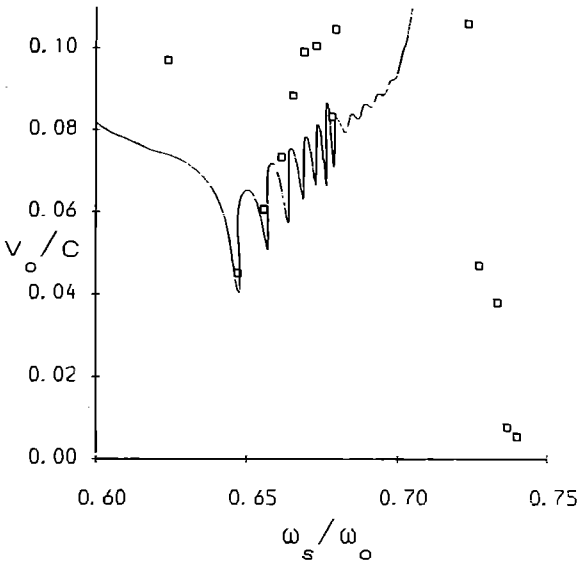


Figure 3: Threshold intensities and the exp(2π) gain contour for SRBS versus scattered frequency including damping ($T_e$ = 1.7KeV)

REFERENCES

1. HC Barr, TJM Boyd and AP Mackwood, Phys Fluids B1 1151 (1987); Annual Report to the Laser Facility Committee Rutherford Appleton Laboroatory RAL-89-045 (1989)
2. RP Drake et al. Phys Rev Lett 61 2387 (1988)
3. RP Drake et al. Phys Rev Lett 60 1018 (1989)

# A SIMPLE METHOD FOR CREATING PULSE-SHORTENING IN X-RAY LASERS

SJ Rose[1], AM Rogoyski[2] and N Tragin[1]

[1]Rutherford Appleton Laboratory
[2]Kings College London

For many years the possibility of developing an X-ray laser has been of interest to scientists, but it is only relatively recently that real progress has been made. Much interest has been shown in the possibility of a water-window (or a near-water-window) X-ray laser but such a laser appears to need pumping by the very largest optical lasers available. Other aspects of X-ray laser design have become important, such as optimising and sustaining gain, developing high gain systems and applications such as X-ray holography. Current X-ray laser schemes involve pumping with high-power (normally multi-terrawatt) optical or ultra-violet lasers with pulse durations of less than a nanosecond. The laser is focused onto a slab or fibre, between a few microns and a few tens of microns wide and a few millimeters to a few tens of millimeters long [1]. The slab or fibre forms a plasma when irradiated by the laser and it is this plasma that forms the gain medium for the X-ray laser. Various schemes exist to create the population inversion, involving different pumping mechanisms and different lasing transitions. Currently, three main types of X-ray laser are being actively investigated: hydrogen and lithium-like recombination schemes, neon and nickel-like collisional schemes and photoexcitation schemes. We have been most involved with the recombination scheme and it is this method that will be used to illustrate the idea for pulse-shortening. Recombination X-ray lasers employ a cylindrical (for a fibre target) or pseudo-cylindrical (for a slab target) plasma, created by direct irradiation by the laser in which the constituent atoms are highly ionised. For the hydrogen-like recombination scheme most ions are initially fully stripped. As the hydrodynamic expansion cools the plasma the ions recombine cascading through the upper states where collisional processes are dominant, reaching the lower states where radiative transitions become more important. For the hydrogen-like recombination scheme population inversion occurs between n=3 and n=2. The lower state of the lasing transition is de-populated by the fast radiative transition between n=2 and n=1.

The pulselength of the X-ray laser is determined by the plasma expansion. Simply shortening the pulselength of the optical pump laser, will not produce ever shorter X-ray laser pulses, although the gain time may be shortened to some extent by choice of optimal irradiation conditions. We have developed a numerical model of recombination X-ray lasers [2]. with which it is possible to optimise the conditions (e.g. incident power, pump laser wavelength, pulselength, etc.) to obtain maximum gain. The calculations also produce the radial gain profile as a function of time. From [3] it can be seen that the region that sustains gain in the plasma is of the order of several tens of microns wide. This region moves away from the solid target/plasma interface and changes shape and magnitude as the plasma evolves (see figure 1). It is the lateral movement of the gain region that provides the opportunity to shorten the X-ray laser pulse. If two slab targets are set end-to-end but so that the irradiated surfaces are opposite to each other (see figure 2) with an appropriate offset between the surfaces, then the pulse can be shortened. As the plasma expands, initially there will be two beams (as observed axially) with an output corresponding to the gain-length product of the two individual lasing plasmas. When the plasmas have expanded to a suitable point, the gain regions will begin to overlap resulting in a corresponding increase in output which will have a maximum value proportional to the gain-length product with the length twice the individual plasma length.

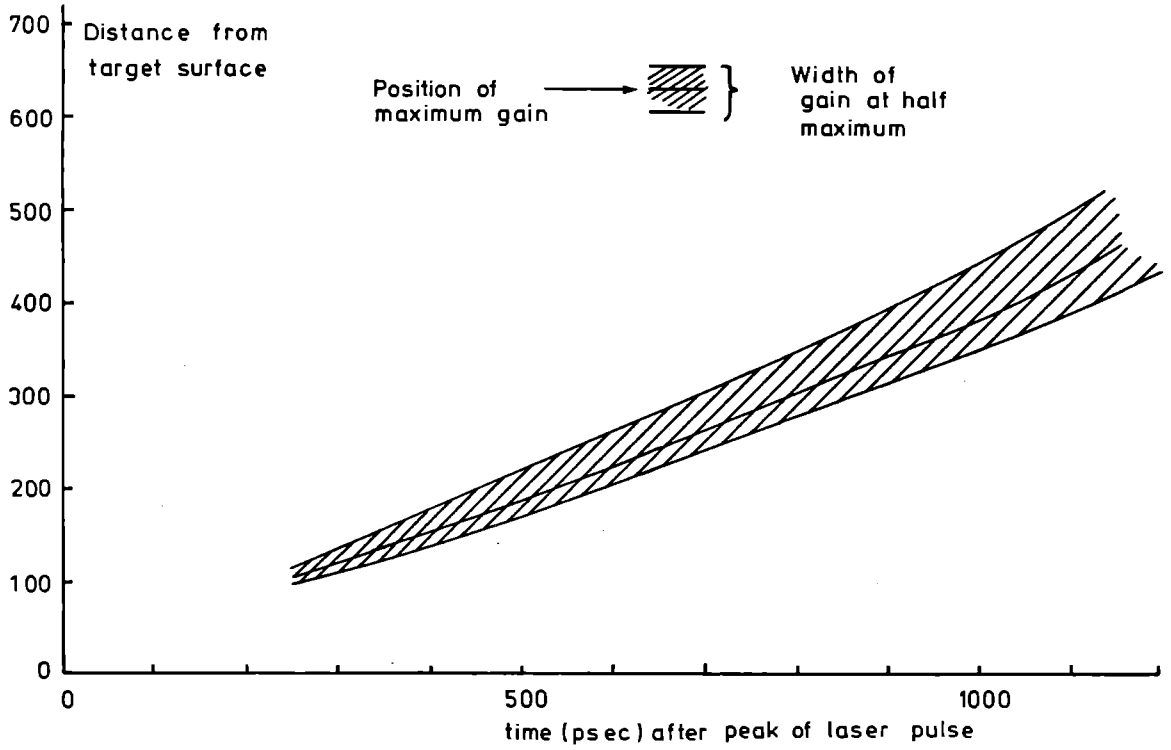


Figure 1: Calculated evolution of gain region for a 100 micron wide stripe irradiated with 0.53 micron light at $6 \times 10^{12}$ W $cm^{-2}$ (absorbed) with a 70 psec pulse (the system reported in figure 4 of reference 3)

The ratio of the observed intensity might be expected to be approximately $e^{\alpha 2l}/2e^{\alpha l}$. The pulse will be shorter because the gain regions will be travelling in opposite directions. Taking the example of a hydrogen-like carbon X-ray laser in slab geometry reported in figure 1 the calculated gain maximum moves at approximately 0.35 micron/psec and the gain width is approximately 80microns wide (figure 2), although it does spread a little as it expands. The time of peak gain is 850 psec after the peak of the laser pulse, corresponding to a distance of 325 microns from the target surface (figure 3) if the offset between the two surfaces is set at 650 microns then the peak gain of the two plasmas will coincide. This will result in the enhanced gain lasting for approximately 230 psecs (the time for the FWHM gain regions to move past one another) which is less than the characteristic lasing time of the system (which is over 0.5 nsec). Furthermore, as the plasmas expand past this point the plasma furthest from the observer will have the gain region overlapping with the higher density, lower temperature region from the near plasma and thus reduce the amount of transmitted radiation. This effect "switches off" the laser more rapidly than for the single plasma case.

The same effect may be obtained by placing an aperture along the axis of the X-ray laser set at the desired distance for maximum gain, thus blocking the radiation emitted as the laser develops until the laterally moving beam coincides with the aperture. However, because of the higher relative velocity the pulse length that can be achieved is smaller with counter-propagating plamas than with an aperture. It may

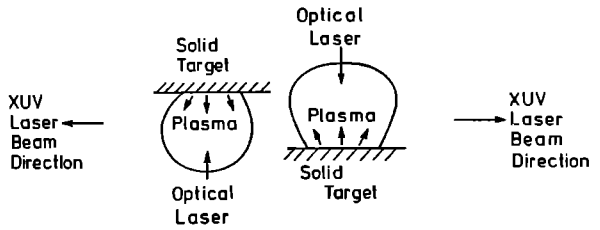


Figure 2: Schematic diagram of experimental arrangement for counter-propagating plasma XUV or X-ray laser pulse shortening

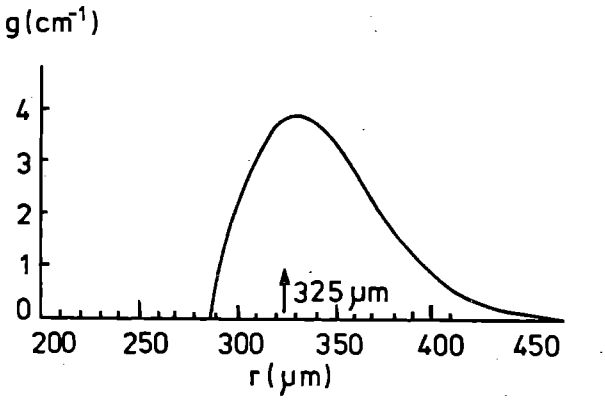


Figure 3: Radial gain profile at the time of maximum gain (850 psec after the peak of the laser pulse)

be possible to arrange several pairs of cross-directed plasmas so that the ratio of the output from the pulse-shortened X-ray laser to that of the output from the individual lasers becomes $e^{\alpha nl}/ne^{\alpha l}$, where n/2 is the number of pairs. Another problem with long plasmas in X-ray laser design is that of refraction. This may be reduced as the density gradients would be opposite in X-ray laser pairs and thus tend to cancel long-range refractive effects.

With optical and XUV lasers, pulse shortening and pulse shaping are achieved by a variety of techniques which do not involve movement of the gain medium. However, with XUV and X-ray lasers which use plasma amplifiers , utilising the motion of the gain medium may turn out to be an effective method of controlling pulse length and shape. It may even be possible to utilise this technique in optical (such as chemical) lasers.

REFERENCES

[1] See for example M Grande et al. Opt Comm **74** 309 (1990)
[2] GJ Pert and SJ Rose Applied Physics **B50** 307 (1990)
[3] N Tragin, MH Key and SJ Rose J Mod Optics **37** 435 (1990)

# INVESTIGATION OF THE EFFECT OF TIME OR SPACE INTEGRATION ON THE APPARENT GAIN IN CVI $H_\alpha$ RECOMBINATION LASERS

N Tragin, M H Key, S J Rose

Rutherford Appleton Laboratory

## INTRODUCTION

In a previous study (1), of the possibility of saturated XUV action in CVI we have performed simulations using a one-dimensional hydrodynamic code (2), for carbon plasmas created from fibres or flat targets. To optimise the gain on the Balmer-alpha line, we have varied the pulse duration of the iradiating laser. Flat targets have been modelled by a fibre giving similar hydrodynamics and having a diameter twice the width of the line focus, so that a 100 micron wide line focus on flat target has been modelled by a 200 micron diameter fibre. The results are presented in table 1. The simulations have shown the advantage of shorter wavelength and shorter pulse.

| Fibre Diameter µm | λ µm | $\tau_\ell$ ps | $I_{abs}$ W/cm² | $g_{max}$ cm⁻¹ | $r_{max}$ µm | $t_{max}$ ps | Ne cm⁻³ | Te eV |
|---|---|---|---|---|---|---|---|---|
| 7 | 0.53 | 70 | 1.6 $10^{13}$ | 9.5 | 155 | 600 | 8.$10^{18}$ | 10 |
| 200 | 0.53 | 70 | 5.7 $10^{13}$ | 4. | 425 | 950 | 9.$10^{18}$ | 13 |
| 200 | 0.53 | 500 | 9.4 $10^{11}$ | 0.8 | 810 | 3300 | 6.$10^{18}$ | 15 |
| 200 | 1.06 | 70 | 2.3 $10^{13}$ | 2.3 | 710 | 1400 | 8.$10^{18}$ | 14 |

Table 1: Theoretical maximum line-centre gain for the different configurations studied. The diameter fibre target and the irradiating laser conditions are specified. The position in the plasma, the electron density and temperature for the maximum gain are given, as well as the time when it occurs.

## APPARENT GAIN AND PEAK GAIN

In practise, the gain measured from the axial to transverse intensity ratio or variation of intensity with length of the Balmer-alpha line in experimental spectra can be much lower than the peak gain and it may even appear that the plasma is absorbing rather than amplifying because of the large amount of emission from plasma which is denser than the gain region but absorbing rather than amplifying. We have studied the case of a 100 micron wide line focus on a flat target with an irradiating laser wavelength of 0.53 micron and a pulse duration of 70 picoseconds. Figure 1 shows the evolution of the line-centre gain versus distance from the target, at the time where the gain is maximum (950 ps). Figure 2 shows the evolution of the line-centre gain versus time, at the distance in the plasma where the gain is maximum (425 microns). On figure 1, the gain region is located between 390 and 550 microns. We have calculated (see figure 3) the apparent gain from the line intensities:

- with time and space integration
  curve 2: gain determined from axial to axial measurement
  $I(2\ell)/I(\ell) = (\exp 2g\ell + 1)/(\exp(g\ell)+1)$
  curve 3: from axial to transverse measurement $(\exp(2g\ell)+1)/2g\ell$
- with time resolution and space integration
  curve 4: gain determined from axial to axial measurement $I(2\ell)/I(\ell)$
  curve 5: from axial to transverse measurement.

The square shows comparison with results from a two-dimensional hydrodynamic code. The apparent gain is 1.6 $cm^{-1}$ for $\ell$ = 1 cm with the one-dimensional code and 1.1 $cm^{-1}$ with the two-dimensional code. The comparison between these two values gives us confidence in the approximation of the one-dimensional code.

Curve 1 shows the peak gain of 4 $cm^{-1}$ which is independant of the plasma length. The circle is the peak gain calculated from a two-dimensional hydodynamic code = 3.6 $cm^{-1}$. Again these two values are in good agreement.

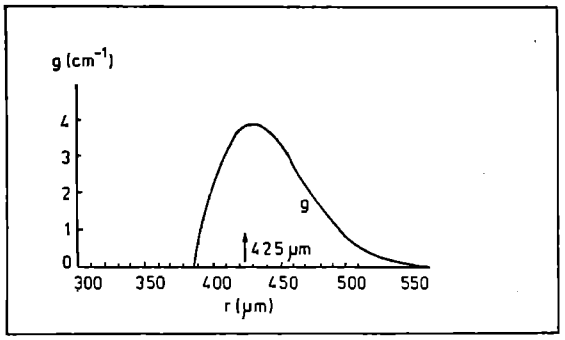


Figure 1: Evolution of the line-centre gain versus the position in the plasma (origin at the centre of the fibre). The position where gain is maximum is shown by an arrow.

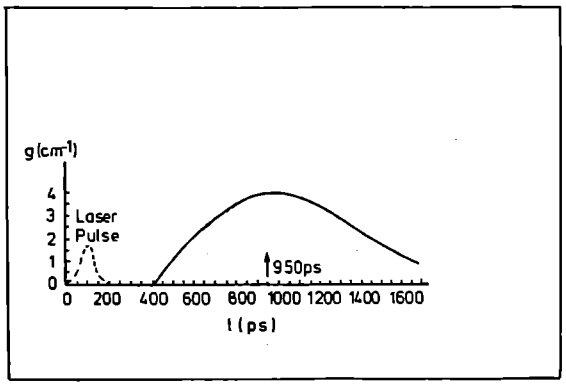


Figure 2: Evolution of the line-centre gain versus time (the shape of the laser pulse is drawn as a reference). The time when gain is maximum is shown by an arrow.

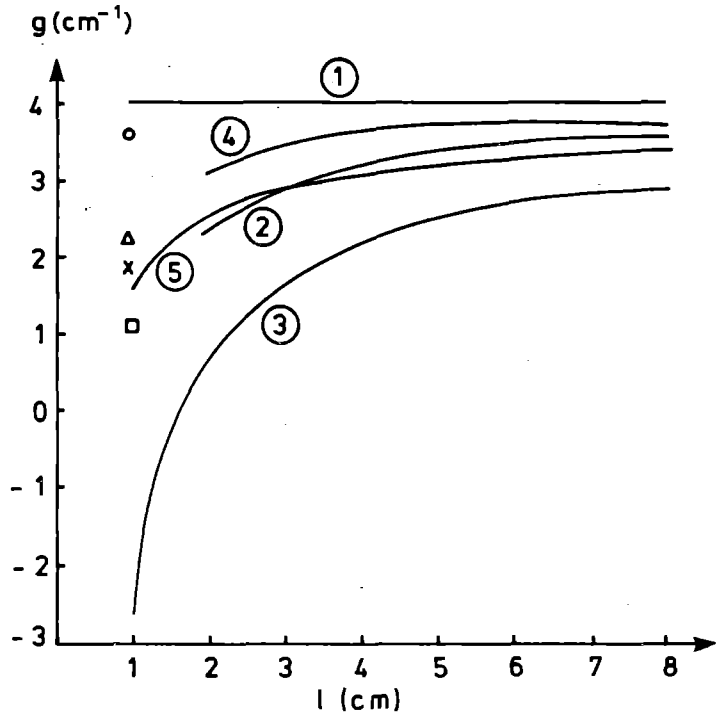


Figure 3: Peak gain (curve 1) and apparent gain versus plasma length for time and space integration (curve 2: measurement from axial to axial intensities, curve 3: from axial to transverse intensities) and for time resolution and space integration (curve 4: measurement from axial to axial intensities, curve 5: from axial to transverse intensities).

For $\ell$ = 1 cm, we have determined the apparent gain with spatial resolution restricted to the gain regions, that is to say from 390 microns to 550 microns. The triangle corresponds to the case of time resolution, and the cross to the case of time integration. With time resolution the apparent gain changes from 1.6 $cm^{-1}$ to 2.2 $cm^{-1}$ with restricted space integration. And with time integration the apparent gain changes from -2.6 $cm^{-1}$ to 1.8 $cm^{-1}$ with restricted space integration.

CONCLUSION:

Axial to axial intensities measurement gives an apparent gain closer to the peak gain. The value reaches 75% of the peak gain for peak values of $g\ell$ >16. For small $g\ell$ < 4 spatial or temporal resolution is necessary to obtain a measurable apparent gain. If the limit for measurement of apparent gain is taken to be $(g\ell)_{eff} \sim 4$, then the necessary values of the peak $g\ell$ are 10 for a time and space integrated measurement and, 5 to 6 for time resolved and 6 for space resolved measurements. An experiment is planned with spatial resolution of 50 microns.

REFERENCES:

(1) N Tragin, M H Key, S J Rose, Journal of modern optics 1990, vol 37, n 1.
(2) P A Rodgers, A M Rogoyski, S J Rose, Internal report 1989.

# CALCULATIONS OF GAIN GENERATED BY SHORT PULSE LASER HEATING

Geoff J Pert

Department of Physics, University of York

For several years it has been appreciated that the highest gain recombination lasers were obtained in a mode in which the pump laser energy was injected in a time short compared to the characteristic times for the development of the population inversion. A very simple heuristic rule for this mode of operation based on extensive computer simulation is that the laser pulse length, $\tau$, is less than $5 \times 10^{-7} Z^4$ secs for the ion of charge Z. The introduction of high power, short pulse lasers has now made this explosive mode of operation accessible for short wavelength (Z - 13) soft X-ray laser design. This short report indicates the range of powers required based on current design understanding.

We have investigated the development of gain on $H_\alpha$ in Aℓ XIII at 38.7Å using the code HYBD3 to model the development of ionisation and population growth from aluminium strips irradiated by 10 ps laser pulses of focal width matched to the strip. A range of strip widths from 25 μm to 100 μm was modelled for differing input power. The laser power was varied over the range 10 - 40 TW/cm, with the absorption at the critical density set to 0.25. The fractional energy absorbed by the strip was thus typically about 25%. The foil thickness was set at 1 μm with burn depths to 0.275 μm at the highest power.

The calculations were used to obtain the peak gain within the plasma, and spatial averaged values for plasma lengths 0.25 - 2.0 cm. We shall present data for a 1 cm length. In accordance with current practice $L_\alpha$ trapping was neglected. When trapping is included the gains are reduced very significantly by about two orders of magnitude to values which are not experimentally detectable.

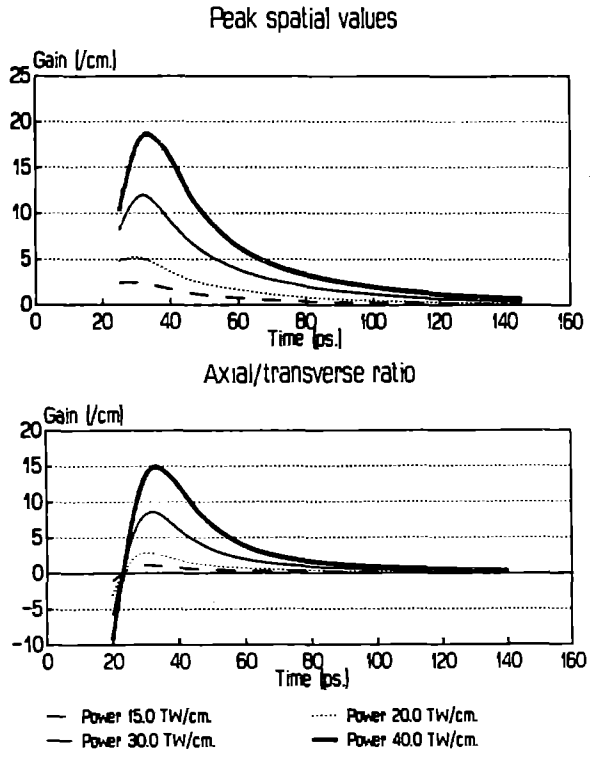


Fig 1 Plots of the spatially averaged/axial/transverse ratio, and peak gain from 100 μm aluminium strips at various powers.

The results are shown in figs 1 and 2. Figs 1 show the variations of peak and spatially averaged gain for 100 μm strips at various powers. For power less than 10 TW/cm no detectable gain is achieved. For higher powers the gain progressively increases, the peak gain length product being obtained for short lengths at high irradiation if the overall power is held constant. Peak gain occurs later, and is longer lived at higher power. In these expansions the flow is essentially one dimensional, and significant cooling by thermal conduction back to the solid occurs.

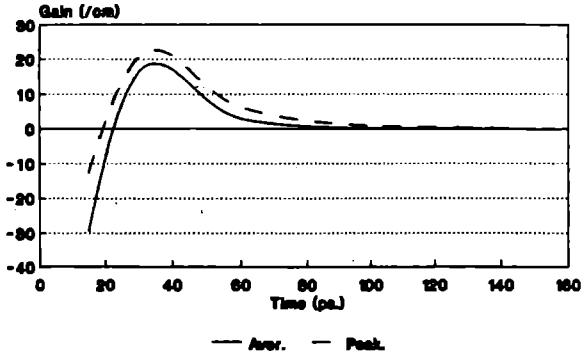


Fig 2 Plots of the spatially averaged and peak gain from 25 μm aluminium strip.

Fig 2 shows the average and peak gain for a 25 μm wide strip irradiated at 10 TW/cm. This is equivalent to the 40 TW/cm case in fig 1. Comparison shows the gain is slightly larger, and occurs later in the expansion. The flow in this case is essentially two-dimensional, axial/transverse velocity ratio 0.6, its nature contributing significantly to the cooling.

The power requirements of these systems are now just within experimental capability for the measurement of gain-length products of about 4. These are subject to the usual identification problems for recombination lasers. However the generation of gain is extremely sensitive to $L_\alpha$ trapping, and experiments in this regime should help to further elucidate this paradoxical behaviour.

# POPULATION COUPLING DUE TO RADIATIVE TRANSFER

Geoff J Pert

Department of Physics, University of York

One of the major theoretical uncertainties in X-ray laser design concerns the role of radiation trapping which inhibits the decay transition and destroys population inversion. Comparison of experiments with simulation indicate that present data can only be reconciled if the trapping is strongly inhibited[1], a result lacking any sound basis. The present modelling of radiative trapping via an escape factor is open to question, and checks using more direct methods are necessary before firm conclusions on this issue should be drawn.

The essential problem involves the coupling of the population distribution at a point in space with that in the surrounding environment. The population growth equations are thus global, rather than local as considered previously. We may approach this problem in two ways either through the calculation of the radiation fields, or through direct coupling coefficients. We have adopted the latter approach, and will report some calculations of these coefficients.

This problem has long been of concern in astrophysics[2,3], where the emphasis is on the output radiation field rather than the detailed internal populations. The problems have considered predominantly the two level atom in planar and spherical geometries using the scattering formalism. This leads to an integral equation for the source function in terms of the kernel function, which is the probability that a photon emitted at a point $\underline{r}_1$ is absorbed in unit volume at $\underline{r}_2$.

Engineering radiation transfer is generally concerned with the transfer of heat from one surface to another, and is determined by the geometric or shape factor, which expresses the fraction of radiation from one surface which is intercepted by the second[4,5]. Shape factors have a useful symmetry property.

The coupling factor required for these calculations is clearly related to both the kernel and the shape factor. In cylindrical geometry we require the probability that a photon emitted in a random direction from the element $R_1 \to R_1 + dR_1$ is absorbed in the element $R_2 \to R_2 + dR_2$, ie the kernel function, but expressed in a form which retains the symmetry of the shape factor.

For a photon of frequency $\nu$ emitted at $\underline{r}_1$, the probability of absorption in $\delta V_2$ at $\underline{r}_2$ is

$$K_M(\underline{r}_1,\underline{r}_2,\nu)\delta V_2 = \frac{\mu(\nu_2)\ \exp\left(-\int_{\underline{r}_1}^{\underline{r}_2}\mu(\nu)\,d\underline{\ell}\right)\delta V_2}{4\pi\ |\underline{r}_2 - \underline{r}_1|^2} \qquad (1)$$

where the integral is taken along the line $\underline{r}_2 - \underline{r}_1$. If the equivalent volumes of the emitter and absorber are $V_1$ and $V_2$ respectively, the number of absorptions of photons of frequency $\nu$ in $V_2$ due to emissions in $V_1$

$$= \int_{V_1} dV_1 \int_{V_2} dV_2\ E_1(\nu)\ \mu_2(\nu)\ \frac{\exp\left(-\int_{\underline{r}_1}^{\underline{r}_2}\mu(\nu)\,d\underline{\ell}\right)}{4\pi\ |\underline{r}_2 - \underline{r}_1|^2} \qquad (2)$$

This result must be averaged over the photon spectral distribution to give the total number of

absorptions of the line in $V_2$ of photons emitted in $V_1$

$$= E_{o_1}\mu_{o_2} F_{12} \cdot V_1 V_2 \qquad (3)$$

where $E_1(\nu) = E_{o_1} f_1(\nu)$ and $\mu_2(\nu) = \mu_{o_2} f_2(\nu)$.

The coupling factor

$$F_{12} = \frac{1}{4\pi V_1 V_2} \int d\nu\, f_1(\nu.)\, f_2(\nu)$$

$$\int_{V_1} dV_1 \int_{V_2} dV_2 \; \frac{\exp(-\int_{r_1}^{r_2} \mu(\nu) d\ell)}{|\underline{r}_2 - \underline{r}_1|^2} \qquad (4)$$

Clearly has the required symmetry $F_{12} = F_{21}$. Its relationship to the kernel and shape functions is obvious.

In cylindrical geometry we obtain, by projection on to a plane normal to the axis; the monochromatic coupling coefficients for unit length

$$f_{12} = \frac{1}{4\pi} \int_0^{2\pi} d\psi \int_0^{\pi} d\theta \exp(-\int_1^2 \mu(R) dL/\sin\theta)/L_{12} \qquad (5)$$

where $L_{12}(\psi)$ is the projection of the path onto the axial plane, ie

$$L_{12}(\psi) = \sqrt{(R_1^2 + R_2^2 - 2R_1R_2\cos\psi)} \qquad (6)$$

Hence

$$f_{12} = \frac{1}{\pi} \int_0^{\pi} d\psi / L_{12} \int_{\tau_{12}(\psi)}^{\infty} dx\, K_0(x). \qquad (7)$$

where $K_0$ is a modified Bessel function of the second kind of order zero: the function $\int_x^{\infty} dx K_0(x)$ being tabulated (ref 6, p.480) and

$$\tau_{12}(\psi) = \int_1^2 \mu(R) dL(\psi). \qquad (8)$$

Uniform Stationary Plasma

In a uniform stationary system $\mu(\nu)$ is everywhere constant, and we may perform the integrals in (4) analytically to give a series of expansions which may be used for calculation. From (7) we obtain using Graf's addition theorem:

$$f_{12} = \mu \int_1^{\infty} dx\, K_0(\mu R_2 x)\, I_0(\mu R_1 x) \qquad (9)$$

where $I_0(x)$ is a modified Bessel function of the first kind of order zero[6] and $R_1 < R_2$. From the expansion of $I_0(x)$ we obtain

$$f_{12} = \frac{1}{2R_2} \sum_{k=0}^{\infty} \left[ \frac{\Gamma(k+\frac{1}{2})}{\Gamma(k+1)} \right]^2 \left[ \frac{\tau_1}{\tau_2} \right]^{2k} \Phi_{2k}(\tau_2) \qquad (10)$$

where

$$\tau_1 = \mu R_1 \text{ and } \tau_2 = \mu R_2$$

and

$$\Phi_{2k}(x) = \frac{1}{2^{(2k-1)}[\Gamma(k+\frac{1}{2})]^2} \int_x^{\infty} t^{2k} K_0(t) dt \qquad (11)$$

satisfies the recursion[6]

$$\Phi_{2k}(x) = \Phi_{2(k-1)}(x) + \frac{1}{2^{(2k-1)}[\Gamma(k+\frac{1}{2})]^2} (x^{2k} K_1(x) + (2k-1)x^{(2k-1)} K_0(x)) \qquad (12)$$

The asymptotic expansion for $\tau_1, \tau_2 \gg 1$

$$f_{12} = \frac{1}{2\sqrt{[R_1R_2]}} \sum_{n=0} C_n E_{(n+1)}(\tau_2 - \tau_1) \qquad (13)$$

where $E_n(x)$ is the $n^{th}$ exponential integral and

$$C_n = \frac{1}{2^n \pi^2} \sum_{m=0}^{n} \frac{\Gamma(m+\frac{1}{2})\Gamma(n+m+\frac{1}{2})}{m!\,(n-m)!} \frac{(-1)^m}{\tau_2^m \tau_1^{(n-m)}} \qquad (14)$$

yields the planar limit.

An alternative expansion is obtained by the direct expansion in $\int_x^{\infty} dx\, K_0(x)$ in (7).

$$f_{12} = \frac{1}{R_2} \left\{ \frac{1}{(1+a)} K\left[ \frac{4a}{(1+a)^2} \right] - \tau_2 \sum_{k=0} \left\{ (C_k - C_k' \ln\tau_2) I_k(a) - \frac{1}{2} C_k' J_k(a) \right\} \tau_2^{2k} \right. \qquad (15)$$

where $a = R_1/R_2$, $K(x)$ is the complete elliptic integral of the second kind and the integrals

$$I_k(a) = \frac{1}{2\pi} \int_0^{2\pi} d\psi (1+a^2 - 2a\cos\psi)^k \qquad (16)$$

$$= \sum_{j=0}^{k} \left[ \frac{k!}{j!(k-j)!} \right]^2 a^{2j}$$

and

$$J_k(a) =$$

$$\frac{1}{2\pi}\int_0^{2\pi} d\psi(1+a^2-2a\cos\psi)^k \ln(1+a^2-2a\cos\psi) \quad (17)$$

satisfy the recursion relations

$$kI_k(a) = (2k-1)(1+a^2)I_{(k-1)}(a) - (k-1)(1-a^2)^2 I_{(k-2)}(a) \quad (18)$$

and

$$kJ_k(a) = (2k-1)(1+a^2)J_{(k-1)}(a) - (k-1)(1-a^2)^2 J_{(k-2)}(a) - I_k(a) + 2(1+a^2)I_{(k-2)}(a) - (1-a^2)^2 I_{(k-2)}(a). \quad (19)$$

The coefficients $C_k$ and $C'_k$ are the expansion coefficients of $\int_x^\infty K_0(x)dx$ given in ref 6 p.481.

Alternative asymptotic expansions may be derived from (5) and (7), but will not be given here. The set of expansions (10), (13) and (15) are extremely powerful, and have been shown by direct calculation to give accurate values for all values of $\tau_1$ and $\tau_2$.

Integration over the line profile is required to give the line coupling coefficient $F_{12}$. For small $\tau_2 \lesssim 10$, this is accomplished directly using (15). For large $\tau_1$ and $\tau_2$ the integration of (13) over the line profile leads to the planar kernel functions whose behaviour is discussed by Ivanov[3], and computationally efficient forms are given by Hummer[7]. The case of small $\tau_1$ and large $\tau_2$ is well treated by equation (10), but requires the direct integration of the functions $\Phi_{2k}(x)$ over the line profile.

Numerical techniques for treating the general case with non-uniform plasma, and line shifts will be discussed in a later report.

REFERENCES


1. GJ Pert and SJ Rose: Appl Phys B in press.

2. D Mihilas: Stellar Atmospheres: Freeman, 1978.

3. VV Ivanov: Transfer of Radiation in Spectral Lines (trans DG Hummer) NBS Special Publication 385, 1973.

4. M Fishenden and OA Saunders: An Introduction to Heat Transfer: Oxford University Press, 1950.

5. JP Holman: Heat Transfer: McGraw Hill, 1981.

6. M Abramowitz and IA Stegun: Tables of Mathematical Functions, NBS Applied Mathematics Series 55, 1963.

7. DG Hummer: J Quant Spectrosc Radiat Transfer 26, 187, 1981.

# A MONTE CARLO SIMULATION OF OPTICAL TRAPPING IN AN EXPANDING LASER-PRODUCED PLASMA

MTM Lightbody and GJ Pert
University of York

## INTRODUCTION

A Monte-Carlo based ray trace of photon paths in a differentially expanding medium of arbitrary optical depth has been devised in order to simulate optical trapping in an expanding laser produced plasma such as is produced in a recombination x-ray laser experiment. This approach was chosen because analytic solutions are available in so few limiting cases and also because those approximate solutions that have been derived in the past are unable to encompass the wide range of physical conditions that are encountered in a laser produced plasma. In the Monte-Carlo "solution" it is possible to simulate a multitude of effects that are not possible analytically. Furthermore, numerical solutions to the radiative transfer equation are notoriously difficult to construct in more than one dimension and for curved geometries. Such solutions include the discrete $S_n$ method of Carlson and Lathrop amongst others. The advantage of the Monte-Carlo solution is the comparative ease with which it can be set up. Features that can be incorporated include:

- Differential expansion, with any velocity from static to high velocity Sobolev limit.
- Arbitrary frequency redistribution.
- Realistic Voigt line profiles with varying Lorentzian and Doppler components.
- Multiple velocity surfaces.
- Any density profile.
- Any optical depth profile.

The Monte-Carlo calculation is described further on. The procedure can best be followed by refering to figure 1 which explains the geometry as well as the various parameters involved. The main features of the basic model are as follows:

- Monte-Carlo based ray trace in 3-D cylindrical geometry.
- Radial coordinate of photon emission is a random variable, weighted by the Gaussian density profile.
- The angle of emission with respect to the initial radius vector and the z-axis are random variables.
- The total optical depth that the photon can travel is a negative exponentially weighted random variable.
- The frequency of the emitted photon is a random variable that is weighted by the emission line profile (a Voigt profile).
- The velocity profile of the expanding medium is chosen to be a linear function of the radial coordinate only, that is, $V(R) = kR$.
- The photon follows a straight line path through the cylinder. The optical depth for each step $\delta y$ is $\delta\tau = \delta y \times \chi(\nu)$ where the absorption coefficient $\chi(\nu)$ for that step is calculated from the line absorption coefficient at that frequency and the line profile function $V(\nu + \Delta\nu)$. $\Delta\nu$ is the total frequency shift undergone by the photon.

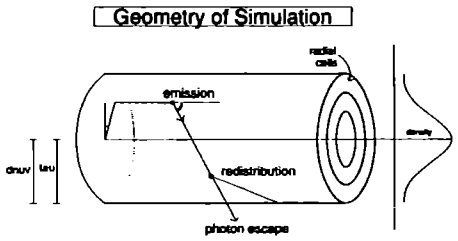


Figure 1: Geometry of Simulation

- The photon is traced until either the total optical depth travelled exceeds the predetermined value or until it escapes the cylinder.
- The total number of photons emitted in each cell is recorded. This gives the source function.
- The number of photons emitted from a cell that subsequently go on to escape is also recorded. This gives an estimate for the local escape probability.

## ANALYTIC ESCAPE PROBABILTIES

The escape probability method was devised by Sobolev [1] for solving line transfer problems in rapidly expanding stellar atmospheres. Doppler decoupling of different regions due to the presence of high velocity gradients reduces the calculation of line transport to a local problem. The escape probability method is used in x-ray laser gain simulations by acting as an inhibitor on the transition probability of various resonance lines, including the lasing line. This is achieved by multiplying the transition oscillator strength by a factor between 0 and 1, the escape probability. Sobolev derived the following general result for the escape probability:-

$$P_s = \frac{1}{4\pi}\int d\Omega \frac{1-\exp(-\tau_s)}{\tau_s}$$

which gives the probability that a photon, emitted at an optical depth $\tau_s$, escapes the system. This was initially evaluated for planar and spherical systems. Recently Eder and Shestakov [2] calculated $P_s$ for an infinite cylinder In all the Monte-Carlo simulations the calculated escape probability is compared with this cylindrical escape probability, as well as with the result for spherical geometry because it is this escape factor that has been used to date in gain calculations. It has been found that agreement between experiment and simulation is only possible if the escape factor is set equal to unity or, in other words, that there is no optical trapping. Therefore the Monte-Carlo calculation was devised in order to determine under what set of model parameters the escape probability could approach unity. The choice of model parameters was guided by results from independent hydrodynamic simulations. The basic Monte-Carlo programme described above is extremely

versatile. The model is characterised by the following free parameters:-

- Mesh size
- Density profile
- Velocity profile
- Total optical depth
- Emission and absorption line profiles
- Frequency redistribution

## MODEL PARAMETERS

### Mesh

The cylinder is divided radially into cells, see figure 1.

### Number of photons

A total of $N$ photons are included in the model. Increasing the number of photons increases the accuracy of the simulation, but the computation time scales with $N^2$.

### Line profile

A Voigt line profile is chosen. This is the result of combining the natural Lorentzian line profile with the thermal Doppler profile. It is given by:-

$$V(\nu) \propto \int dx \frac{\exp(-x^2/\sigma^2)}{x^2+\nu^2}$$

Changing the contribution of the Lorentzian and Doppler profiles alters the Voigt profile as shown in figure (2). The effect of this on the escape probability is also illustrated in figure (3).

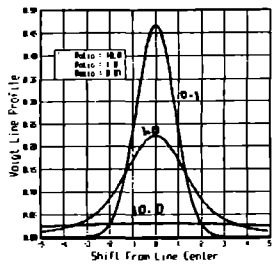


Figure 2: Effect of changing relative contributions to the Voigt profile

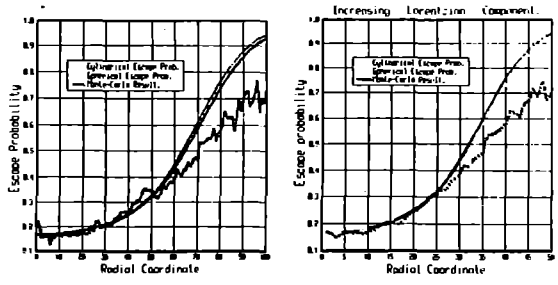


Figure 3: Effect of increasing Lorentzian component on escape probablity

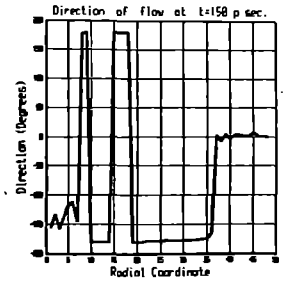


Figure 4: 2-D simulations of plasma velocity at various times in the expansion

### Velocity profile

The initial velocity profile was linearly increasing $V(R) = kR$. In reality this is not likely to be a good model. Results from $2-D$ hydrodynamic simulations, figure (4), indicate the presence of large velocity gradients. Some of these effects can be included in the model by using a multiple velocity surface profile, see figure (5). As can be seen from figure (5), this results in very large (almost unity) escape probabilities in the regions with rapidly changing velocity gradients. If such a rapidly changing velocity gradient occurs in the gain region, then use of the local effective escape probability will make gain simulations agree more closely with experiment. This is because it is largely irrelevant what happens to the photons outside the gain region.

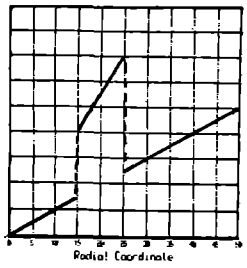


Figure 5: Multiple velocity surface

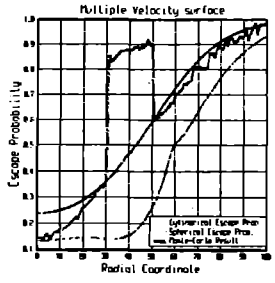


Figure 6: Escape probabilities using multiple velocity surfaces

## CONCLUSIONS

The results of the Monte-Carlo simulation were relatively insensitive to all the free parameters, within realistic bounds. The only way in which the escape probability could be made large was to include regions of high velocity gradient. This can be justified from results of previous hydrodynamic simulations.

# ENERGY OF ATOMS IN HIGH-DENSITY PLASMAS

S. Pfalzner[1,2], S.J. Rose[1]
[1]Rutherford Appleton Laboratory
[2]Queen's University Belfast

## INTRODUCTION

High-energy lasers produce plasmas with densities above $10^{23}$ atoms per $cm^{-3}$. For the analysis of such high-density experiments the equation of state (EOS - i.e. the pressure or energy as a function of density and temperature) is needed.
At high densities the electronic structure is significantly different from the free ion case. Investigation by Hartree-Fock methods is too expensive in computing time, especially for high-Z atoms. However, statistcal models, such as the Thomas-Fermi (TF) model, give energy values which are too high in the low density case. However, the TF model with the two corrections proposed by Schwinger [1] approximates the experimental values of free atoms with less than 1% error. These corrections are due to quantum effects near the nucleus and on the periphery of the atom. This model is generalized to describe ions at high densities and temperatures.

## ENERGY CORRECTIONS

It has been shown that the TF model is an adequate description at very high densities ($> 10^{24} cm^{-3}$),but its use at low densities ($< 10^{22} cm^{-3}$) is more problematic. The deficiencies of the TF model are:

(a) In the case of free atoms Scott [2], Schwinger and Englert [3] have shown that the TF description is only valid when the wavelength of the particle is small compared to the radial distance, $\hbar/p \ll r$ or alternatively there is an inner region where the TF approximation fails.

(b) In the TF model only the electrostatic interaction of the electrons is taken into account. The model can be improved by including exchange and correlation corrections.

With these corrections the energy of the free atom is [1]

$$E = 0.7687 Z^{7/3} \frac{e^2}{a_o} (1 - \underbrace{0.6505 Z^{-1/3}}_{(a)} + \underbrace{0.346 Z^{-2/3}}_{(b)}) \quad (1)$$

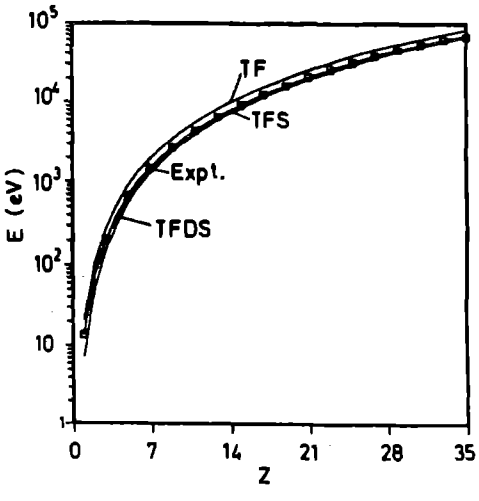


Fig. 1: Comparison of the total energies of free atoms calculated using the TF, TFS and TFDS model and experimental data as a function of the atomic number Z.

Fig.1 compares the results using the simple TF, TF with corrections (a) (TFS) and (b) (TFDS), and experimental data for the energies of free atoms of different Z. For low Z elements the error in the TF model is as high as 25 % . A comparison with energies obtained by the TF model with corrections (a) and (b) shows that for Z > 20 the discrepancy with measured values is less than 1 %.

## TEMPERATURE-INDEPENDENT CASE

The statistical theory of the atom is based on the assumption that the electrons of the system can be treated as a degenerate electron gas within a self-consistent electrostatic field. The electron gas is described by Fermi-Dirac statistics, which in the case of full degeneracy, reduces to the Pauli principle. In the case of full degeneracy the problem becomes temperature-independent. If all effects other than the electrostatic interaction can be neglected, the energies of the atoms and ions are given by

$$E = C_1 \int n_e^{5/3} d^3r - e \int V n_e d^3r + \frac{e^2}{2} \int \int \frac{n_e(r) n_e(r')}{|r - r'|} d^3r d^3r'. \quad (2)$$

with $C_1 = \frac{3}{10}(3\pi^2)^{2/3} e^2 a_o$ and $n_e$ is the electron density.

The Thomas-Fermi equation describes the potential in the atom

$$\Phi'' = \frac{\Phi^{3/2}}{x^{1/2}}. \quad (3)$$

with $x = r\mu$, $\mu = 0.885 a_o / Z^{1/3}$ and $\Phi = r(V - V_o)/Ze$. Using Poisson's equation the electron density can be obtained and eq.(2) can be rewritten as

$$E_{TF} = -\frac{Z^2 e^2}{\mu} \left( -\frac{3}{7}\Phi'(0) + \frac{2}{35} x_o^{1/2} \Phi_o^{5/2} \right) \quad (4)$$

where $\Phi_o = \Phi(x_o)$ is the potential at the boundary of the atom. Correction (a) means now that the integrals of (4) are solved within different limits. Correction (b) means one has to add exchange and correlation energies. Therefore the energy with corrections (a) and (b) is given by

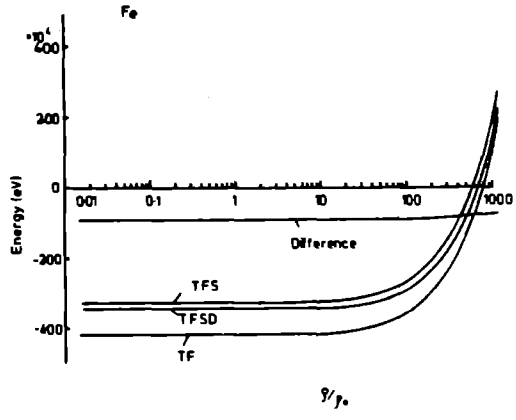


Fig. 2: Comparison of the density dependence of the total energy of an atom using the TF, Thomas-Fermi model with the near nucleus correction (a) and also including exchange and correlation correction (b) (TFSD).

$$E = E_{TF} + 1.195 Z^{7/3} \frac{e^2}{a_o} \left( \underbrace{\frac{3}{7}\frac{C_3}{Z^{1/3}} - \frac{\Phi_o}{x_o}\frac{1}{3Z}}_{(a)} \underbrace{- Z^{-2/3} \int \Phi^2 dx}_{(b)} \right)$$

Fig.2 shows a comparison of the TF equation with correction (a) and (b).

TEMPERATURE-DEPENDENT CASE

To use the EOS for hydrodynamic calculations it is essential to know the density- and temperature-dependence of these corrections. The influence of exchange and correlation effects has been widely discussed in the literature [4,5] in the temperature-dependent case. But because the near-nucleus correction is the dominant correction to the energy, we investigate this near-nucleus correction only.

The temperature-dependent TF model was derived by Feynman, Metropolis and Teller [6], although we use a somewhat different notation. The effect of temperature is to alter the charge distribution of the electrons in the atom.

As with the zero temperature Thomas-Fermi model, the bound and free electrons are indistinguishable and are treated as a partially-degenerate electron gas whose density $n_e(r)$ varies, together with the potential $V(r)$, continuously through the atom:

$$n_e(r) = \frac{4\pi}{h^3}(2m_e kT)^{3/2} I_{1/2}\left(\frac{eV(r)}{kT} + \eta\right). \qquad (5)$$

Poisson's equation relates the potential energy to the electron number density. From $V(r)$ and $n_e(r)$ the energy can readily be evaluated. The electronic potential energy is

$$E_{pot} = \frac{C}{2}\int_0^{r_o} r^2 n_e(r)\left(V(r) - \frac{Ze}{r}\right)dr - C\int_0^{r_o} r^2 n_e(r)\frac{Ze}{r}dr \quad (6)$$

with $C = 4\pi e$.

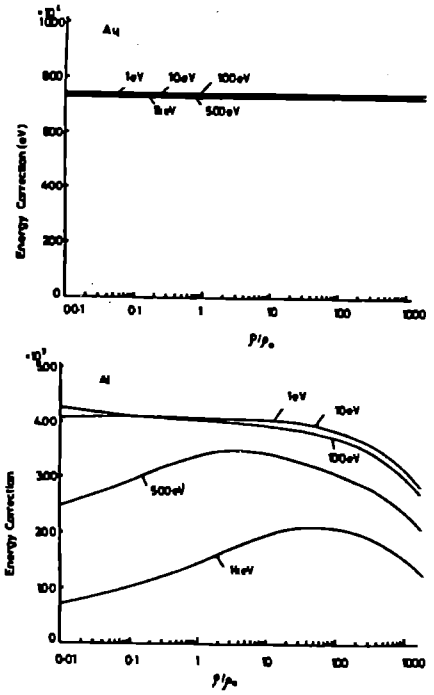


Fig. 3: Near nucleus correction to the total energy for Au and Al using a cut-off radius of $\lambda/2$.

The local electronic kinetic energy $\epsilon(r)$ is

$$\epsilon(r) = kT\frac{I_{3/2}\left(\frac{eV(r)}{kT} + \eta\right)}{I_{1/2}\left(\frac{eV(r)}{kT} + \eta\right)}$$

and the total kinetic energy is then

$$E_{kin} = 4\pi\int_0^{r_o} r^2 n_e(r) kT \frac{I_{3/2}\left(\frac{eV(r)}{kT} + \eta\right)}{I_{1/2}\left(\frac{eV(r)}{kT} + \eta\right)}dr. \qquad (8)$$

As in the temperature-independent case the validity of the approximation used requires that the de Broglie wavelength be small compared with the radial distance, i.e. $\lambda = \hbar/p \ll r$. As before this results in a lower bound for the integration and our choice, which gives an accurate correction at low temperatures and densities, is $r_{cut-off} = \lambda/2$. The de Broglie wavelength varies with radius. Fig.3 shows the energy correction for different elements. For the conditions calculated, for high-Z material (Au) the correction is nearly independent of temperature and density. In the case of a low-Z material (Al) the correction depends strongly on temperature and density.

CONCLUSIONS

It has been shown how the 1st and 2nd Schwinger corrections improve the result for the energy of the free atom. These corrections were generalized to atoms in high-density plasmas, and a new expression for the density-dependence of the energy was obtained. It has been shown how the near-nucleus correction of the TF model can be generalized to the temperature-dependent case. For high-Z atoms the correction is to a good approximation independent of temperature and density ( for the conditions choosen) and it is close to the free atom correction of Schwinger[1]. However, in the low-Z case the correction is strongly dependent on temperature and density. This is because in the temperature and density region considered inner electrons are affected by ionization. In the low-Z case but not in the high-Z case.

REFERENCES

1. J. Schwinger, Phys.Rev.A **24**, 2353 (1981).
2. J.M.S. Scott, Philos.Mag. **43**, 859 (1952)
3. B.G. Englert, J. Schwinger, Phys.Rev.A **26**, 2322 (1982).
4. F.Perrot, Phys.Rev.A **20**, 586 (1979)
5. K.Yonei, J.Ozaki, Y.Tomishima, J.Phys.Soc.Japan **56**,2697 (1987).
6. R.P.Feynman, N.Metropolis, E.Teller, Phys.Rev **75**,1561 (1949).

# THREE DIMENSIONAL HYDRODYNAMICAL SIMULATIONS OF LASER DRIVEN IMPLOSIONS

R P J Town and A R Bell

Imperial College, London

An important issue facing Inertial Confinement Fusion (I.C.F.) is the implosion symmetry. A typical I.C.F. target can be characterised as passing trough three phases: acceleration, coasting and deceleration[1]. Initially the shell is accelerated inwards, defects in target manufacture or non-uniform laser irradiation can seed the Rayleigh-Taylor (RT)[2] instability which grows on the outer, ablation surface. When the shell reaches maximum velocity it coast inwards with little acceleration. Although not unstable the large spherical convergence can further distort the shell. As the pressure inside the filler gas increases so the shell is decelerated and finally brought to rest. In this final stage the shell is again RT unstable, but this time on the inner fuel-shell interface. Maximum density and temperature can only be acheived if the shell converges accurately towards the centre.

Previous numerical simulations[3,4,5] have concentrated on the initial, acceleration phase in two dimensions. The ablation dynamics have been found to play a crucial role in the reduction of the obsevered RT growth rate to approximately one half the classical value. Full implosion simulations have been performed in two dimensions[6] using (R-Z) geometry. However 2 dimensional simulations impose an unrealistic initial perturbation on the target and, unless a hemisphere is modelled the boundary conditions would be incorrect.

We report here on our simulations of the coasting and deceleration phase using PLATO. This is a fully three dimensional, spherical hydrodynamics code with a fixed Eulerian grid. The time dependent equations of mass, momentum and total energy are integrated numerically using the Van Leer[7] algorithm as intepreted by Youngs[8] . The fluid equations are closed using an ideal ($\gamma = 5/3$) equation of state. Currently thermal conduction and laser energy deposition are not included. To model accurately implosions a fine resolution is needed. If the volume modelled is large then a large number of grid points are required. This would need a large amount of computer memory and long run times. It would be prohibitively expensive to model a full sphere so we are using the symmetry of Platonic solids to divide the sphere into a number of self-similar triangles.

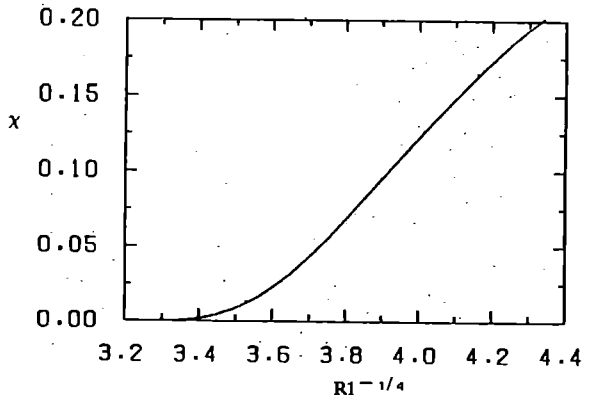


Figure 1: The growth of $\chi$ as a function of the $R1^{-1/4}$

Figure 2: The inner fuel-shell surface at the end of the simulation. This shows the spike-valley arrangement.

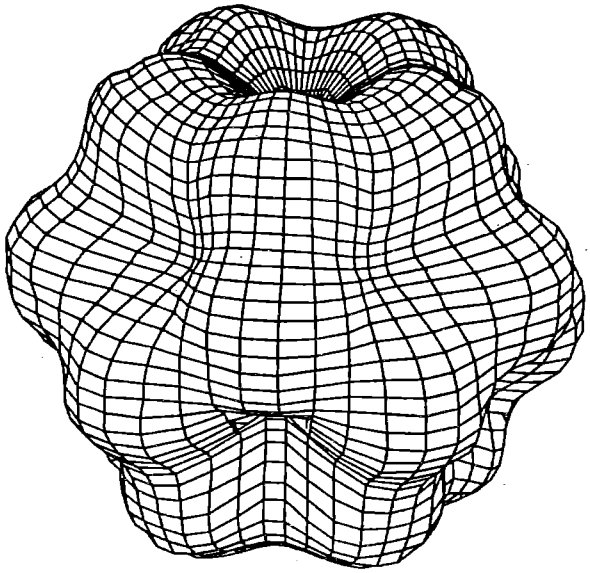

At present we are exploiting the symmetry imposed on the target by the Rutherford Appleton Laboratory's 12 Beam Vulcan laser system. The point of intersection of the centre of each laser beam with the target surface defines the symmetry of the target. These points form the vertices of 20 equilateral triangles on the surface. Since the triangles are equilateral the sides can be bisected and 6 smaller triangles formed for each equilateral one. Hence the smallest self-similar component is 1/120th of the sphere. This is the computational grid that we use in all our simulations.

Since PLATO does not have any laser energy deposition all our simulations were initialised in the coasting phase. To study the coasting phase a 7$\mu$m thick plastic shell was assumed to be coasting inwards with a velocity of $2.10^7$ cm/s at an initial inner shell radius, R1 of 174$\mu$m. The filler gas used was DT at a density of $1.05\ 10^{-2}$ g/cm$^3$ at a pressure of 100 bar. To prevent a transmitted shock travelling in front of the shell a radial velocity proportional to the radius was used in the filler gas. In order to simulate the sffects of non-uniform laser irradiation the radial velocity was perturbed by a sixth order Legendre polynomial summed over the poles of the laser beams. This is the lowest order perturbation a balanced 12 beam system is unstable to.

As the shell coasts inwards it becomes distorted: the more strongly driven part has been driven closer to the origin. Analysis of the flow shows fluid motion away from the strongly driven line towards the weakly driven line. As the shell distorts so the more strongly driven part is no longer

constrained to move purely in the radial direction. The growth of the asymmetry has been characterised by the quantity $\chi$, defined as the difference in integrated mass along the weakly driven radial line to that of the most strongly driven radial line. After an initial transitionary phase figure 1 yields a straight line for $\chi$ against $R1^{-1/4}$. We conclude that during the coasting phase the model of Book and Bodner[1] is valid.

When the pressure inside the filler gas is sufficiently large the shell starts to decelerate. The shell is now RT unstable. We have tried to qualify the nature of the RT instability in this phase. Is it a spike and valley (ie a protuberance of high density) or a ridge and bubble (a protuberance of low density) arrangement? In order that the shell enters the deceleration phase earlier the shell was initialised travelling into a stationary fuel at a constant velocity. We assumed that the shell's inner surface had been deformed by the earlier acceleration and coasting phases. This surface was perturbed by a sixth order Legendre polynomial summed over the laser beams. Figure 2 shows the inner surface at the end of the simulation. The pattern is distinctly a spike surrounded by a valley. However when the perturbation was inverted we produced figure 3 which shows the opposite bubble surrounded by a ridge. Hence the nature of the RT seems to be completely dependent on the initial conditions.

Finally we have undertaken work to quantify the RT growth rate in the deceleration phase. We assume that the mass distribution ($\sigma(\theta,\varphi)$) along a radial line can be expressed as:

$$\sigma(\theta,\varphi) = \sum_n a_n \sum_b \int_{-1}^{+1}\int_0^{2\pi} P_n(\cos(\gamma_b))\ d\cos(\theta)d\varphi \qquad (1)$$

where $\cos(\gamma_b)$ is given by:

$$\cos(\gamma_b) = \cos(\theta)\cos(\theta_b)+\sin(\theta)\sin(\theta_b)\cos(\varphi-\varphi_b) \qquad (2)$$

and $\theta_b$, $\varphi_b$ are the coordinates of the laser beams. The

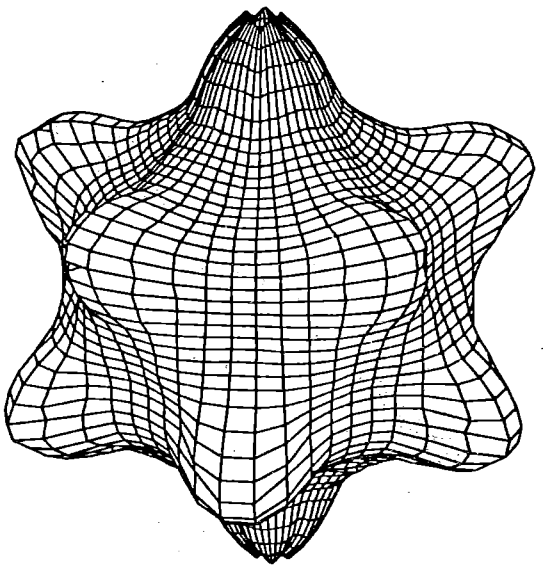

Figure 3: The same as figure 2, but with an inverted perturbation. Notice this shows the ridge−bubble arrangement.

Figure 4: The growth of the sixth order mode.

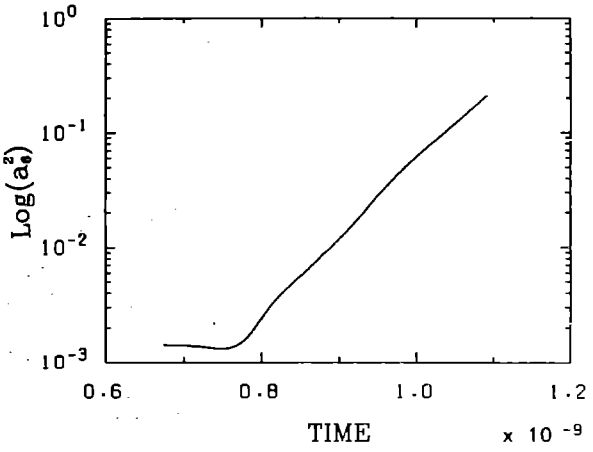


growth of the kth mode is hence obtained by solving the following integral:

$$a_k = \frac{2k+1}{4\pi} \frac{\int_{-1}^{+1}\int_0^{2\pi} \sigma(\theta,\varphi)\ P_k(\cos(\theta))\ d\cos(\theta)d\varphi}{\sum_b P_k(\cos(\gamma_b))} \qquad (3)$$

Figure 4 shows the growth of the sixth mode. This gives a linear growth rate which is 2/3rds the classically expected value.

In conclusion we have written a 3D fluid code to study the growth of assymmetries in ICF targets. We have shown that in the coasting phase the assymmetries scale as $R1^{-1/4}$ in agreement with Book and Bodner. The nature of the RT instablity appears to be dependent on the initial conditions. Preliminary measurements of the growth rate have been made which shows a reduction to 2/3rds the classical value.

REFERENCES


1. D.L.Book and S.E.Bodner Phys. Fluids 30 367 (1987)

2. Lord Rayleigh *Theory of Sound* Dover, New York, (1945) 2nd ed., Vol2;
G.I. Taylor, Proc. Roy. Soc. London, Ser A 201, 192 (1950)

3. M.H. Emery, J.P. Dahlbury and J.H. Gardner, Phys. Fluids 31, 1007 (1988)
and Phys. Fluids B 1, 964E (1989)

4. M. J. De C. Henshaw, G. J. Pert and D. L. Youngs, Plas. Phys. and Cont. Fus. 29, 405 (1987)

5. C. P. Verdon *et al*, Phys. Fluids 25, 1653 (1982)

6. Lab. for Laser Energetics Quarterly Report 23, 125 (1985)

7. B. Van Leer, J Comput. Phys., 276 (1977)

8. D.L. Youngs, *Numerical Methods for Fluid Dynamics* Academic Press, (1982)

# FOKKER–PLANCK SIMULATIONS OF PLASMA IRRADIATED BY AN INCOHERENT LASER

G J Rickard, I R G Williams and A R Bell

Imperial College, London

The Fokker–Planck (FP) code we use has been detailed elsewhere[1]. It has been used to examine the conditions relevant to short–pulse laser–plasma interactions[2], and nonlocal electron transport in long scalelength plasmas[3], in both 1D and 2D. In the present study, we use short density scalelengths (3$\mu$m initially), and impose ISI–type intensity profiles[4]. The Spitzer code uses the classical Spitzer–Harm[5] thermal conductivity, with a harmonic flux limiter. We examine how the ablation pressure responds to rapid changes in incident intensity, and discover a 1D effect caused by thermal conduction. In contrast to lateral smoothing, this effect is not restricted to short perturbation wavelengths, and operates at early times.

Energy is absorbed at or near the critical surface. The variation in absorbed energy is transmitted to the drive pressure at the solid by heat flow. From the heat diffusion equation we can estimate the strength of nonlocal effects:

$$\frac{3nk}{2}\frac{T}{\tau} \approx 7\nu nkT\,\frac{\lambda^2}{L^2} \qquad (1)$$

where $\tau$ is the laser coherence time, $\lambda$ the electron mean free path, $\nu$ the electron–ion collision frequency, and L the temperature scalelength. For T = 1keV, n = $10^{22}$ cm$^{-3}$, Z = 4, this becomes

$$\frac{L}{\lambda} \approx 10\left[\frac{\tau}{\text{psec}}\right]^{1/2} \qquad (2)$$

From previous work[6], we know that nonlocal effects become important whenever $L/\lambda \lesssim 30$, i.e. $\tau \lesssim 10$ psec.

To mimic the fluctuations inherent in ISI, we impose an oscillating laser intensity in 1D,

$$I(t) = I_0(1+\cos(\pi t/\tau))\exp(-(t-t_0)^2/2\sigma^2) \qquad (3)$$

with $I_0$ = 5.10$^{14}$ Wcm$^{-2}$, $t_0$ = 100 psec, $\sigma$ = 45 psec, $\lambda_{laser}$ = 0.25 $\mu$m. The target is fully ionised, Z = 4, with a density scalelength of 3 $\mu$m, and maximum electron density

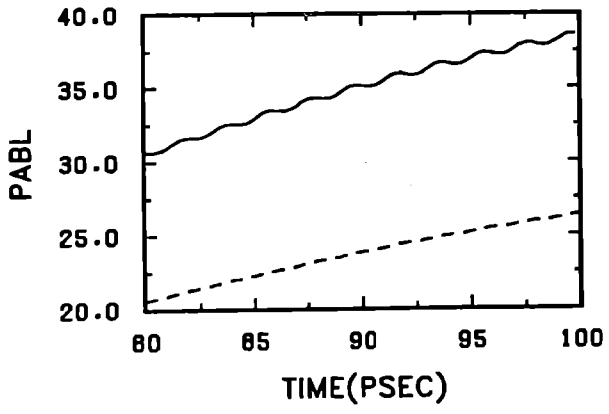


Figure 1: Ablation pressure against time for $\tau$ = 1 psec, for 1D FP (– – –) and Spitzer (——) simulations

Figure 2: $P_{max}/P_{min}$ against time for 2D ISI simulations

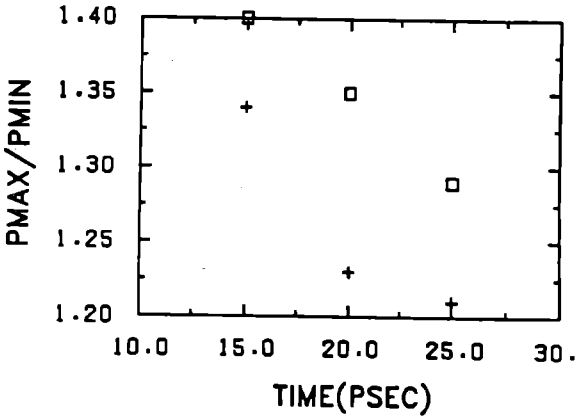


9.10$^{22}$ cm$^{-3}$. The Spitzer simulations show a greater temporal fluctuation in ablation pressure than the FP results (see Figure 1). This is true even when the Langdon reduction factor[7] is used in the Spitzer code (to correct for the reduced absorption due to depletion of electrons at low velocities), and for all values of the flux limiter.

In 2D, an ISI–type intensity profile is used, consisting of multiwavelength time–dependent spatial perturbations in the transverse direction. A coherence time of 1 psec is imposed. Figure 2 shows the values of $P_{max}/P_{min}$ for FP (crosses) and Spitzer (squares) from a typical run. $P_{max}$($P_{min}$) is the maximum(minimum) pressure along the ablation front. $P_{max}/P_{min}$ is thus a measure of the 'smoothness' of the ablation front. The FP always has a smaller $P_{max}/P_{min}$ than that predicted by Spitzer. Hence the 2D results confirm that the FP profiles are smoother than Spitzer.

Nonlocal effects reduce the heat flow from the absorption to ablation regions, so that changes at the absorption surface are not communicated to the ablation surface as strongly with nonlocal transport as with Spitzer. We conclude that $\Delta P/P_{abl}$ for a given $\Delta I/I$ with an incoherent laser (e.g. ISI) is smaller than would be predicted by fluid codes using the Spitzer conductivity. This is encouraging in the context of the high–density, highly symmetric implosions required for ICF.

REFERENCES

1. EM Epperlein et al. Comp Phys Comm 52 7 (1988)
2. GJ Rickard et al. Phys Rev Lett 62 2687 (1989)
3. EM Epperlein et al. Phys Rev Lett 61 2453 (1988)
4. RH Lehmberg & SP Obenschain Opt Comm 46 27 (1983)
5. L Spitzer Jr & R Harm Phys Rev 89 977 (1953)
6. AR Bell Phys Fluids 26 279 (1983)
7. AB Langdon Phys Rev Lett 44 575 (1980)

# COLLISIONLESS ABSORPTION IN SHARP-EDGED, OVERDENSE PLASMAS

P. Gibbon and A.R. Bell

Imperial College, London

Recent experiments[1,2] have demonstrated high absorption of sub-ps laser pulses at various irradiances. The inverse-Bremsstrahlung mechanism[3] used to explain these data appears to give good agreement at low irradiance ($I\lambda^2 < 10^{15} Wcm^{-2}\mu m^2$), but is less adequate for higher irradiance, where the plasma temperature is higher, and the collision frequency correspondingly lower – $\nu_{ei}/\omega \ll 1$. Another possible candidate is the 'vacuum heating' mechanism suggested by Brunel.[4] In this case, electrons are pulled out from the surface of a sharply-bounded solid by an obliquely incident laser field, and return with a speed of the order $v_{osc}$. Because the elctric field vanishes inside the solid (or overdense plasma), the returning electrons penetrate a long way until finally dissipating their energy through collisions. Resonance absorption could also play a role with obliquely incident light, but only at very large angles, since the density gradient L is very much smaller than the laser wavelength $\lambda$. (Owing to the short pulse length, the plasma has little time to ablate significantly, and can be considered as a thin, overdense layer with a very steep gradient.)

We have used a 1½D electromagnetic code $(x, v_x, v_y)$ to investigate the transition between traditional resonance absorption ($L/\lambda > 1$) and the steep gradient regime. Oblique incidence is contrived by giving the particles a boost ($v_{yo}$) in the plane perpendicular to the density gradient. A force $ev_{yo}B_z$ then acts to drive a field $E_x$, whcih can grow resonantly near the critical density.

The angular dependence of the absorption for two different scale-lengths is shown in Fig. 1. The simulation results (squares) on curve 1 ($L/\lambda = 1$) agree well with the fluid theory[5] for $L/\lambda \gg 1$. The results for small scale-length ($L/\lambda = 10^{-2}$) show an unexpectedly high resonance at 52°. In fact, this is in quantitative agreement with the experimental results of Ref. (2) at $I\lambda^2 = 2.5 \times 10^{15}$.

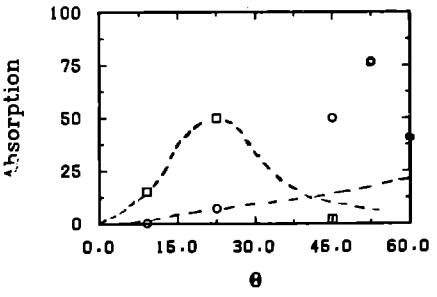


Figure 1. Angular dependence of absorption for a) $L/\lambda = 1$ (squares), b) $L/\lambda = 10^{-2}$ (circles). The fluid theory of Ref.5 is shown by the dashed lines.

To see the variation of absorption with irradiance at small scale-lengths, we choose $L/\lambda = 10^{-2}$, and a fixed angle $\theta = 45°$. Figure 2a shows that the absorption decreases with increasing irradiance. This is because a D.C. magnetic field is generated near the surface which deflects electrons and prevents them re-entering the solid.[4] The magnitude of this field increases with laser intensity, so we expect the 1D model of Brunel to break down at the higher irradiances. The hot electron temperature as a fraction of laser irradiance for the same parameters is shown if Fig. 2b. The scaling is roughly $T_h \propto (I\lambda^2)^{1/3}$. Although we appear to obtain fairly high energies (10-100keV) via this mechanism, the efficiency is low above $I\lambda^2 = 10^{16}$ because the absorption is small. Further study is neede to identify more precisely the nature of the field stuctures and electron orbits in the vacuum-solid interface region, and thus determine whether a 'modified-Brunel' theory best describes the results reported herein.

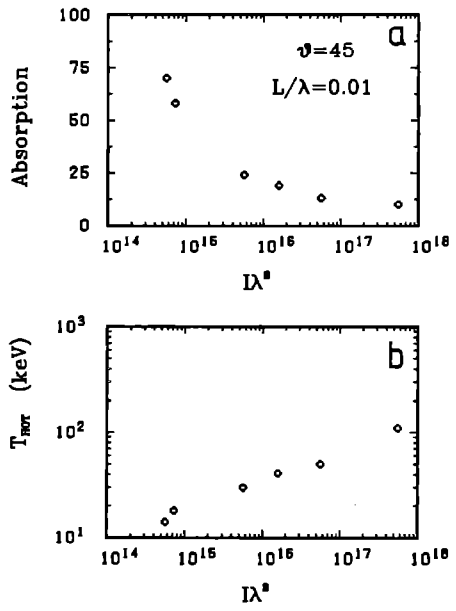


Figure 2. Dependence of a) absorption and b) hot electron temperature on irradiance for $L/\lambda = 10^{-2}$, $\theta = 45°$.

REFERENCES

1. JC Kieffer et al. Phys Rev Lett 52 760 (1989)
2. R. Fedosejevs et al. Phys Rev Lett 64 1250 (1990)
3. HM Milchberg and RR Freeman J Opt Soc Am B6 1351 (1989)
4. F Brunel Phys Rev Lett 59 52 (1987)
5. VL Ginzburg *Propagation of Electromagnetic Waves in Plasma* Pergamon NY (1970)

# LASER WAKE FIELD ACCELERATOR

D.Allen and A.R.Bell

Imperial College, London

## ABSTRACT

A short pulse laser, matched to the natural plasma period, might be used to produce large amplitude plasma waves. These waves in turn can be used to accelerate particles to high energies. We have simulated the generation of plasma waves and their feedback effect on the laser pulse.

## MECHANISM

It was first suggested by Tajima and Dawson[1] that an intense electromagnetic pulse could create plasma oscillations through the action of the non−linear ponderomotive force and hence trapped electrons could be accelerated to high energies.

In the laser wake field accelerator a short pulse high power laser beam is transmitted through the plasma. In 1−D the beam provides an axial ponderomotive force on the plasma electrons. Axially the front (back) of the pulse exerts a forward (backward) force on the electrons. As the plasma electrons flow around the laser pulse, large amplitude plasma waves are generated.

## SIMULATION

1−D wake field simulations have been performed with a code that solves equations (1) and (2), for the wake field produced and its feedback on the driving laser pulse.

$$\frac{\partial^2\varphi}{\partial z^2} = -\left[\frac{\varphi + |a|^2 - \varphi^2/2}{(1-\varphi)^2}\right] \qquad (1)$$

$$2i\omega\frac{\partial a}{\partial t} = (1-(v_g)^2)\frac{\partial^2 a}{\partial z^2} - a\frac{\varphi}{(1-\varphi)} \qquad (2)$$

Where: a is the vector potential of the laser pulse

$\varphi$ is the scalar potential of the wake produced in the plasma

$v_g$ is the laser pulse group velocity

$\omega$ is the laser pulse frequency

Bulanov[2] considers a similar problem, for much shorter time scales.

## RESULTS

The results shown in Fig1 show that as the laser pulse propagates through the plasma, a wake field is produced and this wake field feeds back on the original laser pulse. After $1600(\omega_p)^{-1}$ it can be seen that the back end of the pulse has steepened up and a ripple instability has been produced on the leading edge. The parameters used in the simulation are given with Fig1.

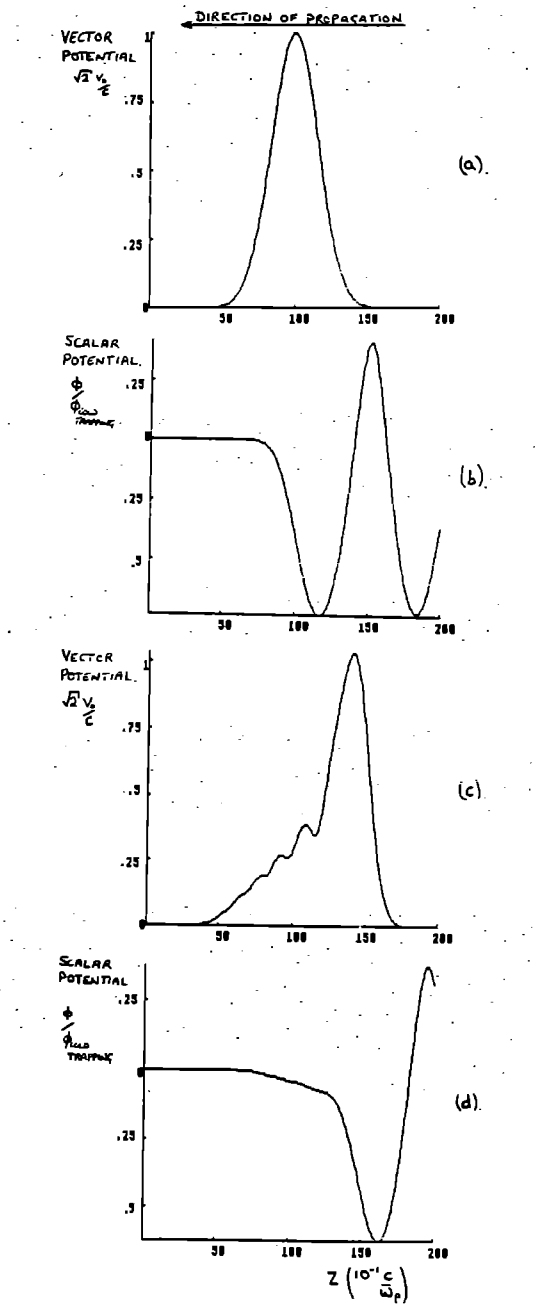


Fig1:

FWHM= 2.6(c/$\omega_p$), $\omega/\omega_p$= 10, $v_o/c$= 1.4, $I\lambda^2$=$10^{18}$W$\mu^2$/cm$^2$, $\varphi_{cold}$= mc$^2$/e

a)Original driving laser pulse

b)Wake field produced by initial pulse

c)Laser pulse after $1600(\omega_p)^{-1}$

d)Wake field after $1600(\omega_p)^{-1}$

## REFERENCES

[1]T.Tajima,J.M.Dawson, Phys.Rev.Lett.43,267,(1979).

[2]S.V.Bulanov,V.I.Kirsanov,A.S.Sakharov, To appear in JETP.

# MED101: A LASER-PLASMA SIMULATION CODE

PA Rodgers and SJ Rose
Rutherford Appleton Laboratory

## INTRODUCTION

This report outlines recent modifications to the laser fusion code MEDUSA [1]. The code has now been renamed MED101 and a user guide is available [2]. This contains complete details for running the code including: an explanation of the input parameters, instructions for running on the Rutherford Appleton Laboratory IBM 3090, Atlas Centre Cray X-MP and DEC VAXs, and information on three new graphics packages. The guide also includes an introduction to CMS (the operating system on the IBM) which should enable those unfamilar with the machine to obtain useful output as quickly as possible.

The operating system on the Cray X-MP was recently changed from COS to Unicos. A sample JOB file for running MED101 under Unicos is given below. To run in SLAC Batch on the IBM see section 2.1 of [2].

Like MEDUSA MED101 is a 1-D Lagrangian hydrodynamic code but is capable of modelling a wider range of experiments and has associated with it a suite of graphics programs. Improvements to the physics in the program include

1) calculation of the ionisation stages of the plasma (as opposed to just the average ionisation)
2) calculation of X-ray laser gain in recombining laser-produced plasmas for H-like, Li-like and Na-like schemes
3) complete control over the design of a three-layer target
4) corrections to the energy exchange and heat conduction subroutines.

MEDUSA needed to be overhauled as different source codes (requiring different input data files) existed for the IBM 3090 and the Cray X-MP computers. This led to confusion as to which version was definitive. MED101 now runs transparently to the user from the same data file on either machine — this should be of benefit to users who don't have large amounts of Cray time at their disposal. MED101 should also run on all DEC VAXs without modification. You may find that results will differ slightly for identical runs on the Cray, IBM or VAX. This is because the machines have different standard numbers of significant figures and exponents.

## RUNNING MED101 UNDER UNICOS

To access the Unicos system you must first enter `GIME CRAY` and then `CRCHOOSE UNICOS` from CMS. The `CRSUBMIT` and `CRSTAT` commands will work as before. Table 1 shows a Unicos JOB file equivalent to the COS job file given in section 2.2 of [2] using POSTER DATA as the input data file. MED101 now produces a minimum of three and a maximum of five output files when run on the Cray (under COS between two and four output files were produced).

Note that Unicos is very sensitive to case.
Lines 1 defines the Cray username and password.
Lines 2 and 3 define the job name and the Cray account.
Line 4 defines the time limit for the job in CPU seconds.
Line 5 must be included.
Line 6 fetches the input data file from your CMS space. You must include a password even if you haven't set one for your CMS minidisks (in this case the password can be anything). Note that this line has been split to fit within the column.
Lines 7-9 define the output streams for the run. Output is always produced on stream 13. Depending on the input data file output can also be produced on streams 11 and 12. These files will have a filetype CARDS.

Table 1: Unicos job file for running MED101

```
# USER=usid PW=craypw
# QSUB-r meduni1
# QSUB-A crayac
# QSUB-lT 200
# QSUB
fetch data -m VH -t'fn=poster,ft=data,
  tid=usid,pw=random'
assign -a xrl fort.11
assign -a ion fort.12
assign -a flipper fort.13
segldr /atlas/pr2/med101.o
a.out <data>medusa
dispose mdeusa -m VH -t'CC=YES'
dispose xrl -m VH -d PU
dispose ion -m VH -d PU
dispose flipper -m VH -d PU
rm a.out data medusa xrl ion flipper
ls -l
```

Line 10 runs the compiled version of MED101. This is now stored on PR2's Unicos space.
Line 11 puts the easy-to-read output in a file called MEDUSA OUTPUT. Under COS the log file and easy-to-read file were combined. Under Unicos they are seperate. The log file will be called MEDUNI1 OUTPUT for this example.
Lines 12-15 send the output files back to your reader.
Line 16 deletes from usid's Unicos space all the files created during the run. Obviously if you wish to keep any of these files do not `rm` them.
Line 17 lists all the files in usid's Unicos space at the end of the job.

## GRAPHICS PACKAGES

There are three different graphics programs to post-process MED101 output:

1) FLIPPER — this plots the hydrodynamic variables (velocity, density, pressure, electron and ion temperatures, and average ionisation) vs. distance for different times, and also the hydrodynamic variables (cell edge and centre plus velocity etc.) vs. time for each cell
2) IONFLIP — this plots the ground state number density of the different ionisation stages vs. distance at different times during the interaction. IONFLIP also displays the zoning of the run. This can be useful to ensure that there are enough cells in the regions of interest
3) XRLFLIP — this plots the X-ray laser gain vs. distance at different times, and also the space-integrated gain for different lines (i. e. alpha, beta etc.) vs. time as would as measured by experiment [3].

Each graph has a panel at the top containing details of the input data used for that particular run.

The graphics packages run on the IBM and use NAG GKS routines to produce GKS metafiles for printing at Rutherford.

## REFERENCES

1. JP Christiansen, DETF Ashby and KV Roberts Computer Phys Comm **7** 271-287 (1974)
2. PA Rodgers, AM Rogoyski and SJ Rose *MED101: a laser-plasma simulation code. User guide* Rutherford Appleton Laboratory Report RAL-89-127 (1989)
3. GJ Pert and SJ Rose Applied Physics **B50** 307 (1990)

# INTRODUCTION AND OPERATIONAL STATISTICS

CB Edwards and CN Danson
Rutherford Appleton Laboratory

The major facility enhancement during the current reporting year was the completion of the Phase I upgrade. This included the installation and commissioning of two 150 mm diameter disc amplifiers in the laser hall, the re-configuration of the beam switchyard, and the installation of relay optics for six-beam delivery to T.A.East. The installation was completed on time, and the facility was fully operational for the first scheduled experiments in May 1989.

In the course of experiments subsequent to the upgrade, VULCAN has demonstrated output at its design specification. During the October implosion experiments, output of 1.6 kJ was routinely delivered, with a maximum recorded 6-beam output in excess of 1.85 kJ. The highest recorded green energy was 844 J in six beams. During the X-ray laser experiment in T A East 1.007 kJ of infra red was recorded from three beams. It is now a high priority to improve the quality of the target area optics as funds permit to ensure that a higher proportion of Vulcan output is delivered on target.

Current funding limits the availability of the full 150 mm backlighting capability to a single beam in T A West, with an apodised beam at 108 mm diameter available in T A East and T A 2.

Highlights of the development programme during the year have been the introduction of Random Phase Plates for both infra-red and green operations, and a successful demonstration of chirped pulse amplification on Vulcan. Pulse durations of 10 ps were recorded at powers up to 1 TW without significant damage to the system. This work is described in more detail below.

Shot statistics for the period are summarised in Table I. All target areas have been operational, with 1220 full disc shots being delivered during experiments, with a shot failure rate of 3%. TA 4 has also been operational with 278 shots delivered primarily for instrumentation development.

Staff shortages continue to be a problem for laser operations. The target area operations group continues to rely heavily on facility users to assist in both the configuration of the areas during the set-up period, and the routine operation of the area during experiments. The contribution made in this way by the user community in general to the success of the experimental programme at the Facility is gratefully acknowledged.

| | |
|---|---|
| Total Number of shots | 4489 |
| Total Number of disc shots to TA's | 1220 |
| Number of disc shots to TAW | 272 |
| Number of disc shots to TAE | 573 |
| Number of disc shots to TA2 | 375 |
| Number of target shots to TA4 | 278 |

| Experimental Period | Experiment / Number of disc shots to the Target Areas | | |
|---|---|---|---|
| | TAW | TAE | TA2 |
| 26 Mar - 15 Apr | Radiation Transport / 136 | Rayleigh Taylor / 127 | |
| 16 Apr - 8 July | | UPGRADE | |
| 16 July - 5 Aug | | | Soft xray emission / 104 |
| 6 Aug - 26 Aug | | Xray laser / 135 | |
| 3 Sept - 29 Oct | Implosion studies / 112 | Xray laser / 115 | Thompson Scattering / 62 |
| 4 Nov - 22 Dec | Fibre shocks / 78 | EXAFS / 24 | uv moire / 64 |
| 4 Jan - 3 Feb | SHORT | PULSE | DEVELOPMENT |
| 4 Feb - 3 Mar | | Beam smoothing / 118 | Plastic strain / 145 |

Table 1: Shot statistics on VULCAN for the year to March 1990.

# BROAD-BAND OSCILLATOR DEVELOPMENT

R Bann and CN Danson
Rutherford Appleton Laboratory

## INTRODUCTION

The ISI experiments carried out last year showed the value of temporal smoothing[1]. This year time was assigned to further investigate the oscillator used in the ISI system. Previous work has shown that a much broader bandwidth could be supported by an Nd:Glass oscillator by modifying the spectral profile within the cavity[2]. To encourage the lower gain regions of the lasing bandwidths to lase, the peak gain region must be selectively supressed. This can be achieved in several ways:

(i) Etalons can be placed in the cavity and tuned to supress the high gain modes of the cavity.

(ii) A waveplate can be tuned to reject the desired modes from the cavity via the intra cavity polariser.

(iii) Spectrally selective dielectric back mirrors can be used to inject only the lower gain regions back into the cavity.

## DEVELOPMENT

The scheme described used a combination of (i) and (ii) by using a 2mm etalon made of natural quartz. This could be tuned by tilting and rotating the etalon to achive the desired Q profile within the lasing cavity.

A schematic of the oscillator used is shown in figure 1. Time integrated spectral profiles of the oscillator output are shown in figure 2. They start with the profile of the unmodified pulse as used in the main VULCAN experiments. The 13 Å bandwidth reduces the coherence length enough to use with the ISI stack on the main system[3].

Figure 2b is a calibraton shot with a 430 μm glass etalon placed in the cavity to give a known spectral profile to the output pulse. The peaks are separated by 8.9 Å.

Figure 2c was obtained by totally supressing the main lasing area of the bandwidth and shows that there is over 100 Å of lasing bandwidth available if the Q profile can be well matched.

Figure 2d shows the widest continuous bandwidth achieved using the 2mm quartz etalon. The 50 Å gives significantly improved temporal smoothing.

The final figure shows the widest total bandwidth achieved. The noncontinuity does not adversly affect the smoothing of the pulse. The total bandwidth for this pulse ( $\alpha + \beta$ ) is 60 Å but the maximum spectral width is over 80 Å.

## CONCLUSIONS

The enhanced spectral bandwidth obtained would be useful for experiments requiring increased temporal smoothing during experiments using ISI. The oscillator could only be used on I.R. experiments as the 2ω conversion process would be very inefficient and would also reduce the bandwidth significantly. For these reasons it is not planned to make this system a standard option for VULCAN experiments.

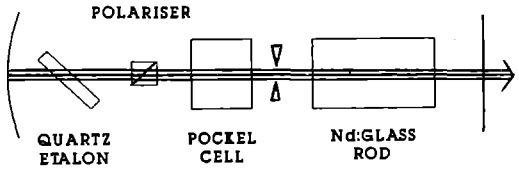


Figure 1: Schematic of Broadband Oscillator

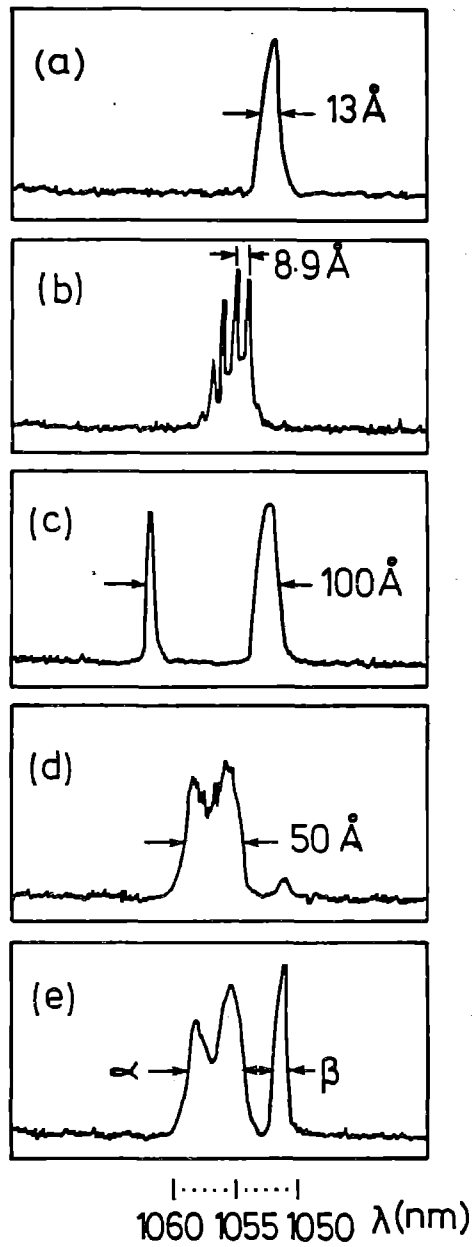


Figure 2: Time Integrated Spectral Profiles.

## REFERENCES

1. Annual Report to the Laser Facility Committee. (1989) RAL Report 89-045. pp 51-56.

2. A Master Oscillator with Tunable Radiation Spectrum for a High Power Pulsed Neodymium Laser. I.V. Aleksandrova et al. Kvantovaya elektronika, 1983, 10, (4), pp 892-895.

3. Annual Report to the Laser Facility Committee. (1989) RAL Report 89-045. pp 141-149.

# PRODUCTION AND OPTIMISATION OF RANDOM PHASE PLATES

R Bann, CN Danson and J Exley
Rutherford Appleton Laboratory

## INTRODUCTION

To improve the quality of data from laser plasma interaction experiments required the development of focal spot smoothing techniques. Techniques described previously[1] have included multi-beam ISI and the use of Random Phase Plates (RPP). These have been produced for interaction experiments at 1 053 nm, 527 nm and 263 nm by standard lithography.

## MASK PRODUCTION

The most important developments in this area were new techniques in mask production which improved the range of focal spots available. The first improved masks were produced by the Electron Beam Lithography (EBL) facility using software written within the group. The masks consist of a chrome coating on a quartz substrate. Using EBL the chrome can be etched with 0.125 micron precision, allowing extremely fine structures to be produced.

The photolithographic process used creates thin non uniform areas of resist between the individual elements. Light passing through these regions is diffracted out of the focal spot. An acceptable maximum of 'wasted' area on the plate has been set at 2% which limits the element size to 50 microns. This mask is currently under manufacture. The other masks shown in Table 1 are all available for the production of RPP's, and have been used in various experiments during the last twelve months.

There are two problems with using masks manufactured by EBL: the first is that the largest apertures that can be provided are 100 mm. This would create some problems in providing RPP's for the 150 mm diameter beams. The second is the delivery times of 1-3 months. To experiment with RPP's for specialist applications, such as line focii, it would be preferable to produce our own masks to maintain a degree of flexibility.

One solution currently under development uses a standard high resolution printing process to produce opaque mask designs on clear plastic film. The film is not UV transmitting and so a second process is required to transfer this design onto a quartz-chrome plate. The whole process could be completed within a week. Trials using this technology are still to be completed.

## OPTIMUM FOCAL CONDITIONS

To obtain satisfactory focal spot smoothing in the far-field the thickness of the resist is critical to about 1%. A discrepency in the thickness will produce a small coherent spike in the centre of the focal profile. Present manufacturing methods would produce too many rejects if the tolerence had to be this tight.

A realistic thickness specification would be $\pm 5\%$. A series of tests were conducted on RPP's with this degree of error to investigate the optimum focussing conditions. These test included equivalent plane monitoring of the beam using both cw and pulsed lasers. These tests concluded that the optimum focussing condition is $f^2\lambda/dD$ in front of the normal focal plane ( where: f is the focal length of the lens, $\lambda$ is the operating wavelength, d is the element size of the RPP and D is the aperture of the beam ). This degree of defocussing is possible due to the large depth of focus generated when using small element size RPP's.

## REFERENCES

1. Annual Report to the Laser Facility Committee. RAL Report-89-045 (1989).
2. Private Communication. T Kessler, University of Rochester, 1989.

| RPP ELEMENT SIZE (mm) | FOCAL SPOT SIZE (FWHM) | | | |
|---|---|---|---|---|
| | $\lambda = 1.053\ \mu m$ | | $\lambda = 0.527\ \mu m$ | |
| | fl = 0.25 m | fl = 1m | fl = 0.25 | fl = 1m |
| 10 | 25μm | 100μm | 25μm | 50μm |
| 5 | 50μm | 200μm | 25μm | 100μm |
| 2 | 125μm | 500μm | 67μm | 250μm |
| 1 | 250μm | 1mm | 125μm | 500μm |
| 0.5 | 500μm | 2mm | 250μm | 1mm |
| 0.25 | 1mm | 4mm | 500μm | 2mm |
| 0.1 | 2.5mm | 10mm | 1.25mm | 5mm |
| 0.05 | 5mm | 20mm | 2.5mm | 10mm |

Table 1: Range of focal spot sizes available on VULCAN using the standard Random Phase Plates.

# SHORT PULSE DEVELOPMENT ON VULCAN

R. Bann, C.N. Danson, D. Pepler, N. Rizvi, I. Ross, I. Watson (RAL)
M. Kalashnikov (Lebedev, USSR)

## INTRODUCTION

The amplification of short pulses (< 20 ps) to high intensities is limited in glass systems such as VULCAN due to the onset of small scale self focussing leading to beam breakup. The technique of Chirped Pulse Amplification (CPA)[1] enables the generation of high intensities since the pulse is amplified through the system as a longer pulse (1ns-100ps) and compressed at the output of the system.

In CPA, an optical pulse is injected into a length of optical fibre which modifies the pulse in two ways:-

a) In fibres greater than a few hundred meters in length, temporal broadening takes place due to normal group velocity dispersion.

b) The bandwidth of the pulse is broadened by self phase modulation (SPM). This also imposes a 'chirp' on the pulse so that there is a frequency gradient in time.

The chirp arises due to the intensity dependent change to the refractive index of the silica based fibre. Although the non-linear coefficient is relatively small, the long pathlengths can generatel substantial SPM[2]

$$\Delta\phi(t) = dn\ kL = n_2\ I(t)\ kL$$

Where: $n_2$ is the non linear kerr coefficient
k is the wavenumber
L is the fibre length

This phase shift gives rise to a time dependant frequency shift:

$$\Delta\omega\ (t) = -\frac{d[\Delta\phi(t)]}{dt} = -n_2\ kL\ \frac{dI(t)}{dt}$$

Hence for an input pulse with a gaussian intensity profile (Fig 1 a), the spectral profile of the output pulse shows the linear frequency ramp (Fig 1 b) that is used in the CPA technique.

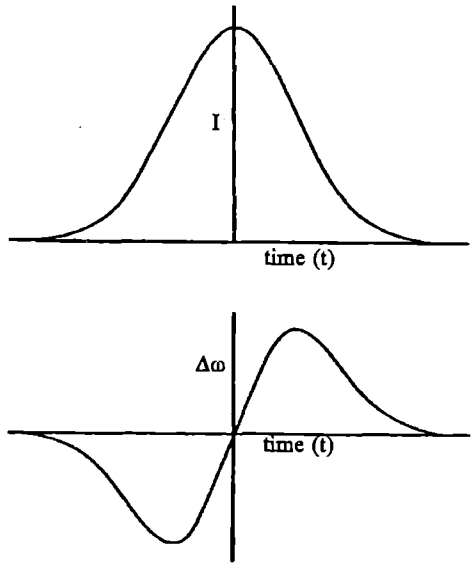


Figure 1: Frequency Chirp Induced by Self Phase Modulation

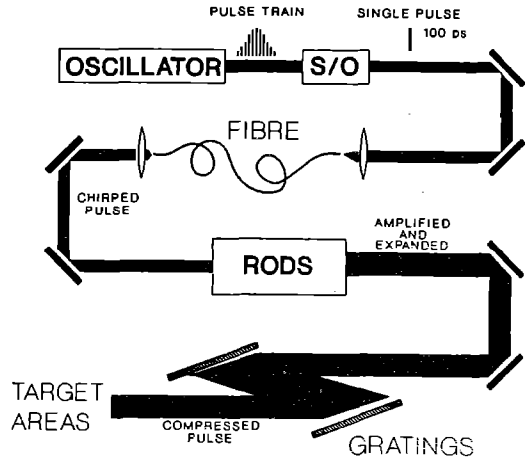


Figure 2: Schematic of CPA System

The chirped pulse can then be amplified to an energy level limited by damage mechanisms at the longer pulse length. Just before the final focussing optics, a pair of parallel diffraction gratings impose a frequency dependent delay, compressing the pulse to a near transform limited pulse-length. A schematic of the system is shown in Figure 2. The grating separation must be such that the leading frequencies of the chirp are delayed relative to the trailing frequencies by a time equal to the uncompressed pulselength. This results in the necessity for complete temporal and spectral stability from shot to shot.

A major problem with this technique is the elimination of non-linear frequency components within the chirped pulse which do not compress but form a low intensity pedestal on which the short pulse sits.

A development program was initiated to develop a suitable CPA system to install on the VULCAN Glass Laser for future use by the user community.

## OFF LINE WORK

An optical system was assembled off line identical to the short pulse generating oscillator of VULCAN. This comprised of an ND:YLF actively modelocked and Q-switched oscillator with a synchronised pockels cell switch-out chain to produce a single 80ps pulse.

For this experiment a short fibre (10 m) was used which would broaden the bandwidth enough to give 5ps pulses. The energy injected into the fibre was accurately matched to the fibre length to ensure a linear chirp: too little energy restricts the spectral broadening; too much and a Raman process causes non-linearity in the broadening and restricts the transmission efficiency of the fibre.

Single shot bandwidth profiles were measured for varying input energies and are shown in figure 3. Using the bandwidth measured in 3 a), it was calculated that a grating separation of 20 m was needed to compress the 80ps pulse.

The chirped beam was expanded and injected into the grating compressor. As the total grating separation was large,

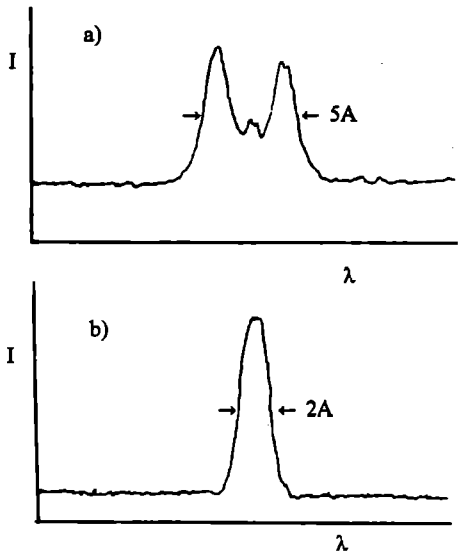


Figure 3: Spectral Profiles of Chirped Pulses

a folded, double passed configuration was adopted.

The output of this system was monitored by a streak camera and the fibre input energy tuned to produce the right frequency gradient across the length of the pulse. This fine tuning gave pulse lengths of around 10 ps , as shown in figure 4, although this did approach the active resolution of the streak camera. The pedestal was shown to have an intensity ratio of 20:1 relative to the short pulse, but due to its length it contained half of the energy in the pulse.

## INSTALLATION ON THE MAIN VULCAN SYSTEM

The fibre was installed under the oscillator covers of the system. Due to space limitations it was placed between the oscillator and pulse selecting switchout chain. In this configuration the whole pulse train was injected into the fibre and the output is shown in figure 5. It can be seen that when the energy in the pulses reaches a critical level, the Raman process limits the transmission of the fibre and the peak of the Gaussian envelope is suppressed. In this region the chirp is non-linear and so a pulse from high on the rising edge of the pulse train was selected for amplification.

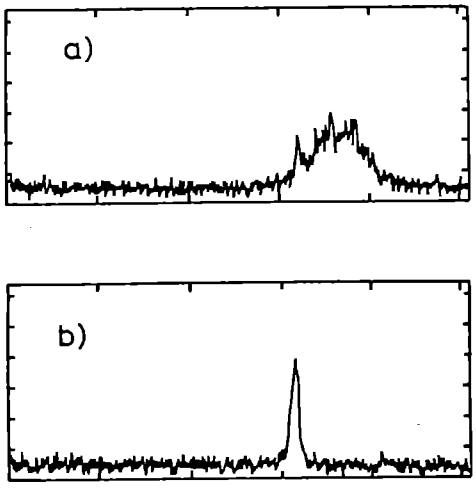


Figure 4 : a) 80 ps input to CPA system
b) 10 ps output pulse

Once amplified to 1J by the outer rod chain, the pulse was injected into a grating pair compressor and the output pulse analysed. Temporal analysis of the spectral content of the output pulse showed that a larger bandwidth could be compressed than that used in the off-line experiment. Since the uncompressed pulsewidth was constant, the spectral/ temporal gradient increased allowing the grating separation to be significantly reduced (< 1m).
The plateau level was measured and seen to be comparable to that seen off-line. This showed that during a 2 J shot, 1 J was present in the 10 ps pulse giving a power of 100 GW.

## AMPLIFICATION TO 1 TW

The grating size was such that a about 80% in area of a 108 mm beam could be passed through the compression system and so the gratings were moved to a position after the double passed disk amplifier stage of VULCAN. Using damage threshold measurements from Osaka, it was calculated that the gratings should be able to operate at 20 J total energy before damaging. Preliminary low energy shots were used to align the gratings to give 10 ps pulses and then full energy shots were fired with calorimetry placed at the output of the gratings. The energy levels were raised to the 20 J level, half of which was in the short pulse. No laser induced damage was detected on the gratings over several 1 TW shots.

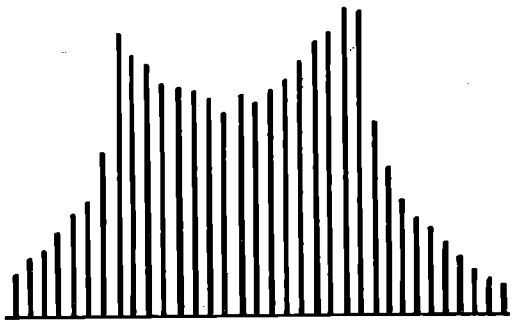

Figure 5 : Modelocked pulsetrain at output of fibre

## FUTURE DEVELOPMENT

In the short-term it is planned to improve the contrast ratio of the pulse as the plateau acts as a prepulse which can preheat a target making the presently available short pulse unsuitable for most experiments. The contrast can be enhanced by reducing the nonlinear areas of the spectral gradient. This can be achieved by spectral windowing in the Fourier plane of the compression stage to suppress any spectral wings. Saturable absorbing dyes may also be used to reduce the lower intensity spectral components which form the plateau.

These experiments will initially be conducted off line before being reinstalled on VULCAN for user experiments.

## REFERENCES

1 P. Maine et al. SPIE Vol 913 (1988) pp 140-146

2 Optical fibre-grating pulse compressors. A.S.L.Gomes et al Optical and Quantum Electronics 20 (1988) pp 95-112.

# COMPUTER CONTROL AND DATA ACQUISITION

C. J. Reason and D. A. Pepler
Rutherford Appleton Laboratory

The GEC 4080 computer after giving more than 12 years service was finally removed, and the control and data acquisition tasks for VULCAN were switched over to two networked IBM PC clones. These computers were installed prior to the GEC 4080 removal and gave very little trouble after the change-over.

The first PC interfaces to a fibre-optically linked ring of CAMAC crates which it uses to control VULCAN, fire laser shots, and to acquire data on capacitor voltages, laser calorimetry, mirror positions etc. This data is then made available on either its hard disk or RAM disk. For high-power laser shots onto a target, the data is permanently stored by transfering it onto a 400 MegaByte optical disk. ( 200 MegaByte per side, Write Once Read Many; WORM drive ).

The second PC gains access to the first PCs disks over a network, and has a HP LaserJet II printer coupled to its LPT1 parallel printer port. This computer controls the colour graphics sytem through the COM1 serial port to display the current layout diagram, and a histogram charging diagram during laser shots. After every target shot, it collates all the data from the control PC and from its own sources, namely video framestore boards, and produces a hard copy on the laser printer. This comprises of text and graphics giving a total description of the shot. A typical printout is shown in Figure 1 below.

VULCAN Glass laser log for shot 20 at 19:48 on 26 Mar 1990 into TAE

Title :
Comment :

| | 9A/C | 9B/D | 16 | Fara | 25 | 45 | Atts | Output J |
|---|---|---|---|---|---|---|---|---|
| Rods | | | | | | | | |
| Inner | 1.56 | 1.55 | 1.89 | On | 1.91 | 1.89 | 99 | 2.39 |
| Outer | 1.48 | 1.44 | 1.92 | On | 1.90 | 0.00 | 60 | 0.66 |

| Faradays | DrU | DrL | BlU | BlL |
|---|---|---|---|---|
| Volts KV | 6.4 | 0.0 | 0.0 | 0.0 |
| Delay us | 300 | 300 | 300 | 300 |

| Disks | DrU | DrL | BlU | BlL | 150U | 150L |
|---|---|---|---|---|---|---|
| Energy J | 0.0 | 0.0 | 0.0 | 0.0 | 0.0 | 0.0 |
| Volts KV | 19.0 | 0.0 | 0.0 | 0.0 | 0.0 | 0.0 |
| Delay us | 300 | 300 | 300 | 300 | 300 | 300 |

| Disks | UW | MW | LW | UE | ME | LE | Total |
|---|---|---|---|---|---|---|---|
| Energy J | 5.8 | 0.6 | 34.4 | 164.7 | 0.8 | 17.6 | 223.8 |
| Volts KV | 0.0 | 0.0 | 0.0 | 19.0 | 0.0 | 0.0 | |
| Delay us | 300 | 300 | 300 | 300 | 300 | 300 | |

| TAEAST Beams | 2 | 4 | 6 | 1 | 3 | 5 | 7 |
|---|---|---|---|---|---|---|---|
| Energy J | 0.1 | 0.0 | 0.1 | 62.4 | 0.1 | 0.1 | 1.2 |

Total energy 62.4 J. - 1 beam mean 62.4 J. - Best/Worst = 1.000

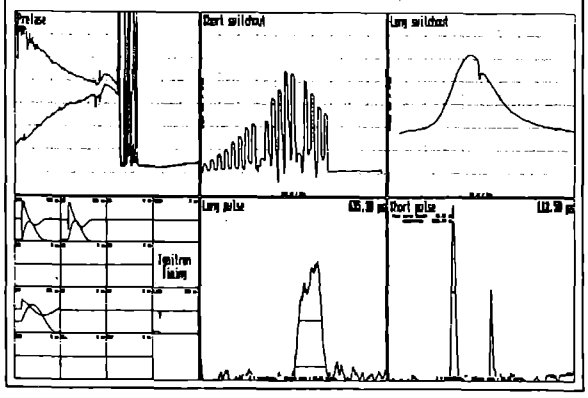


Figure 1.

Also on laser shots, from 2 minute rod-shots through to 20 minute disc-shots onto target, the first PC updates a statistics package detailing the number of times any amplifier has been fired.

Figure 2 below shows the form that the package produces.

Laser Statistics file from 27/ 6/89 to 7/ 3/90 at 11:12

| Amplifiers | UE 274 | ME 590 | LE 364 | LW 419 | MW 572 | UW 403 |
|---|---|---|---|---|---|---|
| | 150U 395 | 150L 0 | BLU 376 | BLL 0 | DRU 571 | DRL 823 |
| Faradays | | | BLU 446 | BLL 0 | DRU 601 | DRL 895 |

| Rod Chain | Inner | Outer | Rod Chain | Inner | Outer |
|---|---|---|---|---|---|
| 16 mm Rod | 4216 | 4200 | 16 mm Probe | | 27 |
| 25 mm Rod | 3807 | 4117 | 32 mm Faraday | 4225 | 4225 |
| 45 mm Rod | 4165 | 4102 | | | |

| Shots | Laser | TAW | TAE | TA2 | TA4 | Total |
|---|---|---|---|---|---|---|
| Total | 1441 | 548 | 1556 | 666 | 278 | 4489 |
| Disk | 132 | 272 | 573 | 375 | 0 | 1352 |
| Failed | 1 | 3 | 16 | 17 | 0 | 37 |

Figure 2.

The framestore boards are required to record the output from an optical streak camera, and to monitor a fast non-storage oscilloscope. Neither framestore had initially produced very reliable results, and the development of the oscilloscope readout was postponed in order to concentrate effort on the more important streak camera system.

It was eventually discovered that it was possible to operate the framestores in a new acquisition mode. This coupled with the use of an interline transfer CCD and a 30 millisecond event post-trigger, instead of a frame transfer CCD and a 20 millisecond event pre-trigger, has improved the reliability to 100% from only 20% for the original configuration. It is now the intention to install the oscilloscope monitor using the modified triggering arrangement.

The two PCs have now been controling the VULCAN laser system, without GEC 4080 support, for the last year and have proved to be extremely reliable. They even survived severe mains-dips during electrical storms, which would have locked-up the GEC 4080. The storms did result in a number of CAMAC modules failing but these were either repaired quickly or replaced from spares, keeping the down-time of VULCAN to only a few hours.

The control, data acquisition, and graphics programs have continually been upgraded to meet the changing needs of the system, and of facility user requirements, with most of the changes being made without effecting facility operation.

# PROPOSED USE OF AN LSM COATED GRATING TO PRODUCE A HIGH DISPERSION SPECTROMETER IN THE EUV REGION

A Ridgeley

Rutherford Appleton Laboratory

## INTRODUCTION

The X-ray laser consortium are planning to build a high dispersion EUV spectrometer for time-resolved studies of X-ray laser plasmas. The resolution of the instrument needs to be high enough to resolve Stark widths and fine structure of x-ray laser transitions.

The resolution required for these studies is not very high (about 0.1A), but the poor spatial resolution of an X-ray streak camera (∿ 5 line pairs/mm) means that a high dispersion (≤ 5A/mm) is required if the spectrometer is to be interfaced to a streak camera.

There is an existing instrument, the Hettrick HIREFS 164-25m[1] which has been purpose built for such an application, but it is expensive and its 7m length would be a handicap in the CLF target areas. The possibilities for building cheaper and smaller options has therefore been explored.

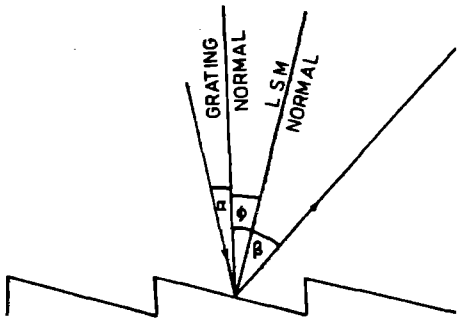


FIG. 1. THE GEOMETRY OF THE LSM COATED GRATING

One possibility is the use of diffraction gratings which have been coated with an EUV reflecting multilayer, sometimes called layered synthetic microstructures or LSMs. The technology of coating LSMs onto gratings is now imminent. Lamellar gratings have already been coated with LSMs[2], and work is in progress on the coating of blazed gratings[3].

## GEOMETRY OF AN LSM COATED GRATING (fig 1)

Consider a diffraction grating of period $d_g$ coated with an LSM of period $d_m$, where $d_m$ is an exact fraction of $d_g$. The grating will then only diffract when both the grating equation

$$n\lambda = d_g (\sin\alpha - \sin\beta)$$

and the Bragg condition for the multilayer

$$\lambda = 2d_m \cos(\phi - \alpha)$$

are satisfied, where $\phi$ is the blaze angle and $\beta$ is the angle of diffraction. This means that the grating will only diffract over a narrow angular range centred on

$$\beta = 2\phi - \alpha$$

and will be diffracting in order $n = d_g/d_m$ in this range.

The LSM therefore causes the grating to be used in high order with correspondingly higher dispersion, and acts as a narrow bandpass filter which enables it to function as an order sorter.

## A PRACTICAL INSTRUMENT

Take a fairly typical grating with 1200 lines/mm blazed at 3.4 degrees (1000Å in 1st order). If this is coated with a 10 layer LSM of period 200Å then we have a grating which will reflect up to 200Å in the 5th order and with a bandpass $\lambda \pm \Delta\lambda$ where $\Delta\lambda$ is about $\lambda/10$, small enough to discriminate against 4th and 6th orders. For the required dispersion of 0.5Å/m to be achieved the throw of the instrument must be at least 1.5m. The aim of designing a significantly smaller instrument than the Hettrick is therefore achievable using an LSM coated grating.

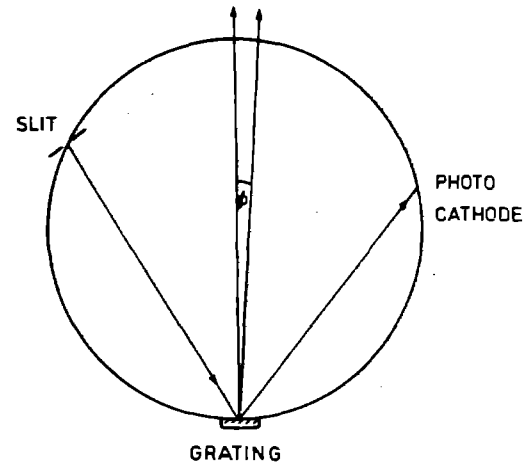


FIG. 2. THE NAMIOKA-SEYA ARRANGEMENT

The simplest working arrangement for a practical instrument is a concave LSM coated grating in a Johann-type geometry. Wavelength changes in this geometry would be accomplished by moving the slit and detector equal and opposite amounts around the Rowland circle. In the application being considered it is impractical to move either the source or the detector, so the Namioka-Seya[4,5] arrangement shown in fig 2 would probably have to be used. In this arrangement wavelength changes in the range $\lambda-\Delta\lambda$ to $\lambda+\Delta\lambda$ can be effected by rotating the grating, but grosser changes in wavelength range would require interchangable gratings. Four or five gratings would be necessary to cover the wavelength range 100A-250A.

## REFERENCES

1. Michael C. Hettrick, James H. Underwood, Philip J. Batson, and Mark J. Eckart App. Opt. 23,pp 200-201, (1988).

2. Yuichi Utsumi, Jun-ichi Takahashi, and Tsuneo Urisu, Rev. Sci. Instrum. 63, pp 2024-2026, (1989).

5. M. Seya, Science of Light, 2, p8, (1952).

6. T. Namioka, Science of Light, 3, p15, (1954).

# AN ACTIVE CRYSTAL SPECTROMETER USING A PHOTO-DIODE ARRAY REMOTE HEAD

A McPhee[1], A Ridgeley[2], D Pepler[2], R Wyatt[2]

[1] Salford University
[2] Rutherford Appleton Laboratory

## INTRODUCTION

Previous measurements in 1, 2 using a commercial RETICON OMA system have shown that a silicon photodiode array (PDA) is an order of magnitude superior to photographic film as a detector of soft X-rays with respect to detective quantum efficiency, dynamic range and sensitivity.

The OMA system is too bulky to be widely applicable to high power laser experiments, which require a detection head which would ideally be smaller than the mini-spectrometer to which the detector head is likely to be interfaced. Some effort (at the level of a sandwich course student project) was therefore directed towards the problem of designing and building a remote head for a set of PDA drive electronics.

## THE PROJECT

A PDA is literally a row of up to 1024 silicon photodiodes which can be read sequentially by means of suitable clocking circuitry onto a common line. The elements of providing a remote detection head using a PDA are

(a) synchronising a start pulse to the laser shot
(b) providing clocking pulses for the PDA readout
(c) obtaining a reliable readout of the individual diodes and digitising
(d) having the PDA remote from the drive electronics.

Problem (a) was solved by linking the start pulse to a three second pulse cycle routinely available to the VULCAN target areas. Clocking pulses (b) were provided by using the makers evaluation board. This leads to a problem with (c), care having to the be taken not to pick up the clocking pulses as signal. This was avoided by using the PC internal clock to drive the clocking and read-out circuitry thus ensuring that each diode was sampled at the same point in its signal profile. The main problem with siting the PDA head remote from the drive electronics is that the photodiodes have a very small capacitance, but this problem can be overcome by incorporating a suitable charge pulse pre-amplifier in the remote head.

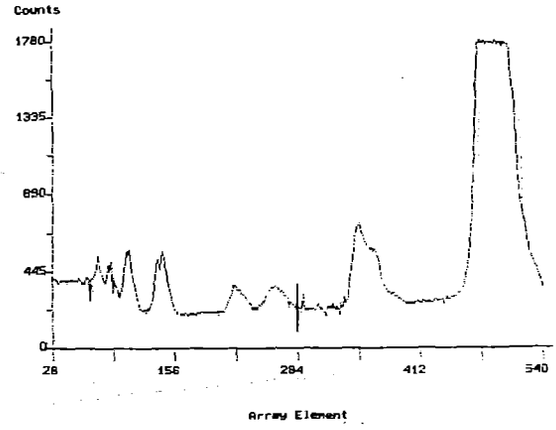


Fig.1. Aluminium spectrum obtained with remote PDA head.

## RESULTS AND FURTHER WORK

A remote head about the same size as a mini-spectrometer i.e. about 5cm square and 1cm deep has been built and has been demonstrated to work. Fig. 1. shows an aluminium spectrum obtained using this device in the TA4 target area. Although this is a reasonably useful device, which also obtained spectra during the August 1989 X-ray laser experiment, it is still somewhat large and is much noisier than the commercial OMA read-out system. Work is in progress to see if the noise level of this device can be reduced, and a smaller design is also being evaluated.

Future developments will include work on 2D CCD read-out systems. It is planned to experiment with a commercial miniature CCD camera as an X-ray detector and Essex University will be purchasing a commercial coated CCD system with 14 bit intensity resolution.

## REFERENCES

1. Annual Report to the Laser Facility Committee 1988 RAL-88-042 pp. 143-145 (1988).

2. J. of X-ray Sci. and Techn. 1 pp. 162-170 (1989).

# A STREAK CAMERA READ-OUT SYSTEM USING A 2D CCD CAMERA

A Ridgeley, K Levitt, D Pepler, C B Edwards

Rutherford Appleton Laboratory

Fig.1. CCD camera record of X-ray streak camera trace.

Streak camera output is normally detected using photographic film in high power laser experiments. Using a 2D CCD system has the potential advantage over film of

(a) increased dynamic range (less shots wasted through overexposure).

(b) faster turn-round (enabling quicker decisions to be made for the next shot)

(c) increased photometric accuracy.

The time history of the laser pulse has for several years now been recorded by CCD camera read-out of the VULCAN operations section streak camera. Recently this technique has been extended to target area use.

A CCD/framegrabber/image analysis system has been set up twice now for timing beams in target areas, and has given a significant increase in the speed of executing this task. In a recent experiment in TA2 the CCD system has also been used to read the output from an X-ray streak camera used as an experimental diagnostic.

Fig 1. shows a streaked image obtained by this method. The experiment was one to study opacities by absorption measurements of backlighted sources. There are three components to the image

(i) the straight through X-rays stimulating the phosphor directly
(ii) the X-ray heated main target (long pulse)
(iii) the backlighter target (short pulse).

This is the first demonstration at RAL that a CCD read-out system works on an experimental diagnostic, and shows that it is possible, in principle, to use a CCD read-out system on any diagnostic which involves an image intensifier system.

We wish to thank OFA Ltd for the loan of hardware and software during these experiments.

# REFLECTION FILTERED OPTICS DESIGNED TO ELIMINATE HIGHER ORDERS ON THE R.A.L. FLAT-FIELD SOFT X-RAY SPECTROMETERS

C L S Lewis,[1] D Neely[1] and A R Damerell[2]

[1]Queens University Belfast
[2]Rutherford Appleton Laboratory

The soft X-ray (1.2-30.0nm) flat-field Hitachi grating[1] spectrometers widely used in our soft X-ray laser program suffers from the problem of short wavelength emisson in multiple order overlapping with the spectral region of interest. Potential solutions to this problem fall into two basic catagories; either a grating may be specifically designed for only the region of interest or, a wavelength selective filter is used to absorb any unwanted radiation. There are two distinct filtering methods available namely, transmission through thin (0.05-5.0μm) self supporting layers of elements or reflection from a high quality mirror with a surface coating (sub 1.0μm) of a desired element. An ideal filter would have a throughput of the form as shown in figure 1. At wavelengths below the region of interest (0-$\lambda_0$) the throughput is very low, it then has a sharp turn on at $\lambda_0$, and remains reasonably constant and high for wavelengths greater than $\lambda_0$. Because dispersion is generally greater in second order, it may in some cases be necessary to record the spectral region of interest in first and higher orders. This would require that the filter throughput falls sharply for wavelengths greater than $2\lambda_0$ as shown by the dashed line on Figure 1.

Figure 2 shows the transmission curves of two commonly used filter materials namely, Formvar (a $(C_5H_7O_2)X$ plastic filter), and Aluminium. As can be observed from Figure 2 the drawback of using transmission filters is that although the transmission immediately below an edge is much lower than above the edge, the transmission tends to increase with shorter wavelength and decrease with longer wavelength. The throughput of a transmission filter is therefore significantly different from that of the ideal case. In soft X-ray glancing angle reflection however, the opposite tends to happen in that (ignoring edge effects), reflectivity generally decreases for short wavelengths and increases for longer wavelengths.

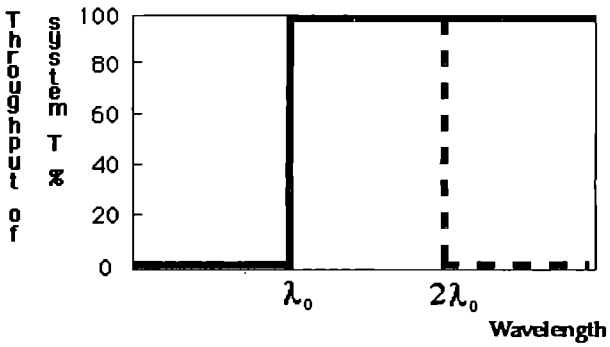


Figure 1: A plot showing the ideal characteristics of a filter for two cases i (A large spectral pass band -- thick line) and ii (A narrow spectral pass band -- dashed line).

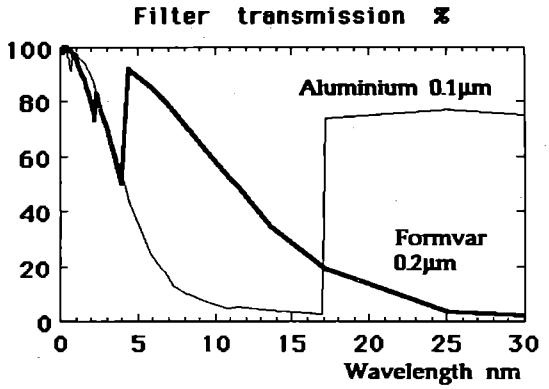


Figure 2: A graph showing the throughput of two transmission filters against wavelength.

The calculated reflectivities (Henke et al)[2] at different glancing angles of many elements were examined in detail. The reflectivity curves can be broadly separated into two groups of either low Z or high Z elements. The reflectivity curves of low Z elements show strong edge effects (acting to some extent as band pass filters) whereas, the curves for high Z elements show much weaker edge effects. In selecting a suitable mirror material not only is the reflectivity curve important, but also the chemical stability should be considered. Because soft X-ray reflection involves only a very thin upper layer of the mirror material, then chemical stability is necessary to ensure that negligible surface contamination ever occurs. Aluminium for example would not be a suitable mirror material since, on exposure to air a sufficiently thick oxide layer is formed that the reflectivity properties of the mirror are totally changed.

The design requirements of a reflection filter for our work at RAL was based on the instrument being used with the flat field grazing incidence spectrometer in four different wavelength regions :-

1. 3.5-10.0nm
2. 7.0-10.0nm
3. 10.0-16.0nm
4. >18.0nm

After considering many possibilities, it was decided that using gold as the reflection filter material at different glancing angles and with either an Al, a Formvar or no absorption filter, all the necessary design requirements could be attained. In the 1.0-30.0nm range the reflectivity of gold is characterized by three regions. In the first region the throughput slowly rises, in the second region the throughput rises very sharply initially and then flattens out and, in the third region ( >13.0nm) the reflectivity remains fairly constant. Figure 3 shows the theoretical throughput obtained from a single reflection of a gold surface as a function of wavelength at different glancing angles, assuming the incident radiation is unpolarised. The form of these curves for glancing angles greater than ≈4° is very similar to that of the ideal case Figure 1. The combination of reasonable reflectivity curves, the known

chemical stability of gold and, the ease with which gold can be deposited on a substrate meant that gold was an ideal choice of mirror material.

The practical problem of using a single mirror reflection filter is that for a given glancing angle g° the output beam is deviated through 2g°. Therefore, for values of 4°< g < 30° the output beam is deviated through 8° < 2g < 60° and this could give rise to considerable spectrometer alignment problems. A simple solution to this problem is to use a second mirror orientated parallel to the first mirror, so that the output beam after two reflections is now parallel to the input beam. The only slight alignment difficulty of this set-up is that the output beam suffers a spatial off-set, s, given by:-

$$s = 2d(1 - \sin g) \qquad ---(1)$$

where d is the spacing between the mirrors. The mirrors of length l are positioned so that the end of one mirror lies over the centre of the other mirror and, the point of rotation is positioned slightly foward of this on the mirror closest to the plasma as shown on Figure 4. The minimum angle $g_{min}$ at which the double reflection filter can be set so that no straight-through emission enters the spectrometer is given by:-

$$g_{min} = \tan^{-1}(2d/l) \qquad ---(2)$$

and the maximum usable angle $g_{max}$ is given by:-

$$g_{max} = \tan^{-1}(6d/l) \qquad ---(3)$$

The mirror length l is choosen so that when the reflection filter is being used, the angular acceptance of the reflection filter is sufficient to allow illumination to reach all points of the spectrometer's grating surface. Using flat precision ground glass spacer bars of d = 0.6, 1.0 or 2.0mm along with mirrors of length l=20.0mm, it is possible to use the double reflection filter at glancing angles of 4° < g < 30°. Figure 5 is a schematic diagram showing the reflection filtered flat-field spectrometer. The operating glancing angle of the double reflection filter may be easily changed during a run, and only requires that the appropiate off set be made to the height of the grating using the motor driven rise stage and digital position read out.

The two important parameters necessary in defining the usefulness of a reflection filter at a glancing angle, g, and at a wavelength, λ, are the percentage throughput T and the second order rejection ratio R which is defined as

$$R(\lambda,g) = T(\lambda/2,g) / T(\lambda,g) \qquad ---(4)$$

Figure 6 shows a plot of T against R for a single mirror gold reflection filter at four wavelengths over the range 0.5° < g < 30.0° and, Figure 7 shows a plot of T against R

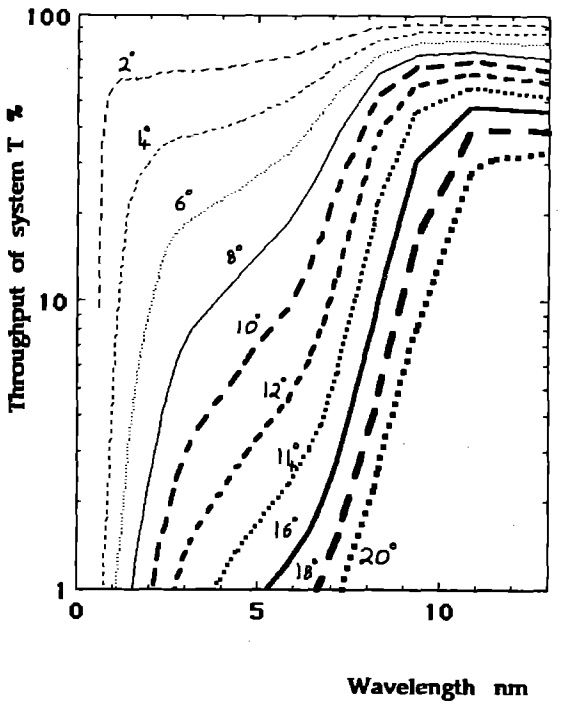


Figure 3: A graph of the reflectivity of a gold mirror at different glancing angles for unpolarised soft X-rays against wavelength.

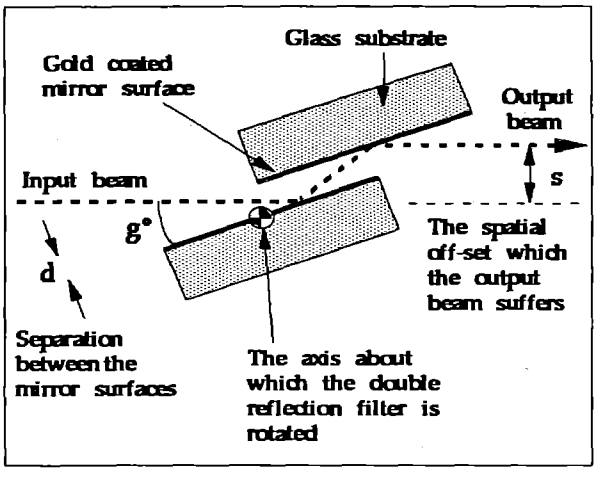


Figure 4: A schematic diagram showing the double reflection filter design.

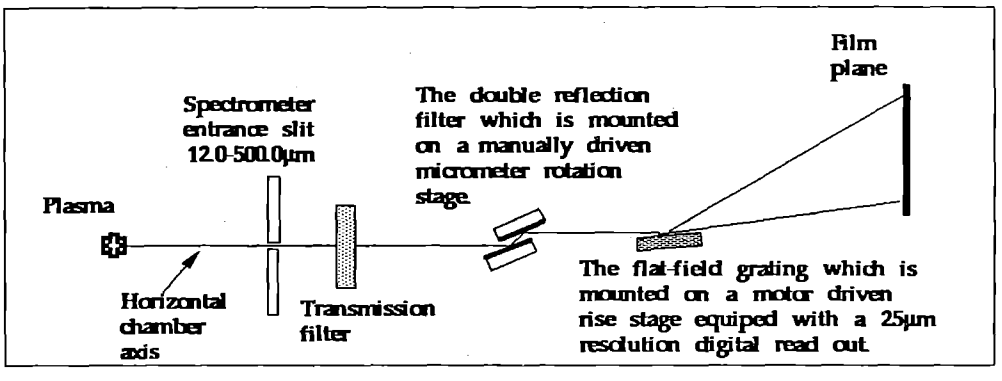


Figure 5: A schematic diagram showing how the double reflection filter is used with the flat-field grating spectrometers.

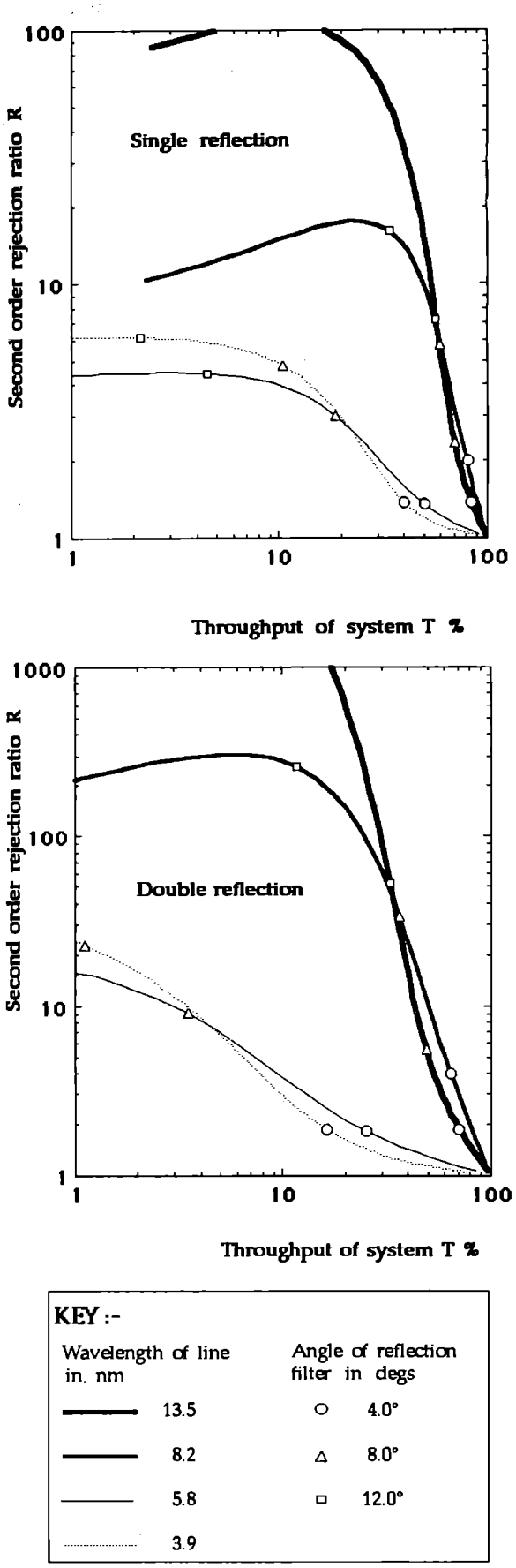


Figure 6+7: Plots showing the second order rejection ratio for four wavelengths from a single (Fig 6) and double (Fig 7) gold reflection filter against throughput.

over the same range but for a double mirror gold reflection filter. An important item of interest to note from these plots, is that as the glancing angle increases the rejection ratio reaches a maximum and then falls, with greater glancing angle being required for longer wavelengths. The implication of this is that for a given wavelength the glancing angle should not be increased beyond this optimum value since, both the rejection ratio and throughput will fall thus making the filter less efficient. From these two plots it is clear that in the region $3.0 < \lambda < 6.0$nm, the achieveable second order rejection ratios at reasonable throughput ($5\% < T < 30\%$), with either a single or double gold mirror reflection filter are quite low ( max value 6). However, in the longer wavelength region $7.0 < \lambda < 30.0$nm at reasonable throughput ($5\% < T < 30\%$) the double gold mirror reflection filter is clearly capable of giving significantly better results. At $\lambda = 8.2$nm a double mirror has a max rejection ratio of $\approx 3 \times 10^2$ at a $T \approx 7.0\%$ whereas, for a single mirror the maximum rejection ratio ever attainable is only ≈18 at a $T \approx 24\%$. Also, for $\lambda > 13.0$nm a double mirror has a rejection ratio of over $\approx 3 \times 10^3$ at a $T \approx 10.0\%$ whereas, at the same throughput a single mirror only has about one tenth of this rejection ratio. The combination of the double reflection filter with a suitably choosen transmission filter can result in achieving a throughput for the combined device which is closer to optimum for the desired spectral region of interest. Figure 8 shows the throughputs readily obtainable which satisfies the design requirements initialy set for this instrument.

The conclusion to be drawn from this work is that, a double mirror reflection filter is much simpler to use experimentally than a single mirror filter and, gold mirrors are ideally suited to examining wavelengths of greater than 7.0nm (using the 1200 l/mm grating). Although gold mirrors are capable of examining radiation in the 3.0 - 6.0nm region (using the 2400 l/mm grating) it is not optimised for this use. A more suitable mirror material such as vanadium (L edge ≈ 2.4nm) will be used for future work in this region.

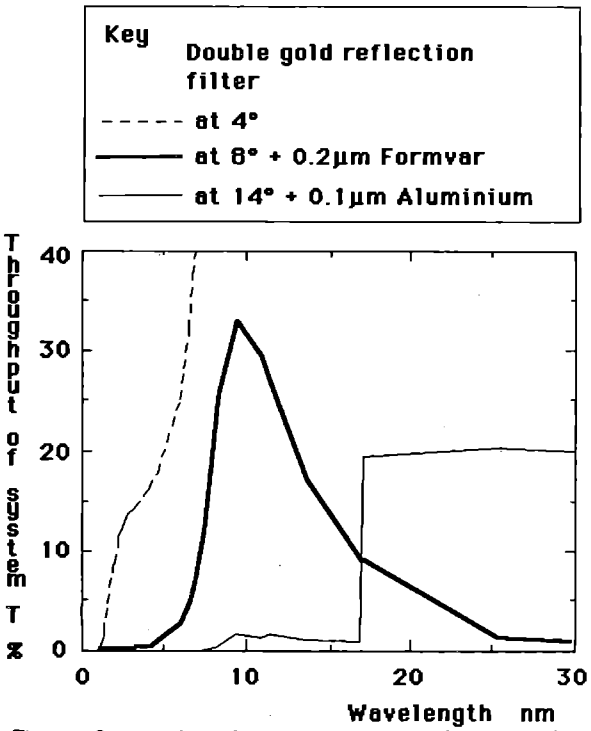


Figure 8: A plot showing the throughput against wavelength obtainable using a combination of transmission and reflection filters.

Figure 10: A 1D spaceresolved spectraobtained from two lollipop targets separatedby 1mm obtained using a toroidal mirror in a spaceresolving mode. The spectral range covered is 3.0-28.0nm with an Al transmission filter 0.2μm thick giving high transmission above the edge at 17.2nm.

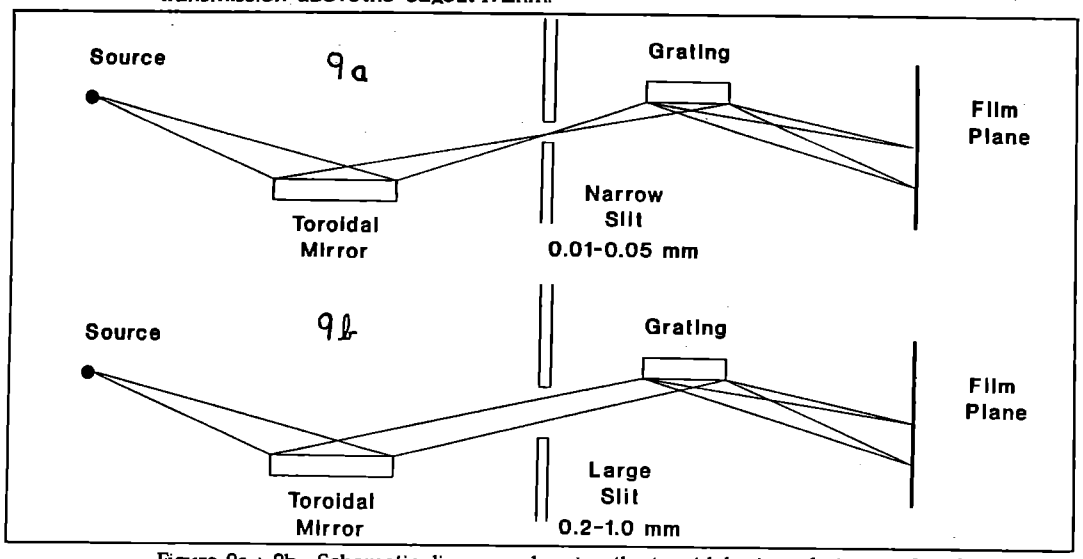


Figure 9a + 9b: Schematic diagrams showing the toroidal mirror being used in the conventional mode 9a (focus on the spectrometer entrance slit), and the new 1D space resolving mode 9b (focus on the spectrometer film plane).

## REFLECTION FILTERED COLLECTIVE OPTICS

In the experimental regime where the two most significant problems are low signal brightness and strong multiple order emission overlap, there is a need for a reflection-filtered collection optic. Both toroidal and cylindrical glancing angle reflection optics have been used very sucessfully previously[3]. These optics were designed to relay an image of the plasma onto the entrance slit of a spectrometer as shown on Figure 9a. By carefully matching the output from the collection optic to the acceptance angle of the spectrometer, it is possible to achieve high collection efficiency. A toroidal mirror with an adjustable major radius 2.0 - 10.0 m, a minor radius of 35.0mm, and size 150.0 mm long by 12.0mm wide, with either a glass surface or a gold overcoated surface was tested at RAL. This mirror was used in the mode as described above with the RAL flat field spectrometer to increase the intensity of recorded emission lines by ≈ 4 and decrease by a factor of ≈ 10 the intensity of unwanted lines.

A new mode of operation capable of giving 1D spatial resolution (better than 40μm) over a large wavelength range (4.0-30.0nm) with increased line intensity (≈ x50 brighter) at resolving powers of ≈ 400 was tested. The toroidal mirror was focused not on the entrance slit of the flat field spectrometer but instead, at the focal plane of the spectrometer see Figure 9b. From a ray tracing analysis and optical measurements, a spatial resolution of better than 40μm can be achieved at distances within a few mm of the ideal focus of the toroidal mirror. The factor therefore, which determines the spectral range over which high spatial resolution is achieveable, is the overall change in distance wrt the toroidal mirror of the focal plane at different wavelengths. For the flat field 1200 l/mm grating spectrometer this difference in distance is only ≈ 4mm over the complete wavelength range, thus making it an ideal choice for this use. Figure 10 shows an excellent 1D spatially resolved spectra, obtained through a 0.2μm Al filter from two 200μm diameter lollipop targets separated by 1.0mm using the toroidal mirror in the imaging mode.

The toroidal mirror when operated in this 1D spatially resolved imaging mode with the flat-field spectrometer, has now opened up the possibility of investigations where previously due to insufficient signal levels and strong multiple order overlaps experiments were not possible.

---

[1] Hitachi flat-field concave diffraction gratings
Grating 001-0266 1200 l/mm 2.5-40.0nm
Grating 001-0471 2400 l/mm 1.0-12.0nm

[2] B L Henke, P Lee, T J Tanata, R L Shimabukuro and B K Fujikawa
Atomic Data and Nuclear Data Tables **27**, 1-144 (1982)

[3] A Franks
Sci. Prog, Oxf. **64**, 371-422 (1977)

# KrF LASER DEVELOPMENT

M H Key and M J Shaw

Rutherford Appleton Laboratory

## INTRODUCTION

The objectives of the high power KrF laser development programme have undergone rapid and significant changes in response to SERC's evolving policy for high performance laser facilities.

Initially it was planned to implement the recommendations of the Challis Review and therefore to construct an advanced KrF/Raman laser facility Supersprite capable of 3.5 kJ in nanosecond pulses and 300 TW in 10 psec pulses. However, prior to formal commitment to the construction of Supersprite, SERC Council, in revising its corporate plan, included the objective of establishing a European High Performance Laser Facility (ELF) jointly with other European partners and SERC with other European research agencies set up a working group to study the case for ELF.

Accordingly the SERC Science Board decided to redirect the KrF laser development activity into a vigorous R&D programme designed to give proof of principle of ideas for both Supersprite and for ELF. This R&D phase would continue for two years until April 1991 and plans beyond that would be determined in the light of the outcome of the ELF study.

The most immediate objective of the new R&D programme was to verify the concept of optical and Raman multiplexing for the efficient generation of powerful, high brightness, high contrast ratio laser beams using the Sprite facility. A major achievement during the year was the successful operation of Sprite with 40 psec pulses to combine seven pump beams in a final Raman amplifier with 50% overall conversion efficiency to producing an exceptionally bright beam (20 μrad divergence) with power of 120 GW. This beam was then used successfully for target irradiation, demonstrating concentration of energy into less than 10 μm focal spot diameter.

Further progress was made during the year to shorten the duration of the Raman beam pulse in order to operate the laser closer to its ultimate power limit. Preliminary studies were conducted with 15 psec laser pulses generated with the pre-existing sync pumped oscillator. These rather noisy pulses demonstrated the need for a transform limited generator and a 10 psec distributed feedback dye laser was successfully developed.

Progress was also made in theoretical modelling of the behaviour of Raman amplifiers and the year's work has broadly confirmed the design principles for Raman beam combining and effort is now devoted the next stage of Raman multiplexing.

For future high power lasers, larger amplifier modules than Sprite will be required and significant progress was made during the year in the design and testing of pulse power technology for such modules. A 100 kJ Marx generator system was constructed and operated into a test load. Designs were finalised for pulse transmission lines and switches to feed a large diameter ($\sim$ 60 cm) amplifier module. Prototypes of these elements are under construction and will be tested shortly.

An important background to the practical work has been theoretical studies undertaken to assess design options for possible European laser facilities. These are reported in Section D3. The work included analysis of the engineering design and cost of large aperture amplifier modules, analysis of KrF laser pulse amplification and staging for KrF amplifier chains and similarly of Raman amplifier chains. Estimates were made of the overall cost and performance characteristics of systems based on Raman and optical multiplexing. The performance characteristics of ultra-short pulse KrF amplifier chains were considered and conclusions were drawn on design optimisation to achieve high pulse contrast ratio as well as high power. The design basis of pure angular multiplexing with induced spatial incoherence for very uniform irradiation of targets at high energy was compared with the Raman architecture. Finally a hybrid scheme was evolved which combined the best features of the Raman multiplexing for high brightness and high contrast ratio with ISI operation for high beam uniformity, in outline system designs for a 100 kJ laser.

# RAMAN BEAM COMBINING AT 40 PICOSECONDS

E C Harvey, C J Hooker, J M D Lister, I N Ross, M J Shaw
G J Hirst, M H Key, P A Rodgers and J E Andrew [1]
Rutherford Appleton Laboratory
[1]A W E, Aldermaston

## INTRODUCTION

The feasibility of the Raman beam combining laser previously proposed[1] has been investigated using pulses of 40 ps duration. Output beam energies of up to 5J have been obtained, and measurements made to characterise the system have confirmed the ability of the Raman beam combining laser to meet many of its design criteria; namely high power, low beam divergence, good near- and far-field beam quality and low prepulse intensity on target.

## SYSTEM DESIGN

The existing e-beam pumped KrF amplifiers Sprite and Goblin form the basis of the system, which is more fully described in a later section. Eight beams were angularly multiplexed through Sprite and Goblin in double pass, with an interpulse time of 5 ns. (Figure 1.) Almost total repumping occurred between pulses ensuring maximum pulse energy. No special precautions were taken to obtain good beam quality or low background amplified spontaneous emission in the KrF beams which were then used to pump the Raman amplifiers.

The Raman amplifier chain (Figure 2.) was designed for a total amplification of about $10^5$ with high extraction efficiency. Window thicknesses were minimised in order to reduce two photon absorption losses which occur at the several GW/cm² intensities required for high gain. Hence the amplifiers were operated with near-atmospheric pressures of methane. $CaF_2$ crystal windows were used on earlier amplifiers to minimise two photon absorption losses. The small signal gain per module was limited to below the threshold for self generated Stokes emission[2] and stability of the chain of amplifiers against self generated Stokes was obtained by limiting the total gain and solid angle with interstage vacuum spatial filters. One Raman preamplifier and three amplifiers were used. The second and third amplifiers used lightguides and were pumped by angularly separated beams with off axis angles of 1.1° and 5° respectively. The transit time of the Stokes and pump beams differed in these amplifiers by 0.6 ps and 13 ps respectively and were much less than the pulse duration. The 1D numerical code described in a later section of this report predicts an internal efficiency in the final amplifier of 85% for pulses that are Gaussian in time, provided that the transit time difference is less than the coherence time of the pulses. Since the dephasing time in methane is 27 ps and the pulse duration was 40 ps, the gain in the Raman amplifier was not steady state and Stokes and pump pulses had to be accurately timed to achieve maximum gain.

## SHORT PULSE GENERATOR

A synchronously pumped dye laser with a two plate birefringent filter and etalon was used to produce 60 ps pulses at a wavelength of 746 nm and at 82 MHz repetition rate[3]. A two-stage YAG-pumped dye amplifier operating at 8 Hz amplified pulses to 150 μJ. These pulses were passed through two KDP crystals to generate pulses at the third harmonic (249 nm). After spatial filtering the 10 μJ pulses were injected into the first KrF amplifier, a Lambda Physik EMG 103 discharge pumped laser. Operating in double pass the amplifier was heavily saturated producing 15 mJ at 8 Hz. A vacuum spatial filter was placed before the second pass of this amplifier to minimise amplified spontaneous emission in the rest of the laser chain. Approximately half of the output was further amplified in the e-beam pumped KrF amplifiers. The

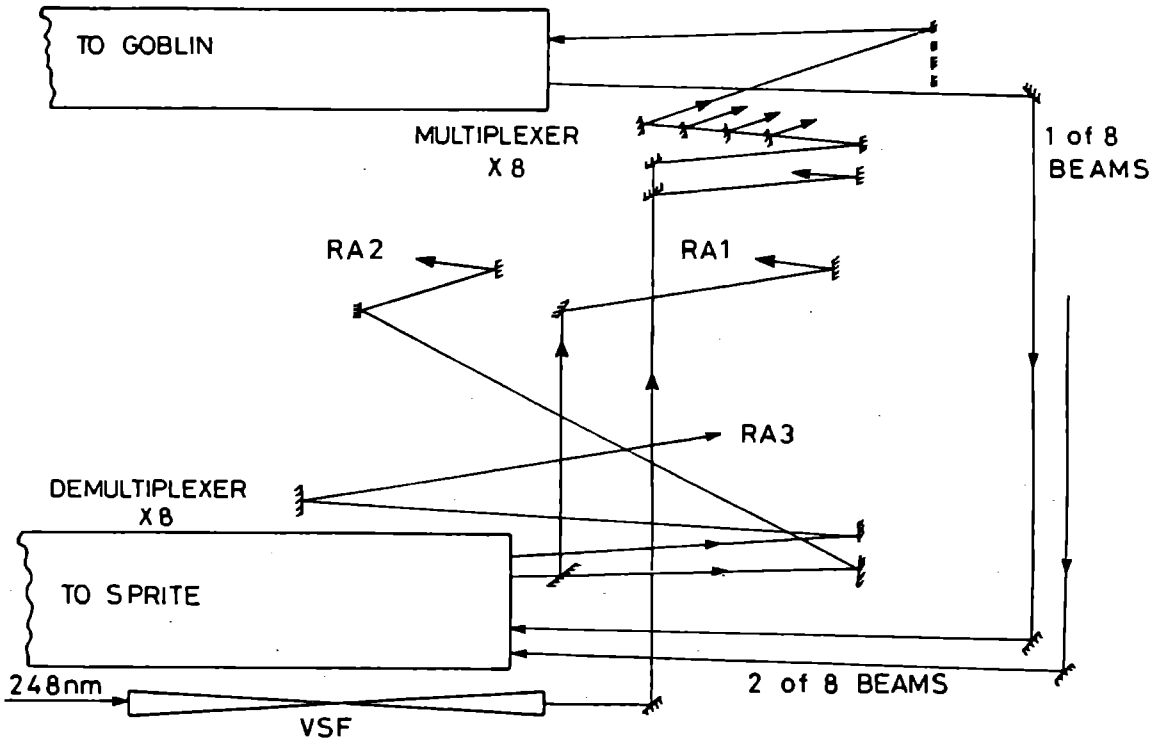


Figure 1. Layout of the multiplexed KrF beams, showing the positions of the Raman amplifiers RA1, RA2 and RA3.

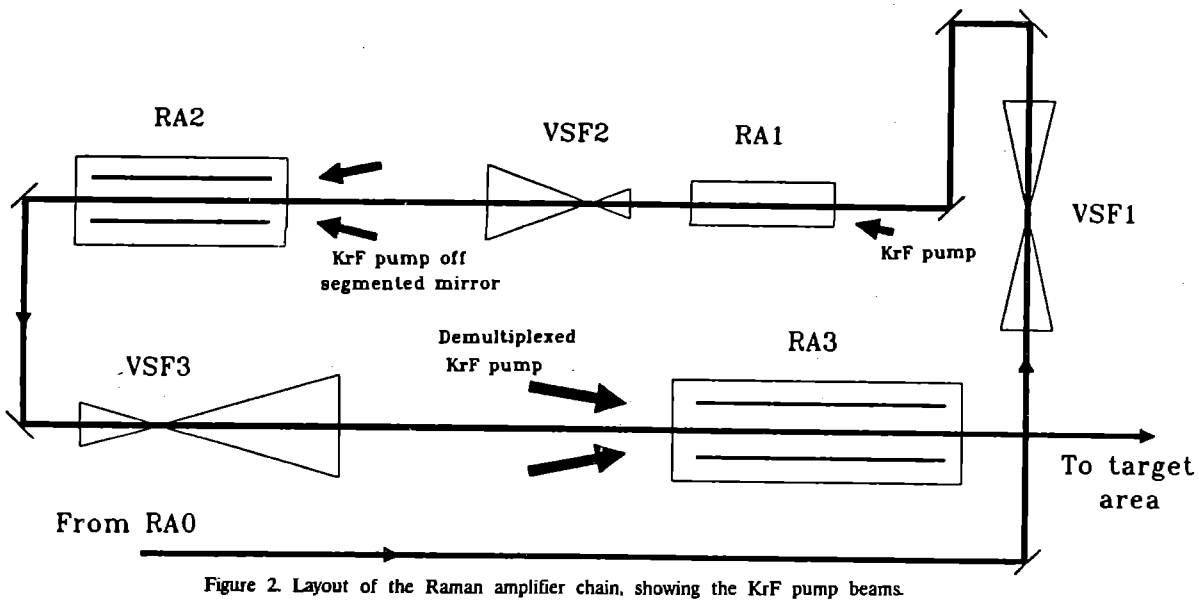


Figure 2. Layout of the Raman amplifier chain, showing the KrF pump beams.

remainder was used to pump a methane Raman generator and preamplifier to produce a near diffraction limited beam of 40 ps duration and 1mJ energy, at 8 Hz, and at the first Stokes wavelength of 268 nm. This Stokes beam was then injected into the main chain of Raman amplifiers.

KrF PERFORMANCE

Total output energies of up to 11 joules in 8 beams were obtained at an average fluence from Sprite of 1.4 x saturation fluence (2.8 mJ/cm$^2$) and a peak fluence of 2.5 x saturation fluence (5 mJ/cm$^2$). This compares with a similar system (ASHURA) in Japan[4] which achieved a fluence of 3 x saturation fluence. A typical KrF pump beam distribution at the entrance window of the final Raman amplifier is shown in Figure 3. The azimuthal variation in intensity is due to the four-sided pumping geometry of Sprite. The pump beam divergence was measured to be about 100 μrad, and the prepulse energy at this plane due to amplified spontaneous emission was approximately 0.3% of the main pulse energy. A total pump energy of up to 10 J was delivered to the final Raman amplifier. A more detailed analysis of the performance and staging of the KrF amplifier chain is presented in a later section of this report.

RAMAN SYSTEM PERFORMANCE

The final Raman amplifier is shown in operation in Figure 4. Table 1 summarises the performance of the Raman system by listing the external parameters of each of the amplifiers, showing a maximum external efficiency of 50% in the final Raman amplifier. When corrected for Fresnel and two-photon absorption losses at the amplifier windows, this corresponds to an internal conversion efficiency of more than 60%.

| Raman Amplifier | RA0 | RA1 | RA2 | RA3 |
|---|---|---|---|---|
| Pump energy | 5 mJ | 25 mJ | 800 mJ | 10 J |
| Pressure $CH_4$ (bar) | 4 | 1 | 1 | 1 |
| Input Stokes energy | 8 μJ | 30 μJ | 5 mJ | 300 mJ |
| Output Stokes energy | 600 μJ | 7 mJ | 350 mJ | 5 J |
| Conversion efficiency | 12% | 30% | 44% | 50% |
| Code prediction | 25% | 35% | 74% | 80% |

Table 1. Performance characteristics of the Raman amplifiers with 40 ps pulses.

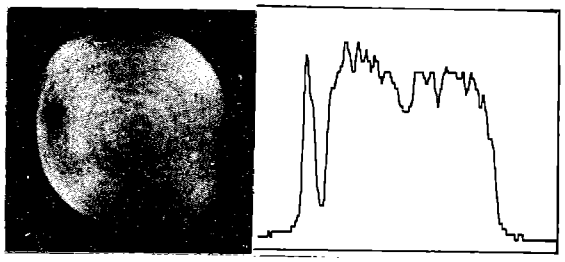

Figure 3. Near-field distribution of one of the KrF pump beams at the entrance to the final Raman amplifier.

Figure 5 shows the near-field Stokes output beam distribution, which in contrast to the KrF pump beams, is remarkably uniform and demonstrates the spatial averaging properties of the lightguide. 2D far-field distributions at full output power and for an unamplified oscillator beam are shown in Figures 6 and 7. These were recorded using a glass

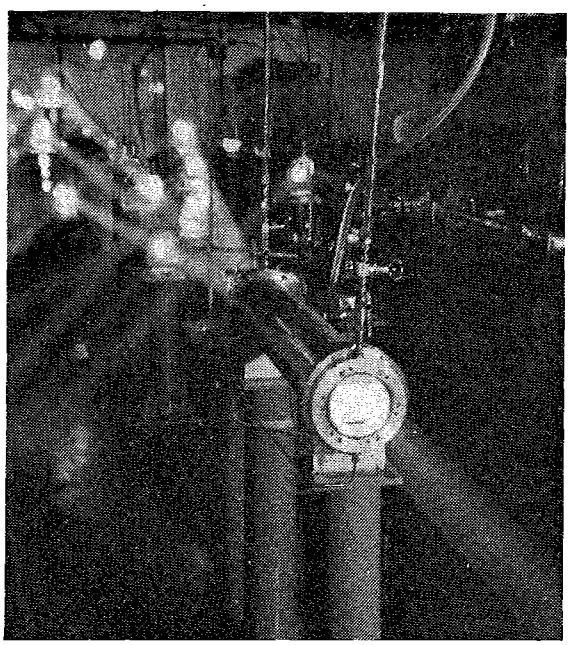

Figure 4. Beam combining in the final Raman amplifier, RA3. In the background the seven KrF pump beams converge on the entrance to the amplifier lightguide. The amplified Stokes beam emerges from the near end of the guide.

fluorescence converter together with a CCD camera coupled to a framestore and image analysis system. The experimental apparatus was located in the Sprite target area, and is shown schematically in Figure 8. The far-field two lens focusing system had an equivalent focal length of 17 m and included an $NO_2$ cell to provide a variable source of attenuation. Both the amplified and unamplified Stokes beams shown in Figures 6 and 7 have a FWHM divergence of approximately 20 μrad. In particular we note that the deterioration due to amplification is small, establishing the ability of the Raman scheme to achieve very high power with high beam quality. For further confirmation of beam quality, the fraction of the total energy lying within a beam divergence of 30 μrad was measured by the pinhole and energy monitor technique. In this technique a partial split from the beam just prior to the focus of the telescope directed light onto an integrating photodiode, and was used to monitor the beam energy. The fraction of light passing through a pinhole placed at the focus of the telescope onto a second integrating photodiode provided a relative measure of the energy lying within a beam divergence of 30 μrad. Values of 60% and 50% were obtained for unamplified and amplified Stokes beams respectively, again showing that the Raman amplification process causes little degradation to the beam quality. Since for a diffraction limited beam, 60% and 50% transmission would occur at beam divergences of 4.1 μrad and 3.5 μrad respectively, the unamplified beam was 7.5 x the diffraction limit while the amplified beam was 9 x the diffraction limit.

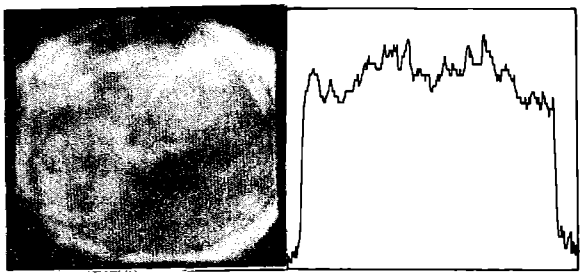

Figure 5. Near-field pattern of the amplified Stokes beam from a full-power shot.

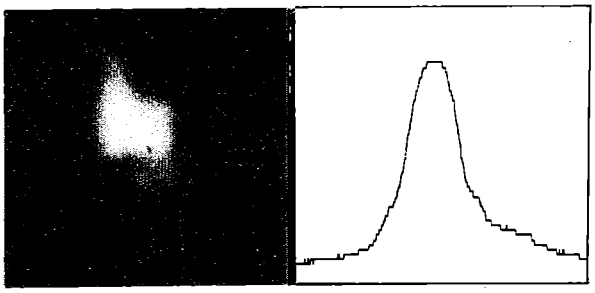

Figure 6. Far-field distribution of the amplified Stokes beam from a full-power shot.

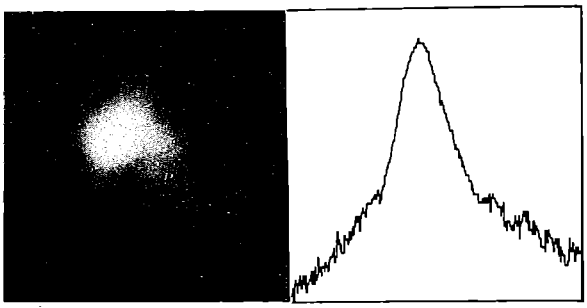

Figure 7. Far-field distribution of the unamplified Stokes beam.

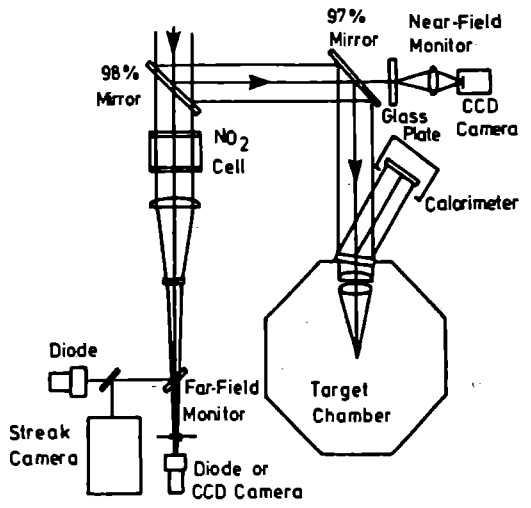


Figure 8. Experimental arrangement for near- and far-field profile measurements in the target area.

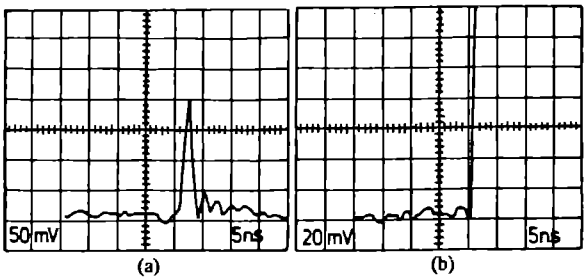


Figure 9. Oscilloscope traces used for determining prepulse levels in the Stokes beam.

(a) is a full-power shot with 2 x $10^8$ attenuation.

(b) is a full-power shot with no attenuation but with the Stokes beam delayed by 200 ps.

PREPULSE MEASUREMENTS

Measurements of the pulse contrast ratio (or prepulse level) were performed at the input to the experimental chamber. A photodiode placed behind an aperture in the far-field measured the transmitted power integrated over 30 μrad. The system had a sensitivity of $10^{-9}$ of the amplified pulse. Since it was not possible to measure a voltage prepulse level of $10^{-9}$ without damage to the oscilloscope and photodiode from the main pulses the voltage contrast ratio was reduced in several ways. The Stokes input pulse to the final Raman amplifier was delayed by 200 ps, thus preventing its amplification whilst still providing amplification for any prepulse (assumed to extend over 10 ns - the duration of the prepulse amplified spontaneous emission in the KrF pump beams). The photodiode was driven as hard as possible into saturation, a fast voltage limiter was placed between the photodiode and the oscilloscope, and a reduced oscilloscope bandwidth was used. Figure 9(a) shows the oscilloscope trace for a full power shot with a beam attenuation of 2 x $10^8$ using an $NO_2$ cell. Figure 9(b) shows the trace for a full power shot with no beam attenuation. We were unable to detect a prepulse level. Taking account of the integrating time constant of the photodiode and oscilloscope these observations gave a power contrast ratio of $> 2 \times 10^{10}$ and an energy contrast ratio of $> 10^8$.

## DISCUSSION

The high quality of the output beam obtained in these experiments was most encouraging. The beam divergence measurements demonstrated focal spots a factor of five smaller than those obtainable using the KrF laser direct[3], and therefore a 25 x increase in focal spot intensity. The majority of the divergence was found to be due to passive optical defects in the system which are correctible. When these effects are eliminated a further factor of 2 reduction in beam divergence and an associated factor of 4 increase in focal spot intensity is possible. This improvement together with the use of a F/1 focusing lens leads to the possibility of focal intensity in excess of $10^{19}$ W/cm$^2$.

An increase in the output of a high power laser requires an associated improvement in the pulse contrast ratio in order to prevent plasma formation on the target before the main pulse arrives. For a pulse intensity of $10^{19}$ W/cm$^2$ and taking the plasma generation threshold to be around $10^9$ W/cm$^2$, a pulse-to-prepulse contrast ratio of $10^{10}$ is required. We have measured the power contrast ratio to be better than 2 x $10^{10}$ for the 40 ps pulses and, perhaps for the first time, have demonstrated this level of performance in a large power laser system.

The internal efficiency of the final Raman amplifier was measured to be 60%, somewhat lower than the prediction of the 1D transient code. The discrepancy between theory and experiment is likely to be due to the simplicity of the code which does not take account of non-transform limited pulses and 2D effects due to the angularly separated pump beams. These finite pump angles give rise to an effective dispersion in the lightguide since the pump wave velocity $v_p = c \cos\theta$, where $\theta$ is the pump angle to the guide axis, and the Stokes wave velocity $v_s = c$ since the Stokes wave travels along the axis. The effect of dispersion in the amplifier is the introduction of a relative dephasing of the pump and Stokes waves in a distance[5]:

$$\ell_d = \frac{c}{\Delta\omega_p(1-\cos\theta)} \qquad (1)$$

For the 40 ps pulses used in this experiment the linewidth, measured using a Fabry-Perot etalon was found to be 0.75 cm$^{-1}$ (about 2 x transform limited). In this case $\ell_d$ = 56 cm, which, in a 1 m long amplifier is small enough to give rise to some reduction in gain and hence conversion efficiency. This conclusion is supported by subsequent measurements made on the final Raman amplifier with somewhat shorter pulses (15 ps) having a very much larger bandwidth of 4.5 cm$^{-1}$ ($\ell_d$ = 9 cm). In this case low conversion efficiencies were obtained.

## CONCLUSION

During the past year the Sprite Raman beam combining laser has produced 40 ps pulses at 268 nm in a single output beam which has a divergence of 20 μrad. An output energy of up to 5 J was obtained with a pulse-to-prepulse intensity ratio of greater than $10^{10}$, and with an internal efficiency in the final Raman amplifier of around 60%. These results are encouraging evidence that an efficient large scale laser system with angularly multiplexed Raman laser output could be successfully constructed and, for high power single pulse applications, would be competitive with Nd glass lasers in terms of beam brightness, pulse repetition rate, pulse contrast, efficiency and cost.

## REFERENCES


1. J R M Barr, N J Everall, C J Hooker, J P Partenan, M J Shaw, *Picosecond Raman pulse combining and compression in light guides for ultra-high power laser systems* Proc SPIE, 874,60 (1988)

2. M H Key, M J Shaw, I N Ross, P A Rodgers, M C Gower, *Annual Report to the Laser Facility Committee* Report RAL-89-133 (1990)

3. J R M Barr, N J Everall, C J Hooker, I N Ross, M J Shaw, W T Toner, *High Energy Amplification of picosecond pulses at 247 nm*, Optics Comm 66 No 2, 3 p127 (1988)

4. T Tomie, Private Communication

5. M J Shaw, J P Patanen, Y Owadano, I N Ross, E Hodgson, C B E/dwards, F O'Neill, *High-power forward Raman amplifier employing low-pressure gases in light guides. II. Experiments* 1466 (1986)

# RAMAN AMPLIFICATION OF NOISY PULSES

P A Rodgers

Rutherford Appleton Laboratory

The 1-D stimulated Raman scattering code previously reported [1] has been modified to include non-transform limited pulses (in both the pump and Stokes modes). The code solves the following set of coupled first order partial differential equations

$$\frac{\partial E_p(z,t)}{\partial z} = - Q(z,t)\, E_s(z,t)$$

$$\frac{\partial E_s(z,t)}{\partial z} = \frac{w_p}{w_s} Q^*(z,t)\, E_p(z,t)$$

$$\frac{\partial Q(z,t)}{\partial t} + \frac{Q(z,t)}{T_2} = C_{12}\, E_s^*(z,t)\, E_p(z,t)$$

A full explanation of the equations is given in [1] and the difference scheme used is described in [2]. The timescale of the interaction is set by $T_2$ (~27 ps in methane). The strength of the interaction is determined by $C_{12}$ and $T_2$ (in the steady state regime the Stokes small signal gain is exp ($\gamma$I L) where $\gamma = 4C_{12}T_2/c\epsilon_0$ (cm/w), I is the pump intensity and L the distance travelled in the gain medium). $E_p$ and $E_s$ are the pump and Stokes field envelopes. For transform limited pulses $E_p$ and $E_s$ are real but in general they are complex.

Two different types of noise are considered.

## COLLISIONAL DEPHASING NOISE

In collisional dephasing noise (CDN) we assume the source radiates coherently for a time $\tau_c$ and then undergoes an abrupt and random phase change (possibly due to a collision) and continues to radiate coherently for a further $\tau_c$ with a different, but constant, phase. However the amplitude of the oscillations are not changed.

$$E_p(t) = |E(t)|e^{i\phi(t)}$$

$$\phi(t) = r_n 2\pi \quad (n-1)\tau_c < t \leq n\tau_c \quad n = 1, 2, \ldots$$

$r_n$ is a random number sequence.

Obviously the pulse becomes 'noisier' as $\tau_c \to 0$ although the pulse intensity will remain smooth in the time domain. In table 1 we show the effect of varying the coherence time, $\tau_c$, for both the pump and Stokes fields for optimally timed 4 ps pulses. For transform limited pulses the energy gain of 1.3 x $10^5$ corresponds to a conversion efficiency of 13% (ie non-saturated). The gain is sensitive to the random numbers used and the figures are averaged over 10 different sets of random numbers, or 'shots'. It can be seen that for $\tau_c$ = 1 ps for both pump and Stokes the gain has been reduced by a factor of 5.

Table 1 Stokes energy gain (÷$10^4$) for different coherence times of collisional dephasing noise on 4 ps pump and Stokes pulses. The input intensity ratio is $10^{-6}$ and the steady state small signal gain is 267. Gains averaged over 10 'shots'.

| Pump / Stokes | ∞ | 10 | 4 | 1 |
|---|---|---|---|---|
| ∞ | 13 | 12 | 8.3 | 2.8 |
| 10 | 13 | 12 | - | - |
| 4 | 8.7 | - | 8.8 | - |
| 1 | 3.5 | - | - | 2.5 |

Table 2 Stokes energy gain (÷$10^4$) for different widths of multimode random phase noise on 4 ps pump and Stokes pulses. The input intensity ratio is $10^{-6}$ and the steady state small signal gain is 267. Gains averaged over 50 'shots'.

| Pump / Stokes | 0 | 1 | 5 | 10 |
|---|---|---|---|---|
| 0 | 13 | 13 | 8.4 | 5.3 |
| 1 | 12 | 12 | 8.0 | 5.1 |
| 5 | 8.2 | 7.7 | 6.5 | 4.5 |
| 10 | 5.6 | 5.3 | 4.6 | 3.7 |

## MULTIMODE RANDOM PHASE NOISE

A realistic noisy pulse can ge generated by (fast) Fourier transforming a sum of amplitude modulated (usually Gaussian) frequency modes with random phases to the time domain and multiplying the resultant (complex) thermal-type noise by a smooth pulse [3]. This produces pulses which have amplitude and phase fluctuations in both time and space.

$$\hat{E}_p(t) = E_p(t) \sum_n \exp(iw_n t + i\phi_n)\, f(w_n)$$

$E_p(t)$ is a smooth pulse, $\phi_n$ is random over $2\pi$ and $f(w_n)$ is typically a Gaussian. For

$$f(w_n) = \exp(-(w_n - \bar{w})^2 / (2\Delta^2))$$

$\hat{E}_p(t)$ becomes noisier with increasing $\Delta$.

In table 2 we show the effect of varying the noise width, $\Delta$, independently for the pump and Stokes fields for optimally timed 4 ps pulses as before. In this case we average over 50 'shots'.

In this regime noise in either the pump or Stokes reduces the gain by approximately the same amount - whether the difference in the second significant figure is statistically significant is being investigated. For $\Delta_s = \Delta_p$ = 10 the pulses are approximately 3 times transform limited.

## REFERENCES

[1] M H Key et al, *Analysis of high power KrF laser Systems* Rutherford Appleton Laboratory Report RAL-89-133, (Section 3.3) (1989).

[2] *Annual report to the Laser Facility Committee* Rutherford Appleton Laboratory Report RAL-89-045 (Section B1.5) (1989).

[3] D J Bradley and G H C New, Proc IEEE, 62, 313, (1974).

# STUDIES WITH THE RAMAN PREAMPLIFIER

C J Hooker, J M D Lister and P A Rodgers

Rutherford Appleton Laboratory

## EXPERIMENTS

In order to obtain information about Raman amplification for comparison with the theoretical model described previously, a series of experiments was performed using the first Raman amplifier, RAØ. This amplifier is a convenient test-bed, since it is part of the oscillator, and derives its pump beam from the EMG 103 at a repetition rate of 8 Hz. All the other amplifiers are pumped by the output beams from Sprite, and thus require full laser shots at intervals of several minutes.

To investigate the performance of this Raman amplifier, we measured the gain and the pump-to-Stokes conversion efficiency at pulse lengths of 4 ps, 8 ps and 40 ps, with variable Stokes inputs but with the pump intensity held constant. The pump beam timing relative to the Stokes was adjusted before each set of measurements to obtain maximum output for the pulse length being used; this is necessary because the optimum timing varies with the pulse length. The methane pressure in the amplifier was adjusted to the highest level consistent with there being no self-generation of Stokes light by the pump beam. Self-generated Stokes would compete with the input Stokes and distort the measurements. Pressures of between 2 and 3 atmospheres of methane were used.

The experimental configuration is shown in Figure 1. The energies of the input and output Stokes pulses were obtained from average-power measurements made with a Laser Instrumentation (L.I) model 14NO power meter. Pump energies were obtained using a Scientech model 362 power meter, which was previously cross-calibrated against the L.I. Both detectors have slow time-constants, of order 10 seconds, so the effects of shot-to-shot variations in pulse energies were averaged out. Before taking each set of data the pump power was measured with the Scientech meter, which was then placed in a spatially split-off part of the KrF beam as a check that the pump power remained constant.

After the dispersing prism at the output of the amplifier, the Stokes beam was directed onto the L.I. meter through an aperture of known area, to restrict the measured part to a region of good uniformity. The Stokes input was varied by attenuating the beam with metallised quartz neutral-density filters, which had previously been calibrated at 268 nm with a spectrophotometer. Calculated adjustments of the pump timing were made to compensate for the extra optical path introduced by the filters. The amplified Stokes power was measured over as wide a range of inputs as the L.I. meter sensitivity would permit, attentuation factors of up to $10^4$ being used. The meter had sufficient sensitivity to measure the unattenuated input Stokes power, and this was monitored at intervals during the data-taking to allow slow variations due to timing drifts in the lasers to be corrected.

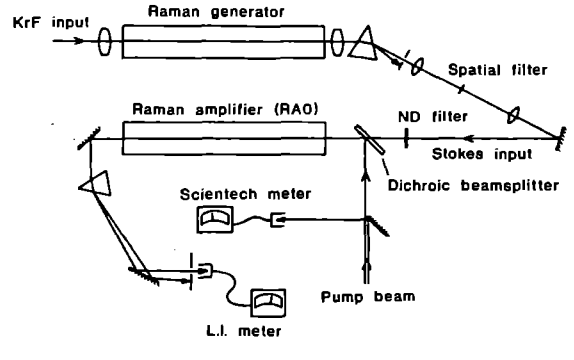


Figure 1. Experimental arrangement for gain measurements on the Raman preamplifier.

The transmission of the amplifier and other optics at 268 nm was measured separately. The intensity of the Stokes beam was assumed uniform across the area measured, and was calculated from the energy per pulse (the measured power divided by the repetition frequency of 8 Hz) and the pulse duration. The actual input intensity was determined from the power of the unamplified beam by applying the attenuation factors of the filters and the system optics. The extraction efficiency was calculated as the ratio of output Stokes energy to input pump energy, both corrected for Fresnel losses in the amplifier windows to give a true internal efficiency.

## RESULTS AND DISCUSSION

Measurements were made of the pulse length and spectrum of the 249 nm output of the EMG103, since these affect the behaviour of the Raman generator and amplifier. Two techniques were used to determine pulse lengths: a streak camera (Imacon 500) was used for the longer pulses and a cross-correlator for the shortest. Streaks were recorded on film at the output of the camera image intensifier and densitometered; the measured pulse length was 39 ps FWHM. This is considerably shorter than the pulse length in the red, and we presume the shortening to have occurred in the tripling stage. The pulse shape was asymmetric, with a rise time of 20 ps and a fall time of 60 ps.

The cross-correlation measurement[1] was performed by mixing the 249 nm and the 746 nm light in a KDP crystal to yield a difference frequency signal at 373 nm. The 249 nm wavefront was sheared by diffraction from a grating (in first order) before mixing. The 373 nm signal was detected with a 1-D diode array, and its spatial extent gives a measure of the pulse length. The pulse length determined in this way was 3.5ps, which is identical to that from the dye oscillator within the limits of error.

No measurements were possible of the intermediate pulse length at 249 nm; we assume it was close to the 8 picoseconds found from the autocorrelation measurement at 746 nm.

The spectrum of the 249 nm amplified beam was examined using a grating spectrometer with a 1-D reticon readout (Exitech Ltd). This instrument has a resolution of approximately 0.8 $cm^{-1}$. The bandwidth of the 40 ps pulses was less than the instrumental limit, but the 4 ps pulses exhibited a spectrum with multiple peaks and marked shot-to-shot variation. These fluctuations orginate in the sync-pumped oscillator, and are a consequence of the leading edge of the pulse picking up cavity noise as it circulates[2]. The average width of the spectrum was 10 $cm^{-1}$, which for a 4 ps pulse is about three times the transform limit. The spectrum of the 40 ps pulses was measured using an etalon with a free spectral range of 1.1 $cm^{-1}$, and was found to be 0.3 $cm^{-1}$, which corresponds to the transform-limited spectral width.

Code predictions of gain and conversion

efficiency are shown in Table 1, alongside the experimentally measured values. The predictions were made using the measured intensities and pulse lengths, full account being taken by the model of transient effects. The theory agrees well with experiment at high Stokes input intensities, but diverges significantly in the small signal regime, where the predicted gain is very sensitive to variations in pump intensity. Small errors in the measured power or in the pulse length could thus account for some of the discrepancy. However, the code does not model the experimental situation exactly, in that it assumes the pulses to be transform-limited with no transverse structure, and neglects higher-order effects. The discrepancy between theory and experiment is largest in the case of the 4 ps pulses, which were known to be non-transform-limited. It is likely that the inclusion of bandwidth effects in the code model would lead to a lower effective value of the gain coefficient, $\gamma$, and to more accurate predictions of the amplifier behaviour.

In order to test this hypothesis, the measured small-signal gain at 4 ps was used to obtain a value of $\gamma$(effective) from the equation:

$$G = \frac{\exp(2u)}{2\pi u^2} \qquad (1)$$

$$\text{where } u^2 = \frac{2t_p}{t_2}\,\gamma_{\text{effective}}\, I_p L \qquad (2)$$

The value obtained for $\gamma$(effective) by this means was 60% of the steady-state $\gamma$. In Figure 2 the experimental date are compared with a code run in which the derived value of $\gamma$(effective) was used; the agreement is seen to be excellent, which is perhaps not surprising. What this analysis shows is that the many factors not included in the model can be allowed for by modifying a single parameter by a modest amount.

Considering the extraction efficiencies, it can be seen that the maximum measured efficiency varied from 75% with 40 ps pulses down to 50% with 4 ps pulses. The dephasing time ($t_2$) for methane is 27 ps so the scattering is already in the transient regime even with 40 ps pulses, leading to lower conversion efficiency than in the steady state. As the pulse length becomes shorter so the calculated efficiency becomes less, a result which is confirmed experimentally. It is clear, however, that this amplifier, in which the pump and Stokes beams are nearly colinear, is capable of quite high efficiencies even with 4 ps pulses.

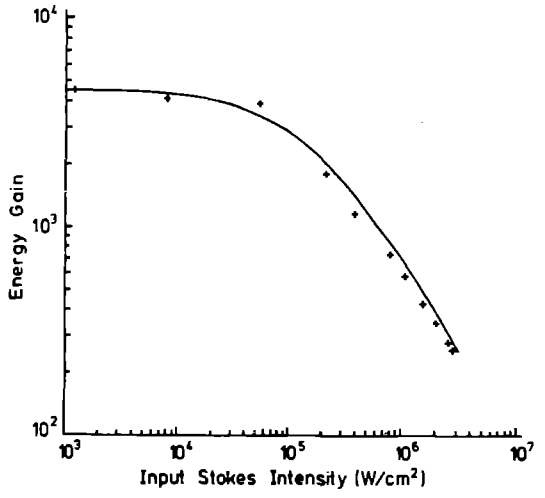


Figure 2. Comparison of measured gain for 4 ps pulses with a theoretical prediction using a derived value of the gain coefficient.

Table 1. Comparison of predicted and observed gains and efficiencies for different pulse lengths.

| Pulse length | Small-signal gain | | Peak efficiency (%) | |
|---|---|---|---|---|
| | Predicted | Observed | Predicted | Observed |
| 40ps | $2\times10^5$ | $4\times10^4$ | 80 | 72 |
| 8ps | $4.7\times10^5$ | $2.7\times10^5$ | 70 | 65 |
| 4ps | $1.3\times10^5$ | $4.5\times10^3$ | 64 | 50 |

REFERENCES


1. I N Ross et al *Single-shot measurement of pulse duration for a picosecond pulse at 249 nm.* Applied Optics **28** 4054 (1989).

2. J M Catherall and G H C New *Role of Spontaneous Emission in the Dynamics of Mode Locking by Sychronous Pumping* IEEE J Quant Electronics **QE-22** 1593 (1986).

# PRELIMINARY OBSERVATIONS OF RAMAN BEAM-COMBINING AT 15 PICOSECONDS

E C Harvey, C J Hooker and J M D Lister

Rutherford Appleton Laboratory

## INTRODUCTION

Successful 40 ps Raman beam combining experiments have been described earlier in this report. It was desirable to be able to generate shorter pulses, and a very simple way of reducing the pulse duration in the Sprite Raman beam combining laser was to change the etalon in the synchronously pumped dye laser that formed the basis of the short pulse generator[1]. Although this method had the advantage of being quick and simple, it is known that the pulses produced in this way are less than satisfactory. In particular the bandwidth of the shorter pulses is broad and has been observed to result in reduced Raman conversion efficiency[2]. Here we report on a preliminary study of Raman beam combining using 15 ps pulses generated in this way, and identify two critical aspects of the system.

## EXPERIMENTAL ARRANGEMENT

The only change made to the experimental arrangement described earlier was to the etalon in the synchronously pumped dye laser of the short pulse generator. Since optimum relative timing depends upon pulse duration and, under high gain the Stokes beam is delayed by the relative timing in each amplifier[2], it was necessary to retime each of the amplifiers whenever the pulse duration was changed. The timing was done for each of the amplifiers in sequence for maximum gain in order to obtain optimum output.

## RESULTS

The performance of the Raman system is shown in Table 1. It can be seen that lower output energies and poorer conversion efficiencies were observed in comparison with those obtained during the 40 ps study. We note that the performance of the lightguide amplifier RA3 has been significantly degraded by the reduction in pulse duration, but that the performance of the preamplifier and first Raman amplifier (RA0 and RA1) did not change significantly.

Figure 1 shows some representative spectra of the KrF beam for (a) a 15 ps pulse amplified by the discharge amplifier and (b) a 15 ps pulse amplified in Sprite and Goblin. Figure 1(c), shown for comparison, is the spectrum of an amplified 40 ps pulse. These were measured using an Exitech spectrometer, and the dispersive axis for each of the graphs is not absolute. Thus relative shifts in the peak position on this axis are an instrumental efect only. The slit used on the spectrometer was 100μm wide giving an instrument resolution of $1cm^{-1}$. Thus the spectral width of the 40 ps pulse was limited by the instrument. Measurements using a Fabry-Perot etalon show the 40 ps line width to be around 0.75 $cm^{-1}$. The linewidth of the amplified 15 ps pulse was found to be 4.5 $cm^{-1}$.

## DISCUSSION

The last two Raman amplifiers were pumped by angularly separated pump beams with off-axis angles of 1.1° and 5.0° respectively. These finite pump angles give rise to an effective dispersion in the lightguide since the pump velocity $v_p = c\cos\theta$, where $\theta$ is the pump angle to the guide axis, and the Stokes wave velocity $v_s = c$ since the Stokes wave travels along the axis. The effect of

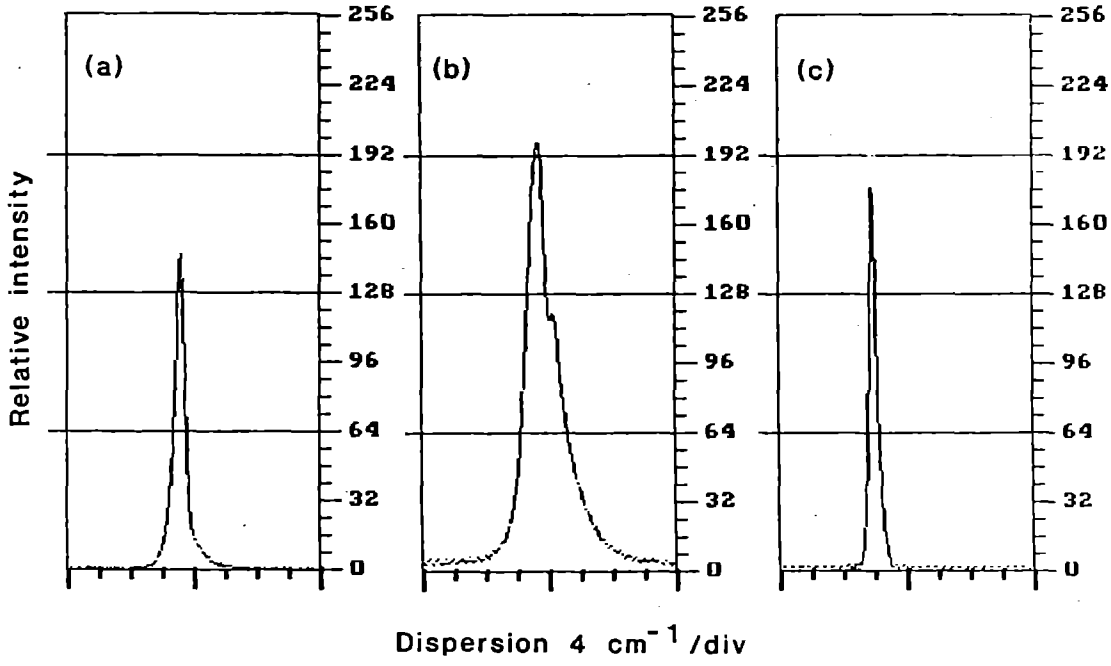


Figure 1. Representative KrF spectra:
(a) 15 ps pulse after discharge amplifier FWHM = 1.25 $cm^{-1}$
(b) 15 ps pulse after full amplification FWHM = 4.25 $cm^{-1}$
(c) 40 ps pulse after full amplification FWHM = 1.0 $cm^{-1}$

Table 1. Operating parameters for Raman amplifiers for 15 ps pulses

| Raman Amplifier | RA0 | RA1 | RA2 | RA3 |
|---|---|---|---|---|
| Pump energy | 5 mJ | 14 mJ | 450 mJ | 4 J |
| Pressure $CH_4$ (bar) | 3 | 3 | 2 | 1 |
| Input Stokes energy | 5 μJ | 40 μJ | 4 mJ | 50 mJ |
| Output Stokes energy | 500 μJ | 5.5 mJ | 70 mJ | 300 mJ |
| Conversion efficiency | 10% | 40% | 15% | 7% |

dispersion in the amplifier is the introduction of a relative dephasing of the pump and Stokes waves in a distance

$$\ell_d = \frac{c}{\Delta\omega_p(1-\cos\theta)} \qquad (1)$$

where $\Delta\omega_p$ is the linewidth of the pump.

At 4.5 $cm^{-1}$, the linewidth of the amplified 15 ps pulse gives rise to a dephasing distance of $\ell_d$ = 9 cm in the lightguide of RA3. This compared with a dephasing distance of 56 cm for the 40 ps pulse. The 9 cm effective length of the amplifier explains the low conversion efficiency seen in the experiments, and also the deviation from the code prediction which assumes a length of 1 metre.

The pump beam angles in the final Raman amplifier have since been reduced from 5° to 2.5° in order to increase the dephasing distance. The dispersion effect was not as serious in RA2 since the pump angles were much smaller than those used in RA3 (around 1°). It is thought that the poor conversion efficiency obtained in RA2 is still associated with the broad spectrum of the pump beam.

The origin of the spectral broadening during amplification is not yet clear, but it is assumed to be associated with the spectral instability of the sync-pumped generator which varies considerably from shot-to-shot. The generator has since been replaced by a Distributed Feedback Dye Laser which is described in more detail in a later section, and which generates pulses that are much closer to the transform limit.

## CONCLUSION

We have identified two related effects which resulted in the poor performance of the lightguide Raman amplifiers with 15 ps pulses. These were the broad pulse linewidths associated with the short-pulse generator, and the dephasing that occurs in the lightguides as a result of an effective dispersion. It is anticipated that the new Distributed Feedback short-pulse generator, and the reduced pump beam angles in the final Raman amplifier will improve the performance of the amplifiers. It was encouraging to note that the performances of the Raman preamplifier and the first Raman amplifier were similar for both 40 ps and 15 ps pulse durations, suggesting that the potential exists for efficient operation of the laser at pulse durations of around 10 ps.

## REFERENCES


1. J R M Barr, N J Everall, C J Hooker, I N Ross, M J Shaw, W T Toner, *High Energy Amplification of picosecond pulses at 248 nm* Optics Comm, 66, 23, 127(1988)

2. C J Hooker, J M D Lister, J Radford, I N Ross, M J Shaw, J E Andrew, G M Davis, E Fujiwara, *Annual Report to the Laser Facility Committee* RAL-89-045, B1.4, 193(1989).

# TARGET SHOOTING WITH A HIGH BRIGHTNESS KrF RAMAN LASER: A COMPARISON OF LASER-PLASMA ENERGY TRANSPORT

G J Tallents[1], M H Key[2], P Norreys[2], N Tragin[2], H Baldis[3], J Dunn[3] and D Brown[4]

[1] University of Essex
[2] Rutherford Appleton Laboratory
[3] National Research Council, Canada
[4] Royal Holloway and Bedford New College

## INTRODUCTION

The processes of energy transport when laser radiation is focussed onto a solid surface to form a plasma are of fundamental importance in understanding laser-plasma interactions[1]. Lateral energy transport (perpendicular to the laser beam) along the surface of the target is important in short pulse laser-produced plasmas when the focal spot dimensions are small. The lateral energy transport reduces the heating of the target material at the focal spot and so lowers the plasma temperature and degree of plasma ionisation. The effect can be very large in nanosecond experiments at long (μm) wavelengths . It is reduced for shorter pulselengths and wavelengths.

Here, we report the results of energy transport experiments using the Raman shifted KrF SPRITE laser with output at 0.268 μm wavelength. This laser is uniquely suitable for energy transport measurements as the focal spot size produced in the experiments is such that half the laser energy is focussed to within only 7.5 μm and the pre-pulse energy is estimated to be less than $10^{-9}$ of the main pulse energy and so does not produce any plasma[2].

We have recently reported[3] energy transport measurements from 20ps, 0.53μm wavelength laser-plasma experiments undertaken using the second harmonic of the VULCAN glass laser with targets of a thin layer of aluminium buried beneath a confining plastic overcoat. Here, we also report some further analysis of these experiments and the results of similar experiments with 0.35μm laser irradiation (the third harmonic of the VULCAN laser) and compare these results with experiments using the Raman shifted KrF SPRITE laser. The irradiation conditions are summarised in Table 1.

Table 1: Target Irradiation conditions

| λ(μm) | Energy (J) | Pulse-length (ps) | Focal spot diameter (μm) | Intensity ($10^{16}$W/cm²) |
|---|---|---|---|---|
| .53 | 6-8 | 20 | 50 | 1-2 |
| .35 | 3-4 | 20 | 50 | 0.8-1.0 |
| .27 | 2-3 | 40 | 10 | 3-5 |

## RAMAN SHIFTED KrF EXPERIMENTS

Experiments were carried out with 40 ps pulses from the SPRITE KrF pumped Raman laser focussed onto layered targets. A 0.2 μm thick Al layer buried below a plastic layer was used to record heat penetration into the target by studying the Al emission spectrum recorded by a flat crystal of Pentaerythritol (PET) (2d = 8.792Å) spectrometer. In addition, KCl and CaF layers were buried deep in the targets to record superthermal electron production from fluorescence of K, Cl and Ca. Energies on target of approximately 2-3J were focussed to ∿ 7.5 μm focal spots giving intensities of 3-5 x $10^{16}$ W/cm². However, recorded $K_\alpha$ emission from the deeply buried KCl layer implies only a few percent conversion of incident laser energy to superthermal electron energy.

Electron densities in the aluminium layer determined from the Stark broadened spectral width of the Al XII $1s^2\ {}^1S_0$ - $1s\,3p\ {}^1P_1$ line[4] are shown in Fig 1.

Pinhole camera pictures of emission less than 2.5Å (passing through a 10 μm Ti filter) show that the spatial extent of the emission is close to that of the laser focal spot size (full width half maximum 10 μm). Similar pinhole pictures with less filtering (6 μm of aluminized mylar) show that the spatial extent of all emission (λ<10Å) varies with the overlay thickness (Fig 2). The large absolute values of the measured spot sizes (fig 2) imply that lateral thermal conduction from the 10 μm diameter laser focal spot is important.
Fig 2 is approximately equivalent to a plot of the diameter of the energy deposition area as a function of depth in the target.

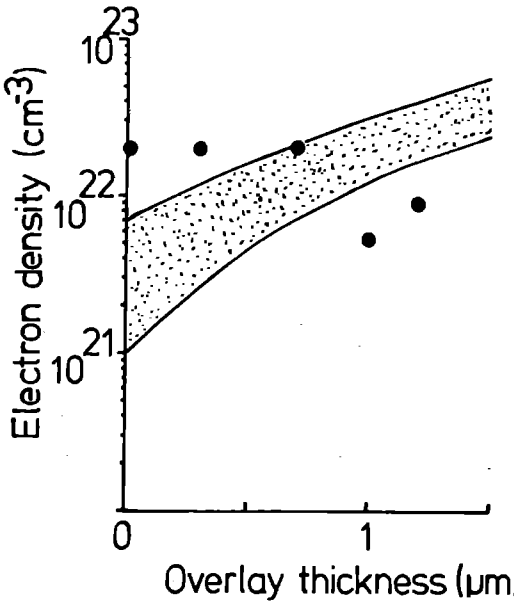


Fig 1: Electron densities measured from the width of the Al XII $1s^1\ {}^1S_0$ - $1s3p\ {}^1P_1$ spectral line as a function of plastic overlay thickness for 0.27 μm laser irradiation using SPRITE. The shading shows the range of electron densities predicted by the MEDUSA code from the inner (top curve) to the outer (bottom curve) boundaries of the aluminium layer.

## .53 μm-EXPERIMENTS

Experiments were carried out with 20 ps pulses from the VULCAN frequency-doubled glass laser at 0.53 μm wavelength in a single beam at energies of 6-8J focussed to a 50 μm focal spot giving intensities of (1-2) x $10^{16}$ W cm$^{-2}$. The energy transport was recorded using layered targets as for the SPRITE experiments.

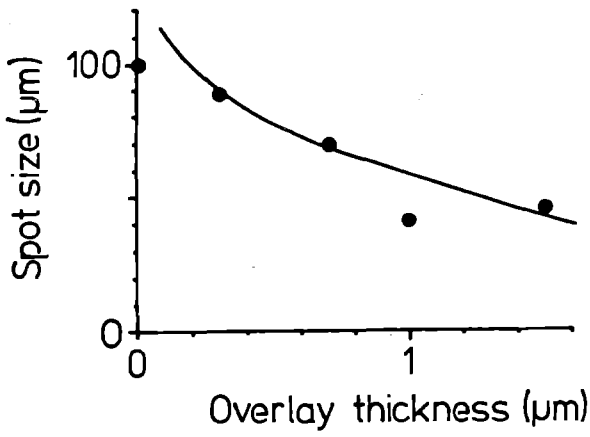


Fig 2: Spot size of X-ray emission ($\lambda < 10$Å) as a function of plastic overlay thickness. The solid curve is a fit of a theoretical curve from Tallents et al[5].

Electron densities in the aluminium layer determined (i) from the Stark broadened spectral width of the Al XII $1s^2\ ^1S_0$ - $1s\ 3p\ ^1P_1$ line[4] (ii) from the intensity ratios of the a-d + q, r to j, k, l satellite lines[6] of Al XII $1s^2\ ^1S_0$ - $1s2p\ ^1P_1$ and (iii) from the intensity ratios of satellite lines of Al XIII $1s\ ^2S$ - $2p\ ^2P$ are shown in Fig 3. The electron densities at the inner and outer boundaries of the aluminium layer at the end of the laser pulse predicted by MEDUSA one-dimensional fluid-code simulations are also plotted on Fig 3. Electron densities significantly above the laser critical density of $4 \times 10^{21}$ cm$^{-3}$ have been measured. The densities deduced from satellites to the hydrogen-like AlXIIII $1s\ ^2S$ - $2p^2\ ^2P$ line show the highest densities. This is consistent with high densities and temperatures co-existing spatially and temporally together.

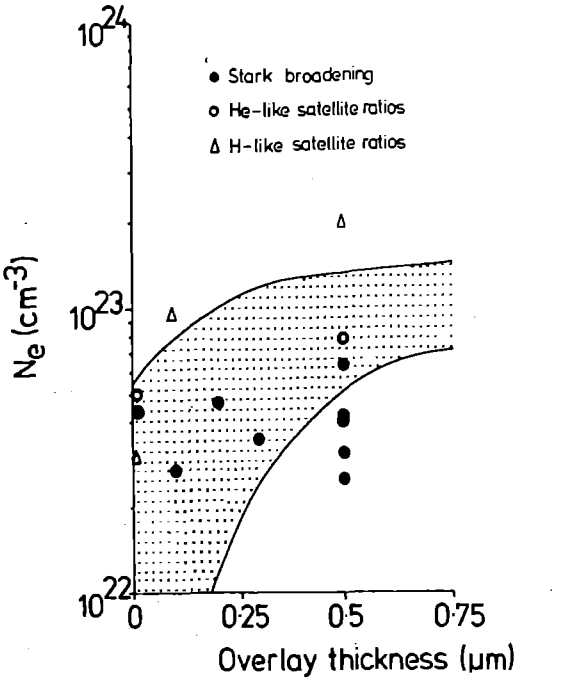


Fig 3: Electron densities deduced by different methods as a function of plastic overlay thickness for 0.53 μm laser irradiation using VULCAN. The shading shows the range of electron densities predicted by the MEDUSA code from the inner (top curve) to the outer (bottom curve) boundaries of the aluminium layer at the end of the laser plasma.

The slope of the hard X-ray continuum between 5 and 20 KeV measured by a filtered diode array indicated a superthermal temperature of 6±2 KeV. Using the analysis of Hares et al[7] the measured absolute flux of potassium $K_\alpha$ emission from a buried KCl layer in the targets implies that the total superthermal electron energy was approximately 0.3 J or 5% of the incident laser energy. Thermal electron temperatures are estimated to be ∿ 1 KeV from the slope of the He-like Al free-bound continuum for all plastic overlay thicknesses 0-0.5 μm.

Pinhole camera pictures show that the spatial extent of emission in the 7.95 - 18Å band (passing through a 10μm Al filter) is localised to within 50-70 μm. There is no evidence for plasma formation outside the laser focal spot area as we found using the SPRITE laser.

## 0.35 μm EXPERIMENTS

A limited number of frequency-tripled VULCAN laser shots at 0.35 μm wavelength onto layered targets were also made. Energies of 3-4J focussed to a 50μm focal spot gave intensities of 8-10 x $10^{15}$ W cm$^{-2}$. $K_\alpha$ emission from the deeply buried KCl and $CaF_2$ layers could not be detected, which implies a small (energy < 5% of incident laser energy) production of superthermal electrons. The He-like $1s^2\ ^1S_0$ - $1s3p^1P_1$ emission from the aluminium layer enabled measurements of electron densities from the Stark broadened spectral widths. For the studied plastic overlay depths of zero and 0.6 μm, we measured densities of $4 \times 10^{22}$ cm$^{-3}$[3]. Pinhole camera measurements again show that the spatial extent of emission in the 7.95-18Å band is localised to within 50-70 μm - the same size as the laser focal spot.

## CONCLUSION

We have reported the first results of target shooting experiments using the Raman shifted SPRITE KrF laser. The transport of laser energy from the small (∿ 7.5 μm) focal spot produced by the laser has been measured and compared with similar measurements undertaken using the second and third harmonic (0.53 μm and 0.35 μm wavelength) of the VULCAN glass laser. Significant lateral movement of energy was seen using the SPRITE, but not the VULCAN laser, probably because of the longer (40 ps) pulse-length and smaller focal spot size obtained in the SPRITE experiments.

The longer pulse-length used in the SPRITE experiments has produced plasmas of lower average density than was found with the 20 ps pulse-lengths from VULCAN. However, the intensity of the H-like lines relative to the He-like lines is increased by a factor of two with the SPRITE experiments. The electron temperature may be greater or possibly the longer pulse-length allows an ionisation equilibrium with more H-like ions to be more closely approached.

## REFERENCES

1. M.H. Key, W.T. Toner, T.J. Goldsack, J.D. Kilkenny, S.A. Veats, P.F. Cunningham, and C.L.S. Lewis. Phys. Fluids 26, 2011 (1983).
2. See this Annual Report.
3. G.J. Tallents, M.H. Key, P. Norreys, D. Brown, J. Dunn and H. Baldis. Phys. Rev. A40, 2857 (1989).
4. R.W. Lee, J. Quant. Spect. Radiat. Trans. 40, 561 (1988).
5. G.J. Tallents, M.H. Key, P. Norreys, N. Tragin, H. Baldis, J. Dunn and D. Brown 1990 Proc. SPIE 1229-18.
6. V.L. Jacobs and M. Blaha. Phys. Rev. A21, 525 (1980).
7. J.D. Hares, J.D. Kilkenny, M.H. Key and J.G. Lunney. Phys. Rev. Lett. 42, 1216 (1979).

# A DISTRIBUTED FEEDBACK DYE LASER FOR SPRITE

Michael Steyer, Ian N. Ross and James M. D. Lister
Rutherford Appleton Laboratory

## INTRODUCTION

This section reports on the measurements made during the assessment and installation of a new Sprite oscillator system based on a Distributed Feedback Dye Laser (DFDL). The DFDL is a promising source of short transform limited laser pulses[1] and as such offers a significant improvement over the previous synchronously pumped oscillator.

Unlike conventional lasers, a DFDL does not have discrete external mirrors. Instead feedback is provided by a volume grating in the dye, set up by generation of a spatially periodic modulation of the pump intensity $I_P$ (figure 1). This modulation gives rise to both an amplitude grating (through the resulting gain modulation) and a phase grating (through the resulting refractive index modulation). A pump laser beam (vacuum wavelength $\lambda_P$) is divided into two partial beams which are focussed into a dye solution, using a cylindrical lens, where they recombine to form a 3D standing wave interference pattern with periodicity $\Lambda=\lambda_P/(2\cdot n_L\cdot\sin\theta_L)$, where $n_L$ is the refractive index of the solvent, and $\theta_L$ is the angle of incidence in the solution. Note that $n\cdot\sin\theta$ is invariant on refraction. The DFDL only provides feedback and consequently only lases at a wavelength meeting the Bragg condition of the grating. Thus $\lambda_L=2\cdot n_L\cdot\Lambda$, where $\lambda_L$ is the vacuum wavelength of the DFDL.

The DFDL has a very fast 'turn on' because not only is the gain increasing with the pump intensity but also the feedback grows rapidly with pump intensity. Likewise the DFDL will also quickly turn off when the gain saturates. At well above threshold the output will typically consist of relaxation oscillations where the first pulse has a pulse duration less than 10% of the pump pulse duration. By lengthening the pump region of the dye it is possible to ensure that the pumped length determines the pulse rise time and hence the pulse duration.

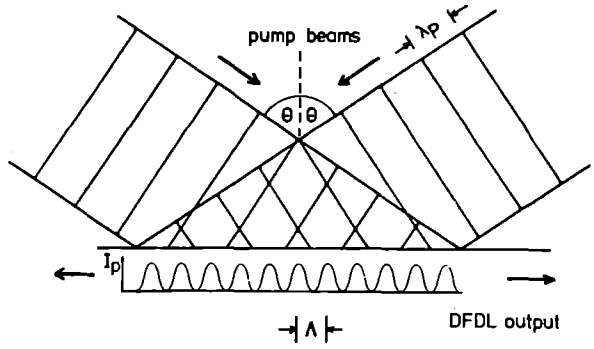


Figure 1: DFDL principle

The DFDL will typically generate pulses of between 5 and 50 times shorter than the pump pulse and is a valuable tool in picosecond pulse generation. In addition to this strong pulse compression there is also a strong spectral narrowing due to the Bragg feedback, and the combination of these leads to operation at close to transform limit. It is this property which makes the DFDL attractive as an oscillator for the Sprite system and particularly so when Sprite is used for pumping Raman ampifiers.

## OSCILLATOR DESIGN

The design of pump geometry of the Sprite DFDL is shown in figure 2. Following a cylindrical lens, the pump beam is divided by a cube beam splitter and recombined in the dye by internal reflections from two prisms. Glycerol provides index matching between prisms and between prism and dye cell. This prism arrangement is achromatic and fine tuning of the output wavelength is achieved simply by rotation of the arrangement about the appropiate axis (figure 2) or by tuning the wavelength of the pump source. For small angles of incidence $\Phi$ of the pump beam onto the front prism face, the laser wavelength $\lambda$ is given by

$$\lambda_L = \frac{n_L\cdot\lambda_P\cdot\sqrt{2}}{n_G+\Phi} \qquad (1)$$

where $n_G$ is the refractive index of the glass prisms.

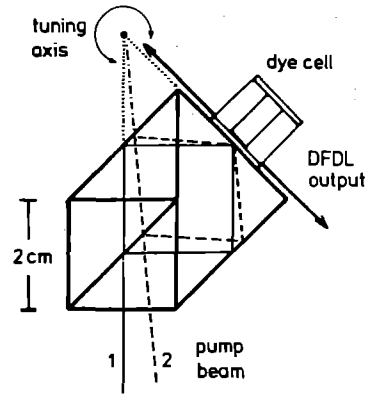


Figure 2: Pump geometry for the present DFDL

To match a given output wavelength $\lambda_L$ to a given pump wavelength $\lambda_P$ it is possible to coarse tune the system by adjustment of $n_L$. This is accomplished in the Sprite arrangement by mixing Ethanol and DMSO in the appropiate proportions (1:1). A $2\cdot10^{-2}$ M solution of Pyridine 2 is used.

The Sprite DFDL has been incorporated into the Sprite oscillator as shown in Figure 3. The pulses of a synchronously pumped dye laser operating at a wavelength of about 581nm are stretched to about 100ps (FWHM) using an intracavity etalon (FSR=17cm$^{-1}$) and amplified in two dye amplifiers pumped by a Q-switched and frequency doubled Nd:YAG laser. The output energy is several μJ in a pulse of duration 50ps (shortened due to strong saturation in the amplifiers).

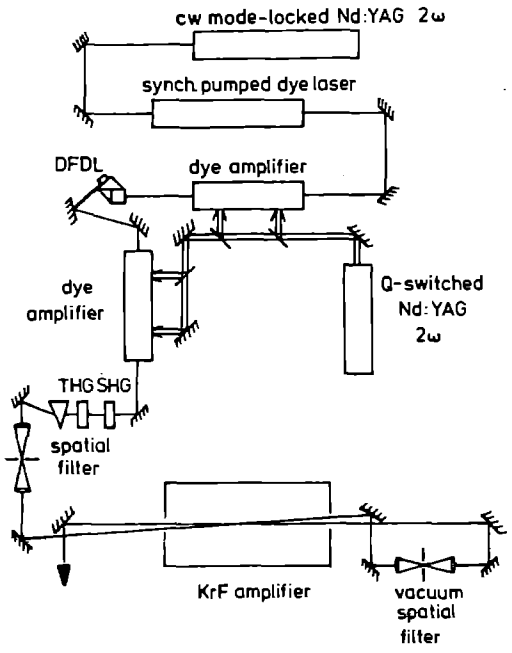


Figure 3: Schematic of the modified SPRITE oscillator

A homogeneous part of the beam is selected by a rectangular mask (2x2 $mm^2$) and focussed into the DFDL using a f=10cm cylindrical lens. Absorbing filters are used to adjust the pump energy into the DFDL.

The output pulse of the DFDL at 746nm is amplified in two dye amplifiers. Frequency tripling using two KDP crystals in series generates a source pulse at 249nm which is amplified by a discharge pumped KrF excimer laser (EMG103) used in double pass. Due to the strong saturation in all these visible and UV amplifiers and due to nonlinear response of the frequency tripling it was important to assess the performance of the DFDL at several points: after the DFDL; after the dye amplifers; after frequency tripling and after the excimer amplifier.

## PERFORMANCE

A number of features of the performance were tested: the threshold and pump energy requirements; the pulse duration; the spectral profile and coherence length; the shot-to-shot consistency. In particular the variation of these parameters with pump pulse energy was measured.

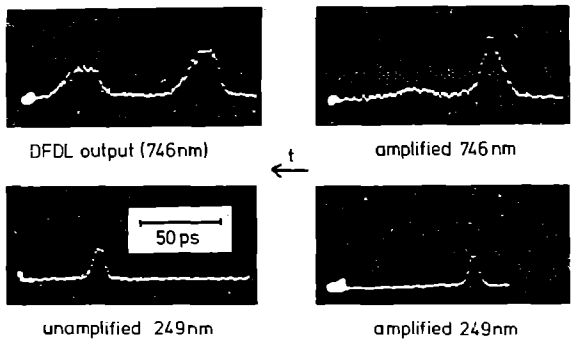


Figure 4: Streak records at various places in the Sprite oscillator for 2μJ pump energy.

The pump threshold for single pulse operation is ≈0.5μJ. At a pulse energy of ≈2μJ, a second pulse follows the first after typically 50ps with an occasional appearance at a later time of a third pulse. Streak traces at various points in the system are shown in figure 4 for a 2μJ pump energy. Second pulses are suppressed by the combined effect of saturation in the dye amplifiers and the frequency tripling process. Suppression in the amplifiers results from saturation which gives less gain for postpulses. Suppression in the frequency tripling process results from a change of wavelength from one pulse to the next probably due to heating effects in the DFDL (see Reference 2). The local heating due to the pump beam leads to a time varying refractive index and hence a time varying output wavelength (Equation 1). The pulse duration is reduced between DFDL output and amplified 249nm primarily due to the expected √3 reduction in the frequency tripling process.

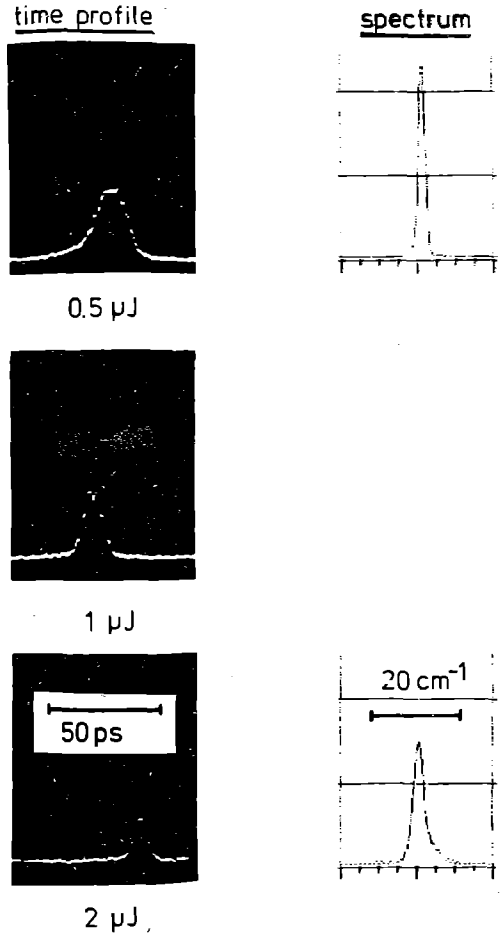


Figure 5: Time shape and spectrum of the amplified UV pulse for various DFDL pump levels

Figure 5 shows typical streak records which demonstrate that, by driving the DFDL with varying pump levels, the UV pulse duration (which remains unaltered in the EMG 103) can be varied from ≈7ps to ≈14ps. Shot-to-shot stability of all pulse parameters, as expected, is better at higher DFDL pump leves where pulses are generally shorter than 10ps.

The amplified UV pulses were observed simultaneously with a streak camera (Hadland Imacon 500) and with a spectrometer (EXITECH). With the existing pulse parameters both instruments work fairly close to their resolution limits (3ps and $1cm^{-1}$, respectively) and hence a correction procedure was required in the evaluation. Figure 5 shows a comparison of temporal and spectral pulse shape on the same pulse for different DFDL pump levels. Both temporal and spectral shape are typically smooth and symmetric. It is seen that a shorter pulse corresponds to a broader spectrum and vice versa as expected if the pulses are transform limited. For a more quantitative analysis of pulse quality, the raw data for pulse duration and spectral width were deconvolved with the instrument resolutions and the product $\Delta\nu\cdot\Delta t$ (FWHM) was plotted as a function of the pulse duration $\Delta t$ (figure 6). It can be seen that the pulses are reasonably close to being transform limited. The average value for $\Delta\nu\cdot\Delta t$ is 0.62 which is 1.35 times transform limit for Gaussian pulses, while the maximum value is 1.6 times transform limit. It is thought that with improved accuracy in alignment of the DFDL and more uniform pump distribution it will be possible to approach closer to the transform limit.

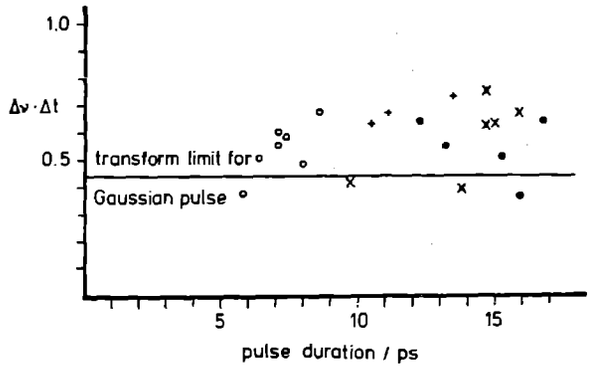


Figure 6: Time-bandwidth (FWHM) product as a function of pulse duration. The symbols correspond to different DFDL pump levels

In order to obtain data to cross check the spectral width measurements and to directly measure the tolerance to time slippage in the SPRITE Raman amplifiers, an arrangement was set up to measure the time coherence function of the output pulses. The beam was split into two partial beams which were allowed to interfere at a small angular separation on a glass plate. This plate acted as a fluorescence converter to allow the interference pattern to be observed in the visible at high magnification using a microscope objective and a CCD camera.

The partial beams could be delayed with respect to each other by introducing quartz plates of various thicknesses into either beam. The visibility of the fringe pattern $(I_{max}-I_{min})/(I_{max}+I_{min})$ is a measure of the coherence corresponding to the time difference due to the inserted plate. The coherence curve (assuming unity coherence with zero path difference) of visibility versus time difference gives a value for the coherence time $\Delta\tau_{coh}$ (FWHM).

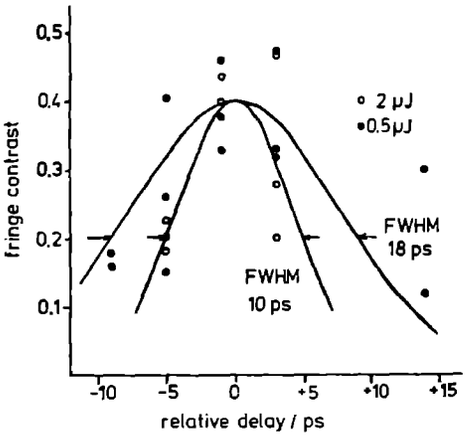


Figure 7: Result of the coherence time measurements

The spectral width is then given by $\Delta\nu\cdot\Delta\tau_{coh}=0.88$ for a Gaussian pulse. It is noted that for a transform limited Gaussian pulse, the coherence time is twice the pulse duration.

Figure 7 plots the coherence time measurements for two different DFDL pump levels (2μJ and 0.5μJ). Although there is a large scatter in the measured points, curves can be plotted giving a reasonable fit to the points and the coherence times given by these curves give spectral widths comparable with directly measured values.

## CONCLUSIONS

A DFDL has been designed, constructed and installed as part of the Sprite oscillator system.

Its operating parameters have been established and a number of measurements made to assess the performance of the Sprite oscillator containing the DFDL.

Although the pulse to pulse energy stability of the DFDL is poor (largely due to fluctuations in the pump energy), the energy is sufficiently high to strongly saturate the dye amplifiers and the output energy stability of the EMG103 has been satisfactory. Spectral and temporal stability is best at DFDL pump leves sufficient to give double pulses. The second pulse is strongly suppressed before injection into the multiplexer room, and under these conditions the output pulse duration is 8-9ps.

Simultaneous measurement of temporal and spectral profile suggest that the pulses are currently less than 1.6 times transform limit, with some prospect for making improvements to get reliably closer to transform limit.

## REFERENCES

1. Zs Bor and A Müller IEEE J. Quantum Electron. 22, 1524 (1986)

2. IN Ross and M Steyer This Report Sect C3

# MULTIPLEXING AND RAMAN SYSTEM MODIFICATIONS

C J Hooker, J M D Lister, E C Harvey and J E Andrew [1]

Rutherford Appleton Laboratory

[1]A W E, Aldermaston

## MODIFICATIONS TO THE KrF MULTIPLEXING

The previous arrangment of the Goblin multiplexer used four double-passed beams, each of which was split into two before entering Sprite. With this arrangement the output energy appeared to be clamped at a maximum of around 30 mJ per pulse. In order to increase the drive energy for Sprite, the optics of the multiplexer were changed to provide eight beams into and out of Goblin, which now propagate to Sprite without being split. The inter-pulse interval is unchanged at 5 ns, and four beam lines for the new beams were chosen to maximise the extraction of the rectangular pumped region in the Goblin cell.

The effects of this modification were evaluated in a series of tests, during which output energies of 30 mJ per pulse were measured routinely. The total energy available to drive Sprite has thus been doubled, and Goblin is now being used more efficiently.

## RESTAGING OF THE RAMAN AMPLIFIERS

The gain of a single Raman amplifier is limited by self generation of Stokes radiation in the pump beams and by two-photon absorption in the amplifier windows[1]. In order to achieve the required overall gain it has therefore been necessary to introduce a fourth stage in the Raman amplifier chain between the 0.5 cm aperture pre-amplifier (RAØ) and the 2.5 cm lightguide amplifier (RA2). Table 1 lists the parameters of the amplifiers in the reconfigured system.

RAØ and RA1 are pumped by single KrF beams. A small angle between the pump and Stokes beams provides some averaging of the pump beam intensity.

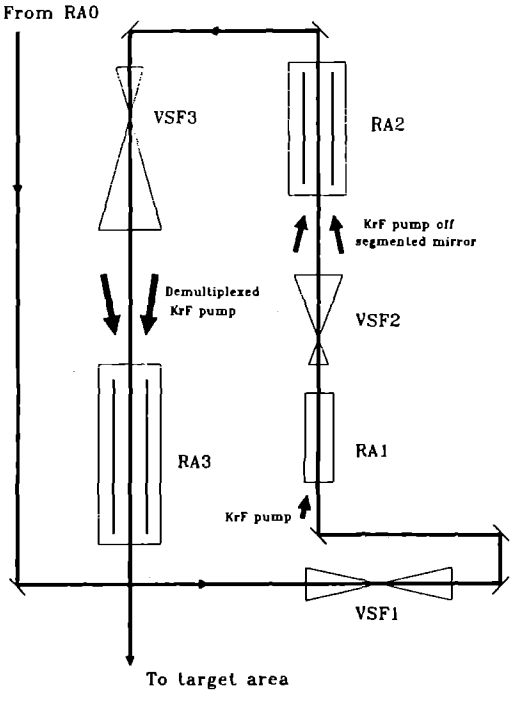


Figure 1: Raman amplifier chain

Table 1: Raman amplifier parameters

| Raman Amplifier | RA0 | RA1 | RA2 lightguide | RA3 lightguide |
|---|---|---|---|---|
| Raman beam diameter (cm) | 0.7 | 1.0 | 2.5 | 8.0 |
| Ampl. length (cm) | 300 | 150 | 100 | 100 |
| Pressure $CH_4$ (bar) | 4 | 1 | 1 | 1 |
| No. of pump beams | 1 | 1 | 8 | 7 |
| Pump angle | 0.5° | 0.9° | 1.1° | 5.0° |
| Operational gain | 200 | 200 | 70 | 15 |

RA1 and RA2 are pumped by one of the eight Sprite output beams. A 10% amplitude split provides about 25 mJ of pump energy to RA1. The remaining 90% is split into eight smaller beams by a segmented mirror to pump the first lightguide amplifier, RA2. The remaining seven output beams are de-multiplexed to pump the final amplifier, RA3.

## INSTALLATION OF VACUUM SPATIAL FILTERS

In order to preserve the high beam quality of the Stokes pulse through the amplifier chain to the target area, vacuum spatial filters have been introduced between the amplifiers. The spatial filters also expand the Stokes beam to fill the aperture of each successive amplifier. Figure 1 shows the layout of the VSF's and the three final amplifiers.

## NEW RAMAN AMPLIFIER LIGHTGUIDES

The final two amplifiers in the Raman chain use square section lightguides to contain the KrF pump beams. Previous guides were constructed from "Reflectafloat"[2] silicon-coated glass, and were found to have poor reflectivity and surface flatness[3]. The flatness of the guide walls has now been improved by careful selection of thicker (10 mm) float glass substrates.

A 150 nm thick aluminium film with a protective $MgF_2$ overcoat provides a hard coating of high reflectivity. To maximise the transmission of the vertically polarised pump beams along the lightguides, different thicknesses of $MgF_2$ were specified for the horizontal and vertical walls. Coating thicknesses of 150 nm and 75 nm gave the highest P reflectivity for the horizontal walls and S reflectivity for the vertical walls.

## REFERENCES

1. M H Key, M J Shaw *Analysis of High Power KrF Laser Systems*, Rutherford Appleton Lab Report RAL-89-133 Sec 3.4.1 (1989).

2. Trademark of Pilkington Glass Ltd, St Helens, Lancs, UK.

3. J E Andrew *Annual Report to the Laser Facility Committee*, Rutherford Appleton Lab Report RAL-89-045 Sec B1.6 (1989).

# DIAGNOSTICS DEVELOPMENT

E C Harvey, C J Reason, P Bowker and C Ansah

Rutherford Appleton Laboratory

Many new diagnostics have been introduced onto the Sprite Raman Laser in the last year, and several significant purchases have been made. Among these are a Hadland Photonics IMACON 500 Streak Camera with a 1-D reticon-based digital readout system, an Exitech Profile 256 spectrometer, also with a 1-D reticon readout system, three Hewlett-Packard digitizing oscilloscopes and a Tektronix 2467B 400 MHz analogue oscilloscope with integral microchannel plate intensifier.

The streak camera and spectrometer have been used during the development and installation of the DFDL oscillator, and are now used to provide single-shot measurements of the amplified KrF pulses. It is particularly important to know the spectral characteristics of the KrF pulses before and after amplification since broadened spectra are known to lead to poor Raman conversion efficiencies[1]. When combined with pulse length data from the streak camera, spectral information can be used to monitor the extent to which the nearly transform-limited pulses are degraded by amplification.

The near-and far-field distributions of the final amplified Raman pulses have been measured in the target area using the setup shown in figure 1. Light passing through the second partial reflector was directed onto a glass fluorescer, and a CCD camera and computer framestore system were used to capture the near-field pattern.

The light passing through the first partial reflector was attenuated using an $NO_2$ cell and focused onto a fluorescer using a telescope with an effective focal length of 17m. A CCD camera and computer framestore system were used to capture the far-field distribution of the laser pulse. An amplitude split from this beam path was directed into the streak camera to measure the pulse length of the final Raman output beam. We have also used a pinhole method to measure the beam divergence. In this case the beam was split as shown, and a pinhole placed at one of the foci. Cross-calibrated integrating photodiodes monitored the relative pulse energies in each of the beam paths and produced results that were in good agreement with the CCD camera measurements.

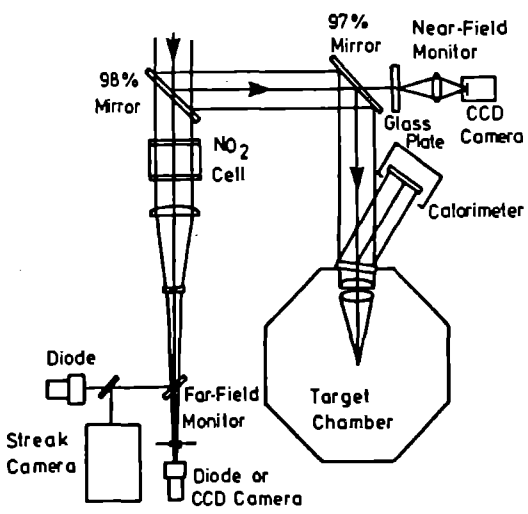


Figure 1. Schematic of the beam diagnostics showing the experimental target chamber

The prepulse was also measured on this beam path by attenuating the beam with the $NO_2$ cell and recording the photodiode signal on a Tektronix 7104 analogue scope using a fast voltage limiter placed between the photodiode and the oscilloscope, and using reduced scope bandwidth. The pulse rise time was limited by the photodiode to about 1 ns. The Stokes pulse was then delayed by 200 ps before the final Raman amplifier, thus only the prepulse (assumed to extend over 10 ns - the duration of the prepulse ASE in the KrF pump beams) was amplified in the last stage. The $NO_2$ was removed from the cell and the photodiode driven into saturation. The signal was recorded as before. The ratio of these two measurements gives the pulse to prepulse contrast ratio.

The performance of the Raman amplifier chain is now routinely monitored using a combination of calibrated photodiodes (RA1 and RA2 Stokes input), a Gentec calorimeter (RA1 and RA2 KrF pump), a Laser Instrumentation energy monitor (RA2 Stokes output) and 4-inch Scientech calorimeters (RA3 KrF pump and RA3 Stokes output). The specific electron beam pump energies to Goblin and Sprite are measured by recording the pressure jump in each amplifier, and the electrical pulsed power performance is monitored via the voltage traces in Sprite's water capacitor and Goblin's pulse forming line. The relative timing of Sprite and Goblin with respect to the oscillator is checked using photodiodes to detect the depletion in the axial ASE from each amplifier caused by the passage of the short pulses[2]. In the past most of these signals have been captured using chart recorders for the slow calorimeters, and on a variety of ageing analogue oscilloscopes using 612 Polaroid film. This cumbersome and often unreliable system is now being replaced by an integrated digital diagnostic system incorporating a 12 Channel A/D card in an Amstrad PC1512 PC clone for the calorimetry, and three digitizing oscilloscopes. Two 2-channel HP54502A scopes are used one for the pulse power and the other for the Stokes photodiode signals. An HP54111D scope is used to digitize the ASE signals. A Tandon 386/20 PC clone is used to drive the digitizing scopes on a GPIB interface, and is networked to the Amstrad computer so that calorimetry data may be transferred after each shot. A single page log report is then produced on a laser printer with a text and graphic shot summary. This system has been designed to allow for further expansion so that networking the framestores, streak camera and spectrometer readouts, and any other PC based controlling system will be possible in the future.

REFERENCES

1. C J Hooker et al *Annual Report to the Laser Facility Committee* Rutherford Appleton Laboratory Report RAL-89-045 Sect B1.4 (1989).

2. M J Shaw et al *Annual Report to the Laser Facility Committee* Rutherford Appleton Laboratory Report RAL-89-045 Sect B1.2 (1989).

# ANALYSIS OF THE PERFORMANCE CAPABILITIES OF THE SPRITE LASER SYSTEM AND OF OPTIONS FOR ITS OPTIMISATION

M H Key and A K Kidd

Rutherford Appleton Laboratory

## INTRODUCTION

The SPRITE system illustrated in Figure 1 comprises an optically multiplexed KrF laser amplifier chain and a parallel Raman amplifier chain. Pulse generators produce near transform-limited KrF and Raman shifted pulses of duration from 40 psec down to 10 psec, as discussed elsewhere.

The performance of the system has theoretical limits due to laser and nonlinear optics considerations which are assessed here for various modes of operation. The ultimate limits are assessed assuming that the KrF amplifier chain operates at output energy limits of about $3E_{sat}$ but in practice the level is about 3x below this and an assessment is made of the reasons for this relatively low output and the best way to achieve an output driven to $3E_{sat}$.

In the following sections we consider

- passive optical losses
- KrF amplifier small signal and saturated behaviour
- the effects of ASE
- options to optimise the KrF chain
- limiting nonlinear effects
- options to optimise the nonlinear limits

## PASSIVE OPTICAL LOSSES

The passive optical losses in the laser system were measured experimentally by propagating a signal at 8 Hz from the oscillator. Calculated values are based on Fresnel losses. The major discrepancy between the calculated and measured transmissions is due to the insertion of a pinhole in the vacuum spatial filter VSF (Figure 1 overleaf).

Table 1: Comparison of measured and calculated transmissions in the SPRITE laser system

| Path | Transmission (%) | | % Error |
|---|---|---|---|
| | Measured | Calculated | |
| Output of EMG103 to after spatial splitter | 50 | 48 | 4 |
| After spatial splitter to output of VSF (no pinhole) | 64 | 68 | 6 |
| To input to Goblin beampipe (incl.1:8 multiplex,pinhole) | 3.7 | 6.4 (a) | 42 |
| Goblin beam pipe transmission | 40 (b) (c), 31 | 40,31 | 0 |
| Output of Goblin beam pipe to input to RA3 | 33 (b) | 35 | 6 |
| Overall system transmission | 0.15 | 0.29 (a) | 48 |

Notes: (a) Calculated transmission does not take account of effect of pinhole in the VSF on beam energy transmitted.

(b) Goblin and Sprite fluorine fill evacuated to remove non-saturable absorption losses.

(c) Calculated transmission takes account of absorption due to fluorine in cell.

## KrF AMPLIFIER SMALL-SIGNAL GAINS

The ssg of the EMG103 is estimated from ASE measurements to be 2.3 x $10^8$ (double-pass). Experimental data on the input vs. output characteristics of Goblin is presented in Figure 2. A KrF amplifier simulation code[1] is used to estimate the ssg from the large signal behaviour. A small-signal gain of 4.4 x $10^3$ (double-pass) and a gain-to-loss ratio of 13.5 produced the curve-fit shown.

Cylindrical diode : voltage = 70 kV
Pulse length $t_p$ = 40 ps
Ar:Kr:F 800:100:90

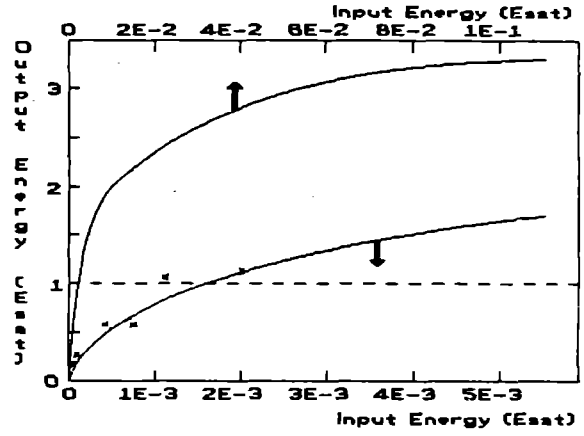


Figure 2: Comparison of experimental data with code predictions for Goblin gain

Experimental data concerning the saturated gain behaviour of Sprite is more limited. The data points that are available (input energy range 0 . 2 -0.3x$10^{-3}E_{sat}$) suggest a small-signal gain of 1.1x$10^3$ (double-pass). The curve-fit is shown in Figure 3, assuming a gain-to-loss ratio of 13.5.

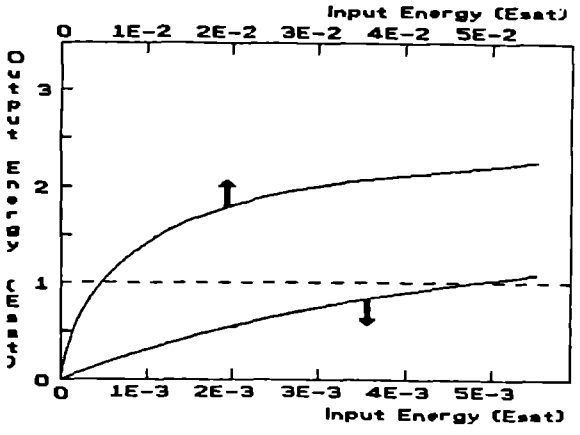


Figure 3 : Code predictions for Sprite gain
$E_{sat}$ = 735 mJ

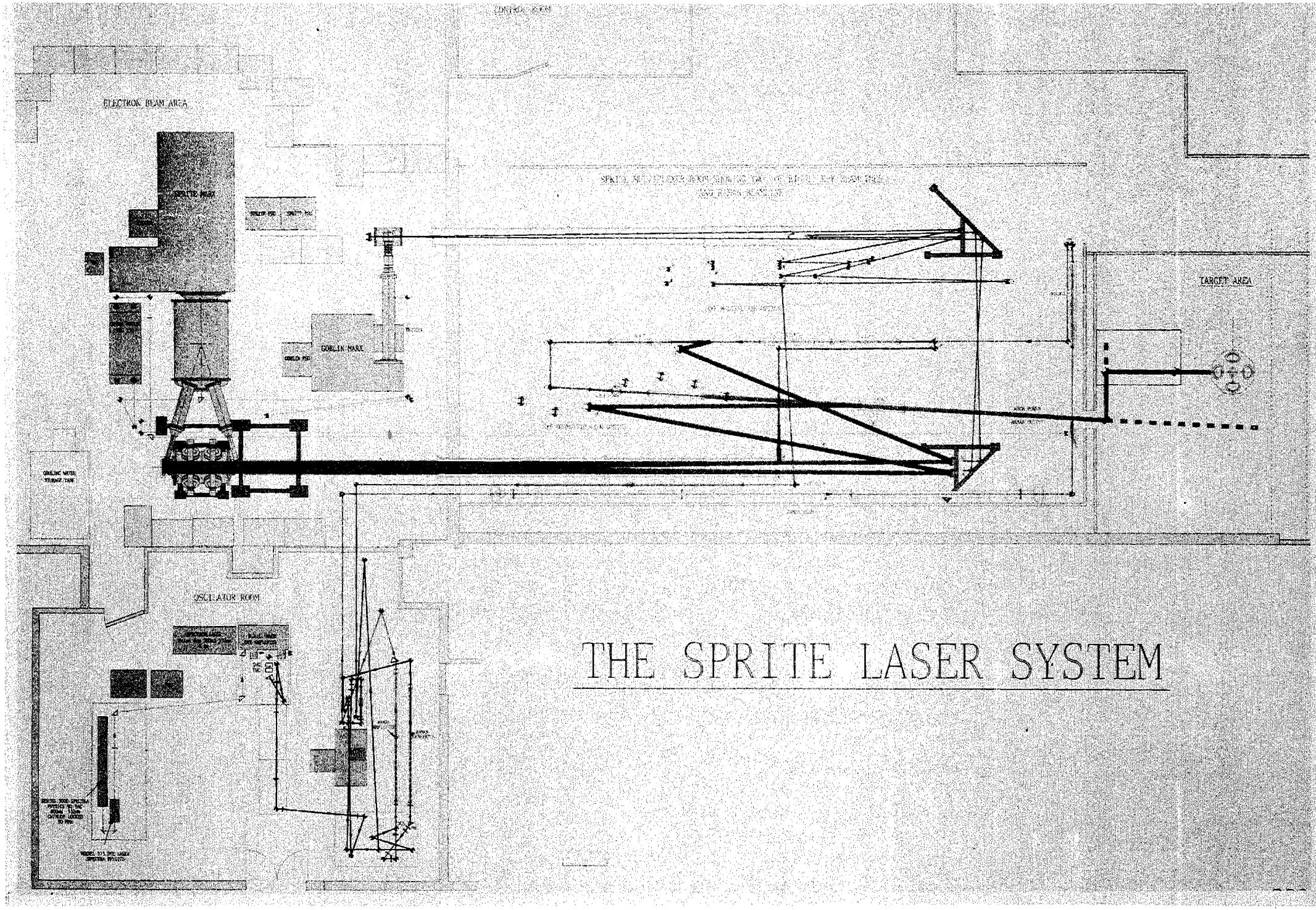


# THE SPRITE LASER SYSTEM

SATURATED PULSE AMPLIFICATION

Table 2 summarises the energies per pulse at various points around the SPRITE laser system for a typical shot (6 μJ per pulse into EMG103). Table 3 summarises the corresponding gain saturation factors of the three amplifiers, obtained by dividing the measured gain by the calculated ssg per pass.

Table 2: Comparison of measured and calculated pulse energies in the SPRITE laser system for a 6 μJ input pulse

| Position | Picosecond Pulse Energy | |
|---|---|---|
| | Measured | Calculated |
| Output of EMG103 (2nd pass) | 8 mJ | 7.0 mJ |
| Input to Goblin beam pipe | 64 μJ | 69 μJ |
| Output fom Goblin beam pipe | 31 mJ | 45 mJ |
| Output from Sprite beam pipe | 1.6 J | 1.5 J |

Table 3 : Gain saturation factors of the three KrF amplifiers for a 6 μJ input pulse

| Module | Pass | LSG/SSG |
|---|---|---|
| EMG103 | 1st | 4.0 |
| | 2nd | 8.7 |
| GOBLIN | 1st | 1.0 |
| | 2nd | 2.0 |
| SPRITE | 1st | 1.0 |
| | 2nd | 9.7 |

EFFECTS OF ASE

The predominant source of ASE from the EMG103 is double-passed within the amplifier. Table 4 presents a comparison of the calculated (based on the ssg estimates above) with measured (where available) ASE energies per pulse due to each of the three KrF amplifiers at points around the SPRITE laser system. The ASE pulse out of EMG103 sees a net system ssg of $4.9 \times 10^6$ (corresponding to a gain-length product of 15.4). The transmission of the ASE pulse originating in the EMG103 module to the input to RA3 is approximately $10^{-6}$. Hence, for 60 μJ of ASE out of the oscillator, the ASE pulse energy at the output of Sprite is calculated to be approximately 10 mJ ie the total ASE energy in the seven pump beams is less than 100mJ. This is confirmed by experiment (see Table 4). This is the predominant source of ASE on-target.

OPTIMISATION OF THE KrF AMPLIFIER CHAIN

Figure 4 illustrates the effect of increasing the gain of Sprite whilst simultaneously halving the retroflector losses (Curve (4)), increasing the gain of Sprite only (3), increasing the input energy to Goblin (2) and increasing the Goblin aperture (1), on the input energy to RA3. In each case, a multiplication factor is used to compare the effects of each modification. It can be seen that increasing the aperture of Goblin or the input energy has little effect on the output energy. However, if the small-signal gain of Sprite can be multiplied by a factor of four, and the losses within the laser halved, such that the performance of Sprite matches the present performance of Goblin, then an increase in output energy of 70% is possible.

Table 4: Comparison of measured and calculated ASE energies per pulse for the three KrF amplifiers

| | EMG103 | Goblin | Sprite | Total ASE energy | |
|---|---|---|---|---|---|
| | | | | Calc | Meas. |
| Input to Goblin beam pipe | 14 nJ | N/A | N/A | 14 nJ | - |
| Output of Goblin beam pipe | 25 μJ | 0(a) (4.7mJ) | N/A | 25 μJ | (b) 12.4 mJ |
| Input to Sprite beam pipe | 23 μJ | 0(a) | N/A | 23 μJ | - |
| Input to RA3 | 10 mJ | 0(a) (210mJ) | 0(a) (1.4J) | 10 mJ | <100 mJ |

Notes: (a) In presence of spatial filter, these calculated energies are negligible.
(b) In presence of spatial filter, measured ASE energy is <1 mJ.

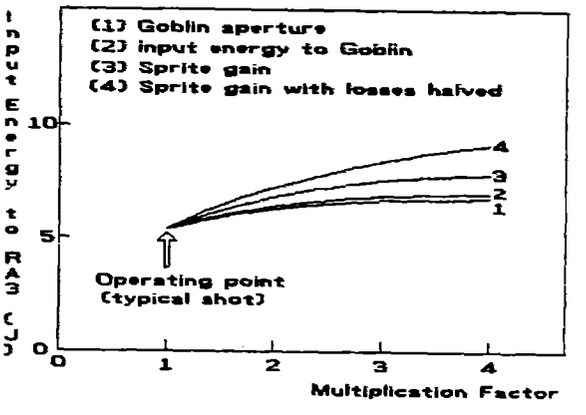


Figure 4 : Effect of increasing various parameters on input energy to RA3

The expenditure associated with each modification must be weighed against the benefits to be obtained. Fortunately, it appears that a relatively inexpensive modification - an increase in the gain of Sprite to its predicted level of performance - produces a greater increase in output energy than, say, a complete re-building of the Goblin amplifier.

LIMITING NONLINEAR EFFECTS IN HIGH POWER UV LASER BEAMS

At high beam intensities, several nonlinear optical effects become significant and may impose limitations on the final output power of a laser amplifier chain. These processes include:

(1) Two and three photon absorption,
(2) Self-focusing,
(3) Self-phase modulation
and (4) Stimulated Raman and Brillouin scattering.

These topics are discussed in reference 2. We provide here estimates of the threshold intensities relevant to each process in critical optical components and air paths at 248 nm and 268 nm in the output stages of the SPRITE laser system and indicate whether these thresholds are being exceeded. The results are discussed more fully in reference 3.

The intensity for a 15% two-photon absorption (TPA) loss is given by

$$I_T\ (TPA) = \frac{0.23}{\beta L} \qquad (1)$$

where L is the thickness of optical component (cm) and the parameter $\beta$ is the two-photon absorption coefficient ($cmGW^{-1}$). For the present laser configuration (fused silica optics in the output stages), two-photon absorption is greatest in the Sprite beam pipe output lens. This limits the intensity at that point to 2.2 $GWcm^{-2}$. For a $3xE_{sat}$ pulse out of Sprite, the minimum pulse length acceptable is 22 psec.

Self-focusing effects become significant for values of integrated laser intensity > $40GWcm^{-1}$. At this intensity, TPA losses dominate in fused silica. In air, the threshold value is 30 $TWcm^{-1}$. This implies that an air path length of 150 m following the Sprite beam pipe is acceptable. It is concluded that significant self- focusing does not occur in air.

The threshold intensity for self-phase modulation at 248 nm is

$$I_T(GWcm^{-2}) = 14/L. \qquad (2)$$

This value is not exceeded at any point in the present laser system.

Finally, the threshold for stimulated Raman scattering in fused silica lies above the point at which the beam breaks up due to self-focusing, and hence does not require consideration. The maximum value of intensity-length product encountered in air in the laser system is after the Sprite beam pipe, which, for a path length of 15 m, has a value of $3TWcm^{-1}$. At this level, the pump depletion caused by steady-state stimulated rotational Raman scattering is negligible.

## OPTIONS TO OPTIMISE THE NONLINEAR LIMITS

A comparison is made between the maximum focused intensity on-target possible with a Raman beam-combined laser output at 268 nm and direct target irradiation at 248 nm. The replacement of the fused silica optics in the output stages of the present laser system with calcium fluoride is considered.

Table 5 summarises the results of calculations performed for various configurations of the laser system. Included in this table are the power and focused intensity available on-target, maximum energy and duration per pulse and total transmission (including Fresnel and TPA losses) and integrated laser intensity through the optics stages. In each case, spatial and temporal fill-factors of 0.8 are assumed in the calculation of beam intensities. Integrated laser intensities greater than 40 $GWcm^{-1}$ correspond to the onset of significant self-focusing of the beam. Cases (1)-(4) show the effect of calcium fluoride components on a pulse propagated through the system Case (1) is for a 15% TPA loss in the Sprite output lens. Cases 1 and 2 demonstrate that a factor of two increase in power, focused intensity and energy on-target is possible with a 30 psec pulse ($E_{max}$ is then 1.68 J in Sprite) if the fused silica optics are replaced by calcium fluoride. If the energy in Sprite is $E_{sat}$-limited ($3xE_{sat}$, 2.75J) and the pulse length is 10 psec, as in cases (3) and (4), then the improvement in these parameters is by a factor of three. The power has doubled with respect to cases (1) and (2), but the energy has halved.

Cases (5) to (7) refer to a system in which the target is directly irradiated with a single pulse at 248 nm. The pulse length in each case is determined by the specified intensity and energy within Sprite.

Table 5: Summary of parameters for pulse propagated through the SPRITE laser system.

| System | λ (nm) | P (TW) | I ($x10^{-11}$ W $cm^{-2}$) | E max (J) | t max (ps) | T total | Total $\int I.dl$ ($GWcm^{-1}$) |
|---|---|---|---|---|---|---|---|
| 1. Raman $SiO_2$ optics. 15% TPA in beam pipe o/p lens (1.68J per beam in Sprite). Lens focused. | 268 | 0.10 | 6.1 | 3 | 30 | 0.26 | 12.1 |
| 2. Raman $CaF_2$ optics. 2% TPA in beam pipe o/p lens (1.68J per beam in Sprite). Mirror focused. | " | 0.20 | 13 | 6.5 | 30 | 0.55 | 8.8 |
| 3. Raman $SiO_2$ optics. $3xE_{sat}$ limited in Sprite (2.75J per beam in Sprite). Lens focused. | " | 0.17 | 11 | 1.7 | 10 | 0.17 | 19.1 |
| 4. Raman $CaF_2$ optics. $3xE_{sat}$ limited in Sprite (2.75J per beam in Sprite). Mirror focused. | " | 0.47 | 29 | 4.7 | 10 | 0.51 | 20.4 |
| 5. Full aperture to target. $SiO_2$ optics. B-integral limited (2.75J per beam in Sprite). Mirror focused. | 248 | 1.46 | 1.6 | 0.44 | 0.3 | 0.17 | 21.2 |
| 6. Present aperture to target. $SiO_2$ optics. B-integral limited (2.75J per beam in Sprite). Lens focused. | " | 0.10 | 1.2 | 0.18 | 1.8 | 0.065 | 28.9 |
| 7. Present aperture to target. $CaF_2$ optics. B-integral limited (2.75J per beam in Sprite). Mirror focused. | " | 0.57 | 7.1 | 1.32 | 2.3 | 0.48 | 49.5 (B>3) |

*Note: B-limited pulse @ 40 $GWcm^{-1}$ in Sprite window (2.75J inside Sprite cell).

Case (5) is a 27cm diameter beam 248 nm pulse, at the $E_{sat}$ limit and the B integral limit.

Case (6) is with the present aperture (B-limited to 40 $GWcm^{-1}$) with fused silica optics. Case (7) is identical, but with calcium fluoride optics. The power in the latter case is high (0.57TW), but the pulse length is limited to 2.3 psec at this power.

It is concluded that in a Raman system a factor of three increase in maximum power and intensity on-target is possible if the fused silica Sprite beam pipe output lens and RA3 input window are replaced by calcium fluoride. If all output stage optics are changed to calcium fluoride, then the maximum focused intensity on-target may reach $2.9x10^{18}$ $Wcm^{-2}$ in a 4 micron diameter spot.

Raman beam-combining represents a more favourable approach than direct irradiation at 248 nm. Focused intensities on-target are an order of magnitude greater, and the effects of self-focusing and self-phase modulation are negligible. This is not the case with direct target irradiation (Table 4).

## CONCLUSIONS AND FURTHER WORK

The higher power and focused intensity available on-target in Raman beam-combined operation of Sprite compared with simple KrF operation at 248 nm

have been demonstrated. The replacement of fused silica optical components in the output stages by calcium fluoride would increase by a factor of three these parameters.

Measurements are under way to measure more accurately the ssg of Sprite and the energy per pulse will be increased by increasing the gain of Sprite. Extension of an existing computer model[1] will be carried out to stimulate the system of KrF amplifiers. This includes the option of modelling either single- or multiple-pass amplification (for the possible re-staging of the system), system transmission optics and the retention of an output pulse train for amplification in subsequent modules. Bi-directional ASE generated in the later, larger-aperture amplifiers is added to that amplified from previous stages.

ACKNOWLEDGEMENTS

The assistance of Dr B A Shiwai in obtaining data from initial runs of the KrF amplifier code is gratefully acknowledged.

REFERENCES

1. C J Hooker, I N Ross and M J Shaw, *"Modelling multiple pulse amplification in KrF lasers"*, RAL Annual Report RAL-87-041, C2.2 (1987).
2. M H Key, M J Shaw, I N Ross, P A Rodgers and M C Gower, *"Analysis of high power KrF laser systems"*, Rutherford Appleton Laboratory Report No RAL-89-133 (December,1989)
3. M H Key and A K Kidd, *"Limiting nonlinear effects in high power uv laser beams"*, Rutherford Appleton Laboratory internal report (1990).

# X-RAY MEASUREMENTS ON THE SPRITE ELECTRON-BEAM MACHINE

G.J.Hirst

Rutherford Appleton Laboratory

## INTRODUCTION

The Sprite electron-beam machine produces pulses of nominal 500 kV electrons which are used to pump a KrF laser amplifier. In this process a small fraction of the electron-beam energy is converted into bremsstrahlung x-rays which then escape into the laboratory. Shielding is therefore necessary to protect the machine operators and a 0.6 m concrete shield wall presently serves this purpose.

The experimental electron-beam generator being developed in building R7 is both a higher voltage and a higher charge-transfer machine and is therefore expected to be a more significant x-ray hazard. As part of an effort to predict its x-ray yield some experiments have been carried out on Sprite to study the dose scaling behaviour.

## EXPERIMENTAL DETAILS

The source of the x-rays is the Sprite laser cell which is a tube of thin titanium foil containing a mixture of rare gases and a little fluorine. The cell is cylindrical, approximately 30 cm in diameter and 1 m long. It is surrounded by a coaxial aluminium vacuum chamber, 70 cm in diameter and with a 1 cm wall thickness. This chamber contains the four radial electron-beam diodes[1].

The detectors used to monitor the x-ray dose are quartz-fibre electroscopes[2] which are sensitive to radiation above 30 keV. They measure the time-integrated dose for each machine shot. All of the results discussed here were taken with detectors placed in the radial plane containing the centre of the laser cell. (Other experiments had suggested little dependence of the dose on angular position in this plane. In fact the detectors were all located along a line vertically above the centre of the diode vessel.)

The Sprite machine parameters are given in table 1 below. A slight timing fault led to a diode voltage droop of 10-20% during the pulse. The diode voltages used here are average values during the flat-topped part of the pulse.

Table 1: Sprite machine parameters.

| | |
|---|---|
| Number of diodes | 4 |
| Diode voltage | 330 - 560 kV |
| Diode impedance | 5 Ω at 500 kV |
| Pulse duration | 60 ns |

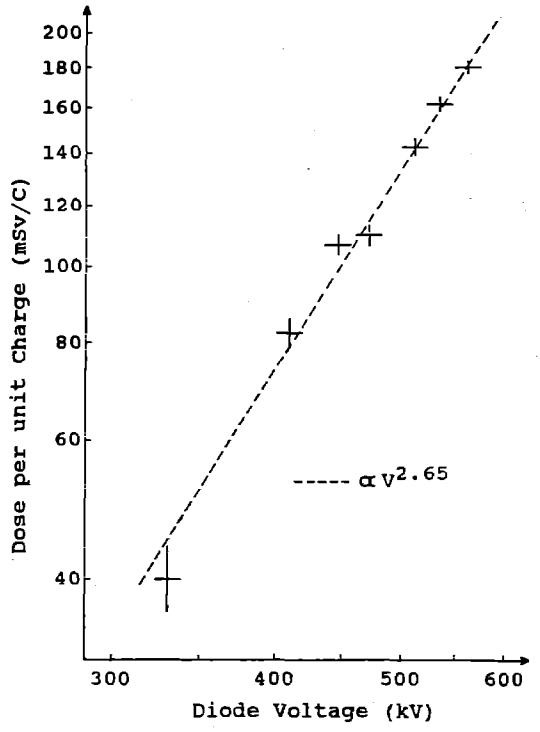


Figure 1: Radiation dose per unit charge as a function of diode voltage.

## RESULTS

The first set of experiments examined the effects of laser gas pressure on the x-ray dose, which was measured 85 cm from the axis and with a diode voltage of 510 kV. There was no systematic variation of the dose with argon gas-fill pressures between 50 torr and 900 torr. The random variation was less then ± 5%. This result is expected since the atomic numbers of argon and titanium are very similar and the only effect of changing the cell pressure is to alter the fractions of the beam stopped by the gas and by the cell walls. The total radiation yield will therefore be unaltered and the dose will only be changed by small differences in the positions at which electrons are stopped. All further experiments were carried out at cell pressures of 800 torr.

Figure 1 shows the results for different diode voltages. The dose per unit charge, again measured 85 cm from the axis, scales in good agreement with the $V^{2.65}$ law[3] for linear accelerators above 1 MV and with the $V^{2.8}$ law[4] for low-Z targets above 0.2 MV. These two references also agree closely on the absolute value for the dose per unit

charge, once corrections have been made for their different target materials. However their mutually agreed value is some 7 times higher than that measured in figure 1, probably because of the very different source geometries and shieldings.

The fall-off of dose with distance from the machine is shown in figure 2. It is initially slow, since the source is large, but it approaches the inverse square law as the radial distance increases. In fact the curve seems slightly faster than $r^{-2}$ at large distances although reading errors on the electroscopes are then also large. (Air is not a strong enough absorber[5] to account for any observed attenuation if the x-ray energy is above 100 keV.)

The spectrum of the x-rays outside the vacuum vessel is limited at high energies by the diode voltage and at low energies by detector response and by vessel shielding. The distribution within this range decides the extra thickness of shielding needed to protect personnel. One way to study the spectrum is through the effect of shielding thickness on the x-ray dose. The results of such an experiment are shown in figure 3. The diode voltage was 510 kV and the detector was 85 cm from the machine axis, surrounded by copper tubes of different thicknesses. The results are rather noisy, due to Sprite triggering fluctuations, but the general trend is readily apparent. The dose initially falls rapidly as low energy x-rays are filtered out of the spectrum. The slope then settles to a more constant value, corresponding to a mass attenuation coefficient of 0.15 - 0.16 $cm^2/g$. There

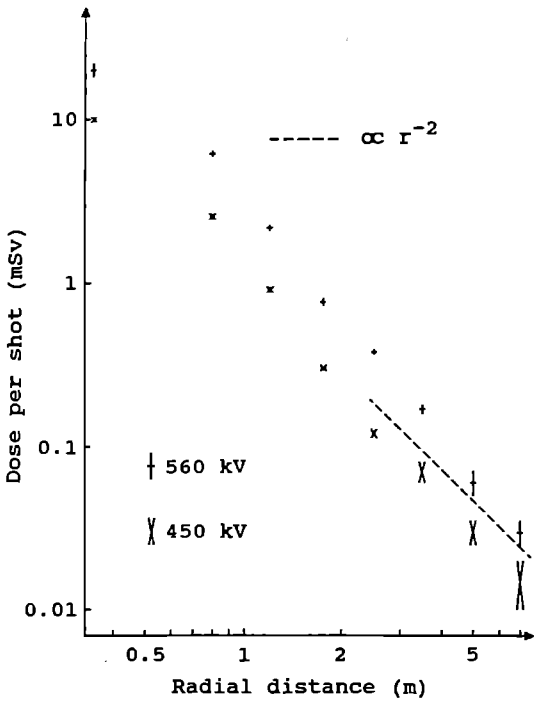


Figure 2: Variation of x-ray dose with radial distance from the machine axis.

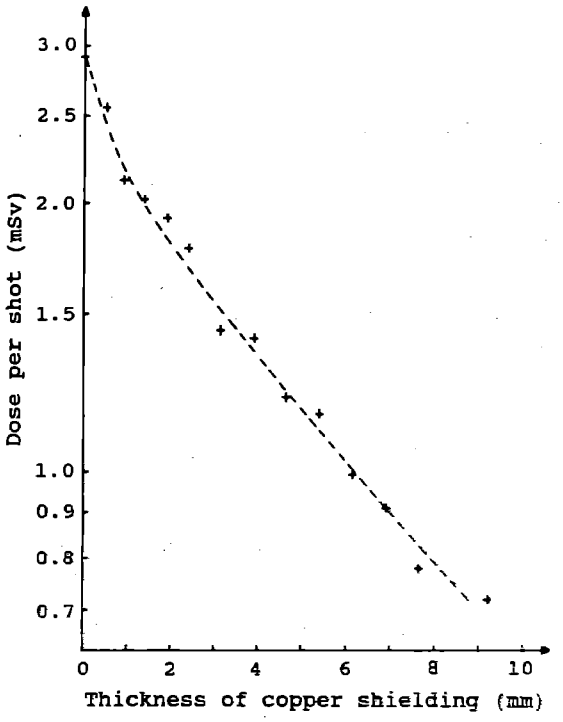


Figure 3: Variation of x-ray dose with thickness of shielding around the detector.

is some evidence that this coefficient falls further at higher shield thicknesses.

The measured value yields an effective x-ray energy of 180 - 200 keV (35% - 40% of the electron energy) which will rise with the shield thickness for two reasons. Firstly the low energy x-rays are more strongly attenuated than the high energy ones. Secondly the published data are for geometries where single scatterings remove photons completely. In real cases some scattered photons do reach the detector, causing the measured dose to increase and leading to a higher deduced energy[6]. This effect becomes greater for thicker shields. Although these processes are difficult to treat quantitatively they both have important consequences for shield design.

REFERENCES

1. Annual Report to the Laser Facility Committee, Rutherford Appleton Laboratory Report RL-82-039 (1982), pp.2.12 - 2.14.
2. R.A.Stephen & Company Ltd., Mitcham, CR4 3YP, England.
3. International Commission on Radiological Protection, Publication 21, p.78.
4. D.W.Forster et al, "Electron Beam Diagnostics Using X Rays", SSWA/JCM/714/162 AWRE Aldermaston.
5. "Reactor Physics Constants", ANL 5800, U.S. Atomic Energy Commission, Argonne National Laboratory (1963).
6. e.g. J.Wood, "Computational Methods in Reactor Shielding", Pergamon Press, Oxford, (1982), Chapter 4.

# SPRITE SHOT STATISTICS

M J Shaw

Rutherford Appleton Laboratory

During the period 5/6/89 to 4/5/90 there were 28 laser shooting weeks including two weeks of target shooting. A total of 1260 shots were fired and 42 were useful target shots. During this time Sprite was configured as a multiplexed amplifier of short duration pulses followed by a Raman beam combining stage. The pulse duration prior to Jan 1 1990 was 40 ps and thereafter 10 ps. Figure 1 shows the distribution of shots per week for the laser shooting weeks.

Over this period the Goblin e-beam foil windows have been changed three times whereas the Sprite foil has remained unchanged.

For the target shooting period between 31/10/89 and 24/11/89 the performance of the final Raman amplifier, RA3 was as follows:

| | |
|---|---|
| Pump duration | 40 ps |
| Average output energy | 2.5 J |
| Average conversion efficiency | 35% |
| Average gain | 9.9 |

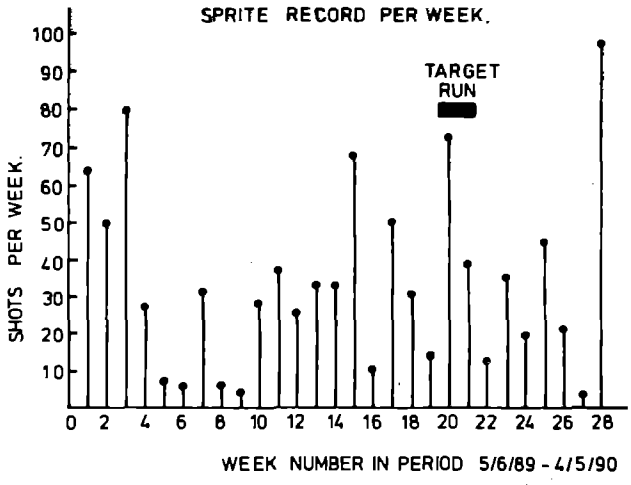


Fig 1 Number of laser shots per week for the 28 Sprite operational weeks between 5/6/89 to 4/5/90.

# DEVELOPMENT OF HIGH ENERGY KrF LASER AMPLIFIERS

G.J.Hirst, M.J.Shaw, E.M.Madraszek and J.E.Boon

Rutherford Appleton Laboratory

## INTRODUCTION

A research and development programme is currently under way to optimise the design of the pulsed power hardware needed for larger KrF lasers. This programme involves the assembly and testing of an experimental electron-beam machine which, like Sprite[1], will use "quasi-radial" pumping.

The design parameters for the machine are shown in table 1. The primary energy store is based on the Sandia Hermes III Marx generator which, in a final system, would be used to pulse-charge three water-filled pulse-forming lines (PFLs) via an intermediate oil-filled "transfer tank". Each PFL would then be connected, by its own laser-triggered output switch, to one of the electron-beam diodes. The number of diodes is dictated by the laser size and the required pump power. Six would be used to pump the table 1 gas volume fully.

The pulsed power R & D facility moved into a new site, in building R7, during 1989-90. Figure 1 shows the layout of the experimental area which, as well as the machine components, contains a number of support systems. These include a 0.6 m thick concrete shield wall, which will absorb the x-rays produced by the electron-beams. There is an oil-handling system, backed up by sealing of the area's floor and walls to contain any spillage from the 16 tons of transformer oil in the tanks.

Table 1: Experimental electron-beam machine parameters.

| | |
|---|---|
| Pumped gas volume | 0.6 m dia. x 1.8 m |
| Static gas pressure | 1.6 bar |
| Diode voltage | 830 kV |
| Diode current | 150 kA |
| Pulse duration | 250 ns |

The PFLs will have a water treatment plant to maintain the water's low electrical conductivity, and a screened room has been set up to provide a noise-free environment for diagnostic equipment.

At present (April 1990) the trigger system and the Marx generator are in place and operational. They are undergoing tests which will be described in more detail below. The transfer tank and one PFL are also on site and will be installed for the next phase of the programme. This will also be detailed below.

## MARX GENERATOR INSTALLATION

The Marx generator has been assembled and tested at low voltage (15 V per capacitor) and the results have been reported previously[2]. It has since been reassembled in its oil tank and the 60 liquid resistors have been attached. The completed generator is shown in figure 2, prior to construction

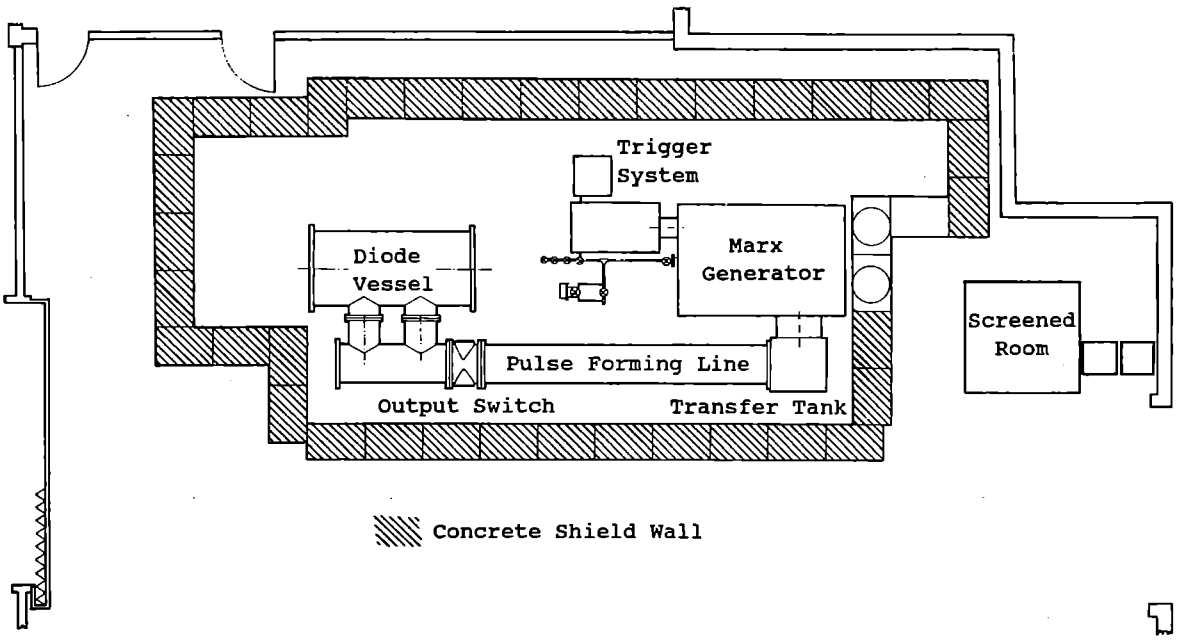


Figure 1: Floorplan of building R7 showing proposed experimental layout.

of the shield wall and sealing of the oil containment area. The output terminal, visible on the bottom right capacitor, now has a nominal 50 Ω copper sulphate dummy load attached.

The trigger system for the main Marx generator consists of a smaller "trigger" Marx which is fired using a thyratron-driven pulse transformer. The resulting output from the main Marx is shown in figure 3 for a d.c. charging voltage of 60 kV per capacitor. The most naive circuit model is a simple series LCR circuit which, when applied to the data of figure 3 with the known Marx capacitance of 56.3 nF, yields an inductance of 6.0 ± 0.1 μH and a resistance of 45 ∓ 1 Ω. The inductance is in good agreement with the low-voltage value of 5.0 μH, given the addition of the spark-channel inductances and the current return path through the load resistor and the tank walls. The resistance corresponds to the load in parallel with the Marx resistors. The measured output voltage was 1.325 MV which was some 4% higher than the model predicted. This agreement seems good, considering that there were no adjustable parameters in the fit. The discrepancy is probably due to calibration uncertainties for the output monitor and charging meters and to simplifications introduced by the model. A more advanced model, based on the BERTHA[3] code, is currently being developed to simulate the whole machine.

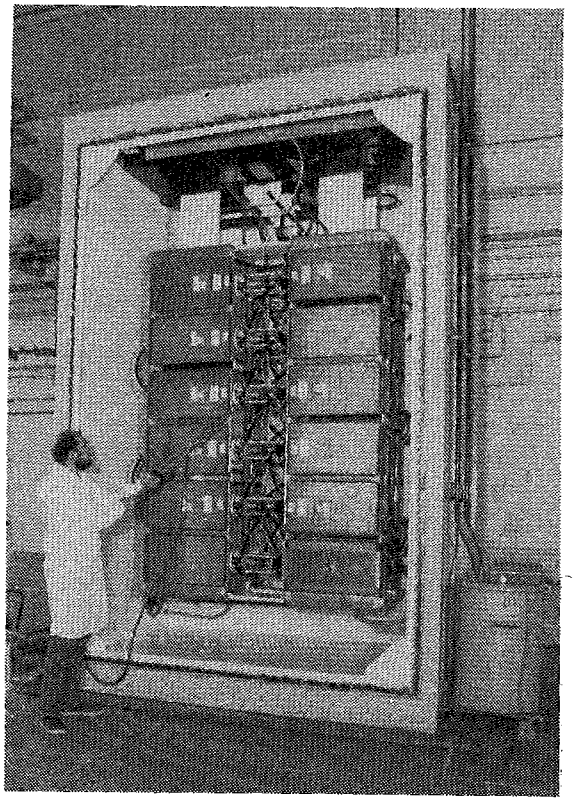

Figure 2: The Marx generator.

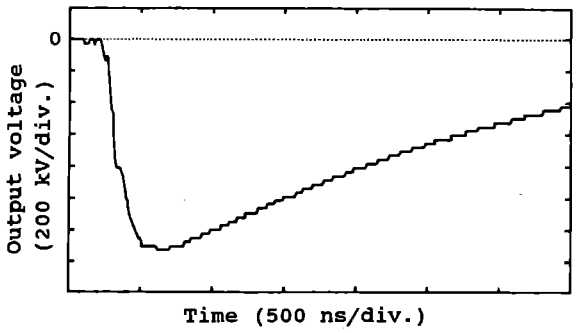


Figure 3: Marx generator output voltage into a 50 Ω load.

## DESIGN OF PULSE-CHARGED COMPONENTS

The transfer tank and PFLs were designed in 1989 and the tank and one PFL have now been manufactured. The laser-triggered output switches, which have also now been designed, are discussed elsewhere in this report.

The transfer tank contains a high-voltage conductor which divides the Marx output between the three parallel PFLs. The shaping of this conductor and of the polythene diaphragms through which its connections pass was carried out using MagNet[4], a commercial electrostatic modelling package, to compute the electric field distribution. The tank is filled with transformer oil and also houses a self-closing oil diverter switch. This will dump the energy from the capacitor bank into a copper sulphate resistor in the event of the output switches failing to close. The diverter switch spacing is remotely controllable, allowing different Marx charging voltages to be accommodated. It is planned eventually to computerise all of the machine controls so that the firing voltage can be set from the keyboard.

The PFLs are 4.2 m long coaxial lines with inner and outer radii of 130 mm and 300 mm respectively. When filled with water their transit time is 125 ns and their characteristic impedance is 5.6 Ω. They are made from aluminium alloy treated with Alochrom 1200 (ICI) to prevent corrosion and are tilted at 1° to the horizontal to allow air bubbles to clear during filling and operation.

## EXPERIMENTAL SCHEDULE

The schedule for the experimental trials is presently divided into three phases which will complete the testing of each of the individual pulsed power components. Table 2 shows the component requirements for each phase, resulting in a single-diode machine at phase 3.

The phase 1 tests are now under way and preliminary results have been given above. The Marx generator will be tested up to its

Table 2: Pulsed power requirements for phases 1 to 3 of the R & D programme.

| Required Components | Phase 1 | Phase 2 | Phase 3 |
|---|---|---|---|
| Oil control system | 1 | 1 | 1 |
| High voltage supply | 1 | 1 | 1 |
| Trigger generator | 1 | 1 | 1 |
| Marx generator | 1 | 1 | 1 |
| Marx dummy load | 1 | | |
| Transfer tank | | 1 | 1 |
| Pulse forming line | | 1 | 2 |
| Output switch & optics | | 1 | 2 |
| PFL dummy load | | 1 | 1 |
| Trigger laser | | 1 | 1 |
| Water treatment plant | | 1 | 1 |
| Switch-to-diode feed | | | 1 |
| Diode vacuum chamber | | | 1 |
| Diode internal assembly | | | 1 |
| Vacuum system | | | 1 |

full rated voltage (± 100 kV per stage) into a dummy load and the spark gap operating pressures will be established. The Marx timing jitter will be studied as a function of gap pressure and trigger voltage and a final trigger generator will be produced from the present prototype. Between phases 1 and 2 the transfer tank and one PFL will be installed, together with a single output switch and a resistive dummy load. The new trigger generator will also be constructed and fitted.

Phase 2 will concentrate on testing the switches. The diverter switch will need to be characterised and the output switch will be tested both under self-break and laser-triggered conditions. It is also proposed to calibrate the diode voltage and current probes using the phase 2 dummy load assembly.

The components needed for phase 3 are presently being designed. The switch-to-diode feed will be a short oil-filled section coupled to the diode via two high-voltage feedthroughs in the vacuum tank wall. It may also house "pulse-sharpening" switches if these are needed to improve the voltage risetime on the cathode. The vacuum tank itself is expected to be approximately 1.2 m in diameter and 2.5 m long. An electron optics and gun design programme EGN2[5] is being used to investigate different designs for the diode internal assembly, which may involve subdivision of the cathode area into smaller sections to control "pinching" of the high current beam.

A second PFL and switch, connected to the phase 2 dummy load, will be needed for the phase 3 tests to ensure adequate matching between the Marx generator and the PFLs. Without this the diode waveform would ring on after the main pulse, making the diode performance difficult to interpret and possibly leading to post-pulse arcing with consequent foil failure. The addition of the second line will also allow testing of gap synchronisation and the study of any faults arising from either gap not closing.

Once phase 3 testing begins it will be necessary to make detailed measurements of the machine's x-ray yield. The results of experiments discussed elsewhere in this report suggest that the dose near to just one diode might approach 20 mSv per shot. This will need to be attenuated by a factor of $10^4$ - $10^5$, depending on the shot rate, to reduce the dose to the operators to an acceptable level.

ACKNOWLEDGEMENTS

It is a pleasure to acknowledge the work of Dave Baker, Harry Medhurst, Dave Wood and the rest of the CLF Engineering Support Group, without whom the project would not have progressed this far.

REFERENCES

1. Annual Report to the Laser Facility Committee, Rutherford Appleton Laboratory Report RL-82-039 (1982), pp. 2.12 - 2.14.
2. Annual Report to the Laser Facility Committee, Rutherford Appleton Laboratory Report RAL-89-045 (1989) pp. 227 - 229.
3. D.D.Hinshelwood, "BERTHA - A Versatile Transmission Line and Circuit Code", NRL Memorandum Report 5185, Naval Research Laboratory, Washington D.C. (1983).
4. Infolytica Corp., 1140 de Maisonneuve, Suite 1160, Montreal, Canada H3A 1M8.
5. G.A. and W.B.Herrmannsfeldt, 451 Patrick Way, Los Altos, CA 94022 U.S.A.

# DESIGN OF A 2400kV, 200kA PULSE FORMING LINE SWITCH

E M MADRASZEK (RAL)
R BAILLY-SALINS (CEA)

UV laser triggered sparkgap insulated by $SF_6$ gas under pressure have been chosen to switch a 5.5ohms pulse forming line with good synchronization. The design maximum applied voltage is 2400kV which could occur under fault conditions. The charging time $T_C$ is 1.0µs and the energy to transfer is 35kJ. The switch has to be simple, reliable, safe as far as the pressure is concerned and accessible for maintenance.

Previous experiences have shown that for continuous effective use, periodic maintenance of the optical componants and electrodes is necessary. The design shown in Fig1, with two removable ports, opposite each other, allows sufficient hand access into the switch housing to remove and replace these elements.

The stainless steel inner parts of the electrodes are easily assembled by means of a bayonet type arrangement and are spring loaded in the brass outer. On breakdown, the inner parts of electrodes are subjected to a shock, causing them to move back. The use of dissimilar metals aids sliding and some of shock energy is absorbed by the springs.

The 2 diaphragms, made of epoxide resin, form the closure plate of the cylindrical switch housing. They have to withstand the $SF_6$ static pressure and the pressure jump following breakdown. The radial stress is the most important one and is expressed by /1/

$$S_R(R,Z) = P\left[\frac{2+\nu}{8}\frac{Z^3}{c^3} - \frac{3(3+\nu)}{32}\frac{R^2 Z}{c^3} - \frac{3}{8}\frac{Z}{c}\right],$$

where $0 < R < b$ = radial coordinate,
$-c < Z < c$ = axial coordinate,
$P$ = total pressure,
$\nu$ = Poisson's coefficient,

when we deal with a simple circular plate of thickness 2c and radius b. As long as the wedge-shaped diaphragm of Fig.1 is concerned, we consider that $|S_R(R,Z)|$ is between the couple of curves $S_R(R,Z=-25mm)$ and $S_R(R,Z=-50mm)$ plotted in Fig2 for P=5bars. $|S_R(R,Z)|$ remains well below the compressive or tensile strength of resin (700bars) leading to a good safety factor.

Previous experiments on SPRITE sparkgap /2/ show that partial traking occurs at 170kV/cm along the inner surface of the resin vessel. The value of 100kV/cm is then chosen as a design criterion for this new sparkgap. A smaller value is even desirable as far as the critical triple points in the sparkgap are concerned. The static field values, shown in Fig1, are satisfactory. They are obtained with the help of a microcomputer code /3/ assuming a 2400kV potential on the cathode. Equipotential lines are also plotted in Fig1.

At time $T_C$, the triggering laser beam (248nm) passes through a sapphire window to a special sapphire prism located in the anode. Sapphire ($Al_2O_3$) is chosen for its transmittance at 248nm and its chemical resistance to hydrofluoric acid which is presumably formed by reaction of $SF_6$ and $H_2$, as impurity, during the breakdowns. The design of the prism is shown in Fig3. The initial laser beam is split by refraction and reflection, into 3 secondary focussed beams to give 3 equispaced plasma channels located at a radius of 4cm from the axis of symmetry. The electrical field is excluded from the ionized channels, while it increases between the channels and the electrodes. The electron avalanche process can then occur and the subsequent streamers can switch the gap in a time T[s] given by the empirical relation /4/

$$T = 97800\ (E/M)^{-3.44}\ M^{-1},$$

where E[kV/cm] = mean value of the electric field in the gap,
M[g/cm$^3$] = specific mass of any used gas.

For instance, with $SF_6$ at pressure p=4bars (M=0.026g/cm$^3$) in a field E=400kV/cm, we get T=15ns and an expected jitter in the region of a few ns.

On the other hand, the self breakdown depends on the sparkgap design and cannot accurately be predicted by any model. But, according to SPRITE data /2/, the probability of this phenomenum seems to be low if

$$E_C = E_A < 380\ \text{kV/cm and } p(SF_6) = 4\text{bars}.$$

Eventually, the inductance of this 3 streamer gap is equal to 40nH instead of 110nH with a single axial streamer and the rise time of the corresponding electrical pulse should be shorter but the efficiency of switches remains to be proved.

ACKNOWLEDGMENTS

We wish to thank Mick Shaw and Graeme Hirst for their helpful suggestions.

REFERENCES

/1/ S P TIMOSHENKO, J N GOODIER. Theory of Elasticity. Mc Graw Hill Ed, 1970.
/2/ Annual Report 1982. Laser Div, RAL.
/3/ MAGNET. Infolytica Corporation, 1988.
/4/ T H MARTIN. An empirical formula for gas switch breakdown delay. 7th IEEE Pulsed Power Conference, Monterey, California 1989.

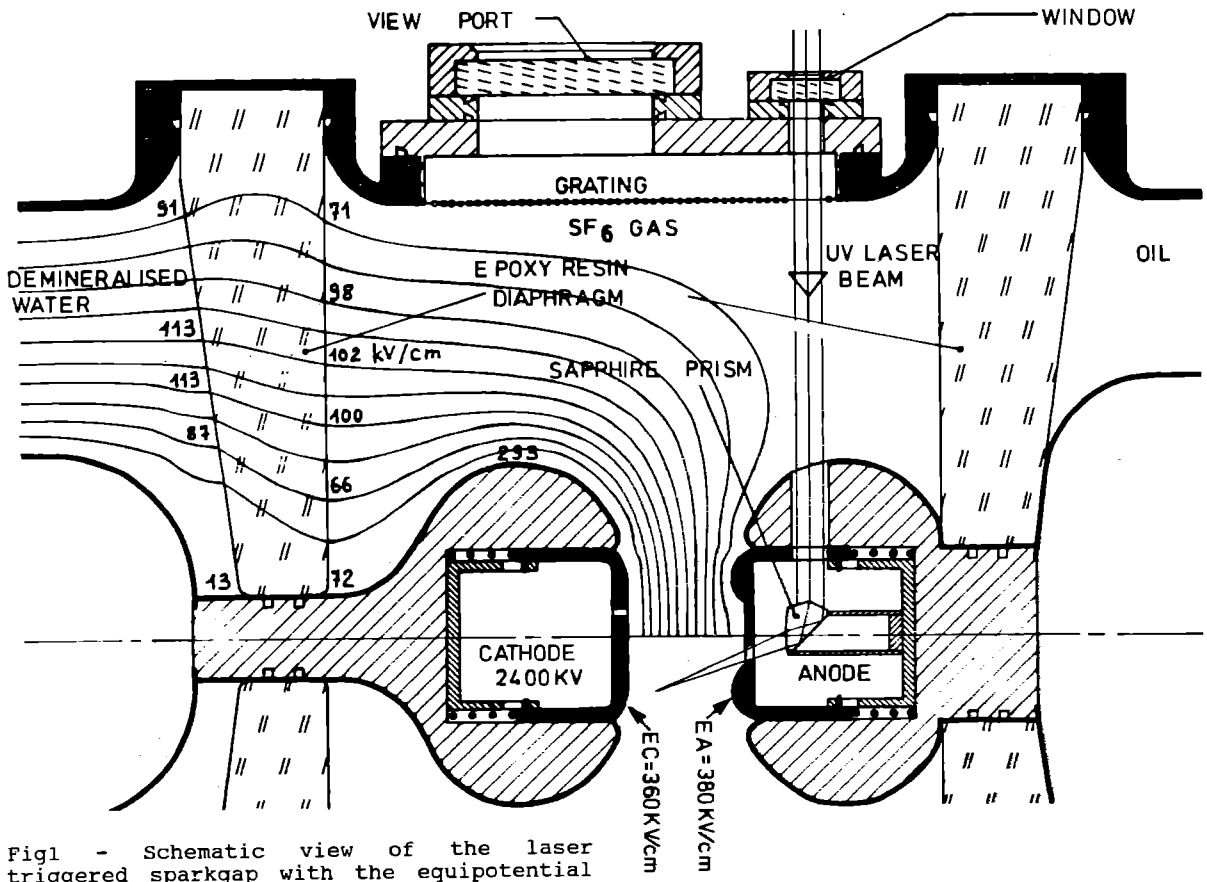


Fig1 - Schematic view of the laser triggered sparkgap with the equipotential lines and the electric field distribution preceding the breakdown.

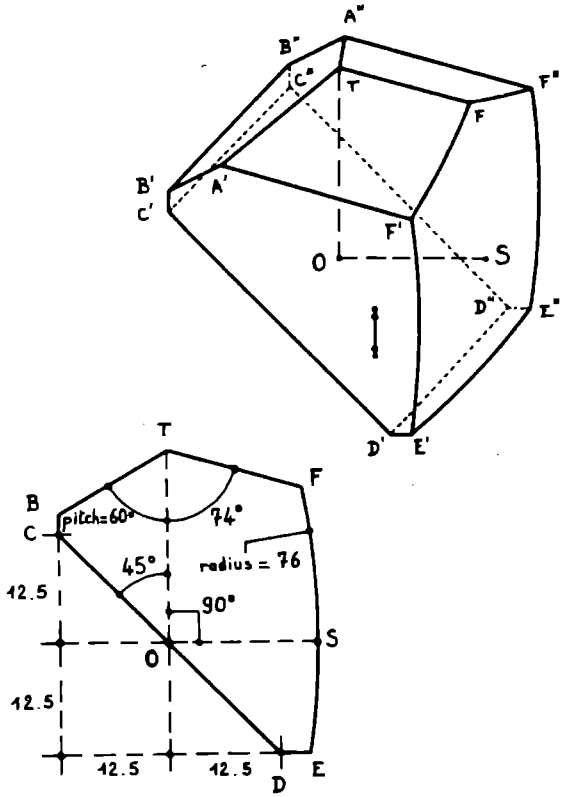


Fig.3 - 3 foci sapphire prism: 3 dimensional view and section in the plane of symmetry.

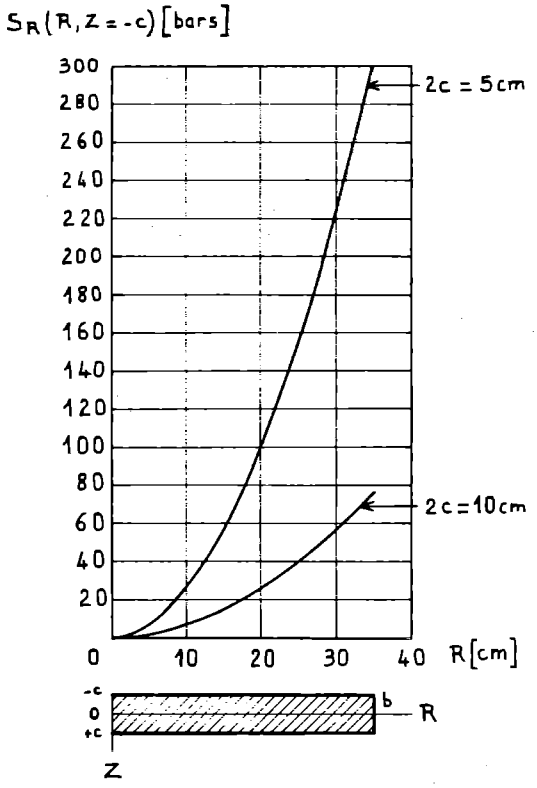


Fig.2 - Radial stresses $S_R(R,Z=-c)$ on one face of a circular plate (thickness 2c=5 and 10 cm) loaded by a 5bars hydrostatic pressure.

# ALTERNATIVE ELECTROLYTES FOR USE IN LIQUID RESISTORS

G.J.Hirst

Rutherford Appleton Laboratory

## INTRODUCTION

Liquid resistors are often used in pulsed power systems because i) they can absorb fast, high-energy electrical pulses without catastrophic damage, ii) they can withstand very high voltages, iii) their resistance is voltage independent, and iv) they can tolerate substantial average power loadings for typical capacitor bank charge-times.

Liquid resistors usually[1] contain copper sulphate solution which is electrolytically and chemically stable if copper electrodes are used. Unfortunately in larger systems both the sizes and the numbers of resistors increase. The copper, which is difficult to machine, can then be very costly. Resistors passing large net charges, such as those carrying d.c. currents, will always need to have electrodes made from the same metal as the electrolyte cations. Cheaper materials, however, may be usable in pulsed circuits. After a suggestion from the Naval Research Lab. in Washington D.C., we have studied aqueous solutions of household cleaning agents with stainless steel electrodes. These liquids also wet the electrodes more easily, helping trapped bubbles to clear.

## RESULTS

The resitivities of five electrolytes are listed in table 1. Beep[2] is a washing-up liquid, Dreft[3] is solid soap-flakes, Kimguard[4] is liquid hand-soap and Shine[5] is a dishwasher powder. Their resistivities were measured using a standard tube of each liquid into which a 64 nF capacitor,

Table 1: Resistivities of five different electrolytes.

| Electrolyte | Concentration | Resistivity |
|---|---|---|
| Beep | As supplied | 38 Ohm cm |
| Dreft | 30 g in 150 g of water* | 15 Ohm cm |
| Kimguard | As supplied | 29 Ohm cm |
| Shine | 30 g in 150 g of water | 11 Ohm cm |
| $CuSO_4$ | 30 g in 90 g of water | 24 Ohm cm |

*May not have dissolved completely.

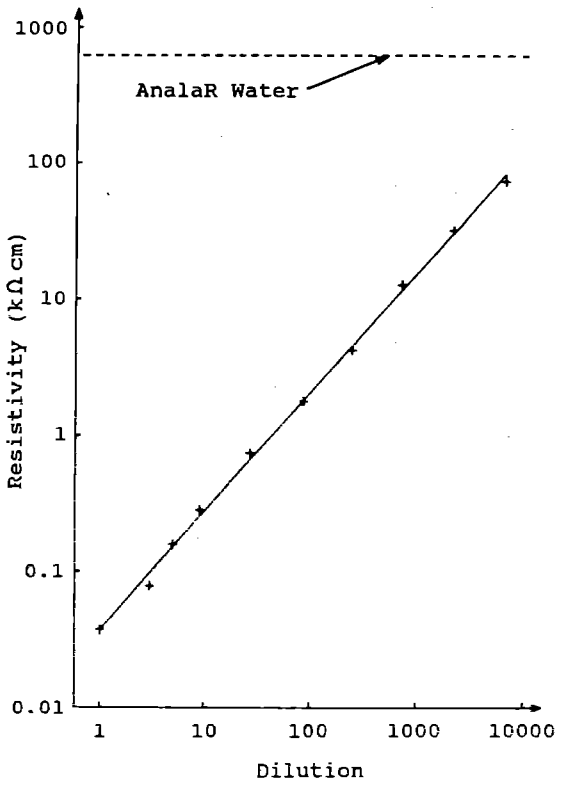


Figure 1: Resistivity of Beep detergent as a function of aqueous dilution.

charged to 15 kV, was switched. The RC decay times yielded resistances between 100 Ω and 350 Ω. Further tests on Beep alone confirmed that its resistivity was independent of electric field from 10 V/cm to 1 kV/cm and that the temperature coefficient of resistivity was less than 2%/K at 300 K. Figure 1 shows the relation between resistivity and dilution, again for Beep alone. Several days' contact with the electrodes produced no apparent changes in the resistors and longer lifetime tests using Shine are now under way.

## REFERENCES

1. J.C. Martin, "Measurement of the Conductivity of Copper Sulphate Solutions", SSWA/JCM/667/67, AWRE Aldermaston.
2. B.P. Detergents Ltd., Pumpherston, Livingston, W. Lothian, EH53 0LQ.
3. Proctor & Gamble Ltd., P.O. Box 1EL, Newcastle, NE99 1EL.
4. Kimberley Clark Ltd., Larkfield, Maidstone, Kent.
5. The Robert McBride Group, Middleton, Manchester M24 4DP.

# C: LASER SUPPORT FACILITY

W T Toner

## INTRODUCTION

This section contains reports from users of the Laser Support Facility (LSF) in Chemistry (C1), Biology (C2) and Physics (C3). Operations and development are reported in section C4.

The facility was set up five years ago to give research workers in HEIs access to up-to-date laser technology which would supplement their own resources and to enable them to draw on the expertise of RAL staff in pulsed lasers and nonlinear optics techniques. The LSF operates three laser laboratories at RAL for scheduled user experiments and a laser loan pool comprising seven laser systems lent for periods of three months at a time to institutions all over the UK: both Edinburgh and Sussex are represented in this report. Table I summarises the main features of the equipment.

Some of the contributors base a large fraction of their research work using lasers on the LSF. Others need only occasional access or will use the facility to obtain data which will establish the case to purchase their own equipment. The user population is large and constantly changing. Of the thirty groups reporting, nine are new users of the facility.

The techniques are diverse and include the use of thermal X-rays from laser plasmas for DNA damage studies employing radioactive tracer assay, laser annealing analysed by synchrotron X-rays and neutron scattering, sub-picosecond transient absorbance; time-of-flight mass spectrometry, high resolution jet-cooled spectroscopy, time-resolved resonance Raman scattering and matrix isolation spectroscopy.

The research covers a very wide range of fields within the Science Board area and has a strong multidisciplinary content.

## CHEMISTRY

There are two substantial groups of papers mostly from loan pool users on gas phase reaction dynamics and jet-cooled high resolution spectroscopy which include noteworthy reports on insertion reactions of phenylsilylene, radical-radical reactions, transition element compounds, the structure of five membered ring molecules, the identification and structural analysis of solvated clusters. Structural studies also include elegant work on reactive metallocenes by a new user group who brought their matrix isolation equipment to RAL and several papers from users of the Raman spectroscopy facilities at RAL in which structural information is used to study solution phase reaction intermediates.

## BIOLOGY

The first two papers are from groups new to the facility who report promising results from trial experiments, one using the Raman facilities at RAL and the other using a loan pool laser for photo - CIDNP studies of protein folding. Substantial progress in the work on the repair of DNA damage by both UV photons and X-rays is reported by the Birmingham-Sussex-MRC collaboration including the observation that exposure to 351 nm light increases the resistance of cells subsequently exposed to the antibiotic adriamycin by a factor of over 100. This dramatic effect is thought likely to be of great significance in research on carcinogensis. Progress has also been made in measurements of transient absorbance changes in Photosystem I which have now established that antenna to reaction centre excitation transfer occurs in less than a picosecond.

TABLE 1

LASER SUPPORT FACILITY EQUIPMENT

Picosecond Systems at RAL

2 cw modelocked pump lasers; sub-picosecond oscillator; 2 cavity dumped oscillators; injection-locked YAG pump and dye amplifier (10 Hz); copper vapour pump and dye amplifier (6 KHz). Pump-probe absorption system; single photon counting; streak camera. Wavelengths from the UV to the far infrared are available, with further amplification at the excimer wavelengths.

Nanosecond Systems at RAL

2 high repetition rate fluoride excimer lasers; laser-plasma X-ray source;
2 high repetition rate XeCl excimer lasers pumping dye lasers; BBO and Raman wavelength conversion. 5 watt ion laser. Raman spectrometer. Flash photolysis system.

Loan Pool

4 YAG-pumped tunable dye lasers with frequency doubling and mixing; Excimer-pumped dye laser; fluoride excimer laser; 5 watt cw Ar ion laser with dye laser or Ti-sapphire laser; streak camera; gated integrators.

## PHYSICS

Though physicists who use small scale lasers for their research purchase and develop their own laser equipment for the most part, the papers in this section illustrate that in physics too modern research frequently requires a variety of techniques going beyond the resources of a single research group. The reports cover quantum well structures, covariance mapping studies of multiphoton ionisation, cluster photodissociation, annealing and non-linear optics.

# OH PRODUCTION IN GROUND STATE OXYGEN ATOM REACTIONS

Fiona Winterbottom and J. Christopher Whitehead

Department of Chemistry, Manchester University,
Manchester, M13 9PL, UK

## INTRODUCTION

Reactions of ground-state oxygen atoms are of considerable importance in atmospheric, combustion and plasma chemistry and in astrochemistry. Yet there have been comparatively few studies of the dynamics of such reactions studied under collision-free conditions due partly to the relatively high activation energies. By using supersonic molecular beam sources; it has been possible to provide enhanced kinetic energy to overcome the barriers. In this way, the formation of OH in reactions of $O(^3P)$ with a wide range of organic molecules, RH, has been studied[1-5] using laser-induced fluorescence (LIF) detection of the OH. Zare has reported[6] a study of OH production in the reaction O + HBr and HCl using "hot" oxygen atoms produced by photolysis of $NO_2$ at 355 nm followed by LIF probing of the OH. The production of OH in the reactions of $O(^3P)$ with organic molecules, RH, was found to yield rotationally-cold OH whereas O + HX (X = Br, Cl) produced rotationally-hot OH. These findings can be rationalised in terms of the anisotropy of the reaction potential energy surface and the geometry of the reaction transition state. The reactions of $O(^3P)$ with $SiH_4$ and $(CH_3)_3SiH$ have recently been studied using the pulse-probe method[7,8]. The reaction O + $SiH_4$ yields an OH rotational intermediate between O + RH and HX, whilst there is evidence that the OH rotational excitation from O + $(CH_3)_3SiH$ is reduced because of steric hindrance caused by the methyl groups during the Si-H abstraction. We have used the pulse-probe method to study the reactions O + $C_6H_{12}$ and $GeH_4$.

## EXPERIMENTAL

The oxygen atoms were generated by the 351 nm XeF excimer laser photolysis of ∿ 60 m Torr of $NO_2$ in the presence of a smaller amount of the hydride (∿ 20 m Torr). After a short enough delay to ensure single-collision conditions (∿ 200 ns), the OH internal state distributions were probed by LIF using a tuneable UV laser system (Spectron YAG, Quanta Ray PDL and WEX) operating on the $A^2\Sigma^+ \leftarrow X^2\Pi$ system of OH. The OH vibrational, rotational, spin-orbit and lambda doublet populations were measured for each reaction using the (0,0) and (1,1) bands.

## RESULTS AND DISCUSSION

For O + cyclohexane, the results for the rotational distribution are shown in Fig. 1 for v = 0. The vibration population ratio N(v = 1)/N(v = 0) = 0.14 ± 0.10 and the spin-orbit ratio $N(^2\Pi_{3/2})/N(^2\Pi_{1/2})$ = 1.66 ± 0.51 with a statistical lambda doublet state population. These results can be compared with crossed-molecular beam studies of the same reaction.[3] The beams reaction has a slightly higher kinetic energy and the cyclohexane is rotationally cold compared with the pulse-probe experiment. The differences between the two sets of results are being rationalised in terms of the initial reagent conditions using a classical trajectory analysis.

For O + $GeH_4$, there is more energy disposed into OH rotation (Figure 1) and the vibrational partitioning N(v = 1)/N(v=0) = 4.1 ± 2.4 with statistical spin orbit state populations. For OH(v = 1) the lambda doublet populations are greater than statistical at low N and decreases with increasing N. The lambda doublet ratio for OH(v = 0) is greater than unity for all rotational levels. This has a parallel with the reaction O + $SiH_4$ [7] where it was suggested that two reaction mechanisms applied. One involves the direct abstraction of hydrogen atom via a collinear (or near collinear) O-H-Ge intermediate and the other occurs by insertion of the O atom into the H-Ge

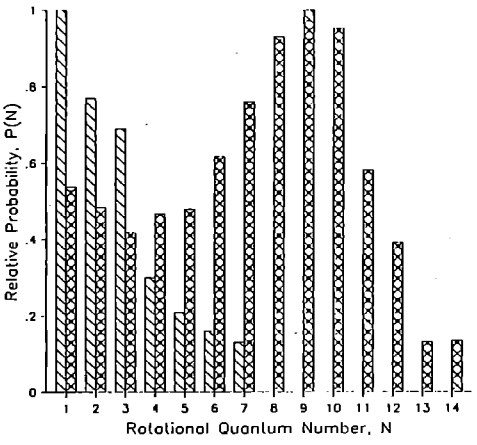


Figure 1 The rotational state distributions for O + $C_6H_{12}$ → OH(v = 0) + $C_6H_{11}$ (single hatched) and O + $GeH_3$ → OH(v = 1) + $GeH_3$ (double hatched).

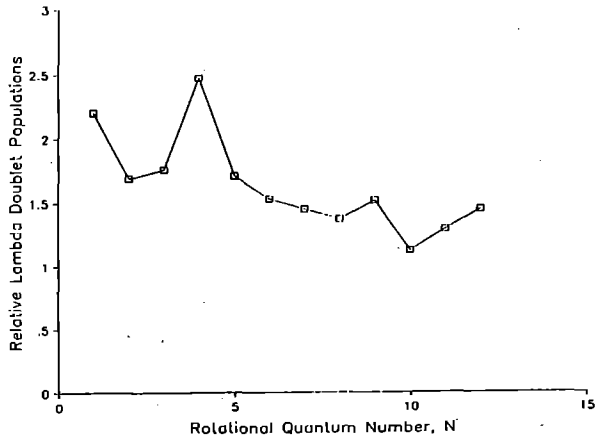


Figure 2 The dependence of the lambda doublet population ratios $\Pi(A')/\Pi(A'')$ for $O + GeH_4 \rightarrow OH\ (v = 1) + GeH_3$.

band to form a long-lived collision intermediate. The dissociation of such an intermediate might show a propensity for planar decomposition giving a $\Pi(A')$ preference and populating low energy states. Such a mechanism might account for all the OH(v = 0) and the low rotational levels of OH(v = 1), It is planned to investigate the formation of OH in v = 2 and v = 3 in future experiments.

REFERENCES

1. P. Andersen and A.C. Luntz, J. Chem. Phys. 72, 5842 (1980).
2. K. Kleinermanns and A.C. Luntz, J. Chem. Phys. 77, 3533, 3537, 3774 (1982).
3. N.J. Dutton, I.W. Fletcher and J.C. Whitehead, Mol. Phys., 52, 2620 (1984).
4. N.J. Dutton, I.W. Fletcher and J.C. Whitehead, J. Phys. Chem., 89, 569 (1985).
5. N.J. Barry, I.W. Fletcher and J.C. Whitehead, 90, 4911 (1986).
6. K.G. McKendrick, D.J. Rakestraw and R.N. Zare, Faraday Disc. Chem. Soc., 84, 39 (1987).
7. C.R. Park, G.D. White and J.R. Wiesenfeld, J. Phys. Chem., 92, 152 (1988).
8. C.R. Park and J.R. Wiesenfeld, J. Phys. Chem., 93, 1365 (1989).

# TIME-RESOLVED STUDIES OF THE TEMPERATURE DEPENDENCE OF GAS-PHASE INSERTION REACTIONS OF PHENYLSILYLENE WITH Si-H BONDS

M.A. Blitz, H.M. Frey, F.D. Tabbutt[1] and R. Walsh

University of Reading

## INTRODUCTION

Silylenes, $SiX_2$, are known to be important intermediates in the thermal and photochemical decompositions of many silicon containing compounds. In 1987 we began a programme of investigation of the kinetics of their gas-phase reactions by time-resolved techniques and have presently published rate constants for a number of reactions of $SiMe_2$[2,3] and also for the reaction of $SiH_2$ with $D_2$[4] and the methylsilanes[5]. These studies have provided substantial insight into the nature of these processes revealing that rates are controlled by a delicate balance between electrophilic and nucleophilic interactions in the activated complex.

No studies have yet appeared involving phenylsilylene, PhSiH. The photolysis of phenylsilane at 193 nm has been observed to produce substantial primary yields of molecular hydrogen[6] thought to occur via the process

$$PhSiH_3 + h\nu \rightarrow PhSiH + H_2$$

Since the effect of phenyl substitution on silylene reactivity is unknown we decided to attempt to detect PhSiH and measure the rate constants for some of its reactions.

## EXPERIMENTAL AND RESULTS

The apparatus for these experiments has been described in detail elsewhere[2-4]. Briefly, transients from the decomposition of phenylsilane were generated by pulsed 193 nm photolysis (Oxford KX2 ArF exciplex laser). Transient absorptions were detected and monitored in the wavelength range 460-600 nm using the Spectra Physics 2025 $Ar^+$ laser provided by the Laser Facility loan scheme (460-520 nm) or an $Ar^+$ pumped dye-laser (Coherent Innova 90-5 and CR-599-01, $\lambda$ =540-600 nm). A multipass arrangement gave total path detection lengths of ca 4.8 m (room temperature quartz reactor) and 1.4 m (elevated temperature stainless steel reactor, with spectrosil photolysis window and crown glass probe beam windows). Absorption signals were detected using a dual photodiode/differential amplifier combination and stored in a transient recorder interfaced to a BBC micro computer used as a signal averager.

Preliminary experiments with 25 mTorr of $PhSiH_3$ diluted in Ar (5 Torr) at 291K revealed absorption signals in the wavelength range 460-600 nm as shown in figure 1 (extrapolated to zero time). This spectrum decayed at a rate independent of wavelength. Its attribution to PhSiH is supported by observations for other known aromatic

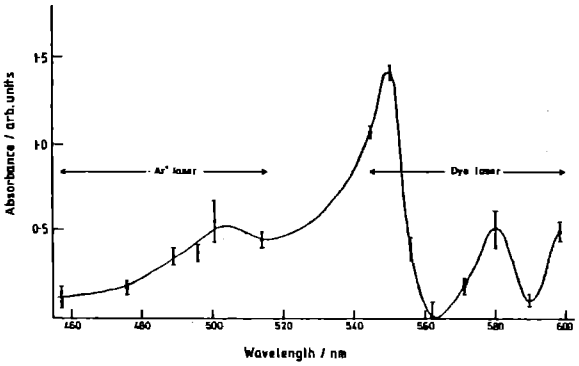


Figure 1 Visible absorption spectrum of PhSiH

substituted silylenes, which have broad band spectra with absorption maxima at ca 500 nm (matrix isolation studies[7]). Kinetic experiments were carried out for mixtures of $PhSiH_3$ with 4 different reagent silanes. Typical experiments employed 25 mTorr $PhSiH_3$ with partial pressures of substrate in the range 0-1 Torr and total pressures of 10 Torr (made up with Argon). Signal decays (averaged for 5-20 laser shots) were single exponential. Bimolecular rate constants were determined by measuring the pseudo-first order decay constants as a function of concentration of added substrate. The reactants investigated were $SiH_4$, $MeSiH_3$, $Me_2SiH_2$ and $Me_3SiH$. Experiments were carried out in the temperature range 291-564K, with at least four different temperatures for each reactant. The measured rate constants are represented by an Arrhenius Plot in figure 2 and the Arrhenius parameters obtained by least-squares fitting are shown in table 1. The scatter in the data is caused, in part, by operation at the limit of the equipment time-resolution for such highly reactive species.

Table 1 Arrhenius parameters for PhSiH insertion reactions

| Substrate | log $A^a$ | $E_a{}^b$ |
|---|---|---|
| $SiH_4$ | -11.54 ± 0.50 | - 7.1 ± 4.1 |
| $MeSiH_3$ | -11.60 ± 0.69 | -12.5 ± 5.7 |
| $Me_2SiH_2$ | -11.31 ± 0.16 | - 9.3 ± 1.2 |
| $Me_3SiH$ | -12.14 ± 0.28 | -15.6 ± 2.3 |
| $PhSiH_3$ | -10.08 ± 0.21 | - 0.7 ± 1.5 |

a. Units: $cm^3$ $molecule^{-1}s^{-1}$ b. Units: kJ $mol^{-1}$

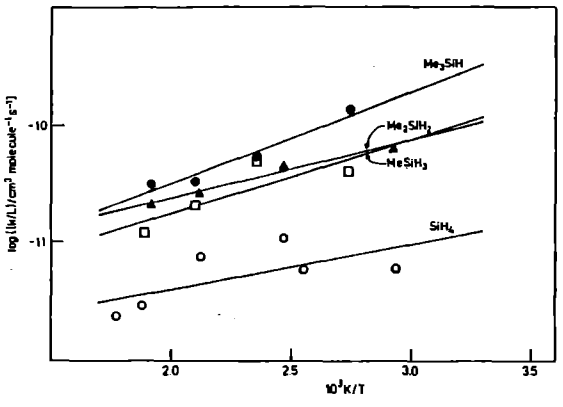


Figure 2 Arrhenius plots for PhSiH insertion reactions (per Si-H bond)

DISCUSSION

Despite some scatter in the data two features stand out clearly: (i) rate constants decrease with increasing temperature, i.e. activation energies are negative; (ii) rate constants for different reactants increase with methyl substitution on the silane substrate (per Si-H bond). Comparison with $SiH_2$[5] and $SiMe_2$[2] show that PhSiH is much closer in reactivity to the former. Thus Ph substitution appears to be much less deactivating that Me substitution (although a strict comparison requires studies with MeSiH, which are planned).

These results offer further support for the idea that the polarity of the substrate silicon atom is important. A picture of the interactions involved in the insertion process is shown in figure 3a. Me-for-H substitution in the substrate silane (substituent Y) causes an increase in positive charge on the Si due to the weak electronegative effect of methyl. This enhances the nucleophilic interaction with the silylene, and facilitates the reaction, as observed here and with $SiH_2$[5] and $SiMe_2$[2]. The failure of phenyl substitution to moderate substantially the silylene reactivity may be attributed to the poor overlap between the C(2p) & Si(3p) orbitals, leading to little, if any, π-type interaction, as depicted in figure 3b.

The negative activation energies may be explained, inter alia, by a mechanism involving an intermediate complex. In the first stage of the process a weak complex is formed reversibly (maybe involving the nucleophilic interaction). In the second stage the complex rearranges via H migration (the electrophilic interaction) to give the final product (disilane). The first stage, involving a loose transition state is highly reversible and redissociation can compete more effectively with H-migration, requiring a tight transition state, as the temperature increases. Hence the rate decreases as the temperature rises. Confirmation of this proposition will require further kinetic tests or a reliable ab initio calculation of the potential energy surface for reaction.

These results represent the first kinetic studies for phenylsilylene. More detailed information is available in the full publication[8].

REFERENCES

1. On Sabbatical leave from The Evergreen State College, Washington 98505, U.S.A.
2. J.E. Baggott, M.A. Blitz, H.M. Frey, P.D. Lightfoot, and R. Walsh, Chem. Phys. Lett. 135 39 (1987).
3. J.E. Baggott, M.A. Blitz and P.D. Lightfoot, Chem. Phys. Lett. 154 330 (1989) and refs therein. See also SERC, Central Laser Facility Annual Report 1989, p. 240.
4. J.E. Baggott et al, J. Phys. Chem. 92 4025 (1988).
5. J.E. Baggott et al, J. Chem. Soc. Faraday Trans. 86 27 (1990)
6. J.E. Baggott et al, Chem. Phys. Lett. 125 22 (1986).
7. M.J. Michalczyk et al Silicon, Germanium, Tin and Lead Compounds 9 75 (1986).
8. M.A. Blitz, H.M. Frey, F.D. Tabbutt and R. Walsh, J. Phys. Chem. 94 in press (1990).

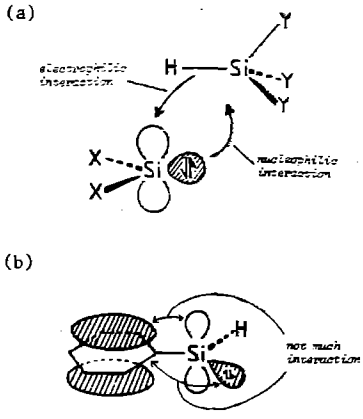


Figure 3 (a) Interactions involved in the silylene insertion process. (b) Potentially important orbitals in PhSiH.

# PRODUCT DISTRIBUTIONS FOR RADICAL-RADICAL REACTIONS

Alistair M.L. Irvine, Leon F. Phillips, Ian W.M. Smith, Richard P. Tuckett, Christopher J. Whitham and Xue-Feng Yang

The University of Birmingham

## INTRODUCTION

As part of a research programme on the dynamical details of radical-radical reactions, we have completed experiments on the reaction

$$H + NO_2 \rightarrow OH + NO; \quad \Delta H^\circ_0 = -123.6 \text{ kJ mol}^{-1},$$

and begun experiments on the reaction

$$CN + O_2 \rightarrow NCO + O; \quad \Delta H^\circ_0 = -27 \text{ kJ mol}^{-1}.$$

The objective is to determine the nascent distributions of products over rotational and vibrational energy levels and, where appropriate, also over spin-orbit states and the $\lambda$-doublet components of rotational levels, in order to improve our understanding of the dynamics of reactions which proceed across potential energy surfaces incorporating deep minima.

## RESULTS AND DISCUSSION

(i) The reaction: $H + NO_2 \rightarrow OH + NO$

Laser-induced fluorescence (LIF) spectra of both products of this reaction have been recorded in an arrangement where two uncollimated beams containing the reagents intersect. Table 1 lists the fractional yields of energy released into the electronic, vibrational and rotational degrees of freedom of both OH and NO.

Table 1: Average fractional yields of electronic, vibrational and rotational energy in the OH and NO products of reaction between H atoms and $NO_2$.

| | OH | NO |
|---|---|---|
| $\langle f_{elec} \rangle$ | 0.006 | 0.004 |
| $\langle f_{vib} \rangle$ | 0.23 | 0.056 |
| $\langle f_{rot} \rangle$ | 0.29 | 0.100 |
| | 0.526 | 0.160 |

For OH, the rotational and the vibrational excitations are both greater than would be expected on a prior statistical basis, whereas in NO these degrees of freedom, despite significant excitation, are less excited than would be the case if energy was distributed randomly. These results are consistent with reaction proceeding via the singlet ground state surface of HONO, but with the intermediate complex unable to survive sufficiently long for complete energy randomisation. In agreement with this hypothesis, there is some propensity for formation of the $\Pi(A')$ $\Lambda$-doublet levels, which would be strongly favoured if products were formed by the break-up of a complex which was tightly constrained to a planar geometry.

Work on the $H + NO_2$ reaction has been written up for publication in the Journal of Chemical Physics.

(ii) The reaction: $CN + O_2 \rightarrow NCO + O$

A major uncertainty in our experiments on the $H + NO_2$ reaction was the average number of collisions suffered by product species before they escaped the observation zone. This not only leads to an uncertain extent of collisional relaxation, but it also means that there is some uncertainty in transforming the observed relative populations into relative rates into product states. Such difficulties are removed when reaction is initiated with one pulsed laser and the product states are observed with a second pulse laser. The delay between pulses and the pressure in the system can be varied systematically and hence relaxation rates measured and nascent distributions obtained accurately. This approach is now being adopted in experiments on the $CN + O_2$ reaction.

CN radicals are generated by photolysing NCNO using the frequency-doubled output from a Nd:YAG laser from the Laser Loan Pool. At delays of 100 ns or greater, LIF spectra of NCO are recorded. So far, we have carried out only preliminary experiments, but two very interesting results emerge. First, the NCO is excited up to its highest energetically accessible level ($v_2$=5) in its $\nu_2$ bending mode. On the other hand, there is evidently rather little excitation of the bond stretching vibrations. Second, by varying the delay between the photolysis and probe lasers, the rise and fall of populations in defined levels can be observed. This is being exploited to obtain rates for collisional relaxation of the $v_2$=5 levels in NCO.

In the immediate future, we intend to improve both the signal-to-noise and resolution of our spectra in order to obtain nascent rotational, as well as vibrational, state distributions.

# RATE CONSTANTS FOR THE REACTIONS OF $CH_3O$ AND $C_2H_5O$ RADICALS WITH NO AND $NO_2$ OVER A RANGE OF TEMPERATURE AND TOTAL PRESSURE

Michael J. Frost and Ian W.M. Smith

The University of Birmingham

## INTRODUCTION AND EXPERIMENTAL METHOD

The reactions of alkoxy radicals (RO) with NO and with $NO_2$ may proceed: (a) to the corresponding nitrite or nitrate as a result of radical-radical association, or (b) to an aldehyde plus HNO or HONO following H-atom transfer. In order to understand these reactions, as well as to assess their roles in combustion and atmospheric chemistry, rate constants have been determined over a range of temperature and total pressure for R + $CH_3O$, $C_2H_5O$.

RO radicals were produced by pulsed laser photolysis of RONO at $\lambda$ = 266 nm and laser-induced fluorescence from the radicals was excited using a frequency-doubled, flashlamp-pumped, dye laser. The time between laser pulses was scanned to observe kinetic decays.

## RESULTS AND DISCUSSION

Each experiment yields a pseudo-first-order rate constant ($k_{1st}$). The variation of the values of $k_{1st}$ with $[NO_2]$ or [NO] at a constant temperature and pressure is linear and the gradient of the plot yields a second-order rate constant.

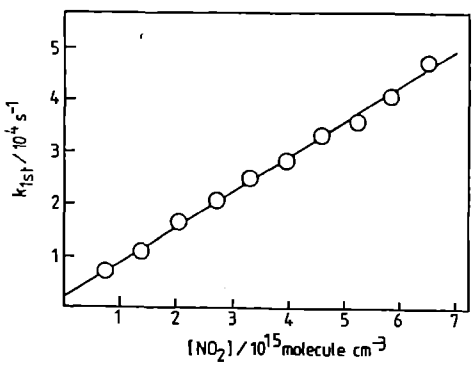


Figure 1: Pseudo-first-order constants for the decay of LIF signals from $CH_3O$ in the presence of 4.9 x $10^{17}$ $cm^{-3}$ (≃ 15 Torr) Ar at 295 K.

Careful analysis of the pressure dependence of the second-order rate constants for reaction between $CH_3O$ and $NO_2$ indicate that it proceeds solely by association. Fitting the rate constants to theoretically based forms for the pressure fall-off curve yields the limiting low pressure and high pressure rate constants for association of $CH_3$ and $NO_2$. Those at low pressure agree well with estimates of $k_o$. The value derived for $k^\infty$ at 298 K is similar to those reported for the association of $NO_2$ with OH and i-$C_3H_7$ and the pressure-independent rate constant, (2.8 ± 0.3) x $10^{-11}$ $cm^3$ $molecule^{-1}$ $s^{-1}$ found in the present work for reaction of $C_2H_5O$ with $NO_2$.

Table 1: Rate constants in the limits of low pressure ($k_o$) and high pressure ($k^\infty$) for reactions of $CH_3O$, $C_2H_5O$ with $NO_2$.

| T/K | M | $k^o/10^{-29}$ $cm^6$ $molecule^{-2}$ $s^{-1}$ | $k^\infty/10^{-11}$ $cm^3$ $molecule^{-1}$ $s^{-1}$ |
|---|---|---|---|
| 298 | He | 1.6 ± 0.6[a] | 2.1$_5$ ± 0.6 |
| | Ar | 2.8 ± 0.6 | 1.9 ± 0.3 |
| | $CF_4$ | 3.4 ± 1.0 | 2.0$_5$ ± 0.5 |
| 390 | Ar | 2.0 ± 0.5 | 1.2 ± 0.2 |

[a] quoted errors correspond to 2 standard deviations.

Analysis of the results for the reaction of $CH_3$ with NO shows that association and H-atom transfer to produce $H_2CO$ + HONO occur in competition. The observed rate constants ($k_{obs}$) are fitted well by an extended Lindemann-Hinshelwood mechanism in which $k^o_{1a}[M]$ and $k^o_{1b}$ are the values which the second-order rate constants for association and reaction to $H_2CO$ + HONO would have in the absence of the other channel and $k^\infty$ is the rate constant in the limit of high pressure. Values of $k^o_{1a}$, $k^o_{1b}$ and $k^\infty$ are given in Table 2. Once again, the rate constants for association are in agreement with what might be expected on the basis of theory and comparison with similar systems.

Table 2: Rate constants for reaction of $CH_3O$, $C_2H_5O$ with NO in the presence of Ar.

| T/K | $k^\infty/cm^3$ $molecule^{-1}$ $s^{-1}$ | $k^o_{1a}/cm^6$ $molecule^{-2}$ $s^{-1}$ [b] | $k^o_{1b}/cm^3$ $molecule^{-1}$ $s^{-1}$ |
|---|---|---|---|
| 296 | $3.6 \times 10^{-11}$ | $1.3 \times 10^{-29}$<br>$1.85 \times 10^{-29}$ | $5.3 \times 10^{-12}$ |
| 370 | $3.2 \times 10^{-11}$ | $5.3 \times 10^{-30}$<br>$1.1 \times 10^{-29}$ | $5.3 \times 10^{-12}$ |
| 452 | $2.8 \times 10^{-11}$ | $2.8 \times 10^{-30}$<br>$5.6 \times 10^{-30}$ | $4.4 \times 10^{-12}$ |
| 573 | $(2.4 \times 10^{-11})$[b] | $(1.15 \times 10^{-30})$[b] | $\sim 4 \times 10^{-12}$ |

[a] upper entry is for M = Ar, lower entry for M = $CF_4$.

[b] derived from values at low temperatures assuming a $T^{-n}$ dependence of the rate constants (see fig. 6).

# The Photolysis of HOCl at 266nm in a Supersonic Molecular Beam: Laser Induced Fluorescence Spectra of OH

Andrew J. Bell, Patrick R. Pardon, C.G. Hickman and Jeremy G. Frey
Department of Chemistry, The University
Southampton SO9 5NH, England UK

**Abstract**

The nascent OH rotational distribution is observed following the 266nm photolysis of HOCl in a supersonic molecular beam. A strong preference for the population of the OH $^2\Pi_{3/2}$ spin state is found and a significant deviation from the statistical population of the OH lambda doublet states is observed. The OH rotational distribution can be characterised by a temperature which is slightly different for the two spin-orbit states. These rotational temperatures decrease as the pressure of the Ar carrier gas used in the supersonic expansion is increased, but the provisional analysis conducted so far indicates that the spin-orbit population ratios and the lambda doublet preference is essentially the same under all the expansion conditions studied.

## 1 Introduction

The ability to detect OH by laser induced fluorescence (LIF) has led to the study of a number of molecules (of the form HOX) that liberate the OH radical on photolysis; some of the most detailed studies have been on hydrogen peroxide. In contrast the photolysis of the triatomic HOCl has been investigated in much less detail despite its potential importance in the upper atmosphere [1] [2]. There has even been considerable debate on the nature of the HOCl uv absorption spectrum, especially at wavelengths around 300nm, however the consensus seems to be that there is a single absorption with a maximum at 250nm and no second peak at longer than 300nm [3] [4]. This is in accord with an *ab initio* calculation on the potential energy surfaces as they relate to the uv absorption spectrum and the photodissociation process[5] [6]. However Molina et al [7] have observed the production of OH from the photolysis of $Cl_2O/H_2O/HOCl/He$ mixtures, between 305 - 310nm, in a gas cell using the same laser to induce the photolysis and detect the OH radical by LIF.

The standard thermodynamic data show that the following are possible products from the photodissociation of HOCl ($\lambda$ is the threshold wavelength and $\Delta H$ the enthalpy change for the dissociation pathway shown assuming the diatomic fragments are in the ground levels of the electronic states, $E_{avl}$ is the energy available to the fragments for a 266nm photolysis).

| | | $\lambda$ nm | $\Delta H$ kJ/mol | $E_{avl}$ kJ/mol |
|---|---|---|---|---|
| HOCl + hv | ——> $O(^3P) + HCl(X^1\Sigma^+)$ | 481 | 248.6 | 201 |
| HOCl + hv | ——> $Cl(^2P) + OH(X^2\Pi)$ | 473 | 252.9 | 197 |
| HOCl + hv | ——> $H(^2S) + ClO(X^2\Pi)$ | 291 | 411.0 | 38.6 |
| HOCl + hv | ——> $O(^1D) + HCl(X^1\Sigma^+)$ | 272 | 439.7 | 9.9 |

Experimental observations and theoretical calculations on the excited state potential energy curves indicate that only Cl + OH pathway is expected to be a significant dissociation route. The spin-orbit states of both Cl and OH mean that there are four asymptotic limits very close in energy. The Cl spin-orbit splitting is 881cm$^{-1}$ while in OH the spin-orbit states are split by only 127cm$^{-1}$.

HOCl is an almost ideal molecule to study the fundamentals of photodissociation processes as other than the possibility of populating either of the Cl atom spin orbit states ($^2P_{1/2}$ or $^2P_{3/2}$) only the OH fragment can be internally excited. Thus the measurement of the OH vibration-rotation state populations by laser induced fluorescence can provide a very detailed description of the reaction dynamics. The properties of the ground state are quite well known; the equilibrium structure of HOCl and a harmonic force field are well established from microwave [8] and infrared [9] spectra. This means that theoretical calculations of the dissociation dynamics are possible and have been investigated by a generalised Frank-Condon approach to the calculation of the OH product rotational distributions[10].

## 2 Experimental

A conventional pump probe geometry was employed with the Nd:YAG photolysis laser propagating anti-parallel to the probe laser and both laser beams entering the molecular beam chamber via brewster angled windows and highly baffled arms. The fluorescence was collected at right angles to both the molecular beam and the laser beams with a single quartz lens. A f1 collection lens was used to image a 12.5mm diameter region on to a photomultiplier tube (EMI 9924QB). The viewing region is sufficiently large so that even the OH radicals with the highest kinetic energy (corresponding to a speed of 4000ms$^{-1}$) will remain within the viewing region during the 1.5$\mu$s fluorescence gate. A band pass filter was used to minimise the amount of scattered 266nm radiation reaching the photomultiplier.

The effusive and supersonic expansions were generated using a 200 micron glass nozzle. A background pressure in the chamber of 5 x $10^{-5}$ torr was maintained when the beam was running by 9" and 4" diffusion pumps. No metal was used in the nozzle and gas entry system thus avoiding most of the problems associated with the catalytic decomposition of the HOCl. An aqueous solution of HOCl was prepared by bubbling chlorine gas through as suspension of HgO in water. This was used as the source of HOCl after degassing without further purification. In the experiments using the Ar carrier gas, the Ar was passed over the top of the HOCl solution. Previous investigations of the photoelectron spectrum of HOCl[11] had established that a reasonable vapour pressure of HOCl exists above an aqueous solution.

The Quantel Datachrome laser produces about 15mJ/pulse at 266nm with our own KD*P type II doubling crystal, with of which about 5mJ/pulse entered the vacuum chamber. The use of a type II crystal resulted in 266nm radiation polarised at 45 degrees to the vertical. An arrangement of mirror was used to ensure that the 266nm photolysis radiation was either vertically or horizontally polarised in the molecular beam chamber. The LIF probe pulse was provided by a JK2000 Nd:YAG pumped dye laser, frequency doubled by an INRAD autotracker system; the linewidth in the uv was estimated at about 0.5cm$^{-1}$ and was polarised horizontally for all these experiments. A 50:50 mixture of DCM and R620 laser dyes was used to cover the OH (0-0) region with we estimate an energy of less than 1-2 $\mu$J/pulse in the 2mm diameter interaction region (we are unable to make accurate measurements of such low powers). The photolysis radiation was gently focused through a 1m baffled arm, to give a spot diameter of about 2mm at a distance of 5mm in front of the nozzle tip. The counter propagating probe laser beam diameter was smaller than the region that was being photolysed.

A pulse delay unit was used to trigger both lasers with the photolysis laser arranged to fire 50-100 nsec before the probe pulse. The signal from the PMT was averaged with an SRS Box Car (SR250) using, as mentioned above, a gate width of 1.5$\mu$s. The box car was triggered from the probe laser with the integration gate delayed by 40nsec to further reduce interference from scattered laser light. The output of the box car was digitised and recorded on a BBC microcomputer along with a measurement of the probe and photolysis laser powers. The dye laser was scanned at a rate of about 0.1nm/min with both lasers operating at a repetition rate of 20Hz. The box car integrators were set to average over 10 laser shots. As it is very easy to saturate the OH LIF signal a set of identical filters was used to check the linearity of the fluorescence with the probe laser power.

## 3 Results

The OH rotational distributions were recorded following 266nm photolysis and a typical LIF spectrum is shown in Figure 1. The normalised line intensities corrected for the transition strengths[12], pump and probe laser powers and any change in the concentration of HOCl during the experiment, were then used to derive the relative populations of the OH rotational, spin-orbit and lambda doublet states.

## 4 OH fragment alignment

The line strengths of the OH rotational transitions are sensitive to the quadrupole moment alignment parameter $A_0^{(2)}$ [13] [14]. The $A_0^{(2)}(J)$ moment can be estimated from the ratio of the intensities of the main and accompanying satellite line originating from the same lower level. However the poor resolution of the dye laser used (0.5cm$^{-1}$) and the relatively large Doppler width arising from the high degree of translational excitation means that it was very difficult to resolve the satellite transitions other than in the $R_1$ branch. The satellite $R_{12}(J)$ transitions are essentially "Q-like" and any bulk alignment will have a different effect on these transitions than it does on the main transition. However since both transition originate from the same lower level the population derived from either must be the same, thus the alignment parameter can be estimated.

The influence of the alignment term is also sensitive to the geometry and polarisations used in the experiment, and it has been shown[15] that a weighted average of the distributions recorded in our experiments with horizontally and vertically polarised photolysis radiation is indepedndent of the alignment. These allows the population rations to be extracted and the value of the alignment to term to be determined.

## 5 OH rotational distribution

The OH rotational distribution from HOCl photodissociation can be approximated by a Boltzmann distribution, as shown in Figure 2 for the experiment with 250torr of Ar. The log of the population corrected for the (2J+1) rotational degeneracy is plotted against the energy of the rotational level, with the energy zero taken as the lowest level of the $^2\Pi_{3/2}$ state. The "temperature" of the rotational distribution falls significantly as the Ar pressure is increased (with the consequent improved cooling of the parent HOCl in the supersonic expansion). The photolysis of HOCl shows a definite preference for populating the lower energy $^2\Pi_{3/2}$ spin orbit state of the OH radical. The lambda doublet state populations can be probed even with a low resolution laser system because the selection rules imply that for a $^2\Sigma$ - $^2\Pi$ transition the Q branches probe only the $\Pi(A")$ lambda doublet component while the P and R branches probe the other $\Pi(A')$ component. The lambda doublet states are distinguished here by their symmetry with respect to reflection in the plane of rotation [16]. The $\Pi(A')$ component is favoured increasingly at higher rotational quantum number. A similar conclusion is again obtained for all the expansion conditions studied.

## 6 Discussion

Hypochlorous acid belongs to the $C_s$ point group with an equilibrium has a bond angle of 102.4°, an OH bond length of 1.83$a_0$ and OCl bond length of 3.194$a_0$ [17]. The electronic configuration of the ground state $X\,^1A'$ is $(1a')^2...(4a')^2(1a")^2(5a')^2...(8a')^2(2a")^2(9a')^2(10a')^2(3a")^2$. The prediction of *ab initio* SCF-CI molecular orbital calculations [5, 10] are that there is an absorption band at 276nm characterised as the promotion of a 3a" electron to the anti-bonding 11a' orbital, giving a $^1A"$ - $^1A'$ transition. Deeper in the uv at 219nm there is a $^1A'$ - $^1A'$ transition arising from the promotion of one of the 10a' electrons to the same anti-bonding orbital. Both these transitions are essentially excitation of a non-bonding chlorine p orbital to an anti-bonding sigma orbital, which is mainly a p orbital on the oxygen atom and directed in the molecular plane. The transition moment for the $^1A'$ - $^1A'$ excitation is predicted to be more than an order of magnitude larger than that for the $^1A"$ - $^1A'$ transition.

The lack of any observable transitions from OH(v=1) together with the relatively cold rotational distribution indicates that the majority of the energy released in the photolysis is deposited into relative translational motion giving a velocity of up to about 4000ms$^{-1}$. The bond length of the OH in the parent molecule is 0.975 Å [17] and is very similar to the bond length of the OH radical (0.97 Å ); the essentially exclusive production of the ground vibrational state is not surprising. The *ab initio* calculations show that the excited state surfaces are bound in the OH coordinate with the same equilibrium bond length as in the ground state. These surfaces are however strongly repulsive along the OCl coordinate; such a dissociation path will give vibrationless products as observed experimentally.

The maximum amount of product rotational energy observed is about 2000cm$^{-1}$, with the average disposal into rotational motion, given by $kT_{rot}$ ranging from for no Ar to 350 cm$^{-1}$ for 250torr of Ar. There are a number of different processes that can lead to rotational excitation. Rotational energy transfer from the parent molecule to the diatomic product is thought to give little product rotational excitation in the photodissociation of HONO but may account for the change in $T_{rot}$ with increasing cooling of the HOCl parent as the Ar pressure is increased.

The most probable origin of the rotational energy is by transfer of vibrational energy of the HOCl modes (the HOCl angle bending and Cl-O stretching vibrations) into OH rotation. These two vibrations will give rise to the rotation of the OH fragments in the plane of the

molecule. The amount of vibrational energy transferred into rotatior can be evaluated by calculating the kinetic energy associated with the rotation of the diatomic unit in the molecule during the bending vibration $\nu_2$ and the kinetic energy associated with the vibrationa motion. A method has been described by Wilson *et al.* [18] which in the case of an angle bending vibration uses an internal coordinate $\phi$ (the valence angle) to derive the components of the displacemen vectors of each atom of the triatomic molecule. A very simila calculation has been performed for HONO [8]. The rotational energy of OH unit which is transformed into that of the fragment OH from the $\nu_2$ vibration is 277 $cm^{-1}$; this is very close to the value obtained for $T_{Rot}$ with the "cold" HOCl beam (high pressure of Ar).

## Conclusion

A relatively cold nascent OH rotational distribution has been observed following the photolysis of HOCl at 266nm this is consisten with the *ab initio* potential energy surface calculations and the quantum mechanical dynamics. The lower energy spin-orbit state is found to be more populated and a distinct preference is observed fo the $\Pi(A')$ lambda doublet levels. The later preference is consisten with the excitation populating the anti-bonding 11a' orbital and the rotational motion of the OH being in the molecular plane.


## Acknowledgments

We thank the SERC Rutherford-Appleton Laboratory Laser Facility for the loan of lasers and additional electronic equipment used in this investigation. AJB would like to thank the SERC for the award of a studentship. PRP would like to thank the British Council for partial support during this investigation.


## References


1. W.C. Fergusson, L. Slotin and D.W.G. Style, 956, (1936).
2. L.T. Molina and M.J. Molina, J. Photochem., 15, 97, (1981).
3. E.A. Mishalanie, C.J. Rutkowski, R.S. Hutte and J.W. Birks, J. Phys. Chem., 90, 5578, (1986).
4. L.T Molina and M.J. Molina, J. Phys. Chem., 82, 2410, (1978).
5. R.L. Jaffe and S.R. Langhoff, J. Chem. Phys., 68, 1638, (1978).
6. G. Hirsch, P.J. Bruna, S.D. Peyerimhoff and R.J. Buenker, Chem. Phys. Lett., 52, 442, (1977).
7. M.J. Molina, T. Ishiwata and L.T. Molina, J. Phys. Chem., 821, 84, (1980).


Figure 1 OH LIF Spectrum 250 torr Ar

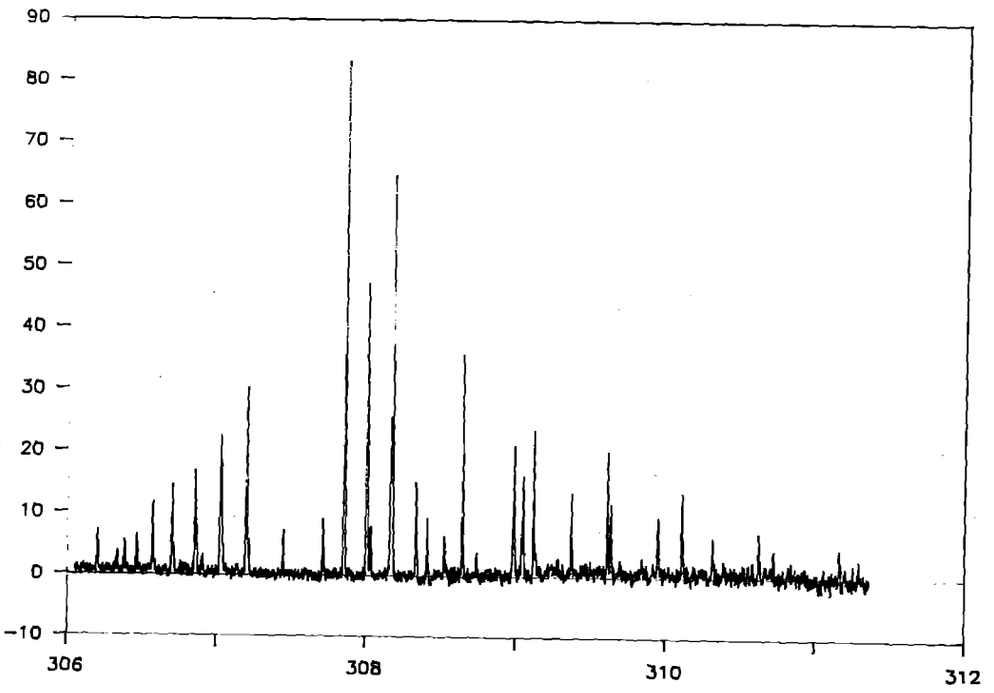

8. H.E. Gillis Singbeil, W.D. Anderson, R. Wellington Davis, M.C.L. Gerry, E.A. Cohen, H.M. Picket, F.J. Lovas, and R.D. Suenram, J. Mol. Spectrosc, **103**, 466, (1984).

9. C.M. Deeley and I.M. Mills, J. Mol. Spectrosc., **114**, 368, (1985).; R.L. Sams and W.B. Olson, J. Mol. Spectrosc., **84**, 113, (1980).

10. M.D. Morse and K.F. Freed, J. Chem. Phys., **78**, 6045, (1983).

11. D. Colbourne, D.C. Frost, C.A. McDowell, and N.P.C. Westwood, J. Chem. Phys., **68**, 3574, (1978).

12. I.L. Chidsey and D.R. Crosley, J. Quant. Spectrosc. Radiat. Transfer, **23**, 187, (1980); J.A. Coxon, Can. J. Phys., **58**, 933, (1980).

13. C.H. Greene and R.N. Zare, J. Chem. Phys., **78**, 6741, (1983).

14. R.N. Dixon, J, Chem. Phys., **85**, 1866, (1986).

15. R. Vasudev, R.N. Zare and R.N. Dixob, J. Chem. Phys., **80**, 4863, (1984).

16. M.H. Alexander, P. Andresen, R. Bacis, R. Bersohn, F.J. Comes, P.J. Dagdigian, R.N. Dixon, R.W. Field, G.W. Flynn, K.-H. Gericke, E.R. Grant, B.J. Howard, J.R. Huber, D.S. King, J.L. Kinsey, K. Kleinermans, K. Kuchitsu, A.C. Luntz, A.J. McCaffery, B. Pouilly, H. Reisler, E.W. Rothe, M. Sahpiro, J.P. Simons, R. Vasudev, J.R. Wiesenfeld, C. Wittig and R.N. Zare, J. Chem. Phys., **89**, 1749 (1988).

17. A.M. Mirri, F. Scappini and G. Cazzoli, J. Mol. Spec. **38**, 218, (1971).

18. E.B Wilson, J.C Decius and P.R Cross, Molecular Vibrations, McGraw-Hill, New York, (1951).

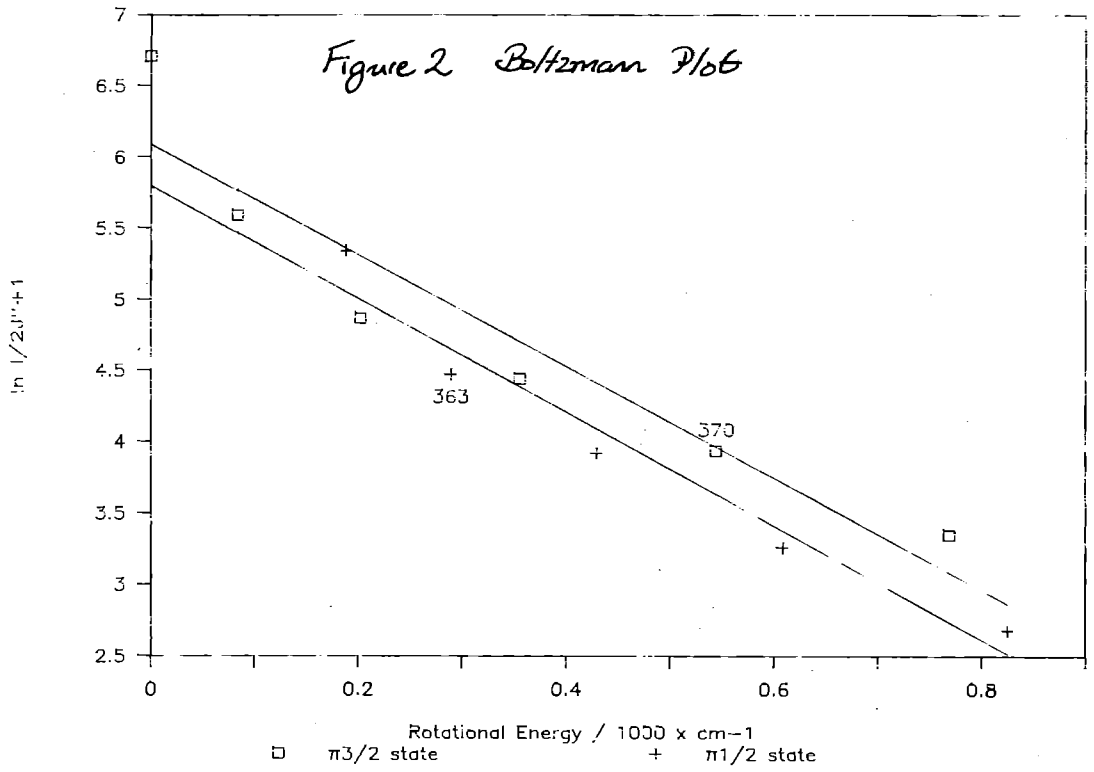

# VAN DER WAALS MOLECULES CONTAINING RADICALS

Colin M. Western

University of Bristol

## INTRODUCTION

The aim of the current study is to characterize a supersonic nozzle design including a discharge to generate cold free radicals in a molecular beam with the aim of looking for van der Waals molecules of simple radicals. This is much simpler than most previous work on species such as ArOH[1] which have required two lasers though Jouvet et al[2] have taken spectra of ground state XeCl using a discharge.

## EXPERIMENTAL

The pulsed nozzle design used in this study is shown in figure 1. It consists of a 1 cm thick plastic (Delrin) endpiece mounted on a fuel injection valve. The endpiece has a 1.5 mm diameter hole through it which carries the gas; half way through the gas meets a pair of tungsten electrodes. In operation a high voltage pulse (500 - 2000 V, ~5 μs) is applied as the gas pulse passes the electrodes. The gap between the electrodes was kept small (<0.5 mm) to minimize the energy deposited in the gas and thus the light from the discharge which would otherwise obscure the laser induced fluorescence.

The nozzle was mounted on a small can evacuated by a roots blower/rotary pump combination to give on operating pressure of a few mTorr. The expansion was probed ~2 cm from the nozzle by laser induced fluorescence using the Spectron Nd:YAG and Quanta Ray PDL-2 combination from the loan pool.

## RESULTS

The A-X transition of OH could readily be seen by discharging a mix of $H_2O$ in Ar. The OH produced was cold; under most conditions the spectrum consisted of just four rotational lines, all that are allowed from the lowest level. A better demonstration of the low temperature achieved was the production of the van der Waals molecule ArOH[1]; to see this required a very dilute mix: 1:4000 $H_2O$:Ar, presumably to minimize water clusters.

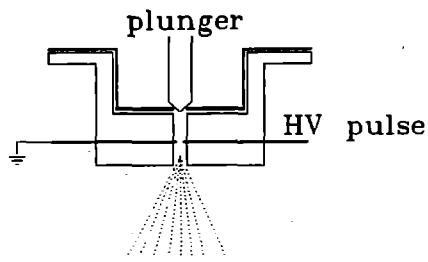


Figure 1: The discharge nozzle.

LIF spectra of the A-X transition of NH were also easily obtained using $NH_3$ instead of $H_2O$, as shown in figure 2. The observed intensities suggest a temperature below 10K though the temperature in the center of the jet may be much lower as no attempt was made to select fluorescence from the coldest part of the jet.

Extensive searches were made around the origin band of the A-X transition of NH for van der Waals complexes. No firm evidence for complexes were seen, though some unidentified lines were observed (see figure) that only became visible at the lowest temperatures.

## CONCLUSION

The discharge nozzle described here is an excellent source of cold free radicals, cold enough even for van der Waals molecules.

## ACKNOWLEDGEMENT

I would like to thank the Royal Society for a 1983 University Research Fellowship

## REFERENCES

1. W M Fawzy et al. J Chem Phys **89** 7030 (1988) and M T Berry et al. Chem Phys Lett **153** 17 (1988).
2. C Jouvet et al. Chem Phys Lett **156** 569 (1989)

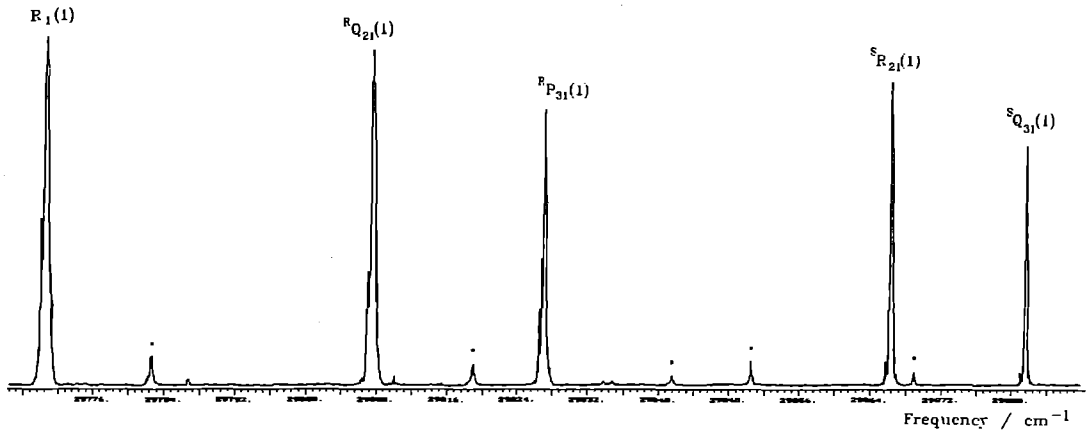


Figure 2: Part of the A-X transition of NH taken in a supersonic jet. The stars mark features not due to NH.

# PHOTOSENSITISERS FOR CANCER THERAPY

D. Phillips[1], A. Beeby[1] and A. J. Langley[2]

[1]Chemistry Department, Imperial College, London.
[2]Rutherford Appleton Laboratory.

## INTRODUCTION

Sulphonated aluminium phthalocyanines have received a great deal of interest as sensitisers for the photodynamic treatment of tumours. Their photoxicity is believed to be mediated by $^1O_2$, which is generated by energy transfer from the electronically excited dye molecule to ground state $O_2$, thus an understanding of photophysical properties of the excited state is critical if the biological activity of the sensitiser are to be understood and optimised. The phthalocyanines are photostable in aqueous or methanolic solution but are known to photodegrade *in vivo*, possibly due to oxidation by $^1O_2$ or by electron transfer reactions with the trypyophan or tyrosine residues of proteins. The streak-camera experiments were carried out in order to study the fluorescence of the sensitiser in the presence of proteins in a single shot, therefore removing any effects caused by degradation products. It is known that these sensitisers may bring about the photooxidation of residues within the proteins.

## EXPERIMENTAL

The phthalocyanines may be pumped by either UV or visible radiation; an excitation wavelength of 650nm was chosen since this is used for the *in vivo* studies. Experimentally this is more complex since the amplified pulses of up to 800μJ per pulse are superimposed upon the 82MHz train of pulses from the synchronously pumped dye laser. To reduce sample photolysis a narrow time window around the 10Hz amplified pulses was selected by a mechanical shutter synchronised with the Q-switched laser. The phthalocyanines fluoresce in the range 680-800nm, beyond the sensitivity of the streak-tube in the Hadland Imacon-500 streak camera, therefore the Delli-Delti streak camera with an extended red response photocathode was used instead. The experimental layout is displayed in fig. 1.

## RESULTS AND DISCUSSION

Single shots of the phthalocyanines in aqueous solution were somewhat noisy, making the fitting of a decay difficult. Co-addition of 24 'binned' images gave data with an acceptable signal to noise ratio; aqueous disulphonated aluminium phthalocyanine showed a single exponential decay with a lifetime of 5ns. From steady state fluorescence and single photon counting studies we have found that in the presence of 100μMol $dm^{-3}$ of human serum albumin, (HSA), the disulphonated aluminium phthalocyanine is completely bound to the protein.

Co-added fluorescence decays from these solutions were indistinguishable to those from the aqueous solution. Individual single shots were noisy, preventing any meaningful shot-to-shot comparisons to be made, and hence the formation and effects of photodegradation products could not be observed.Single photon counting experiments on these phthalocyanine/HSA solutions have shown that the decay is really bi-exponential; $\tau_1 \approx 0.9$ns, $\tau_2$=5.6ns, $A_1$=0.1, $A_2$=0.9. Visually the decay is very similar to that observed from aqueous solution but the better statistical quality of the single photon counting data shows that a single exponential fit is not adequate. These results have been interpreted in terms of two binding sites within the HSA, and this is supported by time dependent fluorescence anisotropy studies.

## CONCLUSION

The raw data obtained from the streak camera system requires many corrections in order to compensate for several instrumental factors, eg. CCD noise, CCD sensitivity, image distortions and the non-linear streak speeds. These result in somewhat noisy data sets which are susceptible to systematic errors and instrumental artifacts. The signal to noise ratios may be improved by the co-addition of many 'binned' images although the fitting of multi-exponential decays to the data is limited because of the poor statistical quality.

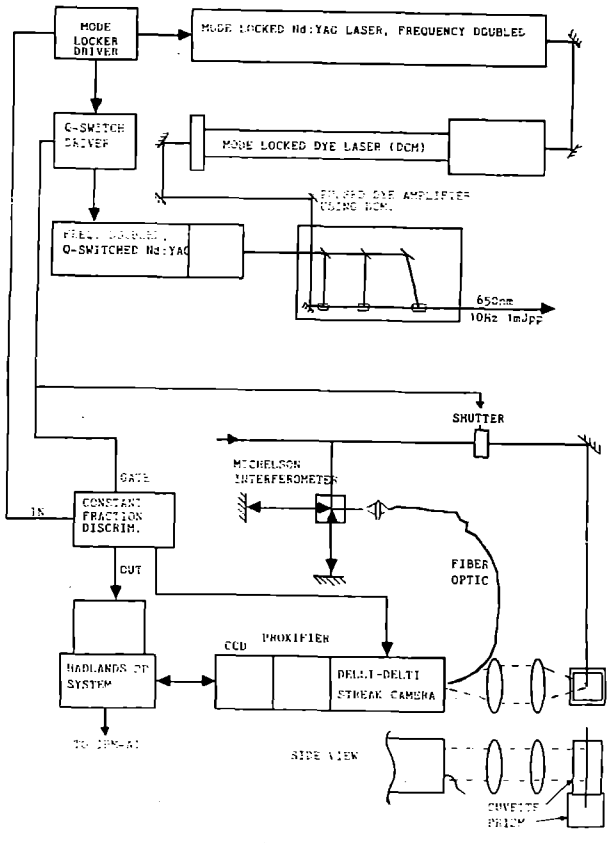


FIGURE 1 EXPERIMENTAL LAYOUT

# PICOSECOND PUMP-PROBE LASER FLASH PHOTOLYSIS OF MODEL PHOTOGRAPHIC PRODUCT DYES AND PHOTOCHROMIC MATERIALS

D.R. Worrall, M. Naftaly and F. Wilkinson

Department of Chemistry, University of Technology, Loughborough, Leicestershire LE11 3TU

## MODEL PHOTOGRAPHIC DYES

### INTRODUCTION

In the course of investigating the photodegradation mechanism of azomethine photographic product dyes, we have conducted pump-probe experiments in the picosecond time domain on both di-n-butyl phthalate (DBP) and methanol solutions of a model pyrazalotriazole (PT) azomethine dye. This dye gives a transient absorption when subjected to nanosecond flash photolysis which decays with a lifetime of the order of 300 microseconds, and which may be attributable to isomerisation about the azomethine linkage. No transient absorption attributable directly to an electronically excited state of these compounds is seen with nanosecond flash photolysis, although there is evidence to suggest that the isomerisation proceeds via the triplet state[1]. The structure of the model PT dye is shown in figure 1. Rotation about the azomethine linkage is postulated as giving rise to very rapid relaxation of electronic excitation energy, with the result that such compounds are very light stable.

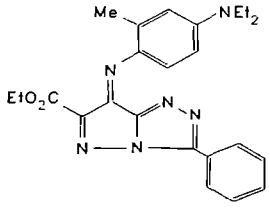


Figure 1: model pyrazalotriazole (PT) azomethine dye

### RESULTS

DBP and methanol solutions of the model PT dye (concentration 4 x $10^{-6}$ M) were investigated using picosecond pump-probe laser flash photolysis, exciting at 584nm (4 ps, 5$\mu$J pulse) and probing between 610nm and 680nm using a picosecond continuum. Pumping a methanol solution at 584nm gave rise to an increase in transmission at 610nm of about 7%, which rapidly decayed with a half-width of approximately 8ps to a point a little below the pre-coincidence baseline, suggesting the presence of a long-lived species having slightly greater transmission than the ground state at this wavelength. A similar decay is obtained from excitation of a DBP solution of the same material under identical conditions, but here the decay is a little longer (Figure 2(a)). The viscosity of DBP is approximately 30 times that of methanol, and hence if we are probing an

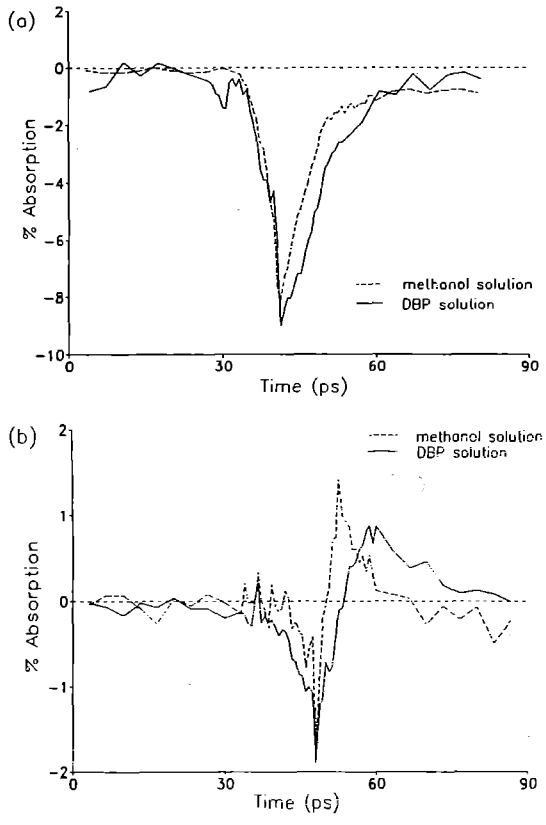


Figure 2: transients observed with (a) 610nm probe and (b) 640nm probe

electronically excited state which relaxes via isomerisation then a longer decay in DBP is expected. This is, so far as we are aware, the first observation of transients of this kind in these compounds. Similar but smaller changes are seen probing at 620nm.

Probing at 640nm produces a somewhat unexpected result, in that initially a small depletion is seen which rapidly becomes an absorption before decaying back to the baseline, the whole transient in methanol solution spanning a time period of only 40ps, while in DBP it is again slightly longer (figure 2(b)). It is difficult to rationalise this on the basis of only one decaying species, and if this effect is due to the photophysics in solution a more complex decay scheme involving more than one intermediate must be postulated. The possibility of it being an instrumental artefact cannot be discounted, however, and further investigations are required.

Excitation of both DBP and methanol solutions of the PT dye (4 x $10^{-6}$ M) at 584nm gives rise to small (< 1%) ps transient absorptions at wavelengths greater than 640nm.

PHOTOCHROMICS

Many classes of organic compounds exhibit the phenomenon of photochromism, i.e. a reversible transition of a chemical species between two isomers possessing appreciably different absorption spectra, such transition being induced by photonic excitation. The photochromic compounds studied in the present experiment were spiro-oxazines. These compounds are particularly stable and can undergo photocolouration reversibly several thousand times without suffering appreciable degradation. They thus offer rich possibilities in nonlinear optical applications. Figure 3 shows the general structure.

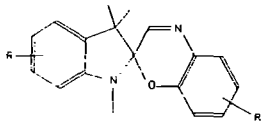

Figure 3: General structure of spiro-oxazines

The colouration mechanism is as follows. The the two halves of the "closed" spiro form of the molecule are arranged in mutually perpendicular planes: as a consequence the molecule absorbs in the near UV (300-400 nm). The photoinduced reaction cleaves the central C-O bond, thus allowing parts of the molecule to rotate so as to achieve near-planar configurations. These "open" merocyanine forms have a characteristic absorption band in the visible region around 590 nm.

Previous nanosecond laser photolysis experiments have established that the colouration is complete within 10 ns. Other workers using similar compounds and employing picosecond excitation[2] showed that the reaction proceeds via one or more intermediate excited non-merocyanine stages and through several unstable isomers of merocyanine corresponding to different angles of rotation about the central bond. The reaction is solvent dependent and is expected to develop differently in a solid matrix. The coloured form has a lifetime of many seconds, depending on compound, solvent and temperature.

In performing the experiment we were interested in clarifying the features of this reaction and elucidating its precise mechanism.

Three photochromic compounds having different substituents were used. The measurements were carried out on $10^{-5}$M solutions in toluene. A flow cell was used to remove the coloured material from the probe path between shots. The pump and the probe were respectively at 295 nm and 590 nm. The pump wavelength was somewhat shorter than we would have wished: the compounds absorb better at 350 nm; moreover, at 295 nm the absorbance of toluene becomes significant. The probe wavelength, however, was placed ideally at the absorbance peak of the coloured species.

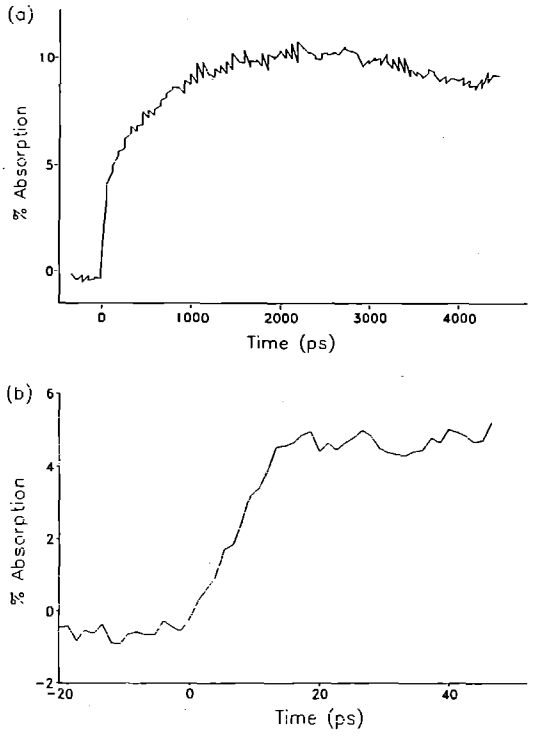


Figure 4: Colouration growth in a spiro-oxazine: pump 295nm, probe 590nm: a) entire rise; b) the fast portion only.

RESULTS

Figure 4a demonstrates the growth in absorption following the pump pulse in one of the photochromics used in the experiment. Figure 4b shows the expanded view of the fast portion of the rise-time curve. Approximately one half of the rise took place within the duration of the pump pulse. Following that, the rest of the rise occupied nearly 1.5 ns. This was true for all three compounds tested, with a slightly different proportion of the entire absorption increase being achieved within the pulse width.

The results obtained demonstrate clearly that photocolouration proceeds in at least two stages. The slow part of the colouration growth may be attributable to the fact the various merocyanine isomers require a relatively long time to rotate to their final position. This could be verified by performing the experiment in solvents of different viscosity: higher viscosity would slow the reaction. The fast portion of the growth curve points to the instantaneous creation of an absorbing intermediate. This may be an excited non-merocyanine isomer, or one or several of the merocyanine forms. Varying the probe wavelength could help to establish which.

REFERENCES

1. W.G. Herkstroeter, J. Am. Chem. Soc., **98**, 330 (1976)
2. S. Schneider et al., Ber. Bunsenges. Phys. Chem., **91**, 1224 (1987)

# LASER PHOTOIONISATION TIME-OF-FLIGHT MASS SPECTROMETRY OF LASER DESORBED POLYCYCLIC AROMATIC HYDROCARBONS

A.C. Jones, G.A. Keenan and P.R.R. Langridge-Smith

University of Edinburgh

## INTRODUCTION

Pulsed laser desorption time-of-flight mass spectrometry is rapidly becoming established as an important mass spectrometric technique. In its most widely used form, sample vapourisation and photoionisation are performed simultaneously using the 4th harmonic of a Nd : YAG laser. This technique can be considerably refined by performing the desorption and ionisation as two separate steps; thus allowing independent optimisation of the two processes, with respect to both laser wavelength and power density. In the present experiments this two stage methodology has been adopted. Pulsed $CO_2$ laser desorption is employed to vapourise involatile or thermally labile molecules without fragmentation or ionisation. The neutral molecules thus produced are then photoionised using UV laser radiation.

## EXPERIMENTAL

The laser desorption time-of-flight mass spectrometer is shown schematically in Figure 1. The apparatus consists of two differentially pumped chambers : the first contains the pulsed molecular beam source and the second forms the ionisation region of the mass spectrometer. The sample of interest is laser desorbed using a pulsed $CO_2$ laser (Pulse Systems LP30) which produces approximately 100mJ of 10.6$\mu$m radiation in a 10$\mu$s pulse. The sample is desorbed from the surface of a stainless steel rod which is mounted with its axis mutually perpendicular to the $CO_2$ laser beam and the pulsed jet. The desorbed molecules are entrained in the helium jet and the resulting molecular beam passes into the second chamber where the entrained neutrals are photoionised. In the present experiments photoionisation was carried out with either 193nm radiation from an ArF excimer laser (Lumonics HE 460) or 266nm radiation from a frequency-quadrupled Nd : YAG (JK Lasers HY750). The resulting ions are mass analysed in a 1.3m linear time-of-flight mass spectrometer equipped with a dual microchannel plate detector. Mass spectra are acquired using a camac-based data acquisition system, employing a transient digitiser with a sampling rate of 100MHz.

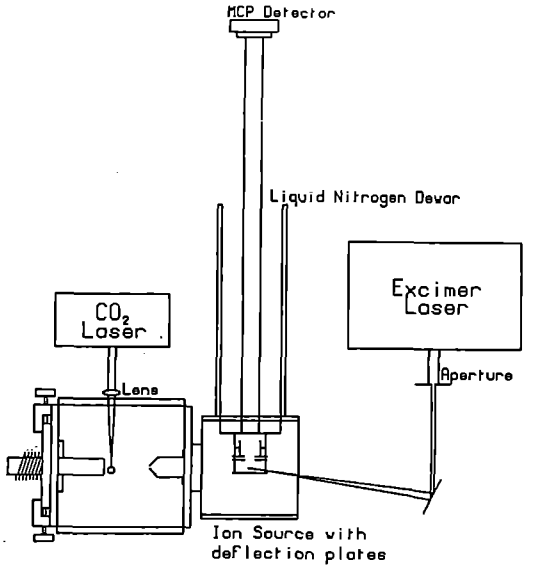


Figure 1 : The laser desorption time-of-flight mass spectrometer.

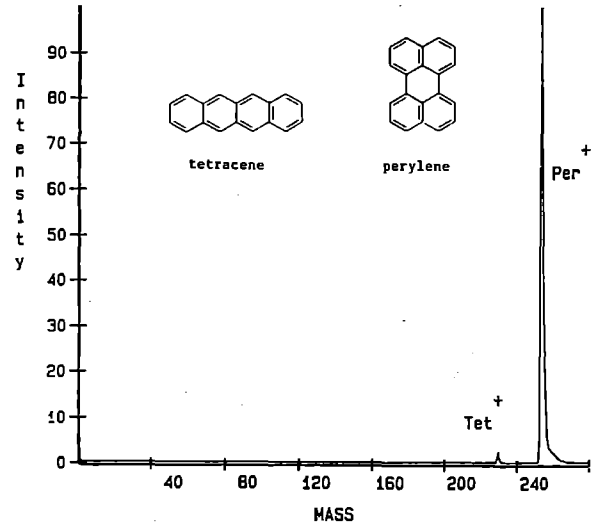


Figure 2 : 193nm photoionisation mass spectrum of an equimolar mixture of perylene and tetracene.

## RESULTS AND DISCUSSION

Mass spectra of the peri-condensed polycyclic aromatics, perylene, coronene and pyrene, and the cata-condensed molecules, tetracene and pentacene, were investigated. The ionisation potentials of these molecules lie in the region of 7eV[1]; photoionisation at either of the wavelengths used is thus a two photon process. In all cases mass spectra recorded under soft ionisation conditions contained only the parent molecular ion peak. For the peri-condensed molecules, it was found that photoionisation at 193nm resulted in much greater detection sensitivities than were obtained by photoionisation at 266nm. This is due to a strong 1 photon absorption to a high lying excited electronic state[2] which results in efficient resonant or near-resonant (1+1) photon ionisation. Detection limits as low as 10fmoles were thus obtained. In the case of perylene, the high lying resonant state can be identified with the $^1B_{2u}$ ($S_6$) state observed in condensed phase absorption spectra[3]. The cata-condensed molecules do not possess a strong absorption in the 193nm region and therefore do not exhibit this pronounced resonance enhancement. The marked difference in ionisation efficiencies, for the two classes of molecules, is illustrated in Figure 2 which shows the 193nm photoionisation mass spectrum of an equimolar mixture of perylene and tetracene.

## REFERENCES

1 R.Boschi et al, J.Chem.Phys. 60 4406 (1974)
2 Y.Kumura et al, Chem.Phys.Lett. 30 35 (1975)
3 K.Fuke et al, J.Mol.Spectrocs. 63 98 (1978)

# PHOTODISSOCIATION STUDIES USING AN ION TRAP MASS SPECTROMETER

C.S. Creaser, M.R.S. McCoustra, D.S. Mitchell, K.E. O'Neill

School of Chemical Sciences
University of East Anglia
NORWICH NR4 7TJ, UK

## INTRODUCTION

The three dimensional ion trap was first described by Paul and Steinwedel[1] in 1960. It consists of a three electrode system, having two end-cap electrodes and a ring electrode. These hyperbolic electrodes create a three dimensional quadrupole field in which ions are trapped by the application of RF, or combined RF and DC, voltages to the ring electrode. The stability of an ion in the ion trap depends upon its mass to charge ratio and the magnitude of the applied voltages. The conditions may be adjusted to enable ions of a single mass to charge ratio to be stored, whilst all other ions are unstable and exit the trap or impinge upon the sides of the trap. An additional RF or Tickle voltage may be applied across the end-caps at the natural frequency of oscillation of the ion. This causes the ion to resonate with an increasing amount of energy in the z direction, and the resultant collisions with the helium buffer gas present induce fragmentation of the ions. This process is termed Collisionally Activated Dissociation (CAD), and has reported efficiencies of up to 100%.

The ion trap has also been used to study Photodissociation (PD) of a trapped ion population.[2,3] In a conventional mass spectrometer ions are irradiated in a single pass through the laser beam, giving low efficiencies of PD, whereas in the ion trap the possible irradiation period is much longer, leading to higher efficiencies. While direct introduction of the laser into the trap is possible, the use of a fibre optic interface facilitates the introduction of light and has been recently demonstrated.[3]

The aims of this loan were firstly to demonstrate the use of a fibre optic link with a Finnigan MAT Ion Trap Mass Spectrometer (ITMS) for photodissociation studies, and secondly to perform preliminary characterisation of some simple systems that will be more comprehensively investigated in the future.

## EXPERIMENTAL

The ITMS was modified by drilling a hole through the ring electrode into which one end of a 1mm fibre optic (Vulman Ltd.) was inserted. The fibre optic passed into the mass spectrometer vacuum system through a modified probe with an o-ring seal, *via* the vacuum probe lock. The other end of the fibre was used with a three axis delivery system (Vulman Ltd., model FD-1000-2) to optimise alignment with a JK 2000 Nd:YAG Laser and Dye Laser on loan from the Rutherford Loan Pool. The dye laser was used with a solution of Rhodamin 6G (Edinburgh Instruments Ltd.) in methanol (HPLC grade, Aldrich Gillingham Ltd.). The experimental configuration is shown in Figure 1.

A series of alkyl benzenes were investigated using photons of 563nm and 573nm from the dye laser, which was pumped with the 532nm line of the Nd:YAG laser. The alkyl benzenes were admitted from a liquid reservoir using a fine control needle valve. The samples were subjected to five pulses of laser light per scan; the timing of the laser was computer controlled *via* the cavity shutter. Background spectra were recorded under the same conditions but in the absence of laser excitation for each of the alkyl benzenes.

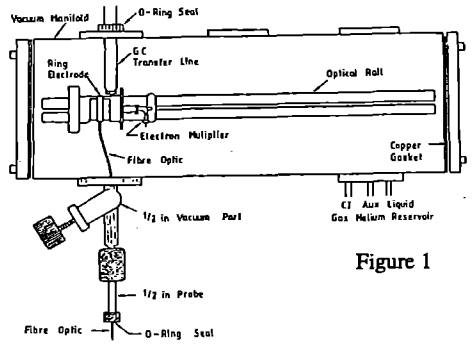


Figure 1

## RESULTS AND DISCUSSION

Preliminary investigations using the fibre optic interface show that photodissociation may be efficiently carried out on the ion trap. The CAD and PD spectra of several alkyl benzenes have been studied. For example, the spectra of the isolated parent ion and the product ions resulting from the process for n-butyl benzene are shown in Figure 2. Differences in the product ions and ion intensities are observed for the CAD and PD processes.

Figure 2

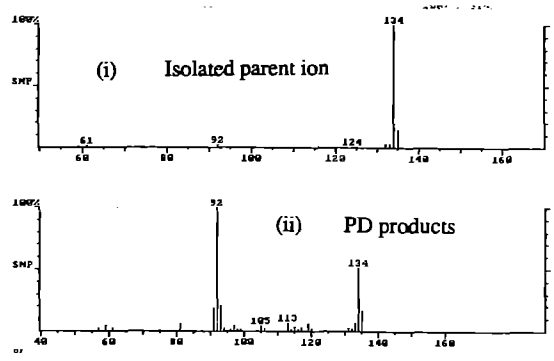


Fragmentation efficiencies of between 57% and 89% were obtained for the butyl-benzene isomers for the photodissociation process, whilst the corresponding efficiencies for the CAD experiment lay between 59% and 99%. The absolute photodissociation efficiencies have, however, proved difficult to determine and need further investigation.

Several difficulties arose during the period of the laser loan. Initial problems with the mass spectrometer hindered our progress. The use of the cavity shutter to control the laser pulses was slow and necessitated the use of a long irradiation period to allow the laser pulses to stabilise. Nevertheless, this preliminary study has shown that photodissociation is possible using the ITMS and a fibre optic interface, and that the fragmentation efficiencies observed are comparable to those obtained by CAD.

In further work, we propose to fit the laser fibre optic at 90° to the current entry point to allow the use of a solid insertion probe and gas chromatography for sample introduction. It is hoped that this will alleviate some of the sample concentration effects observed in the study. We also propose to employ an external mechanical shutter to control the irradiation.

## REFERENCES

1. W. Paul, H. Steinwedel, US Patent 2, 939, 952, (1960).
2. R.J. Hughes, R.E. March, A.B. Young, *Can. J. Chem.*, **61**, 824-833, (1983).
3. J.N. Louris, J.S. Brodbelt, R.G. Crooks, *Int. J. Mass Spectrom. Ion Proc.*, **75**, 345-352, (1987).

# LASER EXCITATION SPECTROSCOPY OF INVOLATILE SOLIDS IN MOLECULAR BEAMS

J.M.Brown[1], I.R.Beattie[2], F.J.Grieman[3], S.H.Ashworth[1] and D.A.Fletcher[1]

[1]Oxford University
[2]Southampton University
[3]Pomona College, California, U.S.A.

Many first row transition elements can be vapourized to give a few Torr pressure at high temperatures around 1000°C. In our experiment molecules are seeded into a high pressure (several atmospheres) of an inert gas, followed by expansion through a jet into a rapidly pumped vacuum system. In this way the rotational and to a lesser extent vibrational energy is converted into translational energy. Such an isentropic expansion results in rotationally cold molecules ( 10K). The jet is irradiated with the beam of a narrow band tunable dye laser and the resultant fluorescence recorded (laser excitation spectroscopy). The excimer pumped dye laser at the LSF has been used in this way to record survey spectra of several species. It has even been possible , in favourable cases, to resolve rotational structure without the intra-cavity etalon.

Two separate visits have been made to the LSF in the current year to carry out experiments of this type. Spectra of $NiCl_2$, $CoCl_2$ and InOH have been recorded and a method for calibration using the optogalvanic effect has been developed. This allows calibration with greater absolute accuracy than previously obtainable.

For calibration the laser radiation is directed into the plasma in the centre of the cathode of an iron hollow cathode lamp. Resonant transitions of any of the plasma species results in a change in the total ionization cross-section of the plasma. This change results in the lamp either pulling more or less current from the high voltage supply. This is monitored by a capacitor attached to the supply (AC coupled). Generally this results in a change of about 50mV which is readily detectable with the boxcar averaging system. The signals observed are mainly from neon, one of the components of the filler gas. The operating current of the lamp is not high enough to sputter sufficient iron to produce appreciable iron signals. Fitting the data shows that the laser scan is linear to 1 part in 1000 of the step size used in burst scanning mode (Step 0.0025 nm). Not all of the transitions which are possible are observed using the optogalvanic effect. To aid future assignments of the transitions we are building up an atlas of lines showing the air wavelength of the assigned transitions. (Figure 1)

Modifications to the nozzle source have meant that the molecules are prepared significantly cooler than before. This has lead to a dramatic simplification of the spectrum of $NiCl_2$ in the 460 nm region. (Figure 2) This confirms our previous assignments[1] and in addition allows us to identify transtions to states with 2 quanta of the upper state bending vibration excited. Consequently we can determine the upper state bending frequency as 60.5 $cm^{-1}$.

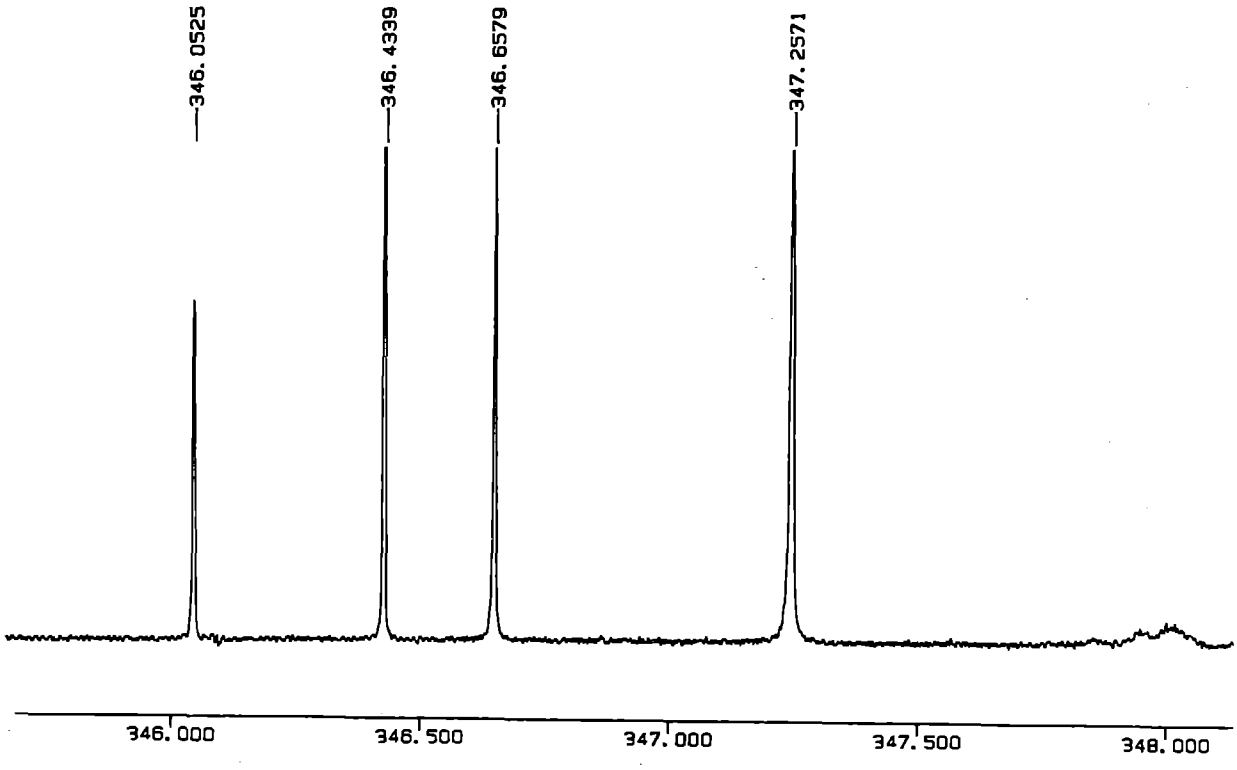


Figure 1. A page of the optogalvanic atlas showing four assigned neon transitions.

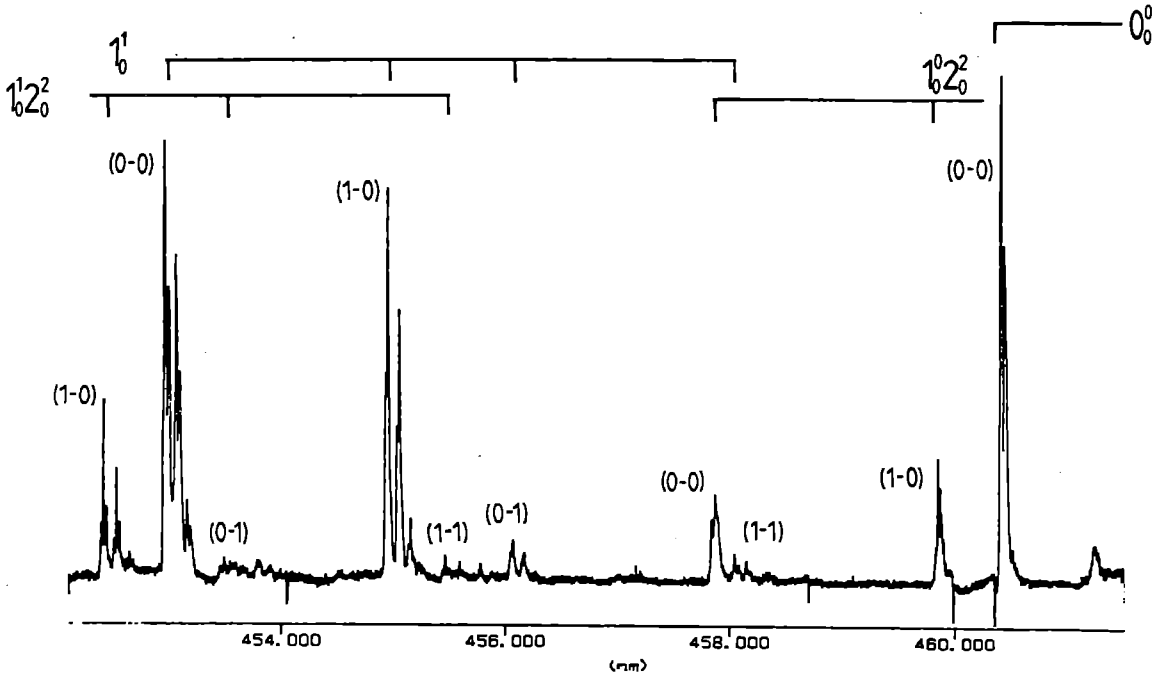


Figure 2. A region of the 460nm band system of $NiCl_2$. Each feature represents a vibrational band or spin component $^{35}Cl/^{37}Cl$ isotope structure can easily be seen on the bands to shorter wavelength.

A similar dramatic simplification was not observed when part of the 360nm system of $NiCl_2$ was calibrated. This lends weight to the assignment of these bands as (v=0-0) bands. The extra cooling was, however, noticeable. Features generally became much sharper and changed relative intensity and the signal to noise ratio was better.

The additional cooling was also apparent in the case of $CoCl_2$. The effect on the spectrum was again dramatic. Many features hitherto not observed were resolved and the spectrum proves to extend beyond our previous measurements at the long wavelength end. The spectrum also becomes much simpler in this region.

Preliminary work was carried out on the spectrum of InOH. These bands have not been reported previously. InOH is formed in the reaction of In with $H_2O_2$ at about 800°C. Unfortunately an inherent problem with this system is nozzle clogging by the refractory by-product of the reaction, InO. Several bands were observed in the near UV (≈340 nm) with rotational fine structure without having to use the intracavity etalon. (Figure 3)

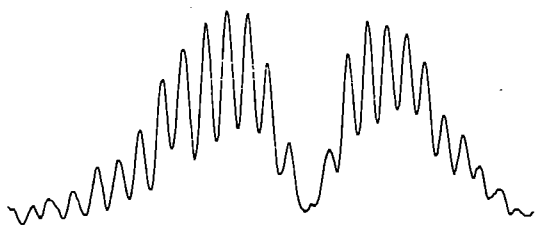

Figure 3: A vibrational band showing rotational structure in the electronic spectrum attributed to InOH. The rotational temperature is about 15K.

Analysis of all these systems is currently under way but further work is necessary particularly on the InOH systems. Diagnostic tests, including isotopic substitution, must be carried out to confirm that InOH is on fact the carrier of the spectrum. We also propose to extend our observations to shorter wavelength and re-record the bands using the intracavity etralon in order to try to resolve In isotope shifts. This will aid the vibrational assignments. We also wish to disperse the fluorescence from $NiCl_2$, $CoCl_2$ and $FeCl_2$ and extend the $CoCl_2$ measurements to longer wavelength.

REFERENCES

1. F.J.Grieman, S.H.Ashworth, J.M.Brown and I.R.Beattie *J.Chem.Phys.* (in press).

# FLUORESCENCE SPECTROSCOPY OF INDAN, CATECHOLBORANE AND PHTHALAN IN A SUPERSONIC JET

A. Camilo P. Alves[1], Karim H. Hassan[2], J. Michael Hollas[2] and Philip F. Taday[2]

[1]University of Coimbra, Portugal
[2]University of Reading

## INTRODUCTION

The series of molecules 1,3-benzodioxole (BDO), indan (IND), catecholborane (CB), and phthalan (PHTH), all shown in figure 1, is of great structural interest. The main problem concerning their structure involves the five-membered ring and, in particular,

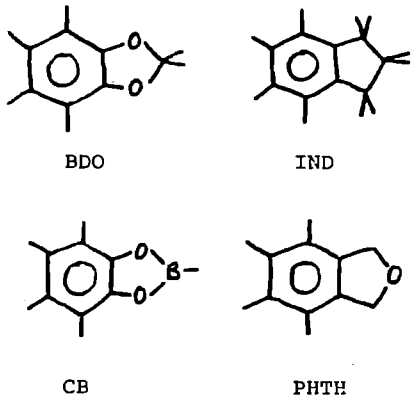


Figure 1: Four molecules whose structures are studied in this work.

whether the three heavy atoms comprising the saturated part of that ring are coplanar with the benzene ring.

Studies of their gas phase far infrared spectra[1,2,3] concluded that, in their ground electronic states $S_0$, BDO[1], CB[3] and PHTH[2] have co-planar skeletal atoms while, for IND[2], the carbon atom in position 2 is puckered out-of-plane with a barrier to planarity of 1900 $cm^{-1}$. Interpretations of the gas phase electronic absorption spectra of BDO[4], CB[4], PHTH[4] and IND[5] were consistent with these conclusions. The spectra of BDO, CB and PHTH all show a nuclear spin intensity alternation with the rotational quantum number $K_a$. That of IND shows a sequence of hot bands in the vibration involving puckering of the carbon atom in position 2. The regular spacing in this sequence, and small splittings with increasing vibrational quantum number, indicate a high barrier in the ground electronic state $S_0$ and a reduced barrier in the excited state $S_1$.

Fluorescence excitation (FE) and single vibronic level (dispersed) fluorescence (SVLF) spectra of BDO[6,7] have shown that, surprisingly, the molecule is twisted into a $C_2$ configuration in $S_0$. One oxygen atom is above and one below the plane of the rest of the skeletal atoms by about 0.16 Å and the barrier to planarity is 157 $cm^{-1}$.

The aim in the work reported here was to use supersonic jet fluorescence spectroscopy to investigate the structures of IND, CB and PHTH.

## EXPERIMENTAL

As for the work reported previously[6] the Quantel Datachrom Nd:YAG pumped dye laser from the Central Laser Facility Loan Pool was used. The dye laser radiation was always frequency doubled into the near ultraviolet and, for the FE spectra, autotracking was necessary. For the supersonic jet, helium carrier gas was used at a backing pressure of about 1.4 atm. A nozzle diameter of 100 μm resulted in rotational and vibrational temperatures of about 10 K and 100 K, respectively.

## RESULTS

INDAN. Figure 2 shows SVLF spectra of IND with excitation in the pure electronic ($0_0^0$)

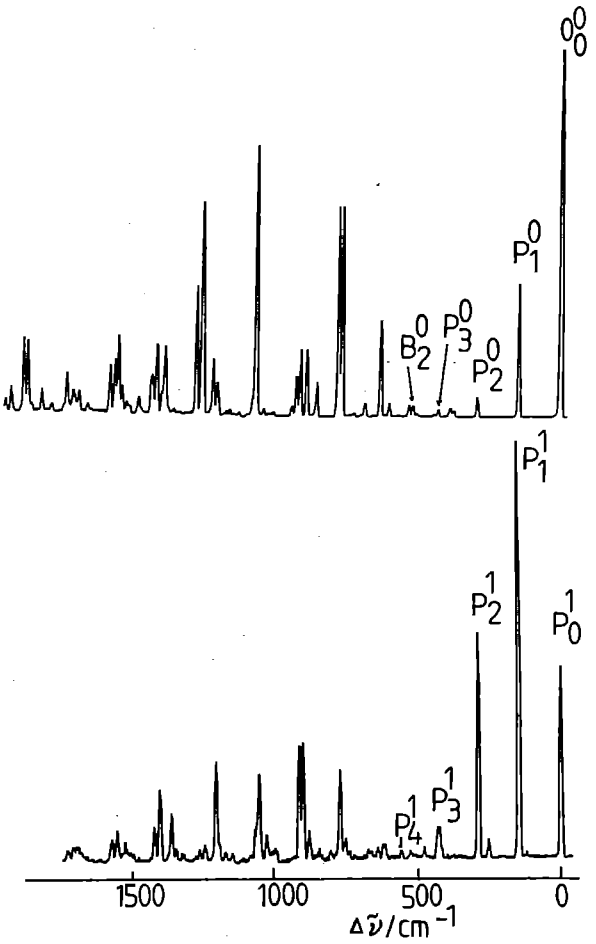


Figure 2: SVLF spectra of indan

band and the $P_0^1$ band, where $\nu_p$ is the puckering vibration of the five-membered ring. Both spectra show transitions with $\Delta v_p$ even and odd. This shows that the vibration $\nu_p$ is totally symmetric and, therefore, that the molecule has a puckered structure with a high barrier to planarity. We have shown that it is puckered in $S_1$ also but with a lower barrier.

CATECHOLBORANE. Figure 3 shows SVLF spectra of CB with excitation in the $0_0^0$ and

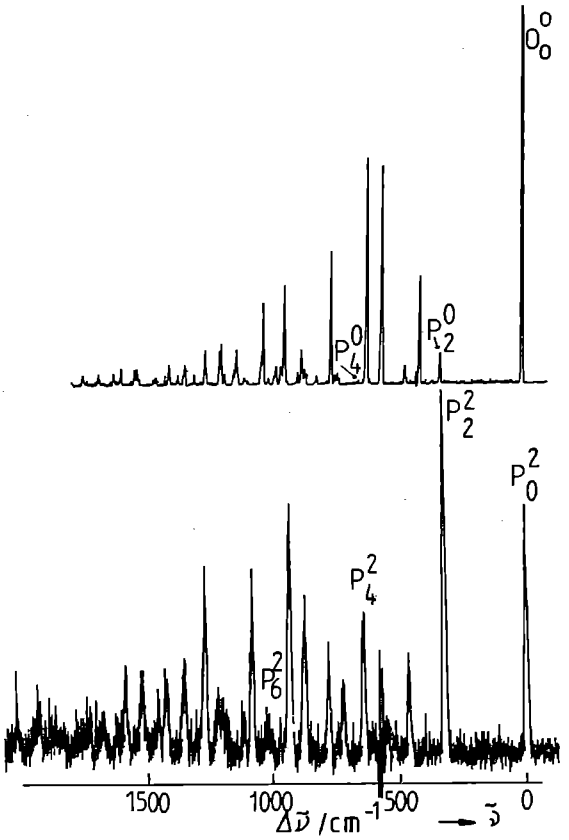


Figure 3: SVLF spectra of catecholborane

$P_0^2$ bands where $\nu_p$ is, again, the puckering vibration of the five-membered ring. In these spectra we observe transitions with $\Delta v_p$ even, only, showing that $\nu_p$ is a nontotally symmetric vibration. The molecule is planar in both the $S_0$ and $S_1$ electronic states. It belongs to the $C_{2v}$ point group and $\nu_p$ is a $b_1$ vibration.

Interpretation of the high resolution absorption spectrum, on the basis of these results, gives the vibrational levels with $v_p$ = 0-3 in $S_0$ and $S_1$ for the isotopomers CB-$^{11}$B and CB-$^{10}$B. These levels have been fitted to a potential function of the form

$$V(x) = Ax^2 + Bx^4 \qquad (1)$$

with A = 70000 cm$^{-1}$ Å$^{-2}$ and B = -95000 cm$^{-2}$ Å$^{-4}$, assuming a reduced mass of 100 u for CB-$^{11}$B, for $S_0$.

PHTHALAN. Figure 4 shows the SVLF spectrum of PHTH with excitation in the $0_0^0$ band. This resembles very strongly the corresponding spectrum[6,7] of 1,3-benzodioxole (BDO, fig.1). The band labelled $23_2^0$ is 92 cm$^{-1}$ from $0_0^0$ and is assigned to two quanta of an $a_2$ twisting vibration involving the $CH_2$ groups. The vibration is very anharmonic and the observed levels have been fitted to the potential function of equation (1) with A = -11600 cm$^{-1}$ Å$^{-2}$ and B = 245000 cm$^{-2}$ Å$^{-4}$ assuming that the reduced mass is 73 u. The potential is W-shaped with a barrier height of 137 cm$^{-1}$. This compares with a barrier height of 157 cm$^{-1}$ in BDO. PHTH

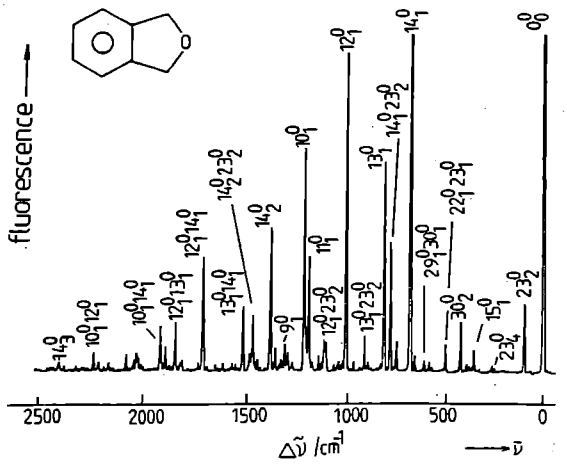


Figure 4: SVLF spectrum of phthalan

has a non-planar, twisted skeleton with the carbon atoms in positions 1 and 3 out-of-plane by about 0.15 Å.

REFERENCES


1. J.A. Duckett, T.L. Smithson and H. Wieser, Chem.Phys.Lett., 64,261(1979)
2. T.L. Smithson, J.A. Duckett and H. Wieser, J.Phys.Chem., 88,1102(1984).
3. T.L. Smithson, R.A. Shaw and H. Wieser, J.Chem.Phys., 81, 4281(1984).
4. A.C.P. Alves, J.M. Hollas and B.R. Midmore, J.Mol.Spectrosc., 77,124(1979)
5. J.M. Hollas and E. Khalilipour, J.Mol.Spectrosc., 66,452(1977).
6. K.H. Hassan, J.M. Hollas, M.Z. bin Hussein and P.F. Taday, Annual Report to the Laser Committee 1989, paper C1.15,285.
7. K.H. Hassan and J.M. Hollas, Chem.Phys. Lett., 157,183(1989).

# HIGH RESOLUTION ELECTRONIC SPECTROSCOPY OF JET COOLED SUBSTITUTED N-PHENYL PYRROLIDINES AND vdW COMPLEXES

Brendan D Howells, T Frank Palmer, John P Simons and Alan Walters

University of Nottingham

## INTRODUCTION

Jet cooling under controlled expansion conditions permits the stepwise growth of size selected solvation clusters and decongests the otherwise impossibly dense spectrum of the host solute molecules.[1] This allows LIF spectroscopy to probe structures via rotational band contour analysis, to identify alternative intramolecular conformers as well as intermolecular cluster geometries and to explore the dependence of solvent induced spectral shifts on the nature and the local structure of the solute-solvent cluster.[2]

The present study investigates the high resolution electronic spectroscopy of pyrrolidinebenzoic methyl and ethyl esters PYRMBE and PYRBEE and the benzonitrile PYRBN The main emphasis concerns the identification and structural analysis of singly and multiply solvated clusters with argon but it has proved possible to resolve individual conformers for the esters and to record spectral data for other solvent clusters.

## EXPERIMENTAL

Experiments were conducted using the pulsed free jet expansion system described elsewhere.[3] The excitation sources used were the Quantel Datachrom Nd.YAG pumped dye laser from the Laser Facility Loan Pool and a Lambda-Physik FL2002 dye laser pumped by a LPX100 excimer laser. The exciting light was frequency doubled to provide radiation in the range 270-350 nm and the laser frequency was calibrated using an iodine reference cell.

## RESULTS AND DISCUSSION

High resolution laser induced fluorescence excitation spectra of PYRBN, PYRBME and PRYBEE and their complexes with argon and a range of other 'solvent' molecules have been recorded under jet cooled conditions. Power saturation studies have confirmed that the doublet structure at the band

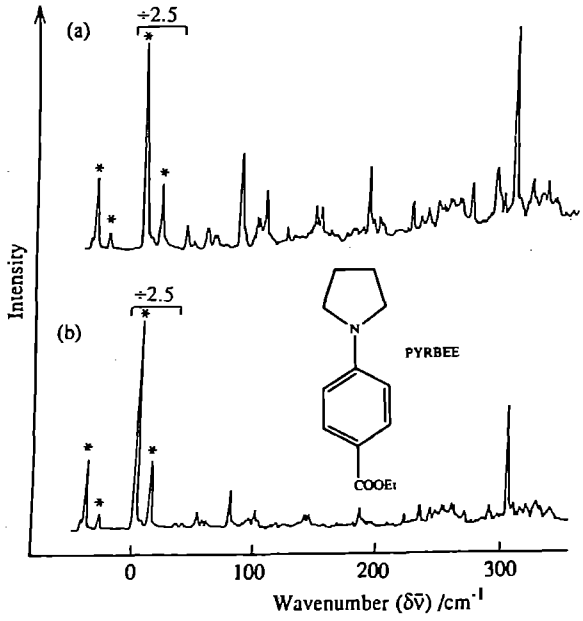


Fig.1 LIF excitation spectra of PYRBEE (a) and (b) low resolution:laser power density (a)/(b) = 100;

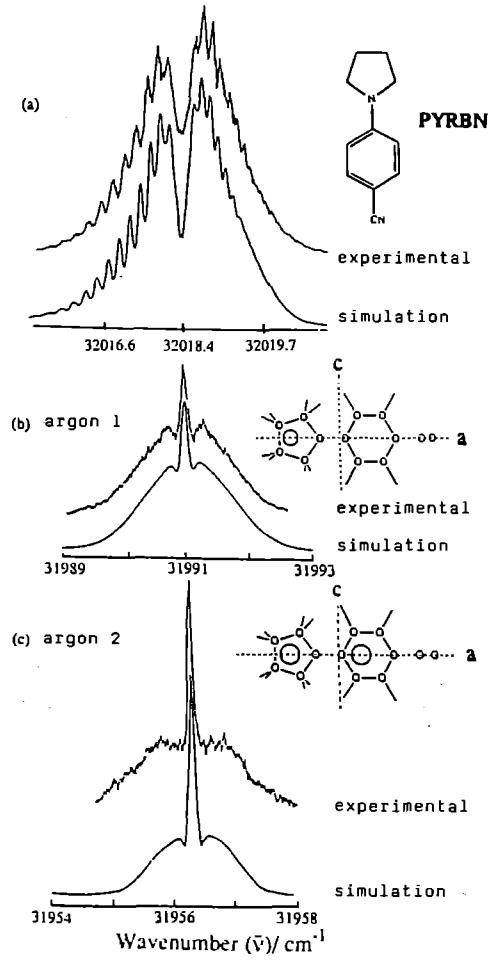


Fig.2. High resolution LIF excitation spectra

origin in the ethyl ester and the weaker singlet and doublet features lying to the red of the band origin in the methyl and ethyl esters respectively are due to the presence of separately stabilised conformers (Fig.1). Since the nitrile PYRBN, shows only a single 0-0 feature, the alternative conformers are likely associated with the ester groups.

Excitation is associated with a short axis polarised $\tilde{A}^1B_2 \leftarrow \tilde{X}^1A$ transition[4] and the origin bands in PYRBN, PYRBME and PYRBEE including their conformers display B type rotational contours. In their vdW complexes with argon the contours are dramatically changed and most complexes display the "P,Q,R" shape characteristic of type C bands, consistent with the siting of argon atoms above (and below) the molecular plane. Rotational band contour simulations have allowed assignment and structural analysis to be completed and optimised results are presented for PYRBN-$Ar_n$(n=0-2) (Fig.2). For nonpolar solvents local site selectivity appears to be the rule. A full report has been presented elsewhere.[5]

## REFERENCES

1. DH Levy Ann.Revs.Phys.Chem. **31** 97 (1980)
2. CA Hayman et al. J.Chem.Phys. **79**, 1581 (1983)
3. J August et al. Chem.Phys.Letters **145** 273 (1988)
4. A Bacon et al. Faraday Discussion Chem.Soc. **86** 129 (1988)
5. BD Howells et al. J.Chem.Soc.Faraday in press

# PHOTOCHEMISTRY OF JET-COOLED COMPLEXES

R J Malcolmson, A J Yates, T L Axon and J Pfab

Heriot-Watt University, Edinburgh

## INTRODUCTION

The structure and dynamics of weakly bound complexes is the target of an important area of current research in spectroscopy and theory aiming to quantify the transition from isolated molecule to condensed phase behaviour. We have carried out a feasibility study aiming to assess the utility of the laser-induced fluorescence (LIF) technique for probing energy and momentum disposal in the photofragmentation of small gas phase clusters. The diatomic fragment AB from the photodissociation of a complexed jet-cooled parent carries information on the dynamics of the fragmentation of an isolated solute-rare gas or solvent complex (R-AB---$X_n$). A typical example of processes to be explored is given by the following equation

$$R\text{-}AB\text{---}X_n \xrightarrow{h\nu} R. + .AB + nX \qquad (1)$$

where R. and .AB are the primary fragments formed by photodissociation and X stands for Ar, $CO_2$, $H_2O$ or $CH_3OH$. The absorption of a UV laser photon projects the parent either onto a repulsive continuum or a rapidly predissociating potential energy surface. Our currently available vacuum equipment only permits mild expansion conditions, and pressures lower than 1 atm have to be used to achieve adequate supersonic cooling with our pulsed expansion chamber. Under these conditions the fraction of the uncomplexed, bare parent will be large and the number of van der Waals ligands n is not likely to exceed 2.

The compounds chosen as parent molecules for the present study are $NO_2$ and the organic nitroso-compound N-methyl-N-nitrosocyanamide (NMCA). The technique used to interrogate the diatomic photofragments NO and CN is laser-induced fluorescence (LIF). The LIF spectra of these diatomic radicals in their ground electronic state provide the opportunity to probe energy and momentum disposal as a function of stagnation pressure of the intended complexation partner.

## EXPERIMENTAL

The experiments were carried out with a small pulsed expansion chamber using colinear, counter-propagating dissociation and LIF probe beams as outlined in detail in previous reports[1] and shown schematically in fig. 1. The loaned excimer pumped dye laser (Lambda Physik EMG 101/FL3002 - laser 2 in fig. 1) was used for LIF excitation spectroscopy of NO near 225 nm. Our own excimer pumped dye laser (EMG 50/FL2002) provided the dissociation beam for the photofragmentation of $NO_2$ between 398 nm and 370 nm. Experiments with NMCA using LIF of CN on the violet bands ($B^2\Sigma^+ \leftarrow X^2\Sigma^+$ transition) were conducted with a single excimer pumped dye laser using most of the 308 nm output for photolysis and the optically delayed (<25 ns) output of the dye laser oscillator and pre-amplifier for LIF probing of CN near 380 nm. Gas mixtures were prepared on a standard glass vacuum line and expanded from blackened glass bulbs using pulsed expansion with a commercial pulsed molecular beam valve (NRCBV-100) with 0.5 mm orifice. The duration of the expanded gas pulse in the probe region 10-20 nozzle diameters downstream of the orifice was 0.5 ms.

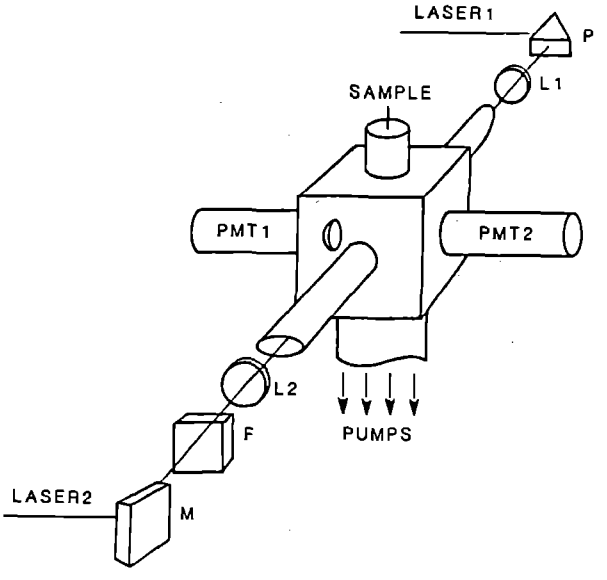


Figure 1: Schematic of apparatus used for dissociation-LIF probe experiments of jet-cooled complexes

## RESULTS AND DISCUSSION

Light absorption will be unselective and both the bare parent and its van der Waals complexes will be excited by the dissociation beam. Provided the primary step is unaffected by complexation, photofragmentation of the complexed parent is anticipated to proceed as shown in the following example.

$$NO_2\text{---}Ar_2 \xrightarrow{h\nu} O(^3P) + NO(X\ ^2\Pi_i) + 2Ar \qquad (2)$$

The disposal of excess energy and angular momentum into NO in process (2) will favour "rotational cooling" due to the increase in phase space available as a consequence of the presence of van der Waals ligands. R-T energy transfer during the scattering process may also contribute to this "cooling". This should become apparent experimentally by marked changes of LIF spectra of the diatomic fragment with stagnation pressure, i.e. a marked cooling of rotationally resolved spectra should be observed.

Nascent NO from the photodissociation of $NO_2$ was seen readily at a variety of photolysis wavelengths ranging from the dissociation threshold (398 nm) down to 370 nm. Cold nascent NO could be discriminated readily from jet-cooled NO present as a contaminant of $NO_2$ by probing NO in the $^2\Pi_{3/2}$ spin-orbit state. No clear effects of Ar pressure could be seen, however, up to the highest stagnation pressure (1 atm) employed. Some rotational cooling of NO could be identified when pump-probe delays were extended beyond 100 ns. These minor effects must therefore be attributed to collisional relaxation in the time interval between generation and LIF probing of the NO. Similar results were obtained for $CO_2$ as expansion gas.

More encouraging results were obtained with NMCA whose photodissociation in a pulsed He expansion has been examined in considerable detail in previous work in this laboratory[2]. At 398 nm NO is formed promptly from a quasi-bound $S_1(n,\pi^*)$ state of $^1A''$ symmetry whereas on excitation to the $S_2$ $(\pi,\pi^*)$ continuum ($^1A'$ symmetry)

at 308 nm both NO and CN ground state fragments have been observed. Two-photon LIF spectra of NO revealed a marked dependence of rotational energy disposal into this fragment on the stagnation pressure of Ar indicating significant complexation under mild expansion conditions where collisional relaxation effects were not apparent. We have now examined energy disposal into CN in the 308 nm dissociation of this compound. LIF spectra of nascent CN have been recorded under a variety of conditions. These spectra provided detailed data on the disposal of excess energy into this fragment. Fig. 2 shows the rotational population distribution of CN(v″=0) from the 308 nm photolysis of NMCA jet-cooled with He. This should be compared with fig. 3 summarising our results obtained on the rotational and vibrational energy disposal into the CN fragment with $CO_2$ as expansion gas. Clearly, in each case CN (v″=0) formed is rotationally hot. A substantial fraction of the population is found vibrationally excited. Note, that the CN LIF signal was found to increase wth the square of the 308 nm pulse energy. This leads us to conclude that the CN fragment is not formed in the primary process but by a fragmentation that occurs after the absorption of a second 308 nm photon by the primary fragment $CH_3NCN$. The drawn out curves in fig. 3 represent rotational population distributions that have been calculated using a prior model which assumes a statistical partitioning of excess energy into the available quantuum states of the fragments. Note, that the model was based on the primary process

$$CH_3NCN \xrightarrow{308\ nm} CH_3N + CN \qquad (3)$$

and that the dissociation energy of the $CH_3NCN$ radical was estimated. The agreement between the observed and modelled rotational distributions is clearly very good. This lends support to the conclusion that CN is formed by the relatively slow predissociation of the intermediate $CH_3NCN$ fragment, and that the $CH_3NCN$ radical absorbs another photon following the initial cleavage of the considerably weaker N-NO bond in the primary step.

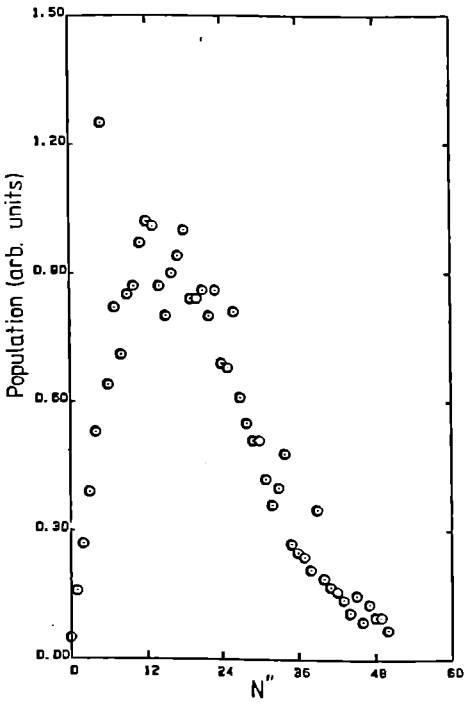


Figure 2: Rotational distribution of CN(X, v″ = 0) from the 308 nm photolysis of NMCA in a supersonic jet of He

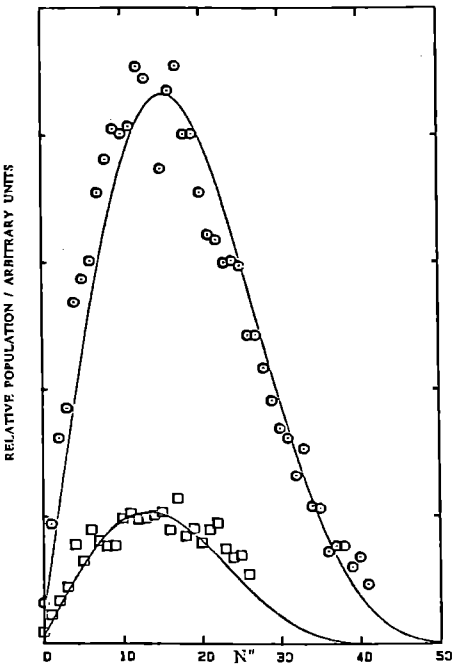


Figure 3: Comparison of observed and calculated statistical rotational distributions for CN(X, v″ = 0 and 1) from the 308 nm photolysis of NMCA jet-cooled with $CO_2$

Comparison of LIF spectra and derived rotational population distributions for the systems NMCA/He, Ar, $CO_2$ and $CH_3OH$ has shown that energy disposal into CN is not affected by the expansion gas within the experimental uncertainty (ca. 10%) in contrast to NO, which is affected markedly by a change from He to Ar. This suprising result is consistent with the interpretation of NMCA photochemistry given above: the primary dissociation event of the uncomplexed and complexed parent, produces bare $CH_3NCN$ fragments, which undergo further fragmentation after absorption of another 308 nm photon, i.e. process 4 is followed by step 3.

$$CH_3N(NO)CN \xrightarrow{308\ nm} CH_3NCN + NO \qquad (4)$$

## CONCLUSIONS

The results obtained indicate that LIF of diatomic photofragments can be useful for studying the dissociation dynamics of van der Waals complexes. The energy disposal deduced results from the superposition of contributions from the bare and complexed parent unless structured and assigned features can be excited, which are attributable to a specific complex. Thus the most interesting systems to study by this approach will be predissociating molecules and their van der Waals complexes. For systems undergoing direct dissociation from repulsive electronic states the effects of complexation by a rare gas or other partner can provide valuable information on the mechanism of photo-dissociation of larger molecules. In the particular case of NMCA the approach used provides a clear identification of the primary and secondary photochemical pathways. This should also prove useful in studies of the dissociation dynamics of more complex parent molecules.

## REFERENCES

1. J A Dyet, M R S McCoustra and J Pfab, J Chem Soc Faraday Trans. 2, 84 463 (1988).
2. P A Giovanacci, M R S McCoustra and J Pfab, to be published.

# LASER SPECTROSCOPY OF TRANSIENT MOLECULES IN A SUPERSONIC EXPANSION

Peter A. Hamilton and Simon K. Bramble
Queen Mary and Westfield College, London

## INTRODUCTION

Laser induced fluorescence (LIF) is an established technique for the spectroscopy of short lived transient molecules. These species are important intermediates in gas phase reactive processes such as found in combustion, the atmosphere and interstellar space. Supersonic free jets have proven to be a nearly ideal source for LIF experiments due to the very high level of rotational cooling inherent in the adiabatic expansion. When transient molecules are generated in such an expansion the reactive intermediates will be effectively "frozen out" in the collision free environment and it is possible, due to the very low temperatures achieved, <10K, to observe "van der Waals" type clusters involving open shell species.

Traditional methods for the generation of radicals and ions such as discharge flow and Penning ionization, cannot be used in a supersonic expansion. A variety of methods have been developed in the last few years most of which rely on the generation of the radical or ion very early in the expansion so that further cooling takes before the subsequent observation in the collision free region. Laser photolysis[1,2], multi-photon ionization[3], electron impact ionization[4] and discharges[5] have all been used to generate ionic and neutral radicals in supersonic expnasions. In this work we developed and used a short duration pulsed discharge in a pulsed supersonic expansion as a source of short lived radicals, ions and metastable molecules for spectroscopic studies by LIF.

## EXPERIMENTAL

A combination of a pulsed supersonic expansion and pulsed electric discharge was used to generate rotationally cold transients. The pulsed nozzle (Newport BV100) was typically operated a backing pressures of 2-3 atmospheres and expanded into a a 60 cm diameter vacuum stainless steel vacuum chamber which was evacuated by a Roots mechanical pump to give average running pressures of <0.1 Torr. The discharge pulse of approximately 3kV was applied to the stainless steel ring electrode 2 mm from the front plate of the nozzle thus creating a discharge between the electrode and the nozzle lasting less than 1 μs. Intense emission was observed from the discharge which had decayed after ~10μs.

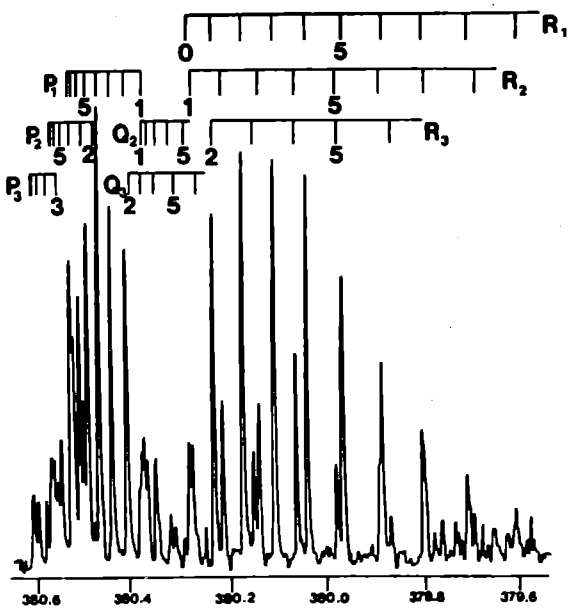


Figure 1: Laser excitation spectrum of $N_2$ C-B (0,2)

The transient molecules were probed by LIF a variable distance from the nozzle, typically 2.5cm, after a delay of about 30μs. The arrival of the discharged gas pulse in the detection region is observable as an increase in the background level of emission due to the presence of long lived (ie >30μs) states excited by the discharge. Extensive cooling of the radicals and ions formed in the discharge takes place after the discharge is off with the effective temperature of the rotational and vibrational degrees of freedom being highly non-equilibrium. The observed temperature of transient species is strongly effected by the distance of the electrode from the nozzle, the timing of the discharge with respect to the gas pulse, and the power dissipated in the discharge.

Excitation spectra were recorded at a resolution of ~0.2$cm^{-1}$ in the region 350 to 420nm using an excimer pumped dye laser system (Lambda Physik EMG101/3002E) operating with PBBO and BBQ dyes. Laser induced fluorescence was collected at right angles to both the supersonic jet and the laser using a band pass filter to discriminate against scattered laser light (and the afterglow emission) and averaged with a boxcar integrator.

## NITROGEN METASTABLE STATES

Specta recorded in the 380 to 410nm. region of a discharge through a pure nitrogen expansion showed the expected and very intense $N_2^+$ (B-X) band at 391nm. In addition several much weaker bands from a neutral species were observed. These bands corresponded to the very well known C-B transitions and showed a 40ns radiative lifetime which is characteristic of the C state. Figure 1 shows a typical high resolution scan of one of the bands and its assignment. The relative intensity of the three spin orbit components was observed to be highly non-statistical in all the spectra, typically being in the ratio of 1.0:0.46:0.35 for the F1,F2,F3 components respectively.

As the B state lifetime is on the order of 5μs under our conditions and we are observing some 40μs after the discharge it is clear that the population we are observing must be formed by some sort of relaxation of the afterglow rather than directly in the discharge. Perturbation allowed radiative cascade via the C state from some high lying metastable state is thought to be the mechanism for this. The lowest Rydberg state, the E state, has been proposed[6] as a likely candidate for the reservior state. This suggestion could be confirmed by direct observation of the E-C transition or possibly by ab initio calculations, although these would have to include extensive configuration interaction and a full treatment of spin orbit interactions.

## A NEW SPECTRUM OF $C_3$

The great importance of small carbon clusters in interstellar space, combustion and the formation of soot has led to intense activity in the study of carbon clusters. There have been many studies[7,8] of the 405nm electronic system and the ground state vibrational levels have been mapped out up to 17000 $cm^{-1}$. Less is known about the upper state which exhibits large Renner-Teller splitting.

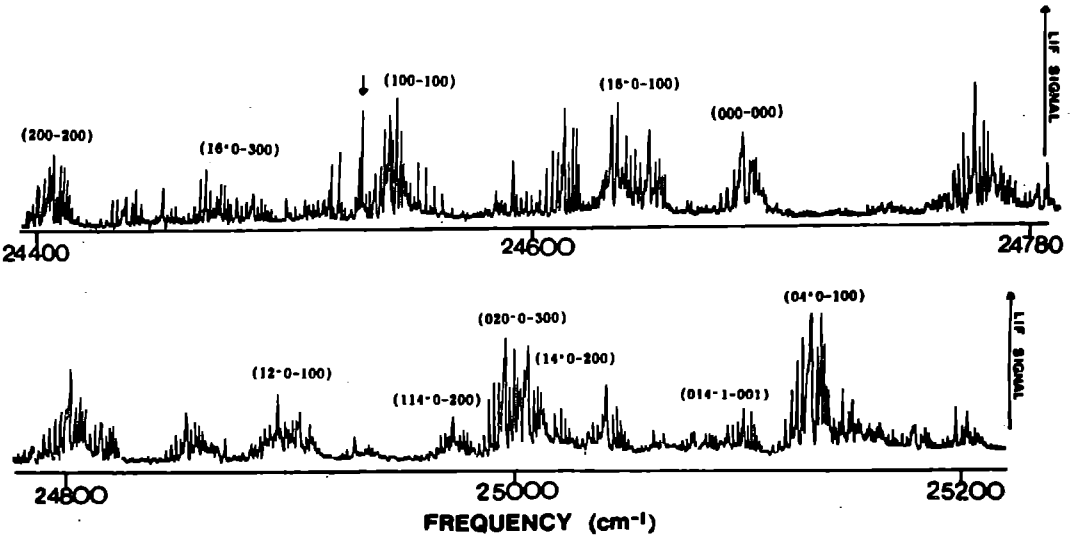


Figure 2: Survey spectrum of $C_3$

We observed an extensive spectrum from $C_3$ arising from our discharge/supersonic expansion source in pure or rare gas dilted carbon monoxide. The reaction mechanism for the creation of the $C_3$ is not known, but may involve clusters. A portion of the excitation spectrum, observed between 397 and 410nm, is shown in figure 2 along with some prelimenary assignments. The apparent lack of regularity in the positions of the vibrational bands is due to the Renner-Teller effect in the upper state which is comparable in magnitude to the bending vibrational frequency. In contrast to previous spectra of the $C_3$ radical there is almost complete cooling of the bending vibration in the ground state but the symmetric and asymmetric stretching motions are both populated. Although the rotational structure of all the observed bands has been analysed many bands are still unassigned and further double resonance studies may be required before the remaining bands are assigned.

## THE A-X SYSTEM OF $Cl_2^+$

The $Cl_2^+$ ions were generated by a discharge through $Cl_2$/argon mixtures in the expansion and a typical LIF excitation spectrum is shown in figure 3. With a normal isotopic mixture, each vibrational band should appear as a 9:6:1 triplet but due to saturation effects and heavy overlapping most bands appear as doublets. A number of previously unobserved bands are seen in this spectrum and are indicated by letters. These new bands appear in the gaps in the previous assignments and arise from the most heavily perturbed levels. As the perturbing state has never before been observed in emission it is probable that it has a very low transition probability to the X state. In the region in which there is extensive mixing of the A state and the perturbing state there will be a substantial decrease in intensity of the A-X emission and a corresponding increase in the possibility of seeing transitions from the perturbing state. Some of the new bands seen in this work are in fact assignable to the perturbing state and calculations are now underway to predict this "intensity stealing" quantitatively. While the theoretical work is by no means complete, at this stage it is already clear that sufficient data is now available to unravel the perturbation and complete the assignment of this important spectrum.

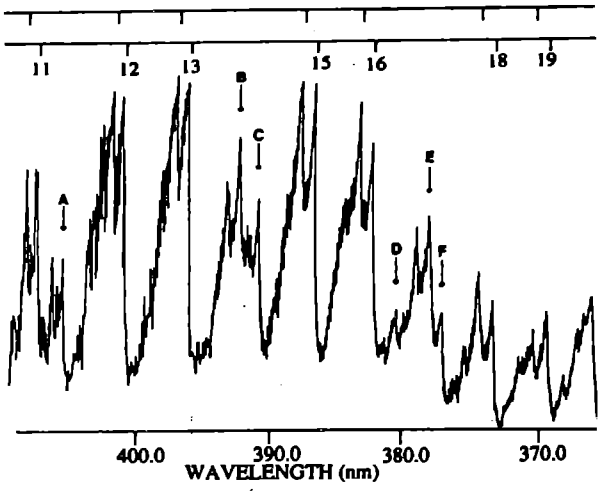


Figure 3: Survey excitation spectrum of $Cl_2^+$

## CONCLUSIONS

In this work spectra were observed from highly excited metastables, neutral radicals and ions demonstrating the range of species which can be generated with the new discharge source. In many cases, eg. $C_3$, the method of formation is not at all clear and it may be possible in the future to carry out kinetic and mechanistic studies of discharges with the products being "frozen out" in the collision free region and probed by LIF. In all cases good rotational cooling was achieved although there was often substantially less vibrational cooling. There is clearly potential for a large number of studies of transient molecules to be made in supersonic sources.

## REFERENCES

1. K. Fuke et al. Chem. Phys. Lett. **126** 119 (1986)
2. M. Heaven et al. J. Chem. Phys. **80** 51 (1984)
3. T.A. Miller et al. Chem. Phys. Lett. **138** 175 (1987)
4. J. Allison et al. Chem. Phys. Lett. **64** 202 (1979)
5. A.T. Droege et al. Chem. Phys. Lett. **96** 316 (1983)
6. R.S. Freund J. Chem. Phys. **50** 3734 (1969)
7. L. Gausset et al. Astrophys. J. **142** 45 (1965)
8. E.A. Rohlfing et al. J. Chem. Phys. **90** 6804 (1989)

# CRITICAL WETTING BY TOTAL INTERNAL REFLECTION FLUORESCENCE

Ian A McLure and Ann-Marie Williamson

University of Sheffield

## INTRODUCTION

In critical wetting in a two-phase liquid mixture close to a critical solution temperature(CST), one liquid phase completely wets the other phase. No matter whether the upper or the lower is the wetting phase, a thin wetting layer prevents contact between the wetted phase and the container and, if the lower is the wetting phase, with the coexisting vapour phase also. In either case the liquid phases/vapour phase contact angle is zero and one liquid phase spreads on the other.[1]

At a critical-wetting transition temperature($T_w$) the complete wetting of one phase by the other gives way to normal partial wetting with a nonzero contact angle. The current pivotal question at $T_w$ is whether the change in the contact angle or the wetting-film thickness is abrupt, and hence of first order, or continuous - albeit with a marked change in slope at $T_w$, and hence of second order. Important also is the identification of the wetting phase and its relation to the nature of the container material. In the present research, the principal goal was to study wetting in alkane + perfluoroalkane(A+PFA) mixtures in Pyrex glass.

## EVANESCENT WAVE-INDUCED FLUORESCENCE

A novel route to the resolution of some of these questions was described recently by Fattinger, Togni and Lukosz(FTL) using the total internal reflection fluorescence(TIRF) technique in which a laser dye appreciably soluble in only one of the coexisting phases of a mixture serves as a probe for the presence of that phase in the wetting layer.[2] The essence of the technique is that when a beam of light is incident on the liquid/glass interface at an angle exceeding that of critical reflection, the greater part of the beam is reflected directly from the interface back into the glass but a small part, the evanescent wave, penetrate the liquid for a very small distance and thus probes the immediate vicinity of the interface. If the wetting phase is a poor dye solvent, the interposition of that phase as a thin film diminishes the intensity of the fluorescence arising from dye in the wetted phase close to the interface. If the wetting phase is a good solvent the surface fluorescence increases. High refractive index glass is usually needed in TIRF to minimize the critical angle.

FTL demonstrated the TIRF technique with water+2,6-lutidine, lower CST=33°C, using DCM as the water-insoluble probe. Wetting was studied at the liquid interface with Schott SF6 flint glass.

## EXPERIMENTAL ARRANGEMENT

The sample cell kernel is outlined in Figure 1. The

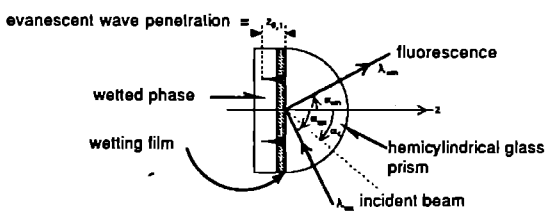


Figure 1: The TIRF sample cell

cell itself was created from an appropriately-recessed metal thermostatting block and the mixture confined within it by a hemicylindrical glass prism mounted with its axis vertical. The cell was illuminated by a horizontal laser beam incident normally on the prism operating at a frequency to excite the dye. Laser stabilty is critical in experiments where the thermodynamic equilibration time in an unstirrable cell can be many minutes and during the loan period this requirement became a limiting success factor.

## WATER+2,6-LUTIDINE

As a precursor to the A+PFA study we reexamined W+L by TIRF with DCM as solute. The initial light source was a JK2000 pulsed laser borrowed from the LSF operating with Coumarin-480 at 488 nm. Our results for this system showed substantial divergences from those reported by FTL, particularly, in the time and temperature(T) dependence of the surface fluorescence. Subsequent work using an $Ar^+$ CW laser confirmed that the latter problem arose chiefly from the the manner of selecting the frequency of the fluorescence to be measured. As the temperature of the sample changes so also do the compositions of the coexisting phases and the more so the further from the LCST. Consequently, the molecular environment of the dye alters with temperature and so therefore does the fluorescence intensity irrespective of wetting-film thickness changes. This effect is particularly pronounced when using a monochromator to select the measured fluorescence at a single frequency , as FTL did, rather than band-pass filters with a wider acceptance window, as we did. We are unsurprised, therefore, that our results differ somewhat from those of FTL. However, we view the TIRF method as validated sufficiently to justify our proceeding to A+PFA mixtures.

## ALKANE + PERFLUOROALKANE MIXTURES

The model A+PFA mixture was methylcyclohexane(MCH) + perfluoromethylcyclohexane(PFMCH), upper CST = 42.6°C. This mixture is advantageous since the perfluoroalkane is readily available in high purity and its bulk and surface thermodynamics is well characterised close to the UCST. The dye probe was 1,6-diphenylhexatriene DPH whose UV absorption in PFMCH is blue-shifted by 20 nm relative to that in MCH thus permitting ready preferential excitation of DPH in the MCH-rich phase. This variation from the original FTL technique was needed due to the lack of a dye sufficiently preferentially soluble in either coexisting liquid phase. Although PFA liquids have low refractive indices, so that TIRF studies are probably feasible using Pyrex prisms, we used an SF4 flint glass prism in this exploratory study. The preliminary results indicate that our modification of the FTL technique in which we exploit the differential solute absorption in the two liquid phases promises wider application of the TIRF technique to wetting in different mixtures than the FTL approach which is entirely dependent on the existence of laser dyes widely partitioned between the coexisting phases of a given mixture.

## REFERENCES

1. RB Heady and JW Cahn J Chem Phys **56** 896 (1973)
2. Ch Fattinger, G Togni and W Lukosz Surface Science **189/190** 405 (1987)

# LASER INDUCED DESORPTION AND ENERGY TRANSFER BETWEEN MOLECULES ADSORBED ON DIELECTRIC SURFACES

S J Clemett[1], A W Parker[2], K v Puttkamer[1], A Takami[1], C J S M Simpson[1]

[1] Physical Chemistry Laboratory, Oxford University
[2] Rutherford Appleton Laboratory

## Introduction

There is a great interest in laser induced processes for molecules adsorbed on surfaces [1-5]. The two main classes of desorption processes are thermal, in which the surface on which the molecules are adsorbed is heated directly by the laser, and non-thermal processes in which the laser excites the molecule and does not directly heat the surface. We use a quadrupole mass spectrometer to measure the flight times of atoms and molecules desorbed from surfaces. We have used pulsed lasers operating in the visible [5], the IR and the UV.

## Thermal Desorption

Thermal desorption time of flight spectra can usually be characterized by a single Boltzmann distribution with temperatures not far different from that of the surface. However, for low coverages on Cu(111) we also have found that $CH_4$, Ar and pyridine/Ar mixtures are desorbed with very broad velocity distributions. For the study of non-thermal processes it is extremely important to avoid surface heating by the laser [1]. This can be achieved using surfaces transparent to the laser light provided that the surfaces are not pumped too hard.

## UV Laser Induced Desorption from Dielectric Surfaces

We have already reported UV laser induced desorption and presented evidence for energy transfer between adsorbed molecules [6]. However, these experiments were not completely conclusive. For this reason we have made major improvements to the apparatus and carried out more experiments in order to firmly establish whether energy transfer occurs. We have installed: (1) A micro-capillary array gas doser to provide controlled dosing (2) A liquid helium cooled cryopump, allowing the main chamber to be evacuated to a pressure of $<4*10^{-11}$ Torr.
We have studied the following systems: 1,3-cyclohexadiene, pyridine, 2-methyl-pyridine, N-methylaniline and mixtures with non-absorbing species including Ar, Xe, $N_2$, $O_2$ and cyclohexane. We have used $MgF_2$, quartz and $N_2$, Ar and Xe coated surfaces.

The laser induced desorption may be divided into three main regions as has been discussed by Domen and Chang for the dissociative desorption of $CH_2I_2$ from sapphire [1]. This is illustrated in Fig. 1

Figure 1 - Types of Desorption

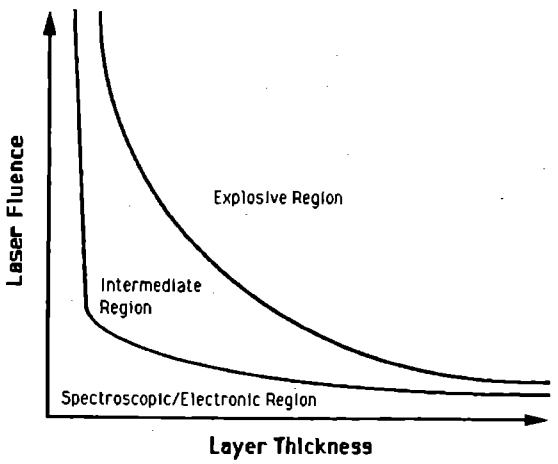


## The Explosive Regime

This is characterized by a very high velocity spike followed by a low velocity tail. We have found that the low velocity tail can be suppressed using pyridine/xenon mixtures and by desorbing the pyridine from xenon coated quartz [6]. We conclude that the spike is due to the molecules which directly absorbed the laser energy and the tail is due to energy released from the upper electronic and vibrationally excited molecules, to the surroundings.

## The Intermediate Region

The very high velocity spike disappears in the intermediate region and the distributions may be fitted by one or two Boltzmann curves, one corresponding to T=1000-1800 K and the second about 200-400 K. The traces resemble those found for the desorption of NO from O atom coated Ni [2] and NO from Ag [3].

## The Spectroscopic or Electronic Region

In this region the thermal effects are negligible. In the case of the dissociative desorption of $CH_2I_2$ coadsorbed with $NH_3$ the unexcited molecules are not desorbed [1]. We have found that a molecule which can accept energy via energy transfer, can also be desorbed.

## Transitions Between Regions

**a) Explosive to intermediate**
This may be shown by plotting yield against peak height for the main peak. In the intermediate region this is linear but as the explosive region is approached there is a rapid increase in the yield.

**b) Intermediate to spectroscopic region**
For some time we considered that there is a fluence cut-off for desorption. This is illustrated in Fig. 2 for 2-methyl-pyridine, and is true of all the molecules we have investigated.

We now realize that this represents an abrupt change in yield rather than a transition to no desorption. Signal averaging small traces at fluences below the "cut-off" gives nearly single Boltzmann distributions with temperatures similar to those in the intermediate region. This may be summarized in Fig. 3 for the case of 20 monolayers

Like Domen and Chuang [1],for sufficiently low coverage, desorption occurs from the spectroscopic region, and no fluence cut-off is observed. This is shown for the case of 2 monolayers in Fig. 3.

Figure 2

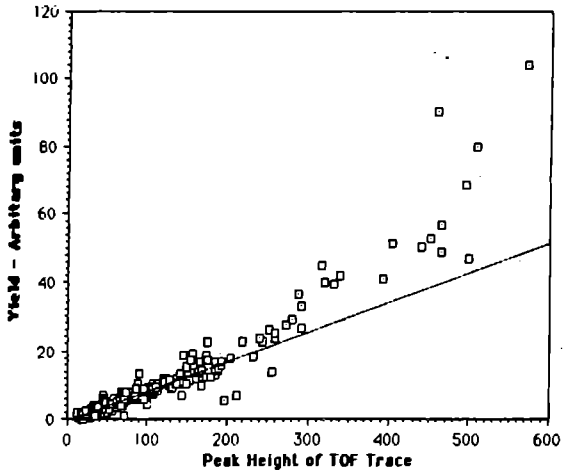


Figure 3 - Desorption of cyclohexane from pyridine-cyclohexane (1:2) mixture

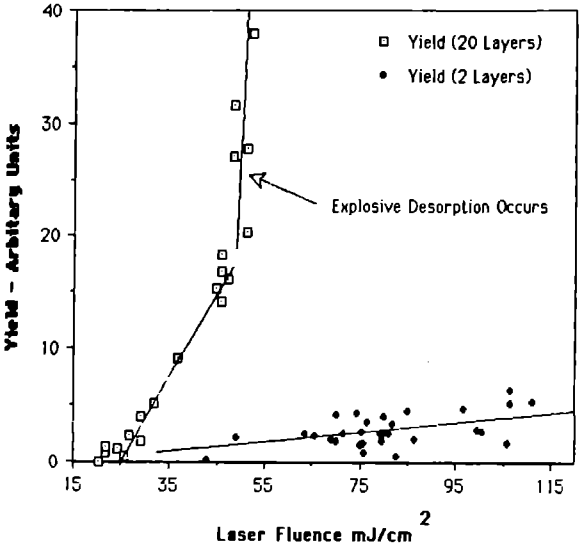


## The Dependence of Yield on Shot Number

Fig. 4 illustates the change in yield with shot number. The first few shots desorb some more loosely bound species. This is followed by a very gradual change in layer thickness until the "fluence cut-off" is reached. This does not mean that all of the molecules are desorbed because the signal re-appears for a small increase in fluence. This is apparent from Fig. 1.

## The Effect of Wavelength and Absorption Coefficient

At constant fluence we found desorption of 1,3-cyclohexadiene between 255 nm and 280 nm, with the translational energy of the desorbed molecules remaining nearly independent of the wavelength, but no desorption at 285 nm. We believe that this change is due to the decrease in the absorption coefficient rather than being a wavelength cut-off. This may be understood from Fig. 1; provided that the conditions do not move into the explosive region changes in the absorption with the wavelength correspond to changes in fluence. We have confirmed this behaviour for 2-methyl-pyridine investigated between 246 nm and 268 nm. That the kinetic

Figure 4

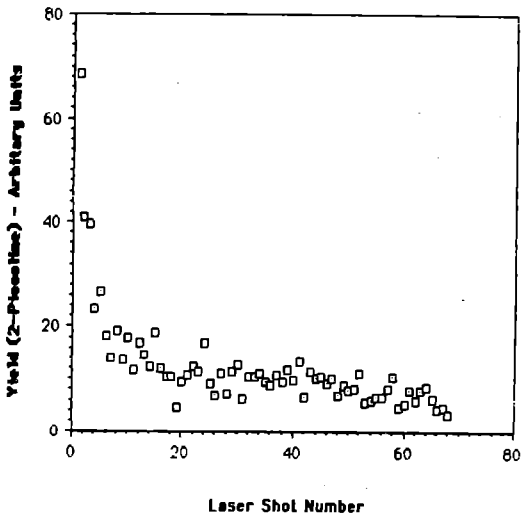


energy of the desorbed species does not change with the wavelength is strongly indicative that the desorption does not occur from the upper electronic state.

## Energy Transfer

Non-light absorbing species may be desorbed as a consequence of local thermal heating due to energy released by the pumped molecule to the surroundings. In this case the desorption temperature is expected to be in the region of 200-400 K with the less tightly bound species being desorbed more readily. However if there is an efficient energy transfer process then the recieving molecule can acquire enough energy to be desorbed with a temperature compareable with that of the pumped molecule. If it is less firmly bound then it will be desorbed with yields greater than that of the pumped molecule. This effect will occur also if energy transfer favours the accepting molecule. These differences enable us to distinguish between the different processes.

For mixtures of 1,3-cyclohexadiene with Ar, $N_2$, or $O_2$, working in the intermediate region we have found little of the non-light adsorbing species to be desorbed with temperatures between 200 and 400 K, whilst that of the 1,3-cyclohexadiene is about 1800 K. Similar results have been found using pyridine or 2-methyl-pyridine as the pumped molecule, dosed on to the crystal using the micro-capillary array doser. We used temperature programmed desorption to show the non-adsorbing species are present on the surface and that they do have small binding energies. For mixtures with cyclohexane, both the pumped species and the non-pumped cyclohexane are desorbed with comparable temperatures of about 1000 K, with preferential desorption of the cyclohexane.

By working at low laser fluences we found conditions for which the yield of pyridine is too small to measure but that of cyclohexane is appreciable with a nearly single Boltzmann distribution with a temperature of about 1000 K.

These experiments establish that energy transfer has occurred to the cyclohexane.

## Luminescence

The aim of these experiments were to find out whether a molecule which fluoresces in the gas phase is quenched on a dielectric surface, and if not whether it has similar laser induced desorption characteristics as pyridine. We selected N-methyl-aniline. This gives very strong fluorescence on the surface which can be seen by eye. Using a photomultiplier its fluorescence lifetime was determined to be 30+/-2 ns. It was found that N-methyl-aniline is desorbed with the same characteristics as pyridine. At high fluences or thick layers there is explosive desorption, and at lower fluences the desorption can be accounted for by a Boltzmann distribution with a temperature of about 1000 K.

In future experiments we shall investigate whether the fluence can be quenched by energy transfer from the excited electronic state, using the fluorescence lifetime as a clock to determine the rate of energy transfer to other molecules. These molecules may then be desorbed in preference to N-methyl-aniline.

## Summary

Our results may be summarized as follows:

(1) The UV desorption of small organic molecules which are not dissociated have qualitatively similar behaviour to $CH_2I_2$ which is dissociated by UV light at 308 nm [1] and to NO which involves the desorption of dimers [3].

(2) The yields in the non-thermal spectroscopic region are very small. Our previous results were in the explosive and intermediate regions rather then the spectroscopic region.

(3) The desorption characteristics from surfaces of $N_2$ coated quartz are qualitatively the same as for quartz or $MgF_2$.

(4) The desorption of cyclohexane from pyridine or 1,3-cyclohexadiene mixtures is not due to the desorbing molecule acting as an antenna to heat the surface since more weakly bond species such as $N_2$ are desorbed with much lower temperatures and yields than the cyclohexane.

(5) The desorption process is complex depending upon the laser fluence, the layer thickness, the absorption coefficient of the molecule at the wavelength used, the shot number and whether the surface has been annealed.

(6) The questions concerning surface cleanliness have been overcome by working with newly formed surfaces of $N_2$, Argon or Xenon coated $MgF_2$ or quartz.


[1] K. Domen and T. J. Chuang, J. Chem. Phys. **90**, 3318 (1989)

[2] F. Budde, A.V. Hamza, P.M. Ferm, G. Ertl, D. Weide, P. Andresen and H.-J. Freund, Phys. Rev. Letters **60**, 1518 (1988)

[3] W.C. Natzle, D. Padowitz and S.J. Sibner J.Chem.Phys. **88**, 7975 (1988)

[4] H.C. Chang and G.E. Ewing Chem. Physics **139**, 55 (1989)

[5] C.J.S.M. Simpson and J.P. Hardy, Chem. Phys. Letters **130**, 175 (1986)

[6] RAL annual report 1987, 1988

# LASER INDUCED FLUORESCENCE STUDIES OF MICROWAVE PLASMAS USED FOR SEMICONDUCTOR ETCHING

G Hancock and M J Toogood

Physical Chemistry Laboratory, Oxford University

ECR plasma chambers are a new design of reactor which are finding many applications in material processing, particularly in the semiconductor field. They employ a microwave generator combined with a magnetic field to produce high plasma densities, which lead to high concentrations of reactive species and hence to rapid processing of materials. The aim of the project at Plasma Technology was to ascertain if techniques developed on a conventional parallel plate plasma chamber could be used on the new reactor, and then to use them to measure relative concentrations of reactive species, which may give information on the physical and chemical processes taking place inside the chamber.

The CF and $CF_2$ radicals were observed by Laser Induced Fluorescence (LIF) in $CF_4$ / $O_2$ / Ar plasmas (Figures 1 & 2) and their relative concentrations were measured as a function of pressure, microwave power and gas composition, in both the generation (ECR) and downstream regions. (During processing, the substrate is generally placed in the downstream region). Optical emission from the plasma was also measured to obtain information on the variation in concentration of fluorine atoms, a key specie in these reactive plasmas, and on the degree of excitation in the plasma, by examining plasma induced emission from Ar atoms.

The results obtained suggest that the concentrations of CF and $CF_2$ in 1 - 20 mTorr $CF_4$ plasmas are determined by rapid diffusion and reactions at the chamber walls. This is in agreement with results obtained in a parallel plate reactor, particularly at low pressures. The degree of dissociation of $CF_4$ by electron impact, appears to be larger than in the conventional reactor, with relatively high CF and C atom concentrations. The presence of $O_2$ in the gas mixture reduces the concentration of CF and $CF_2$ due to their reactions with atomic oxygen, whilst increasing the fluorine atom concentration. This effect is utilised in processing to enhance Si etch rates, which are in part dependent on the fluorine atom concentration.

The rotational temperature of CF, which is equal to the bath gas temperature, was measured in the ECR and downstream regions and found to be lower downstream. Although the precise values varied, measurements indicated a temperature of 600 - 900 K in the ECR region. This is higher than typical values in a parallel plate reactor and is again indicative of the high level of excitation in ECR plasmas.

Time dependent studies using LIF and optical emission have been developed in Oxford on the parallel plate system and give direct measurements of the rates of particular processes in the plasma, but it was not possible to pulse the plasma in such a way as to use these techniques in this case. However, these preliminary results have indicated the high degree of excitation and the domination of diffusion and wall reactions as loss processes in ECR plasma reactors.

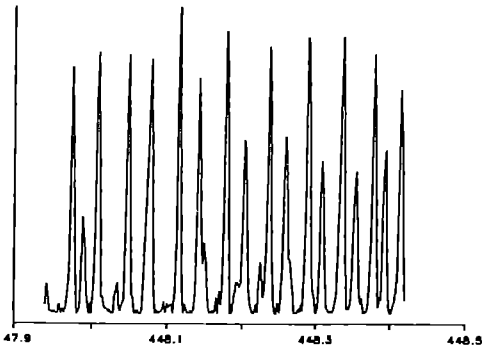


Figure 1 CF : Part of the excitation spectrum of the (1,0) band of the $A^2\Sigma^+ - X^2\Pi$ transition taken in an ECR plasma.

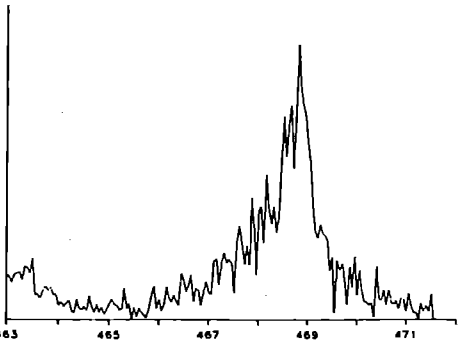


Figure 2 $CF_2$ : Excitation spectrum of the (0,11,0) - (0,0,0) band of the $\tilde{A}^1B_1 - \tilde{X}^1A_1$ transition taken in an ECR plasma.

# LASER-INDUCED FLUORESCENCE OF REACTIVE METALLOCENES $(\eta^5\text{-}C_5H_5)_2M$ (M = Re, W, Mo) AND $(\eta^5\text{-}C_5Me_5)_2Re$

Steven E. J. Bell, Jeremy N. Hill, Andrew McCamley and Robin N. Perutz

University of York, U.K.

## INTRODUCTION

Laser-induced fluorescence (LIF) is an attractive technique for the investigation of small molecules because of its high sensitivity, state selectivity and (in solid or matrix-isolated states) site selectivity.[1] The extension of LIF to larger molecules is productive if the spectra are sharp, a condition fulfilled by electronically unsaturated metallocenes.[2] Molecules such as tungstenocene are of particular interest as transient intermediates in C-H activation reactions. We have previously reported LIF from matrix-isolated $Cp_2Re$ and $Cp^*_2Re$ ($Cp = \eta^5\text{-}C_5H_5$, $Cp^* = \eta^5\text{-}C_5Me_5$).[2-4] Direct population of the ligand-to-metal charge-transfer (LMCT) excited states of these molecules with a cw laser induces emission from the same states in a well-resolved vibrational progression. We have also detected LIF for $Cp_2Mo$,[2] but have been unable to access appropriate laser wavelengths for $Cp_2W$. We now report the LIF of $Cp_2Re$, $Cp_2W$, $Cp_2Mo$ and $Cp^*_2Re$ isolated in nitrogen matrices excited with a pulsed dye laser, recorded at the RAL-LSF. We have also recorded matching UV/vis absorption spectra of $Cp_2Mo$ and $Cp_2W$ in $N_2$ matrices, since they have not been reported previously. These experiments have allowed us (i) to detect fluorescence from $Cp_2W$, (ii) to measure the excited state lifetime of $Cp_2Re$ and to set limits for the lifetimes of the remaining metallocenes, (iii) to record partial excitation spectra.

## RESULTS

Rhenocene: $Cp_2Re$ absorbs in the region from 450 - 490 nm and emits between 485 and 540 nm, corresponding to an allowed LMCT transition between the $E_{5/2g}$ spin-orbit ground state and the $E_{3/2u}$ excited state ($e_{1u}^3e_{2g}^4a_{1g}^2$ <--> $e_{1u}^4e_{2g}^3a_{1g}^2$ expressed in $D_{5d}$ symmetry to emphasise selection rules).[3,4] Both absorption and emission spectra exhibit a strong progression in the ring-metal-ring symmetric stretching mode ($\nu_4$).[7] In absorption, each vibrational component consists of several poorly resolved overlapping bands separated by ca. 70 $cm^{-1}$.[3] The LIF spectrum excited at 457.9 nm does not show this fine structure, but single sharp bands.[3]

Variation of the excitation wavelength not only alters the emission intensity, but reveals a second set of emission maxima (figure 1a). The (0,0) bands of the two sets of emission progressions are designated A and B. The partial excitation spectra (figure 1c) demonstrate that the absorption spectrum may be separated into components for A and B. The excitation spectra show sharp onsets on the long-wavelength side with some fine structure and a longer tail to the blue. The components A and B must belong to separate conformations of $Cp_2Re$ or to molecules occupying different sites in the matrix. The (0,0) bands of the emission spectra of A and B coincide with the absorption maxima to within 0.2 nm. Measurements of the emission as a function of gate delay-time reveal that both components have an emission lifetime of $\tau_F$ = 71.9 ± 1.3 ns (figure 1, inset).

Tungstenocene: The prominent absorption band of $Cp_2W$ in the region 370 - 400 nm has been assigned an allowed LMCT transition from the $e_{1u}^4e_{2g}^3a_{1g}^1$ ground state ($E_{2g}$, $\Omega$ = 3 spin-orbit state). Transitions either from $e_{1u}$ to $a_{1g}$, or from $e_{1u}$ to $e_{2g}$, can give rise to appropriate $E_{2u}$ excited states.[5] Like that of $Cp_2Re$, the absorption spectrum in a $N_2$ matrix shows a strong progression in $\nu_4$ ($\nu_4'$ = 324 ± 8 $cm^{-1}$) and further fine structure (ca. 25 - 100 $cm^{-1}$).

Irradiation into this absorption excites an intense emission spectrum with progressions consisting of three components (A,B,C) which have relative intensities dependent on excitation wavelength (figure 2). The components A-C are assigned to three different conformers/matrix sites. The emission frequencies allow the determination of $\nu_4''$ and $\nu_3''$ ($\nu_3$ is the symmetric ring breathing mode), transitions which are forbidden in the IR. The emission decays within the lifetime of the laser pulse allowing us only to set an upper limit to $\tau_F$ of 10 ns.

Molybdenocene: The absorption and emission spectra of $Cp_2Mo$ are appreciably broader than those of tungstenocene and lie ca. 16 nm to longer wavelength.[5] Nevertheless, they allow comparison of ground and excited state values of $\nu_4$, and identification of multiple components within the spectra. The LIF spectrum shows weak bands to the blue of the (0,0) transition. These bands, which are ca. twenty times weaker than the (0,0) band, are located at frequencies suggestive

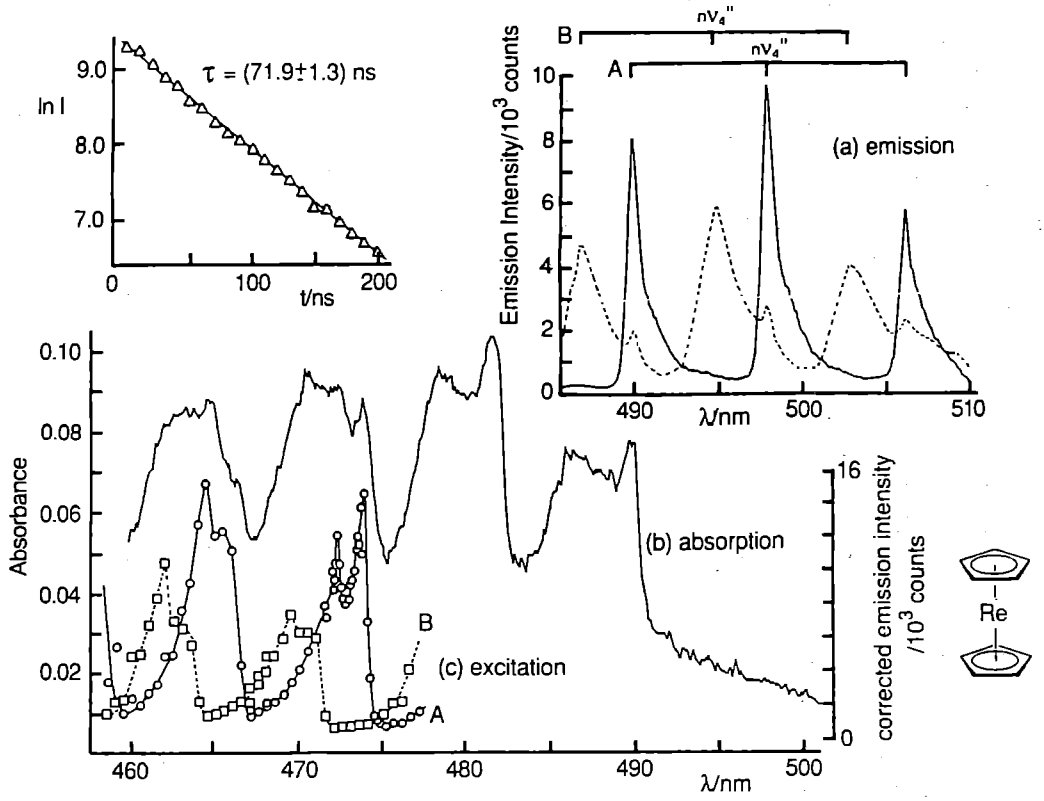


Figure 1. (a) Emission spectrum of $Cp_2Re$ in a $N_2$ matrix at 12 K. ——— $\lambda_{ex}$ = 473.5 nm, - - - - $\lambda_{ex}$ = 469.5 nm. Energy 0.15 mJ, 50 laser shots. The inset shows the logarithmic plot of intensity of emission at 498 nm with $\lambda_{ex}$ = 457.9 nm, yielding fluorescence lifetime. (b) ——— Absorption spectrum of $Cp_2Re$ in $N_2$ matrix. (c) Excitation spectra for $Cp_2Re$: -o-o-o- excitation spectrum for $\lambda_{em}$ = 498.0 nm corresponding to full line in spectrum a; -□-□-□- excitation spectrum for $\lambda_{em}$ = 494.8 nm corresponding to broken line in spectrum a.

of unrelaxed (1,0) and (2,0) emission. The duration of the laser pulse again exceeds the emission lifetime.

Decamethylrhenocene: In previous studies we described the astonishingly sharp absorption and LIF spectra of $Cp^*_2Re$.[3] The LMCT transition is characteristically red-shifted ca. 110 nm relative to $Cp_2Re$. The major progression has a frequency of 389 $cm^{-1}$ in absorption, 46 $cm^{-1}$ higher than the corresponding progression frequency of rhenocene. The high frequency shift has been ascribed to mixing of the symmetric ring-metal-ring stretching mode with a symmetric deformation mode of the methyl groups.[4] Two vibrational progressions (A and B) were observed in absorption which were associated with different conformers/sites on the basis of their annealing behaviour. ($Cp^*_2Re$ is eclipsed in the crystalline state.) We found evidence with cw laser excitation for energy transfer between the minor (high energy) site and the major site which are separated by ca. 130 $cm^{-1}$.[4]

The LIF spectra of $Cp^*_2Re$ in nitrogen matrices excited with a pulsed laser are dominated by emission from the major progression, A, even when exciting into the minor component, B. Nevertheless, the emission spectra did show a smaller variation with excitation wavelength splitting into three subsites $A_\alpha$, $A_\beta$, $A_\gamma$ separated by 18 and 15 $cm^{-1}$. The corresponding excitation spectra show how excitation of different absorption series induces emission in the three subsites. The maxima in the excitation spectra agree with the maxima in the absorption spectra to within 0.2 nm. Once more, we were able only to set an upper limit to the emission lifetime, $\tau_F$, of 10 ns.

## CONCLUSIONS

Most previous measurements of emission properties of stable metallocenes rely on photosensitisation experiments using other absorbers.[8,9] One important exception is $Cp_2Ru$ which exhibits a structured ligand-field emission with a progression frequency of 330 $cm^{-1}$. In this case, however, the emission is spin-forbidden and has a lifetime of ~10 - 130 $\mu$s according to

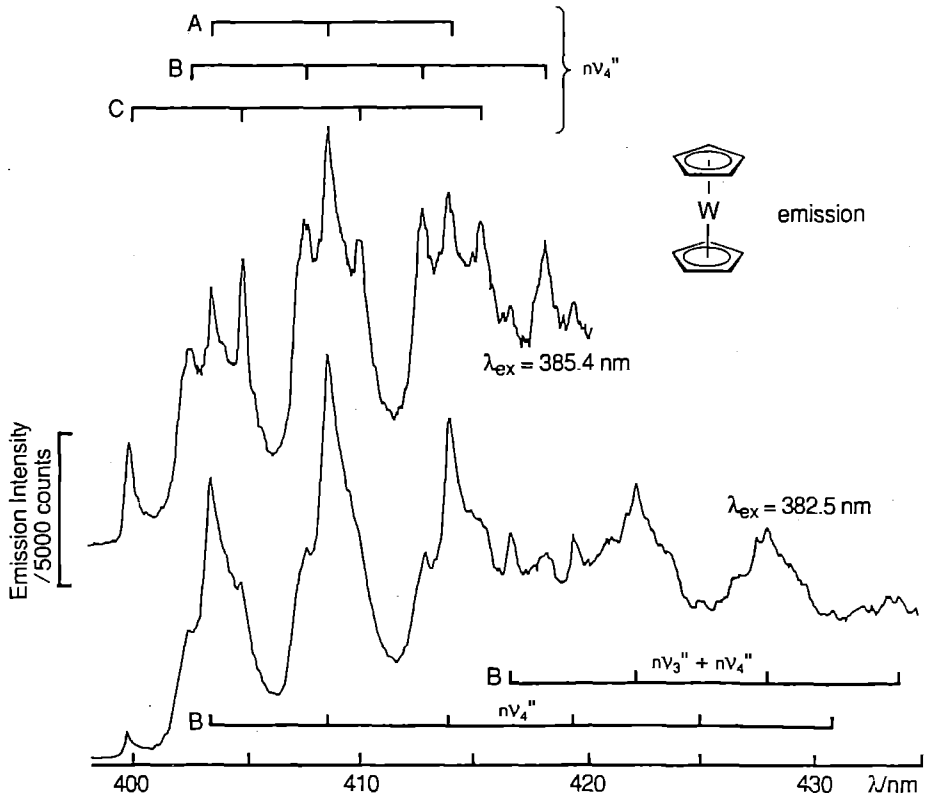


Figure 2. Emission spectrum for $Cp_2W$ in a $N_2$ matrix at 12 K: above $\lambda_{ex}$ = 385.4 nm, below $\lambda_{ex}$ = 382.5 nm. Laser energy = 0.28 mJ, 1650 laser shots. The progressions in $n\nu_4$ and ($\nu_3$ + $n\nu_4$) are marked A, B, and C for the three sites/conformations.

temperature.[10] Our present studies establish the generality of emission from LMCT states of open-shell metallocenes of the second and third row transition metals. The lifetime of rhenocene is 72 ns, while that of the remaining complexes is < 10 ns. The emission spectra are dominated by progressions in the ring-metal-ring stretching mode, so allowing the determination of this and other totally symmetric vibrational frequencies. Changes in emission with excitation wavelength and the associated excitation spectra demonstrate the presence of multiple conformations/trapping sites within the matrices which act as the principal source of fine (10 - 160 $cm^{-1}$) structure in the absorption spectra. Non-resonant electronic energy transfer between minor and major sites/conformers is detected for decamethylrhenocene.

The metallocenes of Mo, W and Re play a key role as reaction intermediates.[2] Their emission spectra not only provide information about detailed photophysical properties, but offer the prospect of a sensitive detection method in fluid phases.


REFERENCES

1. VE Bondybey Chemistry and Physics of Matrix-isolated Species, L Andrews and M Moskovits Ed; North-Holland Amsterdam (1989). RN Perutz Chem Rev **85** 97 (1985).
2. P Grebenik et al. Chem Soc Rev **17** 453 (1988).
3. J Chetwynd-Talbot et al. Inorg Chem **22**, 1675 (1983). PA Cox et al. Chem Phys Lett **108**
4. JA Bandy et al. J. Am. Chem. Soc. **110** 5039 (1988).
5. J Chetwynd-Talbot et al. Inorg. Chem. **21**, 3647 (1982). PA Cox et al. Inorg. Chem. **22** 3614 (1983).
6. DM Haddleton et al. J. Am. Chem. Soc. **110** 1810 (1988).
7. JS Bodenheimer and W Low Spectrochim. Acta **29A** 1733 (1973).
8. GL Geoffroy and MS Wrighton Organometallic Photochemistry Academic Press New York (1979) and references therein.
9. S Rajadurai et al. Chem. Phys. Lett. **129** 244 (1986). A Maciejewskiet et al. ibid. **153** 227 (1988). A Jaworska-Augustyniak et al. ibid. **137** 134 (1987).
10. MS Wrighton et al. J. Phys. Chem. **79** 66 (1975); GA Crosby et al. Chem. Phys. Lett. **28** 497 (1974). KW Hipps et al. J. Phys Chem. **83** 1879 (1979).

# TWO-COLOUR TIME-RESOLVED RESONANCE RAMAN SPECTROSCOPY OF METAL CARBENE COMPLEXES IN SOLUTION.

J. J. McGarvey, A. D. Rooney, K. C. Gordon and K. P. Taylor

The Queen's University of Belfast

## INTRODUCTION

Previous investigations[1,2] at the LSF established the use of TR[3] spectroscopy as a valuable probe of transients and excited states in organometallic complexes.

We present here the results of a two week visit during the current reporting period in which we have carried out two-colour studies on two types of tungsten carbene complex, $(CO)_5W=C(OMe)(Me)$ (1), related to the so-called Fischer complex, $(CO)_5W=C(OMe)(Ph)$ and $(CO)_5W=C(OEt)(SiPh_3)$ (2), one of a series of silyl-substituted carbenes[3], of the type, $(CO)_5W=C(XR)(SiR'_3)$. The studies on (1) extend earlier TR[3] investigations which showed that despite the prompt formation within the laser pulse of a transient with a microsecond lifetime, only minor changes, compared to CW laser-excited spectra, were observed in the frequency region (800 - 1300) $cm^{-1}$ assignable to modes associated with the carbene part (=C(OR)R') of the molecule. This finding was tentatively attributed to the formation of a solvent-coordinated species, $(CO)_4W(S)=C(OMe)(Me)$, following CO loss. One aim of the present study was to examine this proposal more fully by carrying out studies in solvents of varying reactivity and in the presence of other potential ligands and also by extending the measurements to the lower frequency region, $<800cm^{-1}$ where it was hoped that more diagnostically useful changes might be seen in modes assignable to transient and ground state entities.

In the case of the silyl carbenes, the primary aim was to carry out exploratory two-colour experiments to supplement some single colour investigation at QUB and to compare the photochemical behaviour with the thermolysis of these complexes, where previous work elsewhere[4] showed that when XR = $NC_4H_8$ or $NC_4H_{10}$ (but not otherwise), thermally induced CO loss resulted in the formation of stable 16-electron compounds, $(CO)_4W=(NR)R'$.

## EXPERIMENTAL

The two-laser arrangement used for the TR[3] experiments was similar to that described in earlier reports[2]. The pump laser wavelength was 351nm and the probe beam was at 406nm, the energy of the latter being held at sufficiently low levels to effectively eliminate the possibility of secondary pumping. In the case of (1) this requirement amounted to the use of pulse energies of ca. 0.4 mJ or less while for (2), pulse energies as low as 0.1 mJ were necessary. The energies of both pump and probe beams were monitored throughout a given series of experiments to ensure they remained constant. Time delays between pump and probe pulses were controlled by means of a bipolar pulse generator. Comparative singe-colour studies were carried out at 406nm. In this case the laser pulse energies were a factor of 5-10 higher than in the two colour studies.

Argon-purged solution (ca.$10^{-3}$ mol $dm^{-3}$) of the carbenes in the appropriate solvent were cycled from a syringe back and forth through a quartz capillary. Samples were replaced by fresh solution at frequent intervals to minimise the accumulation of possible photodecomposition products. A $90^0$ scattering geometry was employed throughout and all spectra were recorded using the Spex Triplemate spectrometer (1200 grooves/mm grating) and the EG&G 1420B detector controlled from the OMA III console.

## RESULTS AND DISCUSSION

Resonance Raman spectra of (1) generated using single colour (406nm) pulsed excitation are shown in figure 1. The primary feature is a band at 616 $cm^{-1}$ which grows in with increasing laser flux, as shown by the spectra in traces (a) - (c). The position of the band was independent of the solvent used, $CH_2Cl_2$, $C_6H_{12}$, or $C_7F_{14}$. Two-laser TR[3] studies

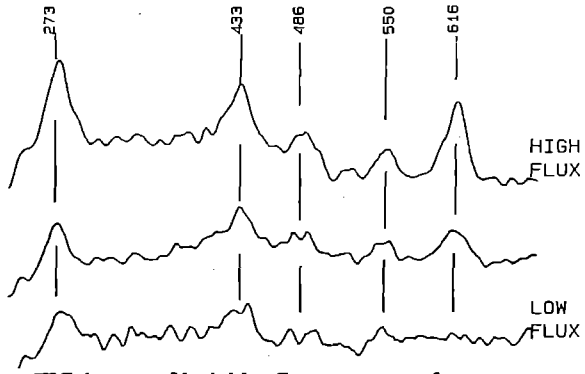


FIG.1. Variable flux spectra of $(CO)_5W=C(OMe)(Me)$ in cyclohexane $\lambda ex$ 406nm

on (1) in different solvents were carried out, using 351nm as the pump wavelength and 406nm as the probe. Representative spectra are shown in figure 2, recorded at several pump-probe time delays. Because of the need mentioned above of maintaining minimum probe energies, the S/N ratio on these spectra

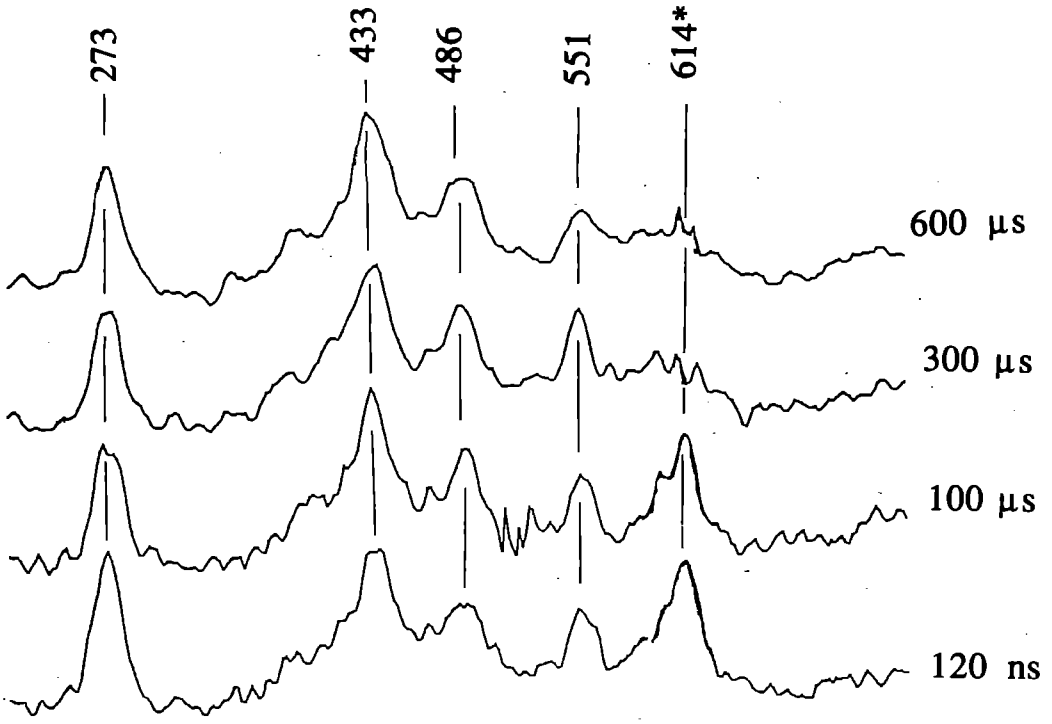


FIG.2. $TR^3S$ of $(CO)_5W{=}C(OMe)(Me)$ in cyclohexane
λ pump 351nm
λ probe 406nm

is rather low. Nevertheless, the same 616cm$^{-1}$ feature appears as in the single colour spectra (figure 1). The decay with increasing pump-probe delay is readily monitored and is consistent with assignment of the 616cm$^{-1}$ band to the same transient as had been observed in independent laser flash photolysis experiments at QUB, carried out at an excitation wavelength of 355nm. Additional two-colour pump and probe experiments demostrated that the decay of the transient Raman feature at 616cm$^{-1}$ was the same within experimental uncertainty in either $H_2$- or CO-saturated solutions as in Ar-saturated solutions. Furthermore, detailed perusal of the $TR^3$ spectra over the frequency range (200-1600 cm$^{-1}$) revealed no additional spectral features to those seen in the single-colour case.

The Raman spectra in figures 1 and 2 indicate that the same transient is formed following irradiation of (1) at either 351nm or 406nm. It should be noted here that in the two-colour experiments, as already mentioned, the probe beam (406nm) energy has been kept sufficiently low to exclude the direct formation of transient at this wavelength. In these experiments, the transient only appears when the 351nm pump beam is turned on. Since 406nm lies within the metal-to-ligand charge transfer (MLCT) absorption of (1) where CO loss would not be expected to occur, the results of the two types of experiment suggest that CO loss from (1) is not a significant primary process at 351nm either, even though this wavelength lies within the ligand field absorption region of the complex where at least some CO loss would be expected.

The absence of any effect of CO- or $H_2$-saturation on the transient decay is consistent with this conclusion. Further support is provided by the fact that CO saturation appears to have no effect on either the $TR^3$ spectra or on the transient decay observed in the inert solvent $C_7F_{14}$. This would also seem to rule out the earlier proposal that a solvent-coordinated species is involved since this would require the formation of a 16-electron CO-loss entity.

Overall therfore, the present $TR^3S$ results are consistent with recent independent studies from two other laboratories [5,6] which suggest

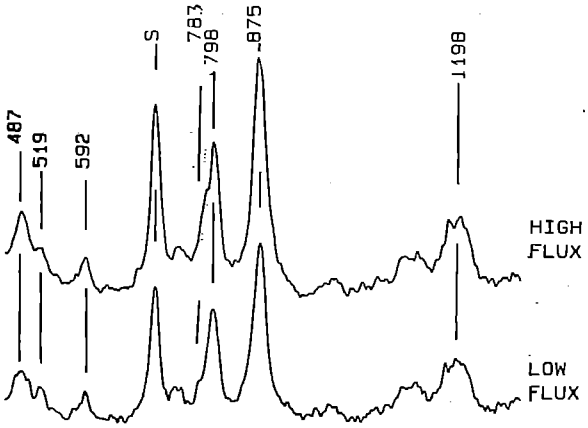


FIG.3. Variable flux spectra of $(CO)_5W{=}C(OEt)(SiPh_3)$ in dichloromethane
λex 406nm

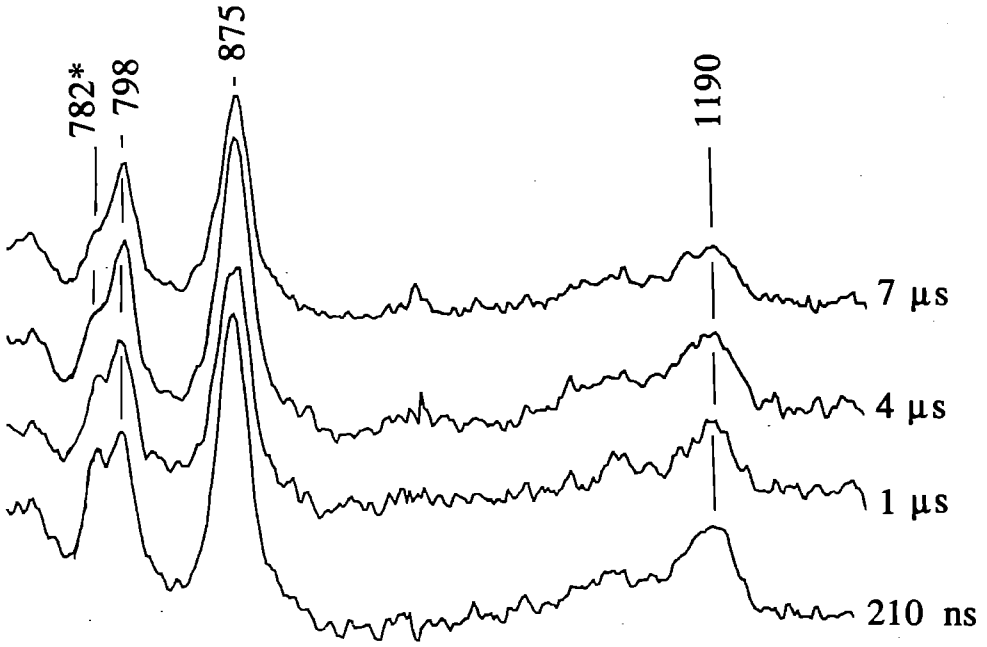


FIG.4. $TR^3S$ of $(CO)_5W=C(OEt)(SiPh_3)$
in dichloromethane
λ pump 351nm
λ probe 406nm

that photoisomerisation rather than CO loss is the principal photochemical process in these tungsten metal carbenes, following irradiation throughout the ligand-field and the charge-transfer absorption regions.

The 616$cm^{-1}$ transient feature which we have used in reaching this conclusion is tentatively assigned to a W-C-O bending vibration but additional work is needed to confirm this. Further studies are under way to try to find satisfactory reasons for the marked differences in the carbene region of the $TR^3$ spectra of (1), compared to the corresponding features observed with other tungsten carbenes, $(CO)_5W=C(OR)R'$, where R' is an aryl group.

Figures 3 and 4 compared the findings from single- and two-colour resonance Raman studies on the silyl carbene, (2). In the two-colour experiments, secondary pumping occurred with such ease that it was necessary to hold the probe beam (406nm) energy at 0.1 mJ. This coupled with the fact that (2) seems to be an inherently weak Raman scatterer resulted in rather low quality spectra being obtained. Only one relatively prominent transient feature at 782 $cm^{-1}$ was observed throughout the range 600-1600 $cm^{-1}$, with a ground state counterpart at 798$cm^{-1}$. The transient decay indicated by the spectra in figure 4 is consistent with recent flash photolysis studies at QUB which also show that the activation energy for the decay is of the same order as that measured for the phototransient generated in (1) and related non-silyl-containing carbenes. This suggests that photoisomerisation may be a common feature in all of these systems, a conclusion with important implications for the catalytic reactivity of metal carbenes.

Preliminary results obtained for the $NC_4H_8$-substituted silyl carbene are in some contrast to the above. In this case no transient species appear to form at any wavelength throughout the range (350-420)nm. Instead, a permanent photoproduct is formed with a distinctive feature at 1503$cm^{-1}$.

ACKNOWLEDGEMENTS

We wish to thank Dr. A.W. Parker and Miss S. Tavender for their assistance in carrying out these experiments. We thank SERC for supporting the work.

REFERENCES

1. J.J. McGarvey et al. *Annual Report to the Laser Facility Committee* Rutherford Appleton Laboratory Report RAL-87-041, B1.4, 128, (1987)
2. K.C. Gordon et al. *Annual Report to the Laser Facility Committee* Rutherford Appleton Laboratory Report RAL-89-045, C1.7, 249, (1989)
3. U. Schubert *J. Organomet. Chemistry* **358**, 215, (1988)
4. U. Schubert et al. *Organometallics* **5**, 173, (1986)
5. P.C. Servaas et al. *J. Organomet. Chemistry* (1990) in press
6. M. Poliakoff et al. unpublished results

# TIME-RESOLVED RESONANCE RAMAN ANALYSIS OF RUTHENIUM(II)TRIS(BIBYRIDINE) EXCITED STATE

S. Umapathy, A.W. Parker[1] and R.E. Hester

Department of Chemistry, University of York, York.
[1]Laser Division, Rutherford Appleton Laboratory, Chilton, Didcot.

## Introduction

Time-resolved resonance Raman spectroscopy (TR3S) has been widely used to establish the vibrational structure and the nature of the metal-ligand charge transfer (MLCT) triplet excited state of $d^6$ transition metal complexes (1-3). In particular, bipyridyl complexes of ruthenium(II) have been studied by TR3S. These have potential use as sensitisers in solar energy conversion processes (2). In this report we discuss the various aspects of the procedures used to interpret the TR3S data, with particular reference to ruthenium(II)*tris*(bipyridine).

## Results and Discussion

The MLCT triplet excited state of ruthenium(II) *tris*(bipyridine) (RBY) has been shown by TR3S studies to have an asymmetric structure with the odd electron being localised on one of the three ligands. This electron localisation is indicated by (a) the presence of two sets of Raman bands, one for the neutral ligands and one for the reduced ligand (where the odd electron is resident), (b) the presence of 2/3 intensity of the neutral ligand bands in the excited state spectrum by comparison with their intensity in ground state spectra, (c) the positions of the bands due to the reduced ligand being consistent with those of the uncomplexed radical anion of the ligand, and (d) the shift in band positions corresponding to the change in electron distribution within the ligand (1). Of these four main criteria used to interpret the TR3S spectra, (a) and (b) have been contradicted by Hopkins *et al.* (3-5) but (c) and (d) have been well supported by various authors (1-6). Therefore, we consider only (a) and (b) here.

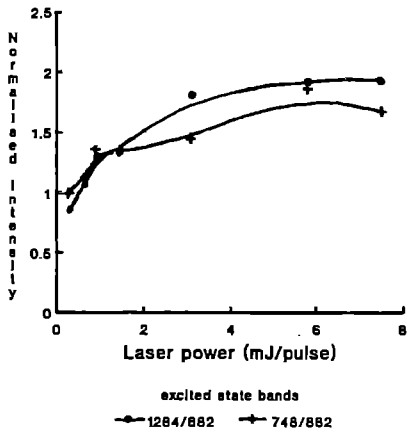


Fig.1: Plot of Raman intensity Vs pulse energy (mJ/pulse).

The criteria (a) and (b) depend solely on whether the photoconversion of the ground state to the excited state is complete, *i.e.* whether the saturation is achieved. Our experiments involved exciting RBY using a variety of laser wavelengths and powers. Fig. 1 shows a plot of the excited state band intensities (normalised against an internal standard) at various laser pulse energies. It is evident that saturation has been reached with high energy pulses, *i.e.* the photochemical conversion to the MLCT excited state is essentially 100%. The wavelength of the laser excitation is *ca.* 363.8 nm, which is in resonance with the reduced ligand absorption leading to specific enhancement of the reduced ligand bands. In Fig. 2 the TR3S spectrum of RBY recorded at the saturation limit (7.5 mJ pulse energy) is shown. the bands due to the neutral ligands are shaded.

From these data and also spectra obtained at other wavelengths, we have shown that the resonance Raman spectra of the RBY MLCT excited triplet state do contain bands due to the neutral ligands, in addition to the bands due to the reduced ligand (7). This is in contrast to conclusions reached by Hopkins *et al.* in a series of recent publications (3-5). We attribute the contradictions to incorrect use of spectral subtraction routines by Hopkins *et al.* without appropriate allowance for absorption of the laser excitation and Raman scatter by the sample.

Using the well-established procedures given above (in para. 2) we were able to interpret the TR3S spectra of ruthenium(II) *tris*(5,5'-dicarboxylate-2,2'-bipyridine) which are shown in Fig. 3. With increasing laser energy the excited state bands (shown as E) also increase in intensity. Analysis of these spectra shows that the electron is localised on one of the three ligands (7).

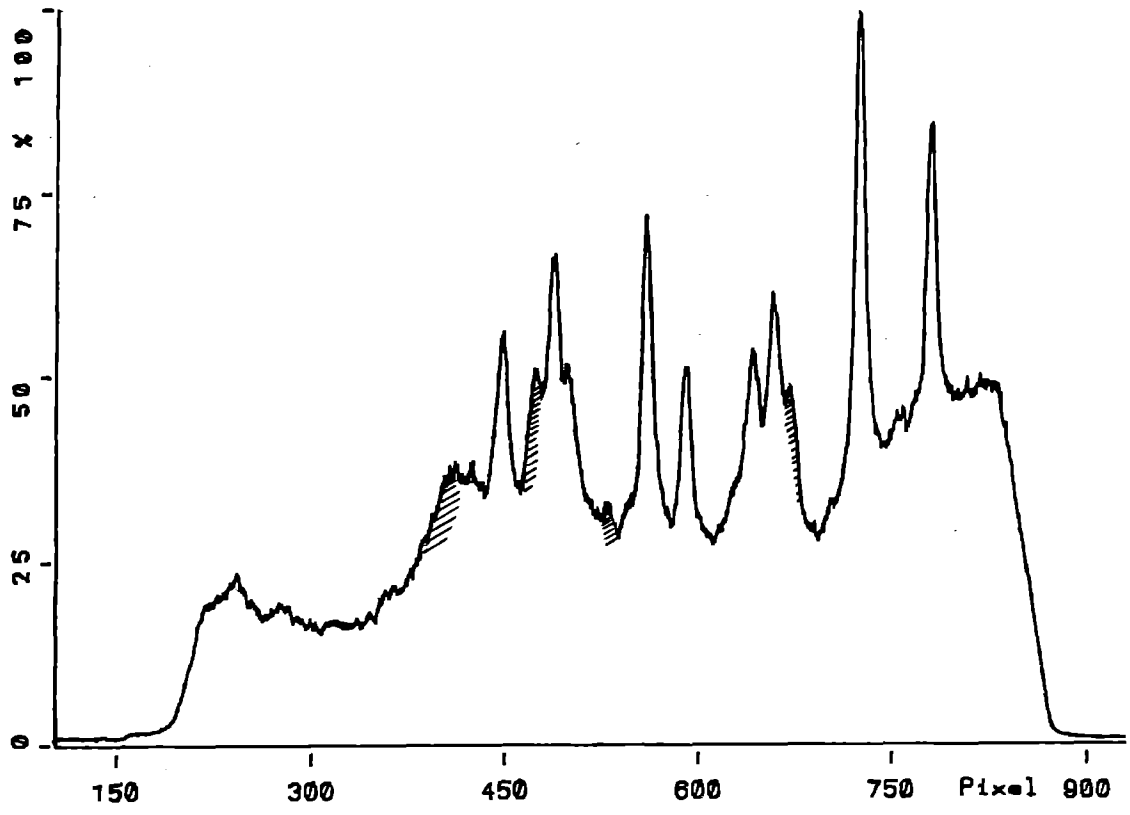


Fig.2: TR3S of RBY triplet excited state - shaded bands are due to neutral ligands.

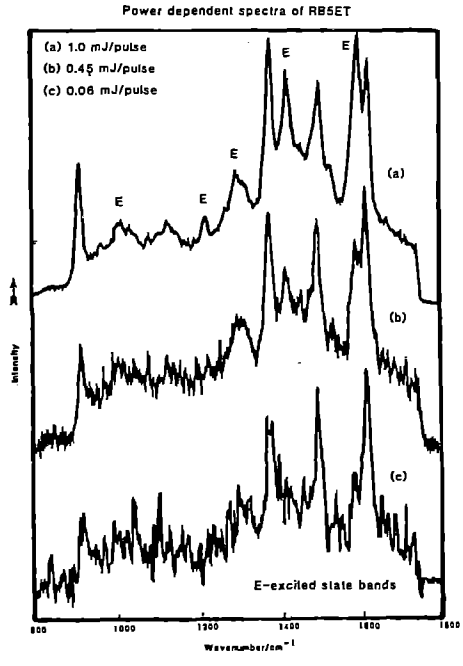


Fig. 3: TR3S of ruthenium(II) *tris*(2,2'-bipyridyl-5,5'-dicarboxylate) at various pulse energies and E-excited state bands.

Acknowledgement:

We thank Dr J N Moore for valuable assistance and discussions, Mr R B Girling for technical assistance and the SERC for financial support.

References:

1. P.G. Bradley, N. Kress, B.A. Hornberger, R.F. Dallinger, and W.H. Woodruff, J. Am. Chem. Soc., 103 (1981) 7441.
2. S. Umapathy, A.M. Cartner, A.W. Parker and R.E. Hester, J. Phys. Chem., in press.
3. L.K. Orman and J.B. Hopkins, Chem. Phys. Letts., 149 (1988) 375.
4. L.K. Orman, Y.J. Chang, D.R. Anderson, R. Yabe, X. Xu, S. Yu and J.B. Hopkins, J. Chem. Phys., 90 (1989) 1469.
5. Y.J. Chang, X. Xu, T. Yabe, S. Yu, D.R. Anderson, L.K. Orman and J.B. Hopkins, J. Phys. Chem. 94 (1990) 729.
6. M. Forster and R.E. Hester, Chem. Phys. Letts., 81 (1981) 42.
7. S. Umapathy, A.W. Parker, R.E. Hester and W.H. Woodruff, manuscript in preparation.

# TIME-RESOLVED RESONANCE RAMAN STUDIES OF ELECTRON TRANSFER

E Vauthey[1], A W Parker[2] and D Phillips[1]

[1]Department of Chemistry, Imperial College, London
[2]Rutherford Appleton Laboratory

## INTRODUCTION

A great deal of experimental work has been concerned with attempts at checking theoretical predictions concerning the rate of fast electron transfer reactions. Since the observation of the 'inverted region' for several systems [1], the influence of the free energy on the electron-transfer rate is now quite well understood. On the other hand, the role of the medium is still under discussion: the so-called semi-classical Marcus-Hush theory predicts a correlation between a solvent reorganisation energy derived from the Born equation of ionic solvation and the rate constant of electron-transfer [2]. Such a relationship has not been generally confirmed by experiments [3], and recently new theories have pointed out the importance of solvent relaxation kinetics for adiabatic electron transfers [4]; correlations between the longitudinal dielectric relaxation time and the rate of electron-transfer have indeed been observed for intramolecular [5] and intermolecular processes [6].

In all solvents, the quenching of the excited state leads to the formation of an exciplex when charge transfer is not complete: this exciplex being an excited state of a 'supermolecule' whose deactivation pathway in low polarity solvents is mainly its fluorescence; in more polar solvents, exciplexes often dissociate to a geminate ion pair formed in the electronic ground state.

If the electronically excited partner in the photoinduced electron-transfer is in a triplet state, it is often held that a 'triplet exciplex' is generated. The absorption spectrum of this species corresponds closely to the superposition of the spectra of the donor's radical cation and of the acceptor's radical anion, indicating that it must be very similar to a geminate ion pair [7]. It is known that back electron-transfer within triplet geminate ion pairs in MeCN is slow, of the order of $10^7 s^{-1}$ [8], because the spin of the electron must change before the recombination. If $k_{sep}$ is even slower than $k_{bac}$ as is the case in solvents of low polarity, it is then possible to observe the geminate triplet ion pair by ns-laser flash-photolysis. In the experiments reported here, time-resolved resonance Raman spectroscopy was employed to attempt to distinguish on structural grounds the 'exciplex' and ion-pair intermediates.

## EXPERIMENTAL

The investigations carried out were standard pump and probe nanosecond $TR^3$ experiments using excimer laser excitation, excimer-pumped dye probe, and OMA III detection, as described in previous reports. The equipment was used to study systems where the electron acceptor is the triplet excited state of (9,10-Anthraquinone, AQ) and the electron donor is either a tertiary amine (Triphenylamine, TPA), or a methoxybenzene (1,2,4-trimethoyxbenzene, TMB). In non-polar solvents, these electron donor/acceptor couples have been reported to form triplet exciplexes, while in polar solvents the free ions are generated. We measured the $TR^3$ spectra of these systems in a polar (acetonitrile) and non-polar solvents (benzene, $CCl_4$) by pumping at 351 nm to excite the acceptor and by probing at 460 nm and 540 nm where the Raman bands of the free ions and of the triplet exciplexes are resonantly enhanced.

## RESULTS AND DISCUSSION

Figure 1 depicts the $TR^3$ spectra recorded with a pump wavelength of 351 nm, probe 460 nm, of the AQ/TMB pair in methyl cyanide, at a delay of 50 ns. Spectra recorded in other non-polar solvents, for example toluene, were identical, leading to the conclusions that the $TR^3$ spectra of free ions and the triplet exciplex are the same, indicating that the species called a 'triplet exciplex' is in fact a geminate ion pair, as indicated in Scheme 1.

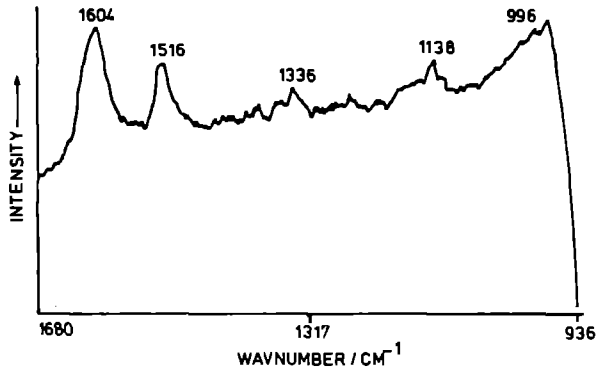


Fig.1: $TR^3$ spectrum (pump/probe - probe only spectra) of AQ ($1 \times 10^{-3}$ mol $dm^{-3}$) + TMB (0.1 mol $dm^{-3}$) in deoxygenated MeCN. Pump 351 nm probe 460 nm; $\Delta t$ = 50 ns.

Contrasting results were obtained in carbon tetrachloride, as shown in Figure 2. By comparison with those in figure 1, it can be seen that the band at 1336 in the MeCN spectrum is absent in the $CCl_4$, and there is a large shift of one band, (1604 $cm^{-1}$ in MeCN) going to 1587 $cm^{-1}$ in $CCl_4$. The probe wavelength in the case of $CCl_4$ solvent was 460 nm, where the radical cation of TMB absorbs.

The difference in spectra in the two solvents could be explained if it is assumed the chlorine atoms in the solvent promote, via a heavy atom effects the intersystem crossing between the triplet and singlet geminate ion pairs. It is thus proposed that the species observed in $CCl_4$ is the singlet geminate ion pair (or a singlet exciplex).

## SCHEME 1:

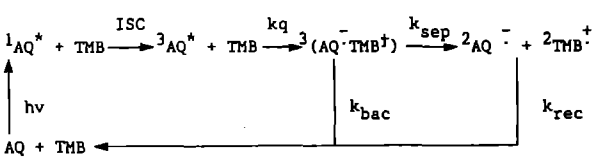

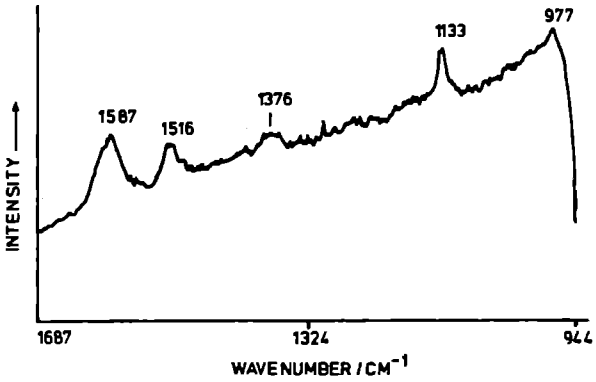


Fig.2: TR$^3$ spectrum (pump/probe - probe only spectra) of AQ (1 x $10^{-3}$ mol $dm^{-3}$) + TMB (0.1 mol $dm^{-3}$) in deoxygenated $CCl_4$. Pump 351 nm probe 460 nm; $\Delta t$ = 50 ns.

The results are preliminary, and require substantiation. However, the implications, which is in accord with previous transient absorption data [7] is that the species generated by the quenching of a triplet excited state by an electron donor is not properly described as a 'triplet exciplex', but rather as a ground-state geminate ion pair populated by a temperature independent spin-flip process. This relaxes by a temperature dependent electron transfer (Scheme 1).

ACKNOWLEDGEMENTS

We are grateful to SERC for financial support of this work, and one of us (EV) thanks National Science Foundation, Switzerland, for the award of a post-doctoral fellowship.

REFERENCES

1. E Vauthey, P Suppan and E Haselbach, Helv Chim Acta 71 93 (1988) and references therein.

2. R A Marcus, Ann Rev Phys Chem 155 (1964).

3. a) E S Yang, M S Chan and A C Wahl, J Phys Chem 84 3094 (1980).

b) P Pasman, C F Mes, N W Koper and J W Verhoeven, J Am Chem Soc 107 5839 (1985).

c) M D Archer, V P Y Gadzepko, J R Bolton, J A Schmidt and A C Weedon, J Chem Soc Faraday Trans II 82 2305 (1986).

d) A B Helman, Chem Phys Lett 135 529 (1987).

e) P Suppan, Chimia 42 320 (1988).

4. a) D F Calef and P G Wolynes, J Phys Chem 87, 3387 (1983).

b) I Rips and J Jortner, J Chem Phys 87 3387 (1983).

5. D Huppert, V Ittah and E M Kosower, Chem Phys Lett 144 15 (1988).

6. E Vauthey and P Suppan, Chem Phys 139 381 (1989).

7. V A Kuzmin, A P Darmanyn and P P Leven, Chem Phys Lett 63 509 (1979).

8. E Haselbach, E Vauthey and P Suppan, Tetrahedron 44 7335 (1988).

# TIME RESOLVED RESONANCE RAMAN SPECTROSCOPY OF HEME PROTEIN MODEL SYSTEMS

J C Austin[1], S E J Bell and R E Hester

Department of Chemistry, University of York, York YO1 5DD.
[1]Current Address: Department of Chemistry, Princeton University, Princeton, New Jersey 08544, USA.

## INTRODUCTION

In a previous report[1] we described single laser resonance Raman experiments on Fe(TPP)Cl in which excitation of $10^{-4}$ mol $dm^{-3}$ solutions of the complex by 10ns duration laser pulses appeared to populate a short lived transient excited state of the complex. We were unable to obtain Raman spectra of the transient and attributed this failure to poor resonance enhancement at the laser wavelenth used. We now report the results of two-colour time-resolved resonance Raman ($TR^3$) experiments.

## RESULTS

In the $TR^3$ experiments, the sample was pumped at high fluence by 406 nm pulses (ie. under conditions where the single-colour experiments showed a large ground-state depletion) and probed at 448 nm, where transient absorption experiments had shown the triplet-state species to be strongly absorbing.[2] Figure 1 shows difference spectra (pump and probe)-(pump only + probe only) recorded at time delays between the pulses of 0 (a) and 15ns (b). A large loss of ground-state signal occurs only when both pump and probe pulses are simultaneously coincident on the sample and thus the signal is associated with formation of a transient species with a lifetime shorter than the laser pulse. In 406 (pump) and 424 nm (probe) two-colour experiments the only strong positive features in the difference spectra are due to solvent. The appearance of more intense (in an absolute sense) solvent bands is associated with a decrease in absorbance of the sample at the Raman probe and/or monitoring wavelength. In 406 (pump) and 448 nm (probe) experiments new positive bands corresponding to the transient species were observed in the zero time-delay spectra but at longer time delays the only observable features were, again, due to a small loss of the ground state species. We have found that this small loss of the ground state species persists with no change in intensity for tens of microseconds and attribute it to a side reaction which gives a photodecomposition product.

The spectra shown in Figure 1 have low signal-to-noise ratios because they are the result of a double subtraction process. The original pump-and-probe spectra are of considerably better quality. Figure 2(b) shows a pump-and-probe spectrum for comparison with a spectrum (Fig. 2(a)) which is the sum of pump only and probe only experiments. In the pump-and-probe spectrum both of the strong bands due to totally symmetric vibrations( $\nu_2$ at 1556 and $\nu_4$ at 1360 $cm^{-1}$ in the ground state) retain considerable intensity but are down-shifted by ca. 15 $cm^{-1}$. The near disappearance of these features from their ground state positions indicates that conversion to the transient species is almost complete.

## DISCUSSION

The above results strongly suggest that the species we have observed is the same excited state of Fe(TPP)Cl reported by Hochstrasser[2] and by Gurinovich[3]. In this state the complex has a strong absorption at 448 nm but considerably lower

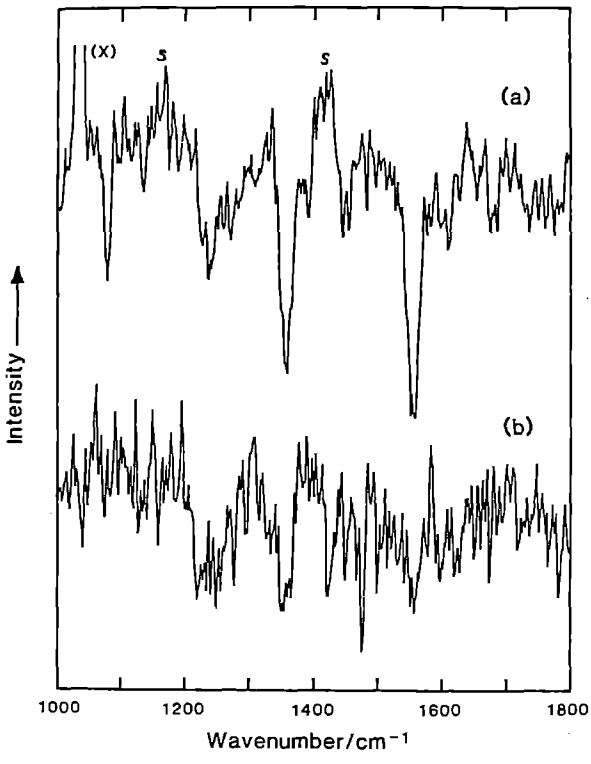


Figure 1: Two-colour (406 nm pump, 424 nm probe) RR difference spectra (pump and probe) - (probe only + pump only) of Fe(TPP)Cl ($10^{-4}$ mol $dm^{-3}$ in $CH_2Cl_2$) (a) at zero pump-probe delay, $\Delta t$ = 0 (b) at $\Delta t$ = 15 ns. Spectrum (b) has been vertically expanded x 2. Feature marked X is an experimental artifact. Solvent bands are marked S.

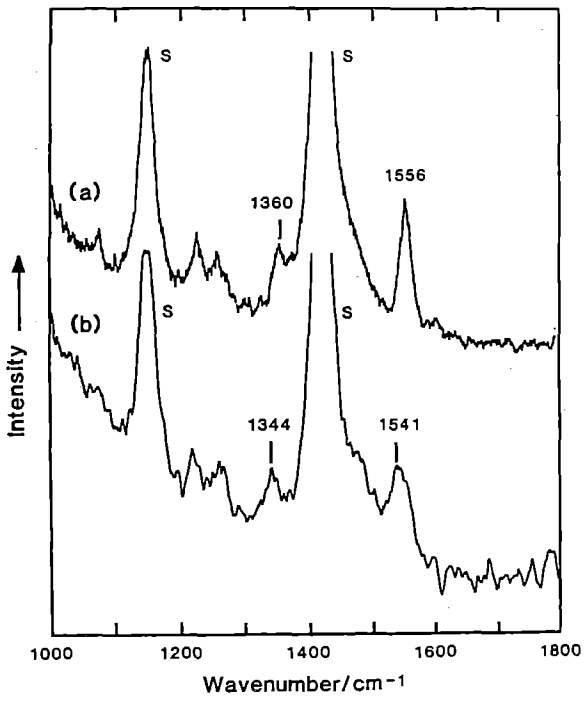


Figure 2: Two-colour (406 nm pump, 448 nm probe) RR spectra of Fe(TPP)Cl ($10^{-4}$ mol $dm^{-3}$ in $CH_2Cl_2$) (a) probe only (b) pump and probe, $\Delta t$ = 0.

absorption at 406 and 424 nm, so it is only at 448 nm that strong resonance enhancement of Raman scattering by the transient species is observed.

Gouterman[4] has shown that for metalloporphyrins with a single unpaired d electron on the metal atom the triplet states associated with $\pi \rightarrow \pi^*$ transitions on the porphyrin are further split into tripdoublets and quartets and that luminescence spectra due to either state may be observed. In the case of Fe(TPP)Cl further complications arise because in this complex the low-lying partially-filled metal $d_{xz}$ and $d_{yz}$ orbitals are of appropriate energy (and symmetry) to mix with the lowest unoccupied ($e_g$) orbital on the prophyrin. Because of this, the low-lying excited states of the complex cannot be described as singlets and triplets but rather are configuration-interaction admixtures of several different sextets with e symmetry. It has been calculated[5] that the lowest-lying of these states arises from a mixture of orbitals associated with tripsextet (ie $a_{1u}$, $a_{2u} \rightarrow e_g$ $\pi \rightarrow \pi^*$) and charge transfer ($a_{1u}$, $a_{2u} \rightarrow d_{xz}$, $d_{yz}$) states, with a minor singsextet ($a_{1u}$, $a_{2u} \rightarrow e_g$) contribution. Although it has previously been recognized[3] that other, spin-forbidden, states of the Fe(TPP)Cl may be populated by intersystem crossing, in the transient absorption experiments of Hochstrasser[2] and Gurinovich[3] the excited state was denoted as a porphryin triplet since the absorption spectra resembled those of simpler triplet metalloporphyrins. We believe that our Raman experiments are probing the same state and have therefore used the "triplet" label, although with some reservations for the reasons outlined above.

The resonance Raman spectrum of triplet Fe(TPP)Cl differs dramatically from that of triplet Zn(TPP) both in the directions of frequency shifts and in the band intensities. In particular, the $\nu_2$ and $\nu_4$ bands (which are strong in the ground state spectra of both complexes) are weak in the RR spectrum of excited Zn(TPP)[6] but strong in that of excited Fe(TPP)Cl. This may be because the strong configuration interaction, which mixes the low-lying porphyrin-centered triplet states with other states in the iron complex, results in a much reduced Jahn-Teller distortion as compared with Zn(TPP)[6]. In the absence of a Jahn-Teller distortion the totally symmetric $\nu_2$ and $\nu_4$ vibrations would be expected to retain their large intensity if the resonance enhancement is through an "A" term mechanism and the absorbance at ca 440 nm is due to promotion of a second electron from $a_{1u}$ or $a_{2u}$ to $e_g$ orbitals [7]. The lowering of the $\nu_2$ and $\nu_4$ frequencies which occurs upon triplet formation indicates a core expansion of the prophyrin[8], which is what would be intuitively expected for a $\pi \rightarrow \pi^*$ excitation of the prophyrins. Furthermore, if the "triplet" we observe is the tripsextet (as seems likely, since it has been shown to form within <8 ps[2]) then it has a significant ligand-to-metal charge-transfer component which would again be expected to give core expansion with a consequent lowering of the $\nu_2$ and $\nu_4$ frequencies.

## REFERENCES


1. J.C. Austin, S.E.J. Bell and R.E. Hester, *SERC Central Laser Facility, Annual Report to the Laser Facility Committee 1989*, RAL-89-045, 323.
2. P.A. Cornelius, A.W. Steele, D.A. Chernoff and R.M. Hochstrasser, *Chem. Phys. Letters* 82 (1981) 9. Y. Liang, D.K. Negus, R.M. Hochstrasser, M. Gunner and P.L. Dutton, *Chem. Phys. Letters* 84 (1981) 236.
3. B.M. Dzhaganov, V.S. Chirvonyi and G.P. Gurinovich, in: Laser Picosecond Spectroscopy and Photochemistry of Biomolecules, ed. V.S. Letokhov (Adam Hilger, Bristol, 1987) p. 137.
4. R.L. Ake and M. Gouterman, *Theoret. Chim. Acta*, 15 (1969) 20.
5. H. Kobayashi, *Adv. Biophys.* 8 (1975) 191.
6. V.A. Walters, J.C. de Paula, C.T. Babcock and G.E. Leroi, *J. Am. Chem. Soc.* 111 (1989) 8300.
7. J. Rodriguez, C. Kirmaier and D. Holton, *J. Am. Chem. Soc.* 111 (1989) 6500.
8. N. Parthasarathi, C. Hanson, S. Yamaguchi and T.G. Spiro, *J. Am. Chem. Soc.* 109 (1987) 3865.

# A RESONANCE RAMAN STUDY OF PENTAAMMINE(5'ADENOSINEMONOPHOSPHATE)RUTHENIUM(II) ISOMERS.

Delwyn R. Evans and Michael Green.
Department of Chemistry, University of York, Heslington, York. YO1 5DD

## Introduction.

The group is interested in the reactions that occur when the pentaammineaquaruthenium(II) ion is mixed with various nucleotides. UV-vis kinetic studies at the University of York have revealed that in the first stage of the reaction, three unique absorption peaks develop, and as there are potentially three sites on 5'AMP, (N1, N3, and N7), at which the ruthenium complex could bind, it seems that a mixture of products initially form. However, during the course of the reaction, the resolution of the bands is lost, and the final spectrum consists of a broad band.

The questions thus posed are:- (i) which UV-vis absorption relates to which binding site ?
and (ii) do the initially formed isomers convert to one favoured species ?

In an attempt to answer these questions, a resonance Raman study was undertaken which involved irradiating the reaction product(s) with light whose wavelength, in turn, matched the position of the three initially observed UV-vis absorptions. It was hoped that the dependence of the Raman spectrum upon incident wavelength would help identify the species present at the end of reaction.

## Experimental.

For each experiment a fresh $[Ru(NH_3)_5(OH_2)](PF_6)_2$ - 5'AMP solution was prepared under argon, using argon flushed deionised water. The solution was left for at least an hour before use. In the sample chamber of the spectrometer, the solution was pumped through a silica capillary tube by argon pressure.

The incident laser wavelengths used were 366, 383, and 397 nm; the last two required an excimer pumped dye laser, and the first an argon ion type. Spectra were collected with a Spex Triplemate connected to a data station.

(Specta were also taken of the individual reactant solutions).

## Results

| Raman bands for $[(H_3N)_5Ru(5'AMP)]$ ($cm^{-1}$) when incident $\lambda$ = x (nm) | | | Raman bands for 5'AMP ($cm^{-1}$)(1) |
|---|---|---|---|
| x=364 | x=383 | x=397 | |
| 1567 | 1576 | 1576 | 1583 |
| | | | 1510 |
| 1478 | 1465 | 1460 | 1485 |
| | 1420 | 1428 | 1425 |
| | | | 1380 |
| 1330 | 1330 | 1332 | 1340 |
| | | | 1308 |

## Discussion.

At each laser wavelength it was found that certain adenine based Raman bands were considerably more intense for the ruthenated nucleotide than the free ligand. For each wavelength it seems that the same adenine vibrations are being enhanced, even though the exact value of the Raman shifts does vary. (For the differences in band position to be significant, further experimentation would be required to improve the resolution of the spectra).

The frequency range of the enhanced bands, 1300 - 1600 $cm^{-1}$, is indicative of adenine ring vibrations with double bond content. They are likely to be enhanced if the ruthenium complex binds to any of the N1, N3 and N7 sites, so there is no obvious evidence that correlates a binding site to a particular UV-vis absorption wavelength. Further work employing a tight control on experimental variables could yield spectra in which any difference in band intensity would be quantitative, and thus of use in product identification. Curiously, the literature mentions an adenine Raman band at 1380 $cm^{-1}$, which is absent in all the product spectra. However, as literature that attempts to assign adenine vibrations to observed frequencies is sparse, the significance of this result is presently dormant.

Although the experiment is inconclusive as it stands, it has illustrated that certain adenine Raman bands are selectively enhanced when using incident radiation that corresponds to the product chromophore. To elucidate further binding site infromation, more sophisticated experiments are needed to highlight and quantify subtle differences in the spectra.

## Reference.

(1) R.C. Lord and G.J. Thomas, Spectrochem. Acta., 1967, 23A, 2551.

# Raman Emission from NOCl

Andrew J. Bell, and Jeremy G. Frey
Department of Chemistry, Southampton University
Southampton SO9 5NH, England, UK.

**Abstract**

Spectroscopic observations during the laser photolysis of NOCl throughout the visible and near uv region allowed the observation of simple resonance Raman spectra. In contrast excitation at 266nm gives rise to vibrational progressions in both the $\nu_2$ and $\nu_3$ vibrational modes[1].

**Introduction**

During a chemical reaction the molecules involved pass through a continuously evolving intermediate species which is neither a true reactant or product, but rather the former turning to the latter. Detailed studies of nuclear motions during a reaction require experimental techniques to probe the process of the order of picoseconds after the reaction has been initiated, finer details, involving sub-Angstrom motions, requiring resolution on the femtosecond timescale.

An approach to this problem is to record the projection of the time-evolving reaction, which is occuring on one electronic surface, onto known vibrational wavefunctions of another. This approach gives the advantage of being able to record sub-Angstrom movements in the frequency domain, eliminating the need for experimental sub-picosecond time resolution.

Nitrosyl chloride (NOCl) is a brown/orange gas at room temperature and pressure. Below -6°C (boiling point) it is a deep red liquid which on solidification at -60°C (melting point) turns pale yellow. The photodecomposition of gas phase NOCl has a quantum yield of $\phi_{NOCl}=2$ over the wavelength region 365-630nm [2]. The first absorption spectrum of NOCl was recorded by Goodeve and Katz [3], and covered the region 190-650 nm. Four broad envelopes lying to the shorter wavelength end of the spectrum being repulsive state transitions correlating with $NO(^2\Pi)$ + $Cl(^2P_{3/2})$, the remaining seven consisting a vibrational progression being broadened by predissociation. Later work performed on the absorption spectrum [4], [5] has shown that there is infact a discrepency in the extinction coefficient at the lowest wavelength ($\lambda_{max} \sim$ 195 nm) band in the Goodeve and Katz spectrum, the absorption cross-section at the peak being just under an order of magnitude higher. The continuous nature of the absorption spectrum is a consequence of the fast dissociation process

$$NOCl + h\nu(\lambda<751.9nm) \longrightarrow NO(X^2\Pi) + Cl(^2P_{3/2,1/2})$$

The quantum yield is greater than unity due to the secondary process

$$Cl + NOCl \longrightarrow NO + Cl_2 \qquad (8)$$

NOCl is a bent triatomic molecule. It has three fundamental vibrations, all of which (from symmetry considerations) are allowed Raman transitions of A' symmetry. Furthermore, electronic dipole transitions from the A' ground state to excited states A' <- A' and A" <- A' are allowed by transition dipole moments lying in the molecular plane, r(A'), or perpendicular to the molecular plane, r(A"), respectively.

Our previous work described the attempts to observe vibrational overtone progression in the resonance Raman emission arising following excitation of NOCl in the B,C and D absorption bands[6]. In contrast to similar experiments on $O_3$ [7], $CH_3I$ [8], $NO_2$ [9], and $CH_2I_2$ [10], the Raman spectra recorded by excitation over the region 514nm to 355nm, showed the $\nu_2$ and $\nu_3$ fundamentals but no overtone transitions [6]. However the work reported here shows that excitation into the long wavelength side of the A band at 266nm gives rise to short but significant progression in both the $\nu_2$ and $\nu_3$ modes; these are associated with the N-Cl stretch and bend.

The 266nm radiation was generated from a Q-switched JK HyperYag Nd:YAG laser (20Hz, 20nsec pulse and 50mj/pulse at 266nm). The 266nm radiation was separated from the Nd:YAG fundamental and other harmonics by a Quanta-ray prism harmonic separator and directed into the flow cell described in the previous publication [6]. The scattered radiation was imaged with a single f1 lens into the Spex 1401D double monochrometer, with 100 micron slits and operated in second order, giving a resolution of about 50cm$^{-1}$.

The Raman spectrum obtained is shown in Figure 1 with the various overtone and combination bands that could arise from $\nu_2$ and $\nu_3$ vibrations shown underneath to indicate a possible assignment. The intensities of the progressions were simply taken in a geometric series as a simple test of the approximate trend of the intensity of the separate transitions. The harmonic and anharmonic constants were taken from reference [11]. The resolution and S/N will need to be improved if the higher overtones and combination bands are to be separated and individually assigned.

**Conclusion**

The NO product state analysis[12] from molecular beam photofragment and NO LIF spectroscopy together with new *ab initio* calculations of the electronic structure[12] have indicated that the C and D absorption bands arise from the same electronic band and differ only in the excitation of the $\nu_1$' vibration. The implication of this on the lifetime of the upper state, long enough for the NO vibration to be established, may explain the fact that no vibrational progression were observed following excitation into these bands. The observation of such a progression following excitation into the higher energy, and stronger A band makes the simple Raman spectra recorded in the B band all the more surprising, as dissociation is expected to be rapid from this state a fact confirmed by the other dissociation studies.

**Acknowledgements**

We would like to thank Chris Dyer for help in preparing the NOCl used in this study.

**References**

1. A.J. Bell and J.G. Frey, Molec. Phys., 69, 943, (1990).
2. G.B. Kistiakowsky, J. Am. Chem. Soc., 52, 102, (1930).
3. C.F. Goodeve, S. Katz, Proc. Roy. Soc. A, 172, 432, (1939).
4. N.M. Ballash, D.A. Armstrong, Spect. Acta., 30a, 941-944, (1974).
5. G.S. Tyndall, K.M. Stedman, W. Schneider, J.P. Burrows, J. Photochem., 36, 133-139, (1987).
6. A.J. Bell, P.R. Pardon and J.G. Frey, Molec. Phys., 67,465, (1989).
7. D.G. Imre, J.L. Kinsey, R.W. Field, D.H. Katayama, J. Phys. Chem.86, (1982), 2564.
8. D.G. Imre, J.L. Kinsey, A. Sinha, J. Krenos, J. Phys. Chem., 88, (1984), 3965.
9. E.A. Rohlfing, J.J. Valentini, Chem. Phys. Lett., 114, (1985), 282.
10. J. Zhang and D.G. Imre, J. Chem. Phys., 89, (1988), 309.
11. A.M. Mirri, R. Cervellati, and G. Cazzaoli, J. Molec. Spectrosc., 71, 386, (1978); G. Cazzoli, R. Cervellati, A.M. Mirri, J. Molec, Spectrosc., 56, 422, (1975).
12. Y.Y. Bai, A. Ogai, C.X.W. Qian, L. Iwata, G.A. Segal and H. Reisler, J. Chem. Phys., 90, 3903, (1989).

Figure 1
The upper part of the figure is the experimental NOCl Raman spectrum at 266nm, for comparison the lower portion indicates where the overtone and combination bands would be expected.

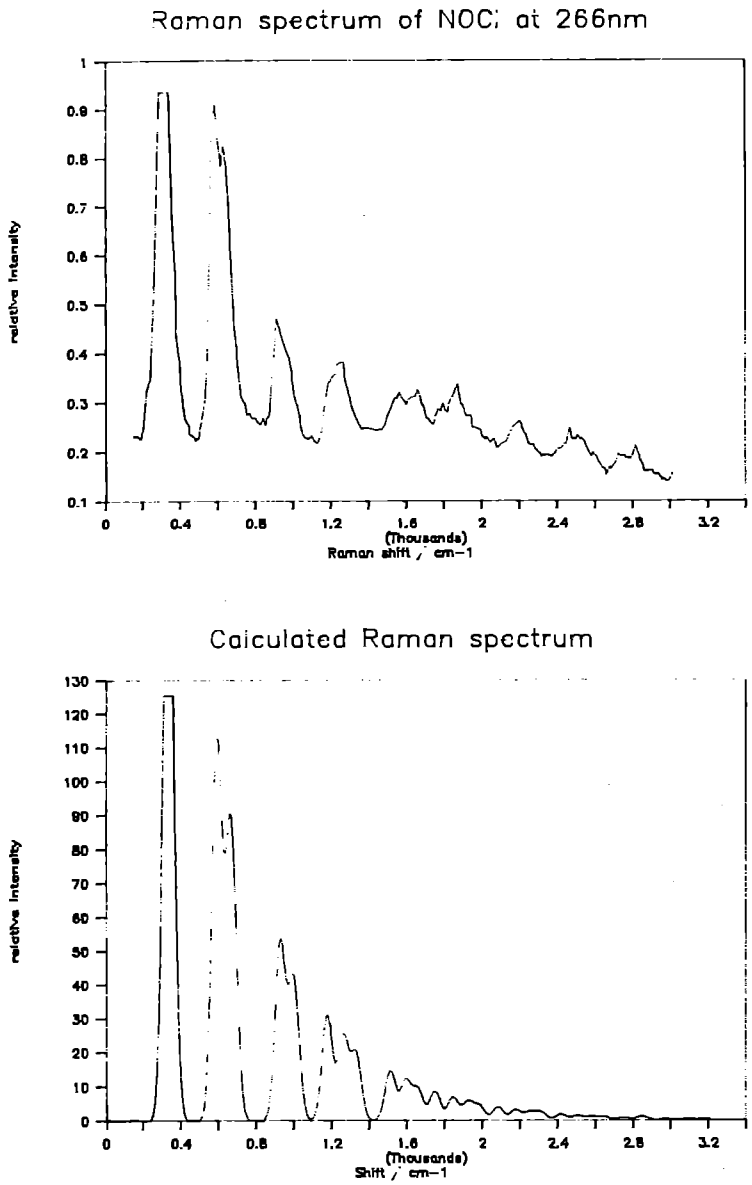

# RESONANCE RAMAN SPECTROSCOPY OF THIOL-SUBSTITUTED NUCLEOSIDES

B A Connolly[1], T Waters[1], C W Wharton[2], A W Parker[3] and S Patel[3]

[1]Department of Biochemistry, University of Southampton.
[2]Department of Biochemistry, University of Birmingham
[3]Laser Support Facility, Rutherford Appleton Laboratory

## INTRODUCTION

The E Coli ECO RV restriction nuclease and methylases are extremely specific enzymes that modify DNA only at the consensus base sequence GATATC. ECO RV endonuclease cleaves the DNA between the two central thymidine (T) and adenosine (A)[1]. The methylase modifies the DNA by methylating the 6-amino group of the outer adenosine[2]. The overall programme is aimed at elucidation of the factors that determine the specificity of these enzymes by using chemical and molecular biological techniques. Chemical and biochemical methods have been developed in Southampton that allow the synthesis of a series of dodecamers with the consensus base sequence but with one of the bases slightly altered (eg changing a C=O group to a C=S). Substitution of sulphur for oxygen at the 2- or 4-positions of thymidine and 6-position of guanidine greatly weakens or prevents interchain hydrogen-bonding in DNA. Such disruption of hydrogen bonding is known to cause perturbation of the geometry of the DNA duplex and so to affect the effectiveness of the binding and catalysis of enzymes that recognise the specific sequences.

This work reports a preliminary investigation on the use of resonance Raman spectroscopy as a method which may provide information concerning the structure and perturbation of the modified dodecamers when bound to the specific enzymes. It is important that the spectroscopic method focusses on the region of the macromolecular complex where the changes will take place, ie, the consensus sequence and the active site of the enzyme. We expect this to be so as thiol-substituted derivatives show strong UV-absorption, eg, 4-thio-thymidine (4-ST) at 340 nm; 2-thio-thymidine (2-ST) at 290 nm, the former is well clear of protein absorption. Also, the C=S chromophore has high polarisability and so will be a strong Raman scatterer.

## RESULTS AND DISCUSSION

In figure 1, curve a, is illustrated the spectrum obtained for 4-thio-thymidine (4-ST) using 340 nm laser excitation. As can be seen the sample is extremely fluorescent. However, on closer inspection weak Raman bands can be just made out above the sloping background. In order to make analysis easier a software correction of the data was made which subtracted away the fluorescent background. The computer programme uses several pre-defined regions of the fluorescent curve, where no Raman bands are present, and constructs a best of fit polynomial equation, see figure 1, curve b. For each point on the curve the fluorescence intensity is calculated and subtracted. The resulting flat baseline spectrum is given in figure 2. The band at 730 $cm^{-1}$ is assigned to the C=S stretching vibration and this is in agreement with that found for 4-thio-uridine[3]. The other bands, mainly due to ring motion, are still to be fully assigned. A sample of thymidine under the same conditions of concentration and irradiation gave a much weaker Raman spectrum showing that the group brings the compound into resonance.

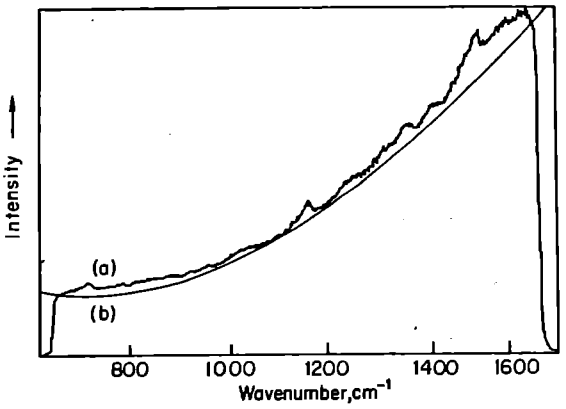


Fig.1. (a) 4-thio-thymidine (5 x $10^{-4}$ mol $dm^{-3}$) in water, 340 nm laser excitation. (b) Fitted background curve for fluorescent subtraction.

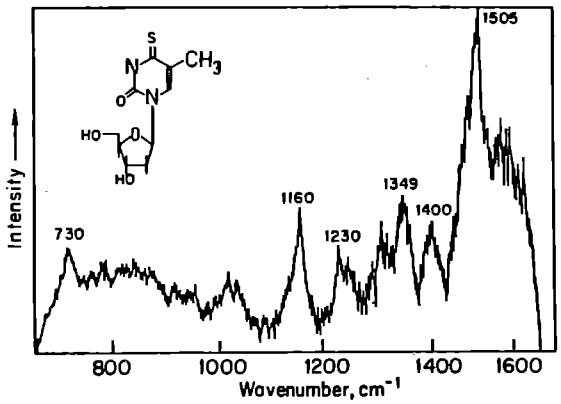


Fig.2. Fluorescence subtracted resonance Raman spectrum of 4-thio-thymidine.

Attempts were also made to obtain spectra of the thio-nucleosides 2-ST and 6-thio-guanosine, but these failed to give as good spectra as 4-ST. The main cause for this failure was these samples were much more fluorescent than 4-ST and problems were encountered with the dynamic range ($2^{16}$) of the OSMA diode array detector.

## CONCLUSION

The resonance Raman spectrum of free 4-ST shows many distinct bands. It is now hoped to incorporate 4-ST into an oligonucleoside and observe any Raman frequency shifts and band intensity changes which take place when bound to sequence specific enzymes. From these results it is hoped to deduce the interactions between DNA and the enzymes that have the ability to modify it.

## REFERENCES

1. I Schildkraut, C Banner, C Rhodes and S Parekh, Gene. 27, 327, (1984).

2. V Nwosu, B Connolly, S Halford and J Garnet, Nuc Acids, Res. 16, 3705, (1988).

3. Y Nishimura, A Y Hirakawa, M Tsuboi and S Nishimura, Nature 260, 173, (1976).

# PHOTO–CIDNP STUDIES OF UNFOLDED STATES OF LYSOZYME

R W Broadhurst, C M Dobson, P J Hore, S E Radford and M L Rees

Oxford University

## INTRODUCTION

A variety of NMR methods have been used to study protein folding, including the nuclear Overhauser effect, relaxation methods, magnetization transfer and hydrogen exchange. A technique that has yet to be used extensively in this context is photochemically induced dynamic nuclear polarization (photo–CIDNP)[1]. The method uses a reversible chemical reaction between a photoexcited dye and the protein to perturb the Zeeman magnetization of protons in the side chains of certain amino acid residues. The polarization is detected as enhancements in the NMR spectrum and is only observed for tyrosine, tryptophan and histidine residues that are physically accessible to the excited dye. The technique therefore probes the surface exposure of these side chains.

In this work we compare photo–CIDNP spectra of native and chemically modified hen egg white lysozyme, denatured in a variety of ways. The native state of lysozyme has been well characterized by NMR and X–ray crystallography and much is known about the thermodynamics and kinetics of its unfolding. In aqueous solution at pH 3.8, it denatures over a narrow temperature range around 77 °C. This temperature can be reduced by the use of chemical denaturants or hydrophobic solvents. Chemically modified forms of the protein with one or all four of the disulphide bonds broken also denature at lower temperatures than native lysozyme.

By comparing the relative CIDNP enhancements of the three tyrosine and six tryptophan residues in the protein, we find evidence for a hydrophobic region in the thermally and chemically denatured proteins in water that is not present in DMSO solution[2].

## EXPERIMENTAL

400 MHz $^1$H photo–CIDNP spectra were recorded on a Varian XL–400 NMR spectrometer. A Varian 5 mm $^1$H probe was modified to permit photolysis of NMR samples by introducing suitable optics. Light from a continuous wave argon ion laser (Spectra–Physics 2025, 5 W, multiline), chopped into 0.1 s pulses by a mechanical shutter, was used to generate CIDNP by irradiating solutions of 1 mM protein in $D_2O$ or DMSO–$d_6$ in the presence of 0.25 mM flavin mononucleotide (FMN) or lumiflavin. Interleaved "light" and "dark" free induction decays were recorded and subtracted prior to Fourier transformation to give difference spectra containing only polarized resonances.

## RESULTS

Thermal unfolding. The aromatic region of the photo-CIDNP spectrum of lysozyme at 30 °C is shown in figure 1a. The main features are the absorptive resonances of the directly polarized indole protons (C2H, C4H and C6H) of Trp–62 at 7.0 – 7.3 ppm and of Trp–123 near 7.5 ppm. This spectrum is essentially identical to that reported elsewhere[3]. As the temperature is raised from 30 °C to 80 °C, the intensity of the tryptophan resonances first increases, reaches a maximum at 60 °C and then falls dramatically. At the same time, an emissive tyrosine peak at 6.8 ppm grows until at 80 °C it is the dominant feature of the spectrum, more than twice as intense as the Trp resonances, figure 1b.

Very similar temperature dependence was found at both pH 2.0 and pH 6.0, except that at the more acidic pH, where the denaturation temperature is 69 °C, the observed changes were shifted to lower temperatures by approximately 10 °C. At pH 3.8, the CIDNP spectra are almost independent of the concentrations of protein and FMN in the ranges 0.2 – 2.0 mM and 0.02 – 1.0 mM respectively.

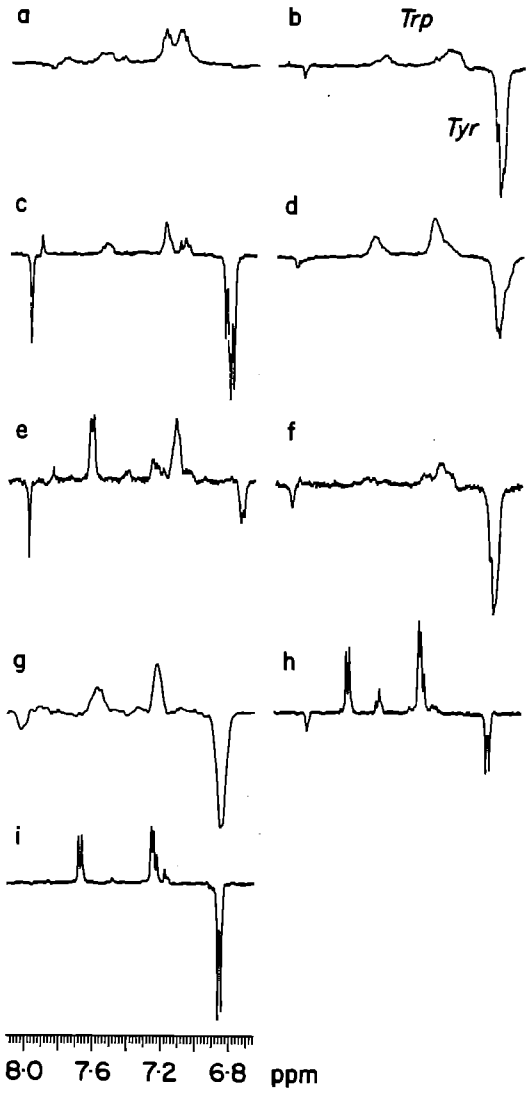


Figure 1: Photo–CIDNP spectra of: (a) lysozyme, 30 °C; (b) lysozyme, 80 °C; (c) lysozyme, 60 °C, urea (10 M); (d) lysozyme, 80 °C, urea (10 M); (e) lysozyme, DMSO, 80 °C; (f) CM–lysozyme, 60 °C; (g) fully reduced lysozyme, 80 °C; (h) N–acetyl–tryptophan amide (3 mM) and N–acetyl-tyrosine amide (1.5 mM), 30 °C, pH 6.0; (i) N–acetyl-tryptophan amide (1 mM) and N–acetyl–tyrosine amide (3 mM), 30 °C, pH 6.0. Unless otherwise stated, the solvent was $D_2O$ and the pH 3.8.

Chemical denaturants. The influence of chemical denaturants on the CIDNP spectrum of lysozyme largely mirrors the behaviour described above. Figures 1c and 1d show the CIDNP spectra of denatured lysozyme in the presence of 10 M urea at 60 °C and 80 °C respectively. Note the larger enhancement of Trp relative to Tyr at 80 °C. Essentially similar changes are seen with guanidinium deuterochloride.

Dimethylsulphoxide. Lysozyme has a random coil structure in DMSO at all temperatures. The CIDNP spectrum of lysozyme at 70 °C, obtained using lumiflavin rather than FMN for reasons of solubility, is shown in figure 1e (similar spectra were found at 30 °C and 80 °C). Compared to thermally denatured lysozyme in water, the tryptophan peaks are much stronger relative to the tyrosine emission.

CM–lysozyme. This modified form of lysozyme, with the 6–127 disulphide linkage broken and the thiol groups carboxymethylated, has a denaturation temperature of 53 ± 2 °C at pH 3.8, some 25 °C lower than the wild–type protein. Its CIDNP spectra at 40 °C and 60 °C, have a similar appearance to those of wild–type protein at 60 °C and 80 °C respectively (figure 1f shows the spectrum at 60 °C). The spectrum in DMSO is essentially identical to that of wild–type lysozyme in the same solvent.

Fully reduced lysozyme. When all four disulphide linkages are reduced, lysozyme is denatured at all temperatures. The CIDNP spectrum at 80 °C (figure 1g) bears a close similarity to that of thermally denatured wild–type lysozyme at the same temperature, except for a 5–fold overall reduction in intensity due to quenching of the excited flavin by the cysteine thiol groups.

Amino acid mixtures. For the purposes of photo–CIDNP spectroscopy, mixtures of amino acids can be used to model a random coil protein. At pH 6, the aromatic region of the CIDNP spectrum (figure 1h) of a mixture of N–acetyl–tryptophan amide (6 mM) and N–acetyl–tyrosine amide (3 mM) comprises absorptive signals from C2H, C4H and C6H of the tryptophan and an emissive doublet from εCH of the tyrosine. The only effect of increasing the temperature of the Trp/Tyr mixture to 80 °C was a slight reduction in the intensity of all resonances. Compared to lysozyme, this mixture shows much stronger tyrosine enhancements relative to tryptophan at 30 °C, and the converse at 80 °C. To reproduce the approximate Trp:Tyr intensity ratio observed for thermally denatured lysozyme at 80 °C, a concentration ratio of between 2:3 and 1:3 Trp:Tyr was required (figure 1i). Finally, the spectrum of 2:1 N–acetyl–tryptophan amide and N–acetyl–tyrosine amide in DMSO was found to be similar to that of the amino acids in water and that of lysozyme in DMSO.

## DISCUSSION

The photo–CIDNP spectrum of hen egg white lysozyme at 30 °C (figure 1a) has been well characterized[3]. Of the ten potentially polarizable residues (6 tryptophans, 3 tyrosines and 1 histidine) only two (Trp–62 and Trp–123) show appreciable CIDNP enhancements, in agreement with estimates of dye accessibility based on crystallographic data.

In contrast, little attention has been devoted to photo-CIDNP of the denatured protein. Compared to 30 °C, spectra recorded above the unfolding temperature (e.g. figure 1b) show dramatically enhanced tyrosine emission and somewhat reduced absorption for tryptophan.

It seems unlikely that this behaviour is an artefact of the method used to generate CIDNP. Under the conditions of these experiments protein aggregation, protein–dye binding, spin relaxation and photo–damage to the protein can all be ruled out[2]. Moreover, the temperature dependence of the spectra of lysozyme, and its modified forms, in water, with and without chemical denaturants, are

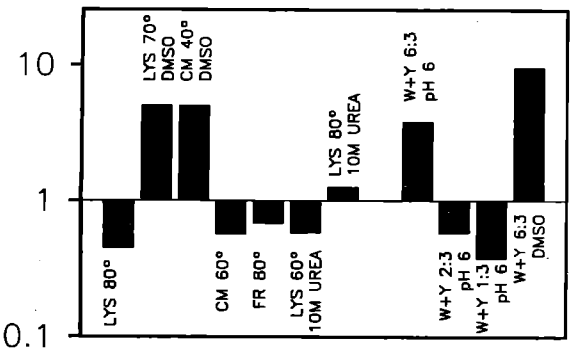


Figure 2: Ratio of tryptophan:tyrosine CIDNP enhancements for unfolded states of native and modified lysozymes and amino acid mixtures. Unless otherwise stated, the solvent was $D_2O$ and the pH 3.8. Key to symbols: lysozyme (LYS), CM–lysozyme (CM), fully reduced lysozyme (FR), N–acetyl–tryptophan amide + N–acetyl-tyrosine amide (W+Y).

all in accord with the known unfolding temperatures. For example, lowering the unfolding temperature by altering the pH, by adding urea or guanidinium deuterochloride, or by reducing one of the disulphide linkages produces a corresponding lowering in the temperature at which the CIDNP spectrum changes from that of the folded state to a spectrum resembling figure 1b.

A clue to the origin of the CIDNP enhancements observed for lysozyme and its modified forms in water is provided by the spectra of lysozyme in DMSO and of the mixture of blocked tryptophan (6 mM) and tyrosine (3 mM), both of which show a much larger tryptophan polarization relative to tyrosine. The similarity of these two spectra (figures 1e and 1h) is consistent with a random coil structure for the protein in DMSO with all 6 Trp and all 3 Tyr residues essentially accessible to the dye. The Trp/Tyr intensity ratio under different conditions, obtained simply by integration of the absorptive (Trp) and emissive (Tyr) signals in the aromatic region, is shown in figure 2.

## CONCLUSION

The most probable explanation of the results described above is that, in aqueous denatured states, the tryptophan residues are in an environment in which they are largely inaccessible to the dye, and by inference, concealed from the solvent. The spectra of amino acid mixtures suggest that if all three tyrosine sidechains are fully exposed, then only one or two of the six tryptophans are accessible (see figure 2). Our results support the idea that this hydrophobic region exists in water for the wild–type protein and its reduced forms and that only the combination of high temperature (80 °C) and high urea concentration (10 M) can loosen it sufficiently to increase the tryptophan accessibility . The hydrophobic cluster is evidently disrupted by DMSO, a more hydrophobic solvent than water.

Further experiments to confirm these conclusions are in progress. Once the factors affecting the CIDNP intensities in lysozyme are fully understood, we plan to move on to a study of multidomain proteins involved in fibrinolysis. The methods described here will be used to probe the interdomain regions to provide an experimental basis for defining the overall architecture of these molecules.

## REFERENCES

1. R Kaptein, Biol. Magn. Reson. **4** 145 (1982)
2. RW Broadhurst et al. Biochemistry, in preparation.
3. PJ Hore and R Kaptein, Biochemistry **23** 1906 (1983)

# THE KINETICS OF DNA REPAIR OF UV DAMAGE IN MAMMALIAN CELLS

R A Meldrum, J Woodbine and C Wharton

Dept of Biochemistry, University of Birmingham,
PO Box 363, Birmingham B15 2TT.

## INTRODUCTION

Previously it was shown that a pulse of DNA synthesis occurred within 30 seconds after UV damage of DNA of mammalian cells (Meldrum et 1, Annual Report Laser Division, RAL 1989). This burst of synthesis fell rapidly between 30 and 120 seconds and was then followed by a slower steady increase from about 120 seconds onward.

The initial burst phase has now been studied in more detail by improving the time resolution. the automatic system devised to collect data has been described previously (Meldrum et al, Annual Report Laser Division, RAL, 1989). Progress curves of accumulated DNA repair enzyme activity were acquired by varying the time delay between the laser pulse and the quench. By contrast the dependence of the rate of DNA repair at any given time after damage were obtained by varying the time delay between the first laser pulse which damages the DNA and the second laser pulse which photoactivates the 'caged' DNA break trapping agent.

## TIMECOURSES OF DNA REPAIR

### Dideoxyadenosine triphosphate incorporation

Progress curves (accumulated incorporation of photoactivated $^{32}$P-ddATP, Meldrum et al 1990a) with the improved time resolution as described above show a decrease from 5-10 seconds after UV after damage. The rates (measured by a 30 second pulse of incorporation of photoactivated $^{32}$P-ddATP at various times after damage) follow a similar profile but a peak at five or ten seconds is more distinct.

### Thymidine triphosphate incorporation

Incorporation of the natural base $^{3}$H-TTP was followed in the same manner. The progress curves show the same initial fall after five seconds but no subsequent rise after 30 seconds, while the rate profiles show a distinct peak at fifteen seconds.

### The effect of added nucleotides

The effects of nucleotide addition on the profiles of progress curves and rates were assessed. ATP (10mM), dGTP, dTTP and dCTP (100fm) showed a similar response to those with caged $^{32}$P-ddATP, but these experiments were not completed owing to a variety of technical problems associated with commissioning of two new Questek lasers.

### What is the nature of the burst phase in DNA repair?

These results to date would suggest that the first burst of synthesis is a 'panic' response of cells to insult where the enzymes are to some extent non-discriminating about the nucleotides which they incorporate into the DNA chain. Subsequently, they attempt to correct this as may be deduced by the fall in incorporation of radiolabelled nucleotide and become more discriminating in the second slower phase of synthesis. This initial 'panic' response of the cells occurs at all levels of 248 nm UV light administered between 25 and 100 J/m².

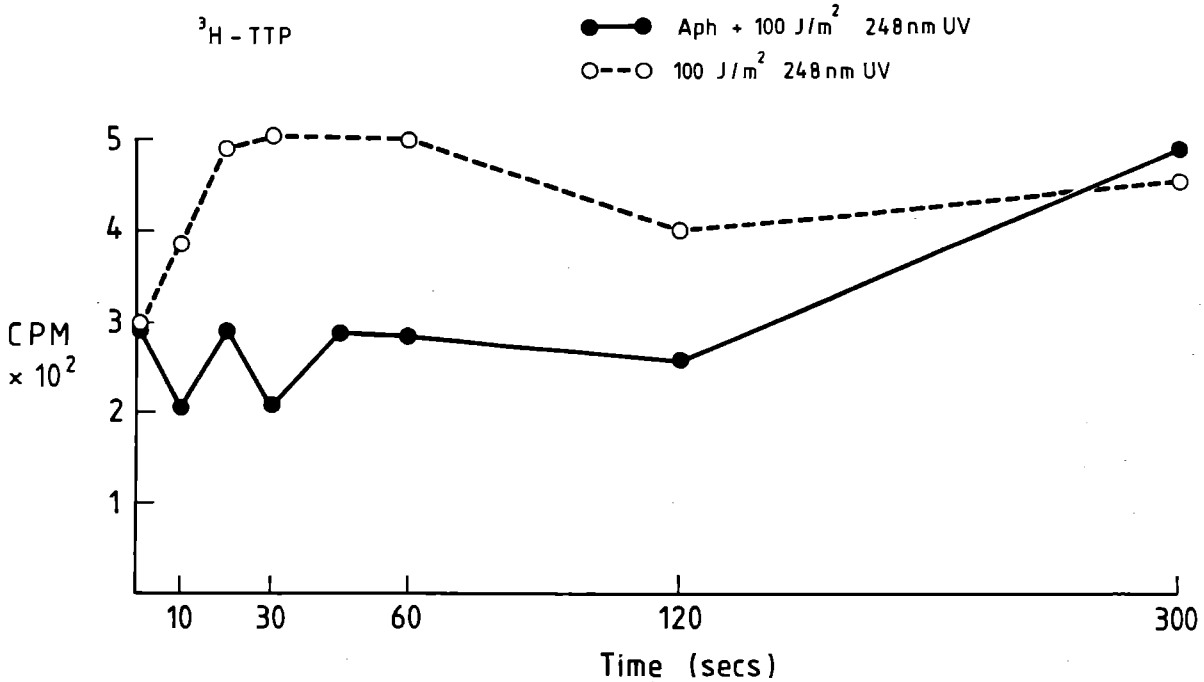


Fig.1. The incorporation of $^{3}$H-TTP in the presence and absence of the polymerase alpha inhibitor after 248 nm UV irradiation (100 J/m²).

Which enzymes are involved during the burst phase?

To determine which of the polymerases are active during the various phases of DNA synthesis immediately after damage, progress curves of the incorporation of $^{32}$p-ddATP and $^{3}$H-TTP in the presence of specific polymerase inhibitors were followed. Aphidicholin inhibits polymerase alpha. The progress curves of incorporation of $^{32}$P-ddATP obtained in the presence of this inhibitor show some suppression of the initial burst phase of DNA synthesis but the second phase progresses as it does in the absence of inhibitor.

The same result was obtained with $^{3}$H-TTP uptake (see figure 1).

Dideoxythymidine inhibits polymerase beta and progress curve following the incorporation of $^{3}$H-TTP in the presence of this inhibitor show partial suppression of the first phase of DNAs synthesis and almost total suppression of the second phase (see Figure 2).

This result is rather surprising as polymerase alpha is thought to be responsible for repair of long patches of DNA and polymerase beta for repair of short patches and it is tempting to assume that short patches of DNA would be repaired first and therefore polymerase beta would be more active during the first phase of DNA synthesis and polymerase alpha during the second. However this does not appear to be the case. These experiments with inhibitors are presently not complete for the reason stated above the considerably more work is required to establish the nature of the activities of the different repair enzymes during the early phases of DNA repair after UV damage.

Effects of 340 nm/351 nm UV irradiation on DNA synthesis.

UV laser light of wavelengths 340 nm and 351 nm have been shown to stimulate incorporation of $^{3}$H-TdR into mammalian cell DNA at doses of between 1-2 kJ/m$^2$ (Meldrum et al Annual Report Laser Division, RAL 1988, Meldrum et al 1990b). It was demonstrated that an enhancement of DNA replication synthesis appeared responsible for this stimulation and DNA repair activity was not involved (Meldrum et al, Annual Report, Laser Division, RAL 1989). This effect has since been shown to be dose dependent between and 2000 J/m$^2$. The uptake $^{3}$H-TdR was assessed at various times during two hours after 2 kJ3m$^2$ of 351 nm UV laser light. This followed a course showing a peak of enhanced incorporation (when compared to unirradiated cells) at 15 minutes after irradiation which was then followed by a steady and slower increase of uptake of $^{3}$H-TdR.

The effect of 351 nm light on adriamycin resistance

A very dramatic result was obtained from a collaborative experiment with I J Stratford and G E Adams of the MRC, Harwell. Cells were irradiated with 2 kJ/m$^2$ 351 nm UV laser light before exposure to the antibiotic adriamycin which intercalates and cleaves DNA. Resistance to adriamycin was induced 30 minutes after irradiation and increased 100 fold by three hours. Cell survival was not affected by 351 nm UV radiation alone.

This spectacular protective effect of 351 nm irradiation against adriamycin is thought to be indicative of a general defence mechanism where cells show a short lived proliferative response to low levels of certain wavelengths of light, electromagnetic fields, heat, hypoxia and ionising radiation (Rajaratnam et al 1981) which then

Fig.2. Cells were pre-incubated for 30 minutes with 100uM dideoxythymidine, an inhibitor of polymerase beta, before irradiation with 248 nm UV laser light (100 J/m$^2$). The incorporation of $^{3}$H-TTP in cell pre-incubated with the inhibitor or cells not exposed to the inhibitor is shown.

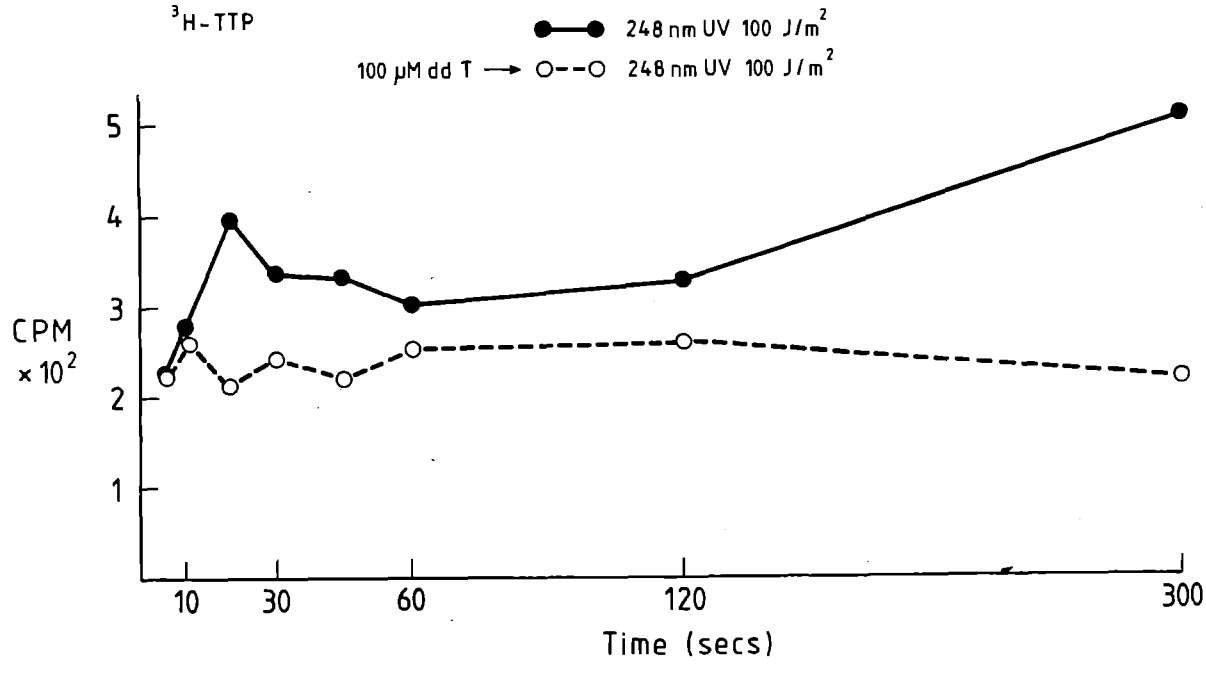

modifies their response to potent levels of a DNA damaging agent.

The implications for the possible effects of the levels of this wavelength which are received from sunlight are at least twofold. The protective effect of this wavelength against DNA damaging agents could be beneficial but a repeated proliferative stimulus induced by multi-exposure could promote mutational changes in the cell.

REFERENCES

R A Meldrum, S Shall, D R Trentham and C W Wharton, J Biochem, 266, 885-890 (1990a).

R A Meldrum, S Shall and C W Wharton, J Biochem, 266, 891-895 (1990b).

S Rajaratnam, E Smith, I J Stratford and G E Adams, Br J Cancer, 43, 551-553 (1981).

# REPAIR OF SOFT X-RAY INDUCED DNA DAMAGE IN MAMMALIAN CELLS

Rosalind A Meldrum[1], Jane Woodbine[1], Christopher W Wharton[1], Edmund Turcu[2] and Fergus O'Neill[2]

[1]Department of Biochemistry, University of Birmingham P O Box 363, Birmingham B15 2 TT.
[2]Laser Division, Rutherford Laboratory, Chilton, Didcot

## INTRODUCTION

We have previously described the use of laser-generated soft X-rays in studies of the repair of mammalian cellular DNA when an iron target was employed (1,2). This system proved in many respects convenient and effective in the induction of DNA damage and the consequent repair process. While the ca. 0.9 KeV photons damaged very well flattened V-79 cells they were less effective if the cells were not in optimum condition and less well flattened. This was ascribed to criticality of the penetration distance of the X-rays with respect to the cellular nuclei and suggested that if more penetrative X-rays could be used then the condition of the cells would become less important. Accordingly some experiments in which a copper target which was used generates X-rays having an energy of ca. 1.1 KeV have been performed. The physical aspects of X-ray generation in these experiments are described in another paper in this volume.

## RESULTS

The X-ray spectrum of the Cu X-rays used in biological experiments is shown in Fig. 1.

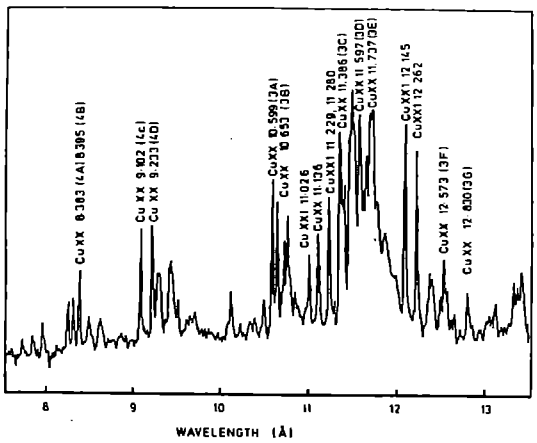


Fig. 1. The spectrum of X-rays generated from a copper target used in biological DNA repair experiments.

The spectrum was recorded as the sum of 120 shots and should be compared with that of the iron target used previously (2). The more intense lines (see Fig. 1) arise from M to L shell (principal quantum number n=3->2) transitions of Ne-like (CuXX) and F-like (CuXXI). O-like (CuXXII) transitions were also observed but these were weak. The spectrum shown in Fig. 1 was determined with 760 mm helium in the target chamber but no significant difference was observed when the pressure was varied from 0.3 torr to 760 torr.

## DOSE RESPONSE OF DIFFERENT CELL TYPES

Cu 1.1 KeV X-rays induced a maximal DNA repair response in V-79 cells at a dose of 50 rads in comparison with the 200 rads required for 0.9 keV Fe X-rays. The dose response curve is shown in Fig. 2.

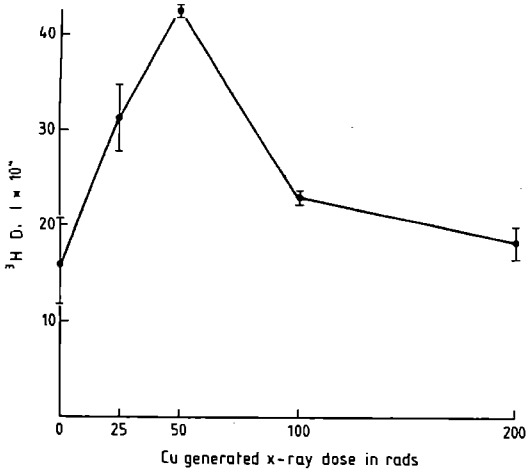


Fig. 2. The induction of DNA repair synthesis as a function of the dose of Cu generated soft X-rays

We associate the reduction of dose needed to stimulate an optimum level of repair with the better penetration to the cell nuclei of the 1.1 KeV Cu X-rays as compared with the X-rays produced from the iron target.

Experiments with AA8 fibroblasts that do not flatten as well as V-79 cells showed that repair could be induced at a dose fo 400 rads in contrast to our previous observation that DNA repair could not be induced in AA8 cells even at 2000 rads. This again illustrates the superior penetrative properties of the Cu X-rays and means that they can be used in studies of various cell types that have different growth habits. Also we expect that the condition of the cells will be less important in the success of repair experiments.

## PRELIMINARY TIMECOURSES OF DNA REPAIR

It has proved possible using $^3$H-thymidine (which has to be phosphorylated after entering the cells, prior to incorporation into DNA) to measure some relatively crude timecourses for DNA repair, the resolution being Ca 5 min. These show a transient of thymidine uptake, a measure of DNA synthesis, in the first 5 min. after irradiation followed by a steady rate. We hope to make progress in the near future with automation of the determination of the timecourses of repair and for this will need to implement rapid permeabilisation so that triphosphates can be used and so avoid the inevitable delay during which intracellular phosphorylation takes place (see above).

ELECTROPERMEABILISATION OF SURFACE GROWN CELLS

For our UV experiments we have successfully exploited the electrical shock method for the rapid permeabilisation of suspension cultured cells. For our initial studies with surface grown cells we have constructed the apparatus shown in Fig. 3, the design being based on parameters deduced from the suspension experiments.

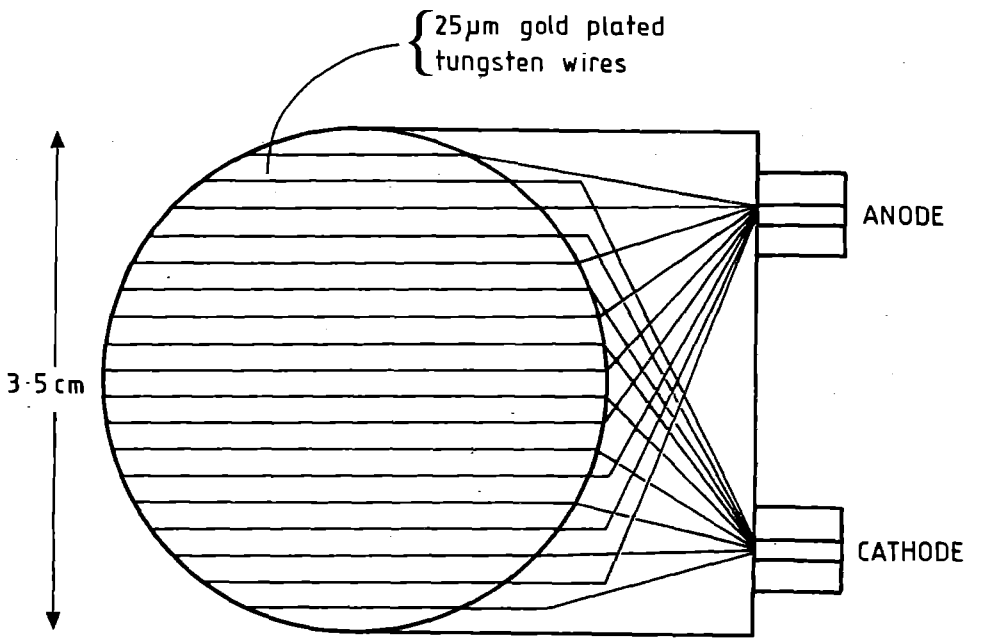


Electropermeabilisation of surface-grown cells for soft X-ray DNA damage studies.
Wires, 1mm apart are connected alternately to anode and cathode

**Fig. 3. Cell culture dish with 25 μm gold wires for electric permeabilisation of surface grown cells. The assembly was fabricated in the Target Preparation Facility, Laser Division.**

Initial tests have proved somewhat successful but as yet not optimal. At 100 V/mm some 40% of cells were permeabilised as determined by trypan blue penetration but not in a uniform fashion. Patches of permeabilised cells are seen within 0.3 mm of the wires with an unaffected population equidistant between the wires. Movement of the wires and gas evolution during the discharge cause some disruption of the cell layer in the vicinity of the wires. Providing constant mechanical tension and a smaller distance between the wires are expected to improve the performance.

STUDIES WITH DNA POLYMERASE INHIBITORS

Inhibitors of polymerase α (hydroxyurea/cytosine arabinoside) and an inhibitor of polymerase β/δ (dideoxythymidine) had an approximately equal effect on the early stages of repair while the α inhibitor had a more pronounced effect after the first 15 min. following irradiation. This implies that all polymerases are active in repair synthesis initially but that α becomes more significant in the later stages. This further implies that there is significant short patch synthesis in the early stages catalysed by β/δ and that long patch (>100 nucleotides) predominates in the later stages. We plan to investigate in more detail the degree of complimentarity between these different enzymes in that they may be involved in the repair of different forms of lesion and the extent to which one can substitute for the others.

REFERENCES

1) O'Neill, F., Turcu, I.C.E., Tallents, G.J. Dickerson, J., Lindsay, T., Goodhead, D.T., Stretch, A., Wharton, C.W. and Medlrum, R.A. (1989) Proceedings of the Internation Congress on Optical Science and Engineering, Paris, SPIE Volume 1140, 232-236.

2) Authors as 1) above; Ann. Rep. Laser Div. SERC (1989) 331-337.

# IMPROVED RISETIME MEASUREMENTS OF COMPONENTS IN THE PHOTOSYSTEM 1 REACTION CENTRE

E H Evans[1], R G Brown[1], R W Sparrow[1], C A S Polter[1], R S Chittock[2], A J Langley[2], W Shaikh[2], W T Toner[2] and M C W Evans[3]

[1] Schools of Applied Biology and Chemistry, Lancashire Polytechnic
[2] Central Laser Facility, Rutherford Appleton Laboratory
[3] Department of Biological Sciences, University College

## INTRODUCTION

In our previous annual reports we showed that Photosystem 1 reaction centres prepared from the cyanobacterium, Chlorogloea fritschii, contain a number of components, excited on a ps timescale, with spectral features in the wavelength range 670-730 nm. In particular, we have measured components at 680 nm, which we have ascribed to bulk light harvesting chlorophyll, and at 706 nm, where we have identified two kinetically different components[1]. Absorption transients have been characterised by decay kinetics, pump intensity saturation behaviour and redox potential. The two components measured at 706 nm exhibit identical saturation behaviour. The fast component decays with $30 < \tau < 45$ psec (the average for many samples is $\tau = 37.5 \pm 1.5$ ps), and is present under all redox conditions, while the slow component, $\tau >> 3$ ns, is only present under redox conditions where the special reaction centre chlorophyll, P700, would be reduced before the actinic flash. We have therefore suggested that the slow decaying component is P700. The fast decaying component is likely to be on a common excitation pathway with P700 because both components have identical saturation behaviour, and is likely to be the 'long wavelength fluorescence' chlorophyll identified by other workers (eg 2), having a fluorescence decay value of $\tau$ = 30-40 ps[3].

Clearly, the establishment of an energy transfer relationship between the bulk light harvesting chlorophyll and the components at 706 nm described above requires measurements of the risetime of the transients. Although our measurements have utilised shorter pulses than other workers, we have not been able to resolve risetimes at any wavelengths, all measurements being within the pulse width.

Here we report our first measurements of Photosystem setting sub-picosecond limits to the transient risetimes.

## RESULTS AND DISCUSSION

Figure 1 shows transients excited by a pulse[4] having an average autocorrelation width (Gaussian FWHM) of 2.3 psec at a wavelength of 600 nm measured by a continuum generated probe at 706 nm. Figure 1a) shows the preparation under redox conditions where P700 is oxidised before the flash where only the fast decaying component is visible. Figure 1b) shows similar transient under redox conditions (approximately 200 mV ambient redox potential) where P700 is partly reduced before the flash. The extent of the transient has increased and the slow decaying component is now clearly visible.

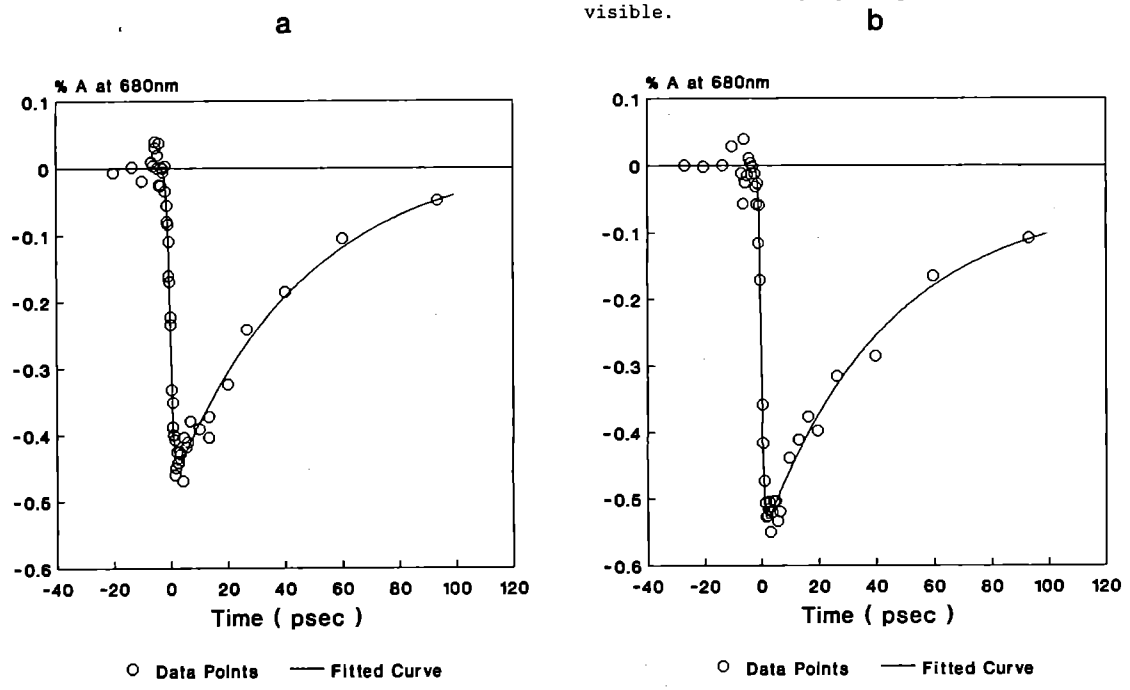


Figure 1. Bleaching transients in PSI. Pump wavelength 600 nm, probe wavelength 706 nm.

(a) Oxidised sample (b) Reduced sample.

The fit to the decay is a single exponential plus a constant.

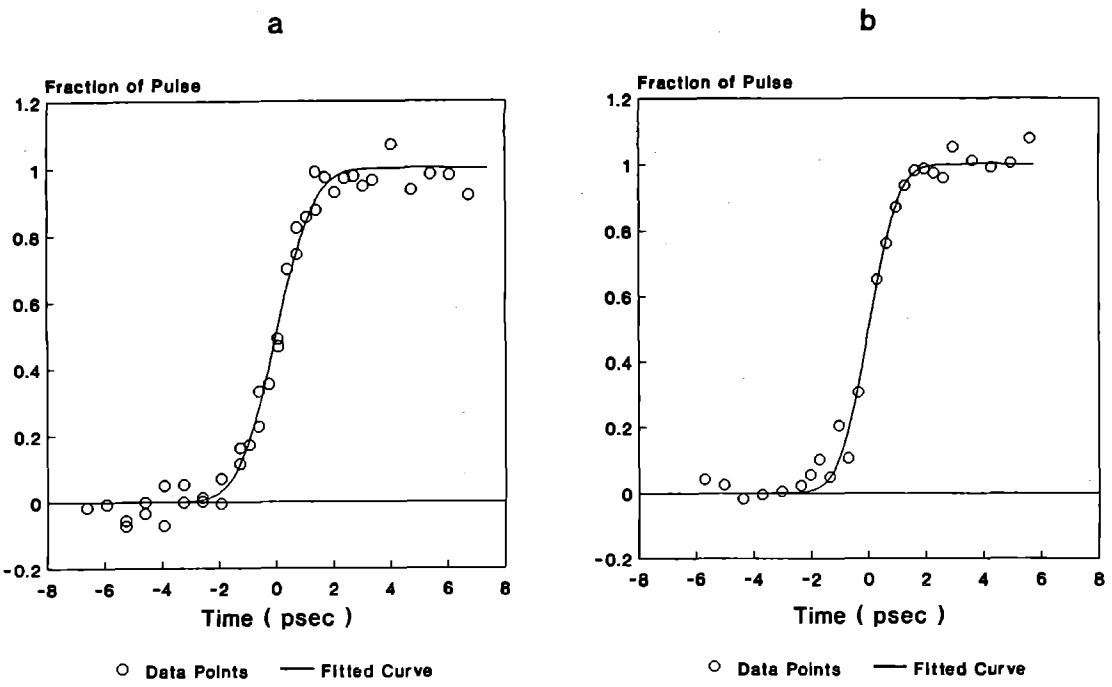


Figure 2. Rising edges of the transients shown in Figure 1 fitted with gaussian excitation functions.

Figure 2 shows Gaussian fits to the rising edges of the transients shown in Figure 1. The widths are 2.5 ps and 2.0 psec (FWHM) for the oxidised and reduced samples, respectively. The difference is not significant. Measurements made on a dye (MEDOTC) give similar values. Using the form $(1-\exp-t/\tau)$ for the intrinsic risetime of the PSI bleach we find $\tau$ less than our resolution. From the variations between measurements we evaluate this as 0.6 psec. We note that the saturation kinetics of this bleach show that it is a collective effect following the absorption of a photon in any of twenty Chl antennae.

The fast decaying component at 706 nm is not redox sensitive and is thus a candidate for a specialised 'funnel' chlorophyll possibly transferring energy between bulk light harvesting chlorophyll and P700. The rapid rise in this transient would therefore suggest very rapid energy transfer from the bulk light harvesting chlorophyll to this 'funnel'. That the transient measured under reducing conditions (Figure 1b) is larger than that measured under oxidising conditions, with a similar fast risetime, suggests that energy transfer to P700 is also rapid, on a timescale of one or two picoseconds. We have not however definitely excluded the possibility that $P700^*$ is formed in parallel with the 37 ps decay of of the 'funnel'. We intend making further measurements to resolve this question.

REFERENCES

1. E H Evans et al, EBEC Reports, 5, 174, (1988).

2. B P Wittmeushaus et al, Biophysics J 532, 829 (1987).

3. R W Sparrow et al, J Photochem Photobiol, in press.

4. A J Langley and W Shaikh Section C4, this report.

# TIME-RESOLVED PHOTOLUMINESCENCE STUDY OF TUNNELLING TIME FOR HOLES IN DOUBLE BARRIER STRUCTURES

DJ Lovering [1], A Gregory [1], RT Phillips [1], MS Skolnick [2], AW Higgs [2], PE Simmonds [3]
GW Smith [2], CR Whitehouse [2]
[1] University Of Exeter, UK
[2] Royal Signals And Radar Establishment, UK
[3] University of Wollongong, Australia

## INTRODUCTION

We have used a 2D streak camera system to study the photoluminescence (PL) arising from transitions between the first confined quantum states in the quantum well (QW) of a double barrier resonant tunnelling structure (DBRT).Our sample consists of a 79Å thick GaAs quantum well clad on either side by 85Å thick $Al_{0.3}Ga_{0.7}As$ barriers.Contacts are arranged such that a current may be passed through the structure perpendicular to the layers. Figure 1 (insert) shows the resulting current-voltage curve; the two peaks are associated with majority carrier electrons tunnelling resonantly through the DBRT at energies coincident with the first and second bound states of the QW. [1]
Currently there is much interest in the characteristic time associated with tunnelling processes in DBRT devices.Several authors have attempted to establish electron resonant tunnelling times from CW PL measurements. [2] However, our measurements have been designed to investigate the way in which the PL intensity is dominated by the tunnelling dynamics of the photo-injected holes. [3]

## EXPERIMENTS AND RESULTS

Our DBRT sample was mounted in an optical access cryostat and connected to a bias source. It was excited by picosecond light pulses at 675 nm from a synchronously-pumped dye laser. The luminescence was collected and dispersed in the vertical direction by a 0.22m monochromator before passing into a streak camera arranged with the synchroscan time streak orthogonal to the spectrometer dispersion. The resultant 2 dimensional image was intensified by a micro channel plate multiplier before being imaged onto a silicon charge coupled device (CCD). The monochromator was set to select light at the wavelength corresponding to the transition between the first confined levels of the QW, and the streak camera was set up to show the time evolution of this signal during the first three nanoseconds following excitation.
This experiment revealed that the lifetime of the PL due to recombination in bulk GaAs was around 1 ns which is shorter than the lifetime of the QW PL. The photogenerated holes form a long lived 2 dimensional hole gas at the edge of the DBRT from which they tunnel into the quantum well. ( The lifetime of holes in such a 2D hole gas can be very long because it is spatially separated from the electrons. )
Figure 2 shows the temporal evolution of the quantum well PL signal for different biases. At low bias the lifetime of the signal was greater than the repetition time of our laser, 13 ns. This gives rise to a non-zero PL signal prior to t=0 which was due to long lived PL emission from previous laser pulses. As the bias was increased both PL rise time and lifetime became shortened. No PL was observed from transitions occurring between higher confined states even when the device was biassed at its second resonance.

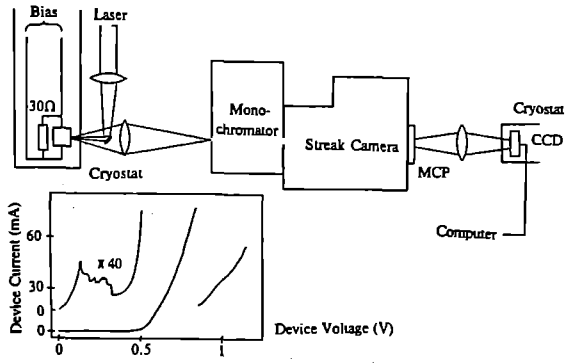


Figure 1: Diagram of the apparatus. The 30Ω resistor was included to prevent parasitic oscillation. The insert shows the current - voltage curve for the DBRT device by itself.

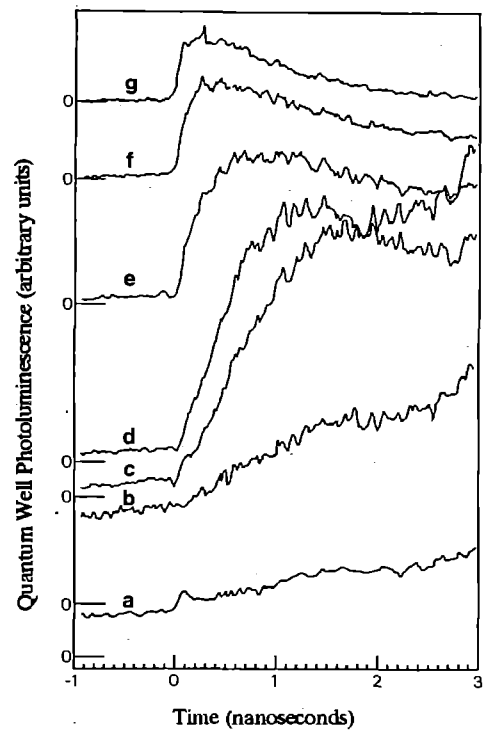


Figure 2: Time resolved PL intensity for different biases. The curves have been displaced vertically for clarity. a)137mV, b)322mV, c)399mV, d)456mV, e)498mV, f)558mV, g)719mV

## DISCUSSION

Most of the light in each laser pulse was absorbed in n-doped GaAs material lying on either side of the DBRT . We have used a finite element simulation to show that the photo-injected electrons represent a small perturbation of the steady state electron population whilst the minority holes rapidly form a 2 dimensional hole gas adjacent to the DBRT.
The PL intensity depends on the product of the electron and hole densities in the QW ( $n_e$ , $n_h$ ). $n_e$ is strongly dependent on bias but since it is largely due to DC tunnelling, remains constant in time, whereas $n_h$ evolves in time and is also affected by bias. We explain the form of the curves in fig. 2 as follows : at low bias the hole tunnelling rate is small. In this case the PL signal rises slowly as the QW is gradually populated by holes tunnelling in from the 2D hole gas, which acts as a reservoir, from which holes are slowly fed into the QW to sustain the PL over several tens of nanoseconds (Fig. 2 a,b). As the bias is increased the rate for holes tunnelling into the QW increases. Hence the PL risetime decreases (Fig. 2 c,d). Further increase in bias results in a greater probability for holes escaping from the QW. At progressively higher bias the non-radiative loss by tunnelling becomes more important in depleting the QW hole population, thereby curtailing its lifetime (Fig. 2 e,f,g).
In conclusion, we have shown that hole tunnelling dynamics are strongly bias dependent and may dominate the PL characteristics of DBRT devices. The absence of PL from the second electron subband when the device is biassed at its second resonance indicates a very rapid intersubband scattering mechanism.

## REFERENCES

[1] LL Chang et al. App. Phys. Lett. 24 593 (1974)
[2] JF Young et al . Phys. Rev. Lett. 60 2085 (1988)
[3] MS Skolnick et al. Phys Rev B. To be published.

# THE ANGULAR DISTRIBUTION OF ATOMIC IONS FOLLOWING THE MULTIPHOTON IONISATION OF CARBON MONOXIDE

Paul A Hatherly[1] , Leszek J Frasinski[1] , Keith Codling[1] , Andrew J Langley[2] and Wasim Shaikh[2]

[1]Reading University Physics Department
[2]Rutherford Appleton Laboratory

In our first publication[1] on the dynamics of the multiphoton ionisation (MPI) of diatomic molecules exposed to intense laser fields, we suggested that the results on $N_2$ might be explained in terms of a field ionisation process. A laser of wavelength 600 nm, pulse length 0.6 ps and repetition rate 10 Hz was focused down to produce an intensity of about $3\times10^{15}$ W/cm$^2$ . This intensity is equivalent to laser E-field of about 15 V/Å, and so this suggestion of field ionisation seemed plausible. We also noted that the angular distribution of the resulting $N^+$, $N^{2+}$ and $N^{3+}$ appeared to be highly peaked along the E-vector of the linearly polarised laser. A similar directionality in the proton emission from HI was observed[2].

The MPI of isoelectronic CO was also studied using the same time-of-flight (TOF) mass spectrometer[2]. The focused laser produced tens of ions per pulse and a field in the region of 10 kV/m accelerated the ions down a drift tube 50 mm in length, to be detected by a pair of microchannel plates. The small size of the interaction region ensured a reasonable mass and energy resolution. The ion signal was fed to a digital oscilloscope and figures 1(a) and (b) are typical of the spectra obtained. In figure 1(a), the E-field of the highly linearly polarised laser beam is directed along the drift tube axis. The field ionisation model suggests that a diatomic molecule is more easily ionised when its axis is along the laser E-field; this is simply because of the molecule's elongated shape. Since there is little time for molecular rotation, the resulting atomic ions are ejected preferentially along the E-vector, either towards or away from the microchannel plates. Ions ejected towards the plates ("forward" ions) have TOF's that vary almost linearly with momentum component along the drift tube axis. The kinetic energy scales shown beneath figure 1(a) are for these forward ions. The "backward" ions of identical energy range reverse their trajectories in the applied field and arrive almost simultaneously at the microchannel plates, regardless of their initial kinetic energies. This produces the sharp peaks in the TOF spectrum and their appearance allows

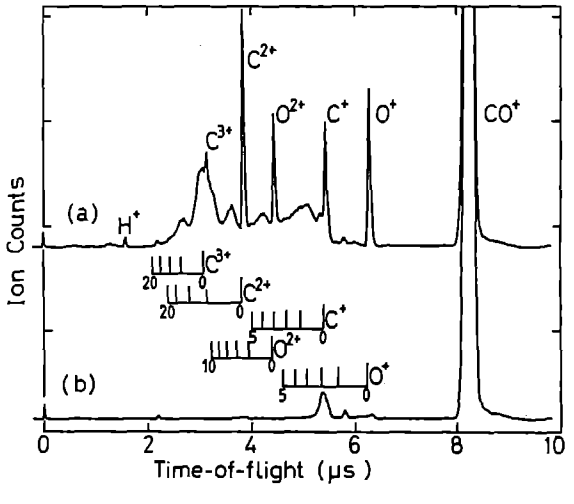


Figure 1. The time of flight spectrum of CO with laser E-field (a) parallel and (b) perpendicular to the drift tube axis. The energy scales are in eV.

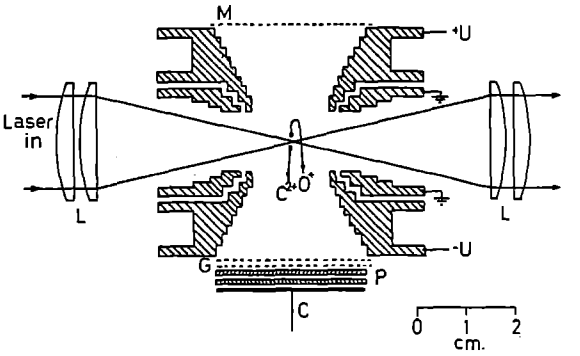


Figure 2. Schematic diagram of experiment. L, doublet lens; G, grids to isolate microchannel plates, P; C, collector plate; M, mesh; voltages U and -U applied to the drift tube (shaded).

immediate identification of the ion stages present in the focal region.

When the E-field is at right angles to the drift tube axis, figure 1(b), the various ions are ejected in this orthogonal direction. The aperture at the entrance to the drift tube is quite small and the field across the interaction region incapable of steering the energetic ions through this aperture and on towards the microchannel plates. Thus the only features observed in the TOF spectrum of figure 1(b) are $CO^+$ and $CO^{2+}$ thermal ions and some low energy $C^+$ and $O^+$ ions. These observations led us to conclude that the angular distributions of the various atomic ions must be highly peaked along the E-vector of the laser. However, we were unable to quantify this conclusion because we were unsure of the effect of the restricting aperture.

There was another, more serious, problem relating to the analysis of the one-dimensional TOF spectra (figure 1). It was impossible to differentiate the process $[CO^{2+}] \rightarrow C^+ + O^+$ from the processes $[CO^+] \rightarrow C^+ + O$ and $[CO^+] \rightarrow C + O^+$, since we could not detect neutral particles (square brackets denote a transient molecular ion). This problem is highlighted in figure 1(b), where one sees a number of low energy $C^+$ ions but very few $O^+$ ions, leading to the conclusion that the process $[CO^+] \rightarrow C^+ + O$ is occuring. To overcome this problem, we devised a triple coincidence technique (photon-photoion-photoion) called "covariance mapping" which allowed the different fragmentation channels involving charged particles to be identified conclusively[3]; see also[4]. However, before this technique could be used, a completely new drift tube had to be designed, differing from the existing one in two specific aspects. Firstly, it was important that ion TOF should be a linear function of ion momentum component along the drift tube axis for both forward and backward ions; this is clearly not the case in figure 1. Secondly , for the covariance mapping technique to work, it was essential that the drift tube should have a much greater ion collection efficiency.

The drift tube used for these experiments is shown schematically in figure 2. The laser light is focused down to a diffraction-limited spot by an f/3 doublet lens (L). The CO gas is admitted at right angles to both the laser beam and drift tube axis. The drift tube is a mere 25 mm in length from focal spot

to 35mm-diameter microchannel plates. Grids, G, reduce field penetration from the microchannel plates (MCP). Mesh, M, is in fact the entrance to a second, longer drift tube used for improved momentum resolution. No restricting apertures are used. This geometry, and the voltages +U and -U applied to the electrodes, ensure that almost 100% of the forward *and* backward ions are collected. This, in turn, allows a definitive study of the angular distribution of the atomic ions relative to the laser E-field.

Before discussing the results of figure 3, it is necessary to describe briefly the covariance mapping technique, and how it allows the unequivocal identification of the fragmentation channels $[CO^{2+}] \rightarrow C^+ + O^+$, $[CO^{3+}] \rightarrow C^{2+} + O^+$, $[CO^{3+}] \rightarrow C^+ + O^{2+}$, $[CO^{4+}] \rightarrow C^{2+} + O^{2+}$ and $[CO^{5+}] \rightarrow C^{3+} + O^{2+}$ seen in the figure. Consider a particular fragment channel shown in figure 2, namely $[CO^{3+}] \rightarrow C^{2+} + O^+$. Suppose that for a given laser pulse a $C^{2+}$ fragment is detected at time $t_1$. There is clearly an enhanced probability of detecting an $O^+$ fragment at time $t_2$; this is considerably less than 100% because of poor detector efficiency. When one calculates, over many laser pulses, the covariance $[C(t_1,t_2) = \langle X(t_1)X(t_2)\rangle - \langle X(t_1)\rangle\langle X(t_2)\rangle]$ between the TOF points at which the fragments are detected, one obtains a positive value. Because one cannot know ahead of time which points in the TOF spectrum are correlated in such a fashion, one must calculate the covariance for each pair of TOF points (ie channels of the digital oscilloscope) and present it in the form of a two-dimensional map as shown in figures 3(a), (b) and (c). The design of the drift tube is such that the TOF(t) of a particular ion of mass m, charge q is given by the expression

$$t = A(m / (qU))^{1/2} + B(mv_{\parallel} / (qU)), \text{ valid for } mv_{\parallel}^2 / 2 < 0.1\ qU$$

Here $mv_{\parallel}$ is the initial momentum component along the drift tube axis and A and B are instrumental constants. This results in the separation of the forward ions ($mv_{\parallel} < 0$) and backward ions ($mv_{\parallel} > 0$). It follows that the covariance map is a *momentum correlation* diagram. In the case of two-body fragmentation, momentum conservation requires the correlated structure to be in the form of a line. The two islands on each line reflect the forward-backward and backward-forward fragment correlation, the tilt angle the ion charge ratio and the intensity variation along the line gives the momentum distribution. In figure 3(a), island 1 involves $C^+_f$ ions (f=forward) correlating with $O^+_b$ ions (b=backward), whereas island 2, close to the autocorrelation line, involves $C^+_b$ ions correlating with $O^+_f$ ions. Island 3 involves $C^{2+}_f$ and $O^+_b$ ions and island 4 $C^{2+}_b$ and $O^+_f$ ions. There are two weak features associated with the $[CO^{3+}] \rightarrow C^+ + O^{2+}$ fragmentation channel. Island 5 involves $C^{2+}_f$ and $O^{2+}_b$ ions and island 6 $C^{2+}_b$ and $O^{2+}_f$ ions. Finally, there are weak features associated with the asymmetric channels $[CO^{4+}] \rightarrow C^{3+} + O^+$ and $[CO^{5+}] \rightarrow C^{3+} + O^{2+}$.

One sees that the broad peak labelled $O^+$ lying at 1.28 μs in the time-averaged, one-dimensional spectrum shown below the covariance map is in reality associated with three different channels on the map: $[CO^{2+}] \rightarrow C^+ + O^+$, $[CO^{3+}] \rightarrow C^+ + O^+$ and $[CO^{4+}] \rightarrow C^{3+} + O^+$ (weak). If one imagines an identical time-averaged TOF spectrum lying along the ordinate axis, one can appreciate that island 1 represents correlation of $O^+_b$ ions lying at about 1.28 μs with $C^+_f$ ions in the "ordinate" spectrum lying at about 0.92 μs whereas the complementary island 2 involves $O^+_f$ ions and $C^+_b$ ions lying at about 1.08 μs and 1.12 μs respectively.

In the case of the $[CO^{2+}] \rightarrow C^+ + O^+$ channel, the momentum spread along the drift tube axis is relatively small; islands 1 and 2 are well resolved. This suggests that both the kinetic energy spread and angular distribution of the ions

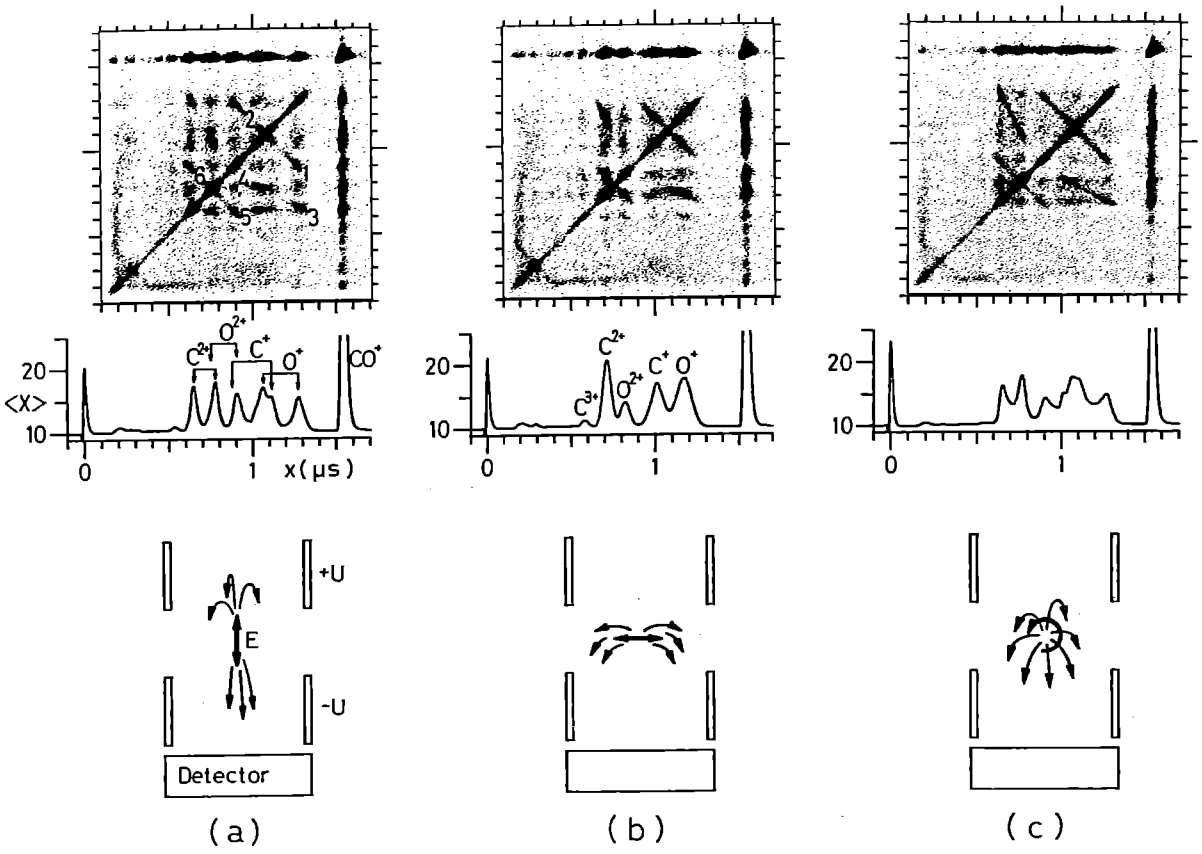


Figure 3. Covariance maps of CO with laser E-field (a) parallel and (b) perpendicular to the drift tube axis, as shown schematically beneath the maps. (c), with circularly polarised laser light.

involved in this fragmentation are quite restricted. In fact the same appears to be true of all channels. To confirm this, a covariance map was taken with the laser E-field at right angles to the drift tube axis, as shown schematically in figure 3(b). Now the atomic ions are ejected as shown, in which case the two islands fuse into one. Since the majority of the ions have a low momentum component along the drift tube axis, a single peak occurs, centred at a TOF equivalent to zero momentum (energy) ions with a width that reflects a different convolution of the same momentum spread and angular distribution as evident in figure 3(a). Once again, the one-dimensional TOF spectrum reflects this behaviour, with the various double peaks (arrowed in (a)) turning into a single peak in (b). The $C^+$ peak occurs at about 1.02 μs and the $O^+$ peak at about 1.18 μs, as expected.

Having achieved the essential objective of separating the various fragmentation channels, one can now attempt to determine the kinetic energy release and angular distribution associated with each. Figure 4(a) shows the covariance for the $C^+ + O^+$ channel when the laser E-vector lies along the drift tube axis. The data points represent the covariance in each channel of the digital oscilloscope, integrated in the y direction and projected on to the x axis, for island 1 in figure 3(a). Island 2 could not be measured because it was too close to the autocorrelation line. Figure 4(b) shows the integrated covariance associated with the single feature in figure 3(b).

The shoulder evident in figure 4(a) suggests that the $O^+_b$ ions have two kinetic energies. The continuous line is a theoretical curve based on the assumption that each peak has an asymmetric momentum profile consisting of composite back-to-back Gaussians with one half-width (the lower energy side) being considerably less than the other. There is no real justification for this assumption but we find that a single Gaussian profile for each does not fit the data. The choice of ion angular distribution parameter has little effect on the agreement between experiment and theory.

The choice of angular distribution parameter does, however, have a marked effect on the agreement between the experimental data points and the theoretical curve in figure 4(b). Here, we make the assumption that the angular distribution is given by $\cos^n\theta$, where $\theta$ is the angle between the laser E-field and the direction of ion emission. An iterative procedure allows improved values of n and kinetic energy to be obtained. The $C^+ + O^+$ angular distribution is found to be characterised by a value of n = 6(±2); peaks in the kinetic energy releases occur at 2.9(±0.5) and 6.6(±1.0) eV. A similar procedure provides the values of n and kinetic energy release for the $C^{2+} + O^+$ and $C^{2+} + O^{2+}$ channels shown in Table 1.

Although it is clear that, within experimental error, the same value of n could describe the angular distribution of all three

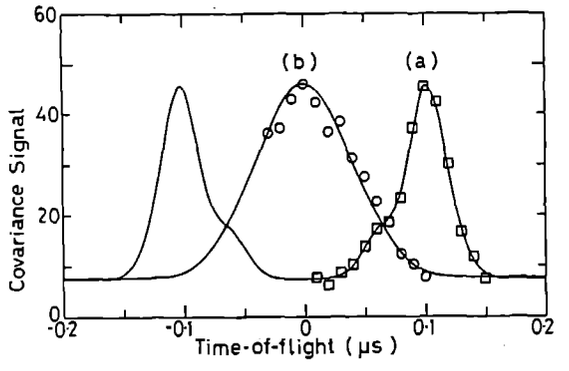


Figure 4. Integrated covariance signal for the $C^+ + O^+$ channel with laser E-field (a) parallel and (b) perpendicular to the drift tube axis. Time of flight is measured relative to the position of zero momentum $O^+$ ions.

Table 1: Angular Distribution Parameter (n) and Kinetic Energy Release.

| Channel | n | Kinetic Energy Release (eV) |
|---|---|---|
| $C^+ + O^+$ | 6(±2) | 2.9(±0.5); 6.6(±1.0) |
| $C^{2+} + O^+$ | 8(±2) | 11.3(±1.5) |
| $C^{2+} + O^{2+}$ | 10(±2) | 13.4(±2.0); 19.0(±3.0) |

fragmentation channels, it nevertheless appears that n does increase slowly with stage of ionisation. The ionisation/fragmentation process is a complex, dynamic sequence of events, where the interplay of the increasing laser E-field and the growing separation of a particular pair of ions are essential ingredients. However, a field ionisation model would tend to suggest this kind of behaviour.

In this model we employ a simple rule of thumb that ionisation occurs at a well-defined laser intensity, when the potential barrier is lowered to about 3 eV above the electron energy level[5]. This potential barrier is lowest when the laser field is applied along the molecular axis. To find the half-width of the ion angular distribution one needs to rotate the molecule until the potential barrier increases sufficiently to halve the tunneling probability. We note that the potential barrier increases faster when either the laser E-field, the internuclear distance or the ion charge state increases. As we move down table 1 all three parameters increase and we therefore expect the ion angular distribution to be more and more peaked. A similar outcome is predicted by a model in which the laser field is quantised[6].

Finally, figure 3(c) shows the map when circularly polarised laser light is used. The ions are now ejected isotropically, in the plane of the rotating E-vector. This isotropic planar distribution is projected on to the axis of the drift tube and gives the continuous covariance lines with higher intensity at the ends.

We are pleased to acknowledge the Science and Engineering Research Council for their financial support and Drs I N Ross and W T Toner of the Laser Support Facility (Rutherford Appleton Laboratory) for their help We are particularly indebted to M P Millard of Reading University Physics Department for his accurate machining of the new drift tube.

REFERENCES

1. LJ Frasinski et al. Phys Rev Lett **58** 2424 (1987)
2. K Codling et al. J Phys B**20** L525 (1987)
3. LJ Frasinski et al Science **246** 1029 (1987)
4. AMHJ Aertsen et al. J Neurophysiology **61** 900 (1989)
5. K Codling et al. J Phys B**22** L321 (1989)
6. A Giusti-Suzor et al. Phys Rev Lett **64** 515 (1990)

# THE UV PHOTODISSOCIATION OF $Ar_2^+$ AND $Ar_3^+$.

Clare A. Woodward, Ben J. Whitaker, and Anthony J. Stace

School of Molecular Sciences, University of Sussex, Falmer, Brighton BN1 9QJ

The cluster ion $Ar_3^+$ has been the subject of numerous experimental[1-6] and theoretical studies.[7-9] Of particular interest recently has been the interpretation of experimental data on the absorption and photofragmentation spectra of the ion.[1-6] There appears to be general agreement that $Ar_3^+$ can best be represented as a weakly bound atom associated with a dimer chromophore, $Ar_2^+$.Ar. However, it is less certain whether the ion is linear or bent, or if the electronic transition observed in the visible region of the electromagnetic spectrum, is analogous to either the $^2\Sigma_g^+ \leftarrow {}^2\Sigma_u^+$ or the $^2\pi_g \leftarrow {}^2\Sigma_u^+$ transitions found in the dimer ion. $Ar_3^+$ has an absorption band in the UV, similar in cross-section and frequency to that observed for the $^2\Sigma_g^+ \leftarrow {}^2\Sigma_u^+$ transition in $Ar_2^+$ and it has been proposed that the band is characteristic of an $Ar_2^+$ chromophore.

Preliminary experiments on the UV photofragmention of $Ar_2^+$ and $Ar_3^+$ have been undertaken. In both cases, the spectra were recorded by monitoring the kinetic energy of the product $Ar^+$, following the excitation of either $Ar_2^+$ or $Ar_3^+$ with 308 nm radiation from a XeCl excimer laser. Approximately $10^{-10}$ A of $Ar_2^+$ and $Ar_3^+$ were generated by the electron impact ionization of neutral argon clusters. Each mass-selected ion beam was crossed at right angles with unpolarized UV radiation, and the kinetic energy spectra of the $Ar^+$ photofragments measured using an electrostatic analyser. Because the excimer laser has only a 10 ns pulse width, the photofragment yields in a crossed-beam configuration are very low; therefore, gated photon counting coupled to a scintillation detector has been used to monitor the product ions.

Figure 1 shows a photofragment kinetic energy spectrum measured for $Ar^+$ following the excitation of $Ar_3^+$ at 308 nm. Although the use of unpolarised radiation should result in an isotropic distribution of photofragments, the magnitude of the excess kinetic energy is such that there is considerable instrumental discrimination. Thus, the dominant contribution to the kinetic energy spectrum comes from those fragment ions which are either forward- or back-scattered. As a consequence of both discrimination and the finite energy window of the electric sector, the spectrum shown in figure 1 corresponds to a detection level of $< 1$ ion $s^{-1}$ and took approximately 10 hours to record. The asymmetry in the spectrum is an instrumental effect which arises because the optimum fixed delay between the laser pulse and the detection of fast forward-scattered ions, is not appropriate for the slower, back-scattered ions. No $Ar_3^+$ ions are produced by direct ionization of the neutral;[17] they all originate from the unimolecular decay of larger cluster ions. The maximum internal energy the ion can have is 0.2 eV; however, there is a possibility that the decay process may leave $Ar_3^+$ rotationally hot. It is evident from figure 1 that the kinetic energy spectrum consists of two components; two wings which can be attributed to a decay step which involves a large release of kinetic energy (≈1.3 eV), and a central feature with a half-width that corresponds to an energy release of just 0.09 eV. Although polarised radiation has not been used in the present experiments, there is a remarkable similarity between figure 1 and those kinetic energy spectra measured previously in crossed-beam experiments,[4-6] where the plane of polarization of the radiation has been orientated parallel to the ion flight direction. In the latter experiments, the use of polarized radiation serves to accentuate the contribution from forward- and back-scattered photofragments.

In an earlier experiment,[6] it was suggested that the two components to the $Ar_3^+$ kinetic energy spectrum, originated from separate excited electronic states. The high kinetic energy component coming from a state which correlates with the formation of an atomic ion, and the low energy component from a state where the formation of $Ar^+$ is preceded by the generation of excited $Ar_2^+$. The fact that the kinetic energy spectrum of $Ar_3^+$ continues to exhibit two separate features in the UV suggests that, in addition to the $^2\Sigma_g^+ \leftarrow {}^2\Sigma_u^+$ transition, other excitation processes may also be taking place.

REFERENCES

1. C.R. Albertoni, R. Kuhn, H.W. Sarkas and A.W. Castleman Jr., *J. Chem. Phys.*, 1987, 87, 5043.

2. N.E. Levinger, D. Ray, K.K. Murray, A.A. Mullin, C.P. Schultz and W.C. Lineberger, *J. Chem. Phys.*, 1988, 89, 71.

3. N.E. Levinger, D. Ray, M.L. Alexander and W.C. Lineberger, *J. Chem. Phys.*, 1988, 89, 5654.

4. J.T. Snodgrass, C.M. Roehl and M.T. Bowers, *Chem. Phys. Lett.*, 1989, 159, 10.

5. Z.Y. Chen, C.R. Albertoni, M. Hasegawa, R. Kuhn and A.W. Castleman Jr., *J. Chem. Phys.*, 1989, 91, 4019.

6. C.A. Woodward, J.E. Upham, A.J. Stace and J.N. Murrell, *J. Chem. Phys.*, in print.

7. W.R. Wadt, *Appl. Phys. Letters*, 1981, 38, 1030.

8. H.H. Michels, R.H. Hobbs and L.A. Wright, *Appl. Phys. Letters*, 1979, 35, 153.

9. P.J. Kuntz and J. Valldorf, *Z. Physik D*, 1988, 8, 195.

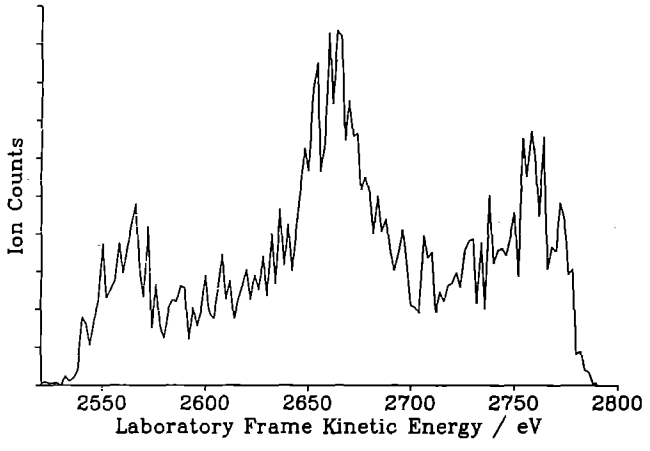


Figure 1. Photofragment kinetic energy spectrum of $Ar_3^+$

LASER ANNEALING OF MAGNETO-OPTIC FILMS

P W Haycock, R H Noyau, W G Stirling and E W Williams

University of Keele

# INTRODUCTION

Rare earth - transition metal alloy thin films are currently the primary media for magneto-optic data storage. Although they possess good magnetic properties, including strong perpendicular anisotropy, high coersivity and large remanent magnetisation,they also have several less desirable qualities. In order to enhance their performance we have concentrated on attempting to modify the film structure by use of pulsed laser irradiation. This technique has several advantages over conventional thermal annealing, in particular the ability to tune the laser wavelength to a region which is absorbing in only one layer of the disc, in order to confine the effects of the anneal to that layer. By tuning a laser to an absorbing wavelength in Tb-Fe-Co media we have been able to produce local transient temperatures approaching 3000°C, modifying the magnetic behaviour of the samples yet without siignificantly affecting their macroscopic layer structure. The structure has been probed by neutron and x-ray reflectivity measurements and the magnetic properties by use of Kerr rotation and vibrating-sample magnetometry. We present here the results of structural and magnetic studies of the effects of laser annealing on commercially produced Tb-Fe-Co based discs. The layer structure of the samples is given in fig. 1. Samples were produced by cutting the 5.25" discs into strips about 5 - 10 cm long by 1 - 2 cm wide.

# LASER ANNEALING

The annealing was carried out in the Nanosecond Laboratory of the Laser Support Facility at the Rutherford Appleton Laboratory. A Lambda-Physik FL3002 dye laser was pumped by a Lumonics HyperX 460 Excimer laser operating at 308 nm using XeCl. The dye was tuned to the optimum wavelength of 390 nm for the dye used (LC3860). At this wavelength the magneto-optic film transmits less than 1beam and the AlN and glass are transparent. The power density on the sample was controlled by use of a diverging lens and the sample was scanned under the beam in a variety of modes, including single shot per area, multiple shot per area and multiple scan per sample. (See fig. 2.)

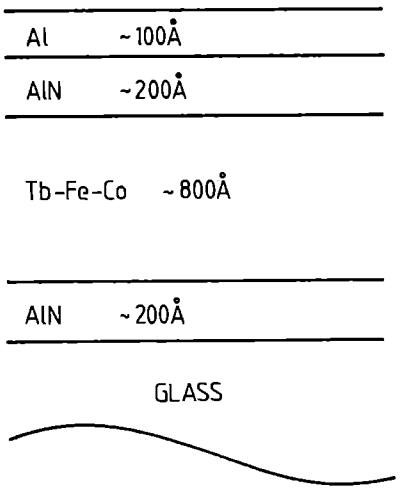


Figure 1

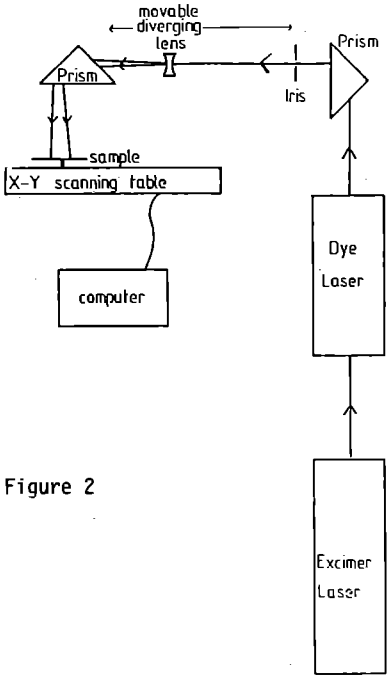


Figure 2

# CHARACTERISATION

Neutron reflectivity measurements were made using the neutron reflectometer CRISP at the Rutherford Appleton Laboratory in unpolarised mode. The white beam was incident at an angle of 0.35° to the sample and the specularly reflected beam detected by a position sensitive detector. The momentum transfer was obtained from time-of-flight analysis.

X-ray reflectivity was carried out on Station 8.3 of the Synchrotron Radiation Source at Daresbury. Theta-2theta mode was used with a monochromatic beam of wavelength 1.734Å.

Magnetic measurements have been carried out using a Princeton Applied Research vibrating-sample magnetometer and Kerr rotation experiments.

# RESULTS

Fig. 3 shows hysteresis loops from the vibrating sample magnetometer for an as-received sample and one annealed to a transient temperature of about 690°C. Here the perpendicular component is shown. There was no in-plane component. It can be seen that annealing has doubled the saturation and remanent magnetisation by the introduction of a soft magnetic contribution in addition to the initial ferrimagnetic loop. Samples annealed to around 2900°C lost their perpendicular anisotropy and a small hysteresis loop was found in-plane but none normal to the plane.

The macroscopic layer structure, on the other hand, has not been significantly affected. Fig. 4 shows the neutron reflectivity from an as-recieved sample and one annealed at 2900°C. Apart from a small offset along the x-axis, due mainly to a slight misorientation between the two samples, these two curves are almost identical. This indicates that there has been no significant change in the structure of the layers on a depth scale greater than 40Å.

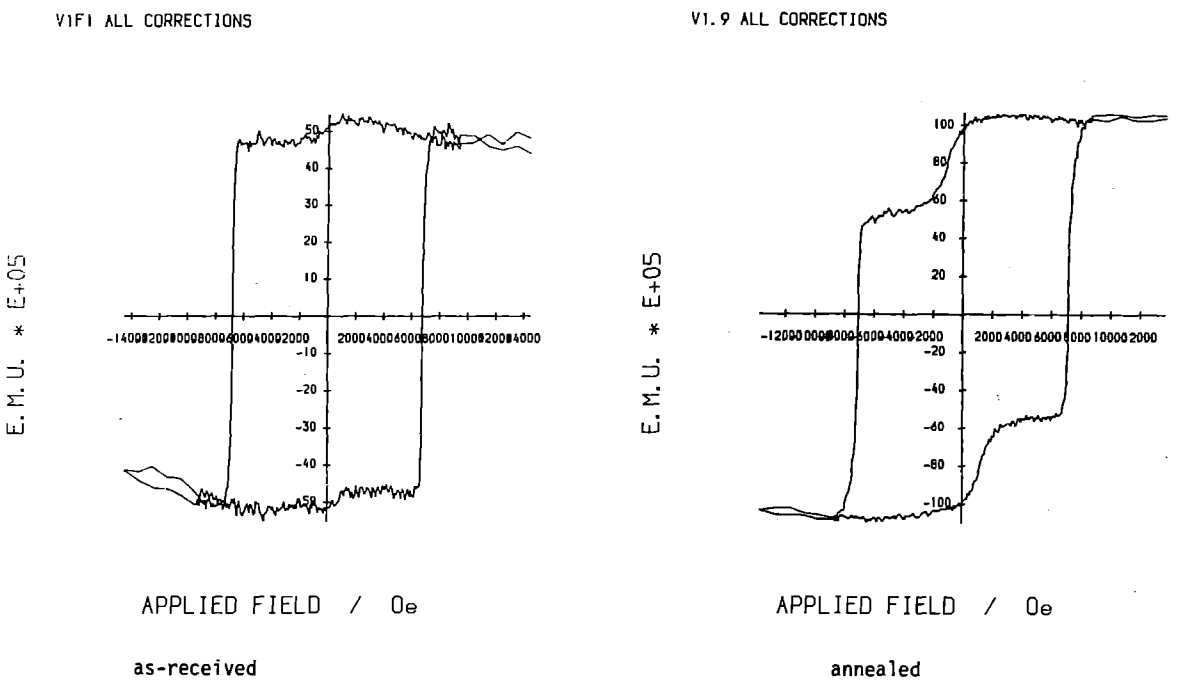


Figure 3

## CONCLUSION

Pulsed laser annealing has been shown to be capable of significatly modifying the magnetic properties of sputtered rare earth - transition metal alloy films while producing only a negligible effect on the large scale structure. In particular an anneal to a transient temperature of about 690°C was found to double the saturation and remanent magnetisation. Further structural work is in progress to correlate these changes with atomic rearrangement on the scale of a few Ånströms.

## ACKNOWLEDGEMENTS

The authors wish to thank G J Herdman for assistance with the neutron data collection and S Collins, M Hagen, C C Tang and T Thomson with the x-ray reflectivity. Advice and help with setting up the laser annealing were provided by A Parker. This work was supported by the SERC.

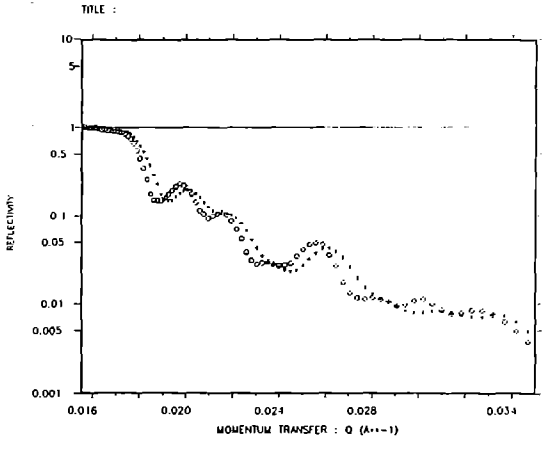


Figure 4

# NONLINEAR SPECTRAL CHANGES IN AIR AT 249 NM

I N ROSS

RUTHERFORD APPLETON LABORATORY

## Introduction

Modification of the spectrum of a pulse due to nonlinear propagation effects in air [1-4] can cause serious degradation to the performance of a high power laser system and hence limit its peak power. This is the case when the spectral nonlinearity is the dominant nonlinear process.

The two principal spectral effects for short pulses are the generation of Stokes spectral sidebands due to stimulated Raman scattering and spectral broadening due to self-phase modulation which is itself due to the nonlinear refractive index. The dominant process of the two is that requiring the lower value of $\int I d\ell$ at 'threshold'. The threshold for significant Raman generation is given by:

$$\gamma_t \int I d\ell = 25 \qquad (1)$$

where $\gamma_t$ = transient Raman gain coefficient = $\gamma_s/[1 + 5.2\ T_2/t]^5$

$$\therefore \int I d\ell = (25 + \frac{130 T_2}{t}) \frac{1}{\gamma_s} \qquad (2)$$

where $\gamma_s$ = steady state gain coefficient;
$T_2$ = dephasing time $(1/\pi\Delta\nu_R)$
$\Delta\nu_R$ = Raman linewidth; t = pulse length.

The self-focusing or self-phase modulation threshold taken to be at B = 1 is given by:

$$\int I d\ell = 60 \lambda n_2 \qquad (3)$$

where $\lambda$ = wavelength in μm
$n_2$ = nonlinear index in esu x $10^{13}$

Figure 1 plots the 'threshold' value of intensity length product obtained by inserting published values of material parameters for nitrogen into the above equations. This shows, for nitrogen, how the dominant nonlinear process depends on the duration of the pulse.

## Experiments

Figure 2 shows the experimental arrangement. A linearly polarised 4 ps pulse at 249 nm was focused in air using a 1 m focal length lens. A reflective grating working in 3rd order dispersed the spectrum and gave a resolution of <1cm$^{-1}$ for the full beam aperture. Figure 3 shows typical spectra at various beam intensities.

It can be seen from Figure 1 that for these very short pulses vibrational Raman should be stronger than rotational Raman by virtue of its very short $T_2$ time (≈7 ps) and that self-focusing effects dominate. We would not expect to see any Raman Stokes lines in air with our short pulses and no evidence of its presence was found.

The dominant effect in air, as shown by Figure 3,

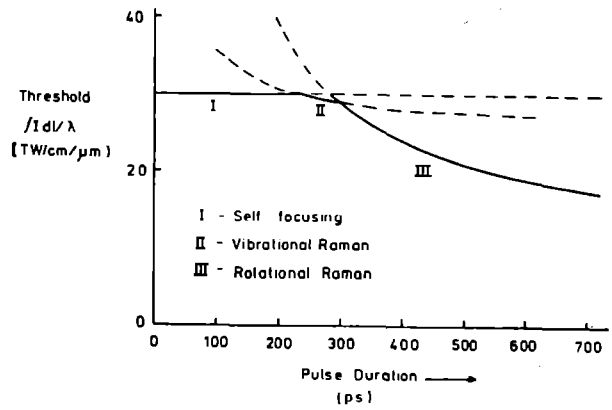


Fig 1 Dependence of threshold values $\int I d\ell$ on pulse duration for self-focusing beam degradation and Raman losses.

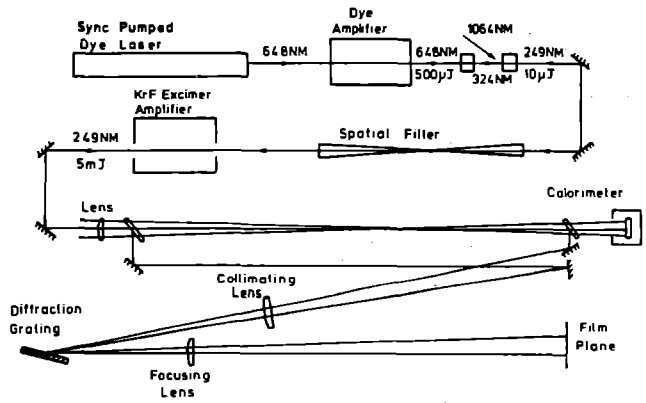


Fig 2 Experimental layout for the measurement of spectral changes resulting from nonlinear propagation in air.

is spectral broadening which increased rapidly above a threshold value for $\int I d\ell$ of 15 TW/cm.

Since there is a possibility of fourwave mixing processes contributing to the observed broadening and since these have phase matching requirements which can make them dependent on the angular content of the beam, a second experiment was conducted in which the beam was not focused but propagated collimated over a long distance. Figure 4 shows the spectral broadening under these conditions. The threshold value for $\int I d\ell$ was measured at 10 TW/cm and this lower value does suggest that effects with phase matching requirements must be considered as possible mechanisms for spectral broadening.

Figure 4 also shows very much less broadening for longer pulses (40ps). The reason for this may be due to the 40 ps pulses being much narrower spectral bandwidth (0.2 cm$^{-1}$) and having time bandwidth products which were much closer to the transform limit.

## Assessment of results

Figure 3 shows rapid broadening of the spectrum at increasing intensities. Figure 3(a) shows a typical double line spectrum at low intensity. Figure 3(b) shows that the spectral broadening is associated with sideband generation. Our interpretation of this process first suggested by Penzkofer et al [6] is that there are efficient four wave mixing processes which enable pairs of wavelengths in the original spectrum to produce sidebands.

This process should depend upon the third order polarisabilities and be closely linked to similar

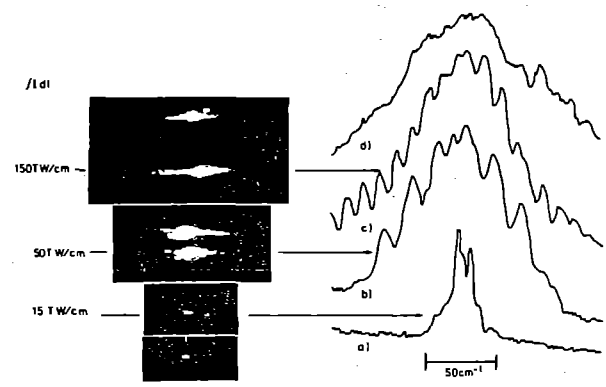


Fig 3 Spectral broadening in air at 249 nm at various intensities for focusing geometry.

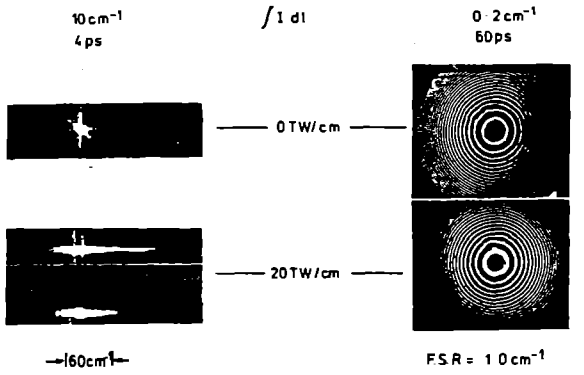


Fig 4 Spectra broadening in air at 249 nm at low and high intensity for collimated beams and for two pulse durations.

processes such as self-focusing and self-phase-modulation. The observed thresholds are close to those expected for $n_2$effects and some spectral broadening due to self-phase-modulation is generally seen as a precursor to 'continuum generation'.

The dominance of continuum generation over other processes including self- focusing depends upon a strong enhancement of the four wave mixing process and this can come from the close proximity of rotational Raman transitions. This 'off-resonant' Raman enhancement of four wave mixing has been considered by Dangor et al [7] in a different context. They show that for the generation of a 10% side-band from a two component spectrum:

$$\frac{1}{2}\lambda_s \frac{\Gamma}{\sqrt{(\Gamma^2 + \Delta\omega^2)}} \cdot \int I d\ell = \sqrt{0.1} \qquad (4)$$

where

$\lambda_s$ = steady state Raman gain coefficient
$\Gamma$ = Raman half-linewidth
$\Delta\omega$ = off-resonant displacement

This is to be compared with the threshold for Raman generation of

$$\lambda_s \int I d\ell \approx 25\ (1 + 5.2\ T_2/t) \approx 130\ T_2 \qquad (2)$$

The large difference in threshold is at once apparent under conditions for which the Stokes shift is not a large multiple of the pulse bandwidth.

Equation 4 applies to a single rotational transition. Inserting the values for the strongest rotational line in nitrogen (S[8]) together with our pulse parameters, the threshold condition, equation 4, reduces to

$$\int I d\ell = 80\ \text{TW/cm}$$

Since there are a number of rotational Raman transitions with appreciable gain, it is necessary to sum the gain over all these lines. Thus our threshold condition now becomes:

$$\int I d\ell \cdot \sum_{\text{all lines}} \frac{\lambda_s \Gamma}{\sqrt{\Gamma^2 + \Delta\omega^2}} = 0.63 \qquad (5)$$

Making use of published data (see for example reference 3), this summation has been evaluated over the rotational lines in nitrogen. The threshold conditions (equation 5) reduces to:

$$\int I d\ell = 9\ \text{TW/cm}$$

which compares well with the experimentally determined threshold value for $\int I d\ell$ of 10 TW/cm.

## Polarisation effects

If the broadening mechanism is associated with stimulated rotational Raman scattering then there should be a strong polarisation dependence. In the case in question we are concerned with the Raman gain for a beam with the same polarisation as the pump beam and then [8]:

$$\frac{\lambda\ (\text{circular})}{\lambda\ (\text{linear})} = 0.25 \qquad (6)$$

Thus we would expect the threshold to increase by a factor 4 to give a threshold value for $\int I d\ell$ of 60 TW/cm. An experiment to test this hypothesis was conducted using the arrangement of Figure 2. A quarter wave plate was introduced to convert linear to circular polarization and a direct comparison was made of the relative spectral broadening in these two cases.

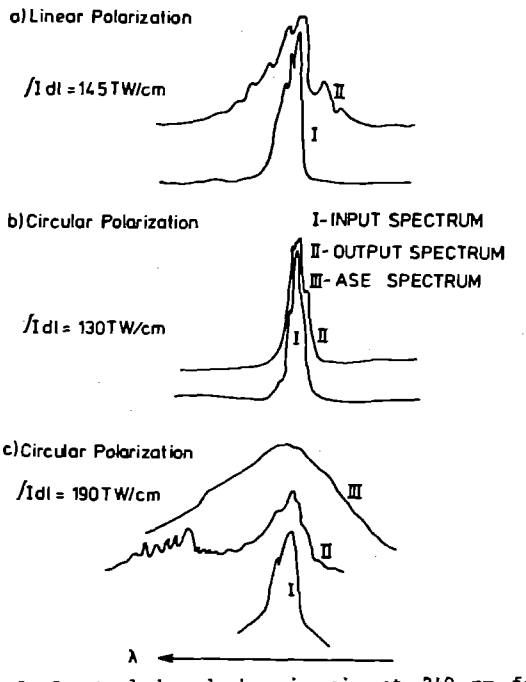


Fig 5 Spectral broadening in air at 249 nm for linear and circular polarisation of the beam.

Figure 5 shows spectral broadening for both linearly and circularly polarised beams. The suppression of this mechanism for circularly polarised beams is immediately apparent and demonstrated a threshold ratio of ~6, even higher than expected. The suppression is so strong that the threshold for generation of rotational Stokes lines can be reach (figure 5) before large spectral broadening severely depletes the beam.

## Discussion

For short pulses at 249 nm the nonlinear effects in air are dominated by spectral broadening rather than Raman Stokes generation or non-spectral effects. A mechanism is proposed for the spectral broadening, based on four wave mixing enhanced by the proximity of rotational Raman transitions in nitrogen. This mechanism gave a calculated threshold in reasonable agreement with the observed spectral broadening threshold ($\int I d\ell$ = 10TW/cm for linear polarization) and with the polarization dependence of this threshold. The threshold for circular polarization is sufficiently high to allow the appearance of rotational Raman Stokes lines, seeded by the amplifier ASE spectrum.

## References

1. P Corkum and C Rolland, Acamdemic Press, R R Alfano (editor).
2. I N Ross, Annual Report to the Laser Facility Committee 1989, RAL-89-043.
3. W E Martin and R J Winfield, App Opt 27, 1988, 567.
4. R H Lehmberg, J Reintjes and R C Eckhardt, App Phys Lett 30 1988, 487.
5. N J Everall, J P Partanen, J R M Barr and M J Shaw, Opt Comm 64, 1987, 393.
6. A Penzkofer, A Laubereau and W Kaiser, Phys Rev Lett, 31, 1973, 863.
7. A E Dangor et al, J Phys B At Mol Opt Phys 22, 1989, 797.
8. M Rokni and A Flusberg, IEEE J Quant Electr, 22, 1986, 1102.

# TEST OF AN ALTERNATIVE OSCILLATOR FOR SPRITE

Ian N. Ross and Michael Steyer
Rutherford Appleton Laboratory

## INTRODUCTION

The synchronously pumped dye laser system in the LSF was used to perform preliminary studies on a Distributed Feedback Dye Laser (DFDL) as a potential future Sprite oscillator. Details of the DFDL principle and pump geometry are described elsewhere[1]. The pump laser is very similar to that employed in the SPRITE system. A mode-locked, frequency doubled Nd:YAG laser synchronously pumps a dye laser at 581nm. The dye laser pulses were stretched by an intracavity etalon (FSR=17cm$^{-1}$) and amplified in a three-stage pulsed dye amplifier to ≈20μJ. The duration of the pump pulse was ≈70ps (FWHM).

After being attenuated and having passed a cylindrical lens (f=10cm) the light enters the prism arrangement near normal incidence, where it is split into two partial beams. The pump beam size and consequently the length of the excited volume was varied by an iris diaphragm. Each of the two partial beams produces a line focus in the dye from which visible red fluorescence is emitted. By horizontal adjustment of the prism holder the two line foci can be made overlap which is essential for DFDL operation.

A $2 \cdot 10^{-2}$ M solution of Pyridine 2 in a 1:1 mixture of ethanol and DMSO was used in order to find a compromise between high solubility, refractive index and absorption depth. The excited volume has a length of ≈3mm and an approximately circular cross-section of 100μm diameter. The DFDL output at 746nm (3x KrF wavelength) was observed with a photomultiplier attached to the exit slit of a monochromator, since it is not visually distinguishable from Amplified Spontaneous Emission (ASE). However, the spectral bandwidth is much smaller and the spectral intensity typically 100 times higher. Another indication for DFDL action is the tunability by changing the angle of incidence. The dye cell is vertically tilted by 10° to suppress laser action between the cell surfaces.

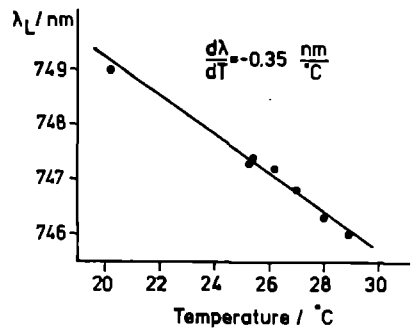


Figure 1: Temperature dependence of the DFDL output wavelength

The output pulse was observed by a Hadland Imacon 500 streak camera. The threshold for the first pulse from the DFDL was found to be ≈500nJ. At about twice that energy, a second pulse occurs after typically 60ps. When pumped far above threshold (≈10μJ) no single pulses were observed but the streak became very blurred. This seems to indicate[2] that separate parts in the DFDL start to lase independently because the risetime of the pump is too fast to allow a common feedback of the whole excited length.

The DFDL beam size at a distance of 50mm was approximately 1.5x2.0mm$^2$. Since it appeared to be of primary importance for the Sprite experiments we concentrated on the single pulse mode. A single DFDL pulse is not visible but it can be conveniently observed with an infrared viewer. The pulse length was determined to be 10±2ps. Attempts to vary the pulse length by altering the pump beam size and consequently the length of the DFDL did not produce convincing results.

A spectral measurement was performed by putting an etalon (FSR=20cm$^{-1}$) in front of the streak camera slit. From the width of the observed spectral peak we conclude that the pulses are certainly within a factor of 2 of the transform limit.

A problem of DFDL operation may be temperature variation of the refractive index of the solvent. We measured the DFDL output wavelength as a function of dye temperature which was simply varied by illumination with a light bulb (figure 1). The temperature coefficient of -0.35 nm/°C indicates that the room temperature has to be kept constant within ±1°C in order to keep the frequency tripled light within the KrF gain bandwidth.

In conclusion, we have demonstrated a simple set-up to produce nearly transform limited 10ps pulses by a DFDL from a synchronously pumped dye laser offering much worse pulses in this respect. The working range for single pulse operation and almost circular beam shape were determined and the sensitivity to temperature changes was measured.

## REFERENCES

1. M Steyer, IN Ross and JMD Lister
This Report Sect B

2. Z Bor, private communication

# COMPUTER CONTROLLED, REPETITIVE KrF LASER-PLASMA X-RAY SOURCE FOR RADIOBIOLOGY RESEARCH

I C E Turcu, F O'Neill, C J Reason, P Gottfeldt, A R Damerell, S Hancock and T Hannon

Rutherford Appleton Laboratory

## INTRODUCTION

The repetitively pulsed KrF laser plasma X-ray source, discussed in this paper has been used to generate photons of energy hν ∿ 1 keV for applications such as the study of radiation damage to biological cells [1] and X-ray lithography [2]. The source has several attractive features: (i) it is compact; (ii) X-rays are delivered to the specimen in the form of intense short bursts of radiation. During the X-ray pulse a number of photons is likely to interact with an individual biological cell nucleus or a macromolecule of a photoresist; (iii) the laser beam is near diffraction limited and can be focused to a small focal spot (∿10 μm) so only a moderate laser energy ∿0.5-1.0 J/shot is required to produce keV X-rays. This reduces the thermal loading on X-ray windows or masks; (iv) the X-ray source can be 'tuned' to different photon energies by changing the target material. However, the exposure time can be limited by debris from the plasma coating the windows and focusing optics [2]. An efficient method of reducing the debris is to introduce helium gas inside the target chamber [1,3,4].

The DNA damage experiments are described in Section C2.5.

The X-ray measurements for different helium ambient pressures in the target chamber are described in Section D2.2.

In this section we describe: (1) the laser and target chamber, (2) the computer control of the X-ray source, (3) the lens mount with helium flow, and (4) the effect of atmospheric helium in the target chamber on lens coating by target debris.

## THE X-RAY SOURCE

The repetitive laser-plasma X-ray source described in Ref 1 was used to produce X-ray photons of energy hν = 1.1 keV by focusing laser pulses from a Lambda Physik EMG150 injection-locked KrF laser onto a rotating precision steel target electroplated with 20 μm of copper. The angle of incidence of the laser beam on target is 22° with respect to the target normal. The experimental arrangement is shown in Fig 1. The KrF laser is operated at 5 Hz repetition rate and produces an energy on target of ≈ 0.5 J in a FWHM ≈ 21 ns pulse duration at a wavelength of 249 nm.

The 9 cm focal length, aspheric singlet, lens focused the laser beam and also sealed the target chamber. The convex surface of the lens was anti-reflection coated hence laser energy losses were limited to one Fresnel reflection. The lens holder was constructed to allow accurate normalisation of the lens to the laser beam. Helium flowing at ≈10 ℓ/min uniformly from a distribution ring around the lens toward the target was used to flush debris away from the lens (Fig 2). The target chamber can operate at any helium pressure between 0-760 torr.

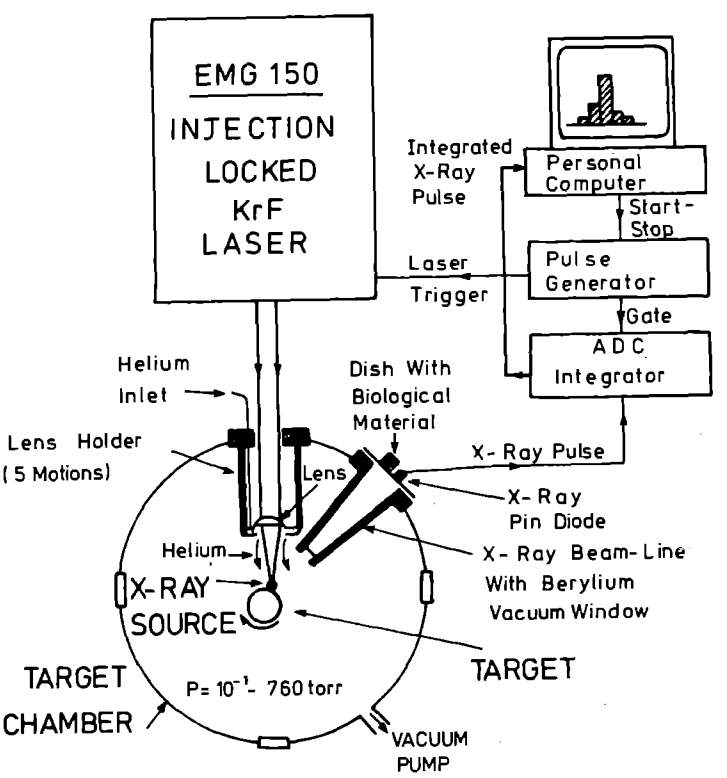


Fig.1 Experimental arrangement.

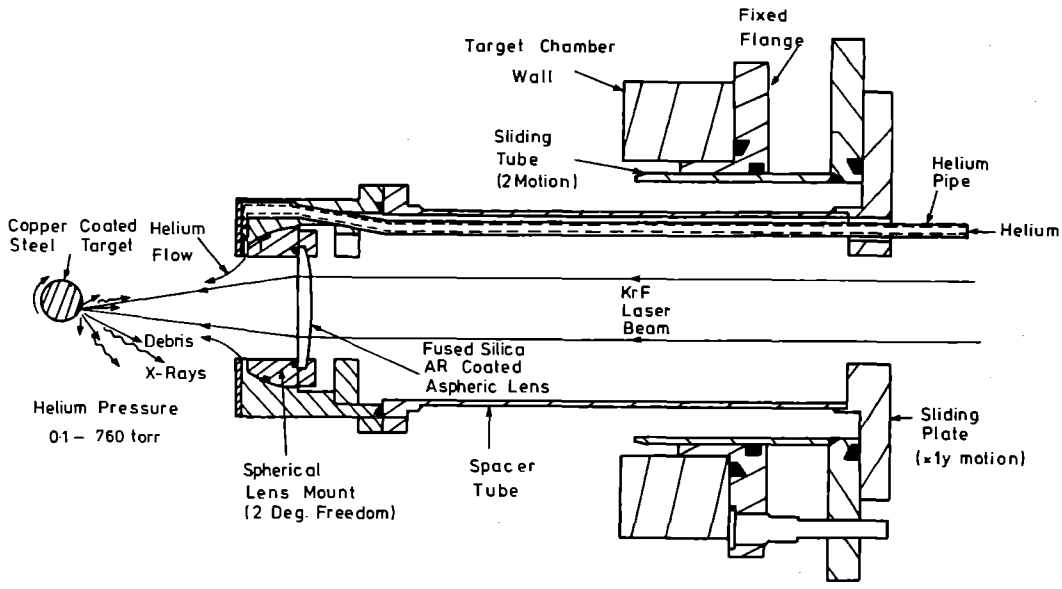


**Fig 2. Detail of lens holder with helium flow. Lens focal length is 90mm.**

The focal spot size was determined using a 5m focal length lens focused to an equivalent plane on a series of pinholes ranging from 0.5mm to 5mm diameter. All the energy was transmitted through the 4mm hole and only 20% through the 0.5mm pinhole. Hence, 20% of the laser energy was delivered to the target in a focal spot of ≈9μm at an irradiance of ≈ $10^{13}$W/cm² and 80% of the energy in a focal spot of ≈ 54μm at an irradiance of ≈$10^{12}$W/cm².

For accurate control of the X-ray dose delivered to the biological specimen the X-ray source was controlled by a personal computer (PC). The PC starts firing the laser at 5Hz via a pulse generator (Fig 1). The signals from the XRD mounted beside the biological specimen dish are integrated by a LeCroy ADC and fed into the PC. The computer displays in real time, on a histogram, the X-ray doses delivered to the specimen each shot and adds them up. When the required total dose is delivered to the specimen the computer stops the laser and prints out: a histogram of the X-ray dose per shot, the total dose, the average dose per shot, the number of shots, the repetition rate and the duration of the X-ray exposure.

## LENS COATING BY TARGET DEBRIS

The transmission of the focusing lens at λ = 249 nm was measured with a UV dual beam spectrophotometer. Despite the use of flowing (10 ℓ/min) helium at 1 atmosphere pressure, plasma debris still coated the f = 9cm focusing lens surface, resulting in an 8% drop in laser (λ = 249) transmission after 8000 shots on Cu coated targets, at 22° incidence. By contrast, in Ref 2, the laser beam was focused at normal incidence, in vacuum, on a silver coated target. The transmission of a fused silica protection plate, placed between the lens and the target at 8 cm from the target dropped by 30% after only 750 shots. Because this plate had both surfaces in the target chamber the transmission of the surface closest to the target has dropped by between 15-30% depending on the amount of debris deposited on the back surface. Assuming that the transmission of the surface coating layer follows Beer's law we estimate, using the absorption coefficients of Ref 5, the thicknesses deposited on an optical surface in the two experiments to be ∿9Å of Cu for 8000 shots in the present experiment and 25-50Å of Ag for 750 shots in the conditions of Ref 2. Clearly, the helium atmosphere and off-normal target irradiation has significantly reduced the rate of debris deposition.

## ACKNOWLEDGEMENTS

The authors wish to thank D Baker and D Wood who assembled the lens holder. This work was partially supported by the UK Department of Trade and Industry through the EUREKA European Research Initiative (EU 213 excimer laser project).

## REFERENCES

1. F O'Neill et al Proc Soc Photo-Opt Instrum Eng 1140, 232-236, SPIE, Washington (1989).

2. E Turcu et al, Microelectron Eng 6, 287-292, North Holland, Amsterdam (1987).

3. M L Ginter and T J McIlrath, Appl Opt 27, 885, (1988).

4. T Tomie et al, Proc Soc Photo-Opt Instrum Eng 831, 224-229, SPIE, Washington, (1987).

5. H J Hageman et al, Report DESY SR-74/7, Hamburg (1977).

# PHOTOCATHODE COOLING FOR THE O-SMA DIODE ARRAY DETECTOR

G J H Simpson and A W Parker

Laser Support Facility, Rutherford Appleton Laboratory

## INTRODUCTION

Figure 1 shows a schematic diagram of the O-SMA detector head. The detector works as follows: photons striking the photocathode generate electrons which are amplified by the microchannel plate (MCP). These electrons then strike the phosphor screen, the light generated is fibre-optically coupled to the diode array where readout operations are addressed. The primary source of noise in the detector head is due to thermally generated photoelectrons. This noise is temperature dependant and in an effort to reduce noise levels various parts of the detector can be cooled.

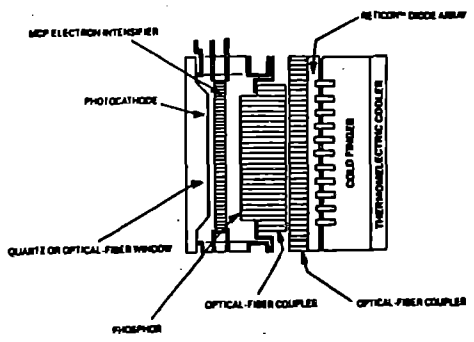


Figure 1: Schematic diagram of the OSMA detector

Firstly, the diode array is cooled by a recirculated liquid coolant in conjunction with a thermoelectric (Peltier) cooler. Using this double method of cooling the array can be maintained at -35°C. Dry nitrogen is passed over the detector head to prevent condensation forming which would damage the array. A second important area for cooling is the photocathode and we report here the incorporation of recirculated liquid (methanol) cooling (-20°C) of the photocathode. The reduction of thermal noise giving an improved signal-to-noise performance is quantified.

## RESULTS AND DISCUSSION

The following experiments were performed to investigate the reduction in noise due to photocathode cooling:

(i) Using a very small aperture on the spectrometer and the photocathode at room temperature, the 405 nm line from a mercury pen lamp was observed through neutral density filters. Spectra were recorded for 4000 exposure units (135 seconds), using successively higher neutral density filters until the Hg line was no longer resolvable from the noise, ie, reduction of signal to less than twice the standard deviation of baseline noise. The photocathode was then cooled and allowed to reach equilibrium at -10°C, and the experiment repeated to find the neutral density filter at which the Hg line was again not resolvable.

Without photocathode cooling, the mercury line was resolvable through a neutral density (ND) filter of 4.2, but not through a ND of 4.3. With photocathode cooling, the mercury line was resolvable through a ND of 4.6, but not through a ND of 4.7, see figure 2.

The difference in ND filters is 4.6 - 4.2 = 0.4. ND filters are on a logarithmic scale, and a factor of 0.4 represents a reduction in light intensity of 2.51. Therefore to be able to resolve this line, the noise must be reduced by the same factor.

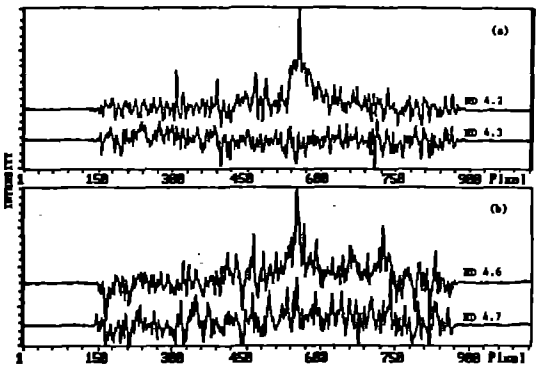


Figure 2: Spectra showing resolution of Mercury line using neutral density filters.
(a) Room temperature photocathode
(b) Cooled photocathode.

(ii) With the detector in complete darkness, readouts were taken with exposures of 4000, 1000, 500 and 100 exposure units with both the photocathode cooling off and on. Readouts were also recorded for the same exposures with the detector in gated mode. This being a special mode of operation for pulsed experiments, the photocathode is only switched on for a preset time duration. In this case, however, it was off all the time and hence the noise level of the readouts give details of the noise from all parts of the detector, including readout noise etc. without any contribution from the photocathode.

The gated spectra were then subtracted from the warm and cooled photocathode spectra, for each exposure time to give the noise contribution of the photocathode in both states.

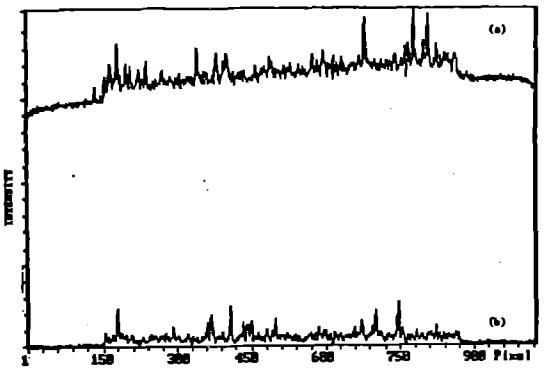


Figure 3: Photocathode noise when (a) at room temperature
(b) cooled to -10°C.

Figure 3 shows the difference between the warm photocathode minus gated and cooled photocathode minus gated spectra for an

exposure of 4000 exposure units. For a region of 100 pixels, the mean intensity is 576.1 for the warm-gated spectrum and 17.4 for the cooled-gated spectrum. This is a reduction in noise intensity by a factor of 33.1 and the increase in signal to noise by $\sqrt{33.1} = 5.75$. For each of the exposure times, the following results were obtained:

| Exposure Units | Reduction in photo-cathode noise Intensity | Increase in Signal to Noise |
|---|---|---|
| 4000 | 33.1 | 5.8 |
| 1000 | 22.9 | 4.8 |
| 500 | 38.9 | 6.2 |
| 100 | 5.6 | 2.4 |

This gives an average increase in signal to noise of 4.8.

(iii) The two spectra for each exposure time, at room temperature, cooled and gated mode were subtracted from each other to produce dark-dark spectra and give a measure of the reduction in noise.

Figure 4a, b & c shows the dark-dark spectra for the warm, cooled and gated photocathode for 4000 exposure units. The noise is reduced for the cooled photocathode compared to the warm.

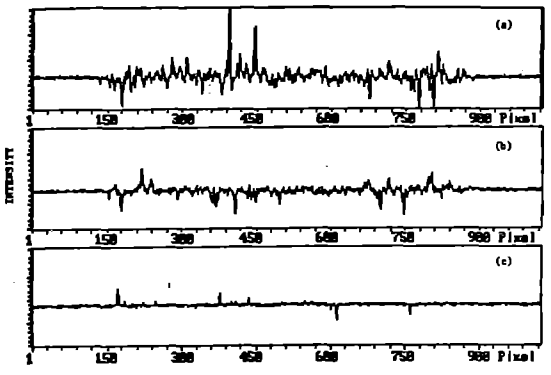


Figure 4: Noise from the detector head

(a) Room temperature photocathode
(b) Cooled photocathode
(c) gated photocathode.

CONCLUSION

The photocathode cooling is a worthwhile addition to the OSMA equipment, giving an increase in signal to noise of 4.8 as determined by both methods. This is an agreement with the theoretical value of a noise drop of $\sqrt{2}$ for each temperature drop of 6.7 K.

The noise is reduced to a little above the noise present in gated mode, when the photocathode is essentially switched off. Further, as background signal levels are reduced longer accumulation times are now possible before saturation occurs. This allows a lower number of detector readout operations which will also limit noise.

This will be very useful in future experiments, particularly in experiments using continuous wave excitation where the signal intensities are low and exposure times are long.

# A DISPERSION CORRRECTED HYBRID MODELOCKED SYNCHRONOUSLY PUMPED DYE LASER TO PRODUCE SUB-PICOSECOND PULSES

A J Langley and W Shaikh

Rutherford Appleton Laboratory

## INTRODUCTION

Synchronously pumped dye laser technology is now well established and many commercially built systems producing pulses of several picoseconds duration exist in hundreds of laser laboratories worldwide. The science driven need for reliable sub-picosecond lasers has led many laboratories to design and build from scratch their own short pulse lasers or to purchase one of the few commercially available systems. An inexpensive and attractively simple alternative is to modify an existing commercial picosecond laser to produce sub-picosecond pulses and this is the approach we took.

## HYBRID MODELOCKING EXPERIMENTS

The basic unmodified picosecond laser source comprised a Spectra-Physics 375B dye laser synchronously pumped by the 800 mW (532 nm) frequency doubled output of a Spectra-Physics series 3000 cw mode-locked Nd:YAG laser. With a broadband coated 30% output coupler and a Spectra-Physics 570B tuning wedge, the dye laser output was typically 100 mW at 600 nm with pulselengths of 3-4 ps. Pulse width measurements were made with a Femtochrome Research FR103 rapid scanning autocorrelator having a resolution of 50 fs.

Initial attempts to shorten the pulses from the dye laser involved adding the saturable absorber DQOCI (concentration $\sim 10^{-5}$ M) directly to the gain medium circulator containing a $\sim 2 \times 10^{-3}$ M solution of R6G in ethylene glycol. An autocorrelation functon FWHM of ca 500 fs was measured indicating deconvolved pulse lengths of 325 fs for sech$^2$ intensity profile pulses. The main disadvantages of this method were firstly a drastic reduction in the useful life-time of the gain dye from several months to $\sim$1 week and secondly, the inconvenience of optimising both dye concentrations in a single circulator.

Following success reported quite extensively elsewhere[1,2] with hybrid mode-locked laser systems, a second intra-cavity mirror fold round another jet for saturable absorber dye was installed near the output coupler end of the synchronously pumped dye laser. The sapphire nozzle used had a 6 x 0.3 mm aperture (Victor Kyburg AG) and was placed at the centre of the two broadband-coated 5 cm radius of curvature mirrors. An optimised concentration of $2 \times 10^{-4}$ M of the saturable absorber DQOCI in ethylene glycol with a R6G gain dye concentration of $2 \times 10^{-3}$ M resulted in substantially shorter satellite free pulses whilst maintaining reasonable output power (see table 1). The shortest pulses were produced between 600-605 nm and assuming sech$^2$ intensity profiles the pulse width at this wavelength was ca 200 fs.

Table 1

| Wavelength/nm | Autocorrelation function FWHM/fs | Output Power/mW (950 mW pump) |
|---|---|---|
| 570-585 | 720 | 70 |
| 590 | 1150 | 65 |
| 595 | 720 | 75 |
| 600-605 | 308 | 60 |

The pulses were further shortened by the introduction of an intra-cavity four-Brewster-angled-prism sequence (see fig 1). The effect of this was to introduce controllable negative group velocity dispersion (GVD) to compensate for pulse broadening caused by intra-cavity self-phase modulation. Careful adjustment of laser alignment

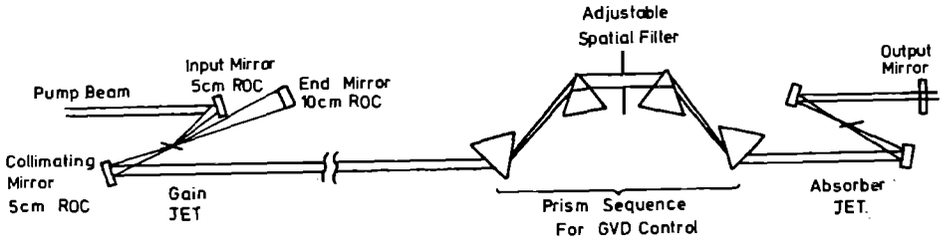


Figure 1: Schematic of the hybrid modelocked synchronously pumped dye laser with four-Brewster-angled-prism sequence for GVD control. The spatial filter between the prisms allowed wavelength and line-width adjustment.

and cavity length resulted in an autocorrelation function FWHM of c.a. 140 fs (at 600 nm) indicating pulse widths of 90 fs assuming sech² intensity profiles (see fig 2).

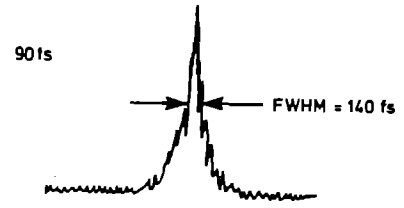


Figure 2: Autocorrelation function FWHM of 140 fs corresponding to 90 fs pulse width assuming a sech² intensity profile.

The short term pulse energy stability for the shortest pulses generated was c.a. ±10%. Less acceptable was the long term pulse stability with break-up of the pulses occuring after approximately 10 minutes observation of the autocorrelation trace. Good pulses could then be regained by simply re-adjusting the cavity length indicating that an active feedback mechanism would be advantageous. By simply not optimising the laser, excellent long term stability was achieved with slightly longer pulses (≥200 fs) that were quite acceptable for most of the range of experiments carried out at the LSF.

For these experiments the 1 nJ pulses from the synchronously pumped dye laser are amplified using a Quanta-Ray DCR3 injection seeded Nd:YAG pumped Quanta-Ray dye amplifier to ∿400 μJ/pulse. Slow scan autocorrelation measurements showed the pulse widths of the amplified pulses were essentially the same as for unamplified pulses. Fig 3 shows a

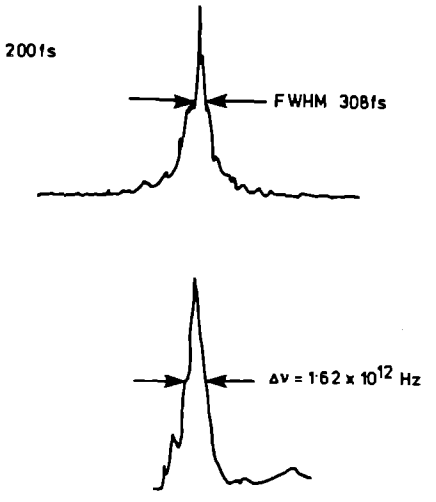


Figure 3: Autocorrelation function FWHM 308 fs corresponding to 200 fs pulse width together with a line width measurement of 1.6 x $10^{12}$ Hz FWHM.

pulse of duraton 200 fs together with a line width measurement. The time bandwidth product $\Delta t \Delta \upsilon$ was 0.324 indicating a sech² intensity profile[3]. (For sech² $\Delta t \, \Delta \upsilon = 0.3148$)[3].

REFERENCES

1. M D Dawson et al, Optics Communications, 60, (1,2) 79 (1986).

2. M Nakazawa et al, Optics Letters, 12, (9), 681, (1987).

3. S L Shapiro Ed, Ultra Short Light Pulses Topics in Applied Physics Vol 18, Springer-Verlag.

# PICOSECOND TIME-RESOLVED RESONANCE RAMAN SPECTROSCOPY
## A PROGRESS REPORT

S. Umapathy, E. Turcu[1], J.N. Moore, S.E.J. Bell and R.E. Hester

Department of Chemistry, University of York, York.
[1]Laser Division, Rutherford Appleton Laboratory, Chilton, Didcot.

This report is presented in three parts. The first part discusses the laser system and, in particular, the development of the copper vapour laser/dye laser amplifier system. This is followed by a discussion of the spectrometer/detector system. The final part details our future plans.

(I) Laser System:

The picosecond laser system involves the use of a cavity dumped dye laser (pumped by a mode-locked Nd:YAG), the output of which is amplified by a copper vapour laser. Although an amplification gain factor of *ca.* 5000 has been reported (1), at the end of last year we were only able to achieve a factor of *ca.* 3500. Further, the amplified picosecond pulse output energy was not stable for more than 10 minutes. Thus, our objective was to improve the gain factor and stability in order to obtain sufficient sustainable energy for efficient frequency doubling of the amplified pulses, as needed for pump-probe time-resolved Raman experiments. We have been successful in achieving these objectives by (a) improving the cavity dumper performance, (b) redesigning the five-pass amplifier configuration for minimum loss and (c) cooling of the dye by using an additional cooling unit along with the standard heat exchanger. These developments improved the stability of the amplified pulse and the gain factor achieved was *ca.* 5000.

(II) Spectrometer/detector system:

The design of the single grating spectrometer, collection optics and a charge coupled device (CCD) detector system has been described previously (2). This set-up has been used extensively in York and we give two further examples here, both relating to systems to be studied in ps-time-resolved resonance Raman spectroscopic experiments. (a) In Fig. 1, resonance Raman spectra of ruthenium(II) *tris*(bipyridine) are shown. The spectra are a two-dimensional representation of a cross-section of the sample excited for Raman scattering along the axis parallel to the spectrometer entrance slit. This figure illustrates the use of the CCD for two dimensional spectroscopy.

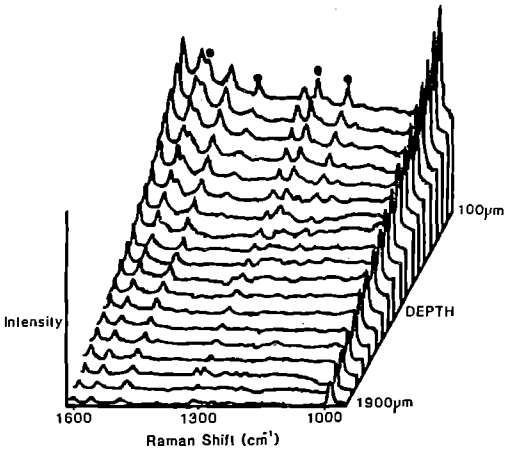


Fig. 1: Resonance Raman spectra of ruthenium(II)*tris*(bipyridine) - a depth profile (see text for details).

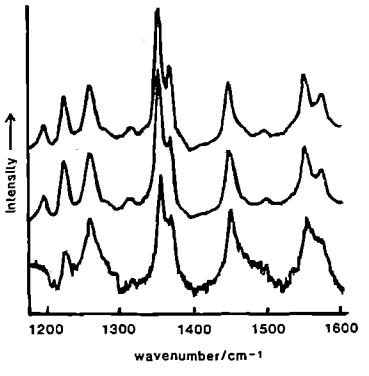


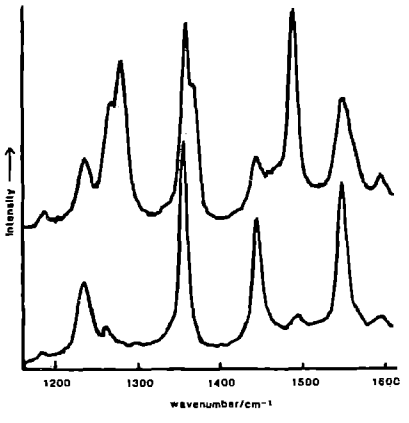


Fig. 2: Resonance Raman spectra of various substituted Fe(II) porphines under several pH conditions.

(b) In Fig. 2 the resonance Raman spectra of substituted Fe(III) porphines under several different pH conditions are shown. The quality of the spectra and the ease with which these spectra were obtained both demonstrate the excellent performance characteristics of this apparatus.

(III) Future plans:

In Fig. 3, the final lay-out of the whole picosecond Raman assembly is shown. All of the components have now been obtained and are assembled in this configuration. The development of the experimental system to the point where Raman spectra can begin to be recorded on the ps timescale requires (a) the reliable operation of the CVL to its specified power output (40 ± 2 W), (b) the achievement of frequency doubling and satisfactory operation of the optical delay line and (c) the installation of the spectrometer/detector system (on test in York) at RAL.

Acknowledgement:

We thank the staff at the central laser facility for their assistance and the SERC for financial assistance.

References

1. D.B. McDonald and C.D. Jonah, Rev. Sci. Instrum., 55 (1984) 1166.
2. I.C.E. Turcu *et al.*, Ruth. Appl. Lab. Ann. Report, RAL-89-045, (1989) 382.

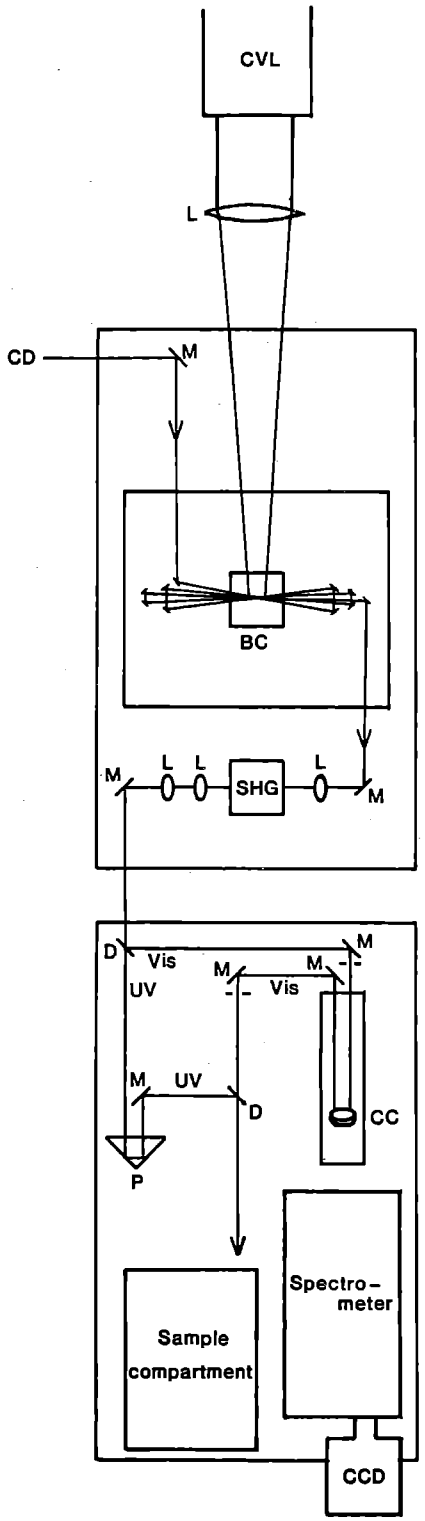


Fig. 3: Lay-out of the picosecond Raman experiment. CVL-copper vapour laser; L-Lens; CD-cavity dumper pulse; M-Mirror; BC-Bethune cell; SHG-second harmonic generation; D-diochroic mirror; VIS-visible laser pulse; UV-ultraviolet laser pulse; P-prism; CC-corner cube; CCD-charge coupled device.

# LASER SUPPORT FACILITY OPERATIONS AND DEVELOPMENT

The Laser Support Facility Panel (LSFP) received around 60 applications for experimental time on the LSF picosecond, nanosecond and loan pool equipment for the period May 1989 to May 1990. Approximately 90% of these experiments were approved by the LSFP and some 90% of approved experiments were scheduled for time. A total of 55 experiments were carried out including those approved for Division Head's or unallocated time. Table 1 shows the distribution of applications and experiments by subject and as in previous years the majority of work was carried out in chemistry related areas.

Table 1

| | Chemistry | Physics | Biology | Total |
|---|---|---|---|---|
| Applications | 59% | 18% | 23% | 60 |
| Experiments | 62% | 22% | 16% | 55 |

Two new members of staff were appointed during the year to bring the total direct scientific staff in the LSF to seven, following the recommendations of the Challis Review Panel.

PICOSECOND OPERATIONS - A J Langley and W Shaikh

During the past year a total of 11 experiments each up to four weeks in duration were carried out using the picosecond laser system. These ranged widely from pump and probe transient absorption studies of photosynthesis, organic dyes and photochromic materials through multiphoton ionisation (MPI) experiments to time resolved LIF measurements.

There were two periods of facility development in which the picosecond synchronously pumped dye laser was modified to a hybrid mode-locked system giving sub-picosecond pulses. (See the report by A J Langley and W Shaikh). The main motivation for this development work came from the multi-photon ionisation experiments but in fact a shorter pulse capability has already proved generally advantageous to experiments notably those employing pump and probe techniques. Not only have shorter pulses increased the time resolution of the transient absorption experiments to ~500 fs but they have also improved the generation of probe light by non-linear techniques. Several new stimulated Raman bands have been utilised recently as has super continuum light to the short wavelength side of the exciting pump light.

Several new lasers have been purchased to upgrade the picosecond system. This will increase the range of short pulse techniques available to the community. In addition to the currently available amplified (~500 μJ) pulses at 10 Hz repetition rate, we shall offer amplified pulses (~10 μJ) at the medium repetition rate of 6 KHz for $TR^3$ or pump/probe experiments and cavity dumped picosecond pulses at ≤4 MHz for time-correlated single-photon counting measurements. Also feasible, in principle, are high repetition (82 MHz) experiments for high sensitivity pump/probe experiments in, for example, Inverse Raman spectroscopy. At any particular time, only one of these systems will be formally scheduled but off-line development time on the other systems will be available to users and RAL staff at lower priority.
The lasers bought and now installed to achieve this upgrade are a Spectron cw mode-locked YAG capable of pumping four dye laser simultaneously, and two Spectra-Physics Model 3290 cavity dumpers.

NANOSECOND OPERATIONS - A W Parker and G J H Simpson

The statistics for nanosecond laser usage are as follows: 81 weeks of laser time were allocated during 1989, incorporating 29 experimental runs. Six of these runs introduced new research groups to the facility. We have been notified of 17 publications/posters resulting from this work.

Experiments have covered a broad range of science including the use of lasers to generate X-rays, laser annealing of metal surfaces, laser induced fluorescence and both resonance Raman and time resolved resonance Raman spectroscopy.

New equipment: The EMG-150 has been replaced with two Questek 2440 fluoride excimer lasers (up to 600 mJ, 100 Hz, KrF). One of the main uses of these lasers will be to generate soft X-rays.

A second Lumonics HE460 and FL2002 dye laser has been installed. For two laser experiments (eg pump/probe, $TR^3$, etc) the double excimer/dye laser set-up within one laboratory allows efficient and full wavelength tuning of both lasers. The ultraviolet region (205-320 nm) is covered by both lasers using β-barium borate frequency doubling. Pump/probe experiments can now be performed at repetition rates of up to 150 Hz, though with the present dye circulators UV efficiency falls off above 30 Hz.

The OSMA multichannel diode array detector has been modified to incorporate photocathode cooling (see report by Simpson and Parker). The OSMA software has also been upgraded to be IBM-PC compatible. This will make analysis of data easier for users who view their results at leisure back at their own institutions.

LOAN POOL OPERATIONS - M Towrie and S M Tavender

In the 1989-'90 period there has been a total of 21 loans. As in previous years the majority were to chemistry users whilst there were 4 loans to physics users and 1 to a biology user.

The Spectron Nd:YAG pumped dye system acquired in 1988 has been a reliable and valuable addition to the loan pool and has to date been used in three successful loans.

The gas lifetime of the fluoride excimer laser was considerably extended by the addition of a purifier, but the laser remains unpopular due to its expensive Neon gas fill and its poor output power on the ArF line. The laser will be returned to the manufacturers for conversion to Helium buffer operation.

The LSF has recently acquired a CW Argon Ion pumped titanium sapphire laser, tunable between 680-1010 nm with 40GHz (200MHz etalon narrowed) bandwidth. This system was bought primarily as a move into state of the art tunable solid state technology. The laser will become part of the loan pool in mid-late 1990, following assessment and development work at RAL.

A 15 Watt air cooled copper vapour laser has been purchased by the Engineering Board for the Laser Loan Pool for use in engineering applications such as flow visualisation and fast photographic techniques. The laser was made available for loan in early April. When not required by Engineering Board funded applicants it will be available to Science Board users.

# REAL TIME ORTHOSCOPIC IMAGE PROJECTION USING PHASE CONJUGATE MIRRORS

N A Vainos and M C Gower
Rutherford Appleton Laboratory

## INTRODUCTION

With the exception of self-pumped and resonator type phase conjugate mirrors (PCM's) which use photorefractive (PR) materials, typical four wave mixing (FWM) schemes for producing PCM's are based on external plane pump waves [1]. While collimated beams may approximate the appropriate FWM boundary conditions, for accurate phase conjugate (PC) generation mutually PC pump waves must be used, otherwise the finite curvature of the beams and their critical alignment over large interaction regions usually lead to phase mismatches and diffraction efficiency variations which limit the fidelity of the generated PC field.
For high fidelity wavefront reconstruction, the self-generated mutually conjugate pumps in a self-pumped $BaTiO_3$crystal (SPPCM) [2], 'cat' mirror, for example, provide the ideal conditions. By using an SPPCM $BaTiO_3$ crystal it has been demonstrated that a $BaTiO_3$ can operate as a wide angle conjugator for a second input beam [3]. Extending this scheme, we have demonstrated a more advanced system which relies on feedback of the PC generated by a $BaTiO_3$ SPPCM into the same crystal interaction region. This secondary input is the PC of the primary input, and a second 'feedback' PC field is produced which is the double phase conjugate of the first.

In this work we perform a comparative study of the above Hi-Fi 'external' and 'feedback' PCMs. In addition, we illustrate an application of this 'feedback' double conjugator by demonstrating for the first time to our knowledge, real-time, real,orthoscopic, 3-dimensional image projection.

## A COMPARISON of Hi-Fi $BaTiO_3$PCMs: SUMMARY

To investigate the differences between the Hi-Fi PCMs produced in $BaTiO_3$ with the SPPCM [2] 'cat' mirror, the 'external' wide angle PCM [3] and the feedback double PCM presented here, we have carried out a comparative experimental study.

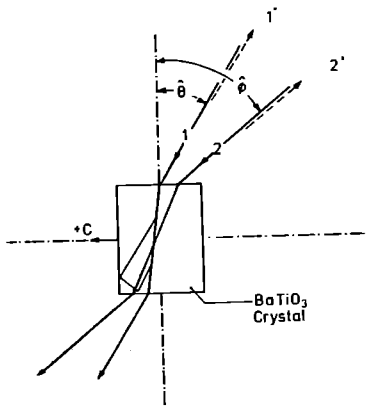


Fig 1. Schematic outline of the experimental geometry used.

As shown in Fig 1, in the typical self-pumping 'cat' mirror arrangement an unexpanded laser beam 1 (∿ 300mW/cm² uncorrected for Fresnel losses) was input into the crystal at an angle θ to the crystal normal (all angles are given in air). The PC beam, 1*, with intensity I1 , was generated by self-pumping. Beam 1 and 1* are a mutually conjugate pair of beams (1, 1*). In the present experiments we have used a signal beam 2 which was either externally supplied or was a part of 1* fed back to the crystal interaction region. In both cases th PC beam 2* was produced by FWM of beam 2 and the pair (1,1*). While low reflectivities of ∿25% were obtained for an external beam 2, the feedback signal was found to exhibit reflectivities as high as 80%. The feedback system also exhibits a much wider field of view and an extremely high output intensity stability. These latter facts are attributed to the high coupling in the crystal owing to the constant phase relationship between the interacting beams. The feedback mechanism also appears to compensate for phase instabilities in the feedback loop. Unlike PC resonators no frequency shifts have been observed here.

Finally, we may regard the feedback Hi-Fi PCM as a single device in which any phase variation in the primary input beam does not affect the output intensity. An extremely stable set of gratings is formed in the crystal and high couplings and PC reflectivities are achieved. According to our experimental results the device characteristics are similar to those of the 'cat' mirror SPPCM, the significant difference of this 'feedback' double PCM being its capability of projecting images orthoscopically. The device can be regarded as a high fidelity repeater based upon phase conjugation.

## DYNAMIC ORTHOSCOPIC IMAGE PROJECTION

When dynamic holographic recording media are used, phase conjugate images are produced in degenerate four wave mixing geometries. However, phase conjugate reconstruction produces real pseudoscopic images (perspective inversion), which is clearly inappropriate for the projection of 3-dimensional (3-D) object scenes. On the other hand, two-wave mixing configurations can produce in forward reconstruction orthoscopic but virtual replicas of the scenes recorded [4]. Furthermore, forward reconstruction lacks the significant abberation correction properties which PC reconstruction by four-wave mixing can provide in real time.

We report here the real time production of real orthoscopic images. To achieve this we use image feedback and double phase conjugation in a $BaTiO_3$ PR crystal.

Figure 2 shows a schematic of the experimental arrangement used. The input

beam 1 is x 20 expanded and diffused by a ground glass plate. After passing through a 3-D transmissive object (parts of a test chart positioned apart) and a large beamsplitter cube (R:T = 1:1), the beam is focused into the $BaTiO_3$ crystal by using a 100 mm focal length F/2 lens, L1. The crystal produces a phase conjugate (pseudoscopic) image by self-pumping, the PC replica 1* of the object being simultaneously fed back into the $BaTiO_3$ as shown. Beamsplitter BS2 is an AR coated flat window glass plate. Lens L2 (f=100 mm; F/2) produces the diffuse Fourier transform (FT) of 1* in the crystal. We have also used non-diffuse illumination of the object although with less visually satisfactory results.

By utilising the mutally PC fields (1, 1*) self-generated in the crystal by self pumping and a part of 1*, a second FWM process is performed. The final field 2* is the real orthoscopic image of the object which can be viewed directly by looking with the unaided eye through BS2. Fig 2 depicts a typical result of this projection operation. In Fig 3(a) the real pseudoscopic image as photographed at camera position A, by using two mirrors not shown in Fig 2 to redirect 1*. Photographs were taken at two focus planes, 'Front and 'Rear', of the camera used to take the photograph. In Fig 3(b) the orthoscopic image photographed at camera position B is shown. We note that the correct perspective of the object is restored in the orthoscopic image in Fig 3(b).

In the present configuration 1* appears with a reflectivity of about 20%, and $R_3^{(FB)}$ was at a low level (~1-3%) since for experimental convenience unfavourable angles were used. Nevertheless, the 4% reflected part of 2* was very bright for a human observer.

We have also performed image projection by using reflective diffusely illuminated more realistic 3-D objects such as coins and other metal or porcelain items.

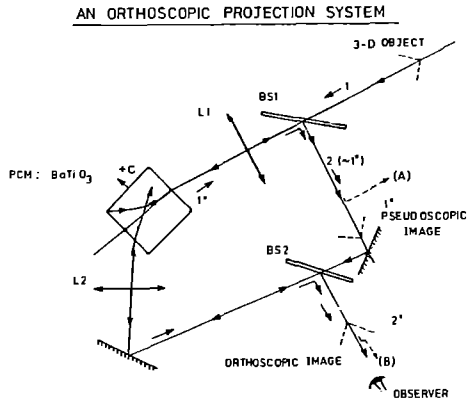


Fig 2. Schematic of the experimental arrangement used to demonstrate orthoscopic image projection in $BaTiO_3$.

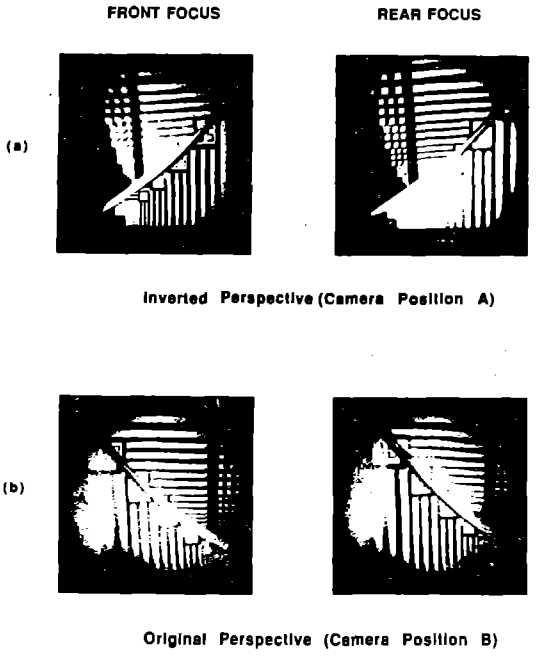


Fig 3. Phase conjugates of images obtained from the system at two camera focus planes. (a) inverted perspective; (b) original perspect.

CONCLUSIONS

To achieve high-fidelity phase conjugate reconstruction of object waves the conjugator must be pumped by a mutually conjugate pair of pump waves. In this work the phase conjugate of the original input is fed back into the SPPCM crystal. A High Fidelity double phase conjugation operation on the original wavefront is thus performed. We have compared this operation to other high fidelity conjugators and shown that it can exhibit very high stable reflectivities and a wider field of view.

We have demonstrated that this 'feedback' Hi-Fi conjugator can be used to project 3-D images in real time preserving the original perspective of the object scene.

REFERENCES

[1] P. Gunter and J.-P. Huignard, in 'Photorefractive Materials and their Applications I', P. Gunter and J.-P. Huignard (eds), Springer-Verlag, Berlin-Heidelberg (1988).

[2] J. Feinberg, Opt. Lett., 7, 486 (1982).

[3] J. Feinberg, Opt. Lett., 8, 480 (1983).

[4] R.J. Collier, C.B. Burckardt, and L.H. Lin, 'Optical Holography', Academic Press, New York (1971).

# HIGH FIDELITY IMAGE AMPLIFICATION AND PHASE CONJUGATION IN $Bi_{12}SiO_{20}$ CRYSTALS

N Vainos and M C Gower
Rutherford Appleton Laboratory

## INTRODUCTION

The potential of photorefractive (PR) materials in real-time holographic applications is now well proven. However, the system performance as far as output image fidelity is concerned has hindered the development of useful devices.

PR crystals with the fastest response times currently used in the visible spectral region are members of the sillenite family: $Bi_{20}$[Si, Ge, Ti] $O_{20}$ [1]. Despite the relatively low electrooptic coefficients of these materials when compared to ferrolectric photorefractives, nonstationary grating recording techniques to enhance coupling constants and achieve high gains and phase conjugate (PC) reflectivities are now well established. These schemes employ either (non-DFWM) under the application of high DC electric fields [2] or DFWM with grating recording under the application of high AC electric fields [3]. Both methods result in the enhancement of the space charge field and provide the necessary $\frac{\pi}{2}$ shift of the grating with respect to the light intensity interference pattern to achieve high diffraction efficiencies and couplings. However, the resonance character of the process severely restricts the useful spatial frequency bandwidth around a low optimum carrier grating frequency [4]. Hence, the space-bandwidth product as well as the field of view of the amplified and/or conjugate image are severely restricted.

In this work we are concerned with image fidelity of B[S,G,T]O amplifiers and conjugators under nonstationary grating recording conditions. We present for the first time to our knowledge techniques which greatly reduce some of the problems discussed above.

## Hi-Fi IMAGE AMPLIFIERS

Moving grating resonant recording in BSO has been intensively investigated [4]. Two beam coupling of energy between beams is produced by the imaginary part of the space charge field where a high DC field is applied to the crystal.

Under resonant recording, the grating spatial frequency (K) dependence of the gain

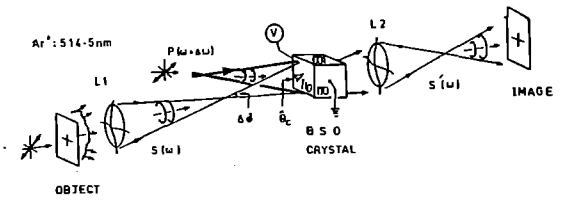


Fig 1. Schematic of the experimental arrangement used to demonstrate high fidelity image amplification.

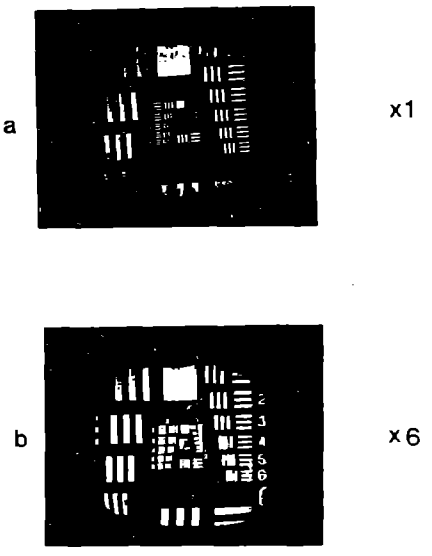


Fig 2. (a) Original image input in the amplifier. (b) x6 amplified output image.

coefficient ($\Gamma$) for a high electric field ($E_o$) and optimum fringe velocity is: a highly nonlinear function of complex Lorenzian-type centered at $K_{max} = (r_E \ell_E)^{-1/2}$ where $r_E$ the electron drift length and $\ell_E$ tightening length depend on the material and applied field. The FWHM bandwidth of the gain is $\Delta K_{1/2} \sim 2\sqrt{3}K_{max}$ which decreases inversely with increasing field implying that the higher the amplification the smaller the operating bandwidth.

In the simplest amplifier, two plane waves a signal S and pump P with wavevectors $k_i$ and $k_j^p$ respectively are mixed. In the useful linear (saturation) regime when $I_p >> I_s$ the gain will be given by

$$G(k_i, k_i^p) \approx \exp [\Gamma(k_i - k_j^p)\ell] \qquad (1)$$

where $\ell$ is the interaction length.

When arbitrary wavefronts S and P are used they may be regarded as compositions of elementary wavefronts

$$S \sim \int s(k_i)dk_i ; \; P \sim \int p(k_j^p)dk_j^p \qquad (2)$$

where the integrations are performed over the angular fields of signal and pump.

The amplified wavefront S' will be given by

$$S' \sim \iint G(k_i, k_j^p)\, s(k_i)dk_i dk_j^p \qquad (3)$$

For a plane pump wave eq. (3) reduces to

$$S' \sim \int G(k_i)\, s(k_i)\, dk_i \qquad (4)$$

and therefore S' is severely limited by the restricted gain $G(k_i)$. The additional degree of freedom provided by eq (3) for non-plane waves can optimise the operation since it can enable the assignment of a set of elementary pump wavefronts each optimally configured to amplify a specific band of the signal field. For the experiments reported here a diverging (Gaussian) pump beam was used. The ideal choice of pump beam would have $p(k_j^P)$ = constant for all $k_j^P$ in eq. (2).

The above principle is experimentally demonstrated by the system outlined in Figure 1. An argon ion laser operating in a single longitudinal mode at $\lambda$ = 514.5 nm and a single $BSO_3$ crystal were used. The laser beam was x10 expanded, filtered and split to provide object (signal) S and pump, P, fields. Both S and P were nominally polarised at 45° with respect to the (001) (horizontal) plane. A piezoelectrically driven mirror was used to frequency shift the pump beam P. A 4 kV DC voltage was applied to the crystal along the [110] direction. Lens L1 (f = 60 mm, F/1.2) was used to relay the object into the crystal. An identical lens (not shown) was used to provide a diverging pump beam. The pump and signal beam divergences, $\Delta\phi$, were both $\sim$ 20° and the central Bragg angle was $\theta_c \sim 1.5°$. Lens L2 (f = 50 mm, F/2) imaged the output onto the camera with a $\sim$ x3 magnification. Several pump beam intensities have been used and in each case a single optimum frequency detuning has been seen to provide the desired flat frequency response of the amplifier over all the available image field. Pump to signal beam intensity ratios were kept high at $\sim$2000:1, and signal beam intensities as low as 60μW/cm² were amplified with high fidelity.

Figure 2 shows a representative result using this setup. In Fig 2(a) the original image in Figure 2(b) the x6 amplified image (as measured with a power meter) is shown. The apparent resolution here is about 60lp/mm and densitometric measurements have verified the flat response of the system amplification over the total spatial bandwidth up to this limit. The resolution is only limited by the numerical aperture of the optical system and the recording film. The amplified beam divergence of $\sim$20° was the same as the input.

## Hi-Fi PHASE CONJUGATOR

Using diverging frequency shifted mutually conjugate pump beams in the setup shown in Fig 3 we have also demonstrated high fidelity phase conjugation by non-DFWM in BSO. A poled single-domain $BaTiO_3$ crystal was used to provide by self-pumping a phase conjugate pair of pump beams [5] for the mixing in BSO.

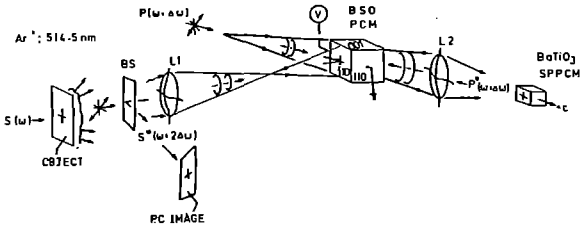


Fig 3. Schematic of the high fidelity phase conjugation system.

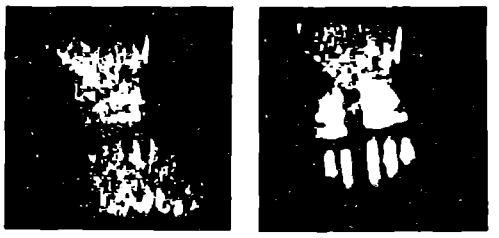

a b

Fig 4. Phase conjugate images observed under (a) 'off-resonance', and (b) 'on-resonance', conditions.

A $\lambda/2$-plate (not shown) used to provide the extraordinary polarisation required for self pumping in $BaTiO_3$. The PC replica of the pump, P*, was found to have the same frequency shift as P while the FWM generated PC beam, S*, had twice the shift as expected for phase matching. Since only 4 kV DC voltage was applied to the crystal relatively low PC reflectivities of $\sim$ 40% were obtained (reflectivities up to 250% have been obtained using higher voltages [6]).

Figure 4 shows first results of these experiments. In Fig 4(a) no PC is observed when the BSO conjugator is 'off-resonance' i.e. when the frequency shift of the pump is different from the optimum required while in Fig 4(b) a very bright PC replica is obtained 'on-resonance'.

Instabilities at high couplings in BSO may affect the self pumping. However the different response times of BSO and $BaTiO_3$ are beneficial since, even at high couplings, the higher inertia of $BaTiO_3$ compensates to preserve self-pumping. In contrast, a highly unstable phase conjugator was produced when the BSO crystal was replaced by another $BaTiO_3$crystal.

## CONCLUSIONS

We have demonstrated high fidelity image amplification and phase conjugation in a BSO crystal by using diverging pump beams and nonstationary grating recording. The wide angle, large space-bandwidth-product and flat frequency response operation of the present schemes may open up new ways for the development of real-time photorefractive systems for use in large scene holographic projection, information processing, and microscopy.

## REFERENCES


[1] P. Gunter and J.-P. Huignard in 'Photorefractive Materials and their Applications I', P. Gunter and J.-P. Huignard (eds), Springer-Verlag Berlin Heidelberg (1988).

[2] J.-P. Huignard and A. Marrakchi, Opt. Commun., 38, 249 (1981).

[3] S.I. Stepanov and M.P. Petrov, Sov. Tech. Phys. Lett., 10, 572 (1984).

[4] Ph. Refregier, L. Solymar, H. Rajbenbach, and J.-P. Huiguard, J. Appl. Phys., 58, 45 (1985).

[5] J. Feinberg, Opt. Lett., 7, 486 (1982).

[6] H. Rajbenbach, J.-P. Huignard and Ph. Refregier, Opt. Lett., 9, 558 (1984).

# EXCIMER LASER SPUTTERING OF PHOTOREFRACTIVE WAVEGUIDES OF BSO/BGO.

K. Youden[1], R.W. Eason[1] and M.C. Gower[2]

[1]Optoelectronics Research Centre, Southampton University
[2]Rutherford Appleton Laboratory.

## INTRODUCTION

Photorefractive materials, such as bismuth silicon oxide ($Bi_{12}SiO_{20}$) and bismuth germanium oxide ($Bi_{12}GeO_{20}$), have been extensively used as real - time media for a range of experiments in optical phase conjugation and real - time holography via two and four wave mixing techniques. So far, studies have almost exclusively used small, bulk, single crystal samples. Howerver, thin films of these materials are an attractive alternative because the guided wave intensity can be very high, thus producing a response time that is correspondingly faster. For example, the response time of $Bi_{12}(Si,Ge)O_{20}$ is around 5 ms at an incident irradiance of 1 W/cm$^2$, whereas, in a crystal guide of dimensions 1 cm by 1 $\mu$m, the response time would be reduced to $\approx$500 ns.

A variety of methods of thin film fabrication have already been employed, such as, RF sputtering, flash evaporation, in - diffusion out - diffusion and ion implantation[1]. however, the films are often of incorrect or variable composition or phase, and are rarely optically perfect, single crystalline waveguides. Excimer laser ablation provides a simple and convenient method for depositing films which allows the stoichiometry of the target material to be easily reproduced. We report here, the progress to date on the deposition of waveguides by excimer laser ablation of the photorefractive materials $Bi_{12}SiO_{20}$ (BSO) and $Bi_{12}GeO_{20}$ (BGO).

## THIN FILM DEPOSITION

The experimental arrangement is shown in figure 1. The BGO target was a 3 mm thick, 1 cm diameter sintered powder pellet, whereas, for the BSO film it was a 3x3x5 mm piece of crystal. The target pellets were prepared from powder by adding a few drops of distilled water, then compressing them under $10^4$ kg/cm$^2$ of pressure. A fused silica tube furnace was used to sinter the pellets by gradually heating them to 800°C then after two hours gradually cooling them. Oxygen was passed through the furnace throughout the ten hour heating and cooling cycle to help maintain the oxygen content of the pellets.

The target material was held on a motor driven holder capable of eccentric rotation at $\approx$7 rpm. This ensured the uniform ablation of the surface. The BSO crystal was not rotated because of its awkward shape. Instead, its position was altered manually every five minutes.

To ablate the material, a Lambda-Physik EMG 201 MSC XeCl Excimer laser operating at $\lambda$=308 nm and 20 pps was used. It was focussed using a lens of 35 cm focal length to a flux of 5.7 J/cm$^2$, incident at an angle of 45° onto the target.

Zirconia ($ZrO_2$) was chosen as the substrate for both the BSO and BGO films because its lattice parameter (5.07 Å) is half that of BSO (10.104 Å) and BGO (10.145 Å) so facilitating epitaxial growth. It

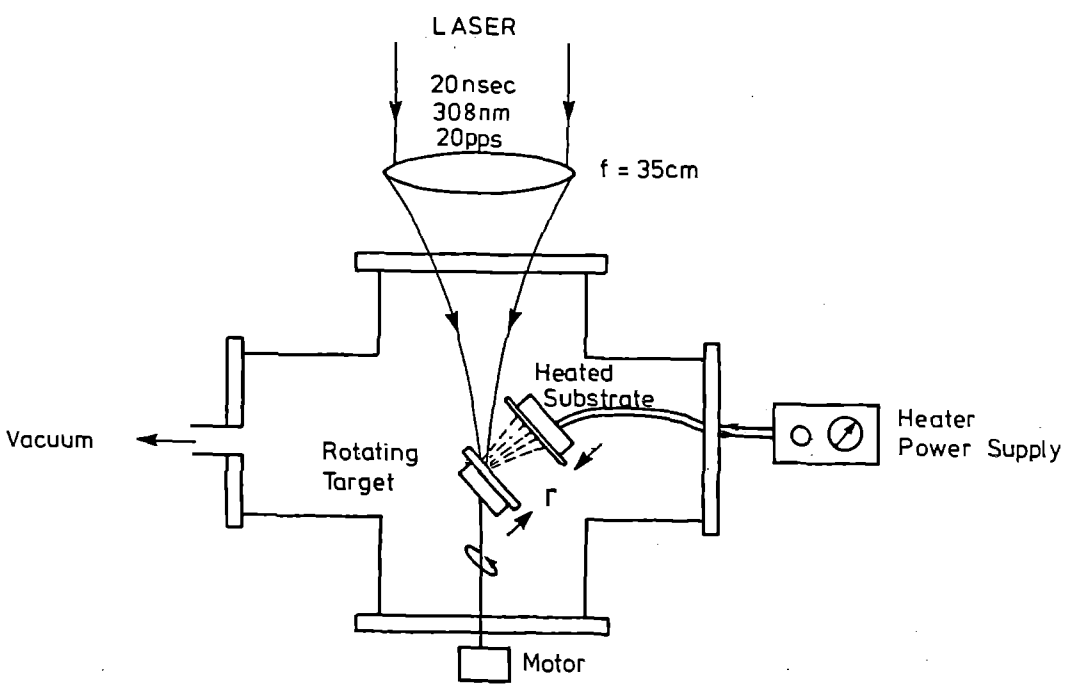


Figure 1: Experimental Arrangement for Thin Film Deposition.

also has a comparable thermal expansivity, is adhesive to and unreactive with the films. The substrate must also have suitable optical properties, and zirconia satisfies the condition for a waveguide, that the refractive index of the substrate (2.20) is lower than that of the film (2.54).

The 10 x 10 x 0.5 mm substrate was clipped onto the heater assembly and positioned parallel to the target plane at a distance of 5 cm. Using a filament heater, the temperature was increased to between 500°C and 550°C and monitored using a standard thermocouple. The substrate and target were contained in a pyrex chamber which was evacuated to a pressure of $\leq 1 \times 10^{-3}$ mbar. The target was ablated for 45 minutes (5400 pulses) to deposit a film approximately 0.5 μm onto the substrate.

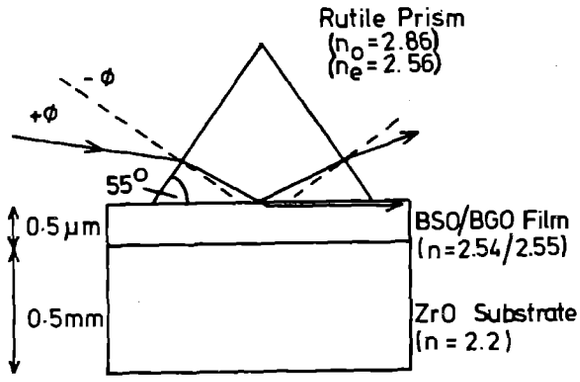


Figure 2: Arrangement for prism coupling light into a waveguide.

## STRUCTURAL ANALYSIS

The crystal structure of the films was determined using an X-ray Texture Camera ( at R.M.C.S., X-ray Unit, Shrivenham ). These showed that the films were polycrystalline with some epitaxial growth of [110] orientation. X-ray Diffractometer Measurements were used to investigate the composition of the films. The peaks obtained corresponded reasonably well with BSO and BGO respectively. Rutherford Backscattering was used to analyse the phase of the material. No information was available on the Si, Ge or O content of the film but the Bi peak had an inclined crest indicating that the Bi ratio might vary as a function of film thickness (there might be more Bi nearer the substrate).

The global thickness and surface quality of the film was measured using an Alphastep. The films were found to be fairly smooth and level. The thickness was 0.5 μm at the centre and 0.2 to 0.3 μm at the edges. The films were also examined under an interference microscope and the results were in good agreement with those of the Alphastep. A Nomarsky microscope was used to observe the film quality. No surface texture could be seen apart from a few pinholes in the film. These were probably caused by tiny dust particles on the substrate and could be minimised by using clean room conditions.

## WAVEGUIDING PROPERTIES

To investigate the waveguiding properties of the thin films, a 55° 'rooftop' rutile prism was used to couple light into the film from a He-Ne laser at $\lambda$=633 nm (See Figure 2). Two film modes are predicted[2] with effective indices and angles ($\phi$) of incidence out of the prism as given in Table 1.

Modes were observed at angles of 2.15° ($TE_0$) and 28.85° ($TM_0$) which are in good agreement with the theory. The mode lines were fairly narrow and experienced a large amount of scatter which was apparent from the length of the lines observed, and indicative of high loss. Measurement of the loss was not possible because the modes were only guided over a few mm due to the polycrystalline nature of the film.

Modes guided in the substrate were observed at angles ($\phi$) in the range +27° to -30°, corresponding to effective indices between 2.2 and 1.5. These mode lines were fairly broad and suffered little scatter because of the comparative thickness and single crystal nature of the substrate.

Table 1: Details of predicted and observed modes guided in the films.

| Mode | $TE_0$ | $TM_0$ |
|---|---|---|
| Effective Index | 2.396 | 2.374 |
| Predicted Angle, $\phi$ | 2.88° | 29.50° |
| Observed Angle, $\phi$ | 2.15° | 28.85° |

## CONCLUSION

It has been shown that waveguides of the photorefractive materials BSO and BGO can be deposited on $ZrO_2$ substrates by excimer laser ablation. The films are polycrystalline with some epitaxial growth and match the stoichiometry of the target materials. Two guided modes have been observed so far in agreement with the theory but to date these suffer fairly high losses due to scattering from the polycrystalline components of the film. Work is in progress at present to routinely deposit high quality singly crystal epitaxial thin films of these materials, with the aim of improving their waveguiding properties.

## REFERENCES

1. G.M. Davis and M.C. Gower. Appl. Phys. Lett. 55(2), 112 (1989) and references therein.
2. J.Wilkinson, Private Communication.

# MULTIPLEXED PERMANENT AND REAL TIME HOLOGRAMS IN $Bi_{12}SiO_{20}$

S L Clapham[1], R W Eason[1] and N A Vainos[2]
[1]University of Southampton
[2]Rutherford Appleton Laboratory

## INTRODUCTION

Bismuth silicon oxide (BSO) is a widely used photorefractive (PR) crystal with numerous applications in the fields of optical phase conjugation, real time holography, and optical information processing[1]. While most of the interest in BSO and other photorefractives stems from its real time recording characteristics, there are also areas where permanent or controlled semi-permanent storage is also required. There are, however to our knowledge no reports of fixing processes or techniques for permanent storage that are not only very simple but also allow the simultaneous storage of permanent and real time holograms within the same crystal volume.

We report here a scheme[2] that allows normal photorefractive real time behaviour in addition to a permanent recording mechanism which is attributable to photochromic behaviour. This photochromic recording has not been investigated before, although holograms have been successfully recorded in other photochromic materials in the past. We present here the characteristics of photochromic hologram formation in BSO including certain dynamic processes observed, such as the variation of the diffraction efficiency of the permanent hologram on its illumination by additional beams and/or on the application of electric fields.

The multiplexing of permanent and real time photorefractive gratings in the same crystal volume has been used here to demonstrate novel applications[3] ranging from image synthesis to holographic interferometry. These operations are mostly based on the inherently separate nature of these gratings, which allows the imposition of relative phase shifts between the simultaneously scattered fields by optically shifting the real time grating with respect to the permanent one. Furthermore, the diffraction efficiency enhancement effect observed has been used for the demonstration of all-optical switching and spatial light modulation[4].

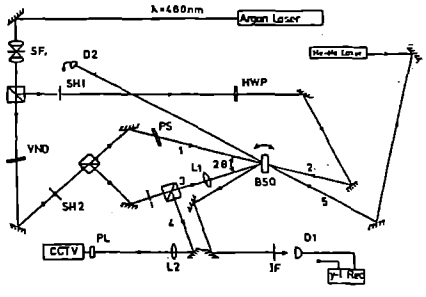


Fig 1. Schematic of the experimental arrangement used.

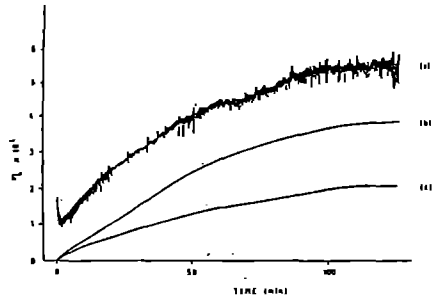

Figure 2. Recorded diffraction efficiency of (a) the combined permanent and real time (PR) holograms $\eta_T$ (b) the permanent hologram in the presence of one of the writing beams $\eta_{pc}$ and (c) the permanent hologram only $\eta_{pc}$ as function of exposure time.

## FUNDAMENTAL STUDIES

Figure 1 shows the experimental arrangement used to investigate the characteristics of permanent holograms. In this typical write-read configuration, beams 1 and 3 record the hologram in the crystal and readout is performed by beam 2. The photorefractive (real time) and photochromic (permanent) holograms were written using an argon-ion laser operating in multilogitudinal mode at $\lambda$=488 nm and at typical intensities or beams 1 and 3 of $I_1=I_3=1.4$ Wcm$^{-2}$. The angle 2$\theta$ between writing beams 1 and 3 was varied between 2° and 30° for the different holograms recorded. Readout was performed by using a He-Ne laser at 633 nm (=5 mW), which was incident on the BSO at the angle for maximum Bragg scattering efficiency. Diffracted beam 4 was monitored by a power meter D1 filtered by a 633 nm interference filter (IF) to minimise the effects of stray light. The output of D1, the combined diffraction efficiency $\eta_T$ of the permanent and real time holograms, was monitored by using a y-t chart recorder. Shutters $SH_1$, $SH_2$ were used for recording $\eta_{pc}$ and $\eta_{pc}$ of the permanent hologram alone and in the presence of one of the writing beams respectively.

Figure 2 shows typical traces of diffraction efficiency $\eta$ (uncorrected for losses) as a function of time recorded on the y-t chart recorder. Curve (a) shows the development of both the real time and permanent holograms $\eta_T$, which are spatially multiplexed in the same crystal volume. The Bragg angle was $\theta$ = 1.25° in this case. The unexpected effect here is the increase of the diffraction efficiency $\eta_{pc}$ on illumination of the recording region by an additional beam. To investigate this behaviour, we monitored the diffraction efficiency $\eta_{pc}$ with only one writing beam present by using shutter SH2 (curve b). A much higher diffraction efficiency is observed in this case.

A possible explanation of this effect is the presence of parasitic PR gratings associated with the photochromic ones. These gratings are activated by the 488 nm enhancement beams. The fields scattered simultaneously interfere to produce the observed behaviour. Furthermore the apparent diffraction efficiency $\eta_{pc}$ can be controlled by the externally applied enhancement beam (488nm) and DC electric fields. A x 6 enhancement effect has been observed so far (depending on crystal nature and orientation), with typical intensity dependent response times in the millisecond time scale.

## APPLICATIONS

The arrangement of Fig 1 can be modified so that PC reconstruction is performed by a readout beam at 488nm. By using a lens in beam 3 a permanent hologram can be recorded with an image placed (or not) at position Q (Fig 1). The reconstructed PC may be expressed as $E_p(x,y)=|A_p(x,y)|\exp[i\phi_p(x,y)]$. Fig 3 shows an image reconstructed by a permanent hologram with ∿25μm resolution. Using exactly the same recording arrangement, a real time grating can be recorded in the very same crystal volume with the same or a different image placed at Q, since the usual PR behaviour is unaffected. The reconstructed real time PC will have exactly the same curvature but will generally be of the form $E_{rt}(x,y) = |A_{rt}(x,y)|\exp[i\phi_{rt}(x,y)]$. The significant feature of the present scheme is that the readout beam 2 is simultaneously scattered off two distinct gratings, having identical carrier grating wavevectors, with comparable diffraction efficiencies. The interference of these two waves will lead to an intensity pattern:

$$I_{out} \sim |A_p|^2 + |A_{rt}|^2 + 2|A_p||A_{rt}| \cos(\phi_p - \phi_{rt}) \quad (1)$$

which is detected by a TV camera. Furthermore, the PR grating can be shifted in real time with respect to the permanent one, for example, optically, by externally imposing phase shifts on one of the writing beams. This additional phase shift will determine the specific interference characteristics of the scattered fields observed at the output plane.

When a different object (other than the one used for permanent hologram recording) is used subsequently for real time recording image synthesis and logic operations (addition, subtraction, differentiation) have been achieved by controlling optically the relative phase between the multiplexed gratings.

Fig 3 PC Image reconstructed by a permanent hologram.

The present system can also be considered as a novel scheme for real time holographic interferometry and phase object detection. The permanent hologram of an object can be stored in the BSO and a real time hologram of the same scene can be simultaneously multiplexed in the same crystal volume. Any real time deformations of the object will be detected interferometrically at the output, providing that they occur over time scales slower than the crystal PR response time.

The fast diffraction efficiency effect has also been used for all optical switching. Another significant application of the observed dynamic behaviour is in spatial light modulation/incoherent to coherent image conversion. This is performed here by spatially modulating the enhancement beam. As shown in Figure 4, a permanent hologram was recorded with a grating spacing, $\Lambda \sim 1.6$ μm. An object (part of a test chart), placed at position "O" in the enhancing beam 5, was imaged onto the crystal by a x2.5 objective lens, L1 (f=45 mm, NA=0.07). The output was monitored by a vidicon camera with the aid of lens L2 (f=100 mm, f/3). The image, corresponding to those parts of the permanent hologram enhanced by the illuminating object beam, is transferred on the readout He-Ne beam and observed on a TV monitor. Fig 5 shows a preliminary result of spatial light modulation. The resolution here is ∿25 μm although an unoptimised configuration is used.

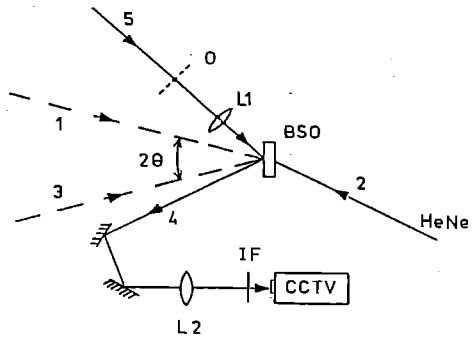


Fig 4 Configuration used to perform spatial light modulation.

Fig 5. Spatial light modulation by the system shown in Fig 4.

## CONCLUSIONS

The simultaneous storage of photorefractive (real-time) and photochromic (permanent) holograms in BSO crystals have been investigated and several dynamic processes have been observed. The subject is undergoing further study. Based on this unique scheme we have demonstrated a number of novel techniques in image synthesis optical logic, interferometry and spatial light modulation with prospective applications in information processing, holographic projection, microscopy and aerodynamic studies.

## REFERENCES

1. 'Photorefractive Materials and their Applications I, II,', P Gunter, J-P Huignard (eds) Springer-Verlag, Berlin (1988, 1989).

2. N A Vainos, S L Clapham and R W Eason, Appl Opt 28, 4381 (1989).

3. N A Vainos, S L Clapham and R W Eason, Appl Opt 28, 4386 (1989).

4. S L Clapham, R W Eason and N A Vainos, Opt Commun 74, 290 (1990).

# X-RAY EMISSION FROM PLASMAS GENERATED BY AN XeCl LASER PICOSECOND PULSE TRAIN

F O'Neill[1], I C E Turcu[1], D Xenakis[2] and M H R Hutchinson[2]

[1]Rutherford Appleton Laboratory
[2]Imperial College, London

Plasma x-ray sources generated by low-energy repetitive KrF lasers have been used for applications such as x-ray lithography, x-ray spectroscopy, and the study of radiation damage to biological cells. However, the applications requiring keV x-ray photons have been slow to develop. This is because the x-ray source brightness is low due to the low conversion efficiency (<1%) from laser light to keV x-rays in plasmas generated by typical discharge-excited KrF laser pulses of 25 ns duration and < 1J energy. Even when 30J, 30 ns KrF pulses were used to generated plasmas, the conversion to x-ray emission at hv=1.2keV from a Cu target was only 2.5%. In contrast, when high-energy, single-shot, subnanosecond, Nd:glass lasers have been used to make Cu plasma x-ray sources, the conversion to keV x rays was ≈10%. Thus, if low-energy excimer lasers are to become competitive as generators of keV plasma x-ray sources, some means must be devised for increasing the x-ray conversion efficiency to the levels attained by Nd:glass lasers.

It has recently been shown that the discharge-pumped KrF gain medium can efficiency amplify a train of subnanosecond laser pulses which thus gives a large enhancement of the laser peak power over the normal ≈25 ns pulse output from these lasers. Such an excimer laser pulse train would appear to be an excellent choice as a generator of repetitive laser plasma keV x-ray sources for the following reasons: (a) The higher peak power will make it easier to achieve the target irradiance $\approx 10^{13}$ W/cm² needed for efficient generation of keV x-ray emission from plasmas. (b) A pulse train focused to high irradiance will ablate less target material than a 25 ns duration pulose of the same energy focused at lower irradiance (I) on target. This is because for UV laser wavelengths the mass ablation rate (m) scales only as I (c) With a pulse train each pulse can act as a prepulse for the nex tone which may lkead to higher x-ray conversion efficiency. We have therefore carried out an experiment to study the generation of laser plasma x-ray sources using a train of picosecond excimer laser pulses. The aim of the experiment was to test if such a pulse train could give improved keV x-ray emission from the plasma when compared to our previousl results obtained using 25 ns pulses.

The experiment reported in this letter was performed using an unstable resonator XeCl laser (Lumonics TE-860) to generate the picosecond pulse train. The 308 nm XeCl laser was chosen instead of a 248 nm KrF laser (as used in the work of Ref 7) because it was more convenient to construct it. This laser is injection mode locked by a train of four low-power pulses at 308 nm generated using a frequency-doubled picosecond distributed feedback dye laser (DFDL) followed by an optical pulse stacker (Fig 1). The energy of each of the four 308 nm injection pulses is a few μJ and the interpulse time is 2.1 ns. This interpulse time is chosen to be exactly one-quarter of the 8.4 ns optical round trip time in the unstable resonator XeCl laser cavity. The mode-locked laser operates at 1 Hz repetition rate and a typical output pulse train (Fig 2) consists of 10-15 major pulses with an interpulse time of 2.1 ns and a maximum total energy of 250 mJ. Streak camera measurements showed that the 616 nm pulses from the DFDL and the 308 nm mode-locked pulses were of = 100 ps duration.

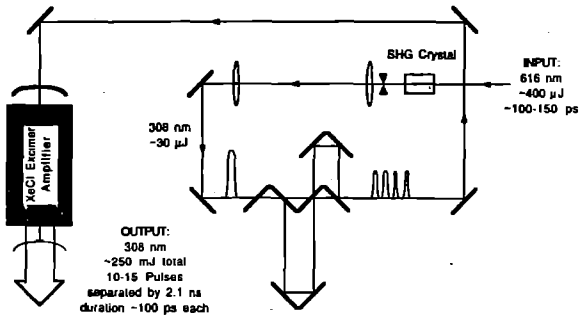


Figure 1. The UV section of the injection mode-locked unstable-resonator amplifier.

Laser plasma x-ray sources were generated by focusing the XeCl laser pulse train to an irradiance $\approx 10^{14}$ W/cm² on Cu and Fe targets held in a vacuum chamber arrangement which has been described in previous publications. Because of losses in the optical components along the laser beam line the maximum pulse train energy on target was only 165 mJ. We have concentrated on performing accurate keV x-ray converison efficiency measurements using time integrating, filtered, Si p-i-n diodes as absolute detectors. One filtered p-i-n diode with subnanosecond response time was also used to monitor the temporal characteristics of the x-ray emission and an exmaple of an oscilloscope record obtained with this detector is shown in Fig 3. The x-rays are seen to be emitted as individual short pulses with the same periodicity as the XeCl laser pulse train and there are fewer x-ray pulses than laser pulses. We believe the double-peaked nature of some of the x-ray pulses may be due to a detector artifact.

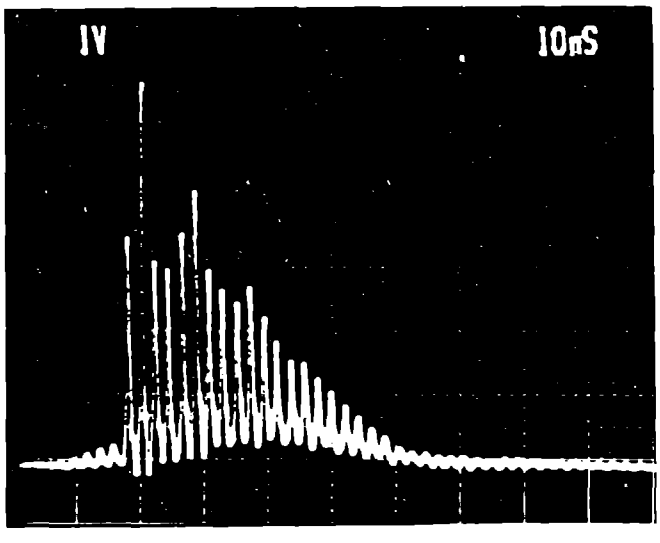


Figure 2. Oscilloscope trace of a typical XeCl laser injection mode-locked pulse train. Time scale 10 ns per division.

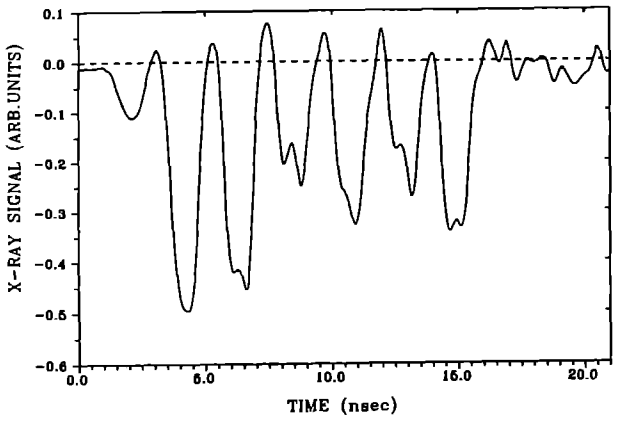


Figure 3. Oscilloscope trace showing fast keV X-ray pulses from Cu plasma generated by mode-locked laser pulse train.

The conversion efficiency from mode-locked laser energy on target to keV x-ray energy emitted from the plasma is plotted in Fig 4. Conversion to keV x rays has been measured as a function of laser energy for Cu targets giving L-shell emission at hv ≈ 1.2 keV (ref 6) and Fe (steel) targets giving L-shell emission at hv ≈ 0.85 keV[4]. For comparison we have also plotted previous data taken with Cu plasmas generated by 25 ns duration KrF laser pulses. The Cu target data clearly show that for a given laser energy the model-locked laser pulse train produces an order of magnitude more plasma x-ray emission than does the 25ns laser pulse. We believe that the difference in the laser wavelengths between the two experiments does not contribute significantly to this increased emission. With the Fe target we have also made a comparison with previous experiments, although here the ong-pulse data are not so extensive. However, as with Cu, it appears that the x-ray emission from Fe plasmas is also increased by approximately one order of magnitude when using the XeCl laser picosecond pulse train. The Fe target gives the best conversion to keV x-rays and for a laser pulse-train energy on target of 165 mJ the maximum conversion efficiency to L-shell emission at hv ≈ 0.85 keV is 2.4%.

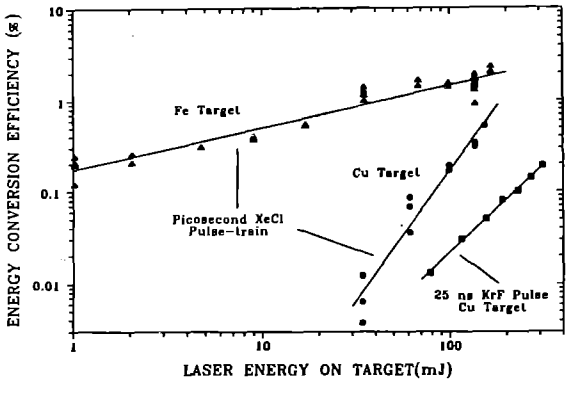


Figure 4. X-ray energy conversion efficiency as a function of laser pulse train energy on target. The KrF data are from Ref 2. Lines are least-squares fits to the data.

In conclusion, we have demonstrated that the keV x-ray emission from a plasma generated by a repetitive low-energy discharge-excited excimer laser can be increased by approximately one order of magnitude if the plasma is generated by a mode-locked pulse train instead of the ≈25 ns pulses more normally obtained from these lasers. There are a number of areas where our experiment could be improved (e.g. use of higher pulse train energy) so it is possible that higher x-ray conversion efficiencies than reported here will be achieved with an optimized mode- locked laser system. A more detailed description of the above x-ray experiment and of the novel injection mode-locked XeCl laser will be published.

The SERC contribution to this work was partially supported by the UK Department of Trade and Industry through the EUREKA European research initiative (EU 213 excimer laser project). D.X. is supported by the State Scholarships Foundation of Greece.

References

1. F O'Neill, M C Gower, I C E Turcu and Y Owadano, Appl Opt 25, 464 (1986).

2. E Turcu, G Davis, M Gower, F O'Neill and M Lawless, Microelectron Eng 6, 287 (1987).

3. M L Ginter and T J McIlrath, Appl Opt 27, 885 (1988).

4. F O'Neill, I C E Turcu, G J Tallents, J Dickerson, T Lindsay, D T Goodhead, A Stretch, C W Wharton and R A Meldrum, Proc Soc Photo-Opt Instrum Eng 1140, (in press).

5. G M Davis, M C Gower, F O'Neill and I C E Turcu, Appl Phys Lett, 53, 1583, (1988).

6. M Chaker, H Pepin, V Bareau, S Boily, B Lafontaine, R Fabbro, I Toubhans, B Faral, J F Currie, D Nagel and M Peckerar, Proc Soc Photo-Opt, Instrum Eng, 733,, 58 (1987).

7. T D Raymon, C Reiser, R G Adams, R B Michie and C Woods, Proc Soc Photo-Opt Instrum Eng, 912, 122 (1988).

8. P D Gupta, Y Y Tsui, R Popil, R Fedosejevs, and A A Offenberger, Phys Fluids, 30, 179 (1987).

9. R Kodama, T Mochizuki, K A Tanaka, and C Yamanaka, Appl Phys Lett, 50, 720 (1987).

10. Z Bor and A Müller, IEEE J Quantum Electron, QE-22, 1524 (1986).

11. C N Danson, C B Edwards and I N Ross, Opt Laser Technol, 17, 99 (1985).

# ATMOSPHERIC PRESSURE OPERATION OF A REPETITIVE KrF LASER-PLASMA X-RAY SOURCE AT hν = 1.1 keV

I C E Turcu[1], F O'Neill[1], G J Tallents[1], T Hannon[1] D Batani[2] and A Giulietti[2]

[1] Rutherford Appleton Laboratory
[2] Instituto di Fisica Atomica e Molecolare, Pisa, ITALY

## INTRODUCTION

In the present paper we describe the operation of a KrF laser-plasma X-ray source with 1 atmosphere of helium in the target chamber. Beside reducing debris, atmospheric operation is particularly convenient for biological work [1] where the living cells require a free surface in the air at atmospheric pressure. This mode of operation is possible because the breakdown threshold of helium for KrF laser wavelength ($\lambda$ = 249 nm) is high [2] and the helium absorption for X-rays of energy $h\nu \sim 1$ keV is low. The laser and target chamber are described in section C4.1. The biological experiments and the X-ray spectrum of the Cu source are described in section C2.5.

To study the effect on X-ray production of ambient helium pressure in the target chamber we have studied the dependence on helium pressure of the following:

(1) Total L-shell X-ray emission,
(2) X-ray source size,
(3) X-ray spectrum, and
(4) X-ray time dependence.

## X-RAY SOURCE EMISSION IN HELIUM ATMOSPHERE

The total, L-shell X-ray emission from the plasma was measured with filtered, absolutely calibrated Si p-i-n X-ray detectors (XRD) with risetimes of a few nanoseconds. From XRD signals in vacuum the total conversion efficiency of X-rays is calculated to be 0.1% for copper targets ($h\nu$ = 1.1 keV) and 0.35% for steel targets ($h\nu$ = 0.9 keV) assuming the $(\cos\theta)^{0.6}$ angular distribution for X-rays as measured earlier with this apparatus. The XRD viewed the plasma at an angle of 20° to the target normal and was filtered by 6μm mylar coated on both sides with 30 nm of aluminium, for copper plasmas, and 10μm of beryllium, for steel plasmas. The helium pressure was varied in the chamber from 0.1 torr to 760 torr to observe the effect of increasing pressure on X-ray emission from copper targets (fig 1). In this experiment the X-rays travelled through ≈ 26.5 cm of helium inside the target chamber, the 6 μm aluminised mylar filter and ≈ 3.2 cm of helium at atmospheric pressure before reaching the XRD. The XRD signal obtained for a given helium pressure was averaged over 3-4 shots and compensated for the absorption in helium (calculated to be 16% at 760 torr) before plotting on fig 1. To eliminate errors due to laser energy variation in time a vacuum X-ray measurement was made immediately before and after the measurement with He in the chamber and the results are normalised to these measurements. The typical range of measurements from shot-to-shot for identical conditions was found to be ±30%. The averaged copper L-shell emission in 760 torr of helium is 80-90% of the signal in vacuum but our estimated measurement errors are larger than this drop in emission. Similar results were obtained for Fe and Zn plasmas in helium atmospheres.

## X-RAY SOURCE SIZE

Single shot keV X-ray pinhole camera pictures of the plasma generated from solid Cu targets in different ambient He pressures are shown in Fig 2. The typical dimension of the hot plasma is ≈ 10-20 μm. As shown earlier, form our equivalent focal plane measurements, the irradiance on target in a focal spot of ≈ 9 μm was ≈ 9 x $10^{12}$W/cm². Hence only the energy delivered by the laser at this irradiance generates the hot plasma required to

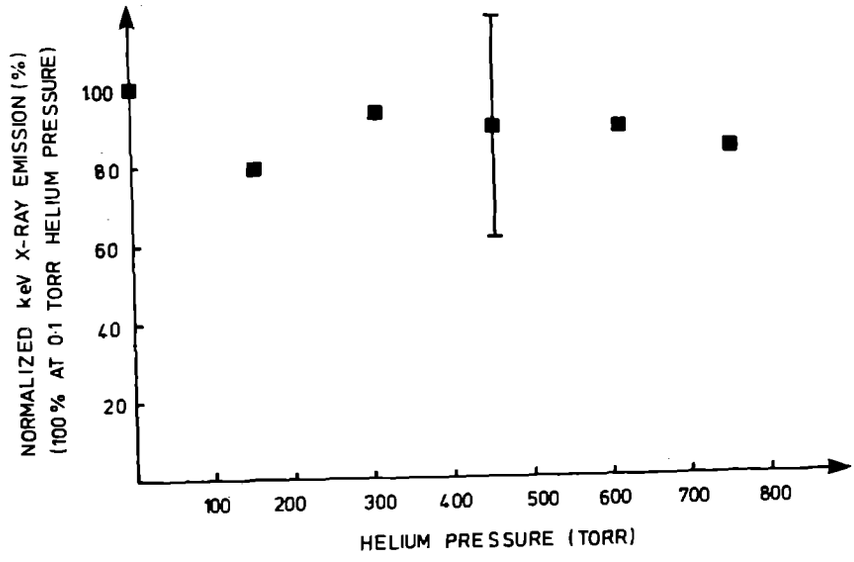


Fig 1: Helium pressure dependence of copper L-shell X-ray emission. The signal from p-i-n XRD filtered with 6μm mylar +60 nm Al is compensated for He absorption of X-rays and normalised to the signal recorded in vacuum (100%). The typical estimated shot-to-shot error range is shown by the error bar.

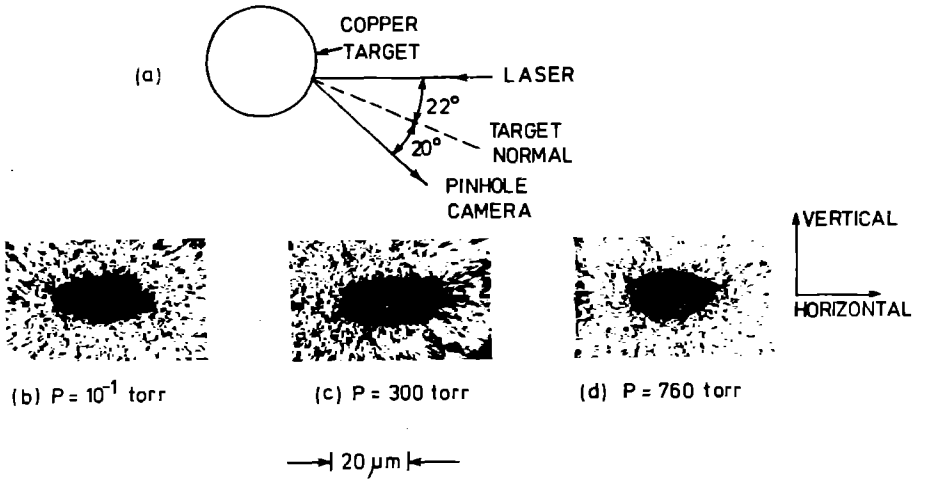


Fig 2: X-ray pinhole camera pictures of the laser- produced copper plasma, recorded on DEF film using single laser shot of = 500 mJ on target, at helium pressures, P, in the target chamber, as noted. (a) Schematic diagram (not to scale) showing the PHC viewing angle and angle of incidence of laser beam on 500 μm diameter copper wire. The plane of incidence is horizontal. The magnification was 11x. The pinhole has 5μm diameter filtered by 15 μm Be and 3μm mylar coated with 100 nm of Al. (b), (c) and (d) are X-ray images.

excite copper, L-shell, emission. The pinhole pictures show an aspect ratio of 2:1 (horizontal: vertical). This is due to the apsect ratio of the KrF laser beam 20 x 10 mm (vertical x horizontal), which results in different F numbers for the focusing lens in the two dimensions. There is little difference between the dimensions of hot plasmas formed in various ambient helium pressures (0.1-760 torr), Fig 5(b, (c), (d).

X-RAY SPECTRUM

A flat crystal (Beryl 2D = 15.95Å) spectrometer was used to record copper, L-shell, spectra on X-ray film (KODAK DEF). The distance between plasma source and X-ray film was 110 mm. A 15μm thick Be filter covered in an entrance aperture to prevent UV/visible light form exposing the film. The same thickness of Be was used to filter the X-ray dose delivered to the biological material. The Cu spectrum obtaied at 760 torr in the target chamber

is shown in Section C2.5. No major differences were noticed between spectra taken at 0,300 and 760 torr for Fe or Cu.

TIME RESOLVED X-RAY EMISSION

A Si p-i-n XRD with subnanosecond response displayed the time evolution of the X-ray signal on a Tektronix 7834 storage oscilloscope with a fast amplifier (7A29). The oscilloscope was externally triggered from a fast UV vacuum diode which was exposed to a reflection from a beam-splitter placed in the laser beam. The signal from the UV photodiode was also synchronously displayed on the oscilloscope by introducing an appropriate delay.

As shown in Fig 3 the X-ray emission starts at the rising edge of the KrF laser pulse and has a very narrow peak, FWHM = 3 ns, sitting on a = 15 ns pedestal with an aspect ratio of 5:1. The X-ray signal is much shorter than the laser pulse duration = 21 ns. Although the energy efficiency of keV X-ray production averaged over the pulse is only =0.1%, the power conversion efficiency is an order of magnitude higher at the peak X-ray emission (Fig 3). Similar measurements were obtained with a fast vacuum XRD for a plasma produced by a 30J, 30 ns KrF laser pulse [3].

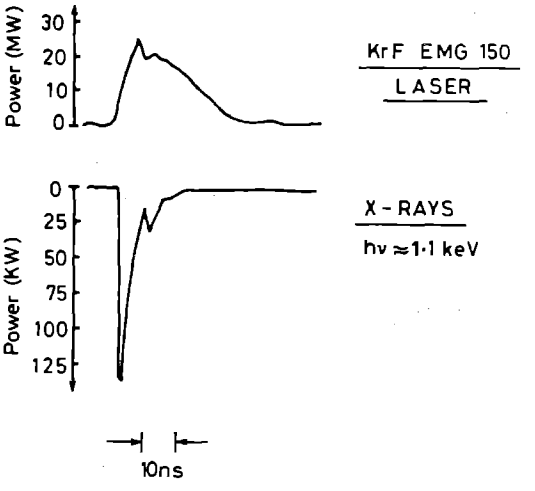


Fig 3: Typical temporal shape of KrF pulse and copper, L-shell, emission. Laser signal recorded with fast UV vacuum diode and X-ray signal recorded with fast p-i-n XRD filtered with 7.5μm Be viewing the target under 20° from normal. The power scale for laser pulse corresponds to a total energy of 500 mJ on target and for the X-ray pulse to 0.5 mJ emitted into 2π steradians. The figure shows synchronised oscilloscope traces. The He pressure in the target chamber was 760 torr.

In conclusion no major differences could be found between vacuum and atmospheric pressure operation of the KrF laser-plasma X-ray source. The SERC contribution to this work was partially supported by the UK Department of Trade and Industry through the EUREKA European Research Initiative (EU 213 excimer laser project). DB was supported by a British Council grant.

REFERENCES

1. F O'Neill et al, SPIE, 1140, 232, 1989.

2. M C Gower Opt Comm 36, 43, 1981).

3. G M Davis et al, Appl Phys Lett 53, 1583 (1988).

# DESIGN STUDIES FOR THE SCIENTIFIC AND TECHNICAL WORKING GROUP FOR A EUROPEAN HIGH PERFORMANCE LASER FACILITY

M J Shaw and M H Key

Rutherford Appleton Laboratory

## INTRODUCTION

This section summarises an analysis of KrF laser systems carried out on behalf of the Scientific and Technical Working Group for a European High Performance Laser Facility ELF and published in more detail as an RAL report (Key et al 1990). The scientific analysis has been applied to preliminary designs of possible KrF lasers for ELF and these designs are outlined here.

The KrF design goals for ELF are for three main target irradiation capabilities:

| | GOAL |
|---|---|
| 1. Ultra short pulse/ultra high power | 100J/100fs |
| 2. High energy laser for ICF and other applications requiring uniform irradiation using broad band, incoherent irradiation and shaped pulse | 100kJ/2ns |
| 3. High power laser for X-ray laser driver and other applications, requiring beams of near diffraction limit and low prepulse | 1000TW/10 to 20psec |

The design of such facilities is constrained by a number of physical considerations as detailed below.

## KINETIC PROCESSES

Kinetic processes impose fundamental limitations on KrF lasers. Non-saturable absorption within the laser medium arises from such species as $F_2$, $Ar_2^+$, $Kr_2^+$, $Ar_2^*$, $Kr_2^*$, $Ar^*$, $Kr^*$. Under typical conditions, the gain-to-non-saturable loss ratio, is in the region of 10 to 20. Non-saturable losses limit the extraction efficiency of the laser medium and impose a maximum achievable intensity of:-

$$I_{max} = (g_0/\alpha - 1)\ I_s$$

Where $I_s$ is the saturation intensity ($I_s = h\upsilon/\partial\tau$) and is typically in the region of 1 to 3 MW cm$^{-2}$ depending on gas composition and pressure. For efficient laser operation, output intensities considerably less than $I_{max}$ must be employed, typical values being in the region of 5 to 15 MW cm$^{-2}$.

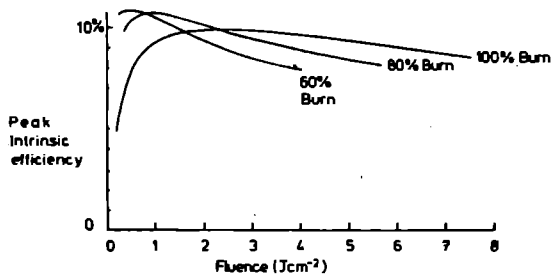


Fig.1 Maximum achievable energy efficiency from a KrF module as a function of output fluence for varying degrees of fluorine burn-up.

This intensity restriction applies to the intensity averaged over times long compared to the upper state lifetime, $\tau$. For pulses of shorter duration much higher peak intensity can be obtained. In this case the limitation imposed by non-saturable absorption is on the pulse fluence. Achievable values are in the region of 6 mJ cm$^{-2}$ corresponding to $3E_s$ where $E_s$, the saturation energy = $h\upsilon/6$.

A further important limitation imposed by non-saturable absorption has recently been studied by Harvey & Shaw (1990). This is a limitation on the maximum fluence which can be delivered by a KrF amplifier module due to the "burn-up" of the fluorine fuel during the laser pulse. If all of the fluroine present in the laser mix is dissociated, then the laser will self-terminate (Kimura and Salesky 1985). The problem is particularly important for high energy KrF facilities since operation for long duration is required to obtain efficient energy load on the module aperture. Increasing the fluorine concentration in the laser gas permits longer pulse operation but at the cost of reduced efficiency since extra fluorine increases the non-saturable losses in the medium. This effect is illustrated in Fig 1 which plots the intrinsic efficiency of a KrF module as a function of the total output fluence assuming different amounts of fluorine burn-up. Since 100% burn-up is unlikely to be useable in practice, it follows that to maintain intrinsic efficiency close to 10% the maximum output fluence will be restricted to between 2 and 3 J cm$^{-2}$.

The limitations imposed by kinetics on the output intensity I and fluence E also lead to an optimum run time for KrF amplifier modules since $T_{run} \approx E/I$. Values of $T_{run}$ in exciting devices are typically in the region of 150 to 600 ns. These times are, of course, very much longer than the pulse durations normally required for target physics experiments which are nanosecond or less, and it is this fact which gives rise to the necessity of serial amplification schemes such as multiplexing where high laser system energy is required.

The design of amplifier modules which meet these constraints and which use radial electron beam pumping with multiple modular diodes operating without guiding magnetic fields is described in some detail elsewhere (Key et al 1990).

## SINGLE PULSE AMPLIFICATION

The design of systems for amplifying subpicosecond pulses imposes very different constraints from those of high energy systems.

Amplifying single short pulses KrF amplifiers is very inefficient compared with glass lasers due to the very much lower upperstate lifetime in KrF. As the pulse duration is reduced, however, the effects of non linear index (B-integral) which is much larger in the solid state compared to gas, makes itself felt and glass lasers become intensity

limited sooner than KrF lasers. For pulses shorter than a few picoseconds duration, KrF amplifiers can significantly outperform glass amplifiers. It is with the amplification of such short pulses that this section is concerned.

A major issue for short pulse systems is the magnitude of prepulse to be expected on target. In KrF this arises primarily from amplified spontaneous emission (ASE) originating at the front end of the amplifier chain. Using a paraxial approximation, the ASE intensity on target can be written:-

$$I_{ASE} = A\ G\ I_s/(f^*)^2 \qquad (1)$$

where A is a constant of the laser medium

$$A = 1/4\pi\ (\tau_r/\tau_a)(\Delta\nu_a/\Delta\nu_s)$$

where the first term in brackets is the ratio of the B state quenched lifetime to the radiative lifetime and the second term is the ratio of the ASE linewidth to the spontaneous linewidth. Typical values of A are in the order of $10^{-3}$. In Eq (1) G is the small signal gain of the amplifier chain and $f^*$ is the focal length/diameter of the target focusing lens. An important requirement is to avoid plasma formation on target by ASE preceding the laser pulse and, since this occurs at $10^9 < I < 10^{10}$ W cm$^{-2}$ it implies that the gain of the amplifier needs to be restricted to values around $10^4$. The "contrast ratio" on target is the ratio of amplified beam intensity to that of the ASE and may be estimated as follows. The beam intensity on targets is given by:

$$I_b = B\ E_s/t_p\ (f^*\ d\theta)^2 \qquad (2)$$

where B $E_s$ is the output fluence B being typically in the region of 2 to 4 and $d\theta$ to the aberration limited beam divergence. Taking the ratio of (2) to (1) gives the intensity contrast ratio:

$$CR\ (intensity) = B/A\ (\tau/t_p)/(G\ d\theta^2) \qquad (3)$$

whereas the contrast ratio in terms of energy is given by:

$$CR\ (energy) = B/A\ (\tau/t_A)/(G\ d\theta^2) \qquad (4)$$

In (3) the time term in brackets is the ratio of KrF lifetime to the pulse duration, $t_p$ whereas in (4) it is the ratio to the amplifier run time, $t_A$. For sub-picosecond pulses intensity ratios in the region of $10^9$ to $10^{10}$ are achievable if the gain is limited to $G \leq 10^4$ and energy contrast ratios of $10^5$ to $10^6$ should be attainable assuming amplifier pumping times can be limited to around 10 ns.

Other factors which need to be taken into account in very high power systems are the nonlinear effects in the laser output window. Such a window is required between the laser medium and the target chamber vacuum (we assume any intervening air can be eliminated by vacuum propagation paths). The two window materials employed in KrF systems are fused silica and calcium fluoride. In fused silica the lowest order nonlinearity is 2-photon absorption with a 2-photon coefficient of 0.=6 cm/GW (Tomie et al 1989). In calcium fluoride, on the other hand, the lowest order nonlinearity is the nonlinear refractive index, $n_2 = 10^{-13}$ esu (Key et al 1989). These figures imply a B-integral of 3 at an intensity-length product of 40 GW/cm in calcium fluoride and a 20% nonlinear absorption in fused silica at an intensity-length product of 15 GW/cm.

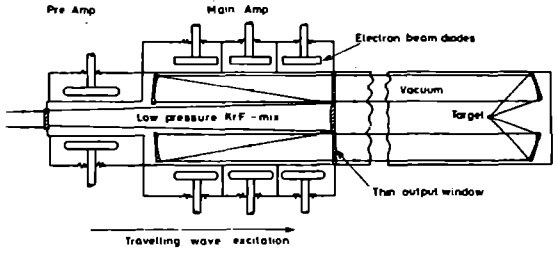


Fig.2 Output stage of a conceptual for a 1000TW KrF facility. Output beam diameter is 2 meters.

The window problem is thus quite serious in KrF especially since large apertures are required to obtain significant power form a single module. One possible solution to this problem is shown schematically in Fig 2. This figure shows a conceptual design for a 1000 TW facility assuming 100 J delivered in 100 fs. The window problem is circumvented by running the amplifier at low pressure. This allows a thin segmented window to be used, thus minimising nonlinear problems. Nonetheless in order to achieve the desired energy on target the total aperture would need to be about 2 m in diameter. In order to improve the energy contrast ratio, a short excitation pulse of 10 ns is assumed. Thus travelling wave excitation would be required for the several metre gain length envisaged. Such short pulse electron beam devices have been demonstrated for laser pumping (eg Hirst et al 1989) as has nanosecond synchronisation of multiple pulse forming lines using laser triggering (Edwards et al 1985).

In order to test one key factor in this design gain measurements were made on Sprite to see how low the pressure could be taken to whilst still providing useful gain. The results are shown in Fig 3. Measurable gain was observed at pressures greater than 40 torr using a krypton rich mix. For the conceptual design shown in Fig 2 a gain coefficient in the order of 1%/cm would be required and so it would appear that this would be readily achievable at pressures in the order of 0.1 bar thus allowing the use of thin windows.

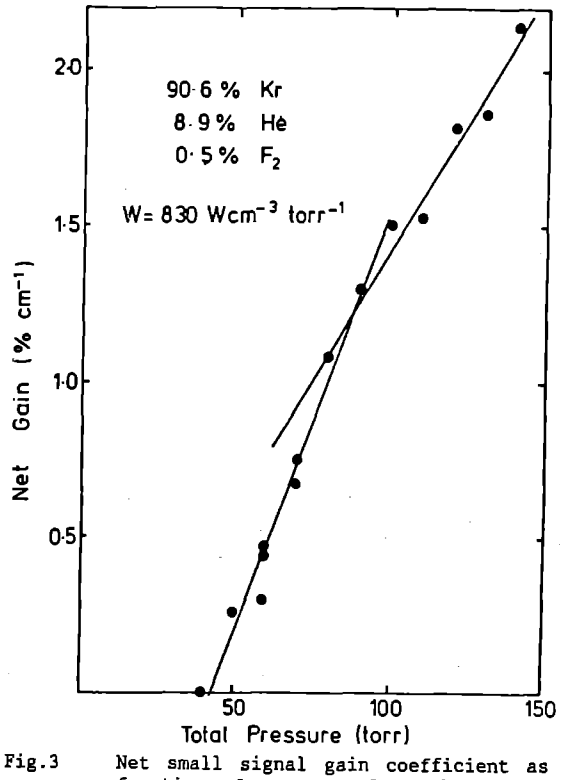


Fig.3 Net small signal gain coefficient as a function of pressure for a krypton-rich KrF mix. Pump rate linear in pressure at 830 W cm$^{-3}$ torr$^{-1}$.

ANGULAR MULTIPLEXING

From the energy loading constraint (and also pulsed power efficiency) the optimum amplifier run time is in the region of a few hundred nanoseconds. In this time approximately 100 pulses at intervals of about the upper state storage time could be amplified sequentially in the KrF laser medium. What is required is a serial-to-parallel converter so that the sequential pulses are made to arrive simultaneously on target.

The simplest form of serial-to-parallel converter is the angular multiplexer. Each pulse travels along a beamline having a unique angle to the axis. At the front end of the system the pulses are multiplexed, ie delays are added to each beamline so that the pulses enter the KrF amplifier sequentially. After amplification the delays are subtracted ie the pulses are de-multiplexed and they all arrive simultaneously on target.

One of the most important points concerning angular multiplexing is the choice of interbeam angle. If this is too small then cross talk between beams can lead to prepulse on target. If the angle is too large then efficiency suffers. For example, for the tightest (circular checker-board) beam array the volumetric extraction efficiency is given approximately by:

$$\epsilon = 1 - (4L/D)(N/\pi)^{1/2}\phi \qquad (5)$$

where $\phi$ is the interbeam (nearest neighbour) angle and L/D is the aspect ratio of the amplifier module. Cross talk is caused by small angle scattering at the points where all the beams overlap ie the amplifier optics and the laser medium itself. Causes of scattering are imperfections in multilayer coatings, etching by fluorine and dust in the laser gas. It would appear that minimum interbeam angles of around 5 mRad (Key et al 1989) will need to be employed giving rise to volumetric extraction efficiencies of around 75% for a typical large multiplexer.

The prime advantage of pure angular multiplexing is that no nonlinear processes are used and so there is no restriction on the bandwidth of the pulses to be amplified. It is thus possible to amplify broadband KrF so that, with a bandwidth capability of 100 $cm^{-1}$, KrF can provide $\Delta\omega/\omega$ of about 0.2%.

The very short coherence length of such pulses (0.1 mm) is important in obtaining uniform illumination on target using induced spatial incoherence (ISI). This technique, pioneered by NRL can be applied to KrF without the use of echelons (Lemberg and Goldhar 1987). Echelon-free ISI is basically an image projection technique that projects the desired spatial profile onto the target via the laser system, using partially coherent light. The information required to reproduce this profile is transported through the laser by a multitude of small coherence zones, rather than by any large whole-beam structure. Thus, the coherence zones play essentially the same role as the beamlets do in conventional ISI, except that their near-field intensity profiles are not "frozen" in by any echelon steps.

Echelon-free ISI is compatible with angular multiplexing techniques. The only requirement is that any spreading of the coherence zones due to diffraction must also remain small in comparison to the apertures and aberration scalelengths. Thus, the technique would not require image relaying at the large-aperture final amplifier, or even in the demultiplexing paths that follow it. Using this technique the NRL group are currently constructing a multiplexed KrF laser system "Nike" which is aimed at demonstrating irradiation uniformity on target of better than 1% at intensities of > $10^{14}$ W $cm^{-2}$. Such uniformity would be required for direct drive ICF.

It has long been known (Kidder 1974) that for isentropic compression of ICF targets some form of shaped pulse is required. The amplification of such a pulse in a single saturating beam line would lead to severe pulse distortion where the low intensity foot of the pulse is preferentially amplified relative to the high intensity peak.

Multiplexing, where many such pulses are overlaid in time, is a solution to this problem, since the amplifier is saturated by the sum of the individual intensities which remains relatively constant. The use of double-pass amplifiers common to KrF multiplexed systems improves this situation.

MULTIPLE SHORT PULSE AMPLIFICATION AND RAMAN MULTIPLEXING

Whereas direct angular multiplexing satisfies the requirements of nanosecond pulse amplification for spherical compression it is less satisfactory when applied to subnanosecond pulses.

A numerical model of multiple-pass amplification has been developed which takes into account the effects of ASE (Barr et al 1988b). The pulse duration is assumed to be long compared to the dephasing time (thus the rate-equation approach is valid), but short compared to the upper state lifetime.

Fig 4 shows results for an amplifier having $g_0L = 10$, $g_0/\alpha = 10$ and an aspect ratio of 3, which are realistic values for a large-aperture output amplifier. For simplicity, it was assumed that no ASE was injected from earlier stages. The input pulse fluence varied over three orders of magnitude for each of several pulse spacings and the steady-state extraction efficiency is plotted against normalised output fluence. The figure shows five plots, corresponding to different normalised pulse spacings, $t/\tau$. Each point represents the steady-state output for a given input fluence per pulse, starting on the left of each plot at $f_{in} = 0.001\ E_s$ and doubling for each successive point. The curves show several significant features, in particular the near-constant peak efficiency at small pulse interval, where the behaviour is effectively CW, and the sharply-limited maximum output energy that corresponds to the pump energy supplied between pulses. The envelope of the curves shows the relationship between spacing and efficiency most

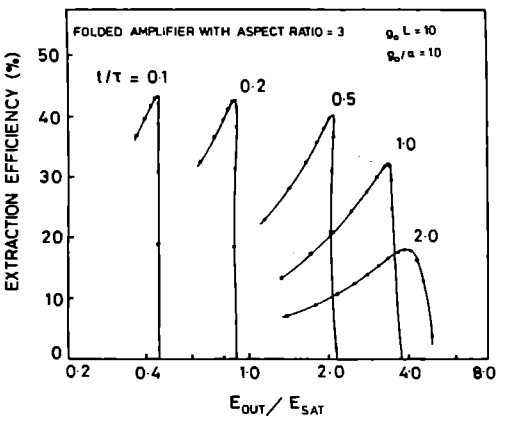


Fig.4 Extraction efficiency of a folded KrF amplifier as a function of output fluence and interpulse spacing assuming extraction by infinite pulse trains.

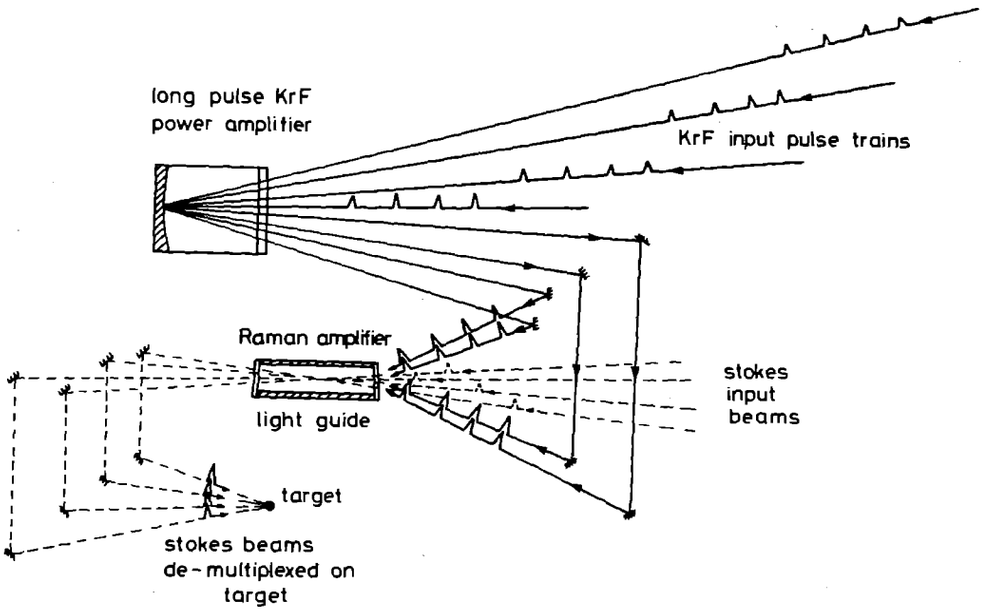


Fig.5 Concept of staged multiplexing using Raman amplifier.

clearly: as the pulse spacing increases beyond $0.5\tau$, ($\tau \sim 2$ ns is the upper state lifetime) the peak efficiency begins to drop sharply. Thus the number of pulses required to ensure efficient energy extraction from a high-power KrF laser is rather large (typically > 100).

A technique which allows amplification a large number of pulses but keeps the number of beams small involves combining KrF beams in Raman amplifiers.

The way such a Raman stage might be used with multiple picosecond pulses is shown schematically in Fig 5. Of major importance is the fact that the number of separate beam lines can be greatly reduced by amplifying a series of pulse trains rather than single pulses. Fig 5 shows 4 pulse trains of 4 pulses each. Each pulse train is amplified sequentially in the KrF amplifier system and thus energy is extracted by a number of pulses per train. The beam quality of the KrF pulses is not too important, since intensity averaging occurs in the Raman stage. Image relaying may also be used to increase the propagation efficiency of highly multi-mode pulse trains around the KrF system. De-multiplexing occurs after the final KrF stage so that the first pulse from each pulse train arrive simultaneously at the entrance to the Raman amplifier.

This technique (results described elsewhere in this report) is capable of providing near transform and diffraction limited beams on target with extremely low prepulse and using staged multiplexing means that such beams can be delivered to target with a high overall system efficiency.

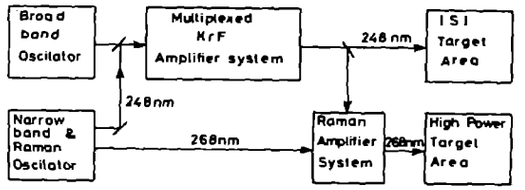


Fig.6 Block diagram of a hybrid KrF system with direct and Raman beam combined target facilities.

Table I : KrF AMPLIFIER STAGES

| Stage | 1 | 2 | 3 | 4 |
|---|---|---|---|---|
| Module diameter | 15cm | 30cm | 60cm | 100cm |
| Pulse duration | 64ns | 128ns | 256ns | 256ns |
| No of beams | 16 | 32 | 64 | 64 |
| Gain | 50x | 50x | 50x | 12x |
| $I_o/I_s$ | 0.03 | 0.17 | 1.0 | 5.0 |
| Output energy | 0.6J | 30J | 1500J | 18kJ |

HYBRID ARCHITECTURE FOR KrF

Requirements 2 and 3 set out in the introduction involve the efficient use of large energies and hence are costly. It is thus if interest to devise a system which uses as many common components as possible for both requirements. The overall block diagram of a proposed solution is shown in Fig 6. Two target irradiation are facilities envisaged because the number of beams or illumination geometry for the two applications are different. There are also two oscillators. One provides transform and diffraction limited pulses at 248 nm and at the Raman shifted wavelength in methane, 268 nm. The majority of the laser amplifier system is common to both systems. The KrF amplifier chain would employ image relaying as much as necessary for ISI purposes and KrF beams at the output are either demultiplexed directly on to target or are switched by moveable mirror to pump Raman amplifiers. One advantage of this scheme is that alignment beams at 268 nm would be available to the high power target area whilst the ISI target area was in operation.

The properties of the KrF amplifier chain are listed in Table I. This chain is designed to

provide 12.5 kJ on target in nanosecond pulses and 100 TW in 20 ps pulses as Phase I of a two phase programme. The output from the final module in Phase I is then envisaged to act as a driver for eight similar modules in Phase II to achieve the design goals on target.

Fig 7 shows a sketch of the electron-beam-pumped KrF amplifiers. The technology adopted is the radial pumping scheme as successfully demonstrated on Sprite (Edwards eat a 1983) and Ashura (Owadano et al 1989). Components of the 60 cm module as at

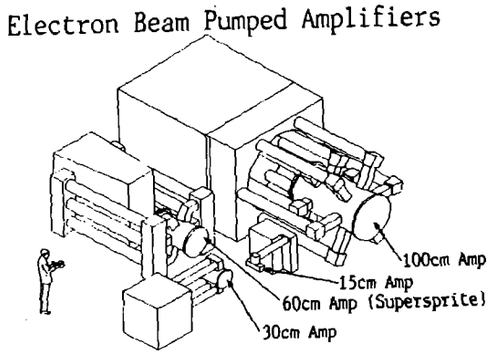


Fig.7 Artists impression of the four electron-beam-pumped amplifier modules.

present being designed and tested at RAL. The larger 100 cm aperture amplifier is envisaged to use essentially identical pulsed power components.

The amplifier modules occupy only a small part of the floor area of a large KrF system. Most of the area is occupied by the large quantity of optics required to multiplex the amplifiers. For the path lengths and intensities envisaged, the nonlinear properties of air, in particular Raman scattering in $N_2$ (Henesian et al 1985) present a problem and propagation in an inert gas (preferably helium) is

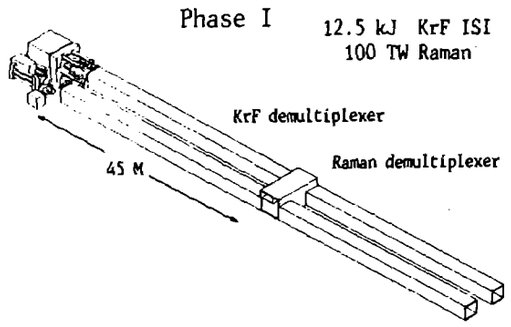


Fig.8 Layout of beam tunnels for a phase I facility.

for maximum power. Fig 8 shows a possible solution to this problem which uses a box section beam tunnel which can act both as an optical bench for the demultiplexing optics and as an enclosure for the helium fill. In this case the beam tunnels could be situated below ground to maintain constant temperature and hence improved stability. The 12.5 kJ on target assumes a 75% geometric extraction efficiency of the 18 kJ module capability and a 90% transport efficiency.

The optical arrangement is shown in Fig 9. There are 64 output beams from the 100 cm final amplifier module which are demagnified to 12 cm diameter at the recollimation array. After demultiplexing the beams are grouped together into 4 beam bundles on compositing mirrors. The reasons for doing this are as follows:
firstly, the square symmetry of the four-beam bundle more closely matches the square section lightguide entrance and, secondly, for the direct illumination using ISI, the cost of transport beams to the target is reduced by using fewer beams of larger aperture. Since it is assumed that ISI will be used with these beams, the fact that the near field is non uniform is not important since the target is irradiated by the beam far field.

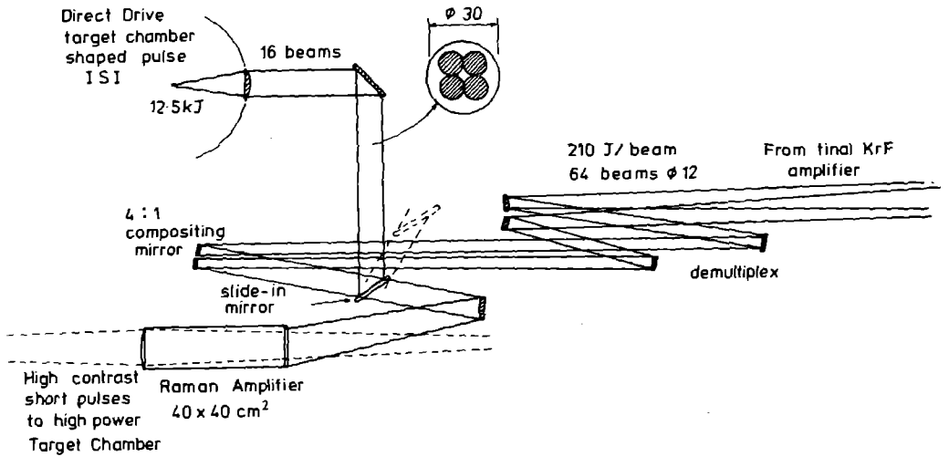


Fig.9 Output beam switching between direct target illumination and Raman amplifier pumping in phase I.

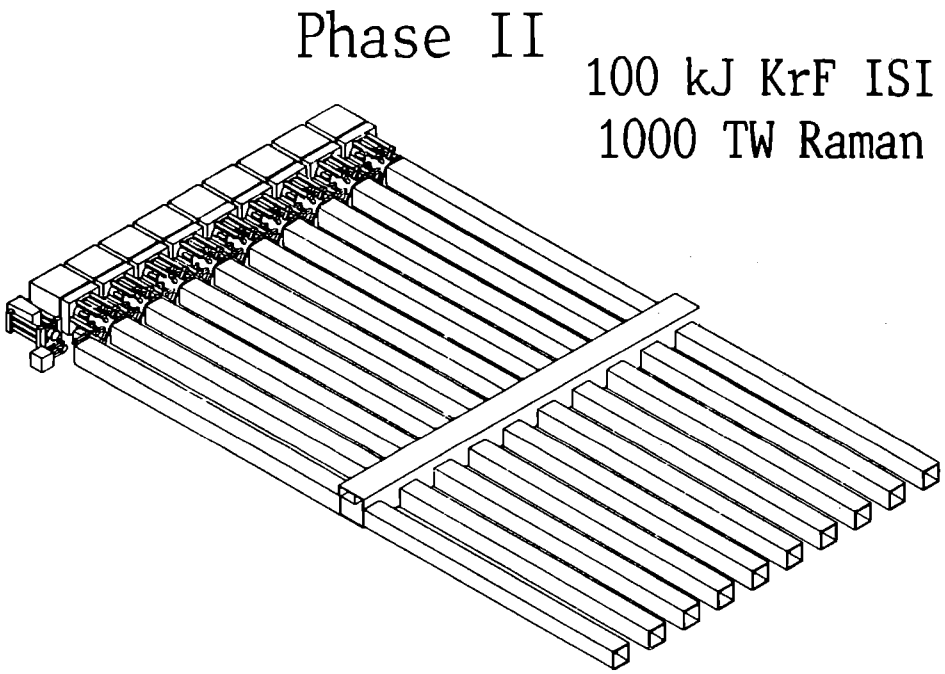


Fig.10 Beam tunnel layout for a phase II facility.

The interpulse space is 4 ns and for Raman beam combined operation four pulses per beam with a 1 ns interpulse spacing would be used. Assuming a short pulse efficiency of 60% of the long pulse, 8 kJ energy would be available to pump the Raman amplifiers. The output window of the Raman amplifier needs to be of high optical quality, sufficiently thin to minimise nonlinear effects and act as an interface between the Raman medium and the target chamber vacuum. These considerations limit the aperture to 40 x 40 cm and four such Raman amplifiers would be required per KrF module. Each Raman amplifier is pumped by four composite KrF beams and if we assume 50% conversion in the amplifier and 80% propagation to target including 2 photon losses in the amplifier windows we would expect 200 J per output beam and a total of 3.2 kJ. Pulse durations of 30 ps or less thus exceed 100 TW on target.

The above figures relate to Phase I of a two phase programme which ultimately will be required to deliver 100 kJ for direct drive and 1000 TW in 20 ps or so. Fig 10 shows one way of accomplishing these aims using the Phase I output module as a driver for eight identical output stages. This approach has the advantage of using tried and tested technology at the output stages and not using any aperture greater than 100 cm. The total number of output beams becomes very large however viz 512 but the four-fold bundling and Raman beam combining reduces the beam number to 128 on target. Target areas (not shown) are probably most conveniently situated above the demultiplexer tunnels. For long pulse target irradiation propagation would be in helium but for the short pulse chamber vacuum propagation after the Raman amplifier would be necessary to avoid nonlinear efects in target chamber windows. All reflective focussing optic would also be required.

REFERENCES

Barr JRM, Everall NJ, Hooker CJ, Partanen JP and Shaw MJ, 1988b, Proc SPIE 874 60.

Edwards CB, O'Neill F, Shaw MJ, Baker D, Craddock D, 1983. In Excimer Lasers - 1983 Eds C K Rhodes and H Egger (American Institute of Physics-New York) 59-65.

Harvey EC and Shaw MJ, 1990. Laser and Part Beams (submited for publication).

Henesian MA, Swift CD and Murray JR, 1985. Opt Letts 10 565.

Hirst GJ, Dane CB, Wilson WL, Sauerbrey R, Tittel FK and Nighan WL, 1989. Appl Phys Lett 54 1851.

Key MH, Shaw MJ, Ross IN, Rodgers PA and Gower MC, 1989. Analysis of High Power KrF Laser Systems - Report No RAL-89-133 Rutherford Appleton Laboratory.

Kidder RE, 1974, Nuc Fusion 14 53.

Kimura WD and Salesky ET, 1985. Proc of the International Conference on Lasers '85, 417.

Lehmberg RH and Goldhar J, 1987, Fusion Tech 11 532.

Owadano Y, Okuda I, Matsumoto Y, Tanimoto M, Tomie T, Koyam K and Yano M, 1989. Laser and Part Beams 7 383.

Tomie T, Okuda I and Yano M, 1989, Appl Phys Lett 55 325.

# ANALYSIS OF GLASS LASER TECHNOLOGY FOR THE SCIENTIFIC AND TECHNICAL WORKING GROUP ON THE EUROPEAN HIGH PERFORMANCE LASER FACILITY

CN Danson, MH Key and PT Rumsby
Rutherford Appleton Laboratory

## INTRODUCTION

The use of glass laser technology in the construction of large scale laser installations has been predominant over the last 15 years. The benefits of using a well established technology, along with the recent developments in short pulse generation and focal spot smoothing, make the use of glass an attractive option for the construction of a European High Performance Laser Facility.

At the present time the two major high power/high energy laser installations operating in the world are both used mainly for ICF related experiments but also for a wide variety of other scientific work. Both can be regarded as versatile laser facilities.

Both installations use the now well established neodymium doped glass laser technology with master oscillator/power amplifier (MOPA) architecture with multiple output beams. This technology is now well assured such that construction of a 100kJ UV laser system based on this technology and architecture could be confidently undertaken. The design details, operational performance, reliability records and construction and operating costs of the installations are fairly well documented and provide a base on which the design and costs for 100kJ UV MOPA architecture system can be based.

Performance details and costs of these systems are outlined below. Also given are brief details of technical advances that are likely to improve the efficiency and reduce the capital cost of neodymium glass laser systems in the future. Requirements for 100kJ laser system to form the basis of a high performance laser facility are outlined, together with capital cost estimates for a system based on MOPA glass laser technology.

## EXISTING MAJOR GLASS LASER FACILITIES

The world's two largest laser systems are the NOVA laser system at LLNL, USA and the GEKKO XII laser at Osaka University, Japan. Their performance details are given in Table 1.

The MOPA type architecture is used on both of these systems. Such systems consist of a master oscillator (or oscillators) feeding small aperture rod-type preamplifiers before splitting into multiple parallel output arms of singly passed box-type disc amplifiers of increasing aperture.

Isolating devices such as Faraday rotators and Pockel cells are placed at strategic positions in each arm to prevent amplifier chain self oscillation, reduce ASE on target, and eliminate backward gain down the system. Vacuum spatial filters are situated at points in each arm to maintain high

| Name | Number of Beams x Dia (cm) | kJ at $\lambda$ = 1 µm | kJ at 3 ω | 3 ω Power (TW) | No of Target Areas |
|---|---|---|---|---|---|
| NOVA | 10 x 75 | 100/3 nsec | 70/2.5 ns | 50(50 ps-1 ns) | 2 |
| GEKKO XII | 12 x 35 | 30/2 ns | 18/2 ns | 15(10 ps-0.8 ns) | 2 |
| KONGOH | 24 x 50 | 200/2 ns | 105/3 ns | 50(10 ps-1.5 ns) | 2 |

Table 1. Performance of existing and proposed major glass laser facilities.

Table 2. Actual and Projected Laser Construction Costs (including in-house labour costs) at 1990/91 prices.

| Name | Costs £M | | | | Normalised cost at 3 ω excluding buildings (£M) | |
|---|---|---|---|---|---|---|
| | Total | Building | TAs | Laser | per kJ | per TW |
| NOVA | 176 | 37 | 139 | | 1.99 | 2.78 |
| GEKKO XII | 121 | 54 | 25 | 42 | 3.72 | 4.47 |
| KONGOH (total inc GEKKO XII) | 291 | 54 | 237 | | 2.26 | 4.74 |

optical beam quality, expand the beam and, very importantly, image relay an aperture at the start of the system right through to the output plane. With such architecture, high output beam quality and high beam fill factors (up to 0.8) are achievable. Conversion of the 1µm wavelength output to shorter wavelength (2ω or 3ω) is achieved with arrays of KDP crystals situated before the target chamber lenses.

The shot rate of such lasers is limited to less than one shot per hour at present for both these systems due to long disc amplifier cooling times. This figure could be improved by changes to disc amplifiers to improve cooling performance.

For both installations output module energy extraction efficiency is low (20-30%) for few nanosecond pulses. This together with the low efficiency of energy transferred from the capacitor banks via the flashlamps to the glass medium (1-2%), and other beam transport, harmonic conversion and fill factor losses leads to an overall system efficiency of 0.1-0.2%.

Osaka University have completed design and development of the hardware needed to upgrade GEKKO XII by a factor of 4 to 5 to the 100kJ (3ω) level. This system is called KONGOH. Performance details are given in Table 1. The number of output beams is doubled to 24 and additional booster amplifiers are added to the end of the system. The technology proposed is conventional single-passed box type disc amplifiers.

## SYSTEM CONSTUCTION COSTS

Actual construction costs for NOVA and GEKKO XII and proposed costs for KONGOH are given in Table 2. These sums include all in-house design, construction and commissioning labour charges and have been scaled to 1990/91 prices at an estimated 5% annual inflation rate. For the NOVA figures a rate of 1.5$/£ has been used.

Table 2 shows clearly that the fraction of the total installation cost, due to buildings varies significantly from system to system. To compare the actual laser construction costs of these systems with each other and to give data that is useful for estimating construction costs of new lasers, it is more valuable to exclude building costs and produce a final costing in terms of pounds per kilojoule of energy and TW of power in the UV region.

Table 2 indicates the costs of the installations on this basis. Rather surprising variations from installation to installation can be seen.

Since the commissioning of the NOVA system occurred in

November 1984, a considerable sum of capital expenditure has taken place (above the published figure used in Table 2) in order to upgrade to achieve the outputs given in Table 1. Much of this expenditure has been needed to replace all the neodymium glass in the system to overcome initial glass impurity problems. The glass replacing the original was cheaper to purchase therefore this would not be an additional factor in calculating the total.

The GEKKO XII installation was built by NEC under contract to Osaka University and hence contains a high level of development costs and also a profit element. This is the reason for the higher cost of this system. The KONGOH upgrade price is a more realistic figure as development work has already been done.

Since the NOVA and KONGOH designs can be used as a base-line for any new installation, the price for similar installation is likely to be lower than those quoted as little new development work is required to be carried out, therefore in the final figure we will only include 50% of the NOVA development work.

In summary a realistic figure for the cost of hardware for a new UV glass laser system of the same scale as NOVA or KONGOH is in the region of £1.8M/kJ.

## NEW GLASS LASER TECHNOLOGIES

Several major new developments are being pursued actively at present in an endeavour to improve glass laser overall efficiency and hence reduce capital construction costs.

LLNL believe a 10-fold improvement in overall efficiency to the 2% level is achievable at 10nsec output pulse duration by improvements to beam transport and harmonic conversion efficiencies, and major improvements (x2.5) to both energy storage efficiency (by using large rectangular element segmented amplifier arrays) and energy extraction efficiency (by double-passing the output module in a Cassegrainian-type architecture). Such designs form the basis of LLNL's proposal for the 10MJ Athena Laboratory Microfusion Facility.

Disc amplifier technology based on solid state diode laser pumping rather than flashlamps is being pursued by Osaka and other groups. It is suggested that this technology will lead to storage efficiency improvements of a factor of 4 or 5 to the 25% level. Using this technology, combined with efficient module energy extraction could lead to overall laser efficiencies of more than 10%.

Clearly capital construction costs for these more advanced technologies could be substantially less than those given in Table 2. However, at this stage when no operating installation exists and no firm data on operational experience and reliability is available, it is difficult to estimate accurately the feasibility or true level of cost.

## CHIRPED PULSE AMPLIFICATION FOR HIGH INTENSITY OPERATION

Chirped Pulse Amplification (CPA) provides a method for amplifying ultrashort pulses to powers >1 TW which takes advantage of the high storage energy density and high saturation density (4 J/cm) of solid state gain media such as neodymium glass. This is achieved by stretching an ultrashort pulse and amplifying it to energy densities comparable with the saturation value of the gain medium (as required for efficient energy extraction) without causing intensity-dependent self-focusing which gives rise to beam distortion and damage to the amplifiers. The amplified pulse is then compressed to its transform limit.

The pulse may be stretched either by propagation through an optical fibre or a pair of diffraction gratings with positive group velocity dispersion. This not only increases the pulse duration but also produces a frequency chirp, and this enables the pulse to be compressed by a pair of diffraction gratings which provide negative group velocity dispersion when suitably arranged.

Development programmes into CPA are being conducted at many of the laser laboratories around the world. At the Institute of Laser Engineering, Osaka University, Japan a chirped pulse has been amplified using the Gekko-MII glass laser. The output aperture of the laser is 20 cm. This beam was compressed using a pair of reflection gratings which limited the beam diameter to 13.5 cm. Using this system they have generated 45 J in a 3.5 ps pulse at 1.052 microns. This is the highest power as yet obtained using a CPA system.

The grating pair used in these experiments had a diffraction efficiency of 90%. The laser damage threshold was measured at 0.8 J/cm at 100 ps using a small aperture laser beam. In the system the gratings have been successfully operated at 0.45 J/cm. These are very encouraging damage threshold measurements which have been verified at RAL.

### System Costs

System costs for CPA beam lines have been estimated for the following scheme: A cw mode-locked Nd:YLF oscillator delivering a train of 35 ps pulses. A single pulse is then selected from the train and is passed through a length of fibre optic. A regenerative amplifier is used to increase the energy in the pulse. The pulse is stretched in a grating pair before being injected into the laser amplifier chain.

The gratings used are assumed to have a damage threshold of 1 $Jcm^{-2}$ and the pulsewidth at the output of the system is assumed to be 1 ps, (a compression ratio of 35). To produce 1 PW in a single beam, 400 mm diameter optics are required at the output of the system. The costs to modify an existing laser system to operate at the 1PW level and with some provision for providing an advanced generator would be £340 K.

The cost of the gratings are based on a quotation from Jobin Yvon for 300 mm square gratings at £30,000/pair. The scaling of this figure to larger aperture is achieved using a linear proportionality with area. A significant cost that would be incurred for any short pulse scheme would be for the provision of a target chamber designed specifically for the purpose. It would be necessary to design the chamber with reflective focusing optics to eliminate nonlinear effects in the normal chamber windows and lenses. The cost incurred to provide this has not been taken into account in these figures but would be of the order of £500K.

It will be possible to directly generate short pulses of the duration required after compression and to temporally broaden it for amplification with a perfectly linear chirp using diffraction gratings. The advantage of this proceedure is that it should be possible to recompress the amplified pulses with very high contrast ratios, reducing pre-pulse problems.

## BEAM SMOOTHING TECHNIQUES

Laser/plasma interaction experiments generally require smooth intensity focused beam profiles onto target. Unfortunately intensity non-uniformities occur because of imperfections in optical components within the system. These impose phase shifts, and generate non-uniformities across the near-field of the beam and in the focal plane produce highly modulated profiles. These random non-uniformities can be somewhat smoothed by overlapping many independent beams but this is generally insufficient. In order to smooth individual beams several alternative techniques have therefore been developed.

The cost of introducing smoothing technology to a multi-beam large aperture system is very dependent on the scheme

under consideration. The spatially separated multi-frequency scheme being developed at Livermore would be the most expensive to implement but does allow 2nd and 3rd harmonic operation together with rapid temporal smoothing. The expected cost of implementation on NOVA is likely to be in the order of £3.5-7M.

## HIGH PERFORMANCE LASER FACILITY REQUIREMENTS

A high performance scientific laser facility able to handle all user experimental requirements must be versatile and flexible in terms of pulse duration, energy output, power output, wavelength of operation, target irradiation conditions, etc. Table 3 shows the projected requirements for such a facility.

| | | |
|---|---|---|
| Number of Beams | : | $20 < n < 60$ |
| Wavelength of output | : | $\leq$ 350 nm |
| Pulse durations | : | variable few ps to 3 ns |
| Energy | : | 100 kJ in UV in 3 ns pulses |
| Power | : | $\geq$ 1000 TW in UV in 10 ps pulses |
| Shot rate | : | $\geq$ 2/hour |
| Target areas | : | $\geq$ 2 |

Table 3. High Performance Laser Facility Requirements.

## CONSTRUCTION COSTS OF A HIGH PERFORMANCE LASER FACILITY

A system to give 100kJ output at third harmonic (351nm), using single-passed amplifiers and MOPA architecture could be the equivalent of double the NOVA laser system (20 beams) or could be similar to a KONGOH (24 beams) system. Consequently the cost figures given in Table 2 can be used as a guide to construction costs for a new system.

Power performance is not so easy to achieve due to nonlinear effects in the glass medium. Note that the power output of the NOVA or KONGOH systems at 3ω are only in the region of 50-100TW, a long way short of the power requirements for a high performance laser facility. Pulse compression in which long duration pulses (few 100 ps) are amplified in the laser and reduced in duration to near the target is vital for effective short pulse performance.

For this argument we assume that adequate power performance can be achieved at pulse durations in the 10-20psec regime by use of presently developing pulse compression schemes based on grating compression of chirped pulses. We estimate that provision of large aperture, high quality, high damage level gratings for a multiple beam system will add approximately 10% to the costs shown in Table 2.

Building costs comprise a major factor in the total construction costs for a high performance laser facility. Excluding office accommodation and target preparation areas, the NOVA installation occupies approximately 10,000m of which over half is clean room, the other half being used for power conditioning and support laboratories. GEKKO XII and KONGOH occupy 17,000m including office space, all support laboratories and target preparation activities. These numbers can be used as a guide to obtain an estimate for building costs for 100kJ glass laser system.

Assuming a total of 15,000 m of space is required made up as follows:

a. 7,000m of clean room area, including target prep, at £2.7K/m = £18.9M
b. 5,000 m of support labs and power conditioning at £1.2K/m = £6M
c. 3,000 m of office accommodation (150-200 persons) at £1.1K/m = £3.3M

TOTAL £28.2M

| | | £M |
|---|---|---|
| Laser and Target Areas (2) | | £177 |
| Buildings | | 28.2 |
| | Total | £205.2 |

Table 4. 100 kJ/1000 TW UV Glass Laser System Costs (including manpower) at 1990/91 prices.

Table 4 summarises total construction costs for a high performance laser facility to the specification shown in Table 3.

## CONSTRUCTION COSTS OF A 1PW CPA FACILITY

The system considered to generate 1kJ in 1ps (1PW) consists of an advanced driver followed by amplification to 250 mm diameter in disc amplifiers. At the output of the system the beam would be expanded to keep below the laser induced damage thresholds of the diffraction gratings. To avoid problems with small scale self-focusing the gratings together with a reflective focusing optic would be housed within the target chamber. It is assumed that the laser and target area would be housed in standard clean areas. The costs of building such a facility are shown in Table 5.

| | | |
|---|---|---|
| Laser Hardware | | £1.0M |
| Building Costs (Clean Area @£2.7K/m²) | | £0.8M |
| Short Pulse Technology:- | | |
| Oscillators (advanced driver) | £500K ) | |
| Gratings | £ 60K ) | £1.06M |
| Target chamber | £500K ) | |
| | £1060 | £2.86M |
| Labour (33% of non building items) | | 0.69M |
| | | 3.55M |

Table 5. Construction Costs of a 1PW CPA Facility.

## CONSTRUCTION COSTS OF A LIMITED APERTURE HIGH PERFORMANCE FACILITY

A study has been undertaken to assess the feasibility of using small output amplifier apertures, 15 cm or 20 cm, in a 20kJ + system.

### Sources of information

To produce a costing the recent experience with this technology at The University of Rochester, AWE (Aldermaston) and at RAL was used. At the University of Rochester an OMEGA system upgrade is planned which will have 60 beams of final amplifier diameter 20 cm. The total figures supplied do not include a significant proportion of the costs, both for manpower and system costs. The University will fund some of the costs and some of the hardware already exists. The figures cannot therefore be used in calculating the total project cost, although costs of components are useful.

A further source of detailed information came from the

Table 6. Component costs for a single amplifier chain with 20.8 cm diameter output amplifiers

208 mm DIAMETER O/P DISC COST ( £ K ) / Beamline

| COMP. | DIAM/mm | GAIN/LOSS | Eout / J | OPTICAL | MECH. | ELEC. | TOTAL |
|---|---|---|---|---|---|---|---|
| VSF | 40 | | 0.44 | | | | |
| ROD | 40 | 7.5 | 3.3 | 1.5 | | | |
| PC | 50 | 0.85 | 2.8 | 15 | 3 | 10 | 28 |
| VSF | 50:108 | 0.96 | 2.7 | 1.5 | 7.5 | - | 9 |
| DISC | 108 | 8.0 | 22 | 15 | 20 | 33 | 68 |
| DISC | 108 | 6.0 | 130 | 15 | 20 | 33 | 68 |
| VSF | 108:150 | 0.96 | 125 | 3 | 10 | - | 13 |
| FAR | 150 | 0.88 | 110 | 38 | 5 | 10 | 53 |
| DISC | 150 | 3.0 | 329 | 31 | 20 | 36 | 87 |
| VSF | 150:208 | 0.96 | 316 | 6 | 12 | - | 18 |
| DISC | 208 | 1.9 | 600 | 40 | 30 | 40 | 110 |
| DISC | 208 | 1.75 | 1020 | 40 | 30 | 40 | 110 |
| DISC | 208 | 1.6 | 1632 | 40 | 30 | 40 | 110 |
| VSF | 208:315 | 0.96 | 1567 | 12 | 15 | - | 27 |
| MISC | | | | | | | 25 |
| | | | | | | | 726 |

recently upgraded HELEN laser system at AWE, Aldermaston. The system was upgraded to provide two beams of 20 cm final amplifier diameter, which are then expanded to 30 cm diameter before being frequency doubled. Costings were made available for major components, all purchased within the last two years.

The final source of information was from experience at RAL following the completion of the Phase I upgrade. For this upgrade new disc amplifiers were designed and installed with clear apertures of 10.8 and 15 cm.

Construction Costs

A system with over one third (37%) of the output capacity of Nova would be obtained with 18 beams at 20.8 cm diameter or 34 beams at 15 cm diameter output amplifiers. A detailed cost of the construction of a single beamline at 20.8 cm diameter is presented in Table 6. Using these figures the total cost of buiding the system is presented in Table 7.

Notes on the Costings:

(i) The front-end costs are based on a number of pulse generators providing a range of pulse-widths and a rod amplification system to provide the required number of beams, including synchronised backlighting capabilities.

(ii) The laser system costs were calculated using 18 beams 20.8 cm in diameter. When calculating for 15 cm diameter outputs the costs are the same to within 5%.

| | |
|---|---|
| Front-end | £ 1 M |
| Laser System | £13.1 M |
| Buildings | £ 7.5 M |
| Diagnostics, alignment and control | £ 3 M |
| System Engineering | £ 2 M |
| Target areas | £ 7 M |
| Labour | £ 8.7 M |
| TOTAL | £42.3 M |

Table 7. Construction Costs of a Limited Aperture System.

(iii) The building costs are based on 2,000 m of clean room at £2.7 K/m and 1,600 m of power conditioning and support laboratories at £1.2 k/m. These figures do not include office accommodation and ancillary laboratories.

(iv) The labour figures are based on a 3:1 ratio of hardware to labour costs for non building items. Building costs are inclusive of contract labour.

(v) The target area costs assume two full target areas of different geometry.

(vi) Costs for beam smoothing and chirped pulse operation are not included.

Scaling Of Costs

The example considered at 37% of the Scale of Nova would operate at about 26 kJ in a 3 ns. The total project cost is £42.3 M therefore the cost per kJ is £1.65 M. For a 100 KJ facility the construction costs would therefore be £165 M. This figure is 16% lower than that estimated for larger aperture (Nova like) beams.

## OPERATIONAL COST

An annual operational budget of £6M would be required for an intermediate energy facility, although a cost analysis has not been completed.

## CONCLUSION

Construction costs for a glass laser system using circa 20 cm amplifier technology and able to deliver 100kJ of energy in nanosecond pulses with smoothing but not including ancilliary buidings (offices and support labs) is likely to be of the order of £190M at 1990/91 prices. The construction costs for building a 1PW stand alone system is of the order £3.6M at 1990/91 prices.